JNC TJ8400 2001-020

分置

人工バリアにおける緩衝材挙動評価研究

（核燃料サイクル開発機構　研究委託内容報告書）

2001年2月

技術情報室
No.
2001.10.12

株式会社　間　組

本資料の全部または一部を複写・複製・転載する場合は、下記にお問い合わせください。

〒319-1184　茨城県那珂郡東海村大字村松 4 番地 49
核燃料サイクル開発機構
技術展開部　技術協力課

Inquiries about copyright and reproduction should be addressed to:
Technical Cooperation Section,
Technology Management Division,
Japan Nuclear Cycle Development Institute
4-49 Muramatsu, Tokai-mura, Naka-gun, Ibaraki, 319-1184
Japan

© 核燃料サイクル開発機構（Japan Nuclear Cycle Development Institute）
2001

JNC TJ8400 2001-020
2001年2月

人工バリアにおける緩衝材挙動評価研究

千々松正和*
雨宮　清*
山下　亮*

要　　旨

地層処分を確実に行なうためには、人工バリアの健全性を確保する必要がある。人工バリアの健全性において重要な要因の一つとなるのが緩衝材の施工技術である。緩衝材が設計要件に基づいて施工されることによって人工バリアの健全性は確保することが出来ると考えられる。本研究では、緩衝材をブロックで施工した場合に考えられるブロック間や岩盤あるいはオーバーパックとの隙間の充填性に関する検討を実施した。

また、施工された緩衝材内には、処分後、廃棄体からの発熱、地下水の浸潤、周辺岩盤からの地圧や緩衝材の膨潤といった連成挙動が発現すると考えられる。これらの現象を理解、評価するためには、人工バリアを対象とした原位置での実規模試験の情報に基づき、適切なモデルを構築する必要がある。ここでは、スウェーデン・エスポ島で行なわれている実規模緩衝材を用いた実証試験（Prototype Repository Project）の技術検討を実施した。さらに熱－水－応力連成現象に関する国際共同研究（DECOVALEX III）に参加し、連成モデルの開発と評価を実施した。

本報告書は、株式会社間組が、核燃料サイクル開発機構の委託により実施した研究の成果である。
サイクル機構担当部課室および担当者：環境保全・研究開発センター　処分研究部
処分バリア性能研究グループ

*：株式会社間組

JNC TJ8400 2001-020
FEBRUARY, 2001

Research on Evaluation of Buffer Materials in the Engineered Barrier

Masakazu Chijimatsu*
Kiyoshi Amemiya*
Ryo Yamashita*

Abstract

In order to achieve the geological disposal of radioactive waste in safe, it is necessary to ensure the stability of the engineered barrier system (EBS). One of the most important factors for the stability of the EBS is the disposal technology. It is considered that the stability of the EBS is secured by the properly emplacement based on the design requirement. In this research, the methods filling the gap between buffer and rock or buffer and overpack were examined. Bentonite pellets were tested as the filling materials.

After emplacement of the engineered barrier system, it is expected that the near-field environment will be impacted by phenomena such as heat dissipation by conduction and other heat transfer mechanisms, infiltration of groundwater from the surrounding rock in to the engineered barrier system, stress imposed by the overburden pressure and generation of swelling pressure in the buffer due to water infiltration. In order to recognize and evaluate these coupled phenomena, it is necessary to make a confidence of the mathematical models and computer codes based on the information about the in-situ experiments regarding the engineered barrier system. In this research, technical investigations about the in-situ full-scale experiment (called Prototype Repository Project) in Äspö HRL facility by SKB of Sweden were performed. Fathermore, the thermo-hydro-mechanical (THM) code named THAMES was validated at the international project, DECOVALEX III.

Work performed by Hazama Corporation under contact with Japan Nuclear Cycle Development Institute (JNC).
JNC Liaison: Waste Technology Development Division, Geological Isolation Technology Section
*: Hazama Corporation

目　　次

図 目 次

3. 隙間充填性の品質評価

4. 実規模人工バリア試験の評価

5. 人工バリアにおける連成挙動の評価

表 目 次

1. はじめに

地層処分を確実に行うためには，人工バリアの健全性を確保する必要がある。人工バリアの健全性において重要な要因の一つとなるのが緩衝材の施工技術である。緩衝材が設計要件に基づいて施工されることによって人工バリアの健全性は確保することが出来ると考えられる。ここでは，緩衝材をブロックで施工した場合に考えられるブロック間や岩盤あるいはオーバーパックとの隙間の充填性に関する検討を実施する。また，施工された緩衝材内には，処分後，廃棄体からの発熱，地下水の浸潤，周辺岩盤からの地圧や緩衝材の膨潤といった連成挙動が発現すると考えられる。これらの現象を理解，評価するためには，人工バリアを対象とした原位置での実規模試験の情報に基づき，適切なモデルを構築する必要がある。ここでは，緩衝材および岩盤を含めた人工バリア周辺における連成現象に関する試験データを収集し，適切な連成モデルを構築する。そして、国際共同研究を通して構築された連成モデルに関しての適用性を検討する。

2. 実施工程

本研究の実施工程は表 2-1 の通りである。

表 2-1　全体工程表

	平成 12 年					平成 13 年	
	8 月	9 月	10 月	11 月	12 月	1 月	2 月
隙間充填性の品質評価	―	―	―	―	―	―	
実規模人工バリア試験の評価		―	―	―	―	―	
人工バリアにおける連成挙動の評価		―	―	―	―	―	
報告書の作成						―	―

3. 隙間充填性の品質評価

3.1 実施内容

緩衝材の隙間充填についての研究フローを図 3-1 に示す。このうち、昨年度実施した「緩衝材製作施工技術の評価」において②、④、⑤を実施し、ベントナイトペレットを用いて充填性の確認を行なった。今年度は、引き続き、ベントナイトペレットの充填性に関しての検討を行なったのでその結果を報告する。今年度は、ブロック間の隙間で発生すると考えられる楔形状の隙間に対する充填性についての検討を行なった。本章では、昨年度得られた成果を合わせてベントナイトペレット充填に関する知見を示す。

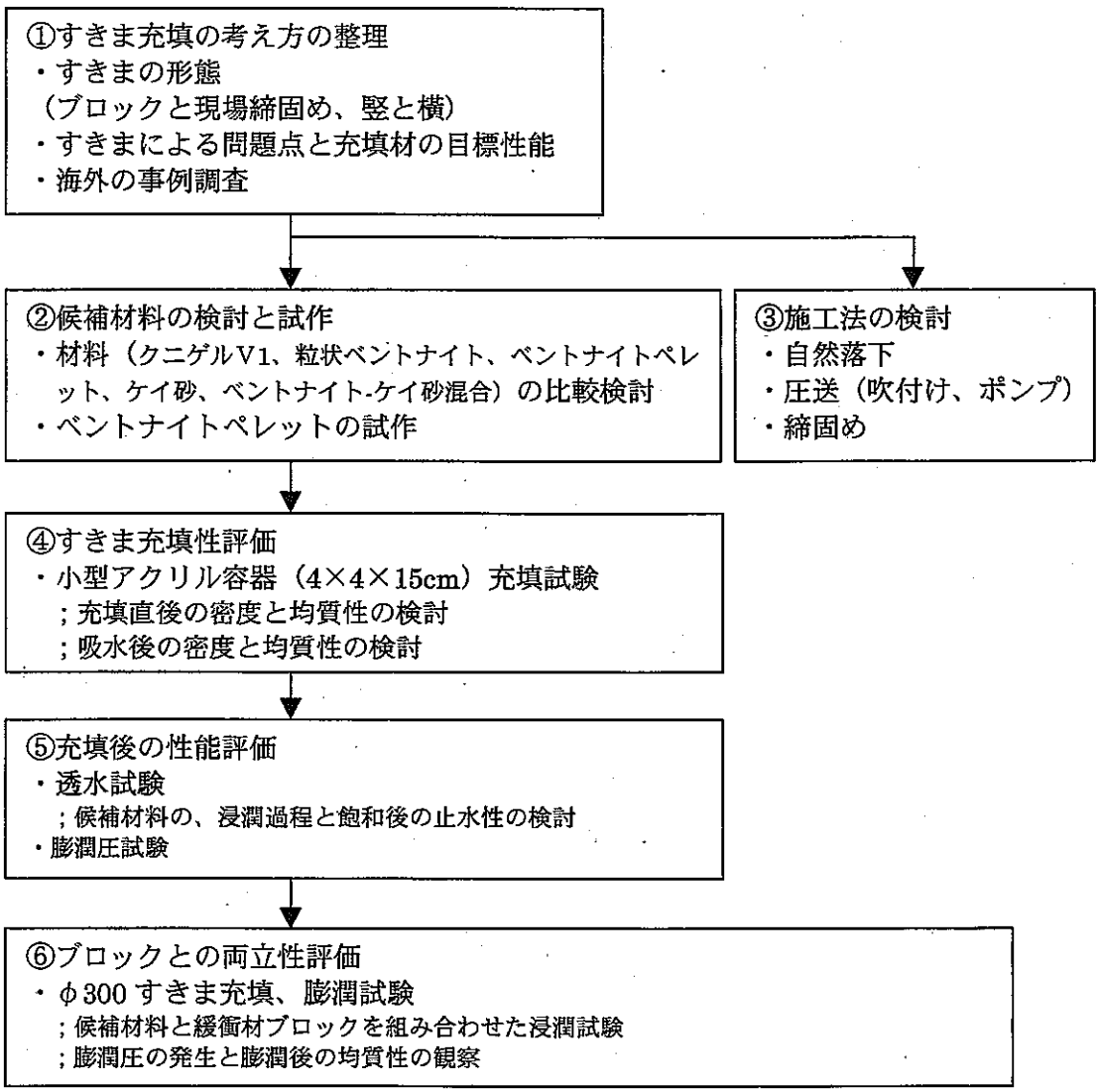

図 3-1 隙間充填の研究フロー

3.2 充填工法

すきま充填は以下の問題に対処するために重要である。

① 緩衝材が流出する
② ブロックの継ぎ目をとおり地下水が廃棄体に接触する
③ すきまの空気層によって温度が上昇する
④ 緩衝材の全体（平均）密度が低下する

隙間の寸法とその処理方法に関しては、内外で表 3-1 のように検討されている。

表 3-1 隙間充填事例

機関	形態	内側すきま 幅/充填材料	外側すきま 幅/充填材料	
JNC	竪・ブロック	2cm/材料未定	4cm/材料未定	
	横・ブロック	同上	同上	
	竪・現場	同上		
	横・現場	同上		
電力	竪・ブロック	1cm/材料未定	4cm/材料未定	
	横・ブロック	同上	同上	
AECL	竪・現場	両側で11cm(片側2.5cm以上)/乾燥ケイ砂の自由落下		AECL-10715
SKB	竪・ブロック	≒1cm/空気(水 or ベントナイトスラリーも検討)	≒5cm/ベントナイト粉(ペレットも検討)	
NAGRA	横・ブロック	数 cm/空気	数 cm/空気	
ENRESA	横・ブロック	2cm/空気（但し内側ライナー付）	すきまなし （ブロックの継ぎ目も合わせて、void 体積を 3-5%に想定）	FEBEX

3.3　ベントナイトペレットを用いた透水試験

3.3.1　ペレット形状

図 3-2 に今回の試験に用いたペレットの形状、図 3-3 に製作器具を示す。

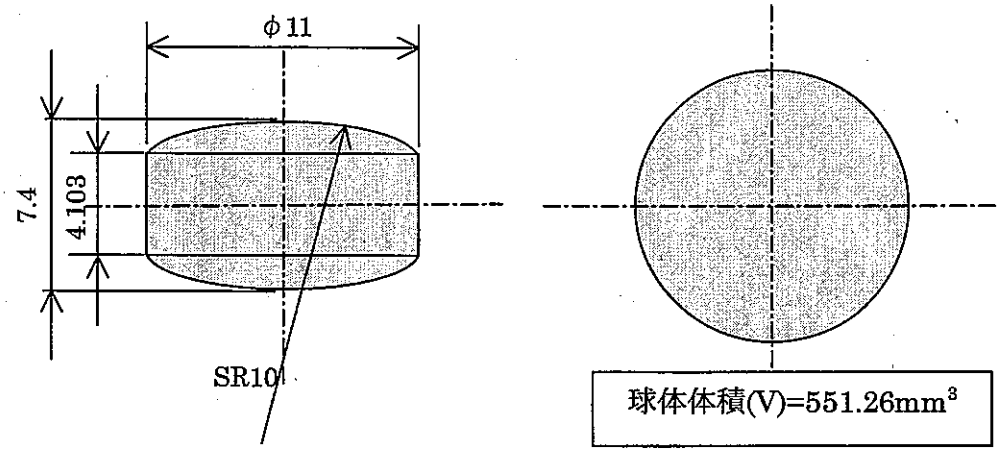

図 3-2　ベントナイトペレット

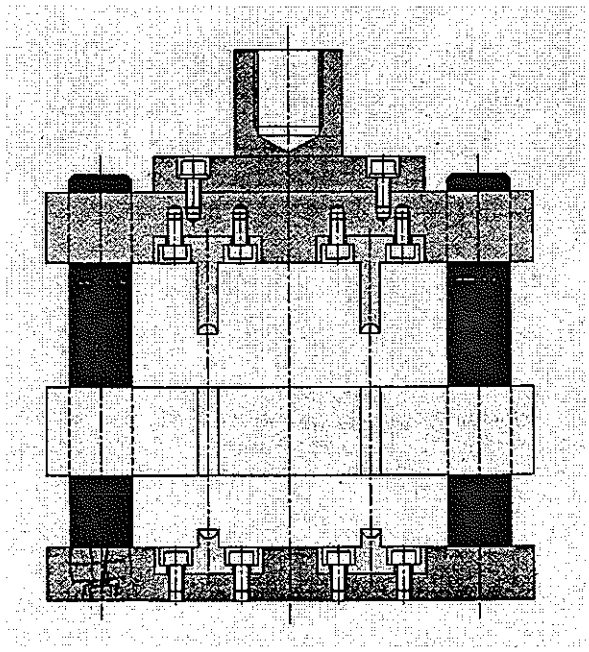

図 3-3　ペレット製作機器

製作するペレットの条件は、以下のとおりとした。

① 目標乾燥密度≧2.0g/cm³

② 製作時の飽和度≦97%

③ 初期含水比10%で製作可能

> 注）製作時の含水比が小さいほど高密度のペレットが製作できる。しかし、本研究ではベントナイトの含水比調整は行なわないものとした。クニゲルV1の含水比は「10%以下（メーカー管理値）」であり、10%の製品を用いても製作可能な密度を目標値として定めるものとした。

④ 含水比管理精度±1.5%

⑤ 秤量精度±0.005ｇ

⑥ リバウンド体積5%(実測値より)

ペレット1個あたりの材料の重量、含水比を変化させたときの製作時と製作後（リバウンド5%を許す）の密度、飽和度を試算し、この試算結果と上記の条件から、ペレットの製作は次の範囲で行なうものとした。

- 湿潤重量1.28±0.005ｇ
- 含水比9±1.5%
- 製作時乾燥密度2.09-2.17g/cm³
- 製作時飽和度73-94%
- 製作後乾燥密度1.99-2.07g/cm³
- 製作後飽和度60-78%

3.3.2 円柱状容器を用いた透水試験

(1) 試験条件

透水試験では、「膨潤前の通水試験」、「飽和後の透水係数測定」、「試験後の密度分布測定」を実施した。試験には、ペレットとクニゲルV1を用いた。ペレットの設計寸法は、図3-2に示すようにφ1.1cm高さ0.74cmである。製作されたペレットから20個を取り出してノギスで寸法を実測した結果を表3-2に示す。この20個の試料について含水比と重量を実測した結果は、それぞれ平均で9.45%、1.237ｇとなった。また、透水試験に供したクニゲルV1の含水比は9.12%であった。以上から、本試験に用いたペレットは、1個あたりの重量1.24g、体積0.5946m³、含水比9.5%、湿潤密度2.085g/cm³、乾燥密度1.905g/cm³となる。

今回、ペレットの乾燥密度の製作目標値は、上記のように1.99-2.07g/cm³である。しかし、実際は1.905g/cm³と、これより小さい値となった。この原因は、製作現場での秤量精度（目標値は1.28g）とリバウンドによる体積の超過によるものである。

透水試験の容器を図3-4に示す。透水試験用セルはアクリル製で、直径5cm、高さ3cm、容積58.9cm³である。ここに、表3-3の3種類の試料（ペレットのみ、ペレット+クニゲルV1、クニゲルV1のみ）を自然落下で充填し試験を実施した。

表 3-2　ペレットの製作実績

	直径 (cm)	高さ (cm)
設計値	1.1	0.74
平均	1.122	0.7705
標準誤差	0.000917663	0.0005
中央値 （メジアン）	1.12	0.77
最頻値 （モード）	1.12	0.77
標準偏差	0.004103913	0.002236068
分散	1.68421E-05	5E-06
尖度	0.698529412	20
歪度	1.624465724	4.472135955
範囲	0.01	0.01
最小	1.12	0.77
最大	1.13	0.78
合計	22.44	15.41
標本数	20	20

表 3-3　透水試験試料

	試料	ペレット個数/重量	クニゲル V1 重量 (g)	湿潤密度 (g/cm³)	乾燥密度 (g/cm³)
T-1-1	ペレット	55/68.43g	0	1.16	1.057
T-2-1	ペレット +クニゲル V1	55/68.43g	21.77	1.53	1.396
T-3-1	クニゲル V1	0/0	45.75	0.78	0.711

容器体積 58.9cm³、ペレットの乾燥密度 1.905g/cm³、クニゲル V1 含水比 9.12%、ペレット含水比 9.45%

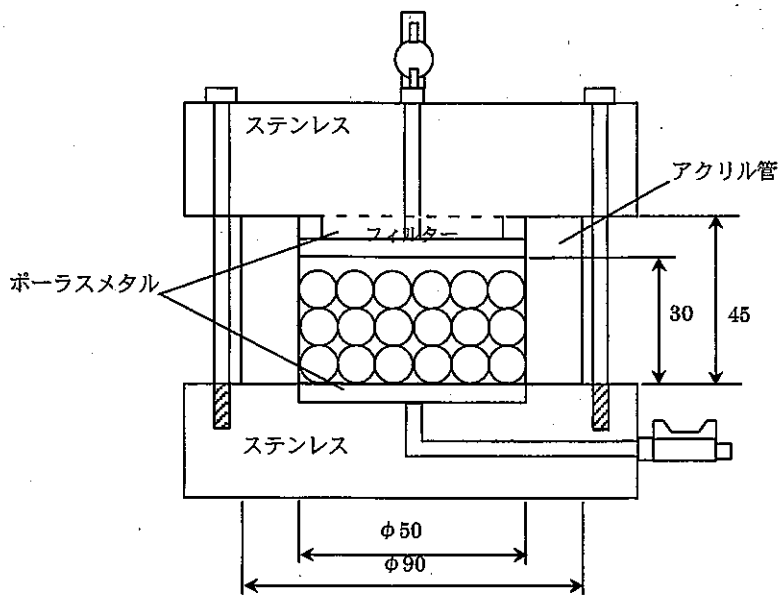

図 3-4　透水試験装置

(2) 膨潤前の通水試験

隙間充填においては材料の投入後、流入する地下水によって充填材料が流出しないことが重要である。ここでは、隙間に投入された 3 種類の材料に、0.01MPa の圧力で水を注水し、流出量の変化を測定、遮水性を検討した。

試験結果を表 3-4 に示す。まず、0.01MPa の圧力で 30 秒通水し、その後、バルブを閉めた。そして、静水中で 5 分間ベントナイトを吸水膨潤させた。この手順を繰り返し、隙間がシールされる状況を観察した。試験ケース T-2-1（ペレット+クニゲル V1）と T-3-1（クニゲル V1）では、通水開始とともにわずかに水が漏れるが、これは第 1 回目の通水で停止し、以後、漏水は生じなかった。一方、T-1-1（ペレットだけのケース）では、隙間を通って水は流出する。この流出量はベントナイトの吸水膨潤によって減少し、本試験条件では、約 2 時間後にゼロとなった。ただし、その後圧力を 0.05MPa まで上昇させると水の流出が再び始まった。これは、図 3-5 に示すように、2 時間の膨潤では密度は均質とはならず、低密度の部分が 0.05MPa の水圧で水みちになったと考えられる。

図 3-6 に通水量の経時変化、図 3-7 には通水量と圧力から計算される（試料は飽和していないので透水係数を意味するものではないが）見かけの透水係数を示す。

これらの結果から、ペレット単体の場合は動水勾配のない状態ではベントナイトの膨潤によって図 3-6 に示すような遮水性を時間とともに発揮する。しかし、水圧が加わる場合はペレット間の空隙にベントナイトの粉末を充填することが、遮水性を向上させる効果があることがわかった。ただし、本試験では、水圧を加える時間は 30 秒ずつの繰り返しであり、連続して水圧を加えた流水環境下での遮水性やベントナイトの流出の程度を観察することは今後の課題として残る。

表 3-4　膨潤前の通水試験結果

透水ﾃﾞｰﾀ						T-1-1 (ペレット)			T-2-1 (ペレット+クニゲル V1)	T-3-1 (クニゲル V1)
	開始	終了	工程	透水量測定	圧力P	透水量 実測値	透水量Q	見かけの 透水係数	透水量 実測値	透水量 実測値
2月18日	(時:分:秒)	(時:分:秒)		ﾎﾟｲﾝﾄ	(MPa)	(cm^3)	(cm^3/sec)	(cm/sec)	(cm^3)	(cm^3)
11:13:00	0:00:00	0:00:30	透水	00:00:15	0.01	160	5.33	8.1508E-03	(5)	(67)
11:13:30	0:00:30	0:05:30	膨潤							
11:18:30	0:05:30	0:06:00	透水	00:05:45	0.01	128	4.27	6.5206E-03	0	0
11:19:00	0:06:00	0:11:00	膨潤							
11:24:00	0:11:00	0:11:30	透水	00:11:15	0.01	106	3.53	5.3999E-03	0	0
11:24:30	0:11:30	0:16:30	膨潤							
11:29:30	0:16:30	0:17:00	透水	00:16:45	0.01	102	3.40	5.1961E-03	0	0
11:30:00	0:17:00	0:22:00	膨潤							
11:35:00	0:22:00	0:22:30	透水	00:22:15	0.01	86.5	2.88	4.4065E-03	0	0
11:35:30	0:22:30	0:27:30	膨潤							
11:40:30	0:27:30	0:28:00	透水	00:27:45	0.01	76	2.53	3.8716E-03	0	0
11:41:00	0:28:00	0:38:00	膨潤							
11:51:00	0:38:00	0:39:00	透水	00:38:30	0.01	117	1.95	2.9801E-03	0	0
11:52:00	0:39:00	0:49:00	膨潤							
12:02:00	0:49:00	0:50:00	透水	00:49:30	0.01	75	1.25	1.9103E-03	0	0
12:03:00	0:50:00	1:00:00	膨潤							
12:13:00	1:00:00	1:01:00	透水	01:00:30	0.01	44.5	0.74	1.1335E-03	0	0
12:14:00	1:01:00	1:11:00	膨潤							
12:24:00	1:11:00	1:12:00	透水	01:11:30	0.01	21.5	0.36	5.4763E-04	0	0
12:25:00	1:12:00	1:22:00	膨潤							
12:35:00	1:22:00	1:23:00	透水	01:22:30	0.01	7.8	0.13	1.9868E-04	0	0
12:36:00	1:23:00	1:33:00	膨潤							
12:46:00	1:33:00	1:37:00	透水	01:35:00	0.01	2.0	0.01	1.2736E-05	0	0
12:50:00	1:37:00	1:47:00	膨潤							
13:00:00	1:47:00	1:52:00	透水	01:49:30	0.01	0.2	0.00	1.0188E-06	0	0
13:05:00	1:52:00	2:02:00	膨潤							
13:15:00	2:02:00	2:03:00	透水		0.03	0				
13:16:00	2:03:00	2:04:00	膨潤							
13:17:00	2:04:00	2:06:40	透水		0.05	23				
13:19:40	2:06:40	2:07:40	膨潤							
13:20:40	2:07:40	2:08:40	透水		0.01	2				
13:21:40	2:08:40		膨潤							

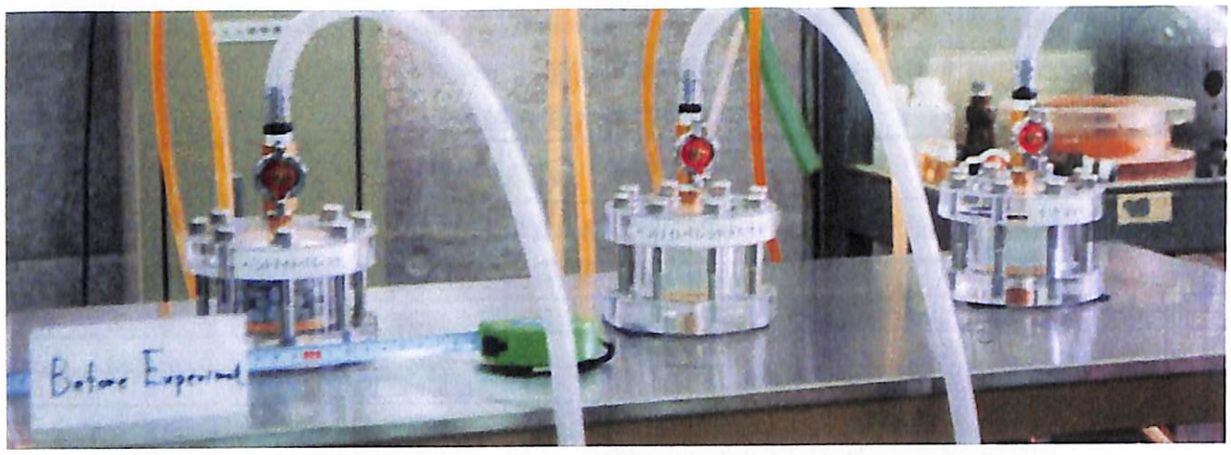

試験前（ペレット）

5.5 分膨潤後（ペレット）

93 分膨潤後（ペレット）

図 3-5　通水試験状況

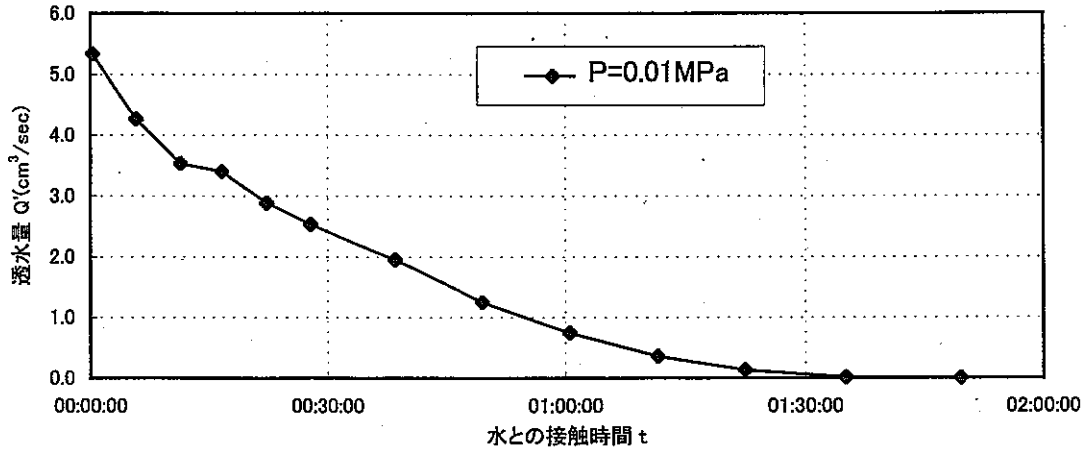

図 3-6　ペレット通水試験（水との接触時間～通水量）

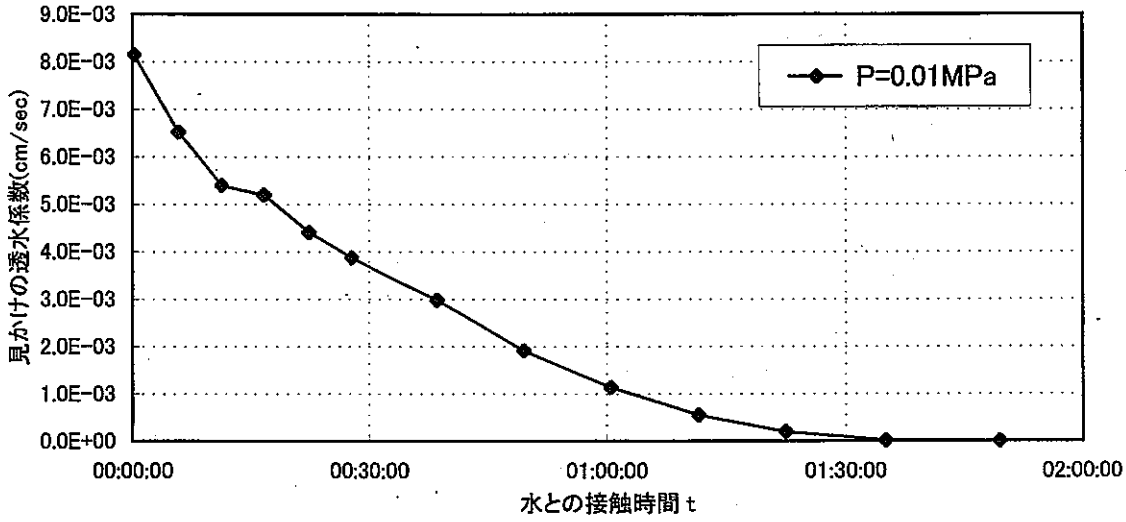

図 3-7　ペレット通水試験（水との接触時間～見かけの透水係数）

(3) 透水試験

通水試験後に、水圧を 0.01MPa から 0.15MPa まで順次上昇させ試料を飽和させた。水の透過が始まるまでの時間（試料が飽和したと判断できる時間）は、ペレットとクニゲル V1 を混合した T-2-1 の場合 47 日であった。その後、0.15MPa の圧力で透水試験を開始した。試験結果を表 3-5 に、透水係数の経時変化を図 3-8 に示す。測定された透水係数は、試験用セル内の粘土全体の乾燥密度が大きいほど小さくなる傾向を示している。また、ペレット単体でも本試験条件では、3 $\times 10^{-10}$cm/s 以下という小さい値を示した。これにクニゲル V1 を添加する（T-2-1 の場合）ことは、透水係数の低下よりも、すでに述べた初期の遮水性向上効果としての意義が大きいことがわかる。

また、図 3-9 には透水係数を固有透過度に換算し、JNC 殿により取得された固有透過度の値と比較したものを示す。有効粘土密度で整理すると固有透過度は図中に示す式でケイ砂混合率に関係なく整理できるとされており、この結果と今回ペレットを用いた試験で得られた固有透過度の値とを比較した。その結果、ペレットを用いた試験の結果得られた固有透過度は関数式に比べ若干大きな値を示したが、傾向はほぼ一致した結果となった。

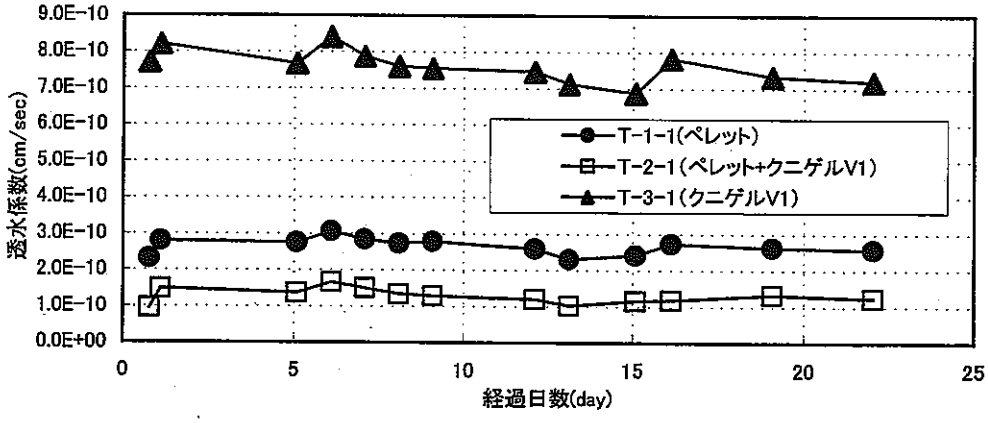

図 3-8　透水試験結果

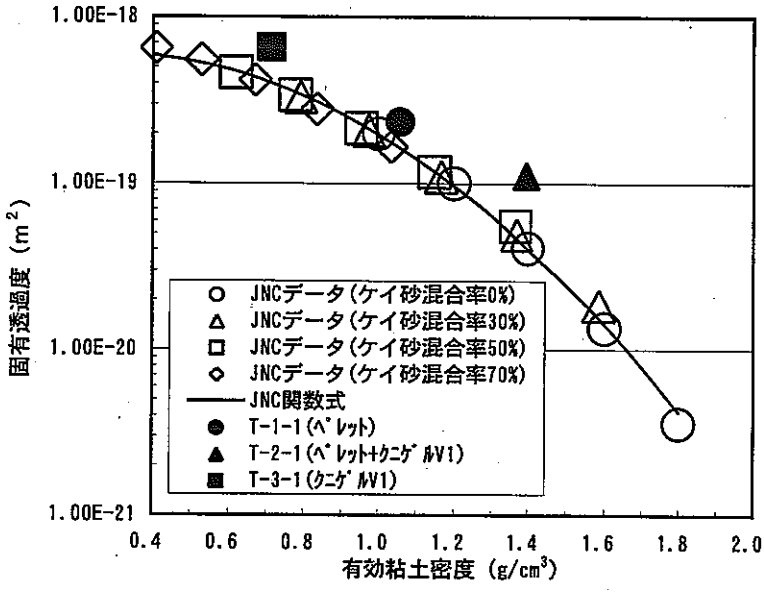

図 3-9　既存データとの比較

表 3-5　透水試験結果

透水データ					T-1-1(ペレット)				T-2-1（ペレット+クニゲル V1）				T-3-1（クニゲル V1）				蒸発量を補正するためのダミー（蒸発皿用）		
測定日時 2000/4/5 15:30	経過時間 (hour)	透水時間 (hour)	透水時間 (day)	圧力P (Mpa)	実測長さ (mm)	量換算 (cc)	透水量 (cm^3)	透水係数 (cm/sec)	実測長さ (mm)	量換算 (cc)	透水量 (cm^3)	透水係数 (cm/sec)	実測長さ (mm)	量換算 (cc)	透水量 (cm^3)	透水係数 (cm/sec)	実測長さ (mm)	量換算 (cc)	蒸発量 (cc)
2000/4/5 17:15	1.75	1.7	0.1	0.15	9.5	1.432			8.7	1.395			11.8	1.536			83.9	4.814	
2000/4/6 9:25	17.92	16.2	0.7	0.15	12.5	1.568	0.13	2.31E-10	10.0	1.455	0.05	9.55E-11	21.6	1.982	0.44	7.72E-10	83.8	4.809	0.005
2000/4/6 17:15	25.75	7.8	1.1	0.15	14.2	1.645	0.08	2.79E-10	10.9	1.495	0.04	1.48E-10	26.6	2.209	0.23	8.21E-10	83.8	4.809	0.000
2000/4/10 17:15	121.75	96.0	5.1	0.15	35.2	2.600	0.93	2.75E-10	21.6	1.982	0.46	1.37E-10	84.4	4.836	2.60	7.68E-10	83.3	4.786	0.023
2000/4/10 17:15					35.2	2.600			21.6	1.982			11.0	1.500			83.3	4.786	0.000
2000/4/11 17:15	145.75	24.0	6.1	0.15	41	2.864	0.26	3.05E-10	24.8	2.127	0.14	1.66E-10	26.8	2.218	0.71	8.41E-10	83.2	4.782	0.005
2000/4/12 17:15	169.75	24.0	7.1	0.15	46.3	3.105	0.24	2.84E-10	27.6	2.255	0.13	1.50E-10	41.5	2.886	0.67	7.88E-10	83.2	4.782	0.000
2000/4/13 17:15	193.75	24.0	8.1	0.15	51.5	3.341	0.23	2.73E-10	30.2	2.373	0.11	1.34E-10	55.8	3.536	0.65	7.61E-10	83.1	4.777	0.005
2000/4/14 17:15	217.75	24.0	9.1	0.15	56.8	3.582	0.24	2.79E-10	32.7	2.486	0.11	1.29E-10	70.0	4.182	0.64	7.56E-10	83.0	4.773	0.005
2000/4/14 17:15					56.8	3.582			32.7	2.486			10.7	1.486			83.0	4.773	0.000
2000/4/17 17:15	289.75	72.0	12.1	0.15	71.5	4.250	0.66	2.59E-10	39.6	2.800	0.30	1.20E-10	52.7	3.395	1.90	7.47E-10	82.8	4.764	0.009
2000/4/18 17:15	313.75	24.0	13.1	0.15	76.1	4.459	0.20	2.30E-10	41.8	2.900	0.09	1.02E-10	66.3	4.014	0.60	7.13E-10	82.5	4.750	0.014
2000/4/20 17:15	361.75	48.0	15.1	0.15	85.4	4.882	0.41	2.41E-10	46.4	3.109	0.20	1.15E-10	92.3	5.195	1.17	6.89E-10	82.2	4.736	0.014
2000/4/20 17:15					5.5	1.250			46.4	3.109			7.3	1.332			82.2	4.736	0.000
2000/4/21 17:15	385.75	24.0	16.1	0.15	10.7	1.486	0.23	2.73E-10	48.7	3.214	0.10	1.18E-10	22.0	2.000	0.66	7.82E-10	82.1	4.732	0.005
2000/4/24 17:15	457.75	72.0	19.1	0.15	25.6	2.164	0.67	2.63E-10	56.3	3.559	0.34	1.32E-10	63.3	3.877	1.87	7.34E-10	81.9	4.723	0.009
2000/4/27 17:15	529.75	72.0	22.1	0.15	40.4	2.836	0.65	2.57E-10	63.6	3.891	0.31	1.23E-10	104.0	5.727	1.83	7.20E-10	81.5	4.705	0.018

(4) 密度測定

透水試験後の試料を 24 分割（鉛直 3 段×8 分割）し、密度分布を測定した。通水試験開始から密度測定までの時間、つまり試料が水と接触している時間は 80 日である。図 3-10 には、試験終了時の供試体表面の状況、および供試体分割の状況を示す。図よりクニゲル V1 のみで製作した供試体は他に比べ表面がきれいであることが分かる。また、ペレットのみの場合と、ペレットとクニゲル V1 を用いた供試体を比較すると、後者の方が若干、斑が強く残っている感じであった。密度の測定結果を表 3-6 に示す。また、含水比と乾燥密度分布の統計量を表 3-7 に示す。表 3-7 から、密度の平均値をみると、T-1-1；1.08g/cm^3、T-2-1；1.41g/cm^3、T-3-1；0.70g/cm^3 である。これは表 3-3 に示した試験用セル全体での粘土の乾燥密度の計算値 T-1-1；1.06g/cm^3、T-2-1；1.40g/cm^3、T-3-1；0.71g/cm^3 とほぼ等しい。試料の分割の人為的な誤差はあるが、平均値としての計測は正確であったことがわかる。また、表 3-7 から、含水比と密度のばらつきは、クニゲル V1 単体がもっとも大きく、ペレットのみの場合がばらつきは小さいことがわかる。以上から、充填時にペレット間の空隙によって密度の不均質性を持つ場合でも、飽和後には比較的均質になり、十分に小さい透水性（顕著な水みちが生じていない）を発揮していることがわかる。ここで、今回の試験においてクニゲル V1 単体の供試体が最も密度のばらつきが大きかった原因としては、初期の充填密度が小さかったために、浸潤面に近い部分に浸潤初期に発生した膨潤の影響が強く残ったことが考えられる。

表 3-6　透水試験後の密度測定結果

T-1-1　ベントナイトペレット				T-2-1　ベントナイトペレット+クニゲル V1				T-3-1　クニゲル V1			
試料位置	含水比 (%)	湿潤密度 (g/cm^3)	乾燥密度 (g/cm^3)	試料位置	含水比 (%)	湿潤密度 (g/cm^3)	乾燥密度 (g/cm^3)	試料位置	含水比 (%)	湿潤密度 (g/cm^3)	乾燥密度 (g/cm^3)
上部 1cm	58.7	1.56	0.99	上部 1cm	37.1	1.75	1.28	上部 1cm	91.1	1.50	0.78
	56.2	1.76	1.12		36.0	1.74	1.28		98.8	1.37	0.69
	58.7	1.67	1.06		39.1	1.68	1.21		94.1	1.47	0.76
	56.6	1.75	1.12		35.7	1.72	1.27		94.1	1.62	0.84
	64.6	1.59	0.97		37.3	1.87	1.36		93.9	1.41	0.73
	54.8	1.59	1.03		38.2	1.71	1.24		96.5	1.37	0.70
	56.3	1.66	1.06		34.0	1.99	1.49		93.8	1.41	0.73
	58.2	1.68	1.06		35.1	1.91	1.42		93.4	1.43	0.74
中央 1cm	50.2	1.60	1.06	中央 1.1cm	31.1	2.12	1.62	中央 1cm	92.0	1.47	0.77
	48.9	1.61	1.08		30.9	1.90	1.45		92.2	1.51	0.79
	49.8	1.69	1.13		30.7	1.97	1.51		91.5	1.55	0.81
	48.6	1.72	1.16		32.3	2.13	1.61		93.4	1.67	0.86
	50.2	1.61	1.07		30.1	2.26	1.73		94.4	1.54	0.79
	50.4	1.54	1.03		31.4	2.09	1.59		95.5	1.60	0.82
	48.0	1.68	1.14		31.5	2.27	1.73		96.6	1.40	0.71
	52.1	1.59	1.05		32.5	2.19	1.65		94.9	1.41	0.72
下部 1cm	61.0	1.73	1.08	下部 0.9cm	39.0	1.86	1.34	下部 1cm	140.1	1.54	0.64
	62.2	1.69	1.04		41.3	1.55	1.10		139.9	1.35	0.56
	63.2	1.66	1.02		41.4	1.64	1.16		137.9	1.36	0.57
	61.6	1.90	1.18		39.4	1.79	1.29		141.5	1.33	0.55
	57.8	1.78	1.13		40.3	1.87	1.34		140.8	1.23	0.51
	60.5	1.94	1.21		36.8	2.02	1.48		141.5	1.33	0.55
	55.7	1.72	1.10		39.1	1.79	1.29		135.7	1.34	0.57
	64.5	1.62	0.99		36.0	1.83	1.34		135.2	1.36	0.58

表 3-7　含水比と乾燥密度分布の統計量

	T-1-1	T-2-1	T-3-1
	ペレット	ペレット+クニゲル V1	クニゲル V1
	含水比		
平均	56.2	35.7	109.1
中央値（メジアン）	56.4	36.0	95.2
標準偏差	5.3	3.7	21.7
分散	28.5	13.3	472.6
範囲	16.5	11.3	50.3
変動係数（%）	9.51	10.23	19.92
	乾燥密度		
平均	1.08	1.41	0.70
中央値（メジアン）	1.07	1.35	0.72
標準偏差	0.06	0.18	0.11
分散	0.00	0.03	0.01
範囲	0.24	0.64	0.35
変動係数（%）	5.72	12.72	15.18

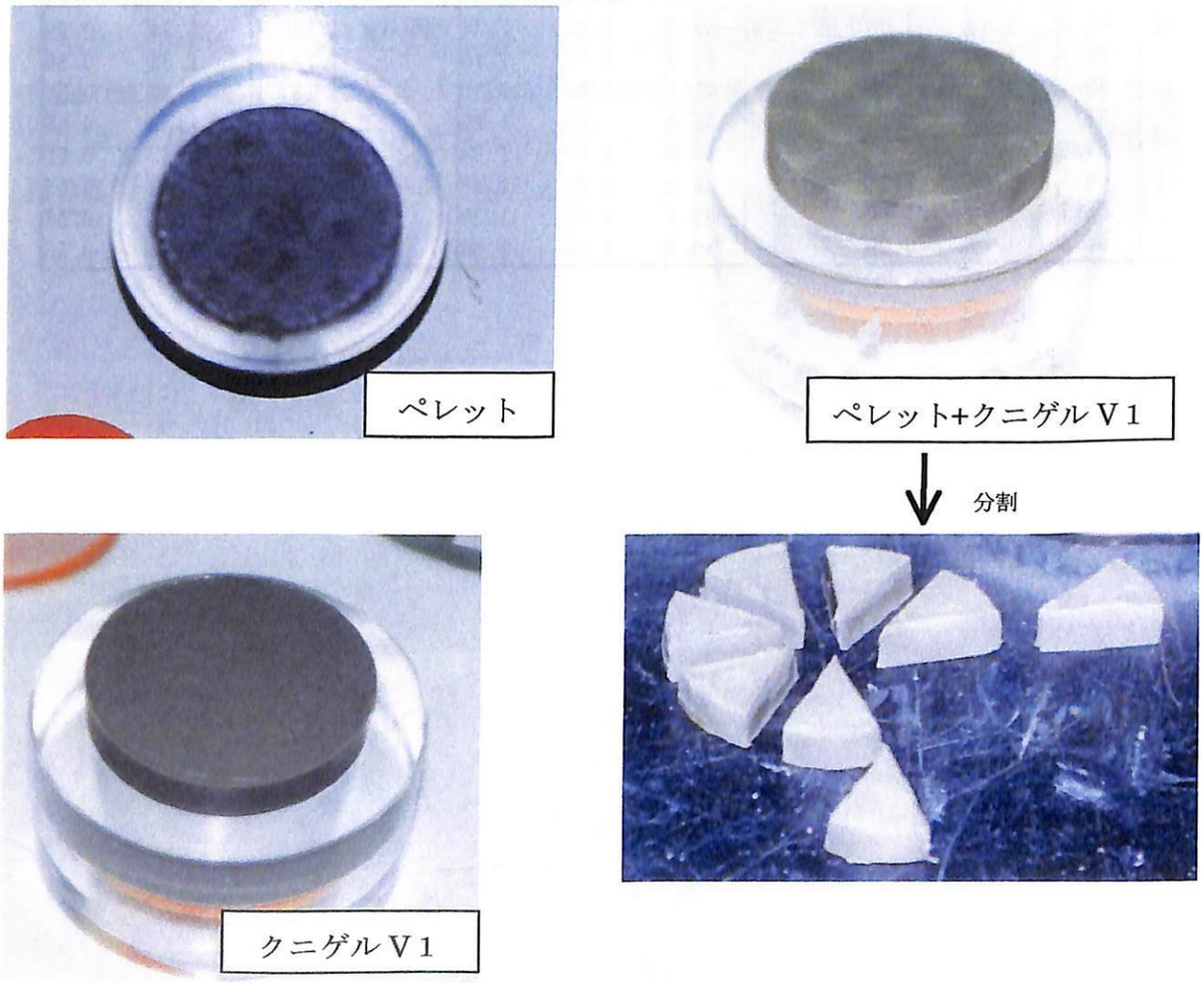

図 3-10　透水試験後の試料（水との接触から 80 日経過）

3.3.3　楔形状の隙間に対する透水試験

鋭角部におけるベントナイトペレットの充填性を確認することを目的に、楔形状の隙間に対するペレット充填および透水試験を実施した。試験用のセルは、3.3.2 節で使用したセルと同じものを用いた。そして、通水部が角度の異なる 3 種類の楔形状となるようなシリコンを作成し、試験用セル内に設置した。

表 3-8 には、実施した試験ケースを示す。また、図 3-11 にはベントナイトペレットの設置状況を示す。試験ケース S-1-1 と S-1-2 は楔部の形状は異なるが、ベントナイトが膨潤後の密度は一緒になるように設定したケースである。また、S-1-2 と S-1-3 は楔形状部は同じであるが充填するベントナイトペレットの個数を変え、最終的な密度が異なるように設定したケースである。図 3-12 には試験の様子を示す。

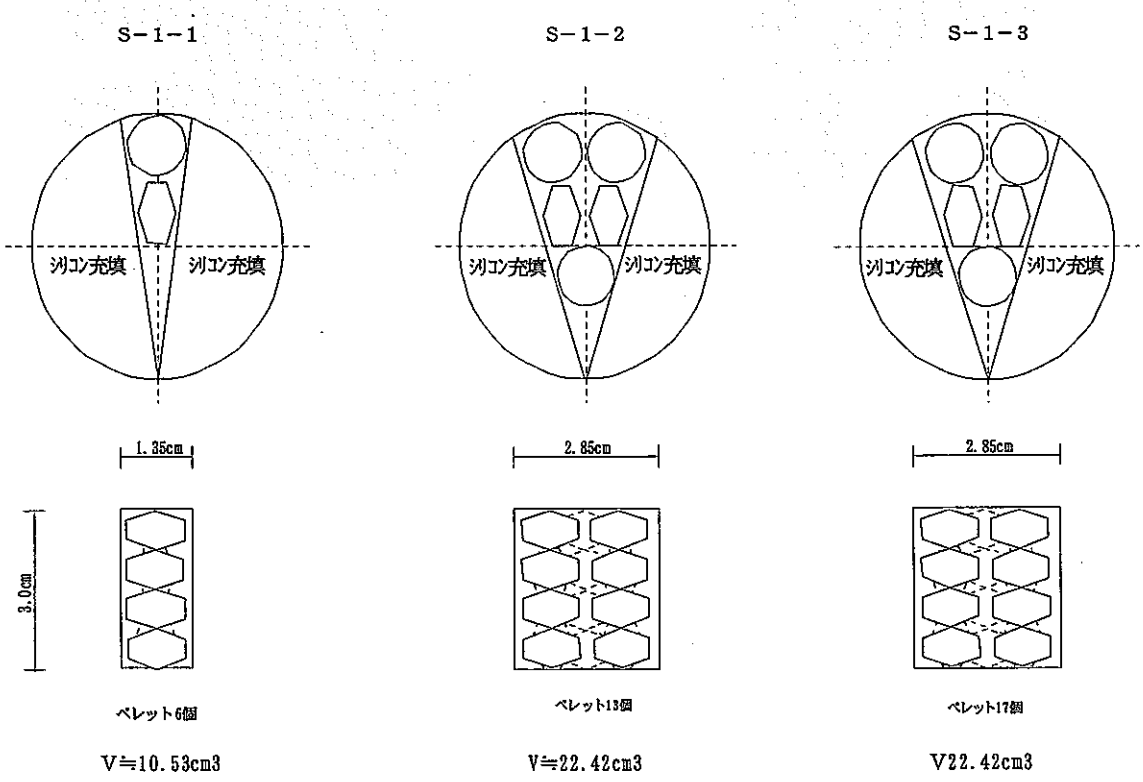

図 3-11　ベントナイトペレット設置状況

表 3-8　楔形状の隙間に対する透水試験の試験ケース

試験ｹｰｽ	試料	楔形状部 体積 (cm^3)	試験前			
			容器質量 (g)	(容器+試料)質量 (g)	試料質量 (g)	初期密度 (g/cm^3)
S-1-1	ﾍﾟﾚｯﾄ6ｺ	10.53	151.07	158.57	7.50	0.71
S-1-2	ﾍﾟﾚｯﾄ13ｺ	22.42	136.06	152.17	16.11	0.72
S-1-3	ﾍﾟﾚｯﾄ17ｺ	22.42	134.92	156.22	21.30	0.95

図 3-12　楔形状の隙間に対する透水試験の様子

表 3-9 に試験結果を示す。同表には、試験開始からの各時間毎の試験セル内の通過水量およびそれから計算される透水係数を示している。また図 3-13 には、計算された透水係数の経時変化を示す。通水開始当初はペレット間の隙間を水が通るため通水量は大きくなっている。しかし、通水開始 1 日後には透水係数は 10^{-9}cm/s 程度となっており、20 日程度経過すれば透水係数はほぼ定常に達している。定常となった透水係数の値を 3.3.2 節に示した透水試験の結果と比べると（T-3-1 と S-1-3)、楔形状部における透水係数の方が若干大きい結果となった。そこで、定常に達した後、試験装置を解体し、内部のベントナイトの状況を観察することとした。

図 3-14～図 3-16 には試験終了後の供試体の様子を示す。全ての図において左側が試験用セルから取り出した状態で、右側がシリコンを外した状態である。全てのケースにおいて鋭角部奥まで十分に粘土が充填されている様子が観察できる。しかし、シリコンを外したところ、鋭角部では粘土の密度がかなり低く、かなり柔らかい状態であった。特に、鋭角部の角度の小さいケース S-1-1 においてその傾向が顕著であった。すなわち、ベントナイトペレットの膨潤により鋭角部奥まで粘土は充填されるが、得られる密度は若干小さくなり、その影響で透水係数も若干大きくなるものと考えられる。しかし、大きいとはいえ透水係数は 10^{-9}cm/s 程度であるため緩衝材の要件である低透水性は十分に確保できると考えられる。

表 3-9　楔形状の隙間に対する透水試験の結果

測定日時	経過時間 (hour)	透水時間 (hour)	圧力 (MPa)	S-1-1			S-1-2			S-1-3		
				管目盛 (cc)	透水量 (cm^3)	透水係数 (cm/s)	管目盛 (cc)	透水量 (cm^3)	透水係数 (cm/s)	管目盛 (cc)	透水量 (cm^3)	透水係数 (cm/s)
2000/8/3 13:40				9.63	0		9.27	0		9.5	0	
2000/8/4 15:40	26	1.1	0.15	9.4	0.23	1.40E-09	8.85	0.42	1.20E-09	9.25	0.25	7.15E-10
2000/8/7 15:40	98	4.1	0.15	8.85	0.55	1.10E-09	7.79	1.06	1.03E-09	8.69	0.56	5.01E-10
2000/8/11 10:00	188.3	7.8	0.15	8.17	0.68	1.12E-09	6.48	1.31	1.01E-09	8.00	0.69	5.27E-10
2000/8/21 9:15	427.6	17.8	0.15	6.28	1.89	1.29E-09	2.97	3.51	1.10E-09	6.13	1.88	5.92E-10
2000/8/25 13:10	527.5	22.0	0.15	5.5	0.78	1.26E-09	1.54	1.43	1.11E-09	5.38	0.75	6.03E-10

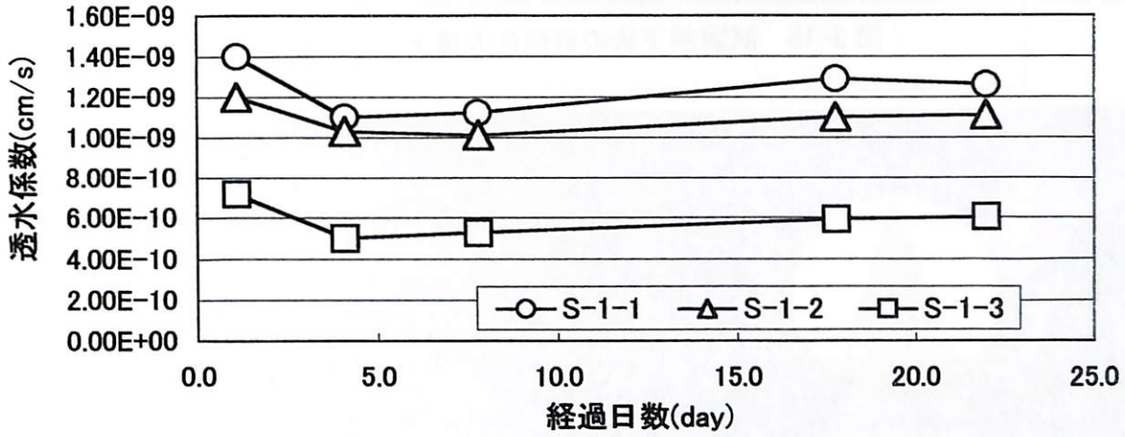

図 3-13　透水係数の経時変化

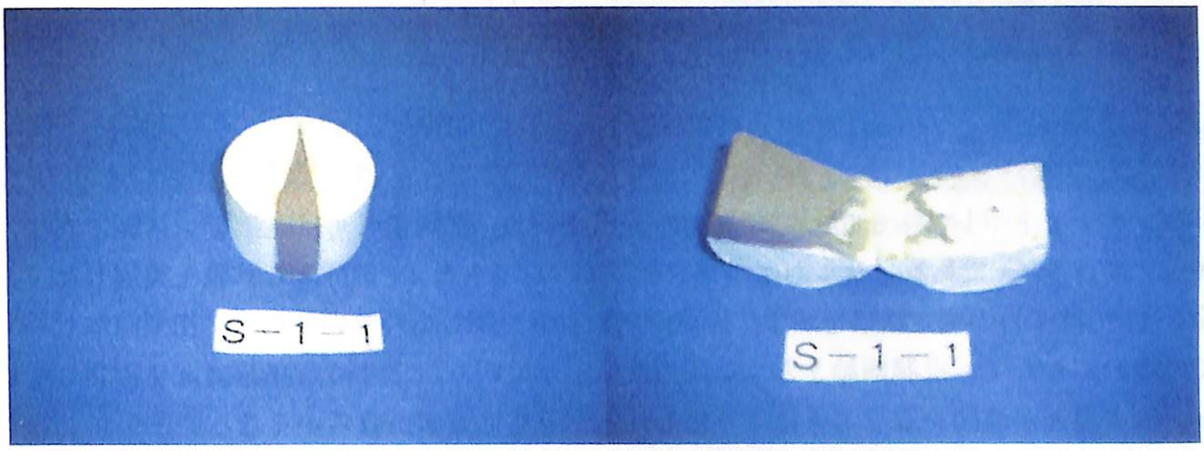

図 3-14　試験終了後の供試体の様子（S-1-1）

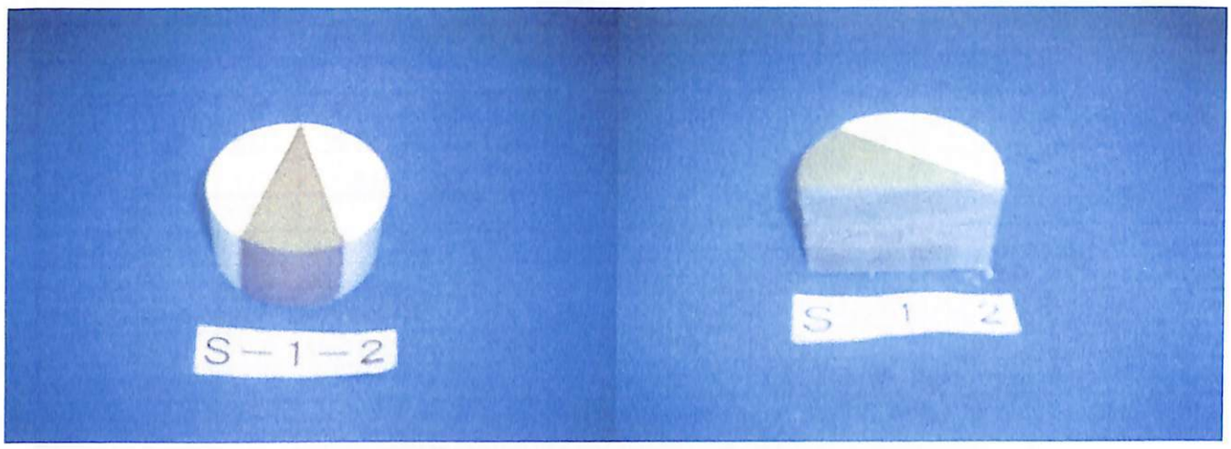

図 3-15　試験終了後の供試体の様子（S-1-2）

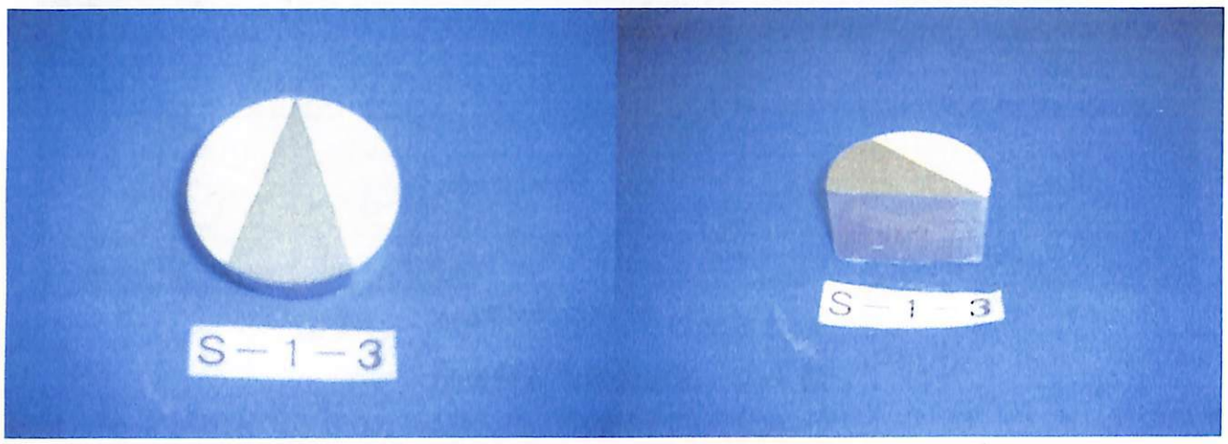

図 3-16　試験終了後の供試体の様子（S-1-3）

3.4 ベントナイトペレットを用いた膨潤試験

ベントナイトペレットを用いて膨潤試験を実施した。試験用セルはステンレス製で内径30mm、高さ 30mm である。セル内にベントナイトペレットを 19 個挿入し試験を実施した。図 3-17 には圧力の測定結果を示す。設置時ペレットを押し込んでいるため、初期値はゼロではない。そして、浸潤開始とともに圧力は低下していく。これは、浸潤により膨潤したペレット表面が隙間を塞ぐことにより使われるとともに表面が軟らかくなることから、設置時の硬いペレット同士のツッパリがなくなり、セル内の形状に合わせてペレットが変形していくため（なじみによる圧力低下）であると考えられる。しかし、さらに浸潤が進んでペレット間の隙間が塞がりセル内でひとつの系としてペレットが膨潤していくことにより徐々に圧力は高くなっており、最終的には約 0.2MPa の圧力となっている。また、図 3-18 には解体時の様子を示す。解体による観察からもペレット間の隙間が塞がれてひとつの固まりとなっていることが分かる。

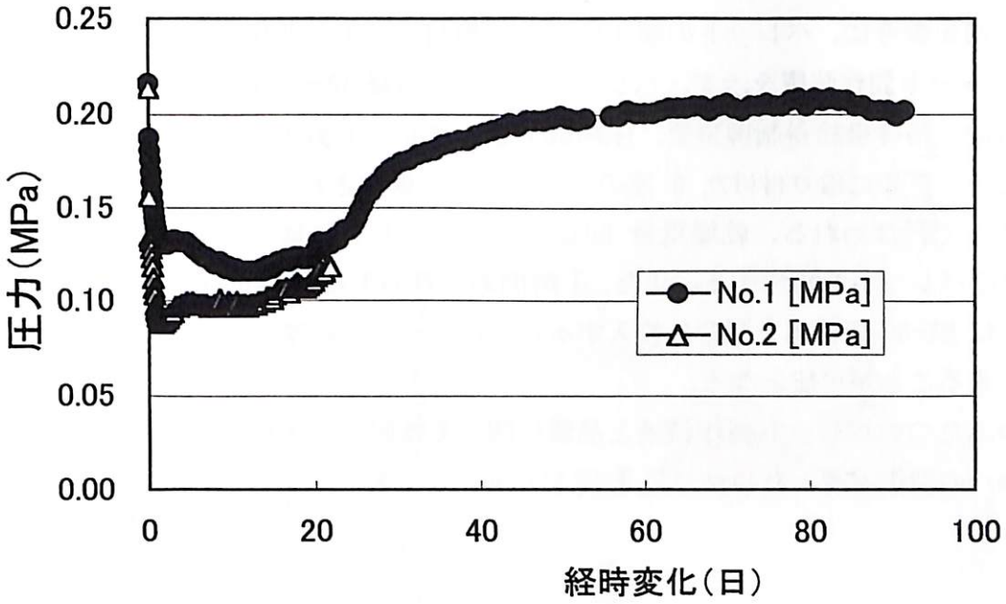

図 3-17　圧力の経時変化

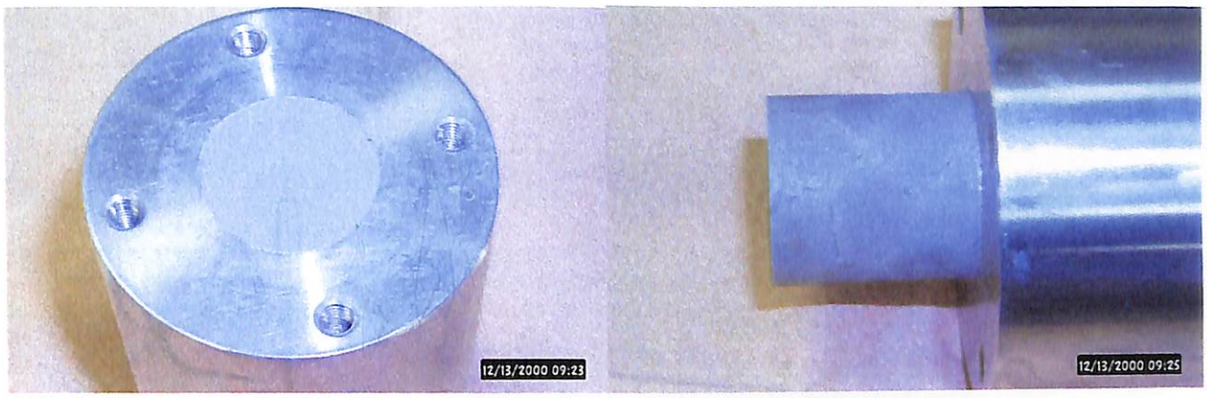

図 3-18　ベントナイトペレット膨潤試験解体時の様子

3.5　ペレット製作技術の検討

本節では、内外の事例を調査し、高密度ペレットの製作の可能性を評価する。また、直径 30mm のベントナイトペレットの製作機械を設計する。

ベントナイトペレットを高レベル廃棄物処分の緩衝材に適応する検討は、フィンランドにおいて 1980 年代に実施されている[3-1)]。ここでは、寸法、直径 24mm 高さ 15mm のペレットの製作を検討している。製作は、一軸のプレスにより行ない、気乾状態での密度は、2.4 g/cm^3 とし、ベントナイトは MX-80 を用いている。製作されたペレットは、ブロック型緩衝材の代替として処分ピットに投入充填される。充填後の密度は、2 種類の寸法のものを用いて、

湿潤密度で 1.8～1.9g/cm³ と示されている。

この事例を参考に、ペレットの製作機器と緩衝材としての使用の可能性を検討する。図 3-19 にペレット製作装置を示す。ペレットの寸法は直径 30mm、高さ 25mm、体積 30cm³ である。これは、粉体供給量制御装置、圧縮成型機、ペレット搬出コンベアーからなる。成型は、回転テーブルに取り付けた 6 連のシリンダーに供給されるベントナイトを油圧でプレスすることで行なわれる。乾燥重量 60ｇベントナイトを秤量供給することで、乾燥密度 2.0g/cm³ のペレットを製作する。また、1 時間あたりの生産量 2400 個の能力を持つ。このペレットに MX-80 の粉体を混合し投入することによって、乾燥密度 1.5g/cm³ の緩衝材を現場で施工することが可能となる。

上記のふたつのペレット製作技術と品質に関する検討を、本研究における小型ペレット（φ11mm）の製作実績とあわせて表 3-10 に示す。

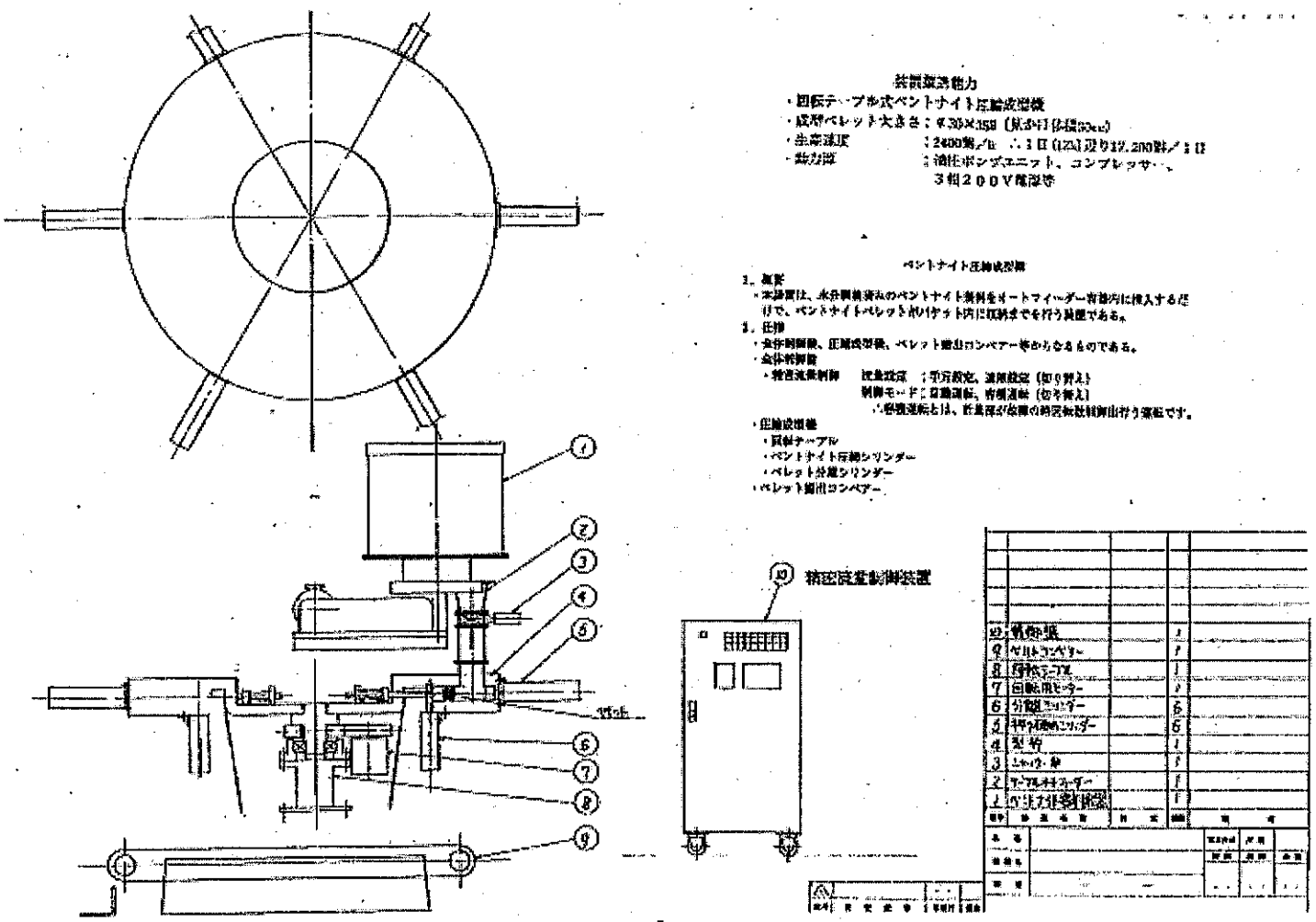

図 3-19　ベントナイトペレット成型装置

表 3-10　ベントナイトペレットの検討比較　（斜線は今後検討が必要な項目）

	TVO フィンランド Salo(1989)	人工バリアにおける緩衝材 挙動評価研究 （製作実績）	人工バリアにおける緩衝材 挙動評価研究 （机上検討）
用途	代替緩衝材	すきま充填（粒径小）	すきま充填（粒径大）
材料	MX-80	ｸﾆｹﾞﾙ V1	ｸﾆｹﾞﾙ V1
寸法	φ30mm、H15mm φ12.4mm も混合	φ11mm、H7.4mm （体積 0.55cm^3）	φ30mm、H25mm（体積 30cm^3） 乾燥重量 60ｇ/個
製作条件	気乾ﾍﾟﾚｯﾄの密度 2.4g/cm^3 ﾌﾟﾚｽ 100MPa	湿潤重量 1.28±0.005ｇ 含水比 9±1.5％ 製作時乾燥密度 2.09～2.17g/cm^3 製作時飽和度 73～94％ 製作後乾燥密度 1.99～2.07g/cm^3 製作後飽和度 60～78％	
製作方法	2.5m^3/day (4.75ton/day)	静的ﾌﾟﾚｽ	回転ﾃｰﾌﾞﾙ式ﾍﾞﾝﾄﾅｲﾄ圧縮成型機 1440 個/hr,17280 個/日（12 時間） ＝1037kg/日
充填密度	緩衝材の目標密度は 1.8～1.9g/cm^3 （湿潤） 2 種類のﾍﾟﾚｯﾄを 80%の充填率で 1.92g/cm^3	充填試験の結果 2.0g/cm^3 のﾍﾟﾚｯﾄ充填で乾燥密度 1.12g/cm^3 すきまにｸﾆｹﾞﾙ V1 を加え；1.41 すきまに MX-80 を加え；1.5	左を参考 ﾍﾟﾚｯﾄ乾燥重量 1.12ton/m^3 MX-80 乾燥重量 0.38ton/m^3
必要量	ﾄｰﾀﾙ 900 ｷｬﾆｽﾀｰ，10 年 90 本/年の処分 9.24m^{3}ﾍﾟﾚｯﾄ/処分ﾋﾟｯﾄ 823m^{3}ﾍﾟﾚｯﾄ/年 必要なﾍﾞﾝﾄﾅｲﾄ 1600ton/年 4m^3/日のﾍﾟﾚｯﾄ型緩衝材必要 1 台で 2.5m^3/日のﾌﾟﾚｽ能力（4.75ton/日）		
透水性	1.9g/cm^3 の透水係数： 10^{-13}～10^{-14}m/s	初期の止水；ﾍﾟﾚｯﾄのみでは水が浸入 飽和後；ﾌﾞﾛｯｸと同等	
膨潤圧	ﾌﾞﾛｯｸ相当というﾃﾞｰﾀがある	測定中	
廃棄体支持力	たぶん十分。さらに強度が必要なときは廃棄体の下にﾚﾝｶﾞ型緩衝材を置く。		
熱伝導率	測定されていない。 但し、ﾌﾞﾛｯｸの熱伝導率（0.75W/mK）より、小さくなる可能性		
長期安定性	ﾌﾞﾛｯｸと同等		

3章　参考文献

3-1) Salo, J. P., et al.,"Bentonite pellets, an alternative buffer material for spent fuel canister deposition holes" Sealing of Radioactive Waste Repositories, Proc. Of NEA/CEC workshop, 1989

4. 実規模人工バリア試験の評価

4.1 エスポ地下研究施設（ÄHRL）の概要

スウェーデンでは、使用済燃料深地層処分場の正確な設計および立地はまだ決定されていないが、20年以上にわたって、様々なデータが室内および現場における広範な研究活動を通じて収集されている。SKBは、現在得られている知識をまとめ、深地層処分場で使用される手法を実際の自然条件の下で実証するために、Äspö島に地下実験施設（Äspö Hard Rock Laboratory、エスポ地下研究施設）を建設した（図4-1参照）。エスポ地下研究施設は、Oskarshamn原子力発電所の近くに有り、その深度は約460mで、坑道の総延長は3600mである。

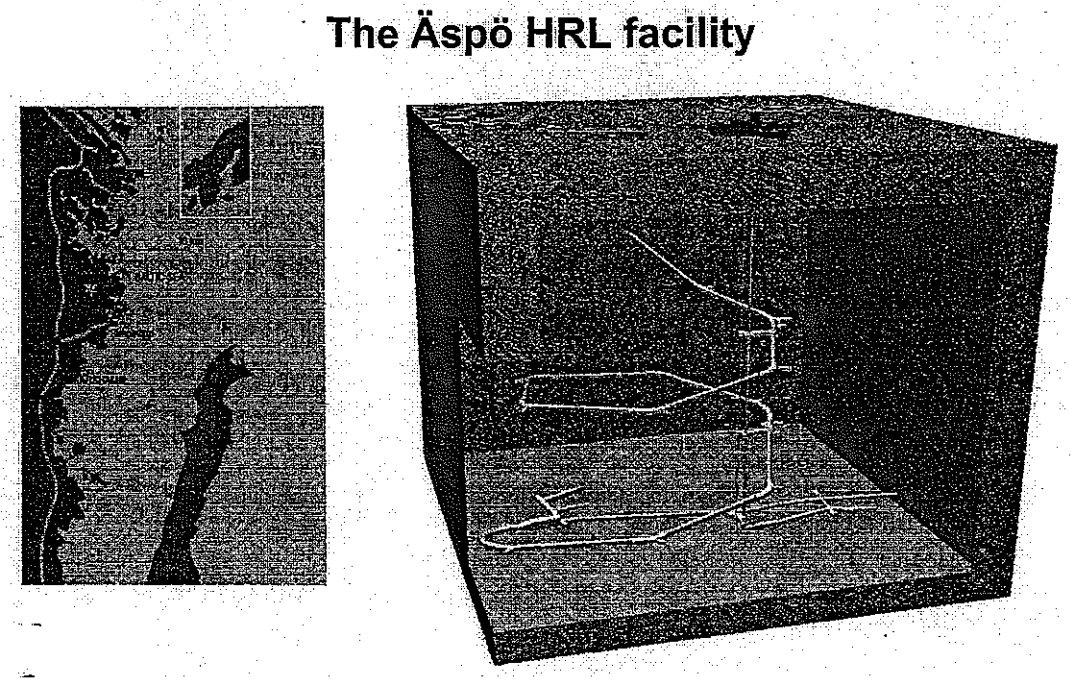

図4-1　Äspö Hard Rock Laboratory

エスポ地下研究施設の目的は、処分で想定される深度の乱されていない地下環境に、研究開発とデモンストレーションの場を与えることにある。つまり、

- サイト調査手法の開発
- モデルの検証
- 天然、および人工バリアの機能の確認
- 処分技術のデモンストレーション

が試験の焦点であり、1986年以降次のような活動が展開されている。

エスポ地下研究施設における試験は3段階（サイト調査段階、建設段階、操業段階）に分けられている。サイト調査段階（1986-1990）においては、サイト調査および詳細な特性調査に関する様々な方法がテストされてきた。また、これらのデータを用い、地質構造モデルの作成、建設段階における水理場の変化予測等が実施された。建設段階（1990-1955）には、地表面下460mまで

の坑道の掘削、ベンチレーションのための立て坑掘削等が実施され、また同時に、さらなる地質調査も実施された。また、地下水の化学的性質や地下水流動の変化等も計測された。こうして得られた結果は、坑道掘削前に実施された予測、すなわち、岩種の分布、破砕帯の分布、地下水の化学的性質の変化、地下水流動に関する予測等のチェックに用いられた。操業段階は1995年半ばから開始された。以下に、各フェーズの概要を示す。

4.1.1 サイト調査 (1986～1990年)

エスポ地下研究施設では、サイト調査および詳細な特性調査に関する様々な方法がテストされてきた。これらの方法は今後、深層処分場候補サイトの特性調査に使用されることになる。また、こうした調査により、岩盤の局所的な特性に深層処分場を適合させる方法に関する情報や、深層処分場の安全評価にとって重要なデータも入手される。地表およびボアホール調査の結果が、エスポ地下研究施設が建設された岩盤内の様々な条件をモデル化するために利用されている。これらのモデルは、岩種の分布、破砕帯の位置および特徴、地下水の科学的な特性、研究施設地下部分の建設が地下水の移動に及ぼすと予想される影響などを記述するものである。

4.1.2 建設期間 (1990～1995年)

建設期間には、坑道掘削と平行して広範な調査が実施された。地下水の化学的性質や地下水流動の変化が、建設期間中および期間後に記録された。そしてこうして新たに得られた結果が、坑道掘削が始まる前になされた予測、すなわち岩種の分布、破砕帯、地下水の化学的性質および地下水流動に関する予測のチェックに用いられた。

その結果、一般的に見て、予測と坑道内で観察された実際の結果の間には良好な一致がみられた。HRLの国際モデル化タスクフォースが地下水流に関する三次元モデルをテストし、これらのモデルが実際の条件を良好に表していることが示されている。

4.1.3 操業期間 (1995年～)

エスポ研究施設の建設は1995年に完了し、この時点から使用済燃料の定置に使用される技術の開発、試験および実証を目的とした計画が開始された。この技術を深層処分場で使用する前に、エスポ地下研究施設の現実的な環境において様々な試験が実施された。

エスポ地下研究施設は国際的にも大きな関心を集めている。このプロジェクトへの参加契約に署名している国として、カナダ、フィンランド、フランス、ドイツ、日本、スペイン、スイスおよび英国が挙げられる。

このエスポ地下研究施設での作業は、今では廃山となっているStripa鉄鉱石鉱山で1977年に開始された現実的な深層処分場環境における国際協力と現場実験の伝統を受け継ぐものである。現在行われている研究とPrototype Repository Project (PRP)での4つのワークパッケージ(WP)を図4-3に示す。

操業段階の試験の目的は以下の通りである。

- サイト調査段階における調査手法の検証
- モデルの検証
- 天然および人工バリアの機能の確認
- 処分技術のデモンストレーション

4番目のデモンストレーション目的のためには種々の要因に関して試験を行なう必要がある。これらの要因を満足するためにÄHRLにおいては以下の試験が実施されている（図4-3参照）。

- Prototype Repository
- Demonstration of Deposition Technology
- Canister Retrieval Test
- Backfill and Plug Test
- Long Term Test of Buffer Material (LOT Project)

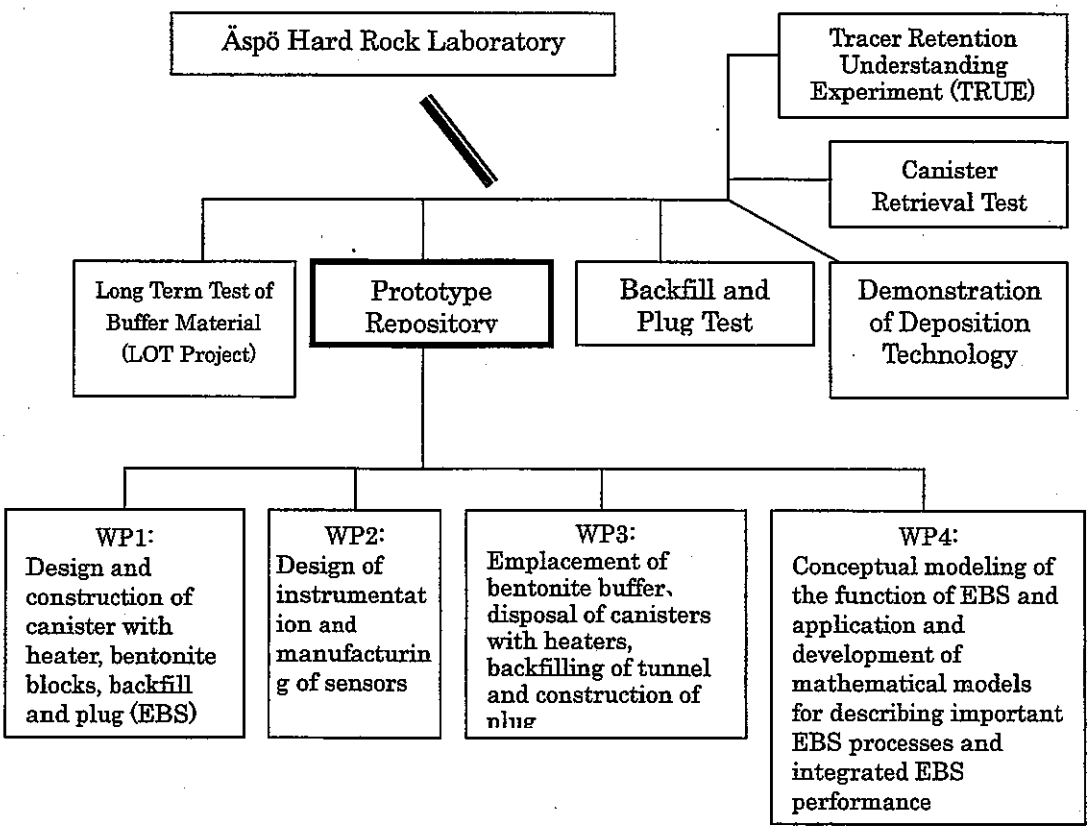

図 4-2　HRL 試験と Prototype Repository Project(PRP)の構成

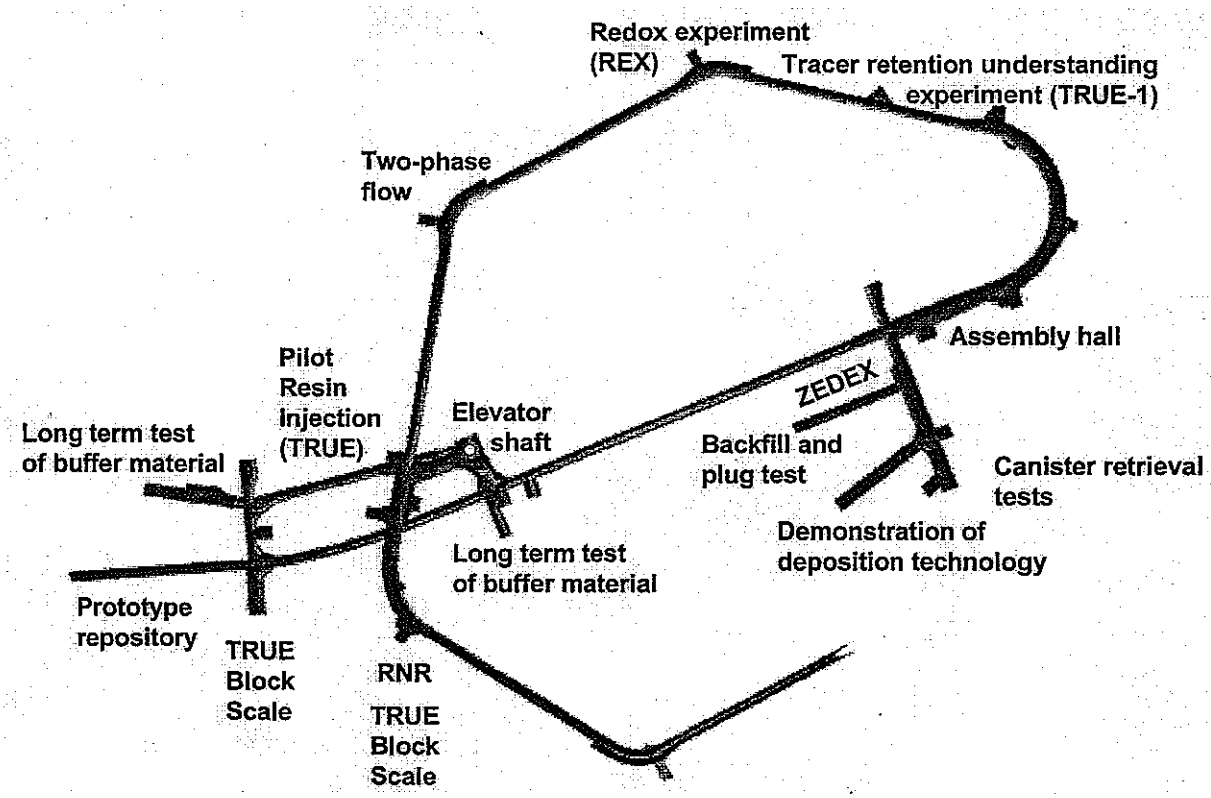

図 4-3　試験場のレイアウト

"Prototype Repository" は、実際の処分を模擬した実規模の試験であり、処分坑道内に６本の模擬処分を行なう。この試験の目的は、処分場の総合機能に関するデモンストレーションと解析モデルによる解析結果との比較を行なうことである。この試験には、処分坑道の構造モデル作成手法の確認、処分孔の掘削工法の確認、緩衝材・キャニスター・埋め戻し材の定置技術の確認、プラクの構築、計測機器の設置等が含まれている。

"Demonstration of Deposition technology" は、４本の実規模の模擬処分孔において実施される。この試験の目的は、実際の処分において必要な定置技術、定置装置等を開発および確証することである。そのために、この試験では、放射線を隔離するという条件のもとで緩衝材およびキャニスターを定置するための装置を実規模で製作する。

"Canister Retrieval Test" においては、２本の実規模の処分孔を使用し、再取り出しのため処分坑道の埋め戻しは行なわない。この試験の目的は、飽和した緩衝材の中からキャニスターを取り出す技術を確証することである。

"Backfill and Plug Test" においては、処分坑道の埋め戻しおよびプラグの構築が実施される。この試験の目的は、種々の埋め戻し材の比較、埋め戻しおよびプラグ構築技術の確認、および、埋め戻し材、プラグ、岩盤の総合機能に関する研究を実施することである。この試験は、"Prototype Repository" の一部を用いて実施される。

"Long Term Test of Buffer Material (LOT Project)" は、実際よりは小規模のサイズにおいて実施される試験である。この試験の目的は、人工バリアの長期の挙動について観測することである。

4.2 Prototype Repository Project の概要

4.2.1 試験の概要

本節では、これらの試験のうち、実規模で実施する連成試験である“Prototype Repository”についてその試験の詳細を記述する。

この試験の主な目的は以下の通りである。

- KBS-3 コンセプトの具現化
- 処分場のふるまいの観察とモデル（概念および理論）による予測との比較
- 工学的な基準と品質保証方法の開発、試験、デモンストレーション
- 処分場設計、建設手順の模擬
- 最低 20 年におよぶ長期のオペレーション
- 参加各機関のモデルに対する Confidence building

Prototype Repository は釜石粘土充填・熱負荷試験や FEBEX などと比べ、これまでに無い特徴として「設計、建設、操業までの一連の作業が実規模で行われること」、「ガスの挙動評価」、「化学、微生物の影響観察」等がある。また、図 4-4 に示すように処分坑道内に計 6 本のキャニスターを設置し、これらの相互作用等についての観察も行なう。各試験ピットでは図 4-5 に示すような形状のキャニスターおよびベントナイトブロックが設置される。岩盤とベントナイトブロックとの隙間にはベントナイトペレットが充填される。処分坑道は図 4-4 に示すように 2 つのセクションに区分けされており、セクション II の試験期間は約 5 年、セクション I の試験期間は約 20 年である。

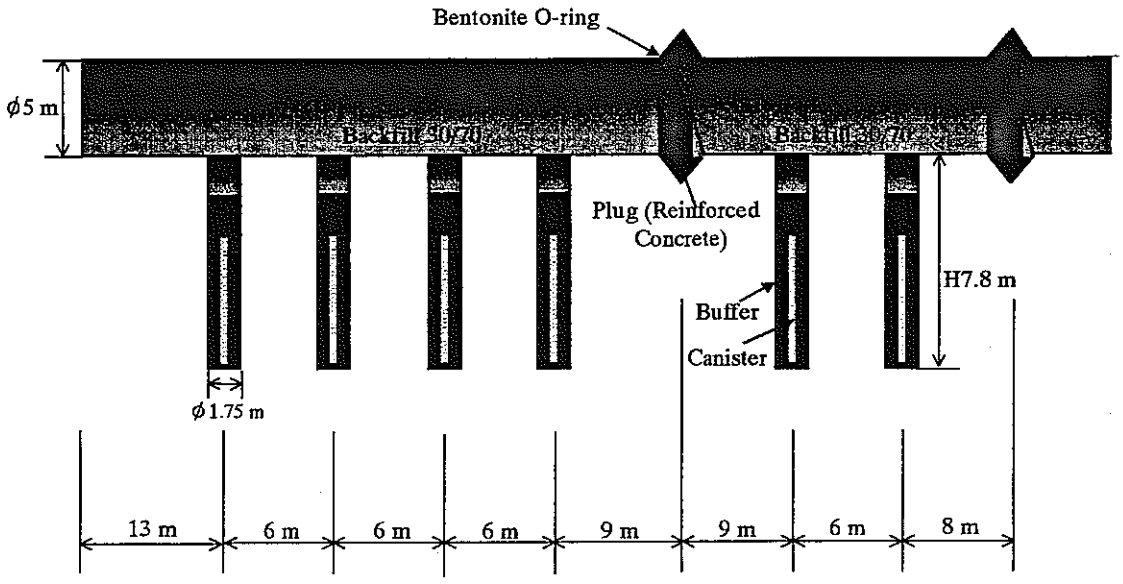

図 4-4　試験坑道の概要

キャニスターは、銅／炭素鋼製で長さ 4830mm、直径 1050mm、重量 21.4ton である。また、ヒーターは表面で温度が 100℃を越えない（設計温度 90℃）ように制御される。さらに、ヒーター

は温度の減少を考慮できるように設計されている。

キャニスターと岩盤との間には高密度に圧縮されたナトリウム型ベントナイト（MX-80）ブロックが充填される。隙間充填後の乾燥密度が一定となるように初期のベントナイトブロックは設計されており、その結果、キャニスターの上部および下部のベントナイトブロックの初期乾燥密度は 1.66g/cm^3、キャニスター周囲のベントナイトブロックの初期乾燥密度は 1.78g/cm^3 となっている。また、初期の含水比は 17%となっている。

試験坑道はベントナイトと砕石を用い原位置施工により埋め戻される。締固め層厚は 20cm で、35° の傾斜で原位置締固めが実施される。ベントナイトと砕石の混合率は 30：70 である。また、試験坑道では２つのコンクリートプラグが構築される。コンクリートプラグは 4.5MPa の水圧と 100kPa の埋め戻し材による膨潤圧に耐えるように設計される。

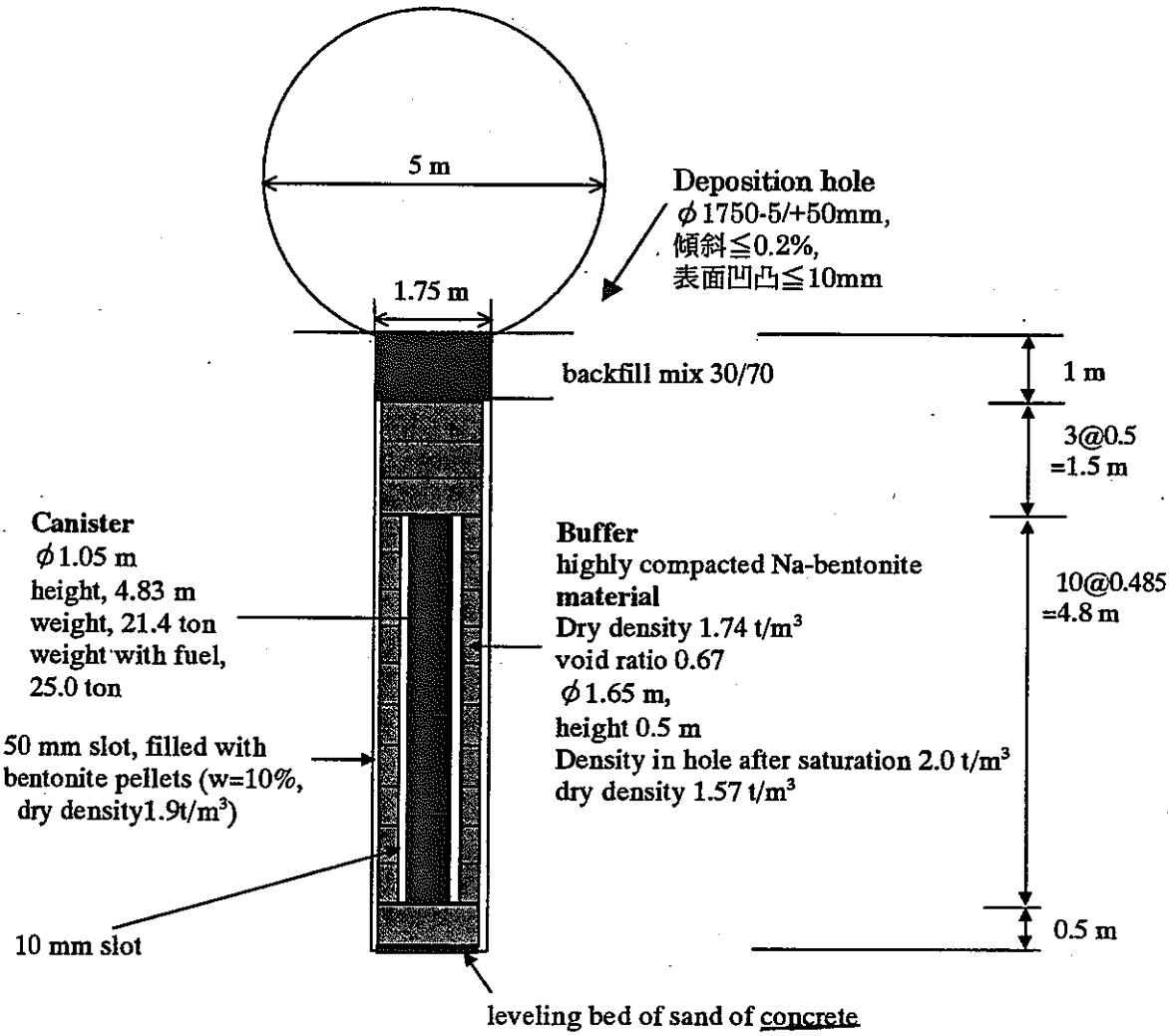

図 4-5　試験ピットの概要

4.2.2　計測機器

試験期間中は岩盤内、緩衝材内および埋め戻し材内において THM に関する種々の計測が実施される。また、ガス挙動、間隙水の化学変化、微生物活動等に関する調査も行われる。THM の挙動は適切な位置に設置された計測機器で計測される。エスポ地下研究施設は海底下であるため地下

水の塩濃度は 1.2%から 1.5%である。また、温度がヒーター近くで 90℃近くにまでなること、応力が 15MPa 程度、間隙水圧が 5MPa 程度と高いこと、および、試験期間が長期に渡ること等を考慮して計測機器の開発が行われた。計測機器の材質に関しては、ステンレス、インコネル（ニッケル 80%、クロミウム 14%、鉄 6%から成る高温、腐食に強い合金）、チタン、プラチナ、プラスチック等の多くの候補材料の中から、最終的に上記の試験環境を考慮してチタンを使用することとなった。表 4-1 には、計測機器による計測項目および数量を示す。

表 4-1　PRP で使用される計測機器の数量

計測項目	計測機器	個　数		
		Section I	Section II	計
温度	熱電対	113	72	185
	光ﾌｧｲﾊﾞｰ	16	10	26
圧力	振動弦式	56	35	91
	光ﾌｧｲﾊﾞｰ	56	35	91
間隙水圧	振動弦式	37	23	60
	光ﾌｧｲﾊﾞｰ	37	23	60
含水比	TDR	45	27	71
	湿度計	84	56	140
	ｻｲｸﾛﾒｰﾀ	50	24	74
計		493	304	797

温度は、T、J、K の各タイプの熱電対により計測される。また、光ファイバーシステム、抵抗式温度計等も使用される。これらの計測機器による計測範囲は 0～200℃である。計測機器は耐食性の材質で作られた外被やシースで保護され設置される。

圧力および間隙水圧は、油圧式の測定器により間接的に計測されるか、圧力計により直接的に計測される。圧力計には振動弦式（Vibrating wire）および電気抵抗式の両者が用いられる。圧力計の計測範囲は、間隙水圧が 0～5MPa、圧力が 0～15MPa である。また、圧力計は以下の温度に耐えうるように設計されている。

- 埋め戻し材内：0～40℃
- 緩衝材内　　：0～120℃

含水比の測定は、以下の方法で行われる。

- 電気容量式センサーによる相対湿度の測定
- TDR による体積含水率の測定
- サイクロメータによる相対湿度の測定
- 抵抗式センサーによる体積含水率の測定

サイクロメータは埋め戻し材内の含水比の測定に主として使用される。また、サイクロメータは緩衝材内においては緩衝材が飽和に近づいた時点で有効となる。各計測機器の測定範囲は以下の通りである。

- 電気容量式センサー　：0～100%（相対湿度）
- TDR　：0～100%（体積含水率）
- サイクロメータ　：95～100%（相対湿度）
- 抵抗式センサー　：0～100%（相対湿度）

また、これらの計測機器も圧力計と同様の温度に耐えうるように設計されている。さらに、圧力および間隙水圧にも以下のように対応している。

- 埋め戻し材内：0～40℃
- 緩衝材内　：0～120℃
- 圧力　：0～15MPa
- 間隙水圧　：0～5MPa

表 4-2 には使用される計測機器の一覧を示す。また、同表には各計測機器の製造元、あるいは、計測機器の適用性を検討し本試験へ提供した機関等も示している。

表 4-2　PRP で使用される各種計測機器の製造元あるいは提供元

測定項目	測定手法	製造元	国
温度	振動弦式	Geokon	アメリカ
	熱電対	Roctest	カナダ
		Geokon	アメリカ
		Pentronic	スウェーデン
		Glötzl	ドイツ
		Fisher-Rosemount	スウェーデン
		BICC Thermoheat	イギリス
	抵抗式温度計	Rotronic	スイス
		Glötzl	ドイツ
	光ﾌｧｲﾊﾞｰ	Roctest	カナダ
		BICC Thermoheat	イギリス
		York Sensors	イギリス
圧力および間隙水圧	油圧式	Glötzl	ドイツ
	電気抵抗式	Geokon	アメリカ
		Kulite	オランダ
		Roctest	カナダ
	振動弦式	Geokon	アメリカ
		Roctest	カナダ
		Glötzl	ドイツ
		Geonor	ノルウェー
	光ﾌｧｲﾊﾞｰ	Glötzl	ドイツ
		Roctest	カナダ
含水比	TDR	Nagra	スイス
		Environmental Sensors	カナダ
		Soilmoisture Equipment	アメリカ
	電気容量式	Rotronic	スイス
		Vaisala	フィンランド
	ｻｲｸﾛﾒｰﾀ	Wescor	アメリカ
	抵抗式	Clay Technology and LTH	スウェーデン

4.3 検討内容

今年度、Prototype Repository Project（PRP）に対して実施した検討内容は以下の通りである。

1)使用センサーに対するレビュー
2)THM 解析コードの概要紹介
3)モデリングの予定作成

上記 1)および 2)に関してレポートを作成し、SKB に提出した。作成した資料を添付資料に示す。使用センサーに関しては、特に、緩衝材中の水分測定のセンサーに関して、釜石試験で使用したセンサーの概要を説明した。釜石試験では水分計として熱電対サイクロメータ（PST-55、WESCOR）および湿度計（HMP233H、VAISALA）を使用しており、その耐久性について示した。

解析コードに関しては、THAMES における基礎式の展開を示し、THAMES に関してこれまで実施してきた Validation の結果を示した。Validation は、加圧浸潤試験、緩衝材大型試験設備（BIG-BEN）における熱-水-応力連成試験の解析評価結果、釜石原位置試験場における粘土充填・熱負荷試験の解析評価結果を報告した。

解析のスケジュール案は表 4-3 の通りである。最初に PartA として、試験孔１本に対しての解析を行なう。解析は軸対称で実施し、対象は Buffer、Backfill、Canister、Concrete、Rock である。解析領域は水平方向が 10m で、鉛直方向は処分坑道底部から上下にそれぞれ 25m である。図 4-6 には解析のモデル図を示す。また、図 4-7 には有限要素メッシュを示す。引き続き、３次元解析を実施する。この場合、２本の試験孔を対象にモデル化し、２本の試験孔の離間距離は実際のサイズに合わせる。図 4-8 に解析モデル図を示す。解析は試験坑道に沿った半断面で実施する。

PRP における解析では緩衝材と岩盤との隙間をどのようにモデル化するかが重要である。したがって、ここでは図 4-9 に示すような解析ケースを設定しモデル化の比較を行なう。実際はケース３に示すように隙間にはペレットが充填されるが、このようなケースを有限要素法で表現するのは難しい。そこで、ケース１およびケース２のような解析ケースを設定する。このように取り扱うことにより、実際の再冠水時間は解析結果の幅の中に入ってくるものと推察される。

表 4-3　解析スケジュール

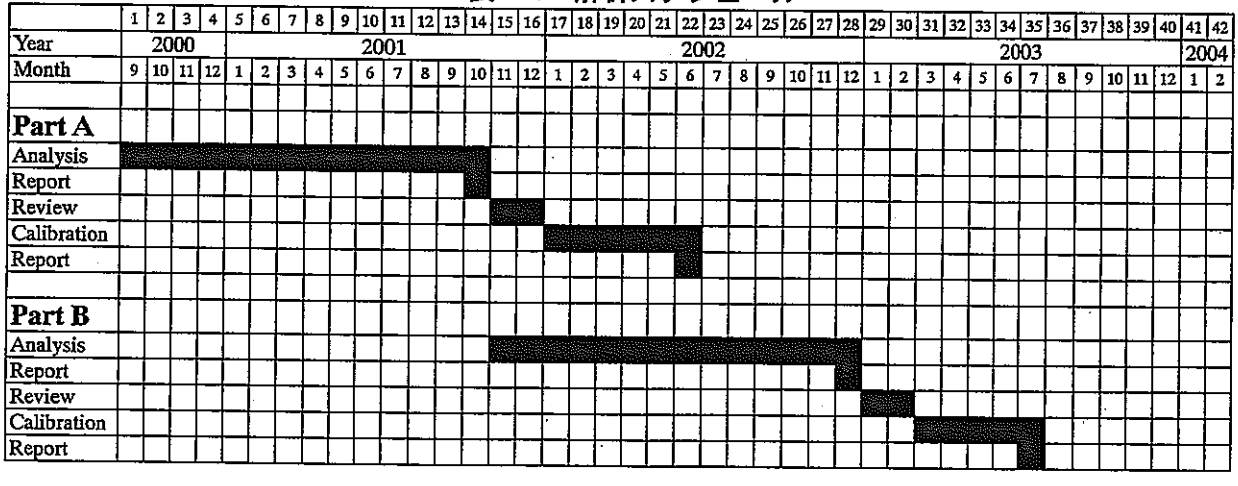

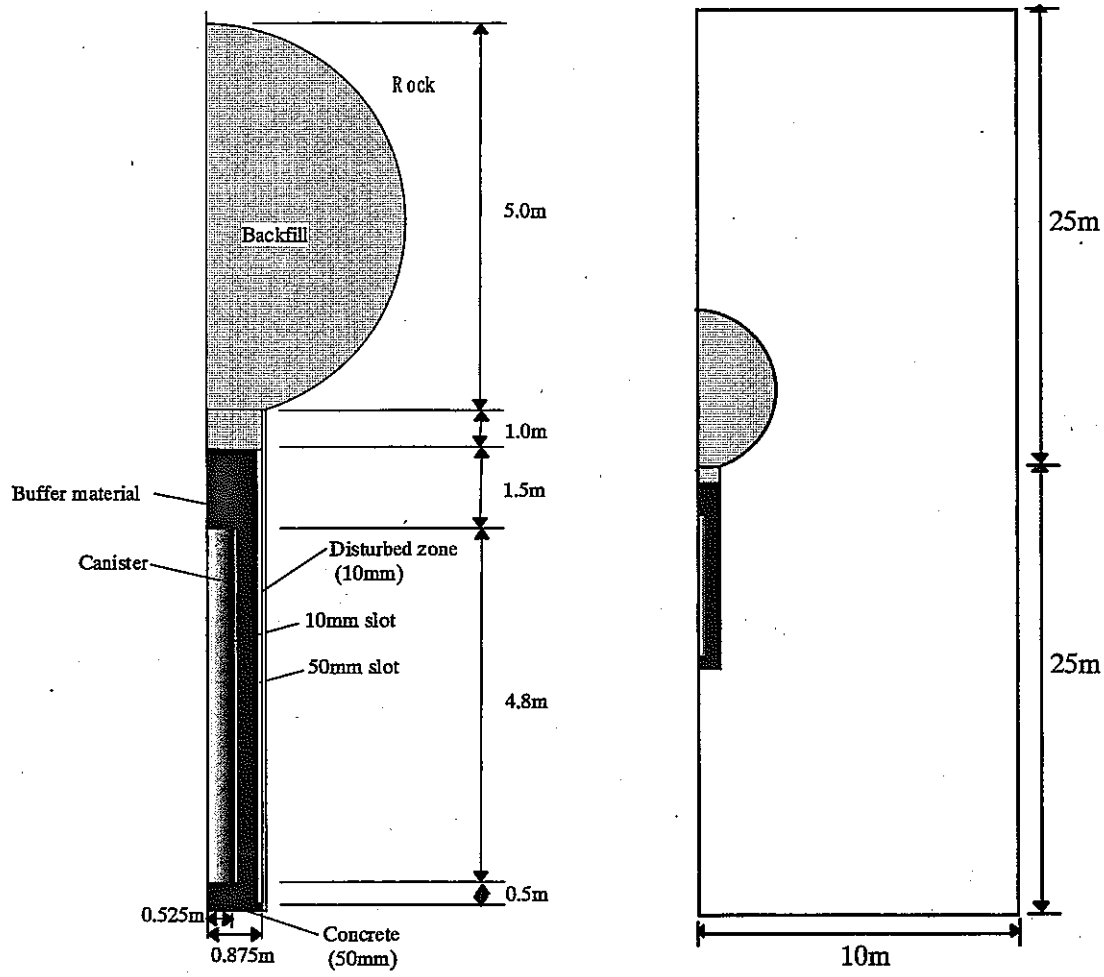

図 4-6　解析モデル概要図（PartA）

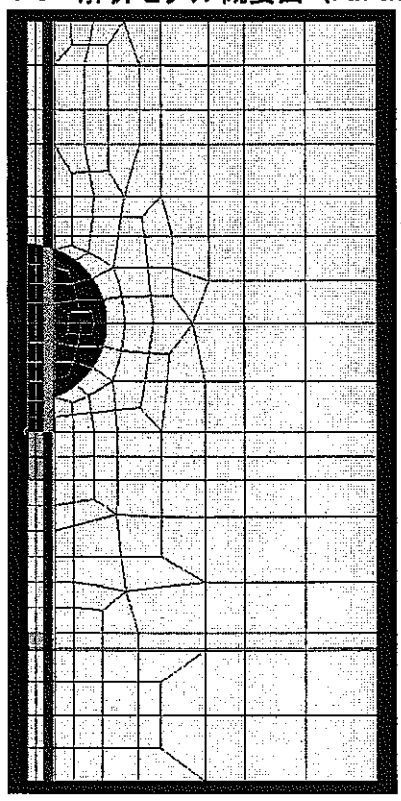

図 4-7　有限要素メッシュ図（PartA）

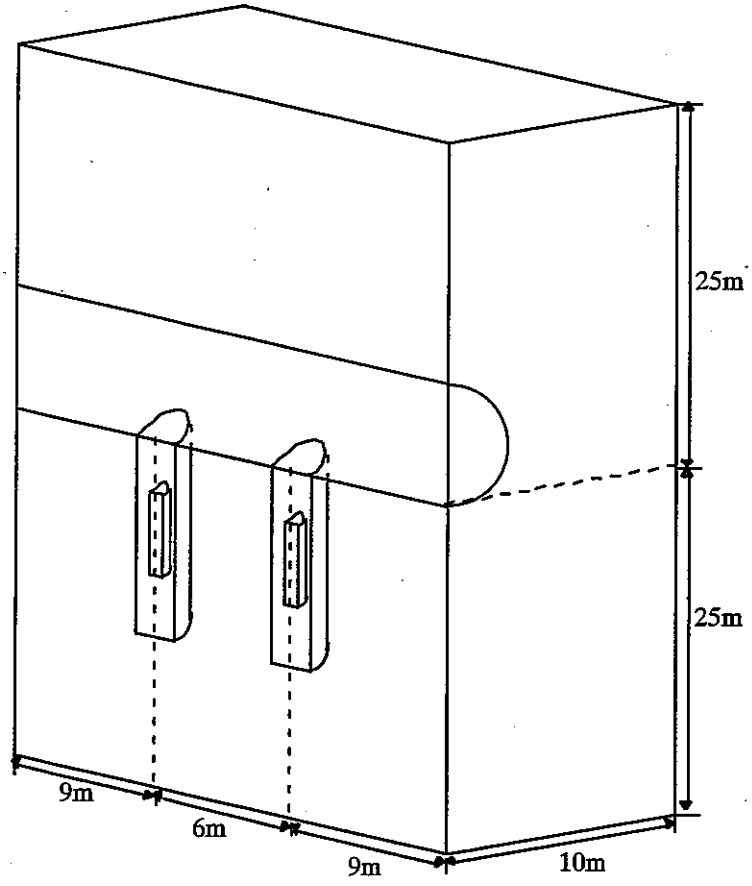

図 4-8　解析モデル概要図（PartB）

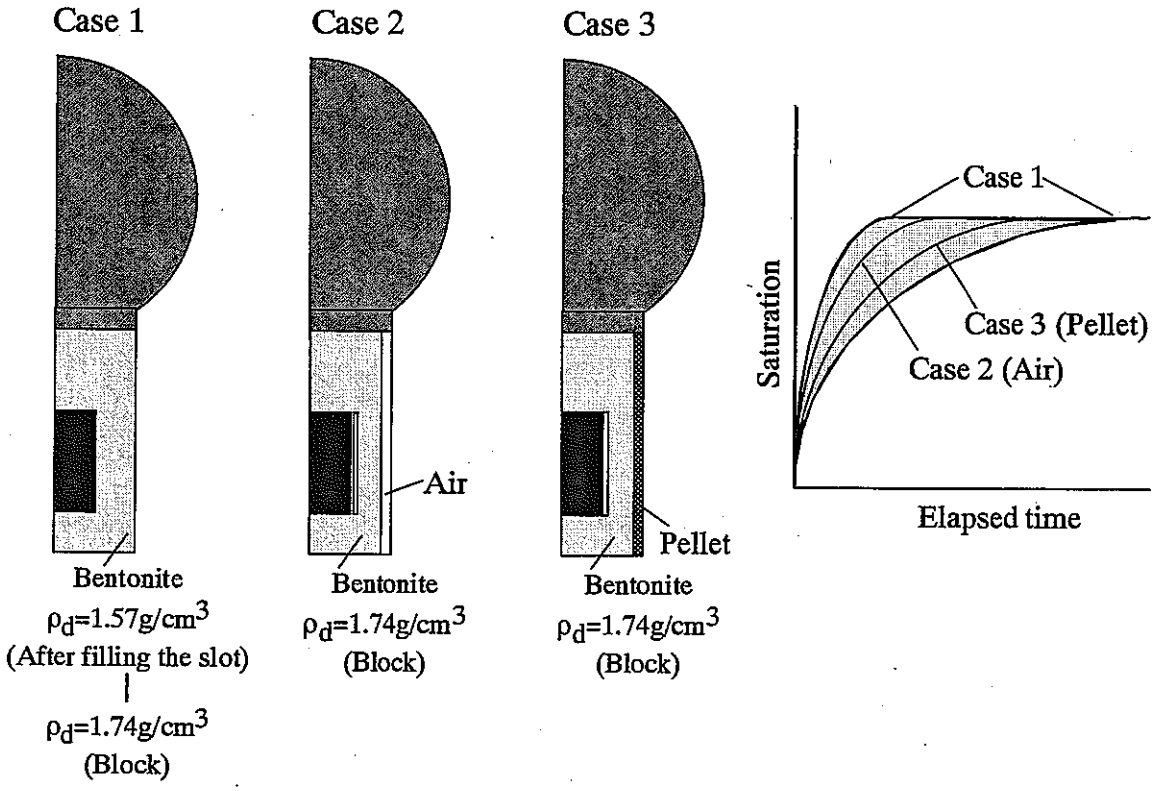

図 4-9　隙間の取り扱い方法に関する検討

5. 人工バリアにおける連成挙動の評価

5.1 DECOVALEX III の概要

連成現象についてのモデルの妥当性評価については、国際共同研究プロジェクト DECOVALEX III に参加し、解析コードを各 TASK に適用することで検討した。DECOVALEX III では DECOVALEX II 同様原位置試験の解析が実施される。今回解析が実施される原位置試験は、スイスのグリムゼルにおいて実施されている FEBEX と、アメリカのユッカマウンテンにおいて実施されているヒーターテストの２ケースであり、それぞれ、TASK 1、TASK 2 と定義されている。また、TASK 3 として PA (Performance Assessment) としての THM に関するベンチマークテストを実施することとなっており、３ケース設定されている。BMT1 は re-saturation に関して、BMT2 は up-scaling に関して、BMT3 は glaciation に関してのタスクである。また、TASK 4 は PA の専門家によるレビューである。各タスクに関して提案された問題は以下の通りとなっている。また、プロジェクト全体のスケジュール案は表 5-1 のようになっている。

TASK 1　The FEBEX in situ experiment
- Part A: Hydro-mechanical modelling of the rock
- Part B: Thermo-hydro-mechanical analysis of the bentonite
- Part C: Thermo-hydro-mechanical analysis of the rock

TASK 2　The Yucca Mountain Drift Scale Heater Test
- Part A: Thermal-hydrologic analysis
- Part B: Thermal-mechanical analysis
- Part C: T-H-M-C analysis

TASK 3　BMTs
- BMT1　THM coupling and near field safety
- BMT2　Upscaling of THM Process
- BMT3　Glaciation

TASK 4　THM/PA Forum

表 5-1　DECOVALEX III のスケジュール（○は会議開催予定）

Task	1999						2000												2001												2002											
	7	8	9	10	11	12	1	2	3	4	5	6	7	8	9	10	11	12	1	2	3	4	5	6	7	8	9	10	11	12	1	2	3	4	5	6	7	8	9	10	11	12
1						○													○				○										○									
2						○													○														○									
3 BMT1										○													○																			
3 BMT2																							○																			
3 BMT3																																										
4																																									
WS				○								○							○									○							○							○

参加機関は DECOVALEX III 開始時点において DECOVALEX II の時から２機関増えていた。一つは DOE（USA）で、もう一つは NRC（USA）である。NRC は DECOVALEX I には参加しており、今回復帰した。また、2001 年よりさらに２機関追加された。CEA（France）および BGR（Germany）である。したがって、現時点での参加機関は９カ国、14 機関である。また、各機関の参加予定タスクが以下のように報告された。日本チームは、TASK 1、TASK 2、BMT1、BMT2 に参加することとしている。

FOs: CNSC (Canadian Nuclear Safety Commission、 Canada)
AECB (Atomic Energy Control Board、 Canada)が組織名変更
OPG (Ontario Power Generation、 Canada)
ANDRA (Agence Nationale Pour la Gestion des Déchets Radioactifs、 France)
IPSN (Institut de Protection et de Sûreté Nucléaire、 France)
CEA (Commissariat à l'Énergie Atomique、 France)
ENRESA (Empresa Nacional de Residoos Radioactivds, S.A.、 Spain)
Nirex (United Kingdom Nirex、 UK)
US DOE (United States Department of Energy、 USA)
US NRC (United States Nuclear Regulatory Commission、 USA)
JNC (Japan Nuclear Cycle Development Institute、 Japan)
STUK (Finnish Center for Radiation and Nuclear Safety、 Finland)
SKI (Swedish Nuclear Power Inspectorate、 Sweden)
SKB (Swedish Nuclear Fuel and Waste Management、 Sweden)
BGR (Bundesanstalt fur Geowissenschaften und Rohstoffe、 Germany)

TASK 1

Funding Organization	Research Team
CNCS	McGill University、 Montreal
ANDRA	G3S Ecole de Polytechnique & Ecole des Mines
IPSN	Ecole des Mines、 Paris
US DOE	Sandia National Laboratory
US NRC	Center for Nuclear Waste Regulatory Analyses

JNC	Kyoto University & Hazama Corporation
STUK	Lab. of Theoretical Mechanics、 Techn Univ Helsinki
SKI	LBNL、 Berkeley
SKB	Clay Technology

TASK 2

Funding Organization	Research Team
US DOE	URS Greniner Woodward Clyde Federal Services
ENRESA	UPC
JNC	JNC
US NRC	CNWRA
SKI	LBNL

TASK 3 (BMT1)

Funding Organization	Research Team
CNSC	CNSC
ANDRA	INERES、 Nancy
IPSN	Wait for result of applied EU funding
US NRC	Center for Nuclear Waste Regulatory Analyses
JNC	Kyoto University & Hazama Corporation
STUK	Lab of Theoretical Mechanics、 Tech Univ Helsinki
SKI	LBNL、 Berkeley
SKB	Clay Technology

TASK 3 (BMT2)

Funding Organization	Research Team
OPG	AECL
ANDRA	INERES
ENRESA	UPV
Nirex	University of Birmingham
US DOE	LBNL、 Berkeley
US NRC	Center for Nuclear Waste Regulatory Analyses
JNC	Kyoto University & Hazama Corporation
STUK	VTT
SKI	KTH、 Engineering Geology

TASK 3 (BMT3)

Funding Organization	Research Team
CNSC	CNSC
OPG	AECL
Nirex	University of Edinburgh
STUK	Not decided
SKB	Chalmers Technical University

今年度は、2回 Workshop が開催された。1回目は6月にスイスで、2回目は1月に日本で開催された。また、各タスクにおける Task Force Group Meeting は適時実施されており、今年度日本からは4月にカナダで開催された BMT1 のミーティングに参加した。

以降では、弊社が担当している各タスクの概要および検討結果を示す。

5.2 Task 1 の概要

5.2.1 FEBEX 試験の概要

FEBEX (Full-scale Engineered Barriers EXperiment) は ENRESA (Spain) および NAGRA (Switzerland) のもと3カ国 (Spain、France、Germany)、7機関の協力により実施されているプロジェクトであり、実規模原位置試験および実規模室内試験から構成されている。試験の形態は図 5-1 に示すようなスペインの結晶質岩における処分形態に乗っ取って実施されている。すなわち、キャニスターは坑道内に水平に定置されており、キャニスターの周囲は高密度に圧縮されたベントナイトブロックで埋め戻されている。実規模室内試験は“Mock-Up test”と呼ばれており、マドリッドの CIEMAT において実施されている (図 5-2 参照)。一方、実規模原位置試験はスイスのグリムゼルテストサイト (Grimsel Test Site、GTS) において、新規に掘削された試験坑道において実施されている (図 5-3 参照)。

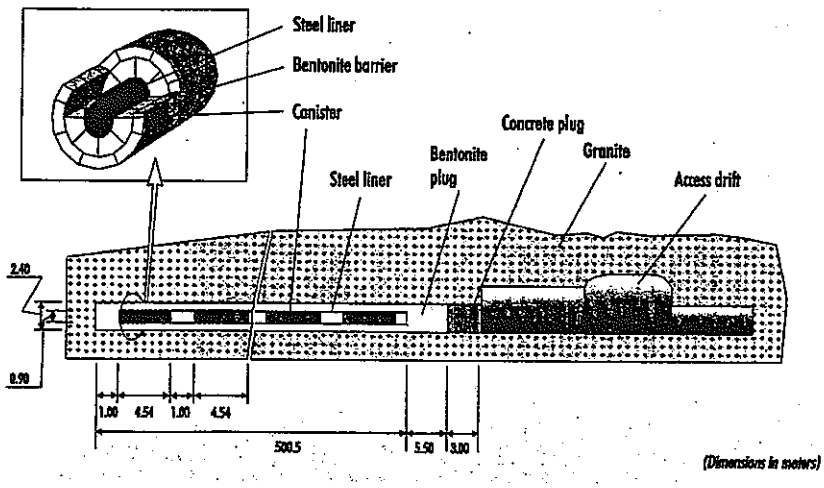

図 5-1 スペインにおける処分形態の概要 (結晶質岩系)

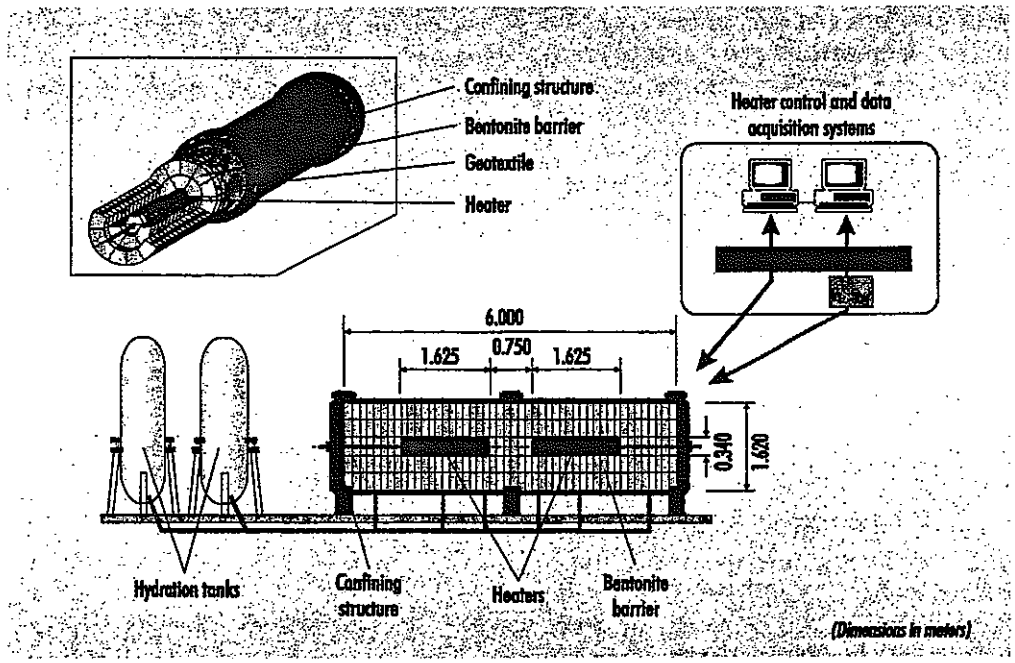

図 5-2　実規模室内試験の概要

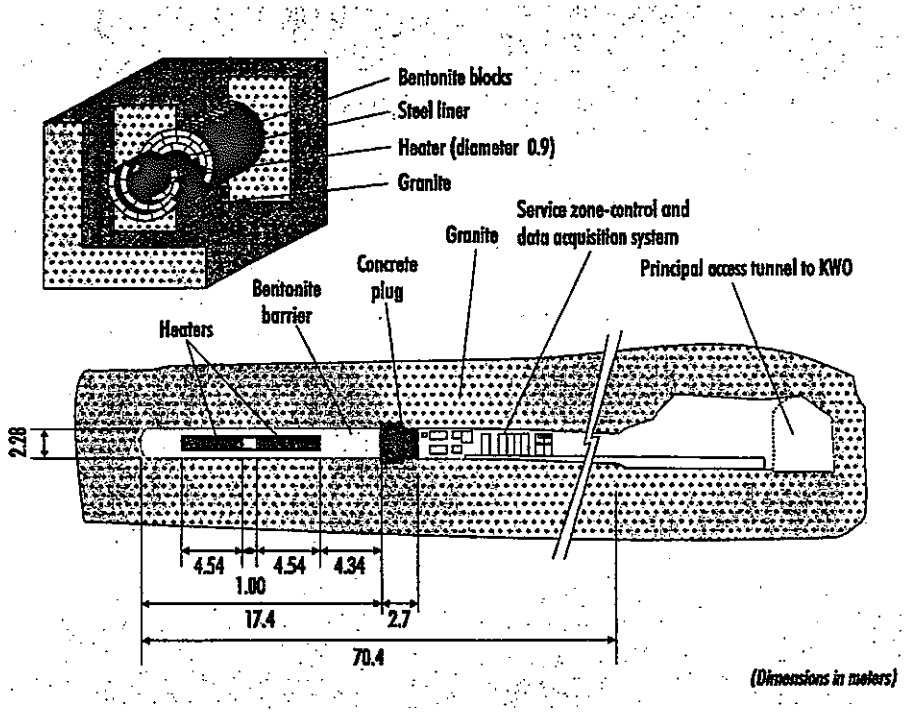

図 5-3　実規模原位置試験の概要

これらの試験の目的は以下の通りである。

・人工バリアシステムの実現性のデモンストレーション

・ニアフィールドにおける熱-水-応力連成現象の研究

・ニアフィールドにおける熱-水-地球化学連成現象の研究

また、ベントナイトはスペイン産であり、その主要物性は以下の通りである。

・モンモリロナイト含有率：88%～96%

・液性限界：98%～106%

・真比重：2.67～2.75

・膨潤圧：4～6MPa（乾燥密度 1.60g/cm³）

・飽和透水係数：4.2×10^{-14}～7.6×10^{-14}m/s（乾燥密度 1.60g/cm³）

以下に、各試験の概要および計測項目等について示す。

5.2.2 実規模室内試験の概要

本試験では、原位置試験と異なり周辺岩盤の不均質性等は考慮できないが、周囲からの浸潤をコントロールすることにより境界条件を原位置試験よりは明確に出来るのが特徴である。本試験結果は解析コードの検証（verification）に使用される。試験装置の概要を図 5-4 に示す。試験は原位置試験と同じ構成で実施されている。キャニスターを模擬した電気ヒーターは２個であり、その周囲に厚さ 0.64m のベントナイトが定置されている。試験装置内空の直径は 1.615m、長さは 6.0m であり、装置は厚さ 7.0cm の炭素鋼および厚さ 0.5cm のステンレスで製作されている。

加熱・浸潤試験は 1997 年 2 月から開始されており、約 3 年間継続される予定である。試験中は Heater Control System（HCS）により温度は自動制御されており、設置された約 500 個の計測機器により自動計測がなされている。計測されたデータは Data Acquisition System（DAS）により収集・整理されている。温度はヒーター表面で 100℃となるように制御されている。また、図 5-5 には人工バリア部分の断面図を示す。左側がヒーターのある部分で、右側がヒーターの無い部分である。製作されたベントナイトブロックは図に示す通りの４種類である。ベントナイトブロックの設計乾燥密度は 1.77g/cm³ である。この密度は、ベントナイト等の設置時に必要な隙間部分がベントナイト膨潤後に埋まった後に、ベントナイトの乾燥密度が 1.65g/cm³ となるように設定されている。また、ベントナイトの初期含水比は 12.5%から 15.5%の間に設定されている。

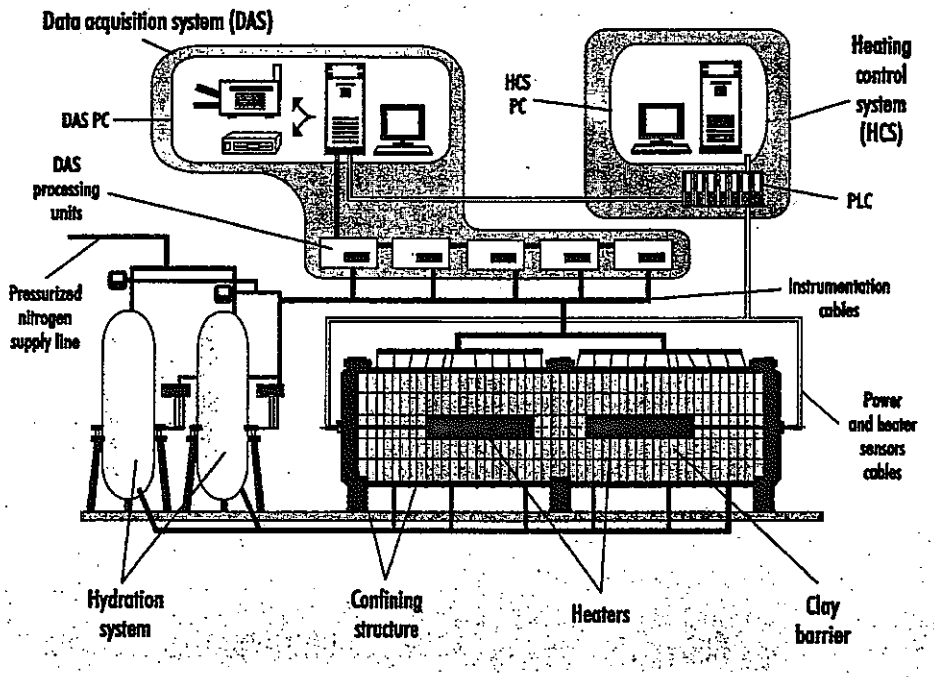

図 5-4 実規模室内試験の詳細図

計測条件が、高圧力下（≧5MPa）、高温下（100℃近く）であることから、計測機器はこれらを考慮し選択された。表 5-2 に設置された計測機器のタイプ、数量および設置箇所を示す。設置された計測機器は全部で 507 個であり、これらのうち大半は自動で計測が実施され、19 個（変形に関する計測機器）のみ手動で計測が実施されている。

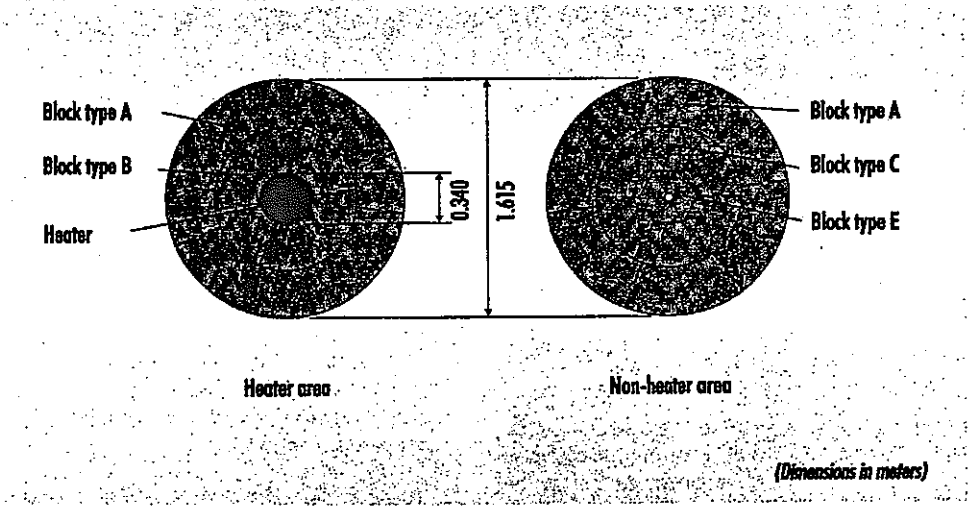

図 5-5　人工バリア部分の断面図

表 5-2　実規模室内試験装置内に設置された計測機器

ﾊﾟﾗﾒｰﾀ	計測機器	設置箇所			計
		ﾍﾞﾝﾄﾅｲﾄ	CS*	外部	
温度	RTD Pt100	328	20		348
室温	RTD Pt100			1	1
注入水圧					
ﾏﾉﾒｰﾀ	DIGIBAR II			1	1
水圧	DRUCK 1400PTX		2		2
注入水量	MVD 2510			2	2
圧力					
周方向	KULITE BG0234	14			14
接線方向	KULITE BG0234	14			14
軸方向	KULITE BG0234	22			22
間隙水圧	KULITE HKM375	20			20
相対湿度・温度	VAISALA HMP233	40			40
変位（ひずみ計）	HBM		19		19
PLC 値					
温度	RTD Pt100			18	18
平均温度	計算値			2	2
出力（電力）	計算値			2	2
DC 出力				2	2
計		438	41	28	507

CS：Confining Structure（図 5-4 参照）

加熱・浸潤試験終了後、試験装置は解体され、人工バリアの抜取、検査およびサンプリングが実施される。

5.2.3　実規模原位置試験の概要

実規模原位置は GTS の地下実験場の北部に新規に掘削された坑道において実施されている（図

5-6 参照)。試験坑道内の配置は図 5-7 に示す通りとなっており、坑道長は 70.4m、坑道径は 2.28m である。ヒーターは２個設置されており、鋼製のライナーで支持されている。ヒーターは実際のキャニスターと同サイズである。ヒーターの仕様は以下の通りである。

・材質：炭素鋼
・外径：0.90m
・長さ：4.54m
・重量：11ton

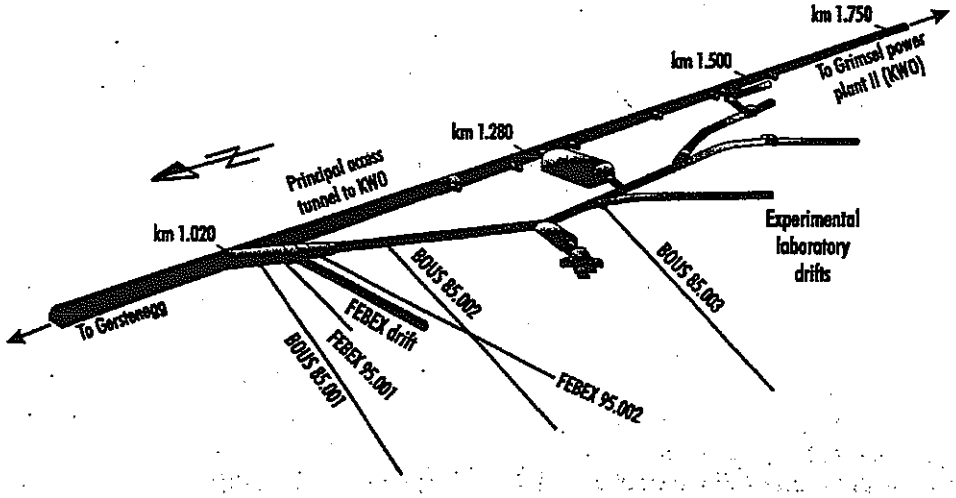

図 5-6　グリムゼル地下試験場

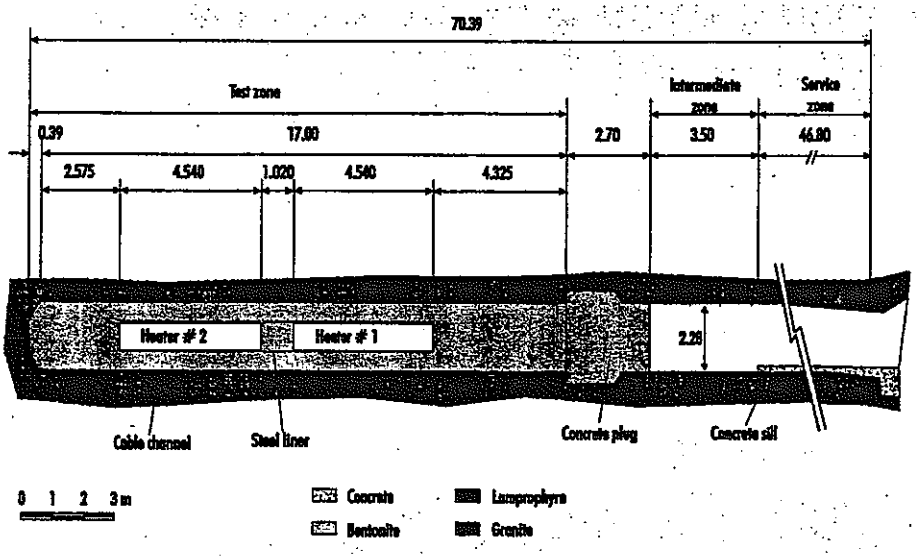

図 5-7　実規模原位置試験の詳細図

緩衝材としては高密度に圧縮されたベントナイトが用いられている。ベントナイトブロックは平均含水比 14.4%、平均乾燥密度 1.70g/cm^3 で製作されている。本仕様のもとでは、隙間充填後の緩衝材の乾燥密度は 1.60g/cm^3 となる。

試験は緩衝材の最高温度が 100℃となるように制御され実施されている。人工バリア内および周辺岩盤内には計 632 個の計測機器が設置されている。表 5-3 には設置された計測機器の一覧を示す。図 5-8 には人工バリア内において計測機器が設置された断面を示す。また、図 5-9 には断

面 F1 における計測機器の配置を示す。図 5-10 には周辺岩盤内に掘削されたボアホール内の計測機器の配置を示す。ここで、図 5-9 および図 5-10 に示す計測機器番号の意味は以下の通りである。

AA-BBn-CC

AA：計測機器の種類（表 5-3 参照）

BB：計測機器の設置位置（人工バリア内 or 岩盤内）

n：各設置断面あるいは各ボアホールの番号

CC：各設置断面あるいは各ボアホールの計測機器の番号

また、図 5-11 にはベントナイトブロックおよび鋼製ライナーの設置状況を、図 5-12 にはヒーターの設置状況を示す。

表 5-3　実規模原位置試験において使用された計測機器一覧

ﾊﾟﾗﾒｰﾀ	計測機器の形式	設置箇所				計
		岩盤	ﾍﾞﾝﾄﾅｲﾄ	ﾋｰﾀｰ	外部	
温度	熱電対	62	91	36		189
ﾎﾞｱﾎｰﾙ内の圧力	振動弦式	4				4
岩盤表面の圧力	振動弦式	30				30
ﾋｰﾀｰ表面の圧力	振動弦式		6			6
ﾎﾞｱﾎｰﾙ内の水圧	Piezoresistive	62				62
ﾎﾞｱﾎｰﾙ内のﾊﾟｯｶｰ圧	Piezoresistive	62				62
ﾍﾞﾝﾄﾅｲﾄ内の間隙水圧	Vibrating wire		52			52
含水比	電気容量式		58		1	59
含水比	ｻｲｸﾛﾒｰﾀ	28	48			76
含水比	TDR	4	20			24
岩盤内の伸張	振動弦式	2×3				6
ﾋｰﾀｰの変位	振動弦式		9			9
ﾍﾞﾝﾄﾅｲﾄの膨張	振動弦式		8			8
ﾍﾞﾝﾄﾅｲﾄ内の変位	ﾎﾟﾃﾝｼｵﾒｰﾀ（電位差計）		2×3			6
傾斜	LVDT		6×2			12
ｸﾗｯｸﾒｰﾀ	LVDT	1×3				3
ﾍﾞﾝﾄﾅｲﾄ内のｶﾞｽ圧	Magnetic		4			4
ｶﾞｽﾌﾛｰ	手動測定		6			6
大気圧	Piezoresistive				1	1
ﾍﾞﾝﾁﾚｰｼｮﾝ時の空気速度	Hot air				1	1
抵抗器の強度	Electric converter				6	6
抵抗器のﾎﾞﾙﾄ数	Electric converter				6	6
計		261	320	36	15	632

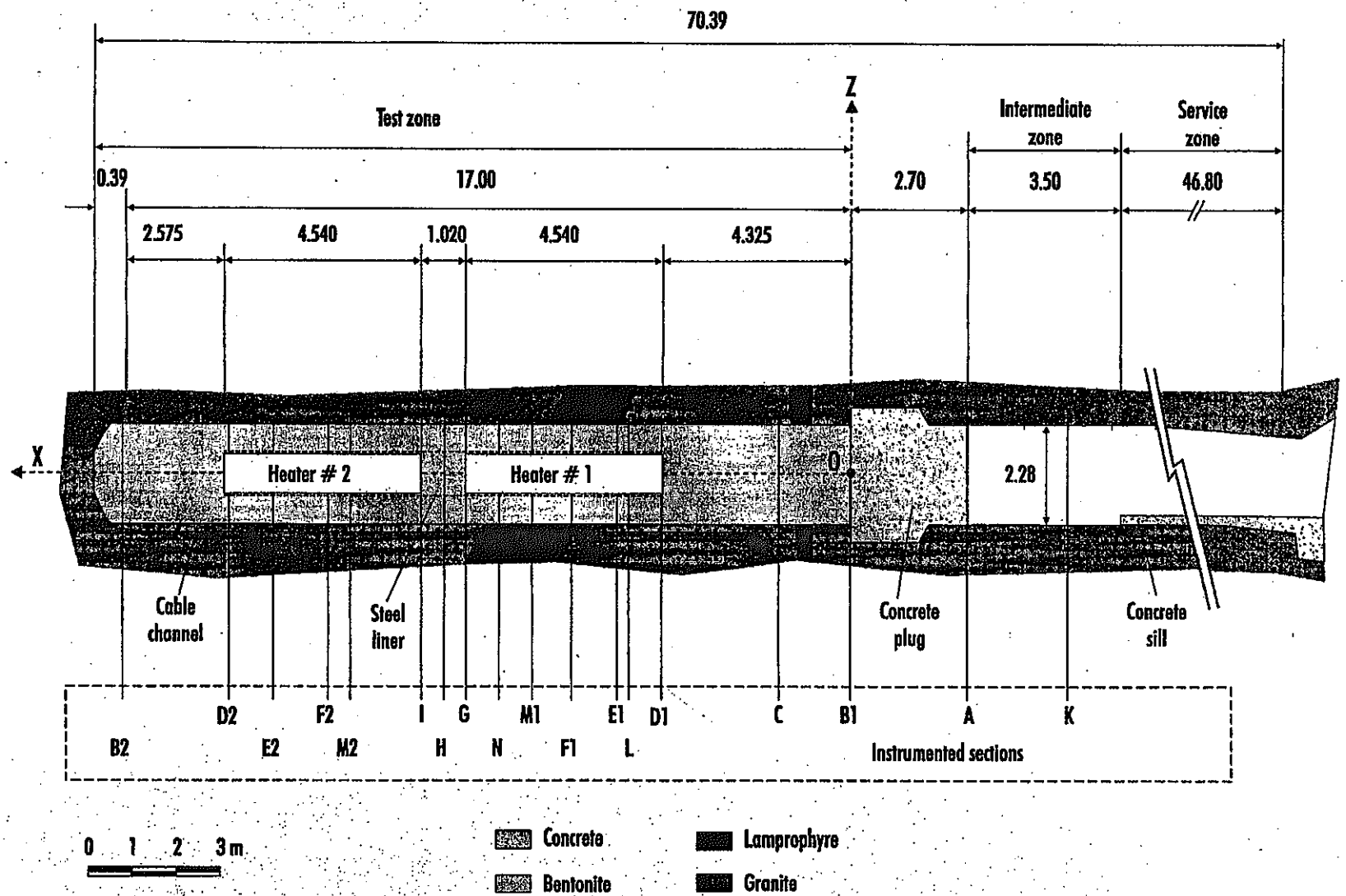

図 5-8　人工バリア内における計測機器設置断面

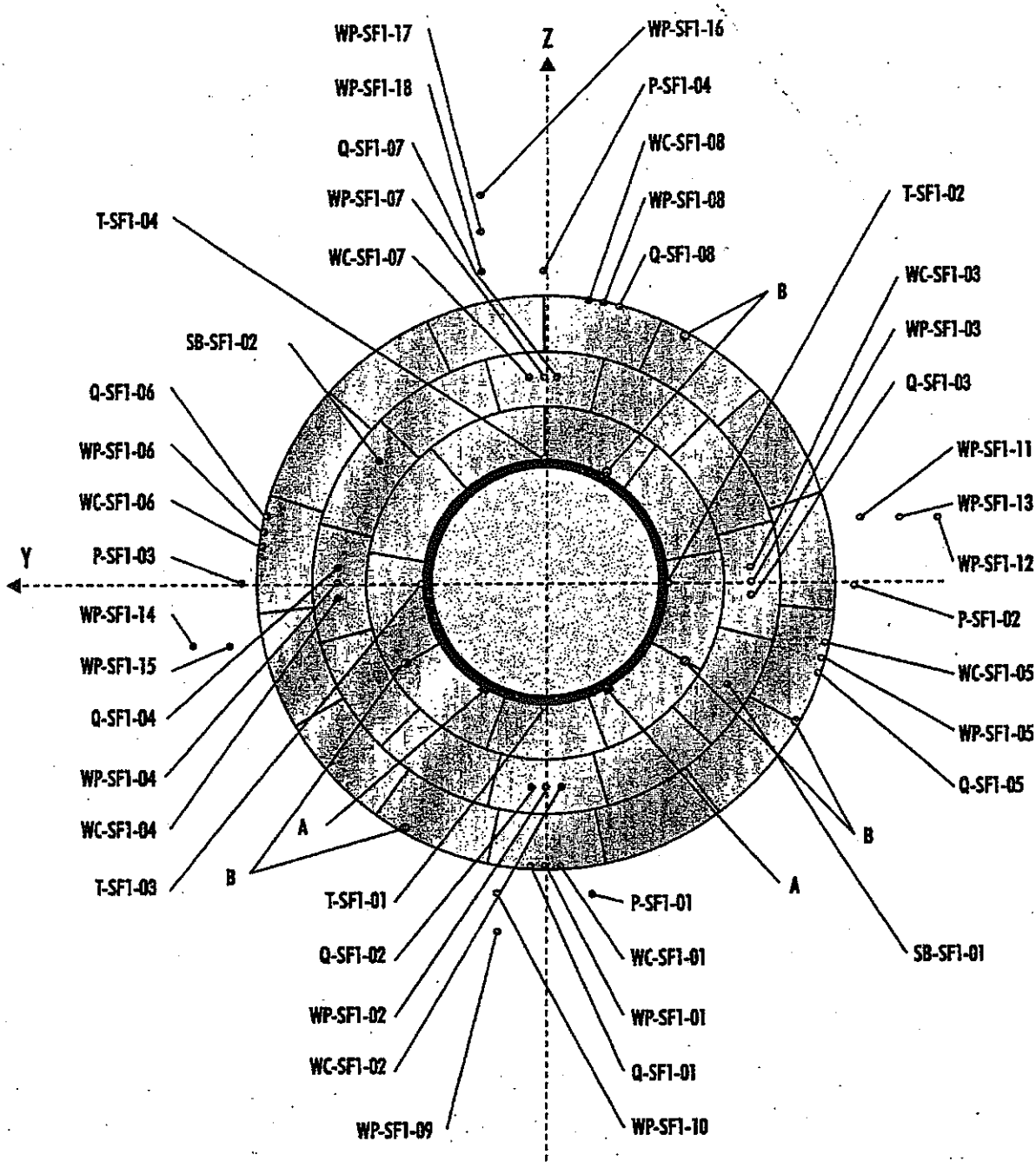

図 5-9　人工バリア内断面 F1 における計測機器設置位置

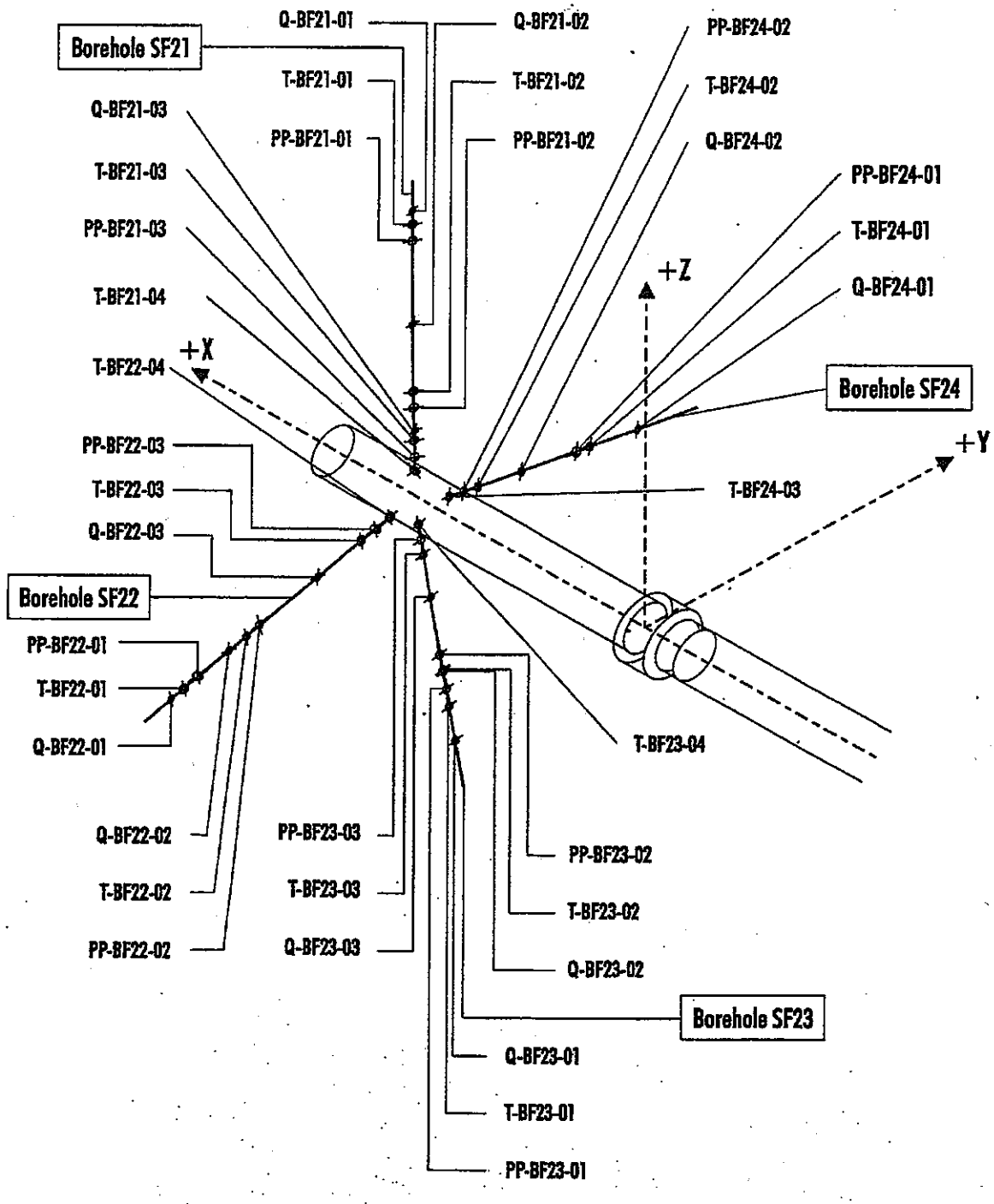

図 5-10　岩盤内における計測機器の設置位置

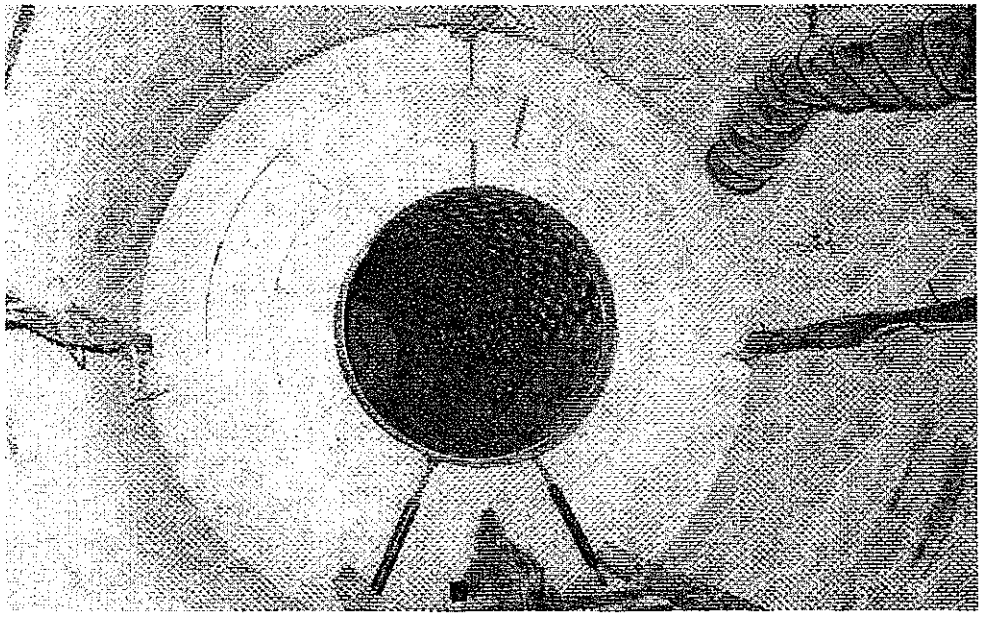

図 5-11　ベントナイトブロックおよび鋼製ライナーの設置状況

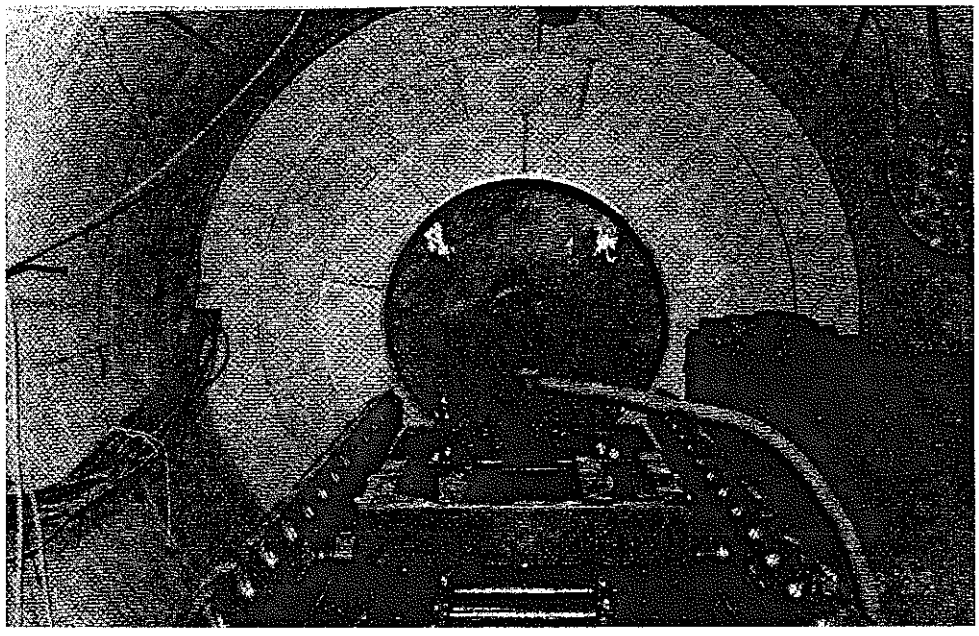

図 5-12　ヒーターの設置状況

5.2.4　解析の概要

(1)水理解析による坑道掘削の解析

DECOVALEX III では Task 1 として FEBEX における原位置試験の解析を実施する。まず、Part A として、試験坑道掘削の解析を行なった。ここでは、最初に実施した水理解析の結果を示す。図 5-13 に解析モデルの概要を示す。試験坑道断面に平行な面は 50m×50m とし、坑道奥行き方向には 150m とした。また、図 5-14 には解析モデルの平面図および断面図を示す。座標軸は東方向を X 軸、北方向を Y 軸、鉛直上向きを Z 軸とした。また、試験坑道の長さは 71.4m である。解析による出力は、試験坑道に平行に掘削されている試錐孔 FEBEX95.002 の観測点 P3 および P4 における間隙水圧の経時変化、試験坑道奥部（54.0-71.4m）における湧水量の経時変化、掘削開始から

100 日後の試験坑道奥部（54.0-71.4m）における湧水量である。また、図 5-15 には解析に用いた有限要素メッシュを示す。掘削は試験坑道部のメッシュを順次除去していき、坑道壁面部に対応する節点の間隙水圧をゼロに固定することにより表現した。図 5-16 には実際の掘削ステップと解析に用いた掘削ステップを示す。

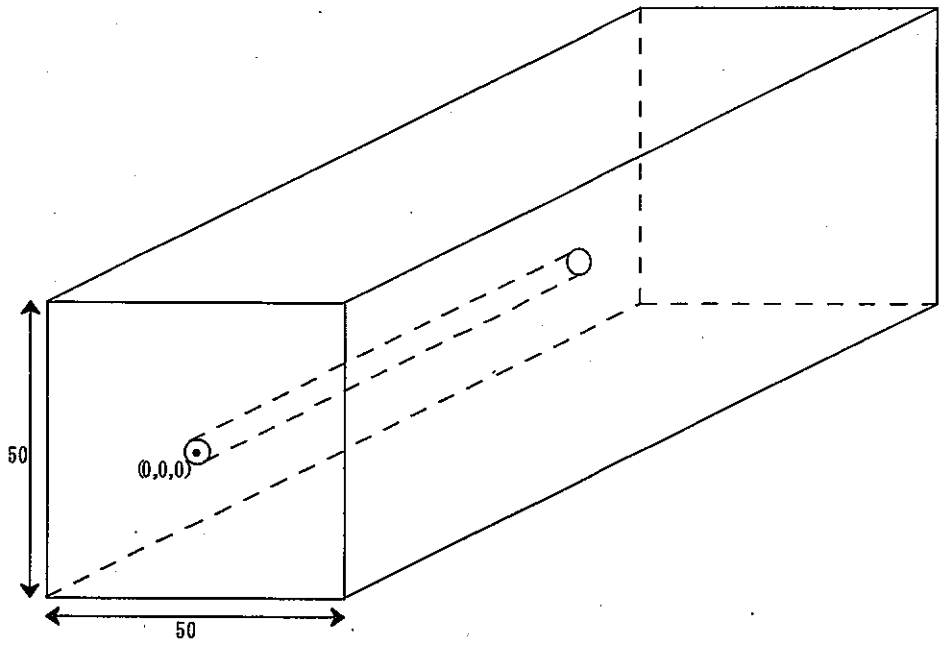

図 5-13　解析モデル鳥瞰図

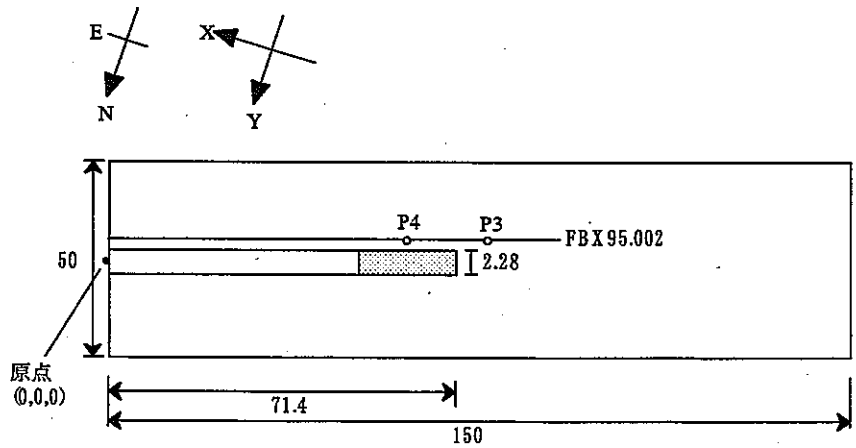

(a)平面図

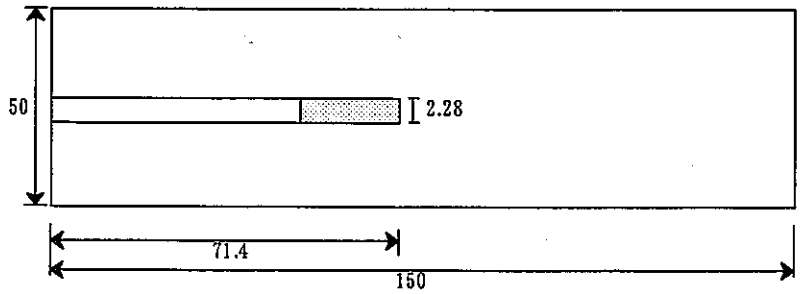

(b)断面図

図 5-14　解析モデル図

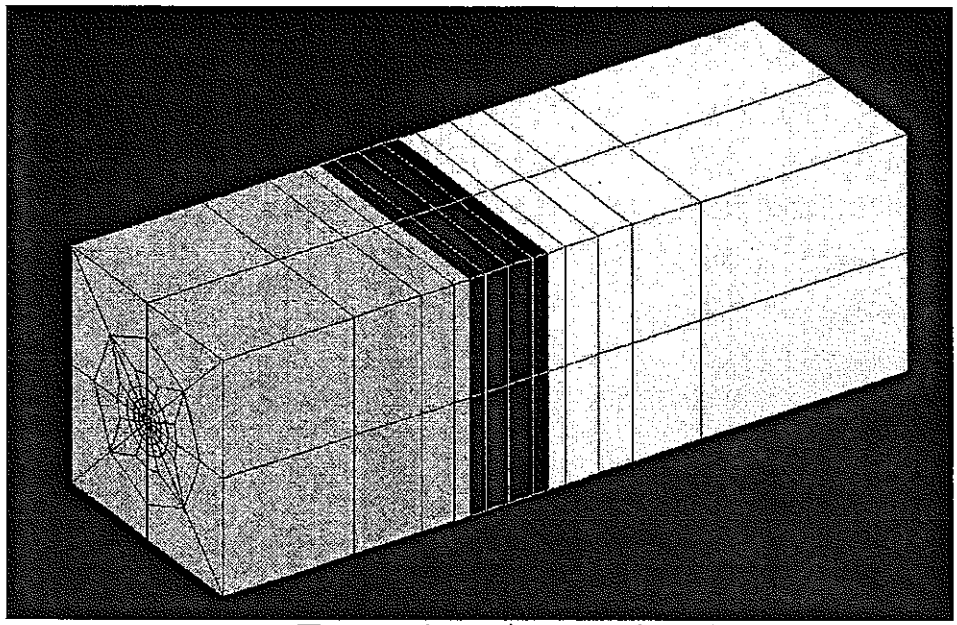

図 5-15　有限要素メッシュ図

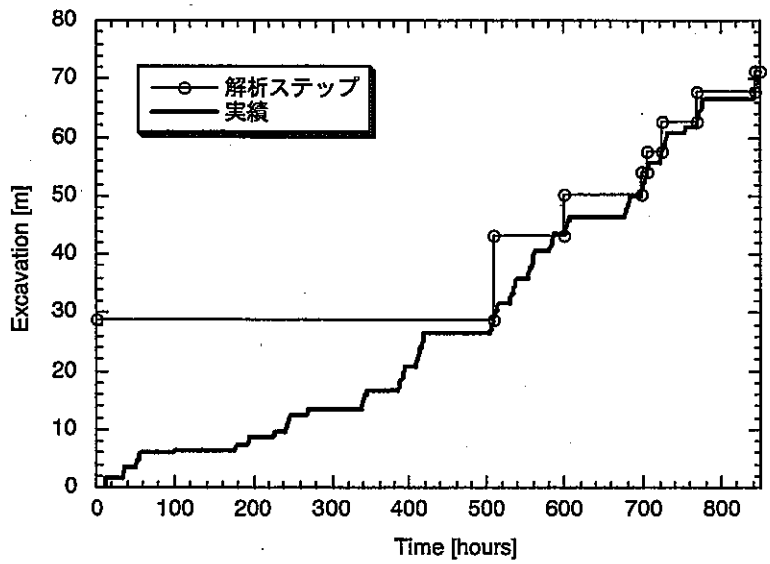

図 5-16　掘削ステップ

今回の解析では、岩盤は均質とし、変形も考慮せずに解析を行なった。用いた岩盤の物性は以下の通りである。

・透水係数：2.0×10^{-11}m/s
・間隙率：0.016
・密度：2640kg/m^3

解析の結果得られた出力点における間隙水圧の経時変化を図 5-17 に示す。また、湧水量算出対象区域（試験坑道奥部 54.0-71.4m）における湧水量の経時変化を図 5-18 に示す。湧水量は算出対象区域を掘削し始めると徐々に増加し始め、掘削が終了した時点で最大となっている。そして、掘削終了後は徐々に減少していき掘削開始から 100 日後では約 7ml/min となっている。間隙水圧は対象区域を掘削中に急激に減少し、掘削終了後は緩やかに減少している。そして初期には

800kPaであった間隙水圧は、掘削開始から100日後には、200～300kPaとなっている。

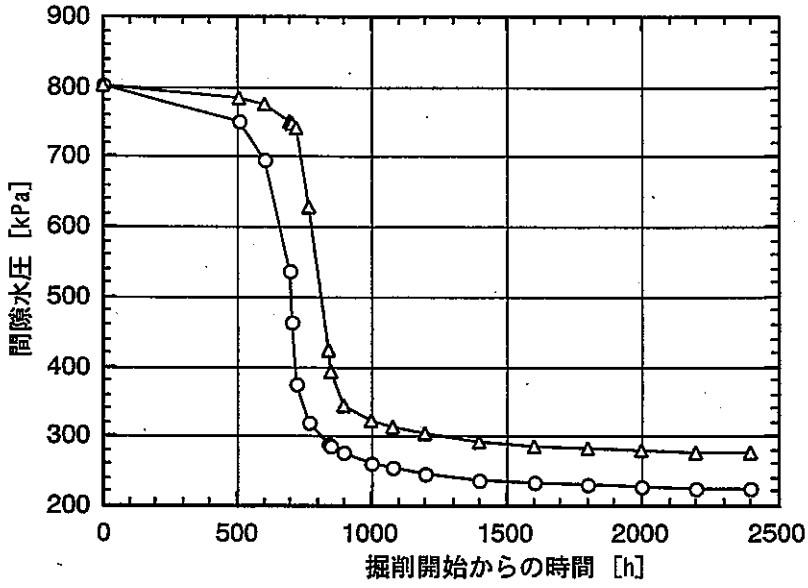

図 5-17　間隙水圧の経時変化

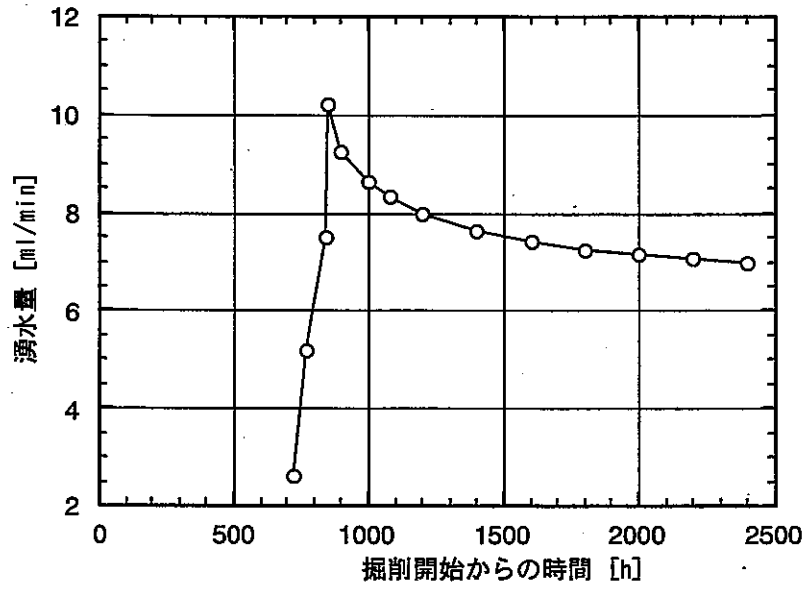

図 5-18　湧水量の経時変化

(2)水理－力学連成解析による坑道掘削の解析

1) 解析モデルの概要

ここでは、水理と力学を連成させた解析による坑道掘削の解析結果を示す。亀裂性岩盤に対する等価連続体モデルはOda (1986) によるcrack tensor theoryと、Barton and Bandis (1985; BB model)による構成モデルを組み合わせることにより作成した。このモデルを用いることにより、crack tensor theoryにより媒体の異方性を、BB modelにより非線形な力学および水理挙動を表現できる。すなわち、媒体内の物性値は掘削過程において不均質そして異方的に変化することになる。

BB modelによると、応力変化に伴う垂直剛性およびせん断剛性の変化は*JRC* (Joint Roughness

Coefficient) および *JCS* (Joint Compression Strength)を用いることによって表現できる。セット I における平均値 JRC_n^I および JCS_n^I (MPa)を用いることによって、亀裂の初期垂直剛性 K_{ni}(MPa/mm)はセット毎に以下のように計算される。

$$K_{ni}^I = -7.15 + 1.75JRC_n^I + 0.02\left(JCS_n^I / a_j^I\right) \tag{5-1}$$

ここで、a_j(mm)は初期の亀裂幅であり、次式で求められる。

$$a_j^I = \frac{JRC_n^I}{5}\left(0.2\frac{UCS}{JCS_n^I} - 0.1\right) \tag{5-2}$$

ここで、*UCS* は岩石の一軸圧縮強度である。

各セットにおける垂直応力 σ_n^I は $\sigma_{ij}n_i^I n_j^I$ となる。ここで、σ_{ij} は各要素において計算された応力であり、n_i^I は各セットにおける単位垂直ベクトルである。したがって、この垂直応力を用い、亀裂の垂直剛性は時間ステップ毎に次式により更新される。

$$K_n^I = K_{ni}^I\left[1 - \frac{\sigma^I{}_n}{V_m K^I{}_{ni} + \sigma^I{}_n}\right]^{-2} \tag{5-3}$$

また、せん断剛性は次式から求められる。

$$K_s^I = \frac{100}{L^I}\sigma_n^I \tan\left[JRC_n^I \log_{10}\left(\frac{JCS_n^I}{\sigma^I{}_n}\right) + \phi^I{}_r\right] \tag{5-4}$$

ここで、式(5-3)における V_m は式(5-2)における a_j^I と等しいと仮定する。L^I は各セットの平均亀裂長(㎜)であり、ϕ_r は残留内部摩擦角である。

$h^I = K_n^I L^I$ および $g^I = K_s^I L^I$ の関係式を用いると、弾性コンプライアンス C_{ijkl} および透水テンソル k_{ij} は次のようになる。

$$C_{ijkl} = \sum_I \left(\frac{1}{h^I} - \frac{1}{g^I}\right)F_{ijkl}^I + \frac{1}{4g^I}\left(\delta_{ik}F_{jl}^I + \delta_{jk}F_{il}^I + \delta_{il}F_{jk}^I + \delta_{jl}F_{ik}^I\right) \tag{5-5}$$

$$k_{ij} = \sum_I \frac{1}{12}e^{I^3}\left(P_{kk}^I\delta_{ij} - P_{ij}^I\right) \tag{5-6}$$

ここで、弾性コンプライアンスおよび透水テンソルはセット毎に求める。また、δ_{ij} は Kronecker delta である。F_{ijkl}、F_{ij} および P_{ij} はそれぞれ次式から求められる。

$$F^I_{ijkl} = \rho^I \frac{\pi}{4} L^{I3} n^I_i n^I_j n^I_k n^I_l \tag{5-7}$$

$$F^I_{ij} = \rho^I \frac{\pi}{4} L^{I3} n^I_i n^I_j \tag{5-8}$$

$$P^I_{ij} = \rho^I \frac{\pi}{4} L^{I2} n^I_i n^I_j \tag{5-9}$$

ここで、ρ^IはセットIにおける亀裂密度である。

F_{ijkl}、F_{ij}およびP_{ij}の値は、解析の過程で変化しない。また、各セットにおける亀裂幅の増加量は次式で与えられる。

$$\Delta V^I = \frac{\Delta \sigma^I_n}{K^I_n} \tag{5-10}$$

したがって、各セットにおいて亀裂幅は次式により更新される。

$$e^I = e^I_{\text{int}} - \Delta V^I \tag{5-11}$$

ここで、e^I_{int}は次式により計算される。

$$e^I_{\text{int}} = \sqrt[3]{\frac{18 \times \mu_l \times K_{mean}}{9.8 \times P^I_{KK}}} \tag{5-12}$$

ここで、μ_lは水の粘性係数であり、K_{mean}は平均透水係数である。ここで、原位置における透水係数の測定結果は平均値であると仮定する。また、K_{mean}の分布は地盤統計学手法により得られる。

上記の非線形等価モデルを熱－水－応力連成解析コードTHAMES (Ohnishi et al.、 1985)に導入し、３次元有限要素法により解析を行なう。地下水の連続式は以下のようになる。

$$\left\{ \frac{\rho_l g k_{ij}}{\mu_l} h_{,j} \right\}_{,i} - \rho_{l0} n Sr \rho_l g \beta_P \frac{\partial h}{\partial t} - \rho_l \frac{\partial \theta}{\partial \psi} \frac{\partial h}{\partial t} - \rho_l Sr \frac{\partial u_{i,i}}{\partial t} = 0 \tag{5-13}$$

ここで、ρ_l水の密度、gは重力加速度、nは間隙率、S_rは飽和度、β_Pは水の圧縮率、u_iは変位ベクトル、hは全水頭、tは時間である。

応力の釣り合い式は以下の通りである。

$$\left[\frac{1}{2} T^{-1}_{ijkl} \left(u_{k,l} + u_{l,k} \right) + \chi T^{-1}_{ijkl} C_{kl} \rho_l h \right] + \rho b_i = 0 \tag{5-14}$$

ここで、$T_{ijkl} = (M_{ijkl} + C_{ijkl})$であり、$M_{ijkl}$は岩盤のマトリックス部の弾性コンプライアンス、$C_{ij}$は$C_{ij}=C_{ijkl}\,\delta_{kl}$である。

2) パラメータの設定

亀裂セットの情報は主としてTechnical Report 87-14Eに示してある。表5-4には、解析に用いたデータを示す。ここで、亀裂長は平均長さの1/10、亀裂密度は単位長さ当りの亀裂数の10倍と仮定している。このように仮定したのは、上記レポートに示してある平均長さは15m以上であり、このような長い亀裂がFEBEXトンネルの掘削に伴う周辺岩盤の物性変化に作用するとは考えにくいためである。したがって、ここでは、平均長さの1/10の亀裂が掘削により影響を受けると仮定した。すなわち、影響範囲は試験坑道から数mである。単位長さ当りの亀裂数はinterlying unjointed zone（上記レポートにおけるFigure 36における*b*）の厚さから求められる。また、全亀裂数と矛盾しないように、亀裂密度は実際の10倍としている。

一軸圧縮強度は、実測の平均値を用いた。また、JCSは一軸圧縮強度の80％であると仮定した。JRCの値は、レポート（Interner Bericht 81-01）における直接せん断試験における図から以下のように推測した。

$$JRC = [\arctan\frac{\tau}{\sigma_n} - \phi_r][\log_{10}(\frac{JCS}{\sigma_n})]^{-1} \qquad (5\text{-}15)$$

ここで、σ_n、τ、ϕ_rは、図から求めた。

Lamprophyreが支配的なゾーンは、それで一つのセットとし、走向傾斜はセット3と同じとした。

表5-4　解析に用いた亀裂特性

Set		System	Density(Num/m^3)	Length(m)	Dip direct./Dip	JRC	JCS(MPa)	UCS(MPa)
Material 1	Set 1	S1+S2	1.00	2.44	155/70	2.99	82.4	103
	Set 2	S3	0.83	1.63	188/81			
	Set 3	K2	1.05	1.83	210/75			
	Set 4	K3	0.72	2.41	258/80			
Material 2	Set 3	Lamprophyre	10.5	1.83	210/75	2.81	63.5	79.4

3) 解析条件

図5-19に、解析に用いた有限要素メッシュを示す。モデルの上面は初期間隙水圧0.8MPaで固定とし、その他の境界は不透水境界とした。また、力学的には全面スライド境界とした。

試験坑道の掘削は表5-5に示すステップで行なった。掘削は試験坑道部のメッシュを順次除去していき、坑道壁面部に対応する節点の間隙水圧をゼロに固定することにより表現した。

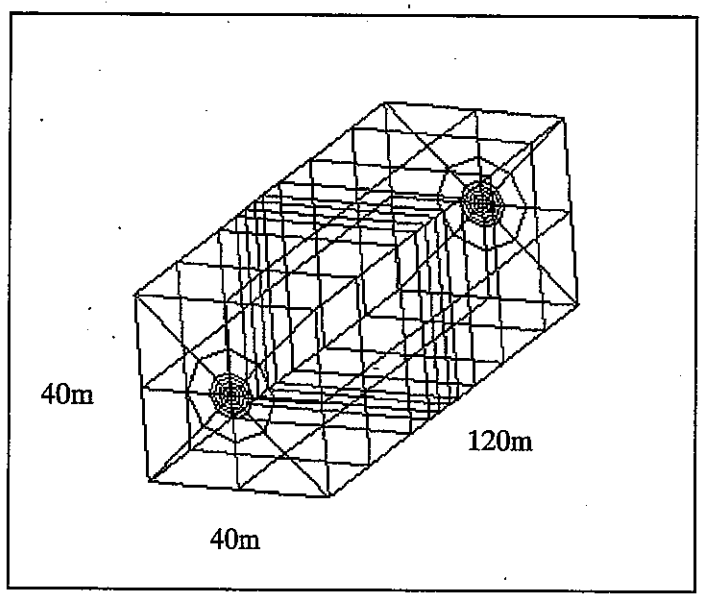

図 5-19　有限要素メッシュ（連成解析）

表 5-5　掘削ステップ（連成解析）

Time(day)	Excavation depth (m)
14	16
22	36
26	50
27	58
28	61.9
29.5	66.65
32.5	71.4
42.5	
53	
73	
100	

4）透水係数の分布

各観測地点における透水係数はレポートに示されている透水量係数の値から算出した。また、クリギングを用い、解析領域全体における透水係数分布を推定した。さらに、式(5-12)から解析領域全体における初期亀裂幅の分布を求めた。クリギングに用いた透水係数の幾何平均値は 4.4×10^{-11}m/s である。図 5-20 にはクリギングにより得られた初期透水係数分布を示す。示しているのは透水係数の対数値（log(K)（m/s)）である。

5）その他の物性値

解析に用いた、その他の物性値を表 5-6 に示す。

表 5-6　解析に用いた力学物性

	Young's modulus of intact rock (GPa)	Poisson's ratio
Material 1	32	0.25
Material 2	25	0.25

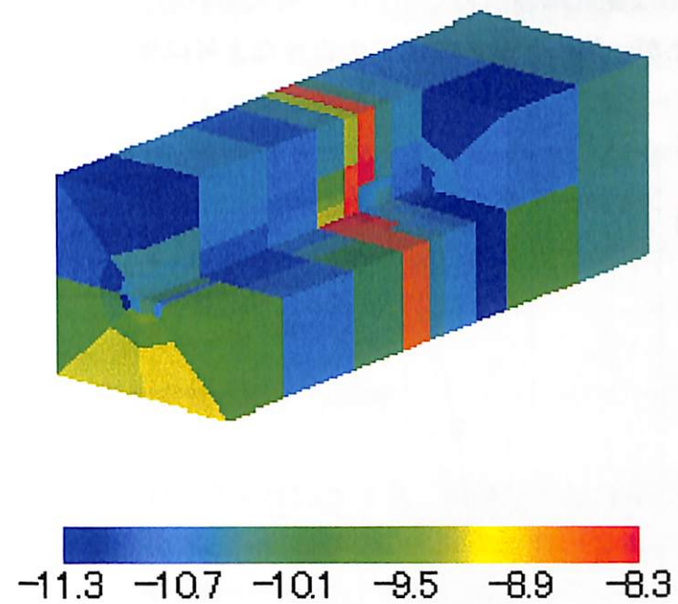

図 5-20　透水係数分布図（log K (m/s)）

6) 解析ケース

解析は２ケース実施した。最初のケースは、上述の異方非線形な力学および水理物性を用いたケース（Case 1）である。２番目のケースは、力学物性は線形等方弾性体モデルで、水理物性は異方不均質なケース（Case 2）である。Case 2 においては、力学物性に関して crack tensor を考慮していない。また、比較のために(1)で実施した変形を考慮しない水理解析の結果を Case 3 として示す。Case 1、Case 2 においては Lamprophyre zone および初期における他の zone の力学物性は均一である。ただし、透水係数に関しては、クリギングにより初期の亀裂幅分布が得られているため不均一となる。Case 3 においては、透水係数はモデル領域全体において均一で 2.0×10^{-11}m/s である。Case 2 および Case 3 においては、物性値は掘削過程において常に一定であるが、Case 1 では掘削に伴い岩盤の水理および力学物性は変化する。Case 1 および Case 2 は力学ー水理の連成解析であり、Case 3 は非連成の水理解析である。

7) 解析結果

図 5 - 21 に試験坑道の区間 50～71.4 m における湧水量の経時変化を示す。Case 2 における湧水量は Case 1 に比べ大きい値となった。これは、掘削に伴い Case 1 では試験坑道周辺の透水係数が減少したためであると考えられる。また、Case 3 は最も大きな値を示した。これは、Case 1 および Case 2 では、透水係数の分布が不均一であることにより流れが複雑になり、その結果、全体の透水性が見かけ上、領域全体に平均の透水係数を与えた Case 3 に比べ小さくなったためではないかと推測される。掘削開始から 100 日後の湧水量は Case 1 で 0.39 ml/min、Case 2 で 1.04 ml/min、Case 3 で 7.0 ml/min であった。

図 5 - 22 には観測ポイント P3 および P4 における間隙水圧の経時変化を示す。Case 1 においては、P3 における間隙水圧は掘削により急激に減少し、負圧も発生している。しかし、その後は緩やかに回復し初期値に近い値まで戻っている。一方、P4 の挙動は Case 1、Case 2 ともほぼ同じである。すなわち、P4 においては掘削の影響は小さく非線形の影響は生じていないといえる。逆に、P3 においては非線形な変形挙動が強く生じたと考えられる。Case 2 においては掘削直前に微量の圧力上昇が見られたが、他のケースではこのような上昇は見られなかった。

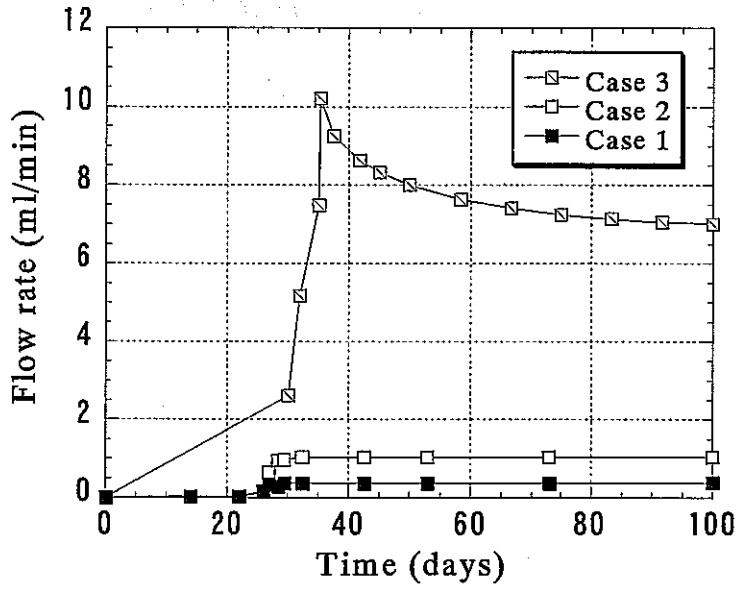

図 5 - 21　試験坑道の区間 50～71.4 m における湧水量の経時変化

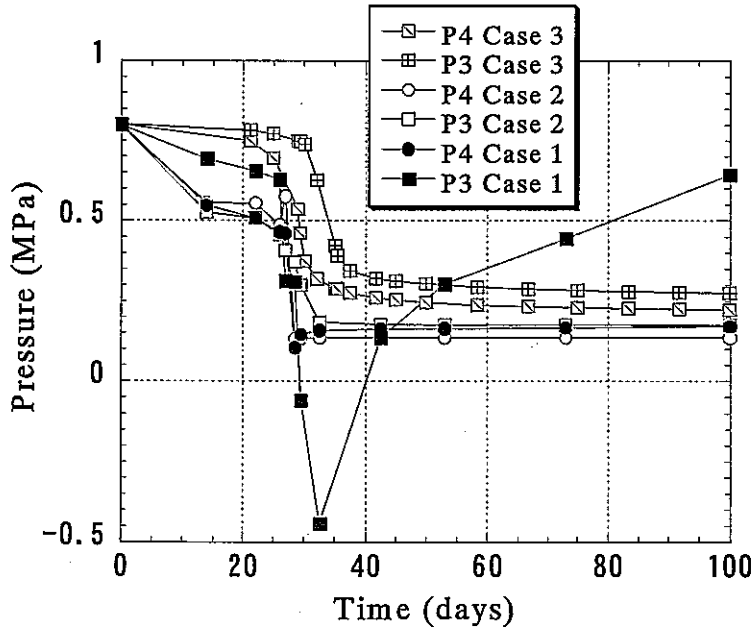

図 5 - 22　観測ポイント P3 および P4 における間隙水圧の経時変化

5.3 TASK3 BMT1 の概要

5.3.1 Task の概要

本ベンチマークテストは、緩衝材の再冠水挙動に関して PA の観点から検討を行なうことを目的としている。ベンチマークの設定に際し、より実際的な問題を解くという観点から、日本の処分仕様をモデルとして検討が進められる。問題は JNC の第２次取りまとめレポートにおける結晶岩系竪置き方式を対象として設定されている。この仕様に対し、周辺岩盤の透水性、亀裂のモデル化等の影響により再冠水挙動がどのように影響を受けるかを解析評価する。BMT1 ではまず、モデルのキャリブレーションということで、釜石粘土充填・熱負荷試験のキャリブレーション解析を実施することになっている。そこで、ここでは実施した釜石粘土充填・熱負荷試験のキャリブレーション結果を示す。

5.3.2 膨潤応力の温度・密度依存性に関する検討

(1) 概要

サイクル機構において取得されたデータに基づき、膨潤応力の温度依存性および密度依存性を考慮したモデル化を行い、実験結果と解析結果との比較を行う。対象とした緩衝材材料はケイ砂混合ベントナイト（ケイ砂混合率 30%）である。

(2) 膨潤応力の温度、密度依存性

1) 温度依存性

図 5-23 にケイ砂混合体の膨潤応力の測定において温度を変化させていった結果を示す。また、表 5-7 には平衡膨潤応力の値を示す。図 5-24 には平衡膨潤応力と温度との関係をグラフにして示す。この試験においては、温度 60℃の時における膨潤応力の値は温度 25℃の時に比べ大きくなっているが、一般には膨潤応力は温度の上昇に伴い減少すると言われているので、ここでは、図 5-24 に示すように膨潤応力の値は温度の上昇に伴い線形に減少すると仮定した。

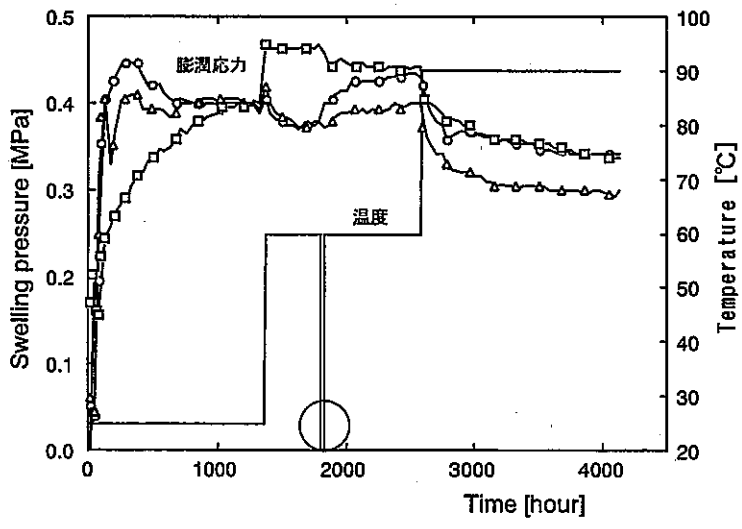

図 5-23 膨潤応力測定結果

表 5-7　平衡膨潤応力の測定結果（MPa）

温度	25℃	60℃	90℃
平衡膨潤応力	0.39	0.43	0.34
	0.40	0.40	0.30
	0.40	0.44	0.34

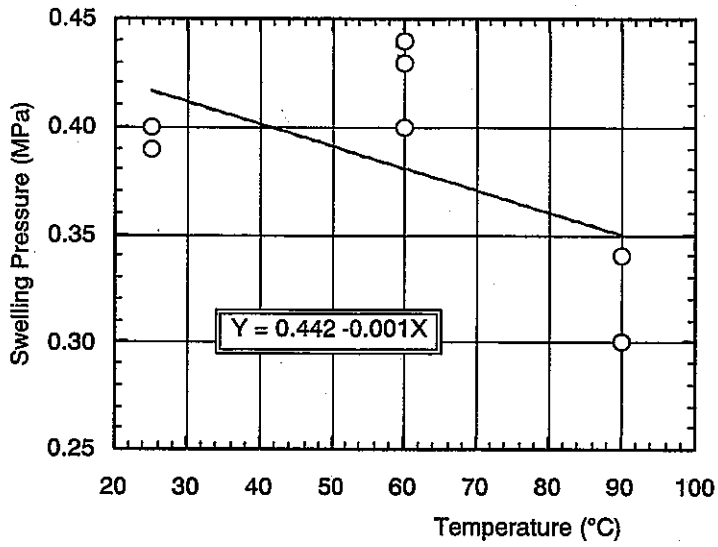

図 5-24　平衡膨潤応力と温度との関係

得られた温度と膨潤応力の関係は式(5-16)の通りとなる。

$$\sigma = 0.44-0.001T \tag{5-16}$$

式(5-16)に基づくと温度 25℃の時の膨潤応力は 0.415MPa となる。

2) 密度依存性

図 5-25 に膨潤応力と有効粘土密度との関係を示す。また、この関係は式(5-17)で与えられている。有効粘土密度は式(5-18)に示す通りであり、ケイ砂混合率 30%、乾燥密度 1.6g/cm³ の場合、有効粘土密度は 1.368g/cm³ となり、式(5-17)によると、その時の膨潤応力は 0.48MPa となる。ここで、土粒子密度は 2.65g/cm³ とした。

$$\sigma = \exp(3.85\rho_e^2-7.33\rho_e+2.09) \tag{5-17}$$

$$\rho_e = \rho_d(100-Rs)/(100-\rho_d Rs/\rho_s) \tag{5-18}$$

ρ_e：有効粘土密度（g/cm³）

ρ_d：乾燥密度（g/cm³）

Rs：ケイ砂混合率（%）

ρ_s：土粒子密度（g/cm³）

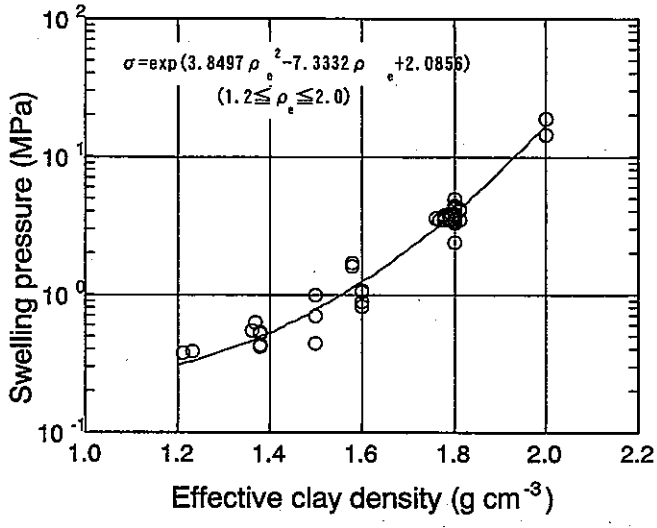

図 5-25　有効粘土密度と膨潤圧の関係

3) 膨潤応力のモデル化

上記の結果より、膨潤応力を式(5-19)のように温度と有効粘土密度の関数として仮定する。また、熱-水-応力連成解析の際には式(5-20)に示すように膨潤応力が水分ポテンシャルの変化に伴い発生すると仮定しモデル化し、式(5-20)における係数 F を実験結果の逆解析から同定している。そこで、温度 25℃、乾燥密度 1.6g/cm³、ケイ砂混合率 30%の状態において得られた膨潤応力値から同定した係数の値を F_o とし、式(5-21)のような F の値を用い解析を行なった。

$$\sigma=\exp(3.85\rho_e^2-7.33\rho_e+2.09)-0.001T \tag{5-19}$$

$$\sigma=F\,|\,\Delta\psi\,| \tag{5-20}$$

$$F=F_o\times\left\{\frac{\exp\left(3.85\rho_e^{\,2}-7.33\rho_e+2.09\right)-0.001T}{\exp\left(3.85\rho_{eo}^{\,2}-7.33\rho_{eo}+2.09\right)-0.001T_o}\right\} \tag{5-21}$$

T_o=25℃、ρ_{eo}=1.368g/cm³

(3) 温度、密度依存性を考慮した解析モデルの評価

1) 膨潤試験の解析

各温度における膨潤試験の解析を行い、解析値と実験値との比較を行なった。解析は図 5-26 に示す軸対称モデルにおいて、温度を 25℃、60℃、90℃として実施した。

解析に用いたケイ砂混合ベントナイトの水分拡散係数、水分特性曲線をそれぞれ図 5-27、図 5-28 に示す。水分拡散係数に関しては式(5-22)に示す実験式、水分特性曲線に関しては式(5-23)に示す van Genuchten による関数モデルを用いて解析を実施した。各式における係数の値は表 5-8 に示す。また、その他の物性値に関しては表 5-9 に示す値を用いた。

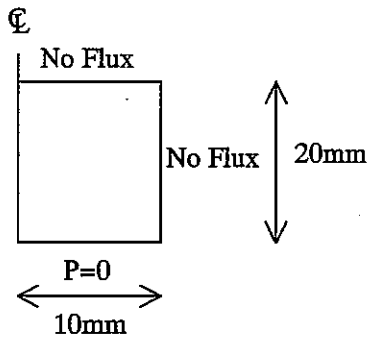

図 5-26　解析モデル

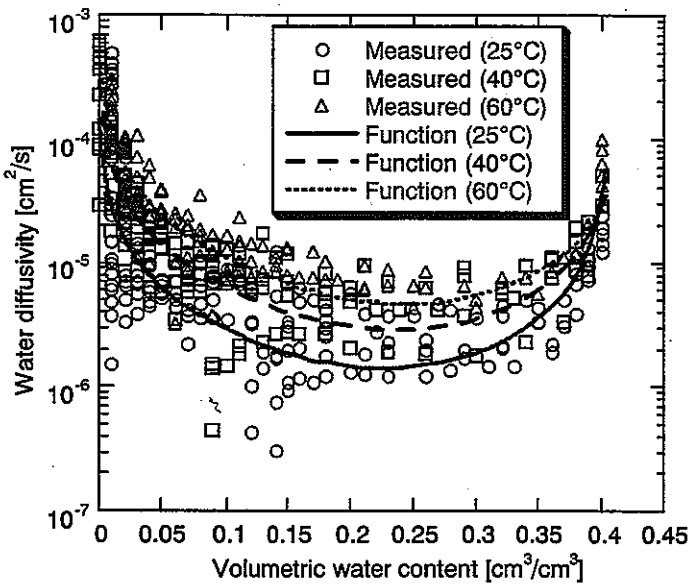

図 5-27　水分拡散係数

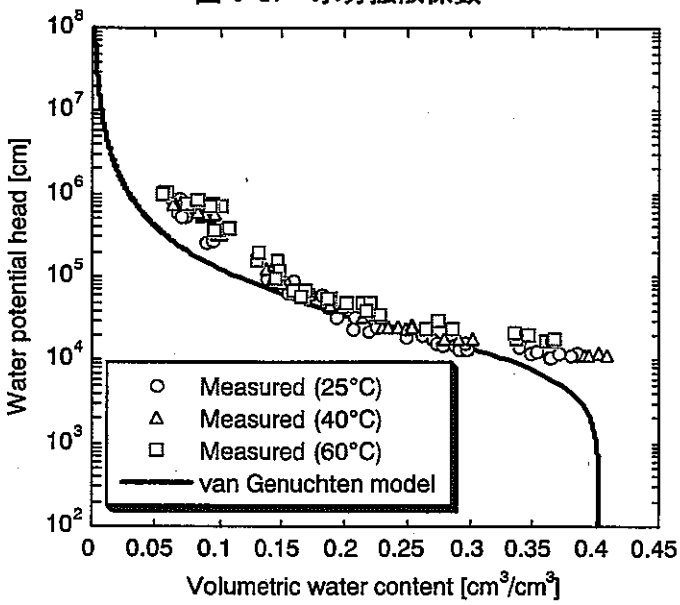

図 5-28　水分特性曲線

$$D_\theta = \frac{a_1(\theta - \theta_s)}{(\theta - b_1)(b_1 - \theta_s)} + \frac{a_2\theta}{b_2(\theta - b_2)} \qquad (5\text{-}22)$$

$$\frac{\theta-\theta_r}{\theta_s-\theta_r}=\left\{1+|\alpha\psi|^n\right\}^{-\left(1-\frac{1}{n}\right)} \tag{5-23}$$

表 5-8　式(5-22)、式(5-23)における各係数の値

係数	値
a_1	$2.99\times10^{-8}T-3.74\times10^{-7}$
a_2	$-1.50\times10^{-8}T+1.49\times10^{-7}$
b_1	-2.49×10^{-3}
b_2	$5.59\times10^{-4}T+3.93\times10^{-1}$
θ_s	0.403
θ_r	0.000
α	8.0×10^{-5}
n	1.6

表 5-9　その他の物性値

物性	値
弾性係数（MPa）	50.0
ポアソン比	0.3
固有透過度（m^2）	4.0×10^{-20}
熱伝導係数（W/m/K）	$4.44\times10^{-1}+1.38\times10^{-2}\omega$ $+6.14\times10^{-3}\omega^2-1.69\times10^{-4}\omega^3$
比熱（kJ/kg/K）	$(34.1+4.18\omega)/(100+\omega)$
熱膨張係数（1/K）	1.0×10^{-5}
温度勾配水分拡散係数（m^2/s/K）	7.0×10^{-12}

図 5-29 には温度が 25℃の時における供試体内の水分ポテンシャルの経時変化を示す。凡例は供試体下部、すなわち浸潤面からの距離を示す。また、図 5-30 には同様に供試体内の含水比の経時変化を示す。供試体内の含水比は浸潤面に近い側から順に増加しており、約 300 時間後に供試体全体が飽和となっている。図 5-31 には供試体内の応力の経時変化を示す。水分ポテンシャルの変化に伴い膨潤応力が発生するというモデルを用いているため、膨潤応力の発生は水分ポテンシャルの変化と傾向がよく似ており、水分ポテンシャルの変化がなくなった時点で、膨潤応力は平衡に達している。また、各供試体高さにおける応力の値を比較してみると、浸潤面に近い側の方が若干小さくなっているが、それほど大きな違いはない。図 5-32 には、供試体内のひずみの経時変化を示す。正が圧縮ひずみ、負が引張ひずみである。浸潤開始直後に浸潤面近く（供試体下部）に引張ひずみが発生しており、それに伴って順次浸潤面と反対側（供試体上部）に圧縮ひずみが発生している。そして、浸潤が進むにつれて、供試体下部の引張ひずみ、供試体上部の圧縮ひずみとも小さくなり、供試体が飽和した時点で、供試体全体においてひずみがゼロとなっている。図 5-33 には供試体内部の乾燥密度の変化を示す。浸潤開始直後に発生した供試体下部における引張ひずみの影響で供試体下部においては乾燥密度が初期の値より低下している。一方、供試体上部においては反対に乾燥密度が初期の値より増加している。乾燥密度のばらつきも膨潤応力が平衡となった時点で終了しており、その後は供試体内で均一となっている。図 5-34 には膨潤応力の解析値と実験値との比較を示す。実験は 5 回実施しているが、実験毎に異なる値を示している。解析はこれらのほぼ平均値を得るように F_0 の値を設定した。

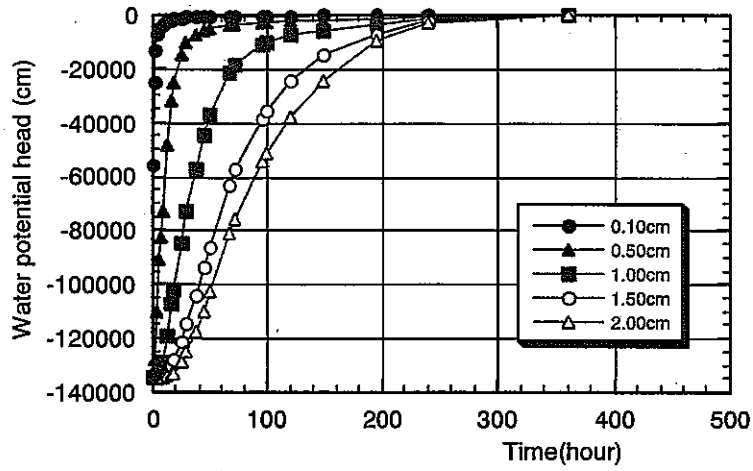

図 5-29　供試体内の水分ポテンシャルの経時変化（温度 25℃）

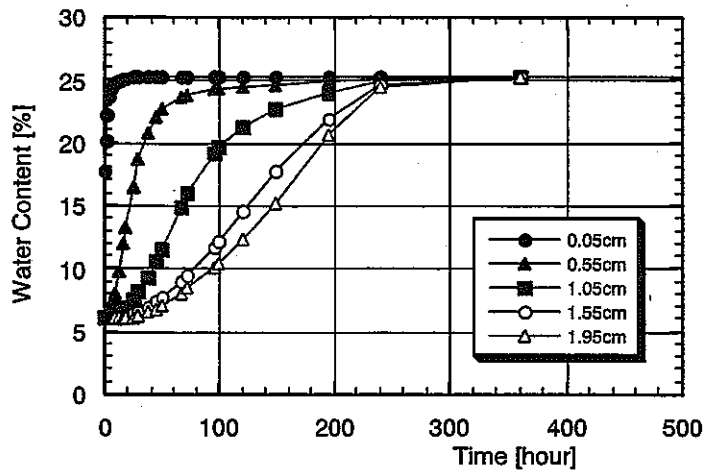

図 5-30　供試体内の含水比の経時変化（温度 25℃）

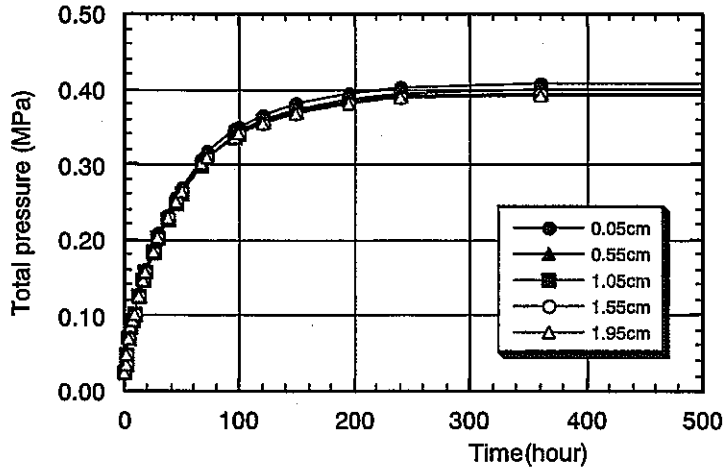

図 5-31　供試体内の応力の経時変化（温度 25℃）

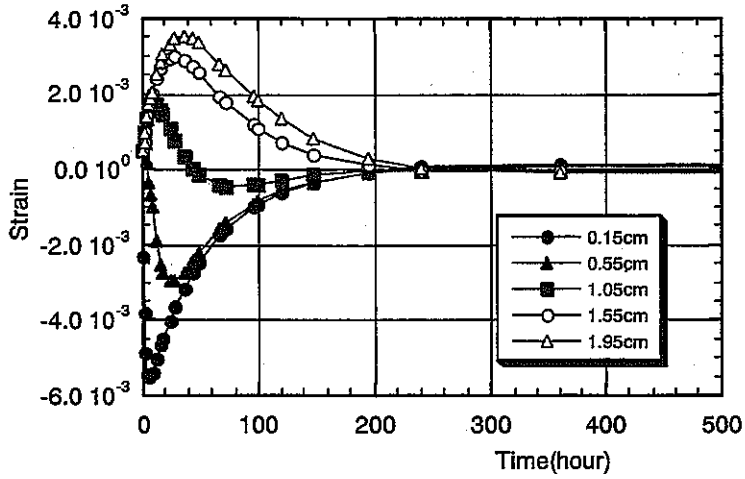

図 5-32　供試体内のひずみの経時変化（温度 25℃）

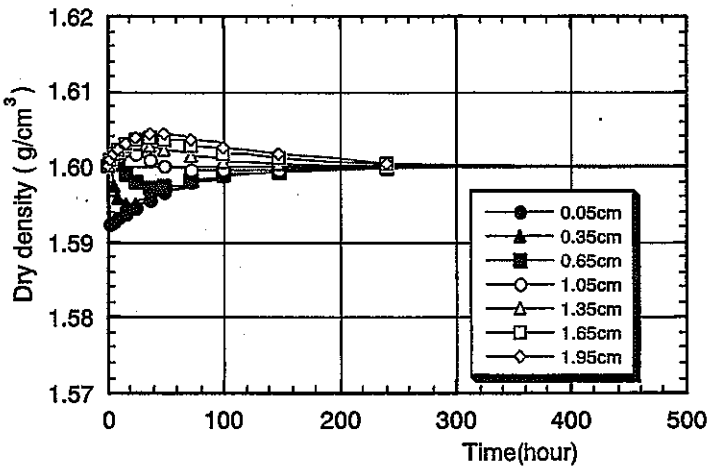

図 5-33　供試体内の乾燥密度の経時変化（温度 25℃）

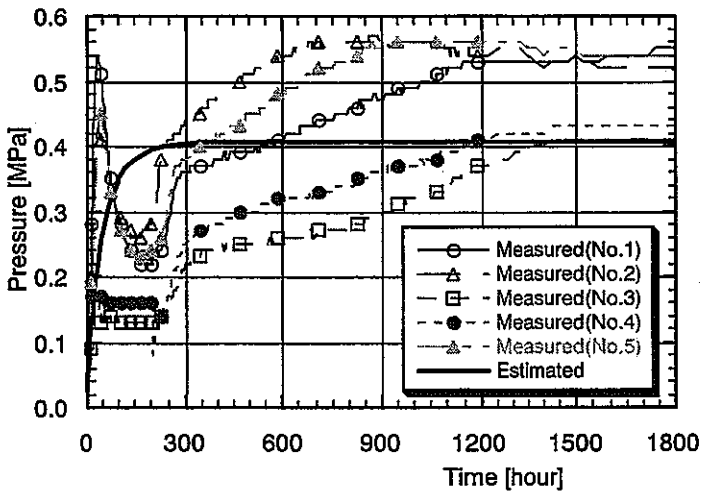

図 5-34　膨潤応力の解析値と実験値との比較

図 5-35、図 5-36 には温度が 60℃の時の供試体内の含水比、応力の経時変化を示す。また、図 5-37、図 5-38 には同様に温度が 90℃の時の供試体内の含水比、応力の経時変化を示す。温度の上昇とともに供試体が飽和となる時間が早くなっており、それに伴って発生する膨潤応力が平衡

に達する時間も早くなっている。また、温度が上昇するにつれて平衡膨潤応力値も小さくなっている。

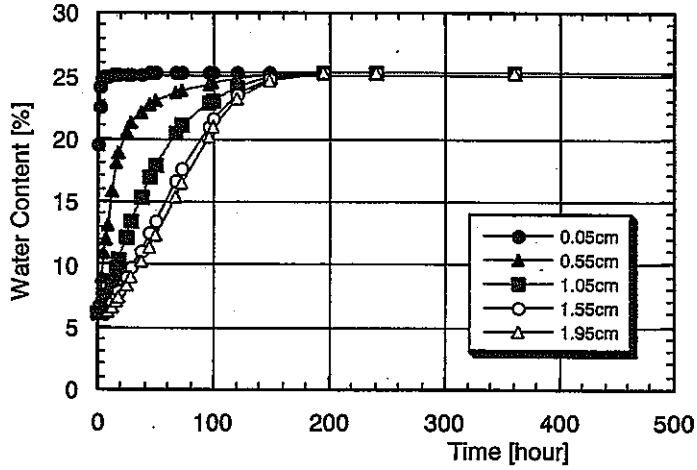

図 5-35　供試体内の含水比の経時変化（温度 60℃）

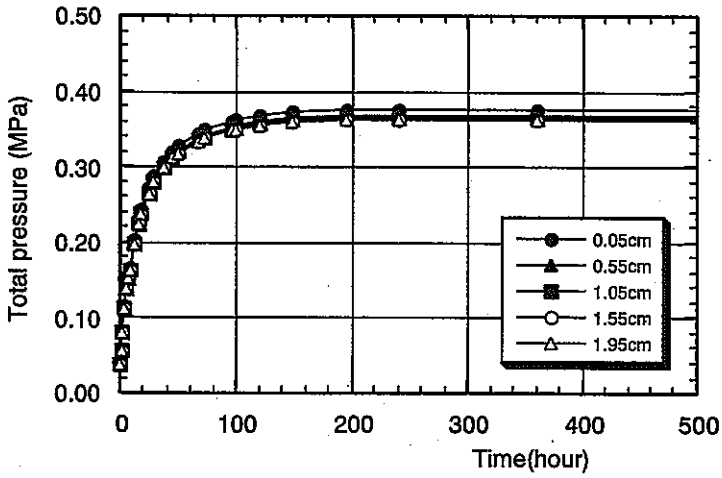

図 5-36　供試体内の応力の経時変化（温度 60℃）

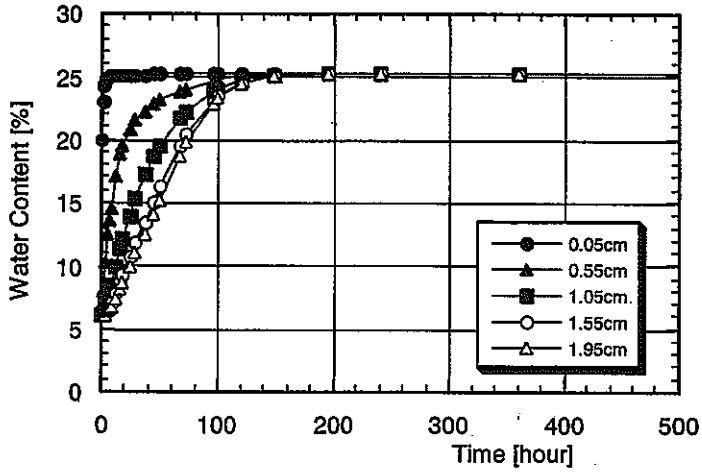

図 5-37　供試体内の含水比の経時変化（温度 90℃）

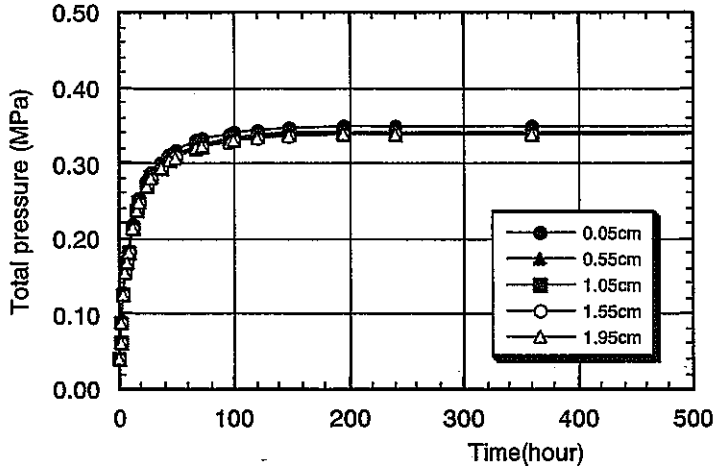

図 5-38　供試体内の応力の経時変化（温度 90℃）

2）連成試験の解析

(a) 試験概要

ここでは，前述のモデルを用い、サイクル機構において実施された室内連成試験の解析を行なった。図 5-39 に試験装置の概要を示す。供試体内の温度勾配は循環式恒温水槽により試験装置の上端、下端を異なる温度で固定し与える。さらに、供試体上部より 100cm の圧力水頭により供試体上面の金属焼結フィルターを介して水を供給する。測定項目は供試体内への水の浸潤量、温度および膨潤応力の分布である。供試体内の温度は、供試体下部より 0.2、2.0、4.0、6.0、8.0、9.8cm の位置に取り付けた計 6 本の熱電対により測定した。膨潤応力は試験装置上面と側面に取り付けた計 6 個のロードセルによって測定した。試験装置側面のロードセルは供試体下部より 1.0、3.0、5.0、7.0、9.0 の位置に取り付けられている。水分分布は、所定の時間経過後に供試体を厚さ 1.0cm の円盤状に 10 分割し、含水比を測定して求める。

(b) 試験結果

供試体内への水の浸潤量の経時変化を図 5-40 に示す。これより、供試体内には約 65cc の水が浸潤し、約 7000 時間で定常となっていることがわかる。理論的に供試体内へ浸潤できる水の量は約 60cc であり、実測値がこの値より大きくなっているのは、試験が長期に渡っていることによる水の蒸発等の影響であると考えられる。また、図 5-41 には応力の経時変化を示す。応力も約 7000 時間でほぼ定常となっており、これは、供試体内への水の浸潤が定常となった時間と一致する。そして、応力は供試体上部で約 0.4MPa、供試体下部で約 0.2MPa であり、供試体上部の方が大きい結果となっている。供試体上部は水の供給側であり、温度勾配を与えた時の低温側である。試験終了後には供試体を 10 分割し、供試体内の含水比を測定した結果を表 5-10 に示す。本試験条件において理論的に求められる供試体の飽和含水比は約 25%であることから、供試体全体を見れば飽和していると判断することが出来る。供試体内の含水比の分布は、水の浸潤面部分と供試体中央部で高い値となっている。浸潤面部分は、浸潤面がゲル化したために含水比が高くなったものと考えられる。また、供試体中央部は供試体の製作上、密度が供試体上下部より低くなってしまうため、その影響で飽和含水比が高くなってしまったものと考えられる。また、全体的な傾向

としては供試体下部の高温側の方が含水比は小さくなっている。

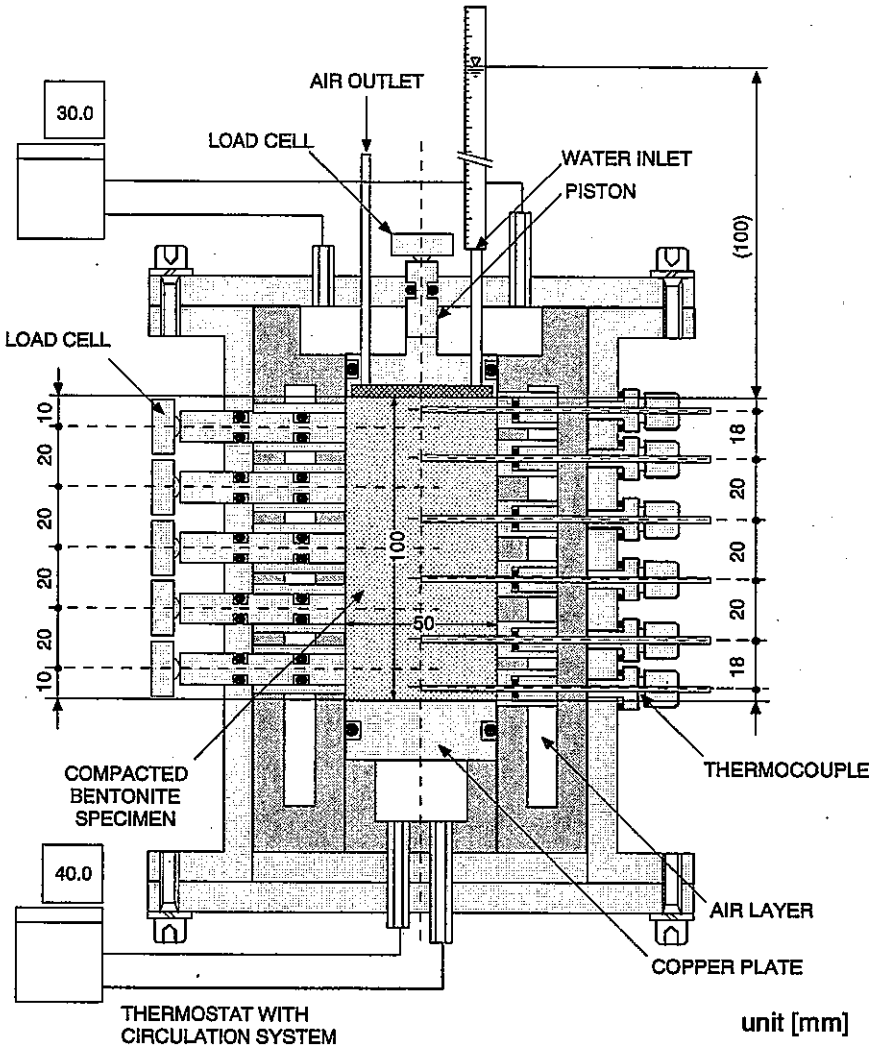

図 5-39　連成試験装置概要

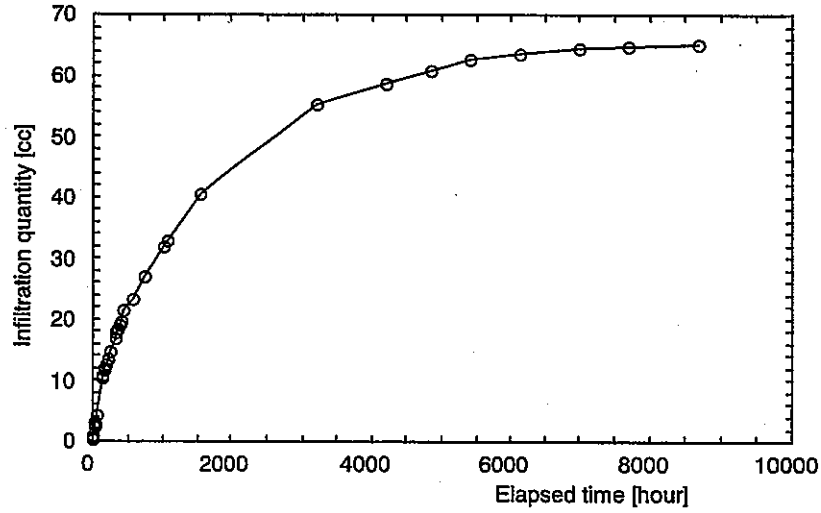

図 5-40　供試体内への水の浸潤量の経時変化（実測値）

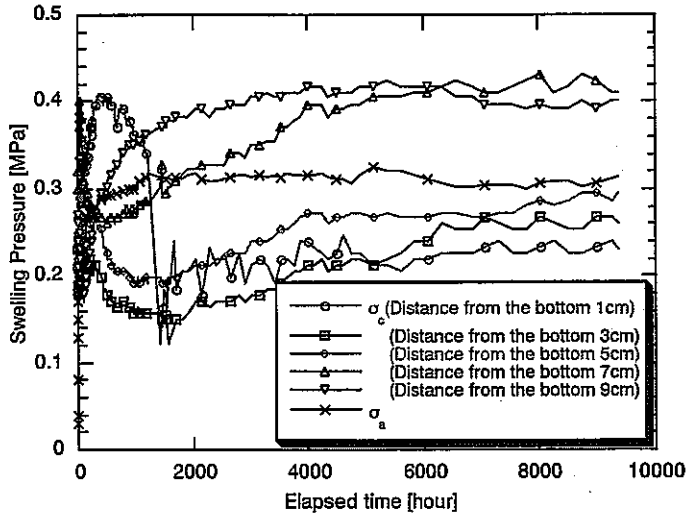

図 5-41　応力の経時変化（実測値）

(c) 解析モデル

解析は軸対称モデルで実施した。図 5-42 に解析モデルの概念図を示す。また、境界条件の概要も図 5-42 に示す。熱に関しては上端を 30℃、下端を 39℃で固定とし、側部は断熱境界とした。また水理に関しては上端に 100cm の圧力水頭を与え、側部および下部は不透水境界とした。また力学に関しては全てスライド境界とした。ベントナイトの初期含水比は 6.0%とした。

表 5-10　含水比分布の測定結果

浸潤面からの距離（cm）	含水比（%）
0.5	27.68
1.5	25.27
2.5	25.18
3.5	25.44
4.5	26.20
5.5	26.43
6.5	25.57
7.5	25.63
8.5	24.77
9.5	24.67
平均	25.68

(d) 解析結果

図 5-43 にベントナイト内の含水比の経時変化を示す。X は供試体下端からの距離を表している。すなわち、X=0cm が高温側、X=10cm が低温側である。100cm の圧力水頭を与えている低温側の方が高温側に比べ早期に飽和に達していることが分かる。また、下端部は温度勾配により初期に若干含水比が低下しているが、その影響は小さく、その後、含水比は上昇している。約 8000 時間後にほぼ定常に達しており、その際に上部の含水比は約 25%と飽和に達しているが、下部の含水比はそれより小さい値となっている。一方、図 5-44 には乾燥密度の経時変化を示す。図 5-44 より、下部は浸潤に伴う膨潤により浸潤面側の上部では初期に乾燥密度が小さくなっているが、最終的には高温側の方が乾燥密度は小さくなっている。その結果、飽和含水比は 25%より大きくなるも

のと考えられる。しかし、解析の結果、下部の含水比は 25%より小さくなっていることから、この部分は解析では飽和に達していないことがわかる。図 5-44 には供試体内への浸潤量の実験結果と解析結果との比較を示す。解析結果は実験結果と傾向的には良く一致しているものの、実験結果の方が若干浸潤量が多くなっている。しかし、初期含水比を 6.0%とした場合の理論的な最大浸潤量は 60cc であるので、解析上は浸潤量がこの値を越えることはない。実験では最終的な浸潤量は 65cc 程度となっており、この理論的な最大浸潤量との差の 5cc は実験上の誤差あるいは実験が長期に渡っているため生じた供試体からの蒸発による影響と推察される。図 5-45 には圧力の経時変化を示す。図 5-41 の実測値と比較すると、値的には差があるものの、高温側の方が発生する圧力が低い点等の傾向は一致している。

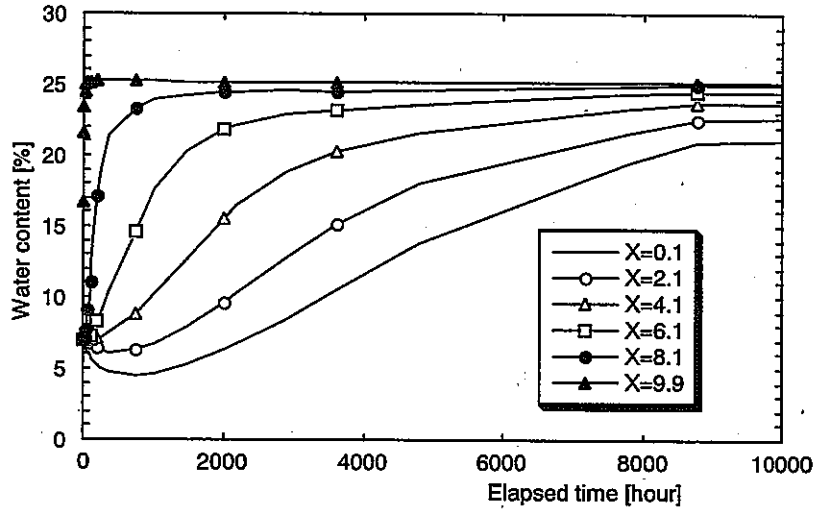

図 5-42　含水比の経時変化（解析結果）

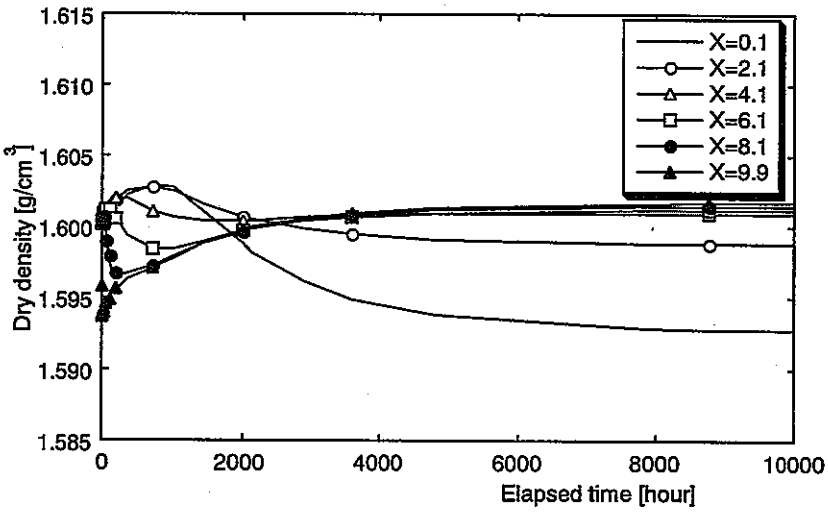

図 5-43　乾燥密度の経時変化（解析結果）

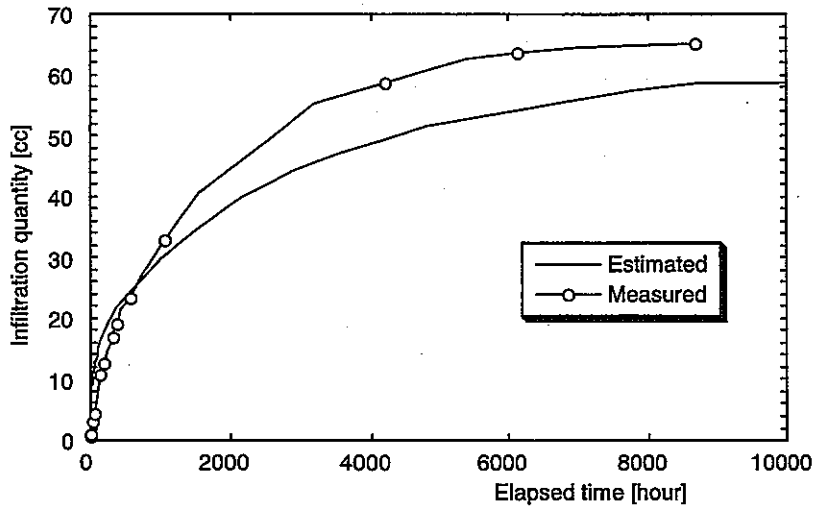

図 5-44　供試体内への浸潤量の解析結果と実験結果との比較

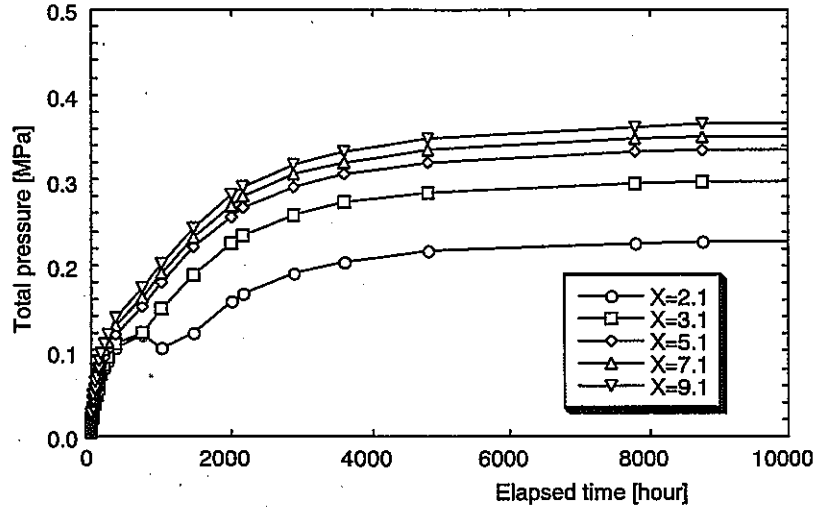

図 5-45　圧力の経時変化（解析結果）

5.3.3　釜石試験のキャリブレーション解析

(1) 概要

上記の検討の結果を踏まえ、釜石粘土充填・熱負荷試験の解析を実施した。解析は、図 5-46 に示す簡易モデルを用い行なった。

解析の境界条件および初期条件は以下の通りである。

【境界条件】

r=0.47m

・T=100℃（加熱フェーズ）

・不透水境界

r=10m

・T=12℃

・変位固定

・水圧固定（p=3.9kPa）

【初期条件】

- T=12℃
- 岩盤内の水圧（p=3.9kPa）
- 緩衝材の含水比（ω=15%）

解析は加熱フェーズ（258 日間）、減熱フェーズ（180 日間）の両フェーズに対して行い、出力ポイントは次表の通りである。

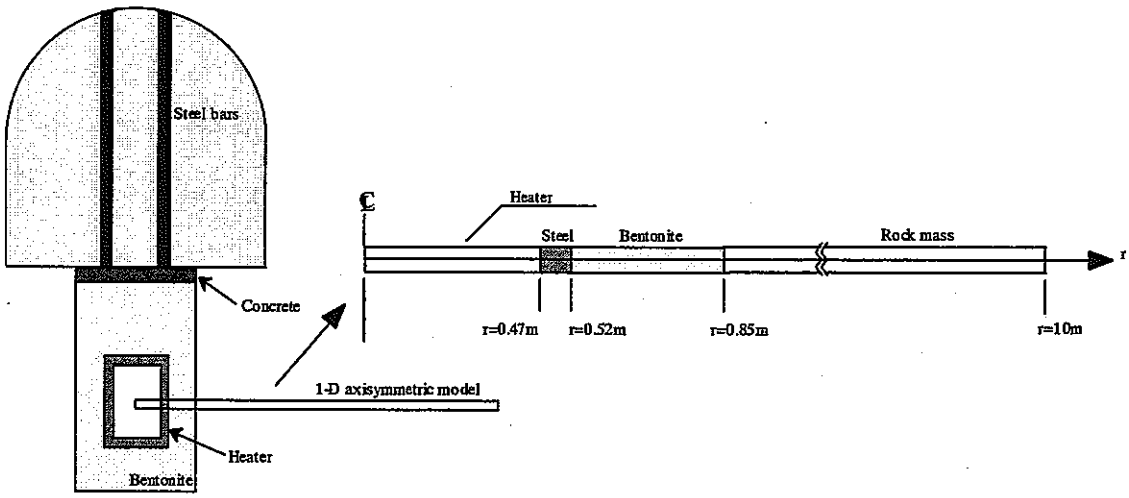

図 5-46　解析モデル

表 5-11　解析の出力ポイント

Point	r (m)
1	0.52
2	0.685
3	0.85
4	1.45

(2) 解析に用いたパラメータ

緩衝材の物性は基本的には室内要素試験から直接算出される。しかし、水分拡散係数、水分特性曲線、温度勾配による水分移動の係数及び膨潤応力に寄与する係数に関しては、室内試験の結果から逆解析的に同定した。以下に設定した各物性値を示す。

1) 水分拡散係数及び水分特性曲線

解析に用いた緩衝材の固有透過度 K [m^2]及び水分拡散係数 D_θ[cm^2/s]は以下の通りである。固有透過度は透水試験から、水分拡散係数は水分拡散試験から直接算出した。水分拡散係数 D_θは水蒸気による拡散係数 $D_{\theta v}$ と液状水による拡散係数 $D_{\theta l}$ の和として式(5-25)のように表している。図 5-47 には測定された水分拡散係数値および式(5-25)の関数式による値を示す。本関数モデルにより、含水量の低いところおよび高いところで水分拡散係数の値が大きくなっていること、および、温度が高くなるに従い水分拡散係数の値が大きくなっていることが良く表現できている。

$$K = 2.00 \times 10^{-20} \tag{5-24}$$

$$D_\theta = D_{\theta v} + D_{\theta l} = \frac{(3.68\times10^{-8}T - 2.08\times10^{-7})(\theta - \theta_s)}{(\theta + 1.00\times10^{-3})(-1.00\times10^{-3} - \theta_s)} + \frac{\theta(-3.58\times10^{-9}T - 2.19\times10^{-7})}{0.41(\theta - 0.41)} \tag{5-25}$$

ここで、θ_s は飽和体積含水率である。

サクションψ [cm]はサイクロメータを用い直接計測されるが、解析を行なう際にはサクションと体積含水率の関係（水分特性曲線）を関数式として与えておく必要がある。ここでは、実測されたサクションと体積含水率の関係を直接用い、水分特性曲線を作成した。図 5-48 には用いた水分特性曲線を示す。水分特性曲線には、水分拡散係数ほど顕著な温度依存性は見られなかった。

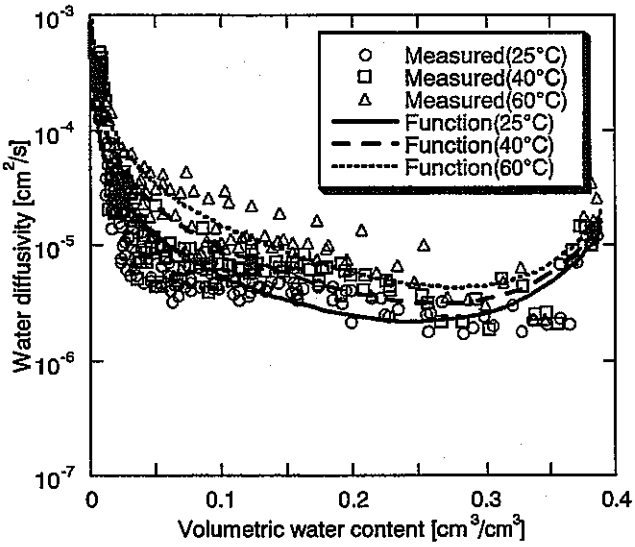

図 5-47　水分拡散係数の測定値および関数式

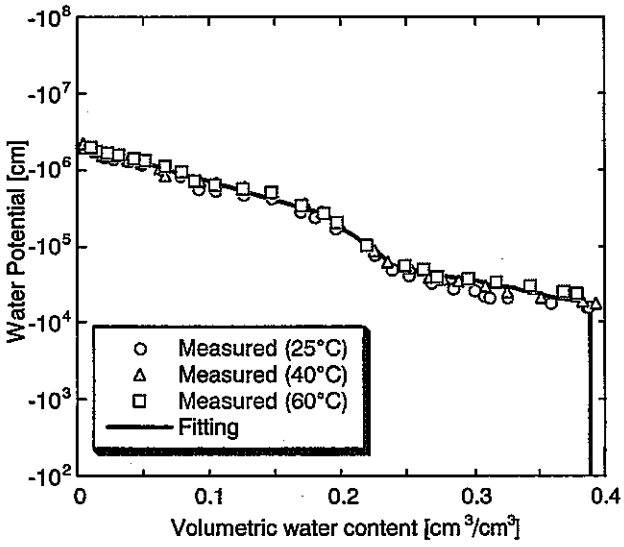

図 5-48　解析に用いた水分特性曲線

2) 温度勾配による水分移動に関する係数

温度勾配による水分移動に関する係数 D_T[cm²/s℃]は次式のように温度の関数として設定した。

$$D_T = D_{To} \exp\left(\alpha_T \frac{T - T_o}{T_o}\right) \tag{5-26}$$

ここで、D_{To} は基準となる係数の値、T_o は基準温度、α_Tは温度に対する非線形性の度合を調整するパラメータでスカラー量である。

これらの値は、室内要素試験結果から逆解析によって求めた。同定された式(5-26)における各パラメータは以下の通りである。

$$D_{To} = 8.5\times10^{-8} \tag{5-27}$$

$$\alpha_T = -1.5 \quad (T<60℃)、1.5\ (T\geqq60℃) \tag{5-28}$$

$$T_o = 60℃ \tag{5-29}$$

3) 膨潤応力に寄与する係数

供試体内部において膨潤圧が発生したときに拘束境界面に作用する応力を膨潤応力と定義する。膨潤応力の値はベントナイトの微視的構造による影響等により膨潤圧とは必ずしも等しくならない。したがって、膨潤応力に寄与する膨潤圧π'は、膨潤圧πにある係数 F を乗じて表わされると考える。ここでは原位置試験の結果得られた応力の値をもとに F の値を定めた。設定された F の値は以下の通りである。

$$F = 0.010 \tag{5-30}$$

また、緩衝材の熱膨張係数も原位置試験結果をもとに設定した。

4) その他の物性値

表 5-12 には解析に用いた物性値を示す。材料としては、ヒーター（スチール)、緩衝材（粒状ベントナイト)、岩盤の 3 種類とした。ここで、緩衝材の弾性係数 E、比熱 c、熱伝導率λに関しては、含水比ωの関数とした。

表 5-12　解析に用いた物性値一覧

物性値	ヒーター	緩衝材	岩盤
弾性係数 [MPa]	2.0×10^{5}	式(5-31)	2.81×10^{4}
ポアソン比 [-]	0.3	0.3	0.3
密度 [g/cm³]	7.80	2.04	2.75
固有透過度 [m²]	1.0×10^{-27}	2.0×10^{-20}	1.98×10^{-16}
比熱 [kJ/kg℃]	0.46	式(5-32)	0.833
熱伝導率 [W/m℃]	53.0	式(5-33)	2.71
熱膨張係数 [1/℃]	1.64×10^{-6}	1.0×10^{-5}	1.0×10^{-6}

$$E = 254.9 - 8.854\omega \tag{5-31}$$

$$c = \frac{42.6 + 4.18\omega}{100 + \omega} \tag{5-32}$$

$$\lambda = 0.050\omega + 0.503 \tag{5-33}$$

(3) 解析結果

図 5-49、図 5-50、図 5-51、図 5-52 に解析結果を示す。図 5-49 には各出力ポイントにおける温度の経時変化を示す。当初の問題設定における温度の境界条件は r=10m の地点で 100℃に固定であったが、この場合、計算結果と実測値に大きな隔たりがあったため、r=2.5m の地点で温度を 100℃に固定した。加熱時には温度はどの地点も急激に上昇し早期に定常となった。また、減熱時の温度低下も急激であり、早期に温度が低下した。図 5-50 には緩衝材内の含水比の経時変化、図 5-51 には応力の経時変化を示す。加熱時の応力は全出力点とも上昇しており、Point 1 における応力の値が最も大きくなっている。ヒーターを停止すると同時に Point 1 における応力の値は瞬時に減少しているが、その後、緩衝材内の含水比が上昇するに伴い緩やかに上昇している。Point 2 および Point 3 においてはヒーター停止後も引き続き応力は緩やかに上昇している。図 5-52 には緩衝材内および岩盤内のひずみの経時変化を示す。正が引張、負が圧縮である。加熱試験開始とともに緩衝材内には圧縮ひずみが発生し、岩盤内には引張ひずみが発生している。ヒーターを停止することにより、それぞれひずみの絶対値が小さくなっている。

図 5-53～図 5-57 には出力ポイントにおける計算結果と実測値の比較を示す。図 5-53 は温度の比較、図 5-54 は緩衝材内の含水比の比較である。温度に関して、計算結果は実測値と良く一致している。また、含水比関しても Point 2 以外は良く一致している。図 5-55 には Point 1 における応力の経時変化の比較を示す。実測値は計測断面によって絶対値が異なっているが、ほぼ同じ傾向を示している。すなわち、過熱時に値が上昇し、ヒーターの停止とともに値が減少している。解析結果もほぼ同じ傾向を示しており、BBC 断面における計測結果と良く一致している。また、図 5-56、図 5-57 には緩衝材内および岩盤内におけるひずみの経時変化の比較を示す。緩衝材内、岩盤内とも過熱試験開始初期に大きな引張応力が出ているが、解析では十分に表現できていない。しかし、その後は実測値と計算結果でほぼ同じ傾向を示している。但し、緩衝材内に関しては絶対値に大きな違いがあり、岩盤内に関しては、ヒーター停止後、実測では圧縮ひずみが発生しているが、計算結果では圧縮ひずみは発生していない。この原因としては、力学構成則の問題、岩盤および緩衝材の物性値の問題等が考えられる。

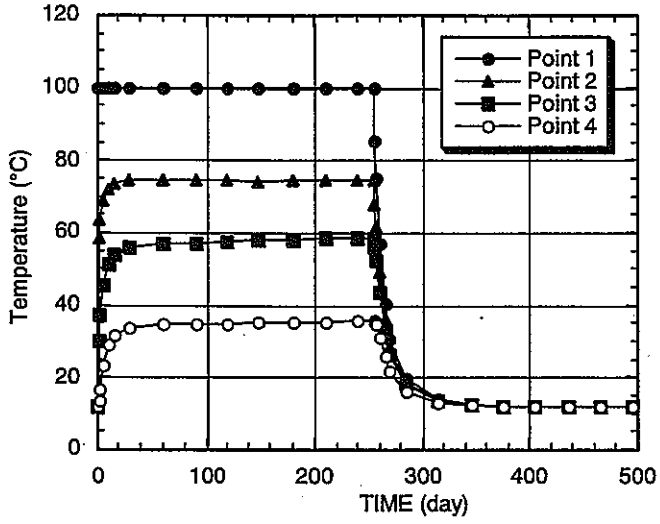

図 5-49　解析の結果得られた各出力ポイントの温度の経時変化

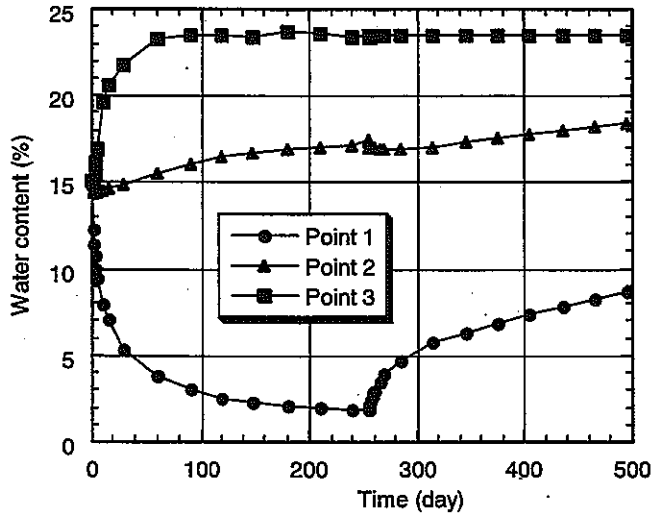

図 5-50　解析の結果得られた各出力ポイントの含水比の経時変化

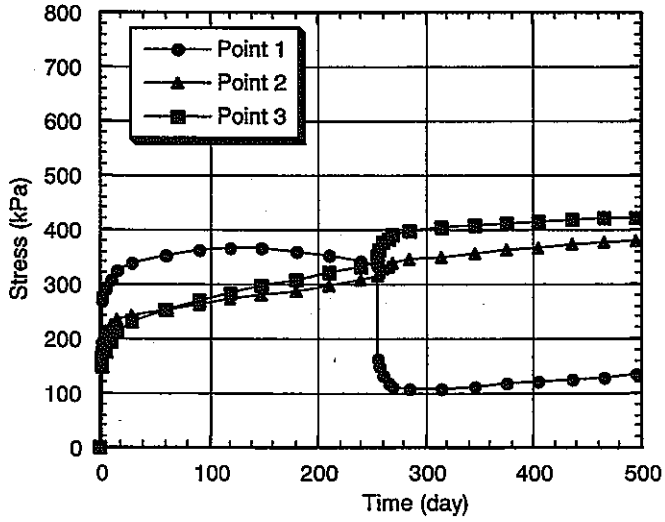

図 5-51　解析の結果得られた各出力ポイントの応力の経時変化

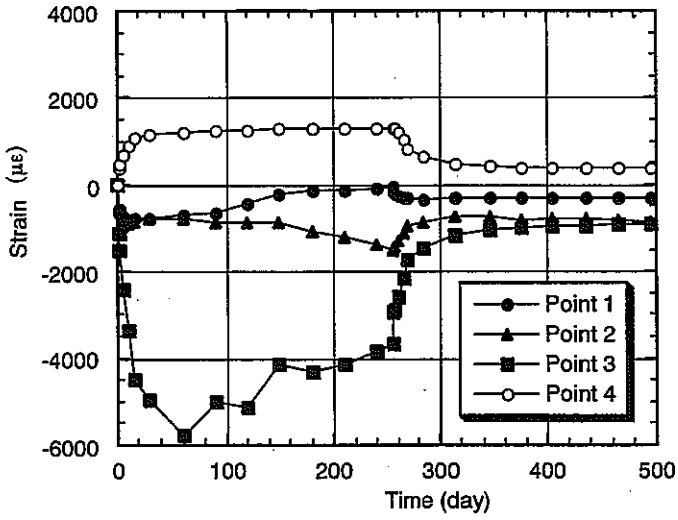

図 5-52　解析の結果得られた各出力ポイントのひずみの経時変化

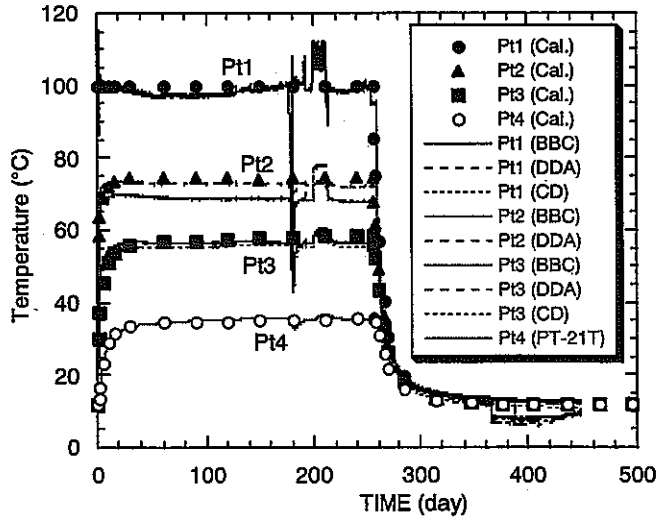

図 5-53　計算結果と実測値との比較（温度）

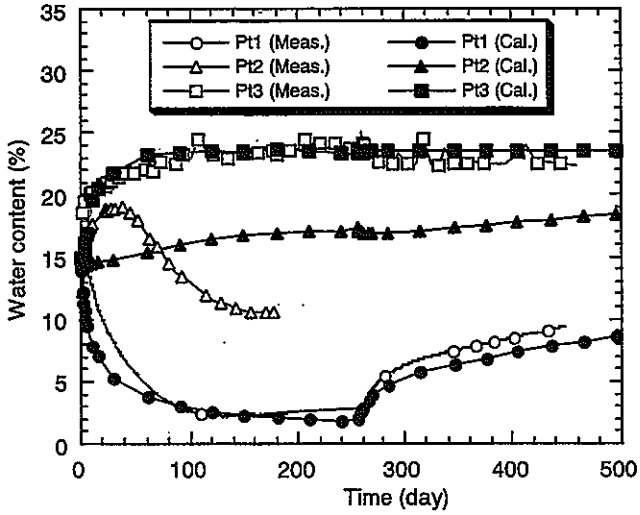

図 5-54　計算結果と実測値との比較（含水比）

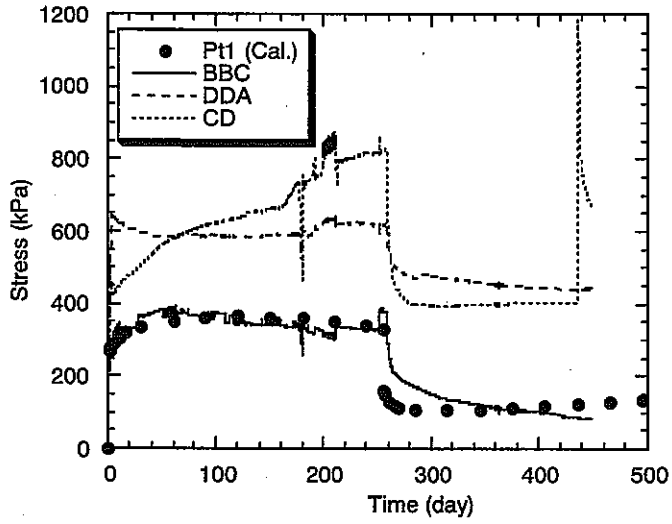

図 5-55　計算結果と実測値との比較（応力）

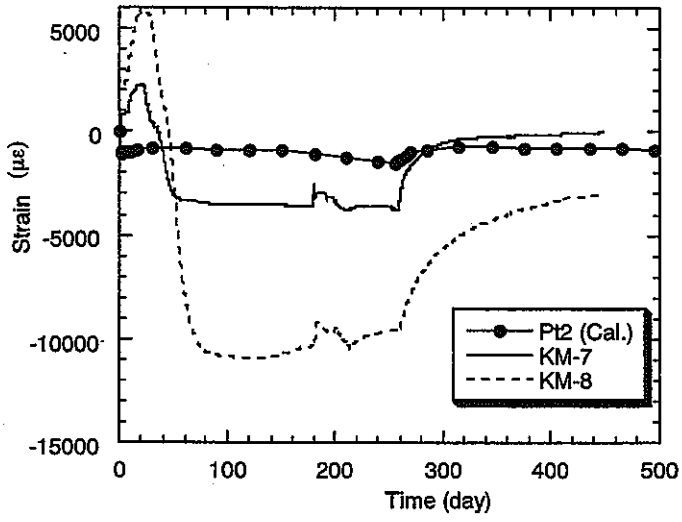

図 5-56　計算結果と実測値との比較（緩衝材内のひずみ）

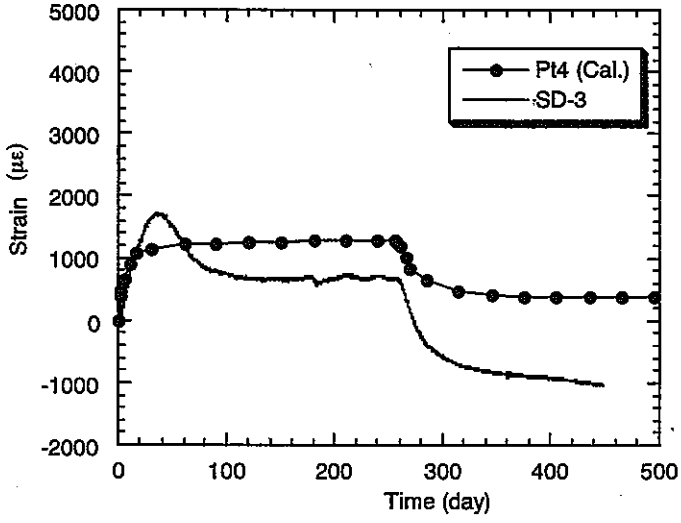

図 5-57　計算結果と実測値との比較（岩盤内のひずみ）

5.4 TASK3 BMT2 の概要

5.4.1 Task の概要

Task3 BMT2 は、モデル化する対象領域を小さいスケールから大きいスケールへと Upscaling することによる、不連続性岩盤の評価の違いを考察することを目的としている。具体的には、DECOVALEX 事務局により示された原位置でのデータに関して、クラックテンソル理論を用いて下記の２点に着目し考察していく。

- Upscaling することでどれだけの情報が失われるか？
- Upscaling することが、不連続性岩盤を評価する際にどれほど有効な手法であるか？

5.4.2 亀裂の幾何学的情報

(1) 方向性

表 5-13 は、亀裂の幾何学的情報を方向性で区分したものである。亀裂は Formation 1、Formation 2、Fault Zone の３種類に分類されている。

表 5-13 亀裂の幾何学的情報

Formation 1 (Based on Bulk Longlands Farm Member)

	Mean dip (º)	Dip direction (º)	Max spacing Vertical (m)	Mean spacing vertical (m)
Set 1	8	145	5.35	0.29
Set 2	88	148	2.21	0.26
Set 3	76	21	2.01	0.28
Set 4	69	87	3.54	0.31

Formation 2 (based on Altered Longlands Farm Member)

	Mean dip (º)	Dip direction (º)	Max spacing vertical (m)	Mean spacing vertical (m)
Set 1	25	28	4.29	0.51
Set 2	81	156	2.5	0.35
Set 3	72	20	3.83	0.28
Set 4	68	90	2.26	0.41

Fault Zone (based on Faulted Longlands Farm Member)

	Mean dip (º)	Dip direction (º)	Max spacing vertical (m)	Mean spacing vertical (m)
Set 1	8	21	1.43	0.18
Set 2	76	150	1.41	0.18
Set 3	72	21	1.06	0.19
Set 4	74	85	1.32	0.22

(2) 亀裂長さ

亀裂長さは、スキャンラインサーベイ・岩盤露頭面のトレースマップ・航空写真より測定されたデータであり、亀裂長さ L(m) と単位面積当たり(km²)の亀裂本数の関係式は式(5-34)で与えられる。また、式(5-34)にはトレース長の短い亀裂はあてはまらず、0.5m 以下の亀裂を考慮しないことが望ましい。

$$N = CL^{-D} \tag{5-34}$$

N: 単位面積当たり(km²)の亀裂本数
C: 4×10^{6}
D: 2.2 [+/- 0.2]

(3) 亀裂密度

Cut-off length x (m)と亀裂密度の関係は式(5-35)で与えられる。つまり x(m)以上の長さの亀裂の亀裂密度を表す式である。

$$Density(m^{-1}) = a \times x^{-E} \tag{5-35}$$

x : Cut-off length (m)
E = -1
a = 2.4

式(5-34)、(5-35)で求まる密度は、それぞれ二次元、一次元であるが三次元でも同じ値を持つものとする。また、各セットの密度はそれぞれ等しいとし亀裂総数を等分する。

5.4.3 クラックテンソル理論

(1) クラックテンソル

クラックテンソル理論は、不連続面を含む岩盤あるいはそれによって形成される異方性岩盤を等価な連続体に置き換えることのできる手法のひとつである。実岩盤において、調査領域の岩盤に対し対象とするクラックの大きさ・方向・開口幅の頻度分布を求めて式(5-36)、(5-37)に示す無次元量の二階と四階のクラックテンソルを決定する。

$$F_{ij}^{I} = \frac{\pi}{4}\frac{n_i^I n_j^I}{V_r}\sum_{k=1}^{m^I} L_k^{I^3} \tag{5-36}$$

$$F_{ijkl}^{I} = \frac{\pi}{4}\frac{n_i^I n_j^I n_k^I n_l^I}{V_r}\sum_{k=1}^{m^I} L_k^{I^3} \tag{5-37}$$

V_r:体積

m^I:考えている体積 V_r 中に含まれる各セットのクラックの総数

I:セット数

亀裂を含む岩盤全体の変形が岩盤を構成する岩石実質部分の変形と亀裂部分の変形の和で表されるとし、それぞれの弾性コンプライアンスを T_{ijkl}、M_{ijkl}、C_{ijkl} とすれば、これらの間には式(5-38)の関係が成立する。式(5-39)は不連続面の弾性コンプライアンスであり K_n、K_s は不連続面の力学特性を表す垂直剛性、せん断剛性である。

$$\overline{\varepsilon_{ij}} = \overline{T}_{ijkl}\overline{\sigma}_{kl} = (\overline{M}_{ijkl} + \overline{C}_{ijkl})\overline{\sigma}_{kl} \tag{5-38}$$

$$C_{ijkl} = \sum_I \left(\frac{1}{h^I} - \frac{1}{g^I}\right) F^I_{ijkl} + \frac{1}{4g^I}\left(\delta_{ik}F^I_{jl} + \delta_{jk}F^I_{il} + \delta_{il}F^I_{jk} + \delta_{jl}F^I_{ik}\right) \tag{5-39}$$

$$h^I = K^I_n L^I \ 、\ g^I = K^I_s L^I$$

(2) Barton and Bandis モデル

クラックテンソルの決定には、式(5-39)に示されるように不連続面の垂直剛性(K_n)、せん断剛性(K_s)といったパラメータが必要となる。これらの値は、原位置での計測で決定できるものであるが BMT2 ではデータが少ないため（４つのサンプル亀裂でのみ試験を行っている)、Barton and Bandis モデル(以下 BB モデル)を用い、これらの値を推測する。ここでは BB モデルによる K_n、K_s の誘導について簡単に記述する。

1) *JRC* および *JCS*

不連続面の粗度係数(*JRC*)は 0～20 の値に区分され凹凸が大きくなるほど大きな値をとる。不連続面の壁面強度(*JCS*)はシュミットハンマー試験により推定される。DECOVALEX 事務局より示された課題資料の Table2 より方向ごとの亀裂の平均 JRC_{300}、JCS_{300} が求まる。添え字の 300(mm)は室内試験での亀裂長さを表す。*JRC*、*JCS* にはスケール効果があり、室内試験試験で得られた亀裂長さ L_0 の *JRC*、*JCS* を JRC_0、JCS_0 とすると、式(5-40)、(5-41)より任意のスケール L_n の値(JRC_n、JCS_n)を推定できる。

$$JRC_n = JRC_{300}\left(\frac{L_n}{300}\right)^{-0.02JRC_{300}} \tag{5-40}$$

$$JCS_n = JCS_{300}\left(\frac{L_n}{300}\right)^{-0.03JRC_{300}} \tag{5-41}$$

2) K_{ni}(初期垂直剛性)

K_{ni}(初期垂直剛性)は、不連続面の垂直剛性(K_n)を決定する際に必要となるパラメータであり式(5-42)で与えられる。a_j(初期亀裂幅)はJRC、JCSを用いることで式(5-43)により表される。

$$K_{ni}^{I} = -7.15 + 1.75JRC_n^I + 0.02\left(JCS_n^I / a_j^I\right) \tag{5-42}$$

$$a_j^I = \frac{JRC_n^I}{5}\left(0.2\frac{UCS}{JCS_n^I} - 0.1\right) \tag{5-43}$$

3) K_n および K_s

不連続面の力学的特性を表す垂直剛性(K_n)、せん断剛性(K_s)はクラック面への垂直応力に強く依存することが知られている。垂直剛性は2)で示した初期垂直剛性(K_{ni})を用いることで式(5-44)で与えられる。またσ_nはクラック面への垂直応力を表す。BMT2における初期応力は式(5-45)により与えられている。せん断剛性(K_s)は垂直応力の一次関数で亀裂長さに反比例する関数式(5-46)で表される。

$$K_n^I = K_{ni}^I\left[1 - \frac{\sigma^I{}_n}{V_m K^I{}_{ni} + \sigma^I{}_n}\right]^{-2} \tag{5-44}$$

$$\sigma_{vertical} = 0.02494D + 0.26622(MPa) \tag{5-45}$$

$$K_s^I = \frac{100}{L^I}\sigma_n^I \tan\left[JRC_n^I \log_{10}\left(\frac{JCS_n^I}{\sigma^I{}_n}\right) + \phi^I{}_r\right] \tag{5-46}$$

5.4.4 モデル規模と弾性コンプライアンス(C_{ijkl})との関係

Upscaling することによる影響を調べるために、はじめに任意のモデル規模(立方体)とその規模内に存在しうる亀裂情報により求められた弾性コンプライアンスとの関係を求める。また本検討では、Cut-off の影響によるモデル規模と弾性コンプライアンスとの関係についても考察する。手法としては任意のモデル規模に存在する亀裂枚数を、長さの確率密度関数をもとに乱数を用いて発生させその亀裂長さに応じた JRC、JCS より垂直剛性・せん断剛性の規模依存を考慮し、三次元クラックテンソルを用いて不連続面の弾性コンプライアンスを求める。ただし、領域の中心座標が深さ 500m 地点と仮定しているため、式(5-45)より求まる垂直応力は以下の(1)～(3)では一定となる。

(1) Cut-off を考慮しない場合

ここでは Cut-off を考慮しない場合、つまり任意のモデル規模(立方体)に存在する全ての亀裂情報を用いて弾性コンプライアンスを作成する。つまりモデルの一辺を超える長さの亀裂が存在したとしても、それを不連続体として取り扱うことはしていない。ただし、0.5m 以下の長さを有

する亀裂は考慮しないこととする。また、原位置で観測された最大亀裂長さは250mである。

1) モデル規模と発生亀裂枚数の関係

すべてのモデル規模に対して存在しうる最小亀裂長さ L_{min}、最大亀裂長さ L_{max} は L_{min}=0.5(m)、L_{max}=250(m)であり、式(5-35)を用いることで式(5-47)に示すようにモデル規模(m^3)とその領域内に存在する亀裂枚数が推定可能となる。

$$Number\ of\ fractures = (\mathrm{D}(L_{min}) - \mathrm{D}(L_{max})) \times \mathrm{volume}(\mathrm{m}^3) \tag{5-47}$$

2) 発生亀裂枚数と亀裂長さの関係

任意のモデル規模に存在する亀裂枚数は、式(5-47)より求まることがわかった。次に発生させる亀裂長さが問題となる。そこで式(5-33)を L_{min}=0.5(m)～L_{max}=250(m)で積分することで求まる単位面積あたりの全亀裂本数 7653570 から、任意の長さ L(m)の分布関数 $f(L)$を導く。また $f(L)$を L_{min}=0.5(m)～L_{max}=250(m)で積分することにより、長さ L(m)の確率密度関数、式(5-48)をもとに乱数を発生させ亀裂長さを決定する。

$$\begin{aligned} f(L) &= \frac{4\times10^6}{7653570}L^{-2.2} \\ P(L) &= \int_{0.5}^{L} f(L)dL = \frac{4\times10^6}{7653570}\left[-\frac{1}{1.2}L^{-1.2}\right]_{0.5}^{L} \\ &= \frac{4\times10^6}{7653570}\left(-\frac{1}{1.2}\right)\left(L^{-1.2} - 0.5^{-1.2}\right) \end{aligned} \tag{5-48}$$

3) 力学定数

1)により発生亀裂枚数、2)により個々の亀裂長さが決定される。ただし前述したようにBBモデルを用いることにより、亀裂長さに応じたJRC、JCSより垂直剛性(K_n)、せん断剛性(K_s)の規模依存を考慮した三次元クラックテンソル、弾性コンプライアンスを求める。

4) 結果

上記より求まったモデル規模と弾性コンプライアンスとの関係を図5-58に示す。ここでは、弾性コンプライアンスの代表値として C_{xxxx} を用いる。図より一辺250m以上のモデル規模で弾性コンプライアンスが安定していることが分かる。ここでは、対象とするモデル以上の長さを有する亀裂も考慮しているために、原位置での最大亀裂長さが250mであることを考慮すれば、一辺250mのモデル規模で弾性コンプライアンスが安定することは当然の結果といえる。つまり、モデル規模の一辺を超える亀裂を連続体としてとらえることは非現実的であると考え、今後このような亀裂は不連続体として取り扱うこととする。

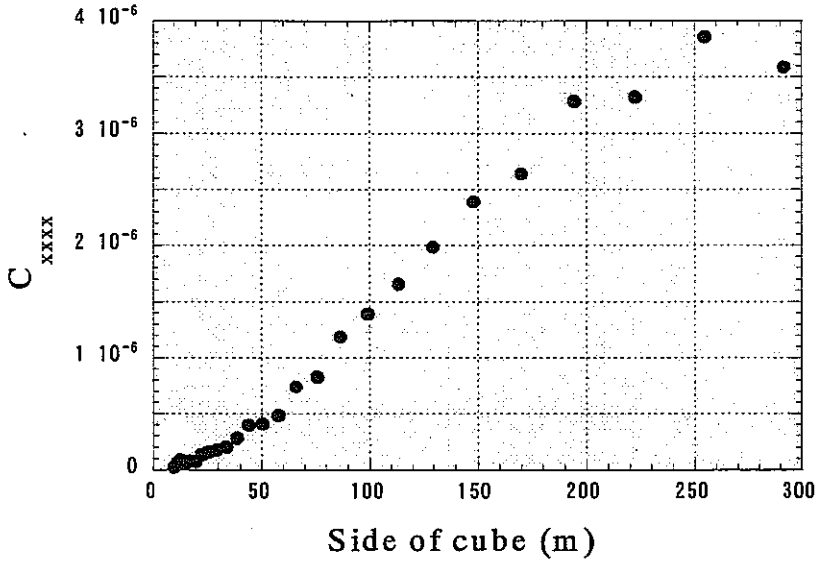

図 5-58　モデルの一辺の長さと C_{xxxx} の関係

(2) 最大亀裂長さを制限した場合

(1)ではモデル規模に存在する全ての亀裂を考慮したが、ここではモデルの一辺の長さを超える亀裂は不連続体(ジョイント要素等)として扱うという条件で、モデル規模と弾性コンプライアンスの関係を求めた。つまり、すべてのモデル規模に対して存在しうる最小亀裂長さ L_{min}、最大亀裂長さ L_{max} は L_{min}=0.5(m)、L_{max}= “モデルの一辺の長さ(m)” として 5.4.4(1) 1)～3)の手順で弾性コンプライアンスを導く。

図 5-59 にモデル規模と弾性コンプライアンスとの関係を示す。図よりモデルの一辺を超える亀裂を不連続体で考えた場合、モデル規模の増加に伴い弾性コンプライアンスは安定しないことがわかった。

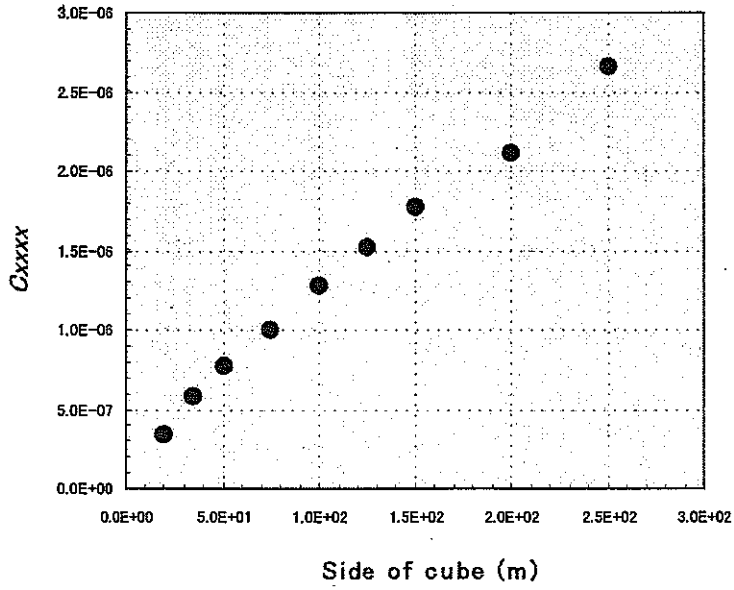

図 5-59　モデルの一辺の長さと C_{xxxx} の関係

(3) Cut-off を考慮した場合

(2)よりモデルの一辺の長さを超える亀裂を不連続体として取り扱った場合、弾性コンプライアンスは安定しなかった。そこで Cut-off という概念を導入することにする。Cut-off とは、長さ L(m)以下の亀裂を考慮しないということである。簡単にいうと大きなモデル規模では、長さの短い亀裂の影響は少ない可能性もあるので、任意のモデル規模において様々な Cut-off length(0.5～一辺の長さ/10)で弾性コンプライアンスを求めてみた。つまり、任意のモデル規模に対して存在しうる最小亀裂長さ L_{min}、最大亀裂長さ L_{max} は L_{min}=Cut-off value(m)、L_{max}="モデルの一辺の長さ(m)" として 5.4.4(1) 1)～3)の手順で弾性コンプライアンスを導く。

図 5-60 にモデル規模と弾性コンプライアンスとの関係を示す。図よりモデル規模が 50m×50m×50m の立方体までは Cut-off length の影響はほとんどないことが分かる。つまり、その領域では、短い亀裂が支配的であるといえる。一方、Upscaling していくことで Cut-off の影響が顕著に生じ、ある Cut-off length 以上で安定した値となっている。例えば一辺 150m のモデル規模では 10m 以下の亀裂を Cut-off したときに、弾性コンプライアンスは安定する。もろい岩盤の弾性コンプライアンスは大きいことより、このモデル規模では 10m 以下の亀裂を考慮せずにクッラクテンソルを作成することは、安全側に岩盤挙動を評価していることにつながるので合理的な手段といえる。

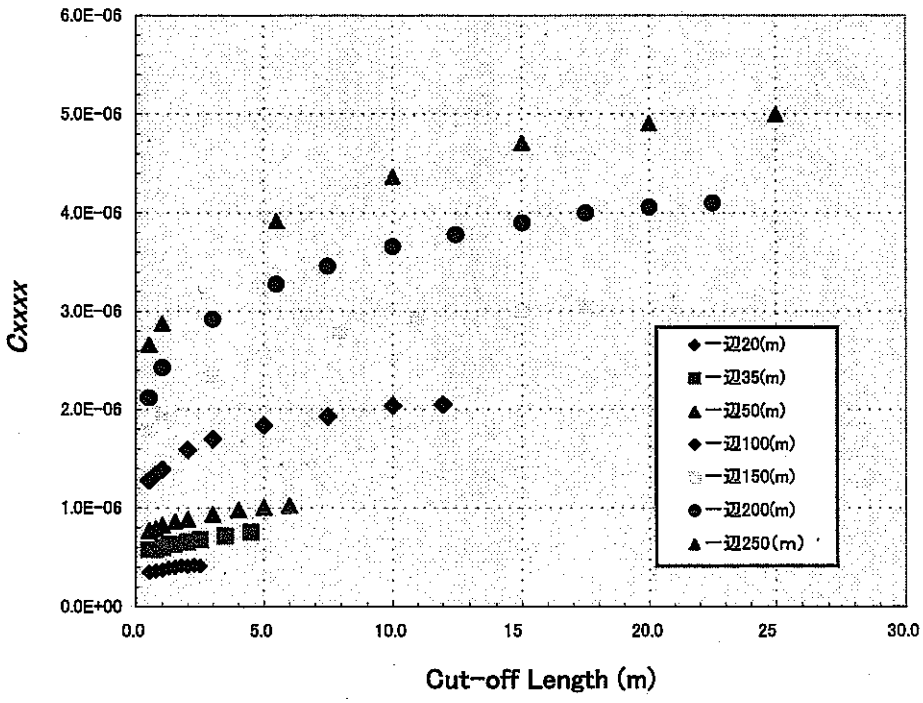

図 5-60 Cut-off length(m)と C_{xxxx} の関係

(4) 垂直応力と弾性コンプライアンスとの関係

(1)～(3)では、深さ 500m 地点における弾性コンプライアンスを求めており、垂直応力は一定である。ここでは、垂直応力を変化させることでの弾性コンプライアンスの影響を調べることにする。ただしモデル規模は一辺 100m と一定とし、垂直応力以外の条件は(3)と同じである。また式

(5-30)より対象領域の中心となる深さと垂直応力は正の比例関係がある。

図 5-61 に対象領域の中心となる深さ(m)と弾性コンプライアンスの関係を示す。図より垂直応力の増加に伴い、弾性コンプライアンスが小さくなることが分かる。また、安定する Cut-off length は全ての領域でおおよそ 5m であり、短い Cut-off length で安定するといえる。また、深さ 100m～200m では垂直応力の変化に伴い弾性コンプライアンスは大きく減少している。これらのことより、不連続性岩盤を、クラックテンソル理論を用いて等価な連続体として評価する際には、モデル規模の影響に加え垂直応力への依存性が大きいといえる。

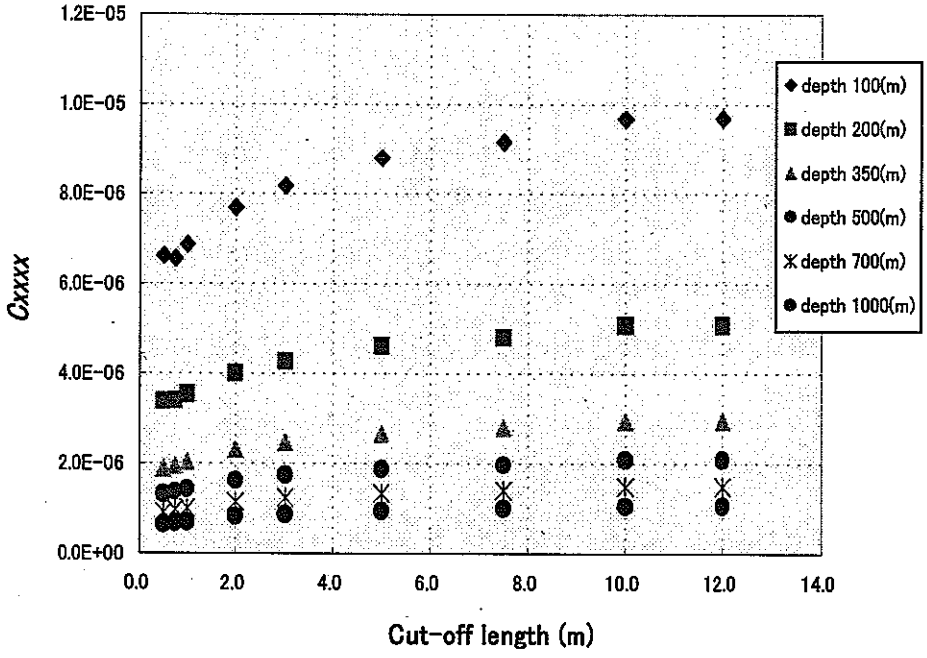

図 5-61　垂直応力(深さ)と C_{xxxx} の関係

5.4.5　モデル規模と異方透水性を示すクラックテンソル(P_{ij})との関係

5.4.4 ではモデル規模と弾性コンプライアンスとの関係を検討したが、ここではモデル規模と式(5-49)で表される P_{ij} との関係を考察する。ただし、ここでは代表値として P_{xx} を用いる。また、弾性コンプライアンスと同様 Cut-off による P_{xx} の影響についても考察する。

$$P_{ij}^{I} = \frac{\pi}{4}\frac{n_i^I n_j^I}{V_r}\sum_{k=1}^{m^I} L_k^{I^2} \tag{5-49}$$

(1) Cut-off を考慮しない場合

5.4.4 と同じ条件、つまり Cut-off を考慮せずにモデルの一辺を超える亀裂は不連続体として扱い、その他のすべての亀裂情報を用いて P_{xx} を作成した。その結果を図 5-62 に示す。図よりモデル規模の増加とともに弾性コンプライアンスは増加しているのに対して(図 5-59 と同じグラフである) は P_{xx} 減少している。クラックテンソル F_{ij}、F_{ijkl} には L^3 の項があるのに対して、P_{xx} では L^2 の項になるために起こったものと考えられる。BMT2 では亀裂長さの確率密度関数が指数関数であり長さの-2.2 乗で減少する。したがって、式(5-34)より長さの-0.2 乗で P_{ij} は変化する。逆に

C_{ijkl}は長さの0.8乗で変化する。このように長さの密度分布が各係数の規模依存性に大きな影響を与えていることがわかる。

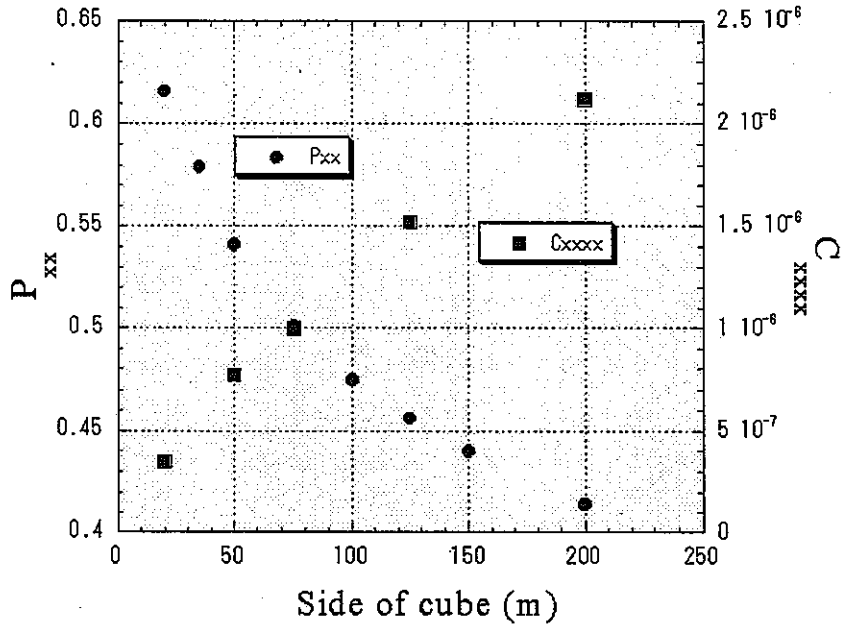

図 5-62　モデルの一辺の長さとP_{xx}の関係

(2) Cut-off を考慮した場合

5.4.4と同じ条件を用いてP_{xx}を作成した。結果を図5-63に示す。図よりP_{xx}と弾性コンプライアンス(図5-60)を比べると、C_{ijkl}は一辺の長さの1/10、P_{xx}は1/20程度で安定することが分かる。またCut-offすることによって、最終的にP_{xx}がモデル規模に依存せず安定した値(0.7)となることより、Cut-offすることで、図5-62で示したP_{xx}の規模依存性の影響をなくすことが可能ともいえる。

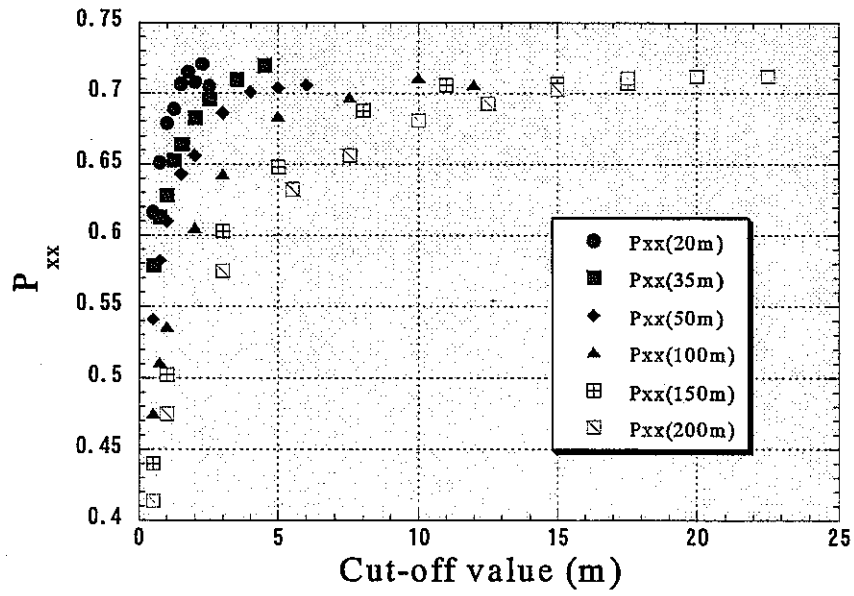

図 5-63 Cut-off length(m)とP_{xx}の関係

5.4.6 まとめ

不連続性岩盤の浸透問題では、Cut-off することでモデル規模に依存しない P_{ij} を得ることができた。つまり、Upscaling することによる規模依存性を Cut-off することで防ぐことができるといえる。一方、変形問題を考える際には Upscaling による規模依存性を防ぐことができないことがわかった。

References

Barton, N, Bandis, S and Bakhtar, K: Strength, Deformation and Conductivity Coupling of Rock Joints, Int. J. Rock M.M.S.G.A, 22,3,pp.121-140, 1985

Oda, M. : An Equivalent Continuum Model for Coupled Stresses and Fluid Flow Analysis in Jointed Rock Masses, Water Resour. Res. Vol. 22, No. 13, pp.1845-1856, 1986

Ohnisi,Y. Shibata,H. Kobayasi,A.,: Development of finite element code for the analysis of coupled thermo-hydro-mechanical behaviors of saturated-unsaturated medium, Proc. Int. Symp. Coupled Porocesses Affectting the Performance of a Nuclear Waste Repository, Berkeley, 263-268,1985.

6. 終わりに

本研究では、人工バリアの健全性において重要な要因の一つとなる緩衝材の施工技術のうち、緩衝材をブロックで施工した場合等に考えられるブロック間や岩盤あるいはオーバーパックとの隙間の充填性に関する検討を実施した。隙間充填材としてベントナイトペレットについて検討し、ペレットを充填し浸潤飽和した後の特性の把握を行なった。その結果、浸潤飽和後の透水係数は、飽和後の乾燥密度相当の値となることがわかった。また、膨潤応力の発現も観察できた。すなわち、ベントナイトペレットを適切に充填すれば所定の品質の緩衝材となること確認できた。また，施工された緩衝材内には，処分後，廃棄体からの発熱，地下水の浸潤，周辺岩盤からの地圧や緩衝材の膨潤といった連成挙動が発現すると考えられる。これらの現象を理解，評価するためには，人工バリアを対象とした原位置での実規模試験の情報に基づき，適切なモデルを構築する必要がある。そこで，緩衝材および岩盤を含めた人工バリア周辺における連成現象に関する試験であるスウェーデン Äspö 等における HRL において実施されている Prototype Repository Project に参加し、試験データの収集等を行なった。さらに、国際共同研究 DECOVALEX III にも参加し、各タスクの解析を実施した。今後の、引き続き、このような国際共同研究に参加し、解析モデルの充足を図っていくことが重要であると考えられる。

添付資料一覧

別添 - 1　Prototype Repository Project　OHP 資料

別添 - 2　Prototype Repository Project　事務局提出書類（検討結果）

別添 - 3　DECOVALEX TASK1　GENERAL SPECIFICATIONS

別添 - 4　DECOVALEX TASK1　PART A ; TASK DEFINITIONS

別添 - 5　DECOVALEX TASK1　PART B ; TASK DEFINITIONS

別添 - 6　DECOVALEX TASK1　事務局提出書類（検討結果）

別添 - 7　DECOVALEX TASK3 BMT1　TASK DEFINITIONS

別添 - 8　DECOVALEX TASK3 BMT1　事務局提出書類（検討結果）

別添 - 9　DECOVALEX TASK3 BMT2　TASK DEFINITIONS

別添 - 1

Prototype Repository Project　OHP 資料

Analysis Plan for PRP

Japan Nuclear Cycle
Development Institute

RADIOACTIVE WASTE MANAGEMENT PROJECT

Analysis code

THAMES (Thermal, Hydraulic And MEchanical System analysis)
-Finite element code for fully coupled T-H-M processes in saturated or unsaturated geological media
-Developed by Prof. Ohnishi and Prof. Kobayashi of Kyoto Univ. with Hazama
-Original code is based on the following assumptions
:The medium is porous and elastic
:Darcy's law is adopted for water flow in saturated/unsaturated medium
:Fourier's law is adopted for heat transfer in both solid and liquid phases when no consideration given for gas phase
:No consideration for phase change between water and vapor
:Density of water changes with both temperature and pressure

RADIOACTIVE WASTE MANAGEMENT PROJECT

Extension of analysis code

Extension of THAMES code for analysis of Buffer material

-Water movement is calculated used by D_θ and ψ -θ curve

-Consideration of vapor flow ($D_{\theta v}$: isothermal vapor diffusivity)

Water movement is occurred in two phases of vapor and liquid water

It is assumed that pressure gradients of vapor and liquid are equal

-Consideration of latent heat by evaporation

-Consideration of water movement by temperature gradient

(D_T : thermal water diffusivity)

-Consideration of swelling pressure

D_θ and ψ-θ curve were obtained by laboratory test

and parameters for water movement by temperature gradient

and swelling pressure were obtained by back analysis of laboratory test

Analysis plan

Part A: Two dimensional axial symmetric model

*One disposal pit

Part B: Three dimensional model

*Two disposal pits

Schedule

	1	2	3	4	5	6	7	8	9	10	11	12	13	14	15	16	17	18	19	20	21	22	23	24	25	26	27	28	29	30	31	32	33	34	35	36	37	38	39	40	41	42
Year	2000				2001												2002												2003														2004	
Month	9	10	11	12	1	2	3	4	5	6	7	8	9	10	11	12	1	2	3	4	5	6	7	8	9	10	11	12	1	2	3	4	5	6	7	8	9	10	11	12	1	2
Part A																																										
Analysis																																									
Report																																									
Review																																									
Calibration																																									
Report																																									
Part B																																									
Analysis																																									
Report																																									
Review																																									
Calibration																																									
Report																																									

Analysis model ; Part A

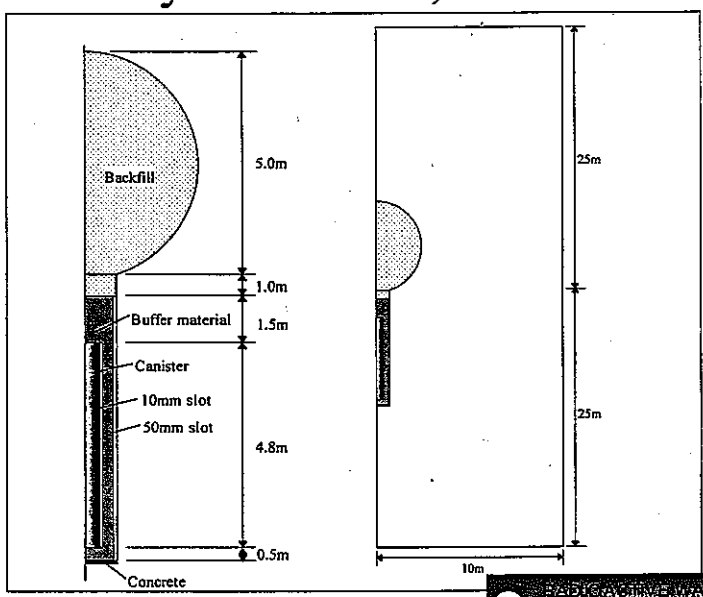

Finite element mesh

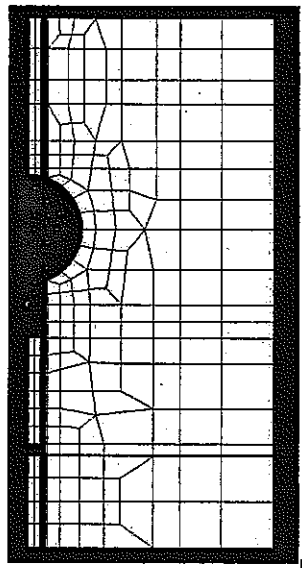

Analysis model ; Part B

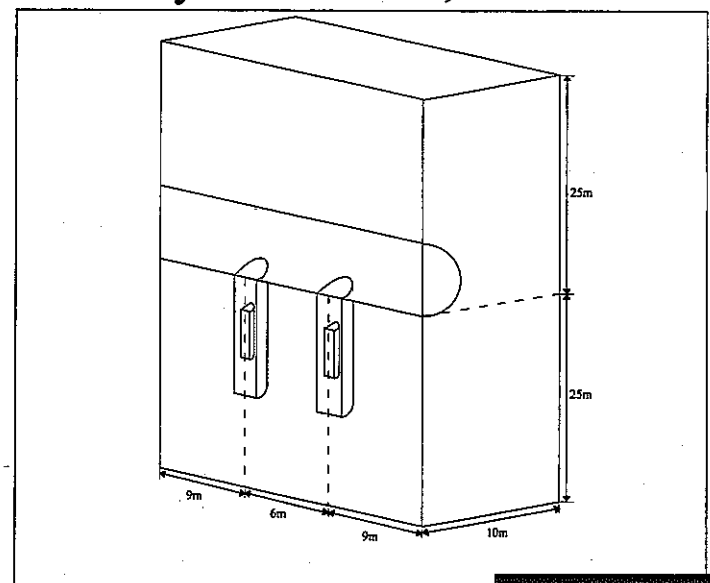

JNC

Analysis condition

Boundary ; Upper and bottom
: Constant temperature
: Constant water pressure
; Side
: Adiabatic condition
: No flux
; All boundaries are fixed

RADIOACTIVE WASTE MANAGEMENT PROJECT

JNC

Output from analysis for comparison with measured data

Buffer ; Water content
Temperature
Stress

Rock ; Pore pressure
Temperature
Stress or Strain (Displacement)

RADIOACTIVE WASTE MANAGEMENT PROJECT

Analysis step (Part A)

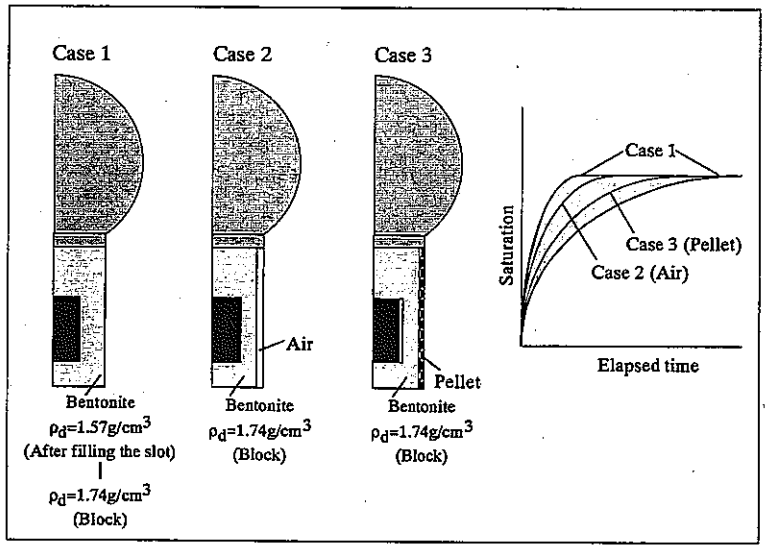

Request for analysis

*Temperature gradient test
- Test conditions
- Test results

*Swelling pressure test
- Test conditions
- Test results

*Properties of concrete at the bottom of disposal pit

*Thickness of concrete

別添 - 2

Prototype Repository Project

事務局提出書類（検討結果）

Description of numerical code THAMES of JNC

1 Analysis objective

Analysis of the coupled thermal, hydraulic and mechanical process is carried out with the computer code named THAMES. THAMES is a finite element code for analysis of coupled thermal, hydraulic and mechanical behaviors of a saturated-unsaturated medium. THAMES is extended to take account of the behavior in the buffer materials such as the water flow due to thermal gradient and the swelling phenomena. The unknown variables are total pressure, displacement vector and temperature. The quadratic shape function is used for the displacements and linear one is used for total pressure and temperature.

2 Governing equations of coupled T-H-M process

The mathematical formulation for the model utilizes Biot's theory, with the Duhamel-Neuman's form of Hooke's law, and energy balance equation. The governing equations are derived with the fully coupled thermal, hydraulic and mechanical relationships.

2.1 Assumption

The governing equations are derived under the following assumptions:

1) The medium is poro-elastic.
2) Darcy's law is valid for the flow of water through a saturated-unsaturated medium.
3) Heat flow occurs only in solid and liquid phases. The phase change of water from liquid to vapor is not considered.
4) Heat transfer among three phases (solid, liquid and gas) is disregarded.
5) Fourier's law holds for heat flux.
6) Water density varies depending upon temperature and the pressure of water

2.2 Equilibrium equation

The equation of motion for a medium in a static case is known as an equilibrium equation. It is written in a total stress expression as

$$\sigma_{ij,j} + \rho b_i = 0 \tag{1}$$

where σ_{ij} is the stress, ρ is the density of as soil-water mixing medium and b_i is the body force.

Terzaghi defined the effective stress principle. Bishop and Blight extended his definition and proposed the following equation for a saturated-unsaturated medium:

$$\sigma_{ij} = \sigma'_{ij} + \chi \delta_{ij} \rho_f g \psi \tag{2}$$

where σ'_{ij} is the effective stress, δ_{ij} is the Kronecker's delta, ρ_f is the unit weight of water, g is the acceleration of gravity and ψ is the pressure head. Subscript f means "fluid". Parameter χ is defined as

$$\chi = 1 \quad \text{(Saturated zone)}, \quad \chi = \chi(S_r) \quad \text{(Unsaturated zone)} \tag{3}$$

χ is a nonlinear function of S_r (the degree of saturation).

The validity of equation (2) is not definite and is still under debate even now. However, here it is assumed that equation (2) holds and that χ is approximately equal to S_r.

Substituting equation (1) for equation (2), the equilibrium equation for the effective stress is a saturated-unsaturated geologic medium is obtained, namely,

$$\left(\sigma'_{ij} + \chi\delta_{ij}\rho_f g\psi\right)_{,j} + \rho b_i = 0 \tag{4}$$

where $(\chi\delta_{ij}\rho_f g\psi)$ is a term which means that changes in the pressure head influence the equilibrium equation.

The effects of temperature can be implemented in a constitutive law for a sold medium. For an isotropic linear elastic material, Duhamel-Neuman's relationship can be used and the following constitutive law is obtained:

$$\sigma'_{ij} = C_{ijkl}\,\varepsilon_{kl} - \beta\delta_{ij}\left(T - T_o\right) \tag{5}$$

where $\beta = (3\lambda+2\mu)\alpha_T$. C_{ijkl} is the elastic matrix, ε_{kl} is the strain tensor, T is the temperature, λ and μ are Lamé's constant and α_T is the thermal expansivity coefficient. Subscript o means that the parameter is in a reference state.

The infinitesimal strain-deformation relationship is

$$\varepsilon_{kl} = \frac{1}{2}\left(u_{k,l} + u_{l,k}\right) \tag{6}$$

where u_i is the deformation vector.

Substituting equation (5) and (6) into equation (4), the stress equilibrium equation is obtained. It takes into account the effects of temperature and pore pressure change, namely,

$$\left[\frac{1}{2}C_{ijkl}\left(u_{k,l} + u_{l,k}\right) - \beta\delta_{ij}\left(T - T_o\right) + \chi\delta_{ij}\rho_f g\psi\right]_{,j} + \rho b_i = 0 \tag{7}$$

$(-\beta\delta_{ij}(T-T_o))_{,j}$ is a term which stands for the influence of heat transfer on the equilibrium equation.

2.3 Continuity equation for ground water

The equation of continuity for ground water in a saturated-unsaturated zone is derived from Richards' theory as follow:

$$\frac{\partial\left(\rho_f\theta\right)}{\partial t} = -\left(\rho_f v_i\right)_{,i} \tag{8}$$

where θ is the volumetric water content, t is the time and v_i is the velocity vector.

The equation of motion for ground water can be explained by Darcy's law. That is,

$$v_i = -k(\theta)_{ij}\,h_{,j} \tag{9}$$

where $k(\theta)_{ij}$ is the permearbility tensor that is a function of θ. h is the total head.

The total head can be expressed as the sum of pressure head ψ and elevation head z.

$$h = \psi + z \tag{10}$$

The volumetric water content θ is a function of the degree of saturation S_r and porosity n, which is expressed as,

$$\theta = n\, S_r \tag{11}$$

Substitution equations (9), (10) and (11) into (8), following equation is obtained.

$$\left\{\rho_f\, k(\theta)_{ij}\, (\psi + z)_{,j}\right\}_{,i} = \frac{\partial}{\partial t}\rho_f\, n\, S_r \tag{12}$$

The right-hand side of equation (12) is expanded to

$$\frac{\partial}{\partial t}\rho_f\, n\, S_r = n\, S_r \frac{\partial \rho_f}{\partial t} + \rho_f\, S_r \frac{\partial n}{\partial t} + \rho_f\, n \frac{\partial S_r}{\partial t} \tag{13}$$

The first term at the right-hand side represents a density change in the pore water. The second term means a change in the skeleton of the porous medium. The third term stands for a change in the degree of saturation in an unsaturated region.

Considering the compressibility and the thermal expansivity of water, the density of water can be expressed as,

$$\rho_f = \rho_{fo}\left[1 - \beta_T(T - T_o) + \beta_P(P - P_o)\right] \tag{14}$$

where P is the pore water pressure and ρ_{fo} is the reference density at $P=P_o$ and $T=T_o$.

β_T and β_P are the thermal expansivity and the compressibility of water, respectively,

$$\beta_T = \left|-\frac{1}{\rho_f}\frac{\partial \rho_f}{\partial T}\right| \quad (P = \text{constant}) \tag{15}$$

and

$$\beta_P = \left|\frac{1}{\rho_f}\frac{\partial \rho_f}{\partial P}\right| \quad (T = \text{constant}) \tag{16}$$

Eaton assumed that buoyancy could be ignored in an unsaturated zone due to its insignificant effect on the fluid flow. Adopting this assumption, β_T is set to be zero in an unsaturated zone.

A combination of the first terms in equations (13) and (14) yields

$$n\, S_r \frac{\partial \rho_f}{\partial t} = \rho_{fo}\, n\, S_r\left(-\beta_T \frac{\partial T}{\partial t} + \beta_P \frac{\partial P}{\partial t}\right) \tag{17}$$

Pressure head ψ is related to the pore water pressure as follows:

$$\psi = \frac{P}{\rho_f g} \tag{18}$$

Taking equation (10) and (18) into account, equation (17) can then be modified to

$$n S_r \frac{\partial \rho_f}{\partial t} = \rho_{fo} n S_r \left(-\beta_T \frac{\partial T}{\partial t} + \rho_f g \beta_P \frac{\partial \psi}{\partial t} \right) \tag{19}$$

Assuming that the strain is infinitesimal, the second and third terms at the right-hand side of equation (13) are expressed as

$$\begin{aligned} \rho_f S_r \frac{\partial n}{\partial t} &\cong \rho_f S_r \frac{\partial u_{i,i}}{\partial t} \\ \rho_f n \frac{\partial S_r}{\partial t} &\cong \rho_f \frac{\partial \left(n S_r \right)}{\partial t} = \rho_f \frac{\partial \theta}{\partial t} = \rho_f \frac{\partial \theta}{\partial \psi} \frac{\partial \psi}{\partial t} \end{aligned} \tag{20}$$

Equation (12) is modified by using equation (19) and (20) as follows:

$$\left\{ \rho_f k(\theta)_{ij} h_{,j} \right\}_{,i} - \rho_{fo} n S_r \rho_f g \beta_P \frac{\partial \psi}{\partial t} - \rho_f \frac{\partial \theta}{\partial \psi} \frac{\partial \psi}{\partial t} - \rho_f S_r \frac{\partial u_{i,i}}{\partial t} + \rho_{fo} n S_r \beta_T \frac{\partial T}{\partial t} = 0 \tag{21}$$

Equation (21) is an equation of continuity for ground water which takes into account the compressibility of the ground water and changes in density by temperature change.

2.4 Energy conservation law

In general, the ground consists of materials with three phases, i.e., solid, liquid and gas. It is not easy to understand the behavior of heat transfer through such a composite material, because the way in which heat is transported is difficult for each phase and a heat transfer may occur between phases. However, the state of the gaseous phase in a ground is too complicated to be modeled. For simplicity, a pore in a porous medium is assumed to be filled with only a liquid phase here. This means that the ground water does not change in phase from liquid to gas or vise versa and that the thermal conductivity of the gaseous phase is disregarded. Since the heat conductivity of the gaseous phase is smaller than that of liquid and the solid phases, the heat conductivity of the composite material is not affected much by the volume of the gaseous phase.

An energy conservation law, based upon the process proposed by Bear and Carapcioglu, is derived for ground water from the above assumptions without the effect of viscous dissipation.

Consideration the existence of an unsaturated zone, the equation of energy conservation is written as,

$$n S_r \rho_f C_{vf} \left(\frac{\partial T_f}{\partial t} + V_f \nabla T_f \right) = -\nabla n S_r J_f - \left(\frac{\partial P}{\partial T_f} \right)_{\rho_f} n S_r T_f \nabla V_f \tag{22}$$

where C_v is the specific heat and J is the heat flux by conduction. In equation (22), the first term at the left-hand side shows the time dependency of energy, the second term shows the change in energy due to heat convection. The first term at the right-hand side express the change in energy by heat conduction and the second term shows the reversible energy change caused by compression.

Similarly, the energy conservation law for a solid phase is written as,

$$(1-n)\rho_s C_{vs}\left(\frac{\partial T_s}{\partial t}+V_s\nabla T_s\right)=-\nabla(1-n)J_s-(1-n)\beta T_s\frac{\partial \varepsilon_s}{\partial t} \tag{23}$$

where subscript s means solid. In equation (23), the second term at the right-hand side indicates the reversible energy change caused by deformation.

Faust and Mercer proposed that the movement of water through porous media is so slow and the surface areas of all phases are so large that it is reasonable to assume that a local thermal equilibrium among phase is achieved instantaneously. This means that the heat transfer between phases in the ground can be disregarded. If this assumption is permitted, the following equation is then valid:

$$T=T_s=T_f \tag{24}$$

Uing this assumption, equations (22), (23) and (24) can be combined and an equation of energy conservation for the ground can be obtained by

$$\begin{aligned}&\left[nS_r\rho_f C_{vf}+(1-n)\rho_s C_{vs}\right]\frac{\partial T}{\partial t}+\left[nS_r\rho_f C_{vf}V_f+(1-n)\rho_s C_{vs}V_s\right]\nabla T\\&=\nabla\left[nS_rJ_f+(1-n)J_s\right]-nS_rT\left(\frac{\partial P}{\partial T}\right)_{\rho_f}\nabla V_f-(1-n)T\beta\frac{\partial \varepsilon_s}{\partial t}\end{aligned} \tag{25}$$

When it is assumed that Fourier's law is valid for heat conduction, the following equation are given:

$$\begin{aligned}J_f&=-K_{Tf}\nabla T\\J_s&=-K_{Ts}\nabla T\end{aligned} \tag{26}$$

where K_T is the coefficient of heat conduction.

The term $(\partial P/\partial T)$ in equation (25) can be modified by applying equation (15) and (16) as follows:

$$\left(\frac{\partial P}{\partial T}\right)_{\rho_f}=\left|\frac{\beta_T}{\beta_P}\right|_{\rho_f=cons\,tant} \tag{27}$$

Disregarding the velocity of a solid, equation (25) is rewritten using equation (6), (9), (26) and (27) in the following form:

$$
\begin{aligned}
&\left(\rho C_v\right)_m \frac{\partial T}{\partial t} + nS_r \rho_f C_{vf} V_{fi} T_{,i} - K_{Tm} T_{,ii} \\
&-nS_r T \frac{\beta_T}{\beta_P} k(\theta) h_{,ii} + \frac{1}{2}(1-n)\beta T \frac{\partial}{\partial t}\left(u_{i,j} + u_{j,i}\right) = 0
\end{aligned}
\tag{28}
$$

where $(\rho C_v)_m$ and K_{Tm} are expressed as follows:

$$
\left(\rho C_v\right)_m = nS_r \rho_f C_{vf} + (1-n)\rho_s C_{vs} \tag{29}
$$

and

$$
K_{Tm} = nS_r K_{Tf} + (1-n)K_{Ts} \tag{30}
$$

Equation (28) is an energy conservation law in which the effects of stress-deformation and ground water flow are considered. The first, second and third terms at the right-hand side express changes in energy due to heat conduction, pore water pressure and reversible energy caused by solid deformation, respectively.

2.5 Governing equations

Equation (7), (21) and (28) represent the governing equations for a coupled tharmal, hydraulic and mechanical problem proposed by Ohnish et al. This model was verified with the available analytical and experimental results. These equations are used by means of a total head expression such as,

$$
\begin{aligned}
&\left[\frac{1}{2}C_{ijkl}\left(u_{k,l} + u_{l,k}\right) - \beta\delta_{ij}\left(T - T_o\right) + \chi\delta_{ij}\rho_f g\psi\right]_{,j} + \overline{\rho_s} b_i = 0 \\
&\left\{\rho_f k(\theta)_{ij} h_{,j}\right\}_{,i} - \rho_{fo} nS_r \rho_f g\beta_P \frac{\partial h}{\partial t} - \rho_f \frac{\partial \theta}{\partial \psi}\frac{\partial h}{\partial t} - \rho_f S_r \frac{\partial u_{i,i}}{\partial t} + \rho_{fo} nS_r \beta_T \frac{\partial T}{\partial t} = 0 \\
&\left(\rho C_v\right)_m \frac{\partial T}{\partial t} + nS_r \rho_f C_{vf} V_{fi} T_{,i} - K_{Tm} T_{,ii} \\
&-nS_r T \frac{\beta_T}{\beta_P} k(\theta) h_{,ii} + \frac{1}{2}(1-n)\beta T \frac{\partial}{\partial t}\left(u_{i,j} + u_{j,i}\right) = 0
\end{aligned}
\tag{31}
$$

where $\overline{\rho_s} = (1-n)\left(\rho_s - S_r \rho_f\right)$ and ρ_s is the density of a solid phase.

3 Governing equations of extended coupled T-H-M model for buffer material

The behavior of the buffer material is influenced by the interdependence of thermal, hydraulic and mechanical phenomena. To treat the water/vapor movement and heat induced water movement, the continuity equation used in the extended THAMES code is as follows;

$$
\begin{aligned}
&\left\{\xi\rho_l D_\theta \frac{\partial \theta}{\partial \psi}\left(h_{,i} - z_{,i}\right) + \left(1-\xi\right)\frac{\rho_l^2 gK}{\mu_l} h_{,i}\right\} + \left\{\rho_l D_T T_{,i}\right\}_{,i} \\
&-\rho_{lo} nS_r \rho_l g\beta_P \frac{\partial h}{\partial t} - \rho_l \frac{\partial \theta}{\partial \psi}\frac{\partial h}{\partial t} - \rho_l S_r \frac{\partial u_{i,i}}{\partial t} + \rho_{lo} nS_r \beta_T \frac{\partial T}{\partial t} = 0
\end{aligned}
\tag{32}
$$

where D_θ is the isothermal water diffusivity, θ is the volumetric water content, ψ is the water potential head and K is the intrinsic permeability. The symbol ξ is the unsaturated parameter so that ξ=0 at the saturated zone, ξ=1 at the unsaturated zone. The symbol μ_l is the viscosity of water, ρ_l is the density of water, g is the gravitational acceleration. D_T is the thermal water diffusivity, n is the porosity, S_r is the degree of saturation, β_P is the compressibility of water, β_T the thermal expansion coefficient of water and z is the elevation head. u_i is the displacement vector, T is temperature, h is the total head and t is time. The subscript 0 means the reference state. This equation means that the water flow in the unsaturated zone is expressed by the diffusion equation and in the saturated zone by the Darcy's law.

The energy conservation equation has to treat the energy change by evaporation. The equation is given as

$$\begin{aligned}&(\rho C_v)_m \frac{\partial T}{\partial t} + nS_r\rho_l C_{vl} V_{li} T_{,i} - K_{Tm} T_{,ii} + L\left\{D_{\theta v}\frac{\partial \theta}{\partial \psi}(h_{,i} - z_{,i})\right\}_{,i} \\ &+ nS_r T\frac{\beta_T}{\beta_P}\left\{\xi D_\theta \frac{\partial \theta}{\partial \psi}(h_{,i} - z_{,i}) + (1-\xi)\frac{\rho_l g K}{\mu_l} h_{,i} + D_T T_{,i}\right\}_{,i} \\ &+ \frac{1}{2}(1-n)\beta T \frac{\partial}{\partial t}(u_{i,j} + u_{j,i})\delta_{ij} = 0\end{aligned} \tag{33}$$

where $(\rho C_v)_m$ is the specific heat of the material consisting of water and the soil particles, C_{vl} is the specific heat of water, V_{li} is the velocity vector of water, K_{Tm} is the thermal conductivity of consisting of water and the solid particles, L is the latent heat of vaporization per unit volume and $D_{\theta v}$ is the vapor diffusivity.

The equilibrium equation has to take the swelling behavior into account.

$$\left[\frac{1}{2}C_{ijkl}(u_{k,l} + u_{l,k}) - F\pi\delta_{ij} - \beta\delta_{ij}(T - T_o) + \chi\delta_{ij}\rho_l g(h - z)\right] + \rho b_i = 0 \tag{34}$$

where C_{ijkl} is the elastic matrix, ρ is the density of the medium and b_i is the body force. χ is the parameter for the effective stress, χ=0 at the unsaturated zone, χ=1 at the saturated zone. The symbol F is the coefficient relating to the swelling pressure process and $\beta = (3\lambda + 2\mu)\ \alpha_s$, where λ and μ are Lame's constants and α_s is the thermal expansion coefficient.

The swelling pressure π can be assumed to be the function of water potential head (ψ) as follows;

$$\pi(\theta_1) = \rho_l g(\Delta\psi) = \rho_l g(\psi(\theta_1) - \psi(\theta_0)) = \rho_l g\int_{\theta_o}^{\theta_1}\frac{\partial \psi}{\partial \theta}d\theta \tag{35}$$

where θ_0 is the volumetric water content at the initial state. This is based on the theory that swelling pressure is equivalent to the water potential.

4. Initial and boundary condition

It is necessary to establish the following initial and boundary conditions in order to solve the governing equations.

Initial conditions:

$$u_i(\tilde{x},t) = \hat{u}_i(\tilde{x},0) \tag{36}$$

$$h(\tilde{x},t) = h(\tilde{x},0) \tag{37}$$

$$T(\tilde{x},t) = T(\tilde{x},0) \tag{38}$$

Boundary condition:

· displacement; $u_i(\tilde{x},t) = \hat{u}_i(\tilde{x},t)$ (39)

or traction; $\sigma_{ij}(\tilde{x},t)n_j(\tilde{x}) = \hat{T}_i(\tilde{x},t)$ (40)

· total head; $h(\tilde{x},t) = \hat{h}(\tilde{x},t)$ (41)

or flow rate; $\left\{k(\theta)h_{,i}\right\}n_i = -\hat{Q}(\tilde{x},t)$ (42)

· temperature; $T(\tilde{x},t) = \hat{T}(\tilde{x},t)$ (43)

or heat flow; $K_{Tm}T_{,i}n_i = -\hat{Q}_T(\tilde{x},t)$ (44)

where, $\tilde{x}$ is the position vector, n_j is the unit normal vector, $\hat{u}$ is the known displacement, $\hat{h}$ is the known head, $\hat{T}_i$ is the known surface traction, $\hat{Q}$ is the prescribed flow rate and $\hat{Q}_T$ is the prescribed heat flow.

5. Numerical techniques

The Galerkin type finite element technique is employed to formulate a finite element discretization. In order to obtain stable solution, linear isoparametric elements are used to represent the behavior of total head h and temperature T. Quadratic isoparametric elements are used to express displacement u_i. In order to integrate time derivatives, a time weighting factor is introduced, and thus, any type of finite difference scheme may be applied.

別添 - 3

DECOVALEX TASK1
GENERAL SPECIFICATIONS

DECOVALEX III, Task 1: Modelling of FEBEX in-situ test

GENERAL SPECIFICATIONS

(Rev. 3)

Table of contents

1 Introduction

The purpose of this document is: (1) to introduce the conventions that will be used throughout Task 1 of the DECOVALEX III project, (2) to give guidelines to prepare the data to be sent to the co-ordinator (3) to introduce the procedure that will be used by the co-ordinator to send information to the participants and by the participants to send information to the co-ordinator and (4) to propose an outline for the Task Force Meetings and the Project Reports. Our experience in the co-ordination of the CATSIUS CLAY project has been the main guidance to elaborate these specifications. Of course, suggestions by participants to improve these specifications are welcome. However, these suggestions should be issued as soon as possible.

2 Codes and symbols assigned to participants and co-ordinator

Within Task 1 of the DECOVALEX III project, a unique 3-character code and a unique symbol is assigned to each participant (Modelling Team). Moreover, a 3-character code and a unique symbol is also assigned to the co-ordinator. The symbol and code of the co-ordinator will be used to identify the experimental data in comparison plots. On the other hand, symbols and codes assigned to the participants will be used to identify the results provided by the various participants in comparison plots. When possible, a colour (shared by 2 participants) will be used to enhance contrast among curves plotted together. Both the co-ordinator and the participants will use their own code to construct the name of the files to be sent by them. The list with the codes, symbols and colours is given in the following table:

Table 2-1 : Codes, symbols and colours assigned to participants and co-ordinator.

F. O.	Participant (Modelling Team)	code	symbol	colour
ANDRA	National Agency for Radioactive Waste Management (G3S-EP), France	ANG	■	red
ANDRA	National Agency for Radioactive Waste Management (LAEGO-EMN), France	ANN	□	red
BGR	Federal Institute for Geosciences and Natural Resources, Germany	BGR	◈	green
CNSC	Canadian Nuclear Safety Commission, Canada	CNC	◇	green
US DOE	US Department of Energy, USA	DOE	▲	blue
IPSN	Institute for Protection and Nuclear Safety, France	IPS	△	blue
JNC	Japan Nuclear Cycle Development Institute, Japan	JNC	⧓	brown
US NRC	US Nuclear Regulatory Commission, USA	NRC	×	brown
SKB	Swedish Nuclear Fuel and Waste Management Co., Sweden	SKB	▪▪	black
SKI	Swedish Nuclear Power Inspectorate, Sweden	SKI	+	black
STUK	Radiation and Nuclear Safety Authority, Finland	STU	◍	orange
	Technical University of Catalonia, Spain (co-ordinator)	UPC	○	orange

The codes have been sorted by alphabetical order according to the acronyms used by the Founding Organizations. Comparison plots will be made using Excel. Therefore, when coincident points are plotted, they overlap each other so that only the last one (UPC) will be clearly visible.

3 Information to be sent to the co-ordinator

Generally speaking, the information to be sent to the co-ordinator corresponding to each part of Task 1 of the DECOVALEX III project will consist of: (1) numerical data and (2) a Modelling Report, as explained below.

3.1 Numerical data

Numerical data refer to the values demanded by the co-ordinator, as stated in section "output specifications" of the pertinent case definition.

The required data should be placed in ASCII files, named according to the specifications to be given in section "output specifications" of the pertinent case definition. In general, the filenames will be of the form "XXXRPNN.txt", where "XXX" is the participant's code, "R" is the revision number (starting at 1), "P" is the Part (A, B, C) within Task 1 and "NN" is the file number. Each of this files should always have a header including the filename, the participant's identification and the date.

The data itself should be given on a tabular form, including a header for each column with the identification of the variable and the units used. There should be a column for each variable. Columns should be separated using spaces. The decimal symbol used should be a point. The data may be in decimal or scientific format. An example of a numerical data file is given below:

```
FILENAME    : XXXRPNN.txt
PARTICIPANT: Participant's identification
DATE        : DD.MM.YY

var1 (units)   var2 (units)   var3 (units)

0.0000E+00     0.0000E+00     0.000E+00
0.0000E+00     0.0000E+00     0.000E+00
...            ...            ...
```

Figure 3-1 : Example of a numerical data file.

An effort should be made to conform with the required units and sign conventions. If the output given by his/her code does not conform with the required format, the participant should perform the pertinent transformations.

Sometimes, the evolution with time or the spatial distribution of a variable will be required. If there are time instants or spatial points where the value of some variables are required, the participant should try to get as close as possible to the required times or points. In fact, these values will be compared against values given by other participants, without any interpolation. On the other hand, the participant is free to provide values at additional time instants or points in order to better define the required curve. In principle, all the points given by the participant will be plotted using the corresponding symbols joined by straight line segments. It should be emphasised that participant's predictions are at the points provided by the participant, whereas

the straight line segments merely join those points together. However, in order that the plotted symbols of points lying too close in the plotted curve do not result in a "thick line", the number of points provided should be kept to a minimum.

3.2 Modelling Reports

The goal of the Modelling Reports is to explain in a concise way what has been done to get the results, by addressing the following issues: (1) justification and definition of the mathematical model used, (2) justification of the values adopted for the parameters defining the mathematical model, and (3) numerical solution of the mathematical model.

Modelling Reports should be self-contained and written in a scientific paper-like form. This will ease their eventual publication. After being reviewed by the co-ordinator, Modelling Reports will be compiled within the Project Reports. In order to ease the reading of the ensemble and to ensure a minimum of coherence of the whole Project Report, the following points should be covered, albeit in a concise way (about 10-15 pages + graphics should suffice) :

- Mathematical setting
    - general balance equations (mass, momentum, ...)
    - constitutive equations (soil model, retention curve, ...)
    - equilibrium restrictions (psychrometric law, ...)
    - additional simplifications (uncoupling, terms neglected, ...)
    - initial and boundary conditions
- Model calibration
    - calibrated parameters (material model parameters, boundary condition parameters, ...)
    - non-calibrated parameters (literature, experience, ...)
- Numerical solution
    - numerical techniques used (finite elements, ...)
    - solving technique (Newton-Raphson, time stepping, ...)
    - other features (convergence criteria, adaptative mesh, ...)
    - characteristics of the mesh (type and number of elements, d.o.f., ...)
- Additional comments
    - sensitivity analysis performed
    - difficulties encountered
- References

Modelling Reports should be in Word97 files named "XXXRP.doc", where "XXX" is the participant's code, "R" is the revision number (starting at 1) and "P" is the Part (A, B, C) within Task 1. In order to ease the compilation of the Modelling Reports, the format to be used should be the same as the format used to prepare the present document (e.g., Times New Roman, 12 point, single space, all margins set to 2.5 cm, ...).

4 Procedure to send information

The use of the available resources to electronically send information is, perhaps, the easiest and fastest way to send and receive data. We also believe that a very robust way to electronically send information is the use of the ftp-procedure. With this objective, the ftp-site "ftp://humus.upc.es/" will be used in connection with the Task 1 of the DECOVALEX III project. The general scheme to be used for sending information is described below.

4.1 Information sent from the co-ordinator to the participants

The co-ordinator leaves the information in the "/decovalex/UPC" subdirectory and warns via e-mail to the participants about the new information. Participants get the information via ftp. The warning will include details of the information to be sent and the name and format of the corresponding files.

4.2 Information sent from a participant to the co-ordinator

The participant leaves via ftp the information in the "/decovalex/XXX" subdirectory (XXX stands for the participant's code) and warns the co-ordinator about the new information by sending an e-mail to "jordi.alcoverro@upc.es". The co-ordinator gets the information. The warning should include details of the information to be sent, as well as the name and format of the corresponding files

Notes:

- The idea is to use the e-mail for short unformatted files and to use the ftp-procedure for longer formatted files.

- The co-ordinator's directory "/decovalex/UPC" will be freely accessible for reading. In contrast, since there are some blind predictions to be made, participant's directories "/decovalex/XXX" will be protected with a password, in such a way that only the participant XXX may read from or write to the directory "/decovalex/XXX".

- To minimise both disk space and transfer time, data to be left in our ftp-site may be compressed using "WinZip 6.2", a windows-based shareware program. Therefore, before sending the files, participant XXX may compress them and put them into files (preferably only one) named XXXRP.zip, where "XXX" is the participant's code, "R" is the revision number (starting at 1) and "P" is the Part (A, B, C) within Task 1. The program WinZip 6.2 may be downloaded from our ftp-site using, for instance, a web-browser by writing "ftp://humus.upc.es/decovalex/tools/" at the URL prompt and clicking on winzip95.exe (a self-extracting file that installs WinZip).

- To get data stored in the co-ordinator's directory, the participant may (1) use his/her web-browser writing "ftp://humus.upc.es/tools/UPC/" at the URL prompt (2) use software as "ws_ftp32", a windows-based program, to perform an anonymous login and copy the pertinent files. This program may be downloaded from our ftp-site using, for instance, a web-browser by writing "ftp://humus.upc.es/decovalex/tools/" at the URL prompt and clicking on "ws_ftp32.zip" (a zip-compressed file containing the installation files of ws_ftp32).

- To write data to his/her directory, the participant may use software as "ws_ftp32" to login in "humus.upc.es" as user XXX and copy the pertinent files from his/her PC to the directory "/decovalex/XXX". To get the program "ws_ftp32", see the previous point.

- Initially, the password assigned to all "/decovalex/XXX" directories will be "Decovalex" (the first D is a capital letter). Each participant should choose a convenient new password and set it by using the following procedure: (1) login as user "XXX" in "humus.upc.es" using telnet (e.g. execute "telnet humus.upc.es" (telnet is included in windows operating system) or use software as "QVT/Term" (a windows-based freeware program) with the telnet option), (2) use the command "passwd" in order to change the password and (3) use the command "exit" to logout. This procedure may be repeated each time that the participant wishes to change his/her password. The program "QVT/Term" may be downloaded from our ftp-site using, for instance, a web-browser by writing "ftp://humus.upc.es/decovalex/tools/" at the URL prompt and clicking on "term32v415e.zip" (a zip-compressed file containing the installation files of QVT/Term).

5 Task Force Meetings and Project Reports

The information provided by the participants will be used in: (1) Task Force Meetings and (2) Project Reports. Both issues will be briefly discussed below.

5.1 Task Force Meetings

Using experimental data and data provided by the participants, the co-ordinator will prepare comparison plots that will be shown to all participants during the Task Force Meetings. Participants should also prepare a short presentation of their results. The following points outline the schedule of a typical Task Force Meeting.

- The co-ordinator briefly recalls the case definition.
- The co-ordinator presents plots comparing experimental data with the predictions provided by the participants.
- Each participant gives a short (10-15 min, say) presentation of the work performed and explains the pertinent details.
- A discussion of the solved case is made, with the participation all participants and the co-ordinator.
- The co-ordinator presents the definition of the next case.

5.2 Project Reports

Using the data and the Modelling Reports provided by the participants, the co-ordinator will prepare Project Reports. These Project Reports will contain the Modelling Reports prepared by the participants and the comparison plots prepared by the co-ordinator, including relevant comments and conclusions. They are thus conceived as a series of contributions by the participants and the co-ordinator, who compiles the report. A typical Project Report would have the following outline:

- case definition (co-ordinator)
- Modelling Reports (participants)
- presentation and discussion of results (co-ordinator)
- conclusions (co-ordinator)

Project Reports should be clear enough in order that the potential reader may easily understand the various models used, how were they calibrated, how were they numerically solved and what conclusions may be derived from their use. In order to achieve these goals, the use of a scientific paper-like style is mandatory. Such Project Reports may easily (as a whole or in part) give rise to eventual publications.

別添 - 4

DECOVALEX TASK1

PART A ; TASK DEFINITIONS

DECOVALEX III, Task 1: Modelling of FEBEX in-situ test

PART A: HYDRO-MECHANICAL MODELLING OF THE ROCK

(Rev. 3)

Table of contents

1 Introduction to Task 1: Modelling of FEBEX in-situ test

The international FEBEX (Full-scale Engineered Barriers Experiment in Crystalline Host Rock) project is a project that is co-financed by ENRESA the European Commission. It is co-ordinated by ENRESA and it is planned to last from 1994 to 2003. The purpose of the project is the study of the various processes occurring in the near field of a high activity radioactive waste storage. Specifically, three objectives were defined: (1) demonstration of the feasibility of the construction of engineered barriers, (2) study of the thermo-hydro-mechanical (THM) processes in the near field and (3) study of the thermo-hydro-geochemical (THG) processes in the near field. The FEBEX project has three main components, namely: (1) an "in situ" test in natural conditions and at real scale, (2) a mock-up test at near-to-real scale and (3) a series of laboratory tests to complement the information of the two large scale tests.

For the present modelling exercise, the FEBEX "in situ" test has been chosen. This test is installed at the Grimsel Test Site, an underground laboratory in Switzerland operated by NAGRA. The experiment is based on the Spanish reference concept of deep geological storage in crystalline host rock. In this concept, steel canisters containing the conditioned waste are placed along the axis of horizontal galleries drilled in a rock formation and an engineered barrier is placed in the annular space left between them. The engineered barrier is made of high density compacted bentonite blocks that will swell due to water input from the host rock, providing thus a very impervious sealing. In the FEBEX "in situ" test, waste canisters are replaced by two cylindrical heaters.

Due to the detailed geological and hydrogeological characterization of the Grimsel Test Site, the comprehensive characterization of the bentonite used to fabricate the engineered barrier and the monitoring performed during the drilling of the FEBEX tunnel as well as during the test, the FEBEX "in situ" test is well suited to be the object of a modelling exercise. In the context of the DECOVALEX III project, the modelling exercise will be divided into three parts, namely:

- Part A: Hydro-mechanical modelling of the rock.

Based on the available geological, hydraulic and mechanical characterizations of the Grimsel Test Site as well as on results of hydraulic tests performed on boreholes, a hydro-mechanical model for the zone around the FEBEX tunnel will be prepared. Using this model, changes in water pressure induced by the boring of the FEBEX tunnel as well as the total water flow rate to the excavated tunnel will be required.

- Part B: Thermo-hydro-mechanical analysis of the bentonite behaviour.

Based on the characterization of the bentonite and on the details of the process of test installation, a thermo-hydro-mechanical model for the bentonite barrier and the heaters will be prepared. Using this model, the thermo-hydro-mechanical response of the bentonite barrier as a result of the heat released by the heaters will be required. Besides local field variables such as temperature, relative humidity, pore water pressure, stresses and displacements, and global variables such as total input power to the heaters will also be required.

- Part C: Thermo-hydro-mechanical analysis of the rock.

Based on the characterization of the rock massif and on the details of the process of test installation and performance, the rock response in the immediate vicinity of the buffer will be required. The rock is now subjected to the heat released by heaters and by swelling pressures resulting from bentonite hydration. The initial hydrological regime (Part A) is also modified by the presence of the impervious barrier. Temperature, stresses, water pressures and displacements in selected points of the rock will be required.

2 Part A: Hydro-mechanical modelling of the rock

The Grimsel Test Site (GTS) has been the object of a number of investigations related to safety emplacement of radioactive waste. Of interest for the present case, are the geological, hydraulic and thermo-mechanical investigations carried out. The reports that are most pertinent to the present case will be made available to the participants. The information contained in these reports should be completed by the participant, based on data available in the literature and on his/her modelling experience. As a result, a hydro-mechanical model of the rock around the FEBEX tunnel should be prepared. This model should be able to predict the changes in water pressure induced by the boring of the FEBEX tunnel and the total water discharge into the FEBEX tunnel test area.

The purpose of the present document is to give an overview of the main features of the Grimsel Test Site (particularly, of the FEBEX area) that are relevant to the present modelling exercise as well as to indicate the sources of additional details. Section 3 is a short overview of the Grimsel Test Site. Section 4 provides information about the FEBEX area. Section 5 deals with the geological characterization of the GTS and FEBEX area. Section 6 presents an overview of the hydrology of the GTS and FEBEX area. Section 7 provides information concerning the thermo-mechanical characterization of the rock, such as characteristic thermo-mechanical parameters and in-situ stresses. Section 8 details the results required in the present modelling exercise. Finally, Section 9 collects the references where additional information may be found.

3 The Grimsel Test Site

3.1 General setting of the Grimsel Test Site

The Grimsel Test Site is at an elevation of 1730 m above sea level, around 450 m beneath the east flank of the Juchlistock mountain in the granitic rocks of the Aare Massif in central Switzerland (see Figure 3-1 and Figure 3-2). It is linked with the northern Grimsel Pass by a short approach road and a horizontal access tunnel around 1.2 km long leading to the Test Site itself. Despite the sometimes harsh alpine winter, all-year-round operation is guaranteed by the infrastructure of the power station company which operates a railway and an aerial cable car when the pass road is closed. The Grimsel Test Site is operated by NAGRA, the Swiss agency for nuclear waste disposal.

3.2 Layout of the Grimsel Test Site

The Grimsel Test Site is located in a tunnel system which branches off from the main access tunnel to the underground power station of the KWO (Kraftwerke Oberhasli AG). The GTS tunnel system consists of a laboratory tunnel with a total length of almost 1000 m and a central building which houses the whole infrastructure such as offices, the ventilation plant, workshops and other installations (see Figure 3-3). The laboratory tunnel has a diameter of 3.50 m and was excavated in 1983 in six months using a full-face tunnelling machine. The conditions for performing experiments at the GTS are particularly favourable because it contains areas of relatively undisturbed homogeneous rock as well as water-bearing zones (shear zones, fracture zones and lamprophyre dykes). The GTS was divided into individual test caverns and drifts where specific experiments are carried out. Figure 3-3 shows the location of the most important experiments which have been performed in the Grimsel Test Site, as well as the exploratory boreholes and the three 150 m long boreholes for the geophysical test field (US). Not shown in these figures are some 120 test-specific boreholes with an overall length of over 2000 m.

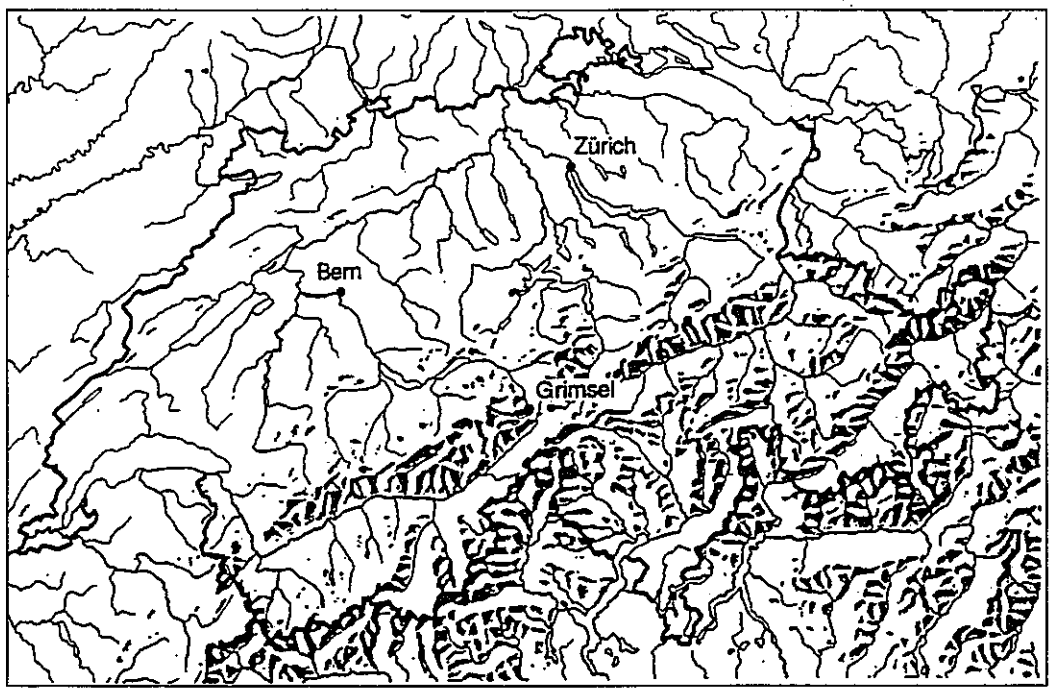

Figure 3-1 : Location of Nagra's underground test facility at the Grimsel Pass in the Central Alps (Bernese Alps) of Switzerland (NAGRA).

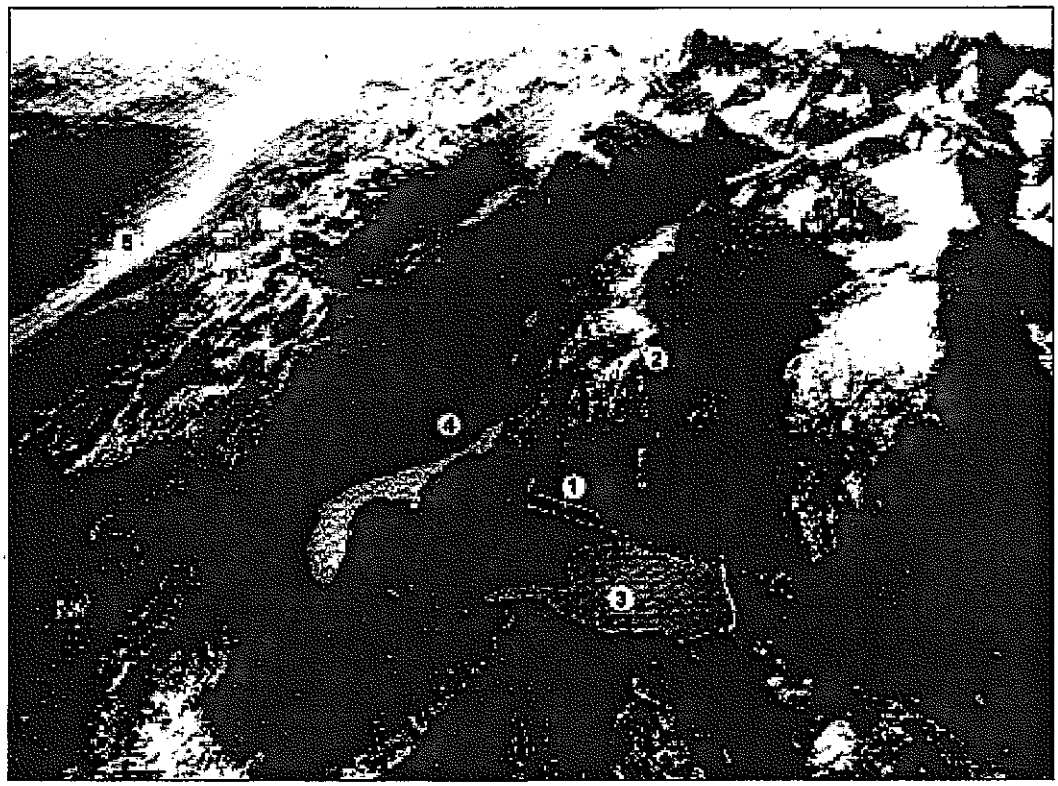

Figure 3-2: Grimsel Area (view looking West) (1. Test Site; 2. Juchlistock; 3. Lake Räterichsboden; 4. Lake Grimsel; 5. Rhone Valley) (NAGRA).

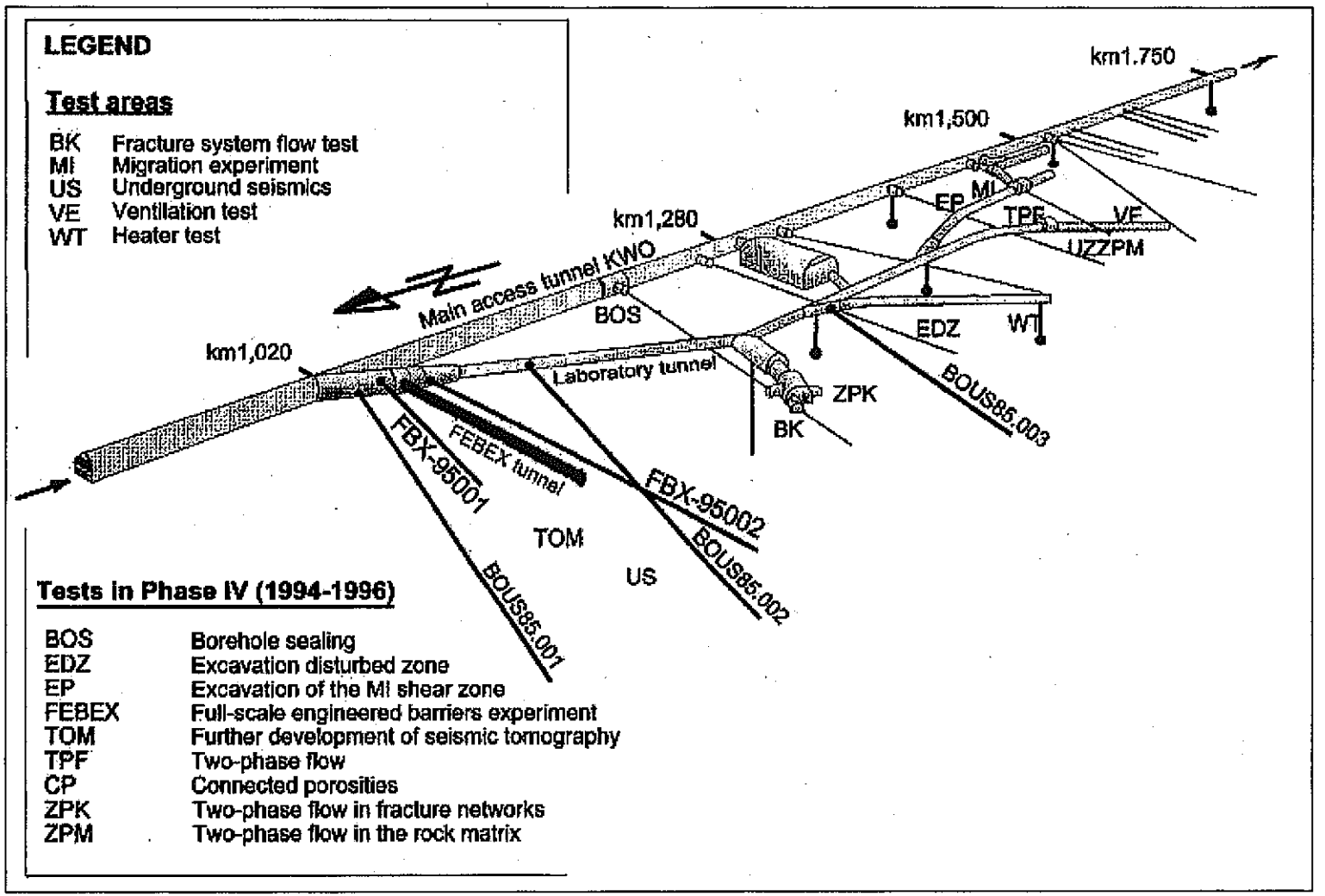

Figure 3-3: Location of tests performed at the Grimsel Test Site during Phase IV (1994-1996) (Pardillo et al., 1997).

4 The FEBEX area

In order to perform the FEBEX in-situ test, it was decided to excavate a new drift in the Underground Seismic (US) test area located in the northern part of the Grimsel Test Site. Prior to the FEBEX drift excavation, two pilot boreholes (FEBEX 95.001 and FEBEX 95.002) were drilled in the area between boreholes BOUS 85.001 and BOUS 85.002. Afterwards, the FEBEX drift was excavated between these pilot boreholes. It was parallel to FEBEX 95.002. Figure 3-3 shows the location of the FEBEX drift and of the aforementioned boreholes in the GTS. From the end of the FEBEX drift, in the in-situ test zone, 19 boreholes were drilled. Figure 4-2 shows a perspective of the FEBEX drift and associated boreholes.

This section summarises the chronology of the works carried out in connection with the FEBEX in-situ test (indicating where the pertinent information may be found), it gives the geometry and location of the FEBEX drift and associated boreholes and provides information about the excavation of the FEBEX drift.

4.1 Chronology of relevant works for the FEBEX in-situ test

The chronology of relevant works carried out in connection with the FEBEX in-situ test presented in this section is summarised in Table 4-1.

In the Underground Seismic (US) test area, located at the northern part of the Grimsel Test Site, three boreholes (BOUS 85.001, BOUS 85.002 and BOUS 85.003) were drilled in 1985 to perform seismic and electromagnetic (radar) investigations. Particularly relevant for the FEBEX in-situ test are BOUS 85.001 and BOUS 85.002, both drilled with a diameter of 101 mm, a length of 150 m and an inclination of 15° (downwards from the horizontal). The location and orientation of these boreholes is given in section 4.2. Geological information may be consulted in Keusen et al. (1985).

In October 1985, the Swedish Geological Co. conducted a radar reflection survey using the three boreholes of the US test area. The combination of radar results and geological information allowed to construct a geological model of the site, as explained in Falk et al. (1988).

In the period 15-19.06.95, Solexperts AG, Schwerzenbach (Switzerland) equipped boreholes BOUS 85.002 (on 19.06.95) and BOUS 85.001 (on 16.06.95) with a packer system and instrumented them. After four weeks of installation, a small leakage in the system was detected in BOUS 85.002. After removal in 03.08.95 of the packer system and reparation, it was re-installed in 08.08.95. Details of packer locations and instrumentation may be found in Fierz (1996).

Borehole FEBEX 95.002, with a diameter of 86 mm and a length of 132.36 m, was drilled during the period 30.06.95 to 24.07.95 with an inclination of 1° (downwards from the horizontal). The location and orientation of this borehole is given in section 4.2. Relevant geological and hydrological information, such as the borehole logs may be consulted in Pardillo et al. (1997).

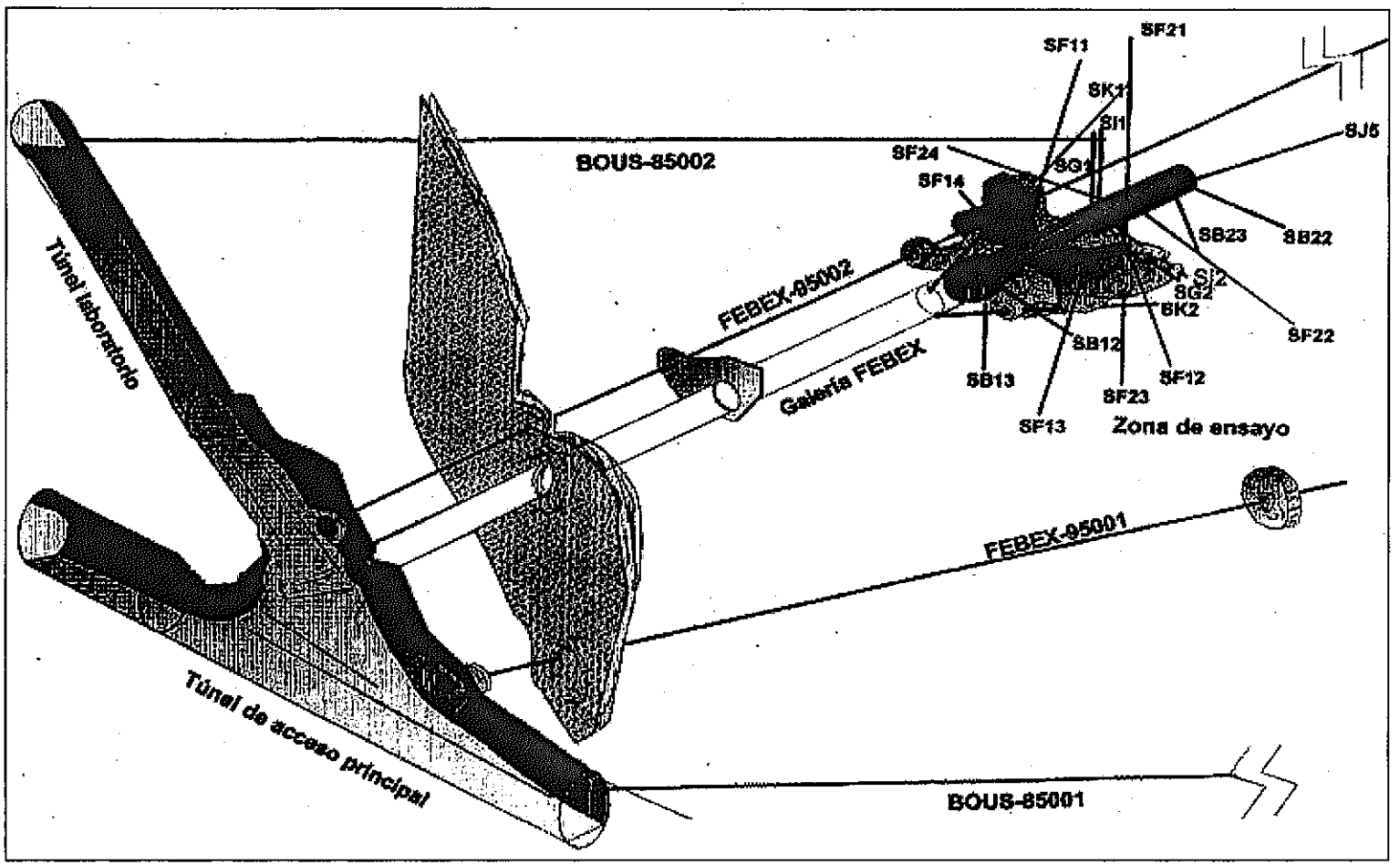

Figure 4-1: Perspective of the FEBEX drift and associated boreholes (Pardillo et al., 1997)

Table 4-1: Chronology of relevant works for the FEBEX in-situ test.

Activity	Dates	References
BOUS drilling	85	Keusen et al. (1989)
BOUS geophysics	10.85	Falk et al. (1988); Keusen et al. (1989)
BOUS instrumentation	06.95	Fierz (1996)
FBX2 drilling	06-07.95	Pardillo et al. (1997)
FBX2 instrumentation	07.95	Fierz (1996)
FBX1 drilling	07-08.95	Pardillo et al. (1997)
FBX1 instrumentation	08.95	Fierz (1996)
FBX1 and FBX2 geophysics	08.95	Häring (1996)
BOUS and FBX hydrotesting	08-09.95	Meier et al. (1995)
FEBEX drift construction	09-11.95	Pardillo et al. (1997)
Discrete flow measurements	11.95	hidden to participants
Geological mapping	11.95	Pardillo et al. (1997)
Second FBX2 hydrotesting	12.95	Guimerà et al. (1998)
Re-location of FBX2 packers	12.95	Fierz (1996)
First bulk inflow measurements	01.96	hidden to participants
Third FBX2 hydrotesting	01.96	Guimerà et al. (1998)
In-drift boreholes drilling	02-04.96	Pardillo et al. (1997)
In-drift boreholes packers placing	04.96	Fierz (1996)
Second bulk flow measurements	05.96	hidden to participants
In-drift boreholes hydrotesting	05-06.96	Guimerà et al. (1996); Guimerà et al. (1998)
In-drift boreholes instrumentation	06-07.96	Fierz (1996)
Start of passive head monitoring	07.96	Guimerà et al. (1998)

Borehole FEBEX 95.002 was equipped with a packer system and instrumented on 26.07.95 by Solexperts AG. The aim of the installation of borehole FEBEX 95.002 was to monitor pore water pressures during drilling of the nearby borehole FEBEX 95.001. Details of packer locations and instrumentation may be found in Fierz (1996).

Borehole FEBEX 95.001, with a diameter of 101 mm and a length of 76.00 m, was drilled during the period 26.07.95 to 10.08.95 with an inclination of 1° (downwards from the horizontal). The location and orientation of this borehole is given in section 4.2. Geological and hydrological information, such as the borehole logs may be consulted in Pardillo et al. (1997).

On 18.08.95, borehole FEBEX 95.001 was equipped with a packer system and instrumented by Solexperts AG. Details of packer locations and instrumentation may be found in Fierz (1996).

After removing the packer system in 09.08.95, boreholes FFBEX 95.001 and FEBEX 95.002 were used to perform geophysical investigations. Radar investigations were made by K-UTEC, Sondershausen (Germany) in the period 10-11.08.95. Geophysical logging was performed by DMT, Bochum (Germany) and EGS (Luxemburg) in the period 14-15.08.95. The results of these investigations are detailed in Häring (1996). The packer system was reinstalled in 17.08.95.

In the period 08-09.95, boreholes BOUS 85.001, BOUS 85.002, FEBEX 95.001 and FEBEX 95.002 were used for hydrotesting. Testing included measuring of the natural outflow, pressure static recovery, pulse withdrawal or constant rate tests (injection or withdrawal) and pressure recovery after constant rate tests. Testing results are detailed in Meier et al. (1995).

During the period 25.09.95 to 30.10.95, the FEBEX drift was excavated using a TBM. The FEBEX drift has a diameter of 2.28 m ± 0.01 and a total length of 71.4 m. The location and orientation of this drift is given in section 4.2. The excavated length of the drift as a function of time is given in section 4.3. Geological and hydrogeological information, such as the geological mapping of the drift wall may be found in Pardillo et al. (1997).

Discrete flow measurements were conducted in 11.95 using diapers (cellulose sheets) located at various points of the FEBEX drift wall. Flow measurements were obtained by dividing the increase of weight of the diapers by the corresponding time. To preserve the blind character of the exercise, this information will remain hidden to the participants.

A geological mapping of the FEBEX drift wall was carried out by CIEMAT in 11.95. Pertinent information may be found in Pardillo et al. (1997).

A second hydrotesting of borehole FEBEX 95.002 was performed in 12.95. Information may be found in Guimerà et al. (1998).

In order to get more detailed information in the vicinity of the test zone in the FEBEX drift, the packer system was removed on 20.12.95 and reinstalled on 21.12.95. Details of the packer locations may be found in Fierz (1996).

First bulk inflow measurements were performed in 01.96 using a gauge. To preserve the blind character of the exercise, this information will remain hidden to the participants.

A third hydrotesting of borehole FEBEX 95.002 was performed in 12.95. Information may be found in Guimerà et al. (1998).

During the period 12.02.96 to 04.04.96, 19 in-drift boreholes (Ø 66 mm and Ø 146 mm) with a total length of 233 m were drilled from the test area of the FEBEX drift (tunnel meters 50-71 m). Initially, the borehole layout was planned to be strictly radial. However, the boreholes were re-oriented in order to intersect the most relevant geological features. The location and orientation of these boreholes is given in section 4.2. Geological and hydrological information, including the borehole logs may be found in Pardillo et al. (1997).

In-drift boreholes were equipped with packer systems by Solexperts AG during the period 17-22.04.97. Packer positions may be found in Fierz (1996).

Second bulk inflow measurements were performed in 05.96 using a gauge. To preserve the blind character of the exercise, this information will remain hidden to the participants.

Hydrotesting of the in-drift boreholes was carried out in the period 05-06.96. Details and results of tests may be found in Guimerà et al. (1996) and Guimerà et al. (1998).

After the hydraulic characterization campaign, the packer systems were removed, equipped with thermocouples and reinstalled by Solexeperts AG in the period 26.06-03.07.96. The

packer locations were not changed. The packer systems of in-drift boreholes SI-1 and SI-2 were removed and not reinstalled. Details may be found in Fierz (1996).

Finally, passive head monitoring was carried out from 07.96 on. Details and test results may be found in Guimerà et al. (1998).

4.2 Geometry of the FEBEX drift and associated boreholes

The co-ordinate system used in the Grimsel Test Site is the Swiss co-ordinate system. In order to define a point, use is made of east, north and height above the sea level. In order to define the direction of a line, use is made of the azimuth (angle formed by the projection of the line onto the horizontal plane with the north, measured clockwise using 0-360 degrees) and the inclination (angle formed by the line with the vertical plane, measured using 0-360 degrees). Figure 4-2 below helps to clarify the aforementioned concepts.

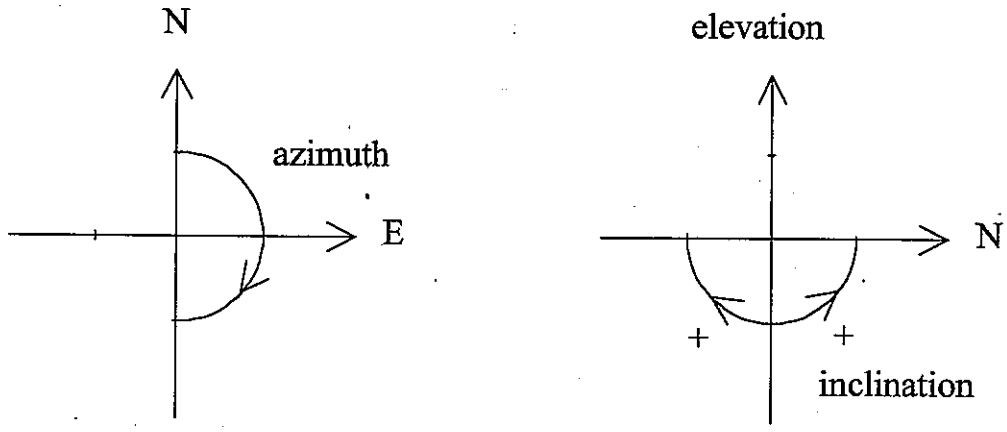

Figure 4-2: The co-ordinate system used in the Grimsel Test Site.

Figure 4-1 gives an overview the location of the FEBEX drift and associated boreholes. Figure 4-3 shows the location of the 19 short in-drift boreholes (7-15 m) which were drilled from test area of the FEBEX drift. All boreholes were equipped with multipacker systems (Solexperts AG) and water pressures were monitored automatically. Details on the instrumentation can be found in Fierz (1996).

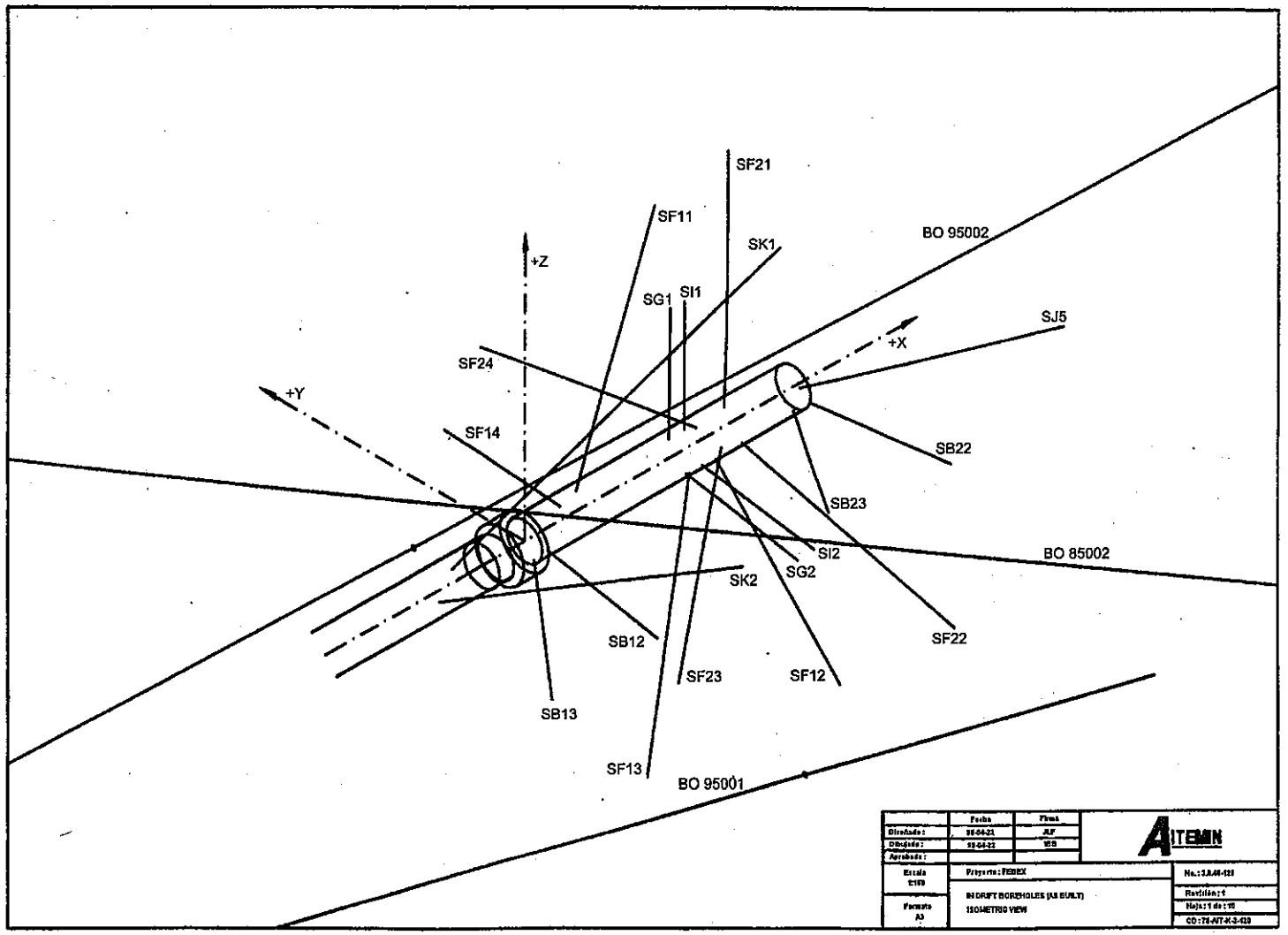

Figure 4-3: Lay-out of the FEBEX in-drift boreholes. Also shown are boreholes BOUS 85.002 (BO 85002), FEBEX 95.001 (BO 95001) and FEBEX 95.002 (BO 95002) (Guimerà et al., 1998)

Table 4-2 and Table 4-3 define the geometry of the FEBEX drift and of the associated boreholes using the Grimsel Test Site co-ordinate system (see Figure 4-2).

Table 4-2: Co-ordinates (borehole mouth centre) and specifications of US and FEBEX boreholes, using GTS co-ordinates (US 1 = BOUS 85.001, US 2 = BOUS 85.002, FEX 1 = FEBEX 95.001, FEX 2 = FEBEX 95.002) (ENRESA).

code	east (m)	north (m)	height (m)	azim (°)	inclin (°)	length (m)	diam (mm)
US 1	667500.46	159357.13	1728.11	290.00	75.00	149.83	101
US 2	667481.95	159287.77	1729.34	290.00	75.00	150.27	101
FEX 1	667496.71	159347.56	1730.04	275.40	89.43	76.00	101
FEX 2	667493.49	159338.67	1730.24	258.47	89.43	132.36	86
Tunnel	667491.92	159342.52	1729.34	258.30	90.69	71.41	2280

Table 4-3: Co-ordinates (borehole-mouth centre) and specifications of in-drift boreholes, using GTS co-ordinates (tunnel = FEBEX tunnel meter at which borehole starts) (ENRESA).

code	east (m)	north (m)	height (m)	azim (°)	inclin (°)	length (m)	diam (mm)	tunnel (m)
SK1	667444.86	159333.22	1731.10	259.10	110.00	22.00	66	48.00
SK2	667445.00	159332.45	1728.96	260.90	70.00	20.00	66	48.00
SB12	667439.41	159332.84	1729.83	349.00	79.20	7.00	66	53.40
SB13	667439.59	159331.93	1728.91	348.40	10.10	7.00	66	53.40
SF11	667436.86	159331.16	1731.17	259.00	159.80	15.00	66	56.25
SF12	667429.04	159330.68	1729.73	10.00	75.00	15.00	66	64.00
SF13	667429.95	159329.94	1728.91	53.40	22.50	15.00	66	63.30
SF14	667436.97	159330.06	1729.74	191.80	72.00	15.00	66	56.40
SG1	667431.11	159329.98	1731.17	209.00	179.40	7.00	146	62.10
SG2	667430.87	159331.07	1729.83	348.00	79.20	7.00	146	62.10
SI1	667430.13	159329.77	1731.17	165.20	179.40	7.00	66	63.10
SI2	667429.89	159330.87	1729.83	348.00	80.00	7.00	66	63.10
SF21	667427.66	159329.26	1731.17	15.10	179.30	15.00	66	65.70
SF22	667427.42	159330.36	1729.83	350.00	76.90	15.00	66	65.70
SF23	667427.68	159329.06	1728.91	168.20	10.00	15.00	66	65.70
SF24	667428.51	159328.29	1729.83	170.00	80.00	15.00	66	65.00
SB22	667423.16	159329.48	1729.83	328.60	80.20	7.00	66	70.00
SB23	667423.38	159328.38	1728.89	258.20	19.90	7.00	66	70.00
SJ5	667423.00	159328.30	1729.93	268.20	80.20	15.00	66	70.40

4.3 Excavation of the FEBEX drift

The FEBEX drift was excavated using a TBM. The boring head had a diameter of 2.27 m. The drift was excavated from 25.09.95 to 30.10.95. The position of the FEBEX drift is given in section 4.2. Geological and hydrogeological information may be found in Pardillo et al. (1997). Table 4-4 shows the excavation status as a function of time.

Table 4-4: Excavated length (in m) of the FEBEX drift as a function of time (when the TBM started (27.09.95), the length of the tunnel was 3.50 m) (Note: the excavated lengths marked with * were measured 30 min earlier than the time indicated in the table) (ENRESA).

	25 sep	26 sep	27 sep	28 sep	29 sep	02 oct	03 oct	04 oct	05 oct	06 oct
07:00			3.50	6.00	6.00	6.50	7.50	8.50	9.50	12.50
08:00			3.50				8.00		9.50	
09:00			3.50				8.50		10.00	
10:00			4.00		6.00		8.50		10.50	
11:00			4.40		6.50			8.50	11.00	12.50
12:00			4.90						11.50	13.00
13:00			4.90			6.50			11.50	13.00
14:00			5.30			6.50		8.50	12.00	13.50
15:00			5.70			7.00		8.50	12.50	
16:00			6.00			7.00		9.00	12.50	
17:00			6.00			7.50		9.00	12.50	
18:00	1.50	3.50	6.00	6.00	6.50	7.50	8.50	9.50	12.50	13.50

	09 oct	10 oct	11 oct	12 oct	13 oct	16 oct	17 oct	18 oct	19 oct	20 oct
07:00	13.50	16.50	16.50	20.90	26.50	26.50	31.70	36.00	40.50	43.65
08:00	14.00		16.90	21.30		26.90	31.70	36.00		43.65
09:00	15.00		17.30	22.10		27.30	31.70	36.00		44.55
10:00	15.00		17.70	22.50		27.70	32.50	36.90		45.00
11:00	15.00		18.10	23.30		28.50	32.90	37.35	40.50	45.45
12:00	16.00		18.50	24.10		29.30	33.30	37.80	40.95	45.90
13:00	16.00		18.50	24.10		29.30	33.30	37.80	41.40	45.90
14:00	16.50		18.90	24.10		29.30	33.75	38.25	41.40	46.35
15:00	16.50		19.70	24.50		30.10	34.20	38.70	41.85	46.35
16:00			20.10	25.30		30.50	34.65	39.60	42.30	46.35
17:00			20.50	25.70		31.30	35.55	40.05	42.75	
18:00	16.50	16.50	20.90	26.50	26.50	31.70	36.00	40.50	43.65	46.35

	23 oct	24 oct	25 oct	26 oct	27 oct	30 oct
07:00	46.35	50.00	55.70	60.95	61.90	66.65
08:00	46.35	50.00	55.70	60.95	62.40	66.65
09:00	46.35	50.95	56.65		62.85	67.15
10:00	46.35	51.45	57.15		63.80	67.60
11:00	46.85	51.90	57.60		64.30	68.55
12:00	47.35	52.40	58.10		64.75	69.05
13:00	47.35	52.40	58.10		64.75	69.50
14:00	47.80	52.85	58.55		65.25	70.00
15:00	48.30	53.80	59.05		66.20	70.45
16:00	48.75	54.30	59.50	60.95	*66.65	70.95
17:00	49.25	54.75	60.45	61.45		*71.40
18:00	50.00	55.70	60.95	*61.90		

5 Geological characterization

5.1 Geology of the Grimsel Test Site

Extensive geological and hydraulic characterizations have been performed at the multiple experiments carried out and ongoing at the GTS. Geology of the area is documented in Keusen et al. (1989), which provides the general frame of the GTS in the context of the Swiss Alps.

The GTS is excavated in a rock mass of intrusive nature. Most of this host rock is granite and granodiorite, which are affected by several tectonic episodes. Keusen et al. (1989) found 12 possible discontinuity systems (see Figure 5-1), from which the systems shown in Table 5-1 were selected as those clearly existing.

Table 5-1: Discontinuity systems shown to exist at the GTS (Keusen et al., 1989).

system	comments
S_2	Main schistosity (azimuth strongly overlapping with S_1; the two systems cannot be separated on the basis of orientation alone)
S_1 and S_3	equivalent system pair (conjugate)
S_4/K_4 and K_2/L_2	equivalent system pair (+ orthogonal)
K_1 and K_3	equivalent system pair (conjugate)
ZK	tension joints

Based on Keusen et al. (1989), and on direct observations, Pardillo et al. (1997) suggest the following geological features as relevant for regional groundwater flow:

- Shear zones S_1 and S_2, of azimuth 140-150/80-90
- Fracture zones and lamprophyre dikes, of azimuth 205-220/80

Shear zones are of considerable thickness at the area (5 to 20 m). At the intersection with tunnels, they display major outflows indicating their relevance as preferential flow paths. Distribution of hydraulic parameters in the shear zone or whether the hydraulic conductivity tensor displays preferential directions is uncertain. Lamprophyre dikes have also considerable dimensions (thickness up to several meters), although their relevance as preferential flow paths is not so important as shear zones. A preferential flow path within these dikes is the contact surface between the lamprophyre and the host rock. Hence, it is not surprising to observe concentrated outflows at these surfaces at their intersections with the tunnels and drifts. Some of the thickest lamprophyres contain smaller fractures parallel to the main azimuth. These fractures enhance the hydraulic conductivity in this plane, but prevent groundwater flow in a normal direction to them. Thus, one would consider the hydraulic conductivity of these dikes as anisotropic. Both shear zones and lamprophyres are traceable from the tunnel daylights to surface outcrops. Figure 5-2 shows the major geological features in a surface exposure, and the position of the GTS excavations. Figure 5-3 shows the general geological model of the Grimsel Test Site. Figure 5-4 correlates the surface outcrops and the intersections of the tunnels. The FEBEX drift which is located at the Northern end of the GTS, is bounded by two main shear zones according to Figure 5-2 and Figure 5-4.

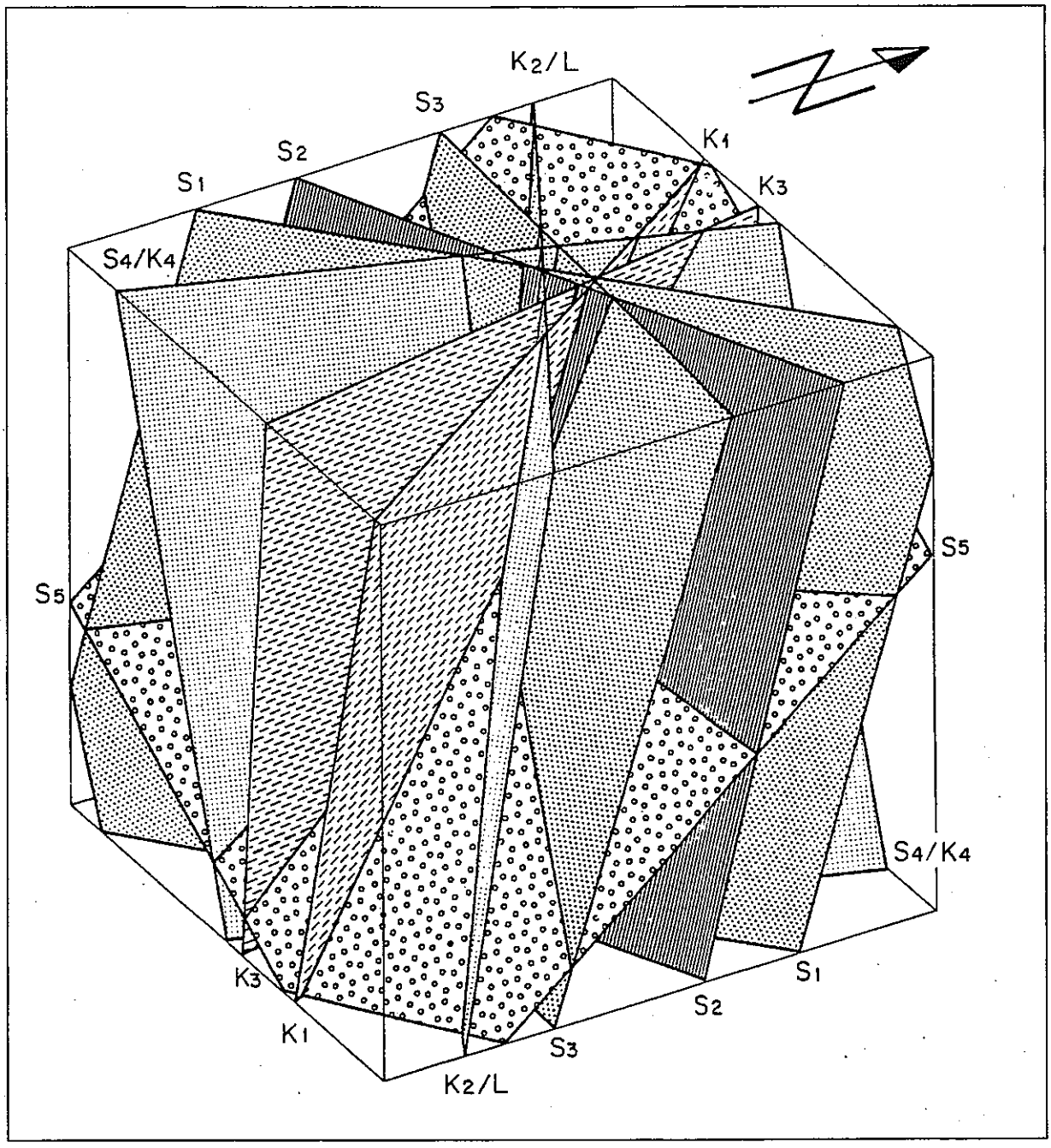

Figure 5-1: Block diagram of the dominant fracture systems (S: schistosity-related systems; K: joint systems; L: lamprophyre). For a better overview, the sub-horizontal system ZK and the hypothetical system S_6 were left out (Keusen et al., 1989).

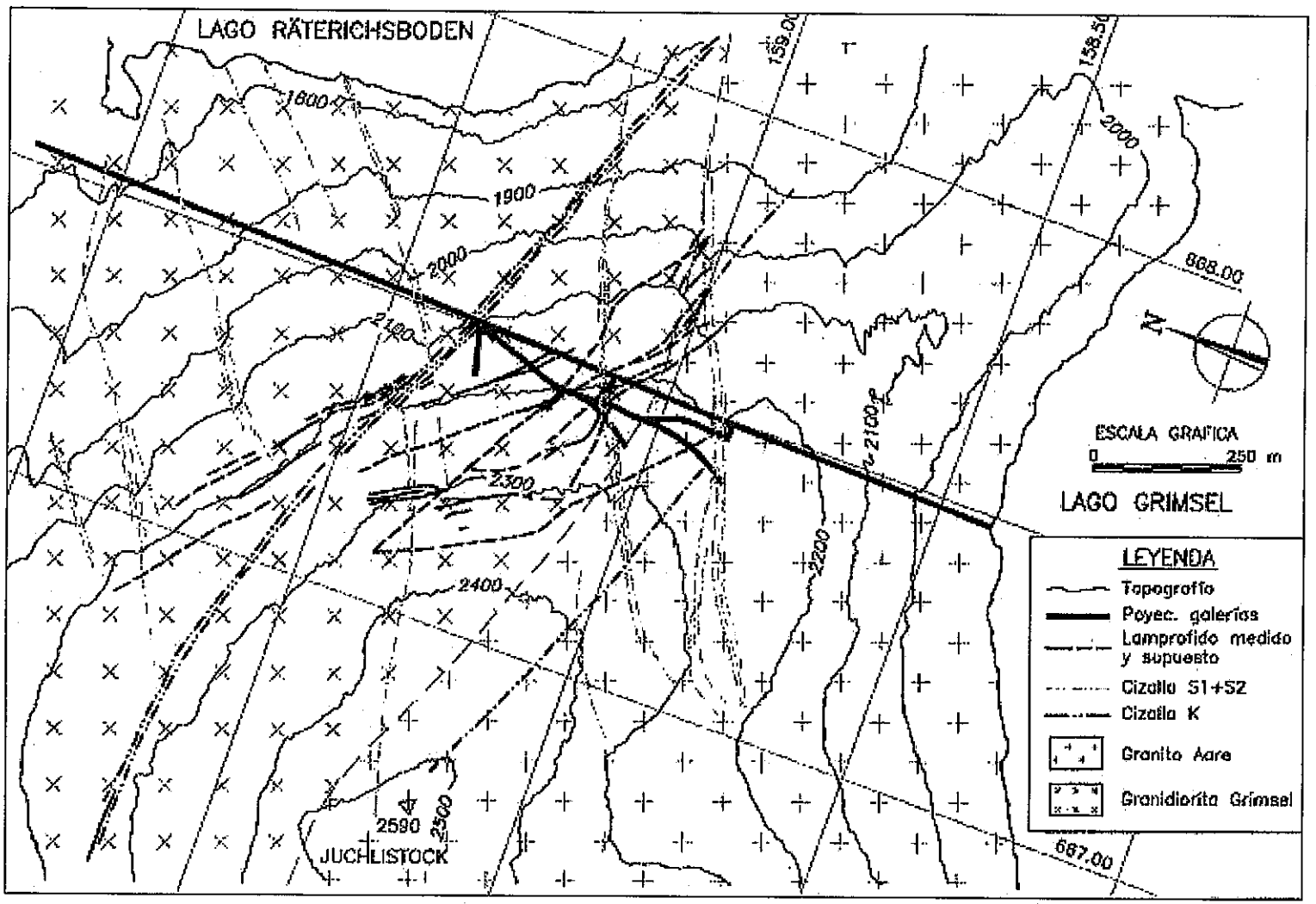

Figure 5-2: Geological map of the Grimsel area (Guimerà et al., 1989).

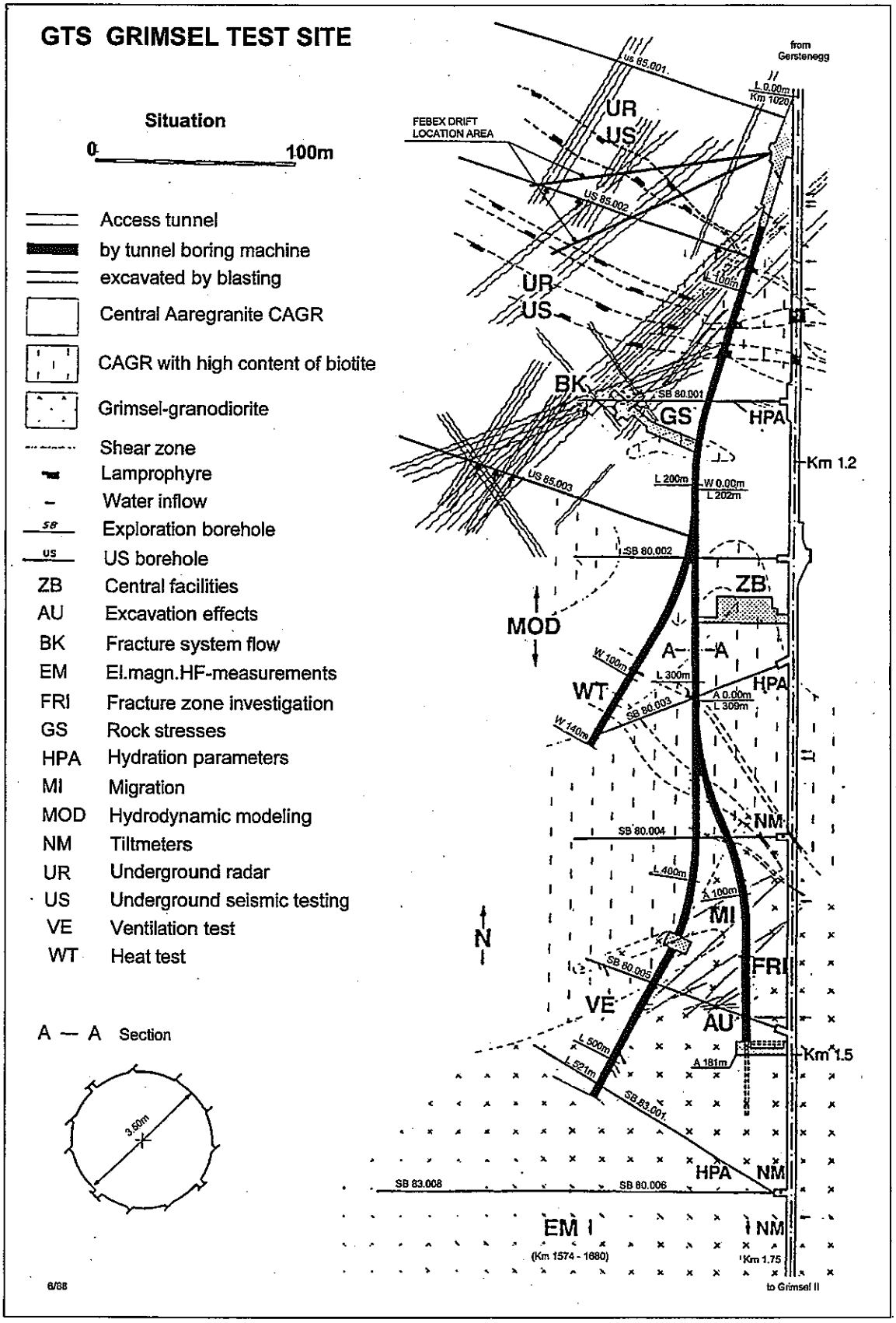

Figure 5-3: Geological model of the Grimsel Test Site (NAGRA).

5.2 Geology of the FEBEX drift area

The site of the FEBEX experiment was explored with 23 boreholes of depths ranging from 7 to 151 m (a total of about 750 m). Available data consist of a geological map of the tunnel wall, the borehole configuration, core descriptions and head monitoring in borehole intervals. Inflow measurements and hydraulic parameters obtained from hydraulic testing will be described separately in the next sections. The main reference to the geology of the FEBEX area is Pardillo et al. (1997). Since this reference is only available in Spanish, a previous report (Pardillo et al., 1996), in English, may be also of some help.

Within this domain, some other geological features are worth mentioning: a shear zone, which actually crosses the FEBEX drift at a depth of about 20 m, and a lamprophyre dike, related to a major set of dikes. It intersects the GTS tunnel in the vicinity of the borehole BOUS 85.002, that is, close to the intersection of the S boundary. Figure 5-5 is a detailed description of geological features observed either in tunnel walls or borehole cores. In this figure, the N boundary of the FEBEX does not show up. However, the S boundary can be easily deduced by the density of fractures which constitute the shear zone. Also, the lamprophyres involved (black) can be traced between the FEBEX drift and the GTS tunnel. The shear zone intersected by the FEBEX drift is also shown.

Figure 5-6 and Figure 5-7 display the geological map of the drift. The last 17.4 m are of immediate concern for the FEBEX experiments because the heater and the bentonite block are installed in this section. Relevant geological features at the tunnel scale include:

- Lamprophyre dikes
- 'en echelon' fractures
- Normal fractures

Note that at about 20 m depth, the drift intersects a series of fractures with the same azimuth as shear zones. We consider this series of fractures as a shear zone because it is highly conductive (measured inflows in the order of ~30 ml/min, which can be considered high for the GTS and comparable to other shear zones).

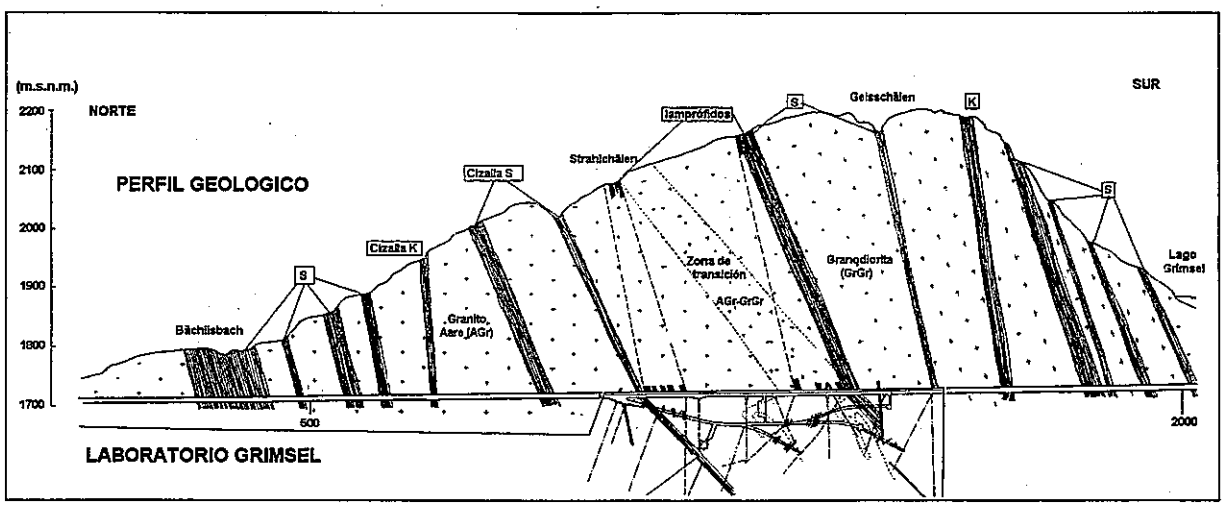

Figure 5-4: Geological cross section of the Grimsel area showing the major geological structures and their relative position at the KWO and GTS tunnels. (Guimerà et al., 1998)

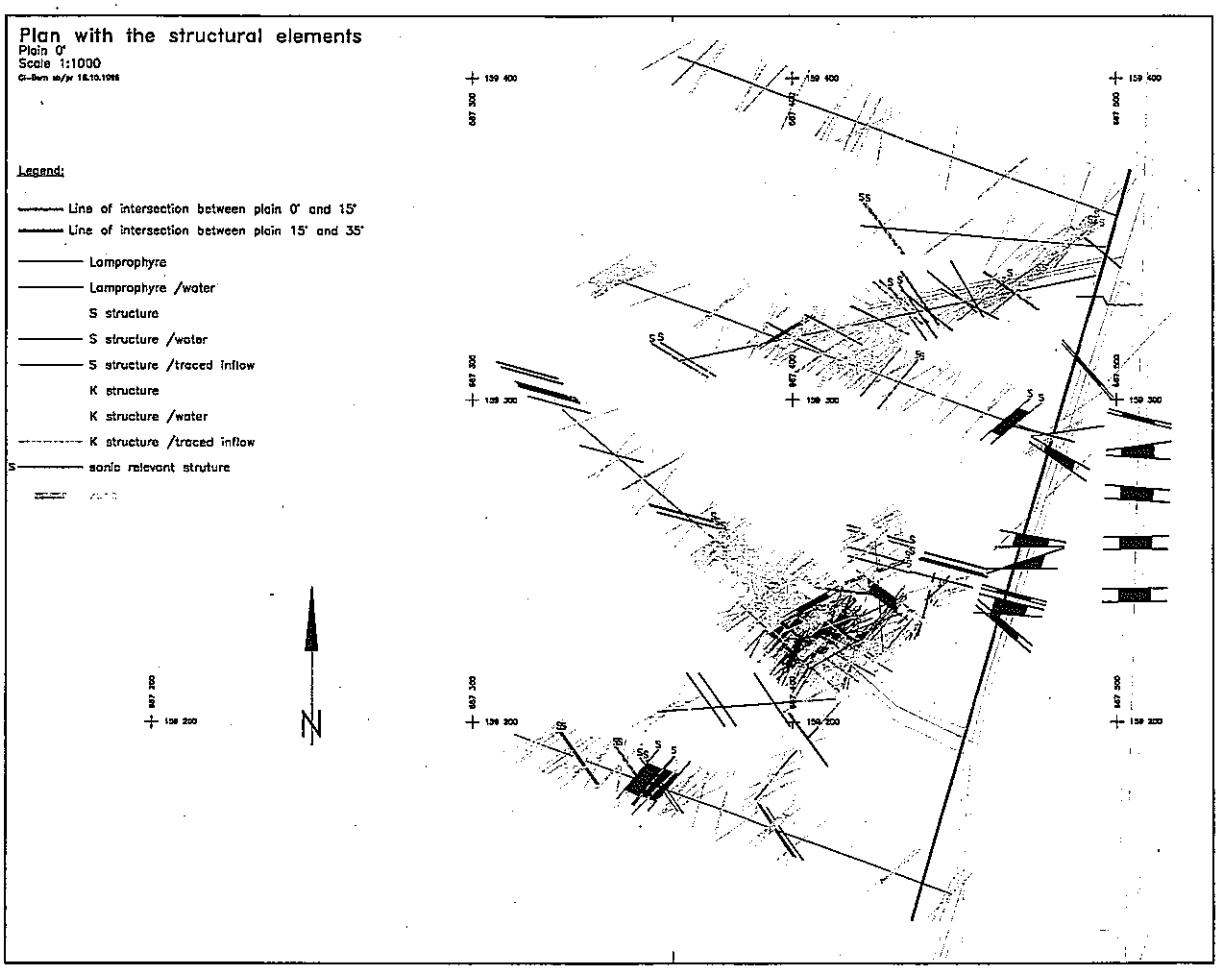

Figure 5-5: Geological map of linear measurements and traces observed at borehole cores and tunnel walls in the BK and FEBEX areas (Guimerà et al., 1998).

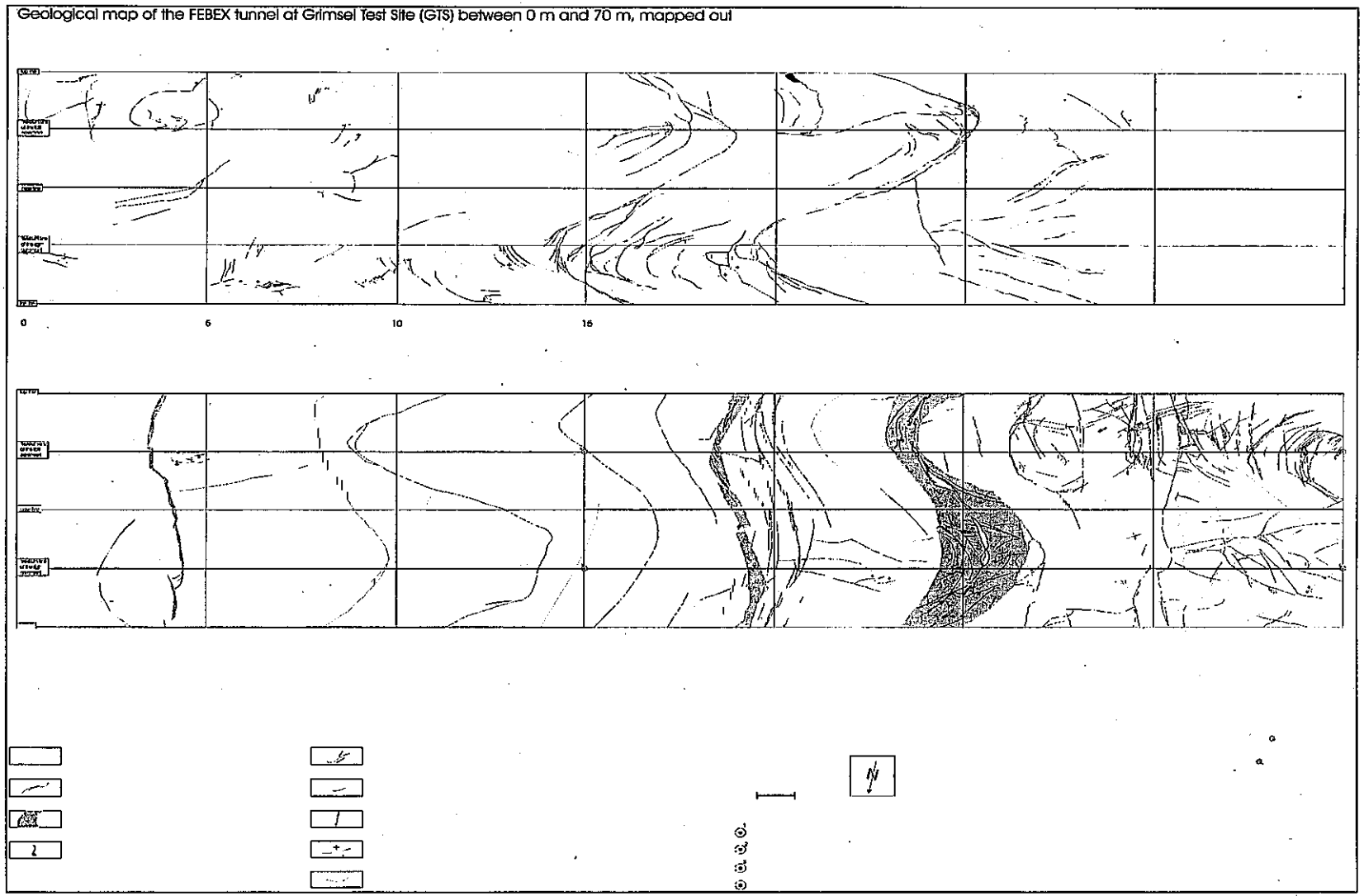

Figure 5-6: Geological map of the FEBEX drift between 0.0 m and 70.0 m (Pardillo et al., 1997).

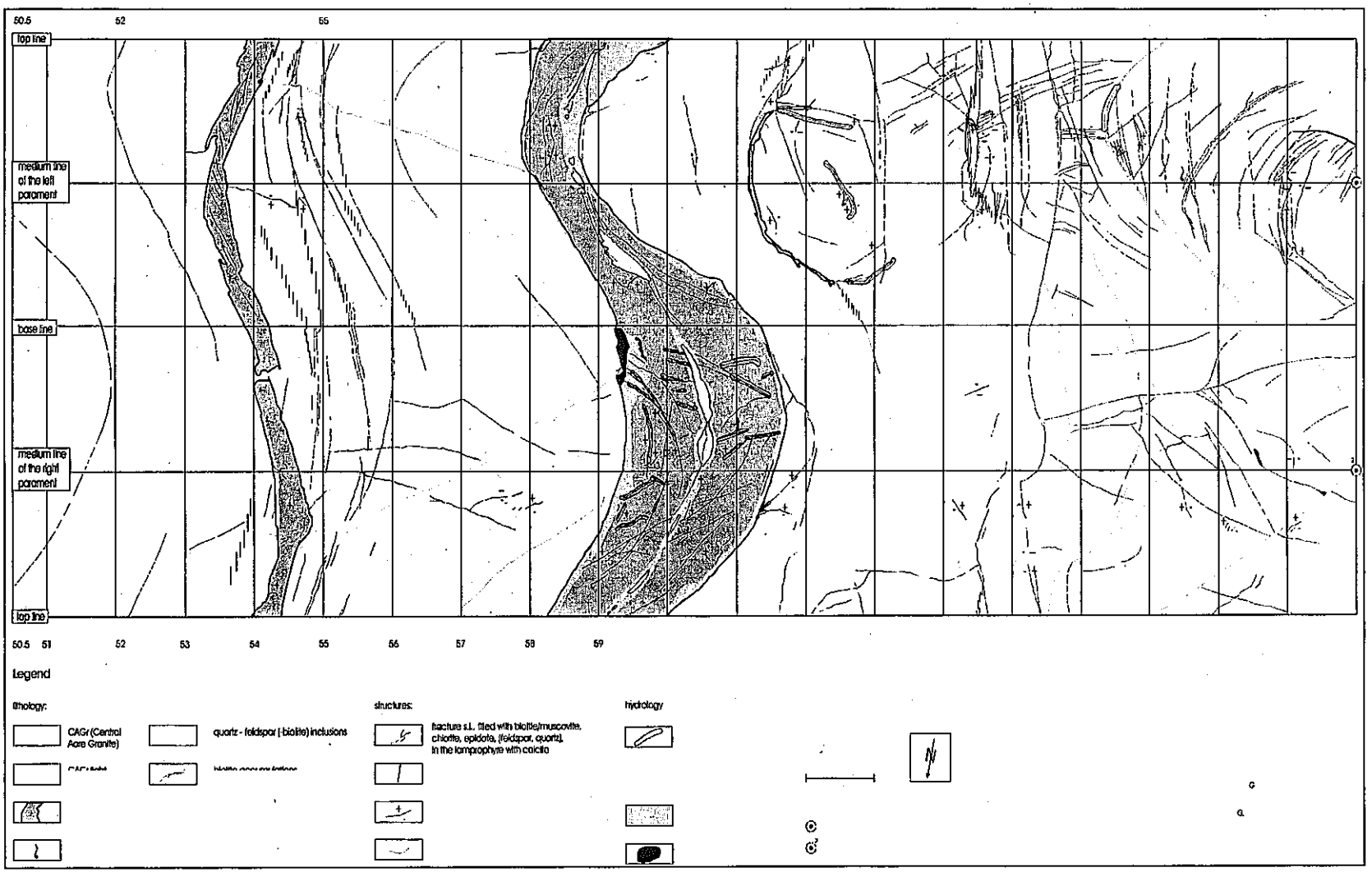

Figure 5-7: Geological map of the FEBEX drift between 50.5 and 70.0 m (Pardillo et al., 1997).

6 Hydraulic characterization

6.1 Hydrology of the Grimsel Test Site

The GTS is excavated in a fractured rock mass of low permeability. Thus, parameter values will display high variability due to the heterogeneity of the medium. When measurable, outflows are small (in the order of ml/min). Groundwater composition displays diluted water, barely detectable tritium contents and highly negative percentage of stable isotopes, which is in agreement with the expected recharge water at a given distance above the tunnel outflows (Figure 6-1). Groundwater composition at the FEBEX environment is also in agreement with such data and no further information will be given here, since it is not considered relevant for the purpose of the exercise.

The numerical model produced by Voborny et al. (1991), described the hydrogeology at two scales: an area of several kilometres around the GTS and the area in the vicinity of the GTS in more detail. For comparison, we will recall that the area of interest of the present exercise is a portion of the GTS.

The regional model evidenced the importance of the topography as the main driving force of groundwater flow. The boundary conditions were of prescribed head on surface, discharge at valleys and tunnels (when present) and nil flow across the lateral and bottom boundaries. Figure 6-2 is a calculated head distribution at a level 1730 m (GTS altitude) which includes the presence of the tunnels. Figure 6-3, is a cross section of the former (BS-BS) not accounting for the presence of the tunnels. Figure 6-3, also shows the effect of the most pervious shear zones as head contours deviations. Groundwater discharges towards the Aare river valley. Therefore, calculated heads of the model points to a regional direction N-NW, according to the main direction of this valley.

The presence of underground excavations disturbs such head distribution. Figure 6-4 shows that the capture zones of both the GTS and the KWO tunnels extends some hundreds of metres. This result was considered an artifact of the coarse discretisation around the tunnels. Thus, the model at the scale of the GTS used a more refined grid. Figure 6-5 shows a head distribution at the GTS plane of this model, where the contribution of the most transmissive features is not so evident as before due to the strong hydraulic gradients imposed by the tunnels.

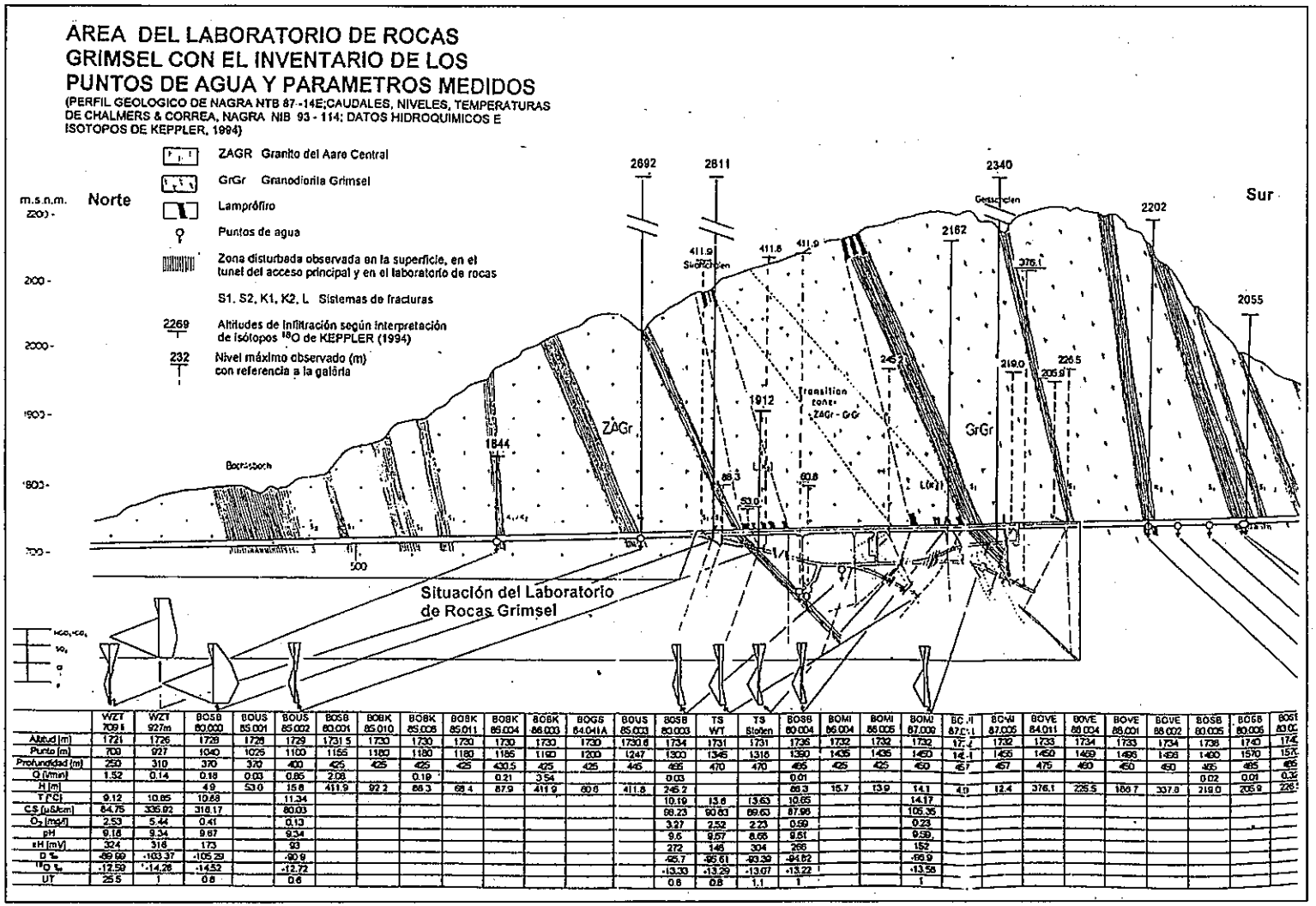

	WZT 709 S	WZT 927m	BOSB 80.000	BOUS 85.001	BOUS 85.002	BOSB 80.001	BOSB 85.010	BOSK 85.008	BOSK 85.011	BOSK 86.004	BOSK 86.003	BOGS 84.041A	BOUS 85.003	BOSB 80.003	TS WT	TS Stollen	BOSB 80.004	BOMI 86.004	BOMI 86.005	BOMI 87.009	BO..I 87.0.1	BO..I 87.005	BOVE 84.011	BOVE 86.004	BOVE 86.001	BOVE 86.002	BOVE 80.005	BOSB 80.006	BOSB 80.00
Altitud [m]	1721	1726	1729	1726	1729	1731.5	1730	1730	1730	1730	1730	1730	1730.6	1734	1731	1731	1736	1732	1732	1732	17..	1732	1733	1734	1733	1734	1736	1740	174
Punto [m]	709	927	1040	1026	1100	1155	1180	1180	1180	1185	1160	1200	1247	1300	1345	1316	1360	1405	1435	1460	14..1	1455	1460	1469	1486	1488	1490	1570	157
Profundidad [m]	250	310	370	370	400	425	425	425	425	430.5	425	425	445	485	470	470	485	425	425	450	457	457	475	460	450	450	485	485	485
Q [l/min]	1.52	0.14	0.18	0.03	0.85	2.08			0.19		0.21	3.54		0.03			0.01											0.02	0.01	0.3
H [m]			4.9	53.0	15.8	411.9	92.2	88.3	88.4	87.9	411.9	60.6	411.8	246.2			88.3	15.7	13.9	14.1	4.9	12.4	376.1	226.5	186.7	337.8	219.0	205.9	226
T [°C]	9.12	10.85	10.88		11.34									10.19	13.6	13.63	10.65			14.17										
CS [µS/cm]	84.75	335.82	318.17		80.03									88.23	90.83	89.63	87.96			105.35										
O_2 [mg/l]	2.53	5.44	0.41		0.13									3.27	2.52	2.23	0.59			0.23										
pH	9.18	9.34	9.67		9.34									9.6	9.57	8.66	9.51			9.59										
eH [mV]	324	318	173		93									272	146	304	266			152										
D ‰	-89.99	-103.37	-105.29		-90.9									-95.7	-95.61	-93.39	-94.62			-89.9										
^{18}O ‰	-12.59	-14.26	-14.53		-12.72									-13.33	-13.29	-13.07	-13.22			-13.56										
UT	25.5	1	0.8		0.6									0.6	0.8	1.1	1			1										

Figure 6-1: Geological cross-section of the GTS area with main geological features, major inflow zones, groundwater composition and available head measurements (Meier and Saavedra, 1995, unpublished).

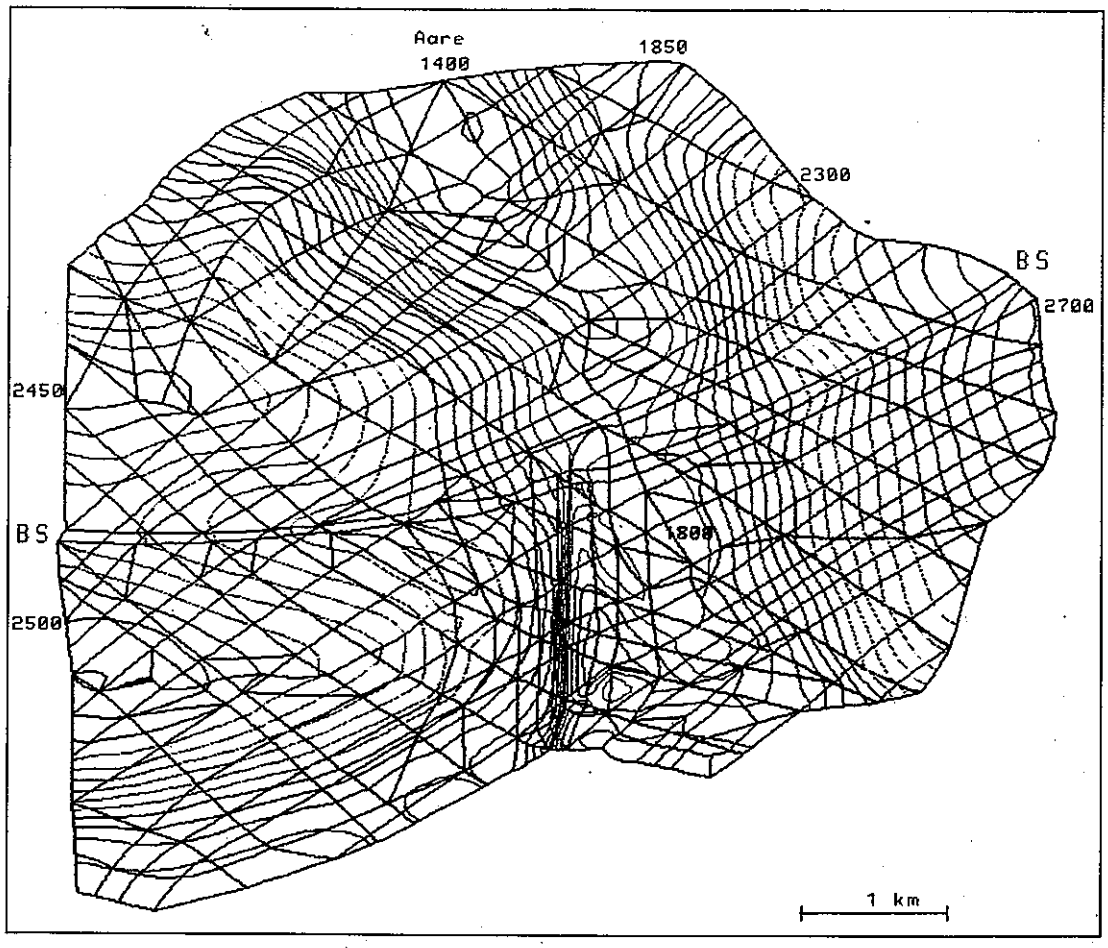

Figure 6-2: Computed head distribution of the regional model at the GTS level (1730 m.a.s.l.) (Voborny et al., 1991). Note the disturbance of the equipotential lines due to the presence of the tunnel.

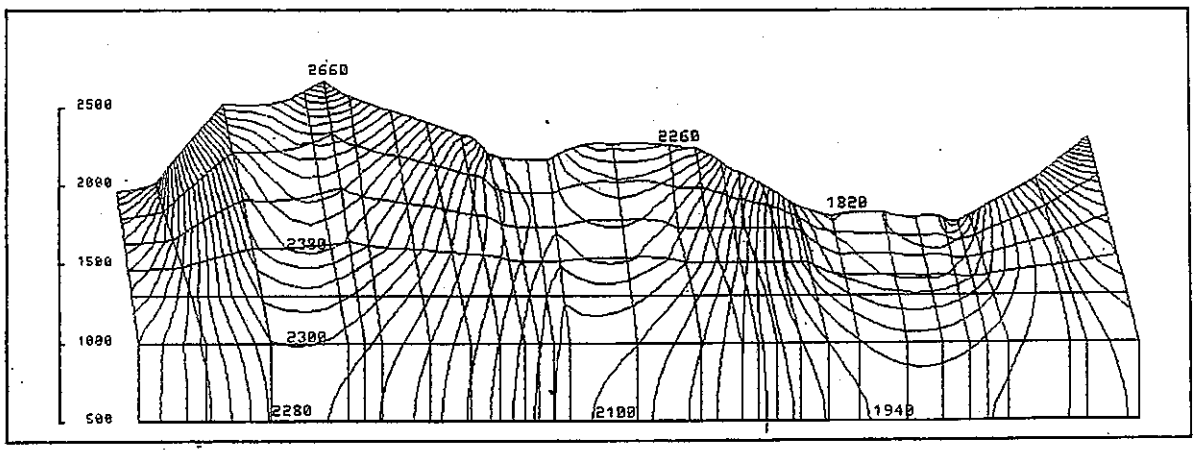

Figure 6-3: Computed head distribution of the regional model at the cross section BS-BS showed in Figure 6-2 (Voborny et al., 1991). Note the disturbance of the equipotential lines due to the presence of the shear zones. Tunnel presence was not simulated

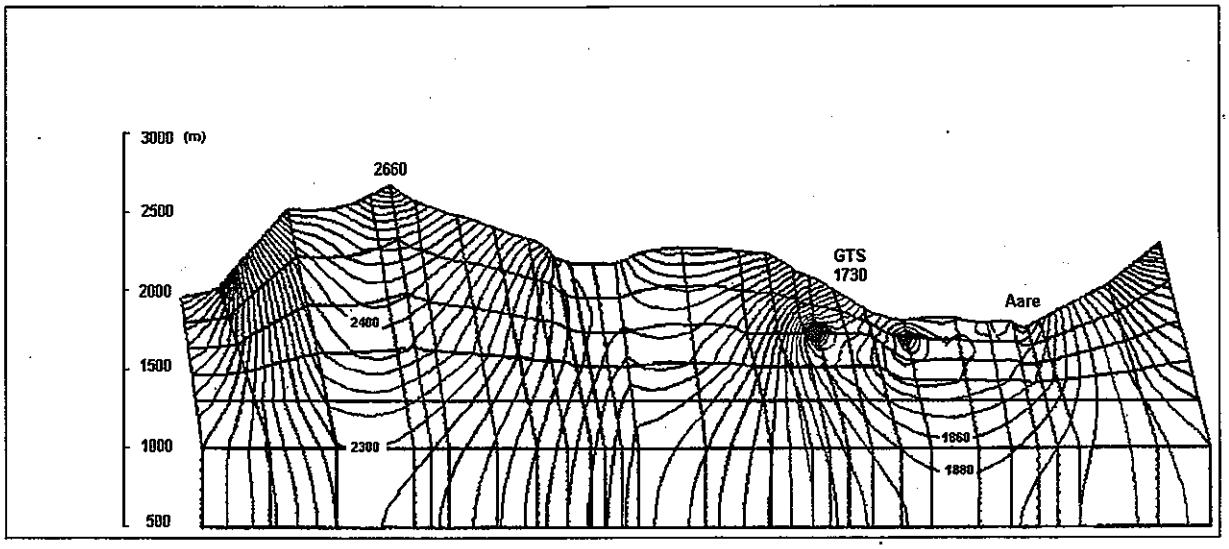

Figure 6-4: Computed head distribution of the regional model at the cross section BS-BS showed in Figure 6-2(Voborny et al., 1991). Note the disturbance of the equipotential lines due to the presence of tunnels and shear zones.

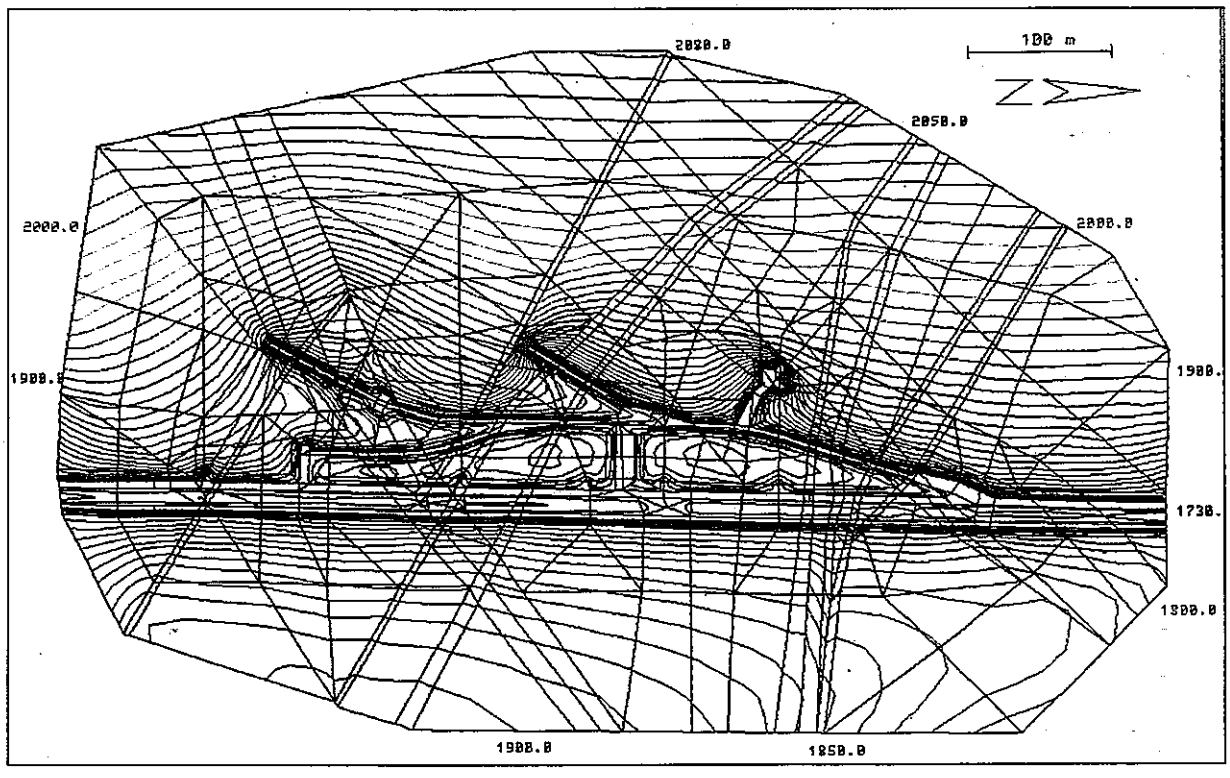

Figure 6-5 : Computed head distribution at the GTS plane (Voborny et al., 1991). Note that in this plan view, heads at the FEBEX vicinity are mainly controlled by the tunnel presence and by the shear zone which is the target of the BK area.

6.2 Hydrology of the FEBEX drift area

The FEBEX drift is located at the Northern bound of the GTS. The most important geological features at this environment are two shear zones (K and S, see Figure 5-2 and Figure 5-4). Such shear zones constraint regional groundwater flow due to their 'high' transmissivity and therefore, they constitute boundaries of the FEBEX environment. Measured inflows of these shear zones towards the tunnels are on the order of 60 ml/min and 23 ml/min (K and S respectively). Such a difference in flowrate measurements mat be attributed to the influence that the BK area, the GTS and the KWO exerts over the S shear zone, while the N one is only intersected by the KWO tunnel.

Topography, the most pervious geological features and the tunnel presence control the hydraulic gradient at the FEBEX environment. Therefore, any model of this rock mass block should take into account such effects.

Extensive hydraulic testing at existing and newly drilled boreholes was carried out. The most relevant results are described below, and the tests are documented in Meier et al. (1995), Guimerà et al. (1996) and Guimerà et al. (1998). Testing protocols are out of the scope of this document, but basically, they progressed from static pressure recovery after a flowing period, pulse test and longer time production or injection period. The instrumentation used (see Figure 6-6 and Figure 6-7) allowed both, injection and extraction.

Hydraulic tests at the boreholes BOUS 85001, 85002 and FBX 001 and 002 (Figure 6-8) consisted of pulse tests, constant head injection and/or extraction and constant rate injection/extraction. Table 6-1summarises the results obtained. They can be viewed as results of a larger scale than the FEBEX drift vicinity, given the distances among the boreholes and the lengths of the borehole intervals.

Hydraulic tests (pressure recovery interpretation and pulse injection) were carried out at all in-drift borehole intervals. The continuous pressure monitoring allowed to detect cross-hole responses during pulse testing (see Table 6-2). This information was used to set up a detailed cross-hole testing campaign, which consisted of 5 long term testing periods at selected intervals, followed by their corresponding recovery.

Cross-hole tests were performed at the intervals indicated in Table 6-3. The corresponding responses were monitored at all borehole intervals, although only few of them displayed noticeable head changes. Table 6-4shows a summary of the results of one-to-one cross-hole test interpretations.

In summary, the hydraulic tests performed allow to determine the hydraulic conductivity and hydraulic head for each borehole interval, as well as the hydraulic parameters of the geologic features involved in the cross-hole tests. This information completed the information of the available geologic map.

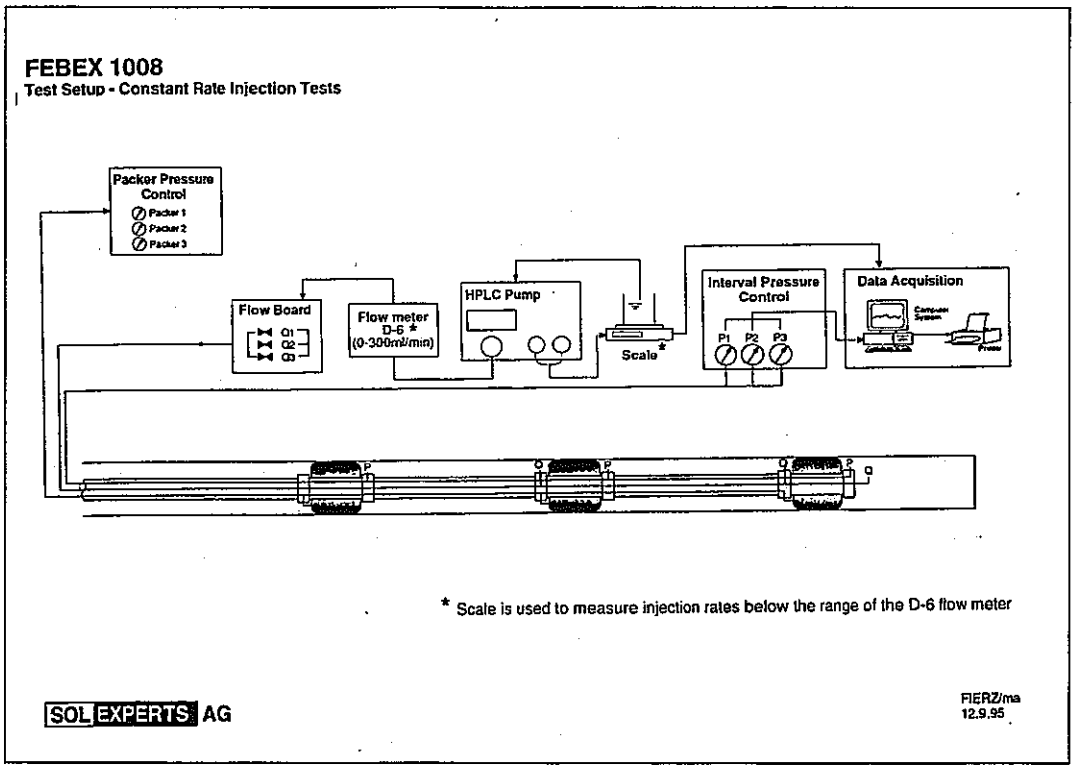

Figure 6-6: Multipackers system with the test set-up used for injection tests (Meier et al., 1995).

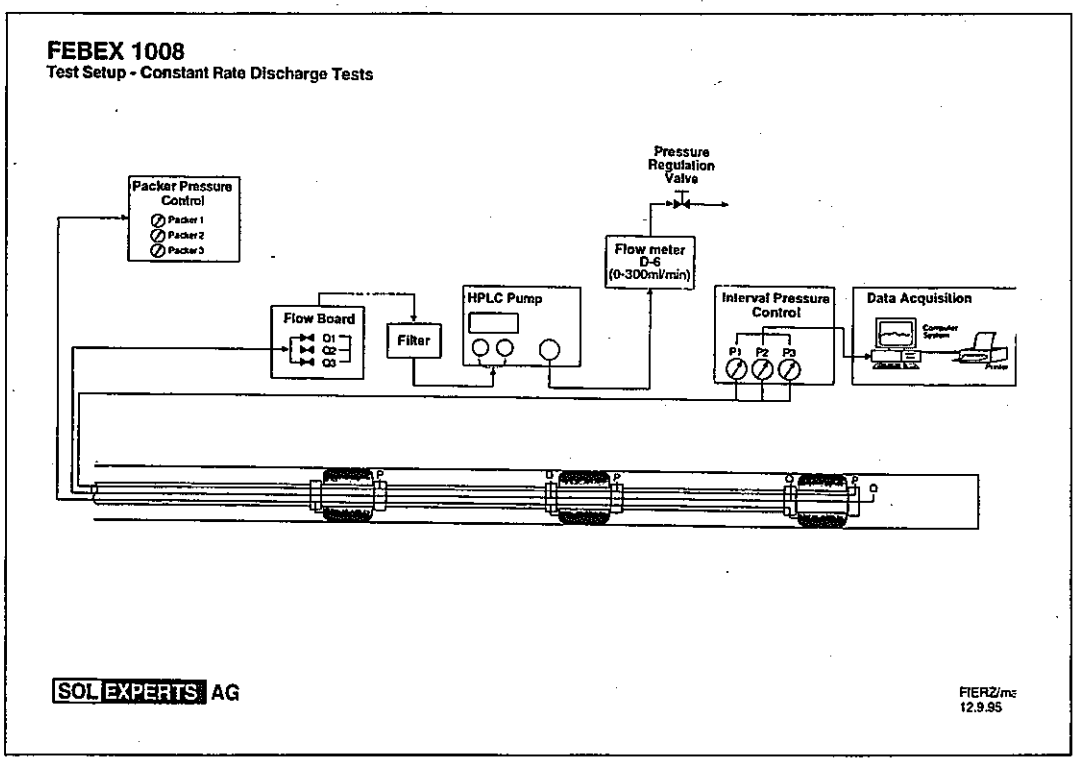

Figure 6-7: Multipackers system with the test set-up used for withdrawal tests (Meier et al., 1995).

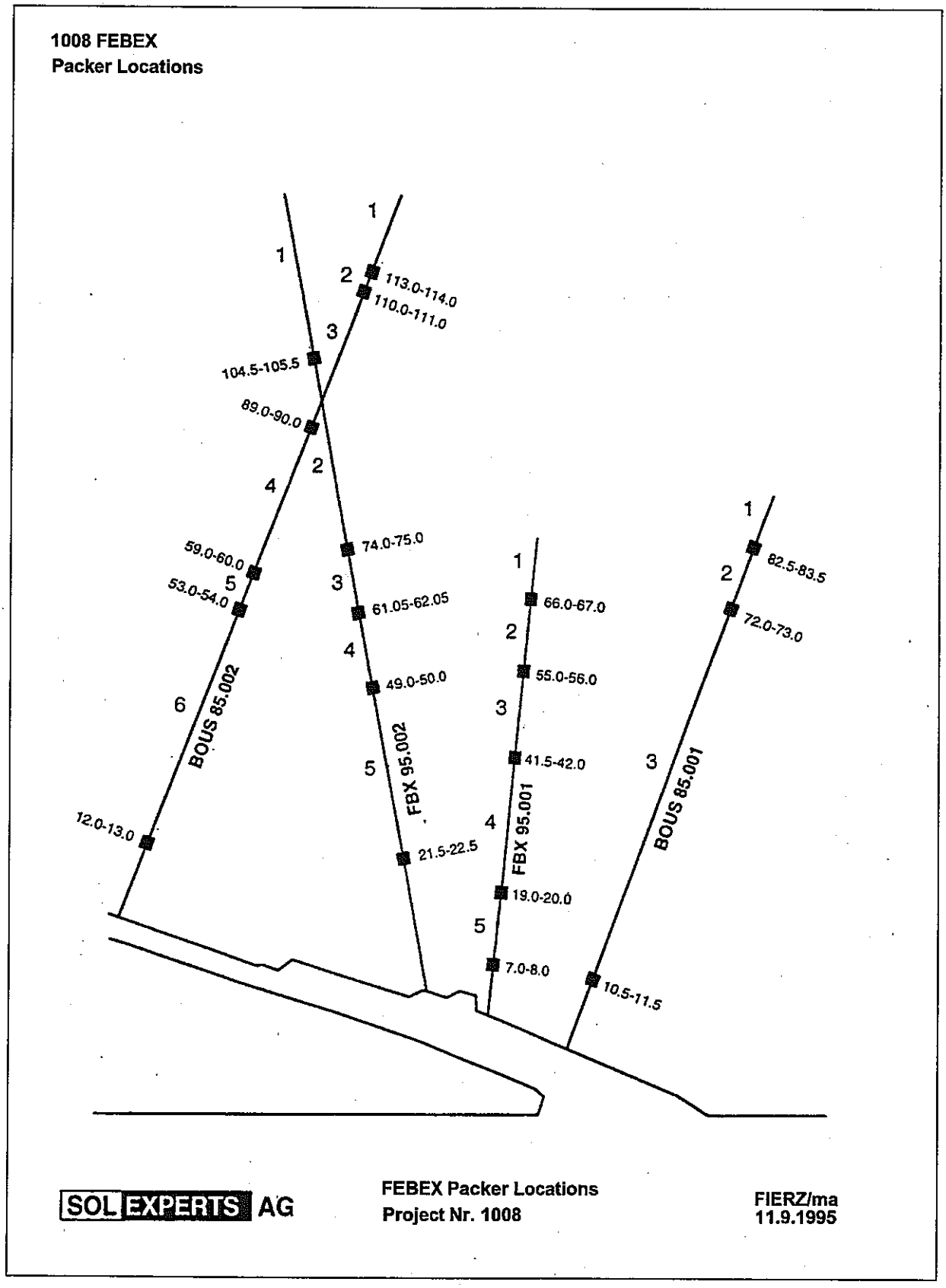

Figure 6-8: Location of packers during hydraulic testing of carried out before the FEBEX drift excavation (Meier et al., 1995).

Table 6-1: Results of hydraulic measurements at BOUS and FEBEX boreholes (Guimerà et al., 1998). (1. transmissivity derived from best estimates for late time data; 2. measured before drift construction on 27.09.95; 3. extrapolated from initial pressure recover data using the Horner method; 4. measured after drift construction on 01.02.96). (NOTES: a. Meier et al., 1995; b. 1994 data; d. 1994 data, dominant zone lies between 10.0 and 17.3 m).

interval (m)	**T** (1) (m^2/s)	**head** (2) (m)	**head** (3) (m)	**head** (4) (m)	**hydraulic communications**
BOUS 85.001					
I1 (83.50-150.00)	$3.6 \cdot 10^{-10}$	1983.0	-	-	-
I2 (73.00-82.50)	$3.2 \cdot 10^{-09}$	1777.3	-	1778.6	I3
I3 (11.50-72.00)	$3.9 \cdot 10^{-10}$	(a)1759.5	-	1758.5	I2
(1.00-150.00)	-	(b)1783.6	-	-	-
BOUS 85.002					
I1 (114.00-150.00)	$8.3 \cdot 10^{-10}$	(a)1909.3	1915.7	1922.2	I2
I2 (111.00-113.00)	$2.8 \cdot 10^{-08}$	1830.1	1844.4	1852.9	I1, I3, FBX2-I1, -I2, -I3, -I4
I3 (90.00-110.00)	$2.7 \cdot 10^{-09}$	1818.6	1835.2	1843.1	I2
I4 (60.00-89.00)	$7.0 \cdot 10^{-08}$	1781.6	1782.7	1783.0	I5, FBX2-I2, -I3, -I4
I5 (54.00-59.00)	$1.6 \cdot 10^{-08}$	1791.0	1792.4	1791.8	I4
I6 (13.00-53.00)	$1.3 \cdot 10^{-07}$	1745.8	-	1745.4	-
(1.00-150.00)	-	(c)1745.6	-	-	-
FEBEX 95.001					
I1 (67.00-76.70)	$3.3 \cdot 10^{-10}$	1788.5	1790.8	1794.0	-
I2 (56.00-66.00)	$8.2 \cdot 10^{-11}$	1776.8	1782.2	1778.5	-
I3 (42.00-55.00)	$6.8 \cdot 10^{-11}$	1772.2	1777.1	1771.7	-
I4 (20.00-41.00)	$1.4 \cdot 10^{-10}$	1757.1	-	1748.1	-
I5 (8.00-19.00)	$>2.0 \cdot 10^{-07}$	1747.2	-	1731.1	FBX2-I5
FEBEX 95.002					
I1 (105.50-132.00)	$5.3 \cdot 10^{-10}$	1889.8	1891.3	-	BOUS-I2
I1 (84.00-132.00)	-	-	-	1881.0	-
I2 (75.00-104.50)	$3.7 \cdot 10^{-10}$	1821.9	1820.4	-	BOUS-I2, -I4
I2 (72.00-83.00)	$1.3 \cdot 10^{-10}$	-	-	1819.5	-
I3 (62.00-74.00)	$5.7 \cdot 10^{-10}$	1807.4	1800.5	-	I4, BOUS2-I2, -I4
I3 (63.00-71.00)	$4.2 \cdot 10^{-10}$	-	-	1786.9	-
I4 (50.00-61.00)	$6.6 \cdot 10^{-10}$	1797.4	1793.4	-	I3, BOUS2-I2, -I4
I4 (50.00-62.00)	$3.3 \cdot 10^{-10}$	-	-	1769.2	-
I5 (22.50-49.00)	$>2.0 \cdot 10^{-07}$	1747.0	-	-	FBX1-I5
I5 (43.00-49.00)	-	-	-	1729.5	-

Table 6-2: In-drift single hole hydraulic testing results (Guimerà et al., 1998). (1. PW = pulse withdrawal; 2. H = Horner; 3. PI = Pulse injection; 4. flowrate = naturally flowing rate after 3-4 days of packer installation, and used to interpret the recovery curve by the Horner method).

interval (m)	pressure (bar)	flowrate (ml/min)	T (H) (m^2/s)	T (PW) (m^2/s)	T (PI) (m^2/s)	responses / comments
B12-1 (6.00-7.03)	1.380	0.065	$1.67\cdot10^{-11}$	$1.98\cdot10^{-11}$	$9.61\cdot10^{-12}$	
B12-2 (1.50-5.00)	0.430	dry		$9.73\cdot10^{-11}$	$3.33\cdot10^{-11}$	
B13-1 (4.00-7.10)	0.870	>0.01		$2.03\cdot10^{-11}$	$2.38\cdot10^{-11}$	
B13-2 (1.50-3.00)	1.425	dry		no recov.	$8.48\cdot10^{-12}$	
B22-1 (1.50-7.07)	8.283	0.32	$2.76\cdot10^{-11}$	$2.87\cdot10^{-10}$	$7.86\cdot10^{-11}$	
B23-1 (3.30-7.16)	8.133	21.9	$3.76\cdot10^{-09}$	$5.20\cdot10^{-08}$	$3.41\cdot10^{-08}$	J5-3
B23-2 (1.50-2.30)	7.218	no measure		$1.04\cdot10^{-10}$	$1.14\cdot10^{-10}$	
F11-1 (13.50-15.00)	5.463	no measure			$2.95\cdot10^{-11}$	
F11-2 (7.50-12.50)	4.772	no measure			$2.37\cdot10^{-11}$	
F11-3 (1.50-6.50)	0.958	no measure			$7.73\cdot10^{-11}$	
F12-1 (9.54-15.19)	3.363	0.22	$5.72\cdot10^{-11}$	$2.52\cdot10^{-10}$	$1.20\cdot10^{-10}$	
F12-2 (6.50-8.54)	2.465	0.04	$9.32\cdot10^{-12}$	$2.53\cdot10^{-10}$	$3.08\cdot10^{-11}$	F24-2
F12-3 (1.50-5.50)	3.315	>0.1		$1.63\cdot10^{-10}$	$5.38\cdot10^{-11}$	F22-2, I2-1
F13-1 (10.50-15.06)	1.435	0.13	$4.08\cdot10^{-11}$	$3.55\cdot10^{-11}$	$2.04\cdot10^{-11}$	
F13-2 (5.00-9.50)	2.382	>0.01		$4.26\cdot10^{-10}$	$4.77\cdot10^{-10}$	
F13-3 (1.50-4.00)	2.380	dry		$9.46\cdot10^{-11}$	$4.19\cdot10^{-11}$	K2-3
F14-1 (11.70-15.00)	5.365	8.7	$9.55\cdot10^{-10}$	$2.14\cdot10^{-08}$	$2.95\cdot10^{-08}$	
F14-2 (8.50-10.70)	4.985	0.012	$1.15\cdot10^{-12}$	$1.00\cdot10^{-11}$	$5.82\cdot10^{-12}$	K2-2
F14-3 (1.50-7.50)	3.698	2.75	$3.90\cdot10^{-10}$	not interp.	$2.83\cdot10^{-10}$	FBX2-4
F21-1 (15.00-11.66)	6.068	no measure			$1.94\cdot10^{-11}$	
F21-2 (10.66-3.70)	4.973	no measure		$5.53\cdot10^{-11}$	$2.53\cdot10^{-11}$	
F21-3 (2.70-1.36)	3.030	no measure			$1.14\cdot10^{-11}$	
F22-1 (15.04-11.50)	6.988	0.38	$5.84\cdot10^{-11}$	$1.66\cdot10^{-10}$	$2.80\cdot10^{-10}$	I2-1
F22-2 (10.50-8.00)	6.745	1.47	$2.03\cdot10^{-10}$	$1.19\cdot10^{-09}$		too rapid rec.
F22-3 (7.00-1.50)	6.340	0.11	$1.05\cdot10^{-11}$	$2.45\cdot10^{-10}$	$8.46\cdot10^{-11}$	
F23-1 (9.34-15.13)	5.100	0.24	$5.70\cdot10^{-12}$	$2.09\cdot10^{-10}$	$7.94\cdot10^{-11}$	
F23-2 (7.54-8.34)	5.198	0.084	$1.06\cdot10^{-11}$	not interp.	$4.96\cdot10^{-11}$	
F23-3 (6.54-1.50)	4.200	0.044	$6.00\cdot10^{-12}$	$2.18\cdot10^{-10}$	$4.80\cdot10^{-11}$	
F24-1 (7.75-15.11)	5.673	236.81	$2.41\cdot10^{-08}$	$1.36\cdot10^{-07}$	no react.	K1-1
F24-2 (1.50-6.75)	4.595	1.17	$1.54\cdot10^{-10}$	$1.29\cdot10^{-09}$	$4.90\cdot10^{-10}$	FB2-3
I1-1 (6.00-7.14)	1.525	no measure				
I1-2 (5.00-1.50)	2.310	no measure		$1.16\cdot10^{-11}$		
I2-1 (3.50-7.14)	6.720	2.5	$3.08\cdot10^{-09}$	not interp.	$5.95\cdot10^{-10}$	J5-2, F12-2, -3, F22-2
I2-2 (1.50-2.50)	2.683	dry		not interp.	$8.44\cdot10^{-12}$	
J5-1 (8.25-15.19)	10.805	1.38	$4.70\cdot10^{-10}$	$2.86\cdot10^{-10}$	$1.73\cdot10^{-10}$	
J5-2 (4.20-7.25)	9.670	0.176	$2.27\cdot10^{-11}$	$9.85\cdot10^{-11}$	$2.28\cdot10^{-11}$	
J5-3 (1.50-3.20)	8.163	26.7	$4.56\cdot10^{-09}$	$3.31\cdot10^{-08}$		B23-1
K1-1 (14.90-21.99)	5.115	no measure			$5.56\cdot10^{-11}$	
K1-2 (9.00-13.90)	1.528	no measure			$1.05\cdot10^{-11}$	
K1-3 (5.00-8.00)	0.108	no measure				
K1-4 (1.50-4.00)	-0.295	no measure				
K2-1 (18.52-20.11)	4.770	0.043	$5.70\cdot10^{-12}$	$4.97\cdot10^{-11}$	$9.07\cdot10^{-12}$	
K2-2 (11.48-17.52)	2.578	0.33	$5.65\cdot10^{-11}$	$4.98\cdot10^{-08}$	$1.24\cdot10^{-07}$	F13-2, F13-3
K2-3 (6.04-10.48)	3.275	0.27	$4.09\cdot10^{-11}$	$6.97\cdot10^{-10}$	$3.28\cdot10^{-10}$	FBX2-4
K2-4 (1.50-5.04)	0.480	dry				no response
Atmospheric	0.8					

Table 6-3: Summary of the 5 performed cross hole tests (Guimerà et al., 1998).

active interval	response intervals
J5-3	J5-2, B22-1, B23-1, B23-2
I2-1	F12-1, F12-2, F12-3, F22-1, F22-2, F22-3
F14-3	FBX2-4, K2-2, K2-3, B13-2, F13-2
FBX2-4	F14-3, K2-2, K2-3, B13-2, F13-2
F24-1	F14-1, F14-2, BOUS2-4, BOUS2-5

Table 6-4: Results of one-to-one cross-hole test interpretations (Guimerà et al., 1998). (1. T = transmisivity; 2. S = storativity).

active interval	resp. interval	T (m^2/s)	S (m^{-1})
J5-3	J5-3	$8.10 \cdot 10^{-09}$	$1.70 \cdot 10^{-04}$
J5-3	J5-2	$7.90 \cdot 10^{-09}$	$2.60 \cdot 10^{-04}$
J5-3	B22-1	-	-
J5-3	B23-1	$7.90 \cdot 10^{-09}$	$1.20 \cdot 10^{-07}$
J5-3	B23-2	-	-
I2-1	I2-1	$1.14 \cdot 10^{-09}$	$1.50 \cdot 10^{-05}$
I2-1	F12-1	$1.45 \cdot 10^{-09}$	$6.20 \cdot 10^{-06}$
I2-1	F12-2	$1.45 \cdot 10^{-09}$	$6.70 \cdot 10^{-06}$
I2-1	F12-3	$1.20 \cdot 10^{-09}$	$1.10 \cdot 10^{-06}$
I2-1	F22-1	$1.17 \cdot 10^{-09}$	$5.40 \cdot 10^{-07}$
I2-1	F22-2	$8.14 \cdot 10^{-10}$	$1.10 \cdot 10^{-08}$
I2-1	F22-3	$7.70 \cdot 10^{-10}$	$2.10 \cdot 10^{-06}$
F14-3	F14-3	$2.10 \cdot 10^{-09}$	$5.60 \cdot 10^{-05}$
F14-3	FBX2-4	$9.90 \cdot 10^{-10}$	$1.90 \cdot 10^{-07}$
F14-3	K2-2	$8.10 \cdot 10^{-10}$	$1.20 \cdot 10^{-06}$
F14-3	K2-3	$1.10 \cdot 10^{-09}$	$5.50 \cdot 10^{-07}$
F14-3	B13-2	$7.60 \cdot 10^{-10}$	$3.40 \cdot 10^{-06}$
F14-3	F13-2	$9.90 \cdot 10^{-10}$	$1.30 \cdot 10^{-06}$
FBX2-4	FBX2-4	$9.60 \cdot 10^{-10}$	$3.10 \cdot 10^{-03}$
FBX2-4	F14-3	$8.60 \cdot 10^{-10}$	$2.70 \cdot 10^{-06}$
FBX2-4	K2-2	$8.40 \cdot 10^{-10}$	$1.80 \cdot 10^{-06}$
FBX2-4	K2-3	$7.80 \cdot 10^{-10}$	$3.70 \cdot 10^{-07}$
FBX2-4	B13-2	$9.40 \cdot 10^{-10}$	$2.90 \cdot 10^{-06}$
FBX2-4	F13-2	$1.10 \cdot 10^{-09}$	$2.20 \cdot 10^{-06}$
F24-1	F24-1	$1.90 \cdot 10^{-08}$	$1.30 \cdot 10^{+00}$
F24-1	F14-1	$2.40 \cdot 10^{-08}$	$8.10 \cdot 10^{-05}$
F24-1	F14-2	$1.60 \cdot 10^{-08}$	$1.40 \cdot 10^{-04}$
F24-1	BOUS2-4	$3.40 \cdot 10^{-08}$	$8.70 \cdot 10^{-06}$
F24-1	BOUS2-5	$2.50 \cdot 10^{-08}$	$1.10 \cdot 10^{-06}$

7 Thermo-mechanical characterization

7.1 Characteristic values of various granitic rocks

Values of important mechanical properties of granitic rocks may be found in Amiguet (1985). This report is a summary from a literature review, including tests carried out in the Grimsel Test Site. The report contains (1) tables with characteristic values of various granitic rocks; (2) a summary table with typical values of intact granite and (3) diagrams showing the behaviour of various characteristic parameters under various mechanical and thermal conditions. For instance, Table 7-1 shows the summary table with the mean and possible values of intact granite properties. The ranges include most results of investigations, but they do not contain all the possible values nor correspond to a statistical standard deviation.

Table7-1: Properties of intact granite (Amiguet, 1985). (* means in-situ stress condition).

property	versus	mean value	range	units
bulk density		2640	2600-2680	kg/m^3
grain density		2680	2650-2700	kg/m^3
porosity		1.6	0.5-2.5	%
uniaxial compression strength		185	150-220	MPa
Young's modulus		60	45-75	GPa
Poisson's ratio		0.25	0.20-0.30	-
tensile strength		10	5-15	MPa
triaxial strength	conf. pressure			
	5 MPa	35	25-40	MPa
	10 MPa	45	35-55	MPa
	20 MPa	65	55-75	MPa
	50 MPa	105	95-120	MPa
	100 MPa	160	140-180	MPa
	200 MPa	240	200-280	MPa
angle of friction (natural joint)		32	25-40	°
p-wave velocity		*5600	5000-6200	m/s
s-wave velocity		*3400	3000-3600	m/s
coef. linear thermal expansion		$8.0 \cdot 10^{-6}$	$(5\text{-}12) \cdot 10^{-6}$	K^{-1}
coef. vol. thermal expansion		$25 \cdot 10^{-6}$	$(20\text{-}30) \cdot 10^{-6}$	K^{-1}
thermal conductivity		3.3	2.7-3.8	W/mK
specific heat		920	800-1250	J/kgK
permeability		10^{-12}	$(0.1\text{-}5) \cdot 10^{-12}$	m/s

Keusen et al. (1989) (see Table 7-2) gives rock mechanical parameters, together with a few geophysical parameters, and makes two important remarks: (1) the majority of measurements were carried out on drill cores in the laboratory and, because the in-situ stresses are higher, do not correspond to true in-situ values; (2) parameters refer to the intact rock on a small scale and not to the whole rock body on a large scale, where fractures and changes in rock type will have an influence.

Table 7-2: Rock mechanical parameters of the main rocks at the Grimsel Test Site (Keusen et al., 1989). (* refers to fractures).

parameter	granite (Central Aare)	granodiorite (Grimsel)	aplite	lamprohyre	units
density	2660±23.8	2706±13.6	2599±17.4	2909±31.0	kg/m^3
porosity	0.4-1.0				vol %
uniaxial comp. strength	169.1±37.1	116.9±47.9	225.6±45.4	127.0±31.8	MPa
Young's modulus E_{50}	53.3±11.0	47.3±15.4	60.2±8.9	42.4±8.5	GPa
Poisson's ratio	0.37±0.12 0.33±0.03	0.33±0.15	0.40±0.12	0.33±0.17	-
tensile strength	9.06±1.48	9.54±2.17	9.27±0.95	12.55±3.59	MPa
triaxial comp. strength	5.0 ; 263.0±29.9	5.0 ; 230.0±70.7	5.0 ; 297.0	5.0 ; 240.0	MPa
(σ_3 ; σ_1)	10.0 ; 333.0±20.6 20.0 ; 410.0±63.8	10.0 ; 287.0±24.7 20.0 ; 355.0±28.3	10.0 ; 395.0 20.0 ; 455.0	20.0 ; 226.0±44	
friction angle	(*) 33	(*) 30±2 29	(*) 34 36	32.5±3.5	°
p-wave vel. (specimen)	3111±278	3351±388	2948±428	2120±480	m/s
p-wave vel. (whole rock)	5600±100	5600±100	5400-5700	5700-6100	m/s
therm. conductivity (wet)	2.58±0.19	2.66±0.19	3.31±0.35	2.21±0.45	W/m·K
therm. conductivity (dry)	3.34±0.35	3.22±0.29	5.32±0.49	2.71±0.60	W/m·K
permeability	$5 \cdot 10^{-17}$ (10 MPa) 3.5-4.5·10^{-12} (5-15 MPa) $5 \cdot 10^{-12}$ (5-30 MPa)				m/s

Unconfined compression tests using two specimens of granite and two specimens of lamprophyre recovered from in-drift boreholes SF22 and SF13 were carried out in the Structural Technology Laboratory of the Construction Department of UPC (Pintado et al., 1997). The procedure adopted was based on the ASTM standard test method D3148-86. Three 60 mm long strain gauges were mounted centrally on each specimen, equally spaced around the circumference and parallel to the longitudinal axis. The stress versus axial strain recorded in the pre-failure regime of each test is shown in Figure 7-1. A straight line was fitted through the linear part of each curve and its slope was used to calculate the elastic modulus. The location and type of rock of the specimens tested with the results obtained are summarised in Table 7-3.

Water retention curves were determined at the UPC (Pintado et al., 1997) for 2 lamprophyre and 3 granite specimens recovered from in-drift boreholes. Table 7-4 shows the location and type of rock of each specimen. Suctions ranging from 2 to 200 kPa were applied using a pressure plate extractor with a porous ceramic plate. In order to apply higher suctions (0.6, 1.0 and 2.0 MPa) a pressure membrane extractor was used. For low suctions (2 and 5 kPa), suction was applied by means of a water column and for higher suctions positive air pressure was applied in the extractors. Figure 7-2 shows the water retention curves obtained.

These curves are coherent with the curves obtained by Schneebeli et al. (1995) performing similar tests but using samples of the ventilation test instead. On this ventilation test, Finsterle et al. (1995) obtained by backanalysis the following expressions for the retention curve and the relative permeability of the Grimsel granite:

Table 7-3: Results of unconfined compression tests performed in specimens recovered from in-drift boreholes (Pintado et al., 1997). (1. depth = distance to FEBEX drift wall; 2. mean Ø = mean diameter; 3. E_{50} = Young's modulus; 4. comp = compressive strength) (Pintado et al., 1997)).

borehole	depth (m)	rock type	mean Ø (mm)	E_{50} (GPa)	comp (MPa)
SF22	0.17-0.27	granite	51.73	61.6	193.5
SF22	0.85-0.95	granite	51.64	50.8	110.0
SF22	12.16-12.26	lamprophyre	51.64	49.8	142.0
SF13	0.70-0.80	lamprophyre	51.78	35.7	85.4

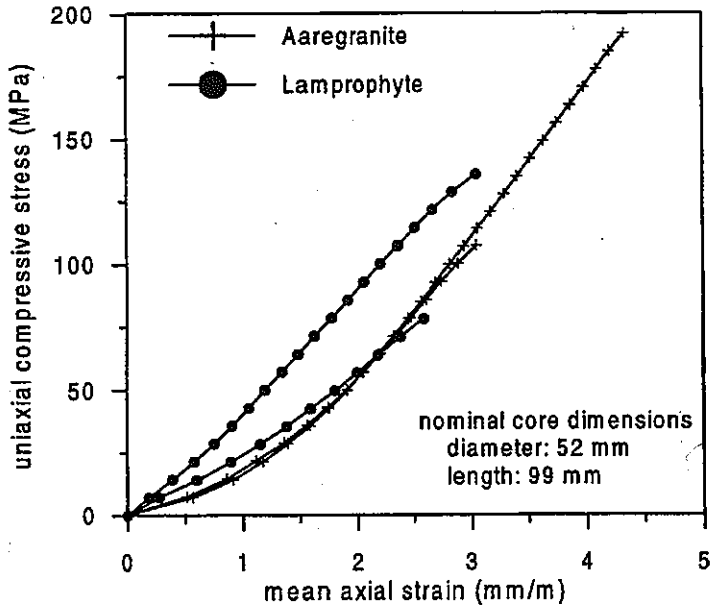

Figure 7-1: Unconfined compression tests performed in specimens recovered from in-drift boreholes (Pintado et al., 1997).

$$s = 1.74\,(S_r^{-1.68} - 1)^{0.405} \tag{7-1}$$

$$k_r = S_r^{0.5}\,[1 - (1 - S_r^{1.68})^{0.595}]^2 \tag{7-2}$$

where s is the suction (in MPa), S_r is the degree of saturation and k_r is the relative permeability.

Values of properties of the rock around the FEBEX area may also be inferred from the geophysical investigations carried out in boreholes FEBEX 95.001 and FEBEX 95.002, and reported in Häring (1996).

Table7-4: Specimens recovered from in-drift boreholes to determine the water retention curve (Pintado et al., 1997) (depth = distance to FEBEX drift wall).

specimen	borehole	depth (m)	rock type
L1	SF13	0.05-0.07	lamprophyre
L2	SF22	12.14-12.16	lamprophyre
G1	SF22	0.04-0.06	granite
G2	SF22	0.06-0.08	granite
G3	SF13	0.95-0.97	granite

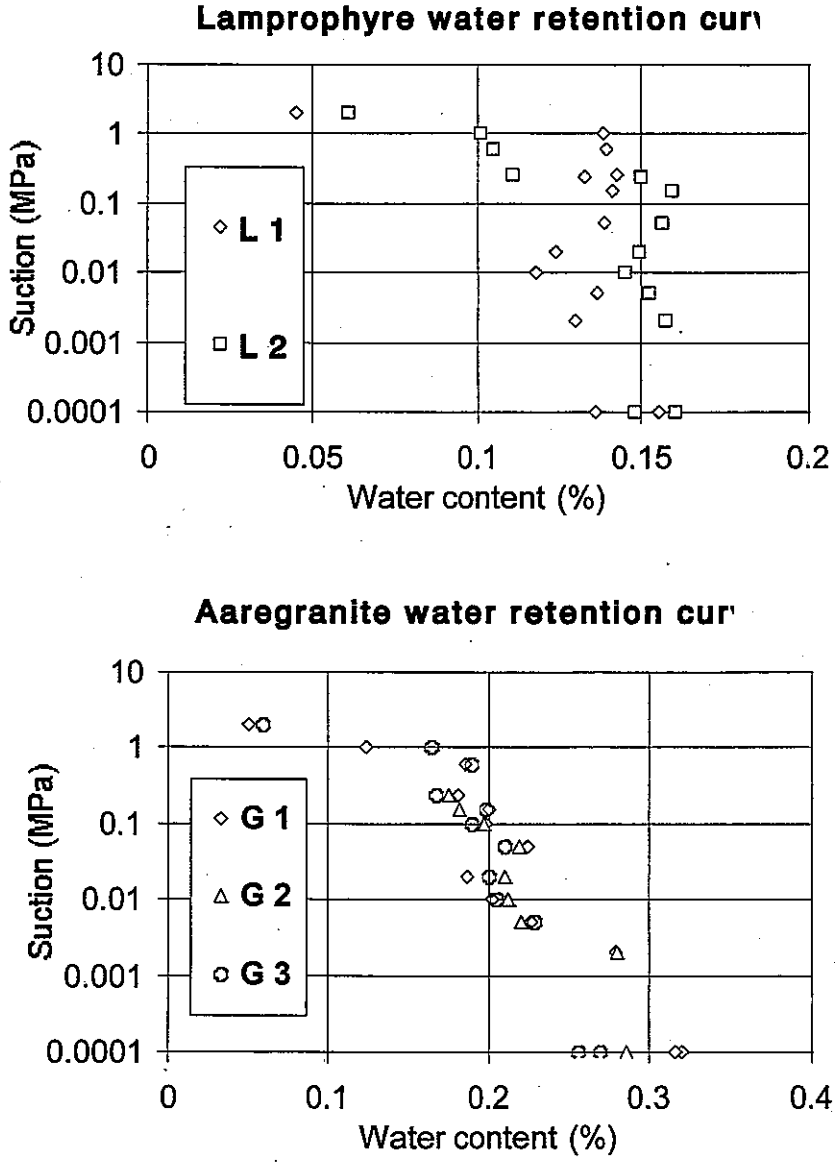

Figure7-2: Water retention curves of lamprophyre and granite specimens (Pintado et al., 1997).

7.2 In-situ stresses in the Grimsel Test Site

In the Grimsel Test Site, investigations have been carried out to determine rock stresses. Information may be found in Bräuer et al. (1989) and Pahl et al. (1989).

General remarks concerning stress measurements carried out by BGR, Hannover (Germany) are provided in Keusen et al. (1989): "(1) there is a difference of more than 10 MPa between the minimum and maximum horizontal stress; (2) the maximum horizontal stress lies between 18 and 45 MPa and the minimum principal stress between 15 and 32 MPa; (3) the maximum horizontal stresses are generally directed towards the SE, i.e. perpendicular to the main alpine schistosty S_2". It is concluded that "the stress, which is 4-5 times higher than the lithostatic pressure of around 9-12 MPa, indicates the presence of significant horizontal forces in the main compression direction NW-SE".

In the context of the project Rock Stresses carried out in the Grimsel Test Site (GS in Figure 5-3) several rock stress investigations were carried out by BGR, Hannover (Germany). In these investigations several overcoring methods, borehole dilation tests and hydrofracture tests were used. Details may be consulted in Pahl et al. (1989). For instance, Figure 7-3 shows the results of horizontal stress measurements using and overcoring method. Referring to this figure, Pahl et al. (1989) remark that "It can clearly be seen that tha maximum stresses are approximately 25 - 40 MPa and the minimum horizontal stresses are between 15 and 30 MPa. We have then that the horizontal stresses (are) substantially higher than the depth-related overburden pressure".

Additional information may be found in Bräuer et al. (1989) where engineering geological investigations were carried out for the Rock Stresses and Fracture System Flow tests performed in the Grimsel Test Site (GS and BK in Figure 5-3). The evaluation of the geological data showed structural tectonic and hence rock mechanical and rock hydraulic differences between closely neighbouring rock sections. The analysis of both test areas enables the transferability of rock stresses and rock hydraulic properties to other areas.

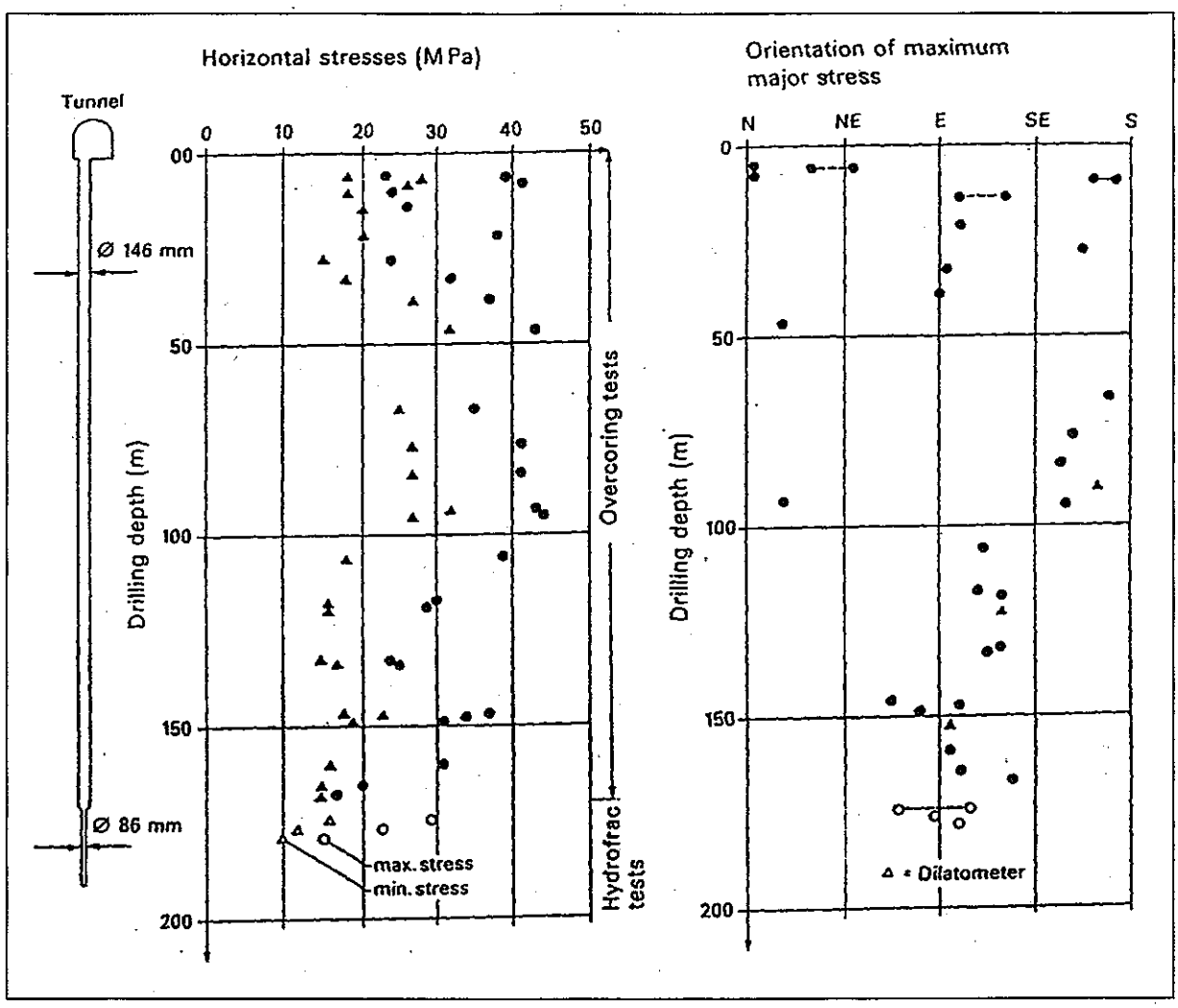

Figure7-3: Size and direction of horizontal stresses obtained from BGR overcoring tests assuming isotropic rock mass behaviour (E = 40 GPa, ν = 0.25) (Pahl et al., 1989)

8 Required results

8.1 Work to be done

Based on the information presented in the previous sections, it is required:

- Preparation of a hydro-mechanical model of the host rock near the FEBEX tunnel.

  Full details of the construction of the model are required, as explained in the general specifications. Specifically, the following issues should be explained: (1) Mathematical setting, (2) Model calibration, (3) Numerical solution and (4) Additional comments.

- Blind prediction of total water inflow to the FEBEX tunnel.

  As a result of the excavation of the FEBEX tunnel, water will flow into the tunnel. The total water inflow to the FEBEX tunnel is required.

- Blind prediction of the response of pore water against the tunnel excavation.

  During the excavation of the FEBEX tunnel, existing stresses around the tunnel were disturbed, as well as pore water pressures. Indeed, water pressure at intervals P3 and P4 of borehole FBX 95.002 against the advance of the excavation front showed the existence of a non-negligible hydro-mechanical coupling. Given the evolution in time of the excavation of the tunnel, it is required to predict the evolution of water pressure at intervals P3 and P4 of borehole FBX 95.002, running subparallel to the FEBEX tunnel.

8.2 Output specifications

The origin of time measurements is set at the beginning of the FEBEX drift excavation (i.e., on 25.09.95). The required output is:

- The total water inflow Q (in ml/min) into the portion of the FEBEX tunnel later occupied by the test (tunnel metering from 54.00 to 71.40 m) 100 days after the start of the tunnel excavation (i.e., on 03.01.96).

- The evolutions of water pressure (in MPa) in intervals P3 and P4 of the FEBEX 95.002 borehole (see Figure 6-8) as a function of time (in days). Of course, packer locations should be those used during the FEBEX drift excavation, as detailed in Fierz, 1996. The evolutions should cover 45 days (i.e., from 25.09.95 to 09.11.95), hence they should include the month used to excavate the FEBEX drift and two weeks more.

The output data should conform with the document "General Specifications". The following points are recalled: (1) the modelling report should be put in the Word97 file "XXX1A.doc"; (2) output data should be put in the ASCII file "XXX1A01.txt", where "XXX" stands for the participant's code; (3) data should be arranged in a way similar to that shown in Figure 8-1; and (4) the points provided should be enough to properly define the evolution curve.

```
FILENAME    : XXX1A01.txt
PARTICIPANT: Participant's identification
DATE        : DD.MM.YY


t (day)         Q (ml/min)

100.000         0.0000E+00

t (day)         P3(MPa)         P4(MPa)

0.0000E+00      0.0000E+00      0.000E+00
0.0000E+00      0.0000E+00      0.000E+00
...             ...             ...
```

Figure 8-1: Example of output file "XXX1A01.txt".

9 References

- Amiguet J.-L. (1985) Grimsel Test Site. Felskennwerte von intaktem Granit. Zusammenstellung felsmechanischer Laborresultate diverser granitischer Gesteine. NAGRA, NIB 85-08, Sep. 1985.

- Bräuer V., Kilger B., and Pahl A. (1989) Grimsel Test Site. Engineering geological investigations for the interpretation of rock stress measurements and fracture flow tests. NAGRA, NTB 88-37E, Apr. 1989.

- Falk L., Magnusson K.-Å., Olsson O., Ammann M., Keusen H.R. and Sattel (1988) Grimsel Test Site. Analysis of radar measurements performed at the Grimsel Rock Laboratory in October 1985. NAGRA, NTB 87-13, Feb. 1988.

- Fierz T. (1996) FEBEX Instrumentation of BOUS 85.001 and 85.002, FBX 95.001 and 95.002 radial boreholes. Solexperts AG, 1008, Jul. 1996.

- Finsterle S. and Pruess K. (1995) Solving the estimation-identification problem in two-phase flow modelling. Water Resour. Res., 31(4), 913-924, 1995.

- Guimerà J., Ortuño F., Vázquez E., Ruiz B., Martínez L., Carrera J. and Meier P. (1996). Pulse tests at "in drift" boreholes. Performance and evaluation. UPC, 70-UPC-L-0-1001, Sep. 1996.

- Guimerà J., Carrera J., Martínez L., Vázquez E., Ortuño F., Fierz T., Bülher C., Vives L., Meier P., Medina A., Saaltink M., Ruiz B. and Pardillo J. (1998). FEBEX Hydrological characterization and modelling. UPC, 70-UPC-M-0-1001, Jan. 1998.

- Häring M.O. (1996) GTS/FEBEX: Supervision and interpretation of geophysical investigations Boreholes FBX95.001 and FBX95.002. NAGRA, NIB 96-14.

- Keusen H.R., Ganguin J., Schuler P. and Buletti M. (1989) Grimsel Test Site. Geology. NAGRA, NTB 87-14E, Feb. 1989.

- Meier P., Fernández P., Carrera J. and Guimerà J. (1995) FEBEX - PHASE 1. Results of hydraulic testing in boreholes FBX 95.001, FBX 95.002, BOUS 85.001 and BOUS 85.002. UPC, Dec. 1995.

- Pahl A., Heusermann St., Bräuer V. and Glöggler W. (1989) Grimsel Test Site. Rock stress investigations. NAGRA, NTB 88-39E, Apr. 1989.

- Pardillo J. and Campos R. (1996). FEBEX - Grimsel Test Site (Switzerland) Considerations respect to the fracture distribution. CIEMAT, 70-IMA-L-2-05, Mar. 1996.

- Pardillo J., Campos R. and Gimerà J. (1997) Caracterización geológica de la zona de ensayo FEBEX (Grimsel - Suiza). CIEMAT, 70-IMA-M-2-01, May 1997.

- Pintado X. and Lloret A. (1997) THM laboratory tests in FEBEX Phase 3. UPC, 70-UPC-L-3-01, Dec. 1997.

- Schneebeli M., Flühler H., Gimmi T., Wydler H. and Läser H.-P. (1995) Measurements of water potential and water content in unsaturated crystalline rock. Water Resour. Res., 31(8), 1837-1843, 1995.

- Voborny O., Adank P., Hürlimann W., Vomvoris S. and Mishra S. (1991) Grimsel Test Site. Modelling of groundwater flow in the rock body surrounding the underground laboratory. NAGRA, NTB 91-03, Oct. 1991.

10 Acknowledgements

The assistance of Dr. Jordi Guimerà during the preparation of this document is gratefully acknowledged. Based on his experience in the hydrogeological characterization and modelling of the FEBEX in-situ test, his suggestions and comments have been an important contribution to this document.

別添 - 5

DECOVALEX TASK1

PART B ; TASK DEFINITIONS

DECOVALEX III, Task 1: Modelling of FEBEX in-situ test

PART B: THERMO-HYDRO-MECHANICAL ANALYSIS OF THE BENTONITE BEHAVIOUR

(Rev. 2)

Table of contents

1 Introduction to Task 1: Modelling of FEBEX in-situ test

The international FEBEX (Full-scale Engineered Barriers Experiment in Crystalline Host Rock) project is a project that is co-financed by ENRESA the European Commission. It is co-ordinated by ENRESA and it is planned to last from 1994 to 2003. The purpose of the project is the study of the various processes occurring in the near field of a high activity radioactive waste storage. Specifically, three objectives were defined: (1) demonstration of the feasibility of the construction of engineered barriers, (2) study of the thermo-hydro-mechanical (THM) processes in the near field and (3) study of the thermo-hydro-geochemical (THG) processes in the near field. The FEBEX project has three main components, namely: (1) an "in situ" test in natural conditions and at real scale, (2) a mock-up test at near-to-real scale and (3) a series of laboratory tests to complement the information of the two large scale tests.

For the present modelling exercise, the FEBEX "in situ" test has been chosen. This test is installed at the Grimsel Test Site, an underground laboratory in Switzerland operated by NAGRA. The experiment is based on the Spanish reference concept of deep geological storage in crystalline host rock. In this concept, steel canisters containing the conditioned waste are placed along the axis of horizontal galleries drilled in a rock formation and an engineered barrier is placed in the annular space left between them. The engineered barrier is made of high density compacted bentonite blocks that will swell due to water input from the host rock, providing thus a very impervious sealing. In the FEBEX "in situ" test, waste canisters are replaced by two cylindrical heaters.

Due to the detailed geological and hydrogeological characterization of the Grimsel Test Site, the comprehensive characterization of the bentonite used to fabricate the engineered barrier and the monitoring performed during the drilling of the FEBEX tunnel as well as during the test, the FEBEX "in situ" test is well suited to be the object of a modelling exercise. In the context of the DECOVALEX III project, the modelling exercise will be divided into three parts, namely:

- Part A: Hydro-mechanical modelling of the rock.

Based on the available geological, hydraulic and mechanical characterizations of the Grimsel Test Site as well as on results of hydraulic tests performed on boreholes, a hydro-mechanical model for the zone around the FEBEX tunnel will be prepared. Using this model, changes in water pressure induced by the boring of the FEBEX tunnel as well as the total water flow rate to the excavated tunnel will be required.

- Part B: Thermo-hydro-mechanical analysis of the bentonite behaviour.

Based on the characterization of the bentonite and on the details of the process of test installation, a thermo-hydro-mechanical model for the bentonite barrier and the heaters will be prepared. Using this model, the thermo-hydro-mechanical response of the bentonite barrier as a result of the heat released by the heaters will be required. Besides local field variables such as temperature, relative humidity, pore water pressure, stresses and displacements, and global variables such as total input power to the heaters will also be required.

- Part C: Thermo-hydro-mechanical analysis of the rock.

Based on the characterization of the rock massif and on the details of the process of test installation and performance, the rock response in the immediate vicinity of the buffer will be required. The rock is now subjected to the heat released by heaters and by swelling pressures resulting from bentonite hydration. The initial hydrological regime (Part A) is also modified by the presence of the impervious barrier. Temperature, stresses, water pressures and displacements in selected points of the rock will be required.

2 Part B: Thermo-hydro-mechanical analysis of the bentonite behaviour.

The FEBEX in-situ test simulates in natural conditions and at real scale the disposal of two canisters containing radioactive waste and surrounded by bentonite blocks in a horizontal gallery, according to the Spanish reference concept of Deep Geological Disposal in Granite. An important component of this test is the set of sensors placed in the bentonite barrier and in radial borings in the host rock. This part focuses on the THM analysis of the aforementioned bentonite barrier.

The purpose of this document is to describe the FEBEX in-situ test and to provide the properties of the bentonite used to construct the barrier. Section 3 describes the main components of the FEBEX in-situ test (bentonite barrier, heating system and instrumentation), their installation and the test operation. Section 4 summarizes the mechanical, hydraulic and thermal properties of the FEBEX bentonite. They have been derived from specific tests as well as from backanalysis of suitably instrumented tests. Section 5 defines the results required for the present modelling exercise. Finally, Section 6 contains the references where more information may be obtained. Most of the references are in Spanish, but the main results are summarized in the present document.

3 The FEBEX in-situ test

3.1 General description of the test and of the Grimsel Test Site

The "in situ" test consists of a full-scale simulation of a HLW disposal facility, in keeping with the ENRESA AGP Granito (Deep Geological Disposal, Granite) reference concept. Performance of this test implied the placing of two electrical heaters, of dimensions and weight equivalent to those of the canisters in the concept, in a 2.28 m diameter drift excavated in granite, the entire space surrounding the heaters being filled with blocks of compacted bentonite to complete the 17.4 m of barrier for the test section. This test zone was closed with a concrete plug. The test has been installed in the underground laboratory managed by NAGRA, located in Grimsel (Switzerland), because of the similarity between the Spanish and Swiss reference concepts. Figure 3-1 shows the general scheme of the FEBEX in situ test.

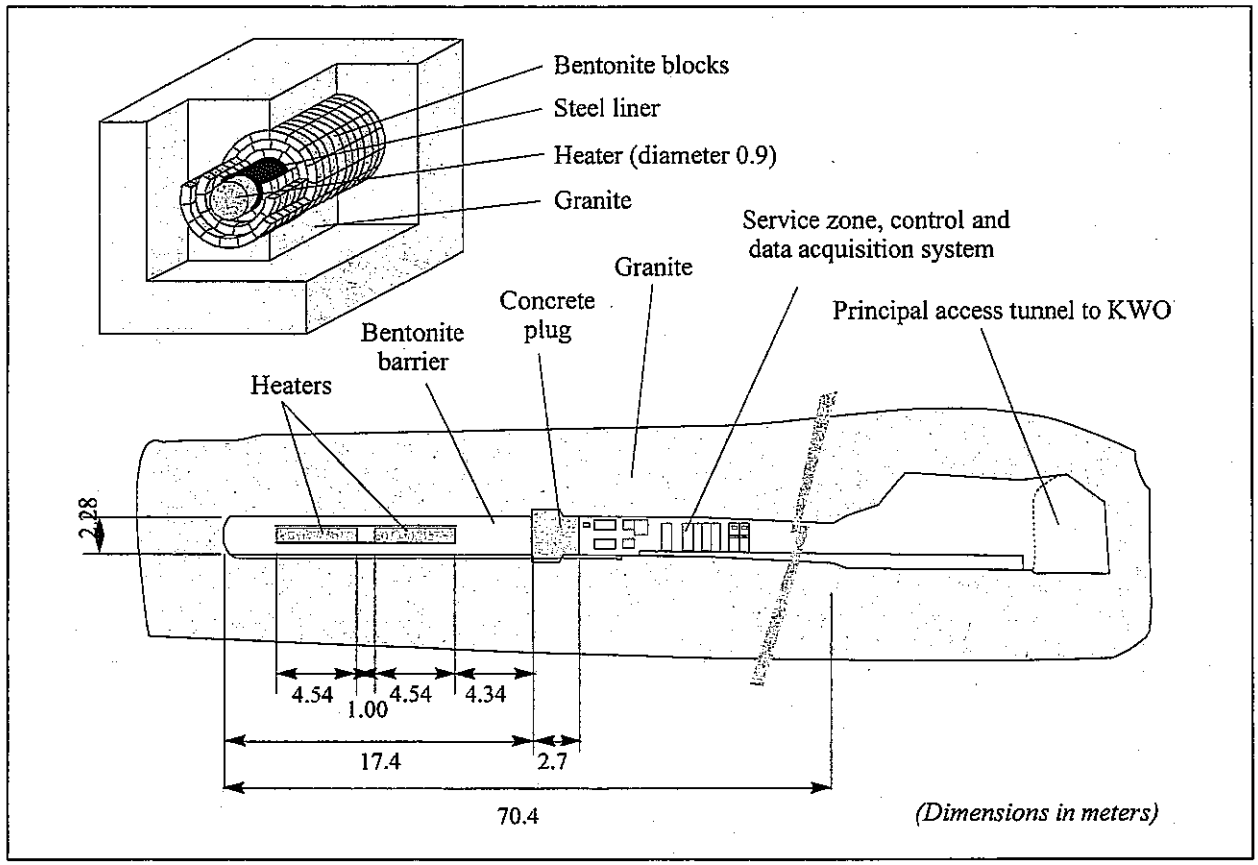

Figure 3-1 : General scheme of the FEBEX in situ test.

In addition to the clay barrier, made up of 5331 bentonite blocks with a total mass of 115.7 t, and the heaters, 632 sensors of very diverse types were installed. The sensors were installed to monitor the different thermo-hydro-mechanical processes that occur in both the clay barrier and the surrounding rock throughout the entire life of the test. In principle, a heating stage of more than three years is planned, followed by dismantling of the test for performance of the appropriate tests and analyses. A series of artificial chemical tracers, specimens of different metals, and gas collectors were installed in the test zone for the study of corrosion and transport phenomena.

A drift was specifically excavated for this test, in an area previously selected in accordance with the existing Grimsel laboratory database. To provide additional information, two exploratory boreholes were drilled in the area, practically parallel to the planned trace of the drift (see Part A of DECOVALEX III, Task 1).

Following excavation of the drift, a detailed reconnaissance of its geometry and geology was performed and 19 boreholes were drilled from its interior, to monitor the rock mass.

A detailed hydrogeological study of the rock mass surrounding the drift was performed, using data taken from the existing boreholes in the area, the two boreholes made for the study, the walls of the drift, and the 19 boreholes drilled from the interior of the drift.

The test has been designed to function in an autonomous mode. Supervision, monitoring, and control are accomplished remotely from Madrid.

The underground laboratory managed by NAGRA, known as the GTS (Grimsel Test Site), is located at an elevation of 1,725 m in the Swiss Alps, near the Grimsel Pass.

The laboratory consists of a series of excavated experimental drifts and caverns connected with the main access tunnel for two subterranean hydroelectric power plants owned by he hydro-electric company KWO. The GTS starts at 1.02 km from the portal of the main access tunnel, at a depth of some 400 m relative to the surface of the terrain. The laboratory has a general service area and is equipped with the infrastructure required for the performance of large-scale tests.

3.2 Components of the test

3.2.1 Blocks for the clay barrier

This section includes a summary of the most important aspects of the processes of designing, fabricating, quality control, packing, handling, transporting, and storing of the compacted bentonite blocks used to construct the clay barrier.

The blocks were fabricated from FEBEX bentonite, the properties of which will be described in Chapter 4. The construction of the barrier is described in Section 3.3.

Design

Figure 3-2 shows the geometry of the barrier in the heater and non-heater areas. In both areas, the three exterior crowns of the blocks are equal; in the heater area the interior crown of this group is in contact with the steel liner, while, in the non-heater area, the interior crown is in contact with a core of blocks. Five types of blocks form this barrier geometry: BB-G-01, BB-G-02, BB-G-03, BB-G-04, and BB-G-05. Figure 3-3 and Table 3-1 show the shapes and dimensions of the block types.

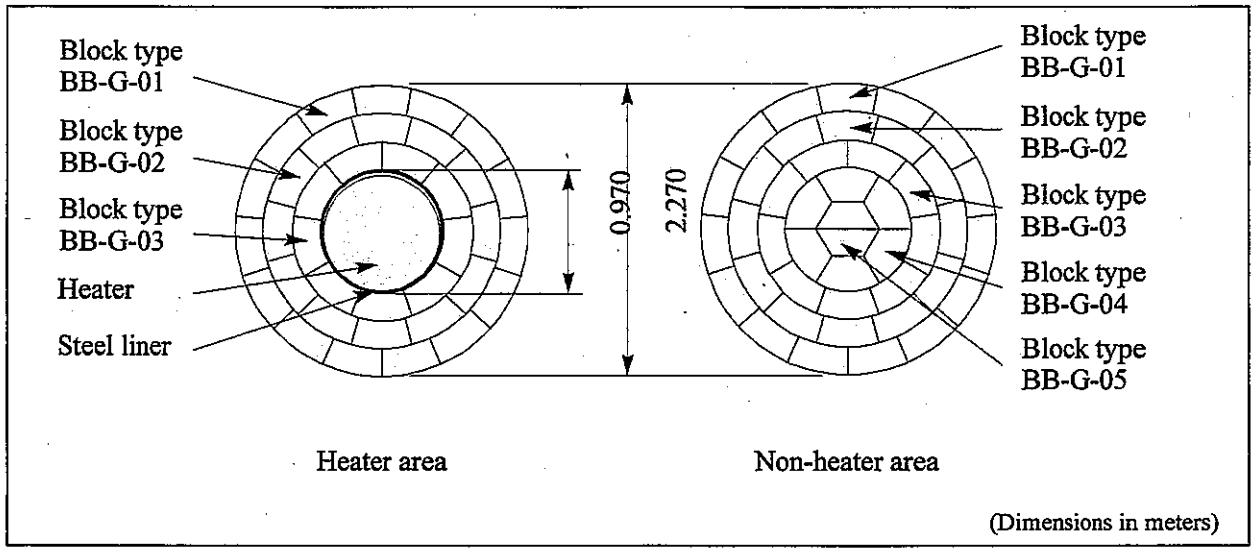

Figure 3-2 : Geometry of the clay barrrier.

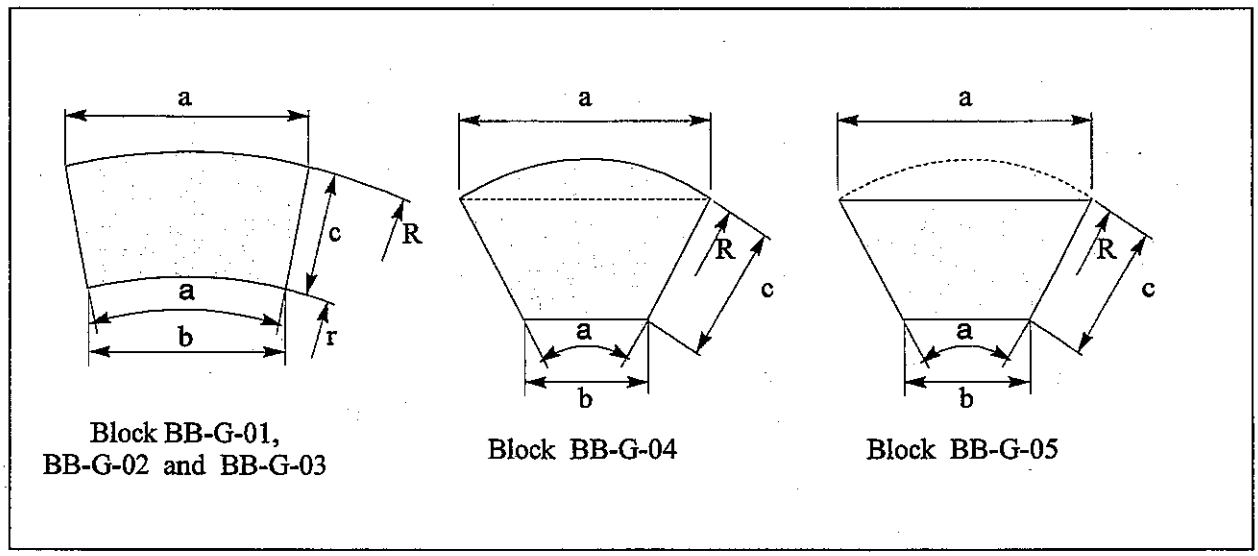

Figure 3-3 : Shapes and dimensions of the blocks.

Table 3-1 : Dimensions for block fabrication.

Type	a mm	b mm	c mm	thickness mm	R mm	r mm	α °
BB-G-01	470.0 (+2.0 –5.0)	380.0 (+2.0 –4.0)	214.0 (+2.0 –3.0)	125.0 (+2.0 –2.0)	1133	919	24
BB-G-02	473.0 (+2.0 –5.0)	361.0 (+2.0 –4.0)	214.0 (+2.0 –3.0)	125.0 (+2.0 –4.0)	917	703	30
BB-G-03	478.0 (+2.0 –5.0)	330.0 (+2.0 –4.0)	214.0 (+2.0 –3.0)	125.0 (+2.0 –4.0)	701	487	40
BB-G-04	483.0 (+2.0 –5.0)	240.0 (+2.0 –4.0)	240.0 (+2.0 –3.0)	125.0 (+2.0 –4.0)	485	—	60
BB-G-05	483.0 (+2.0 –5.0)	240.0 (+2.0 –4.0)	240.0 (+2.0 –3.0)	125.0 (+2.0 –4.0)	—	—	60

The dry density specified in the design of the blocks was 1.70 g/cm^3. This density was determined by taking into account the probable volume of the construction gaps and the need

to have a barrier with an average dry density of 1.60 g/cm^3. For a dry density of 1.60 g/cm^3, the swelling pressure is of the order of 5 MPa, which is the value proposed in the AGP Granito. The water content of the blocks is that specified for the raw bentonite, 12.5% to 15.5% (see Chapter 4).

Fabrication

For the fabrication of blocks BB-G-01, BB-G-02, BB-G-03, and BB-G-04 it was necessary to design and manufacture moulds, whereas block BB-G-05 was obtained from BB-G-04 by machining the curved face with a saw. The blocks were fabricated in the REFRACTA, S. A. plant at Quart de Poblet (Province of Valencia, Spain), by compaction in a uniaxial hydraulic press under a pressure of 40 MPa to 45 MPa. A quality assurance program was applied in fabrication of the blocks: external appearance, dimensions, water content, and dry density were controlled. Table 3-2 shows the average values for the characteristics and the number of blocks fabricated for each type.

Table 3-2 : Average values of the physical properties and number of blocks fabricated.

	BB-G-01	BB-G-02	BB-G-03	BB-G-04	BB-G-05
weight per block (kg)	22.1	21.8	21.3	23.1	18.0
average water content (%)	14.49	14.07	14.87	13.69	13.07
average dry density (g/cm^3)	1.69	1.69	1.69	1.70	1.70
number of units fabricated	2 898	2 310	1 614	562	184
total weight (kg)	64 046	50 358	34 378	12 982	3 312

Taking into account the dimensions of the blocks of each type, the average values of water content and dry density are 14.4% and 1.69 g/cm^3, respectively. A total of 7568 blocks were fabricated, with a total weight of 165 076 kg.

Packing, handling, transporting and storage

Laboratory tests and the study of some blocks placed in the tunnels of the GTS showed that the blocks deteriorate quite rapidly when exposed to an environment of high humidity. For this reason, the blocks were packed in boxes appropriately protected by sheets of plastic. Although the blocks have a high, unconfined compressive strength (of the order of 2.5 MPa), they were packed in boxes inside quilted plastic wrapping to avoid impact damage during their handling and transport.

The appropriately packed blocks were stored away from the GTS, in a warehouse with controlled temperature and humidity. During the construction of the barrier, the FEBEX drift was dried, heated, and ventilated to keep relative humidity low. Also the work was scheduled such that in the work area at the portal of the drift, where relative humidity is high, the time of exposure was compatible with the stability of the blocks.

Since no block was observed to have deteriorated as a result of the aforementioned causes, these precautions were confirmed to be effective.

3.2.2 Heating system

General characteristics

The test uses two electrical heaters inserted within a steel liner. The heaters reproduce the mechanical characteristics of the AGP Granito canister, simulating the thermal effects.

The external dimensions of the heater are identical to those of the canister anticipated in the AGP Granito concept (a cylinder measuring 4.54 m in length with a diameter of 0.90 m) and the weight is of the same order (11 t). Both the material and the shape of the exterior body of the heaters are similar to those anticipated for the canister: carbon steel plate measuring 100 mm in thickness.

As regards the thermal aspect, the aim of the test is to subject the bentonite, at the point of contact with the steel liner, to a maximum constant temperature of 100ºC, which is the maximum value anticipated in the reference concept. Nevertheless, in order to reach this value in a period of time compatible with the duration of the test, and maintain it in an isolated drift, it was necessary to increase the power of the heaters beyond the value anticipated in the AGP Granito concept for the maximum residual thermal power of the canisters, that is 1200 W. Following different analyses and modelling exercises, performed during the design phase of the experiment, the nominal power was fixed at 4,300 W per heater. This power will be the maximum required in the most unfavorable case of the clay barrier being totally saturated, with a certain margin of safety.

Mechanical characteristics

Figure 3-4 shows a general view of the final design of the heater. The exterior casing consists of a forged tube with a wall thickness of 100 mm, and two welded end covers of metal plate, each measuring 150 mm in thickness. The casing is of carbon steel without any treatment or covering, except shot-peening of the exterior surface.

Inside the casing, the heating elements (resistances) are wound around a tube or reel measuring 660.4 mm in diameter and 12.7 mm in thickness. The assembly - reel and resistances - is covered with a copper sheet measuring 3 mm in thickness. This covering serves to distribute the temperatures more uniformly along the heater and to provide mechanical protection for the heating elements during heater assembly.

The thickness and shape of the end covers are based simply on convenience during assembly of the interior elements of the heater and do not correspond to the reference concept. The front end cover has a total of 24 perforations to allow for the exit of cables (6 for the heating elements and 18 for the control thermocouples) and is fitted with a cylindrical, screw-on box on the exterior for mechanical protection of the cable exits. On its outer face there are two key notches located at 36°, to allow for coupling with the pushing mechanism of the insertion system. The other end cover is solid, and its outer edge is chamfered to facilitate insertion into the liner.

The exterior casing is hermetically sealed. The cable exits were sealed with Viton gaskets and filled with epoxy resin, as shown in Figure 3-5.

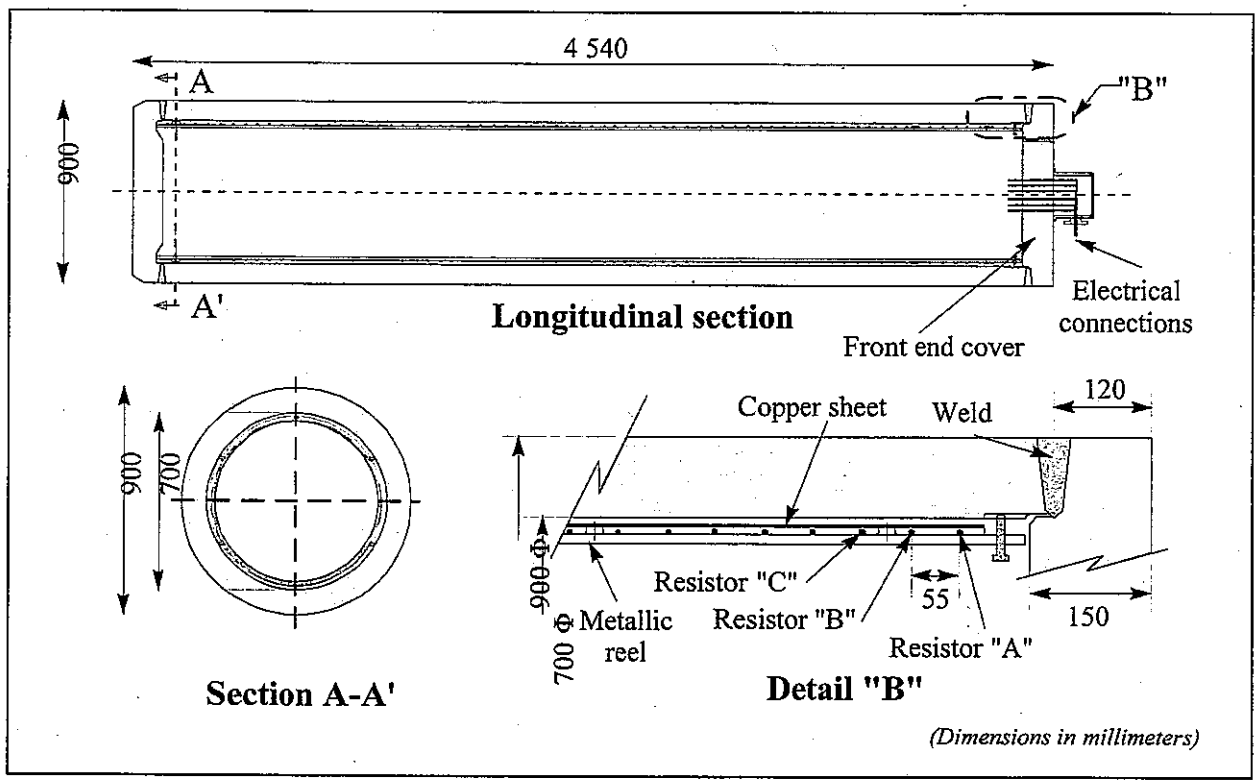

Figure 3-4 : Dimensions and construction details of the heaters.

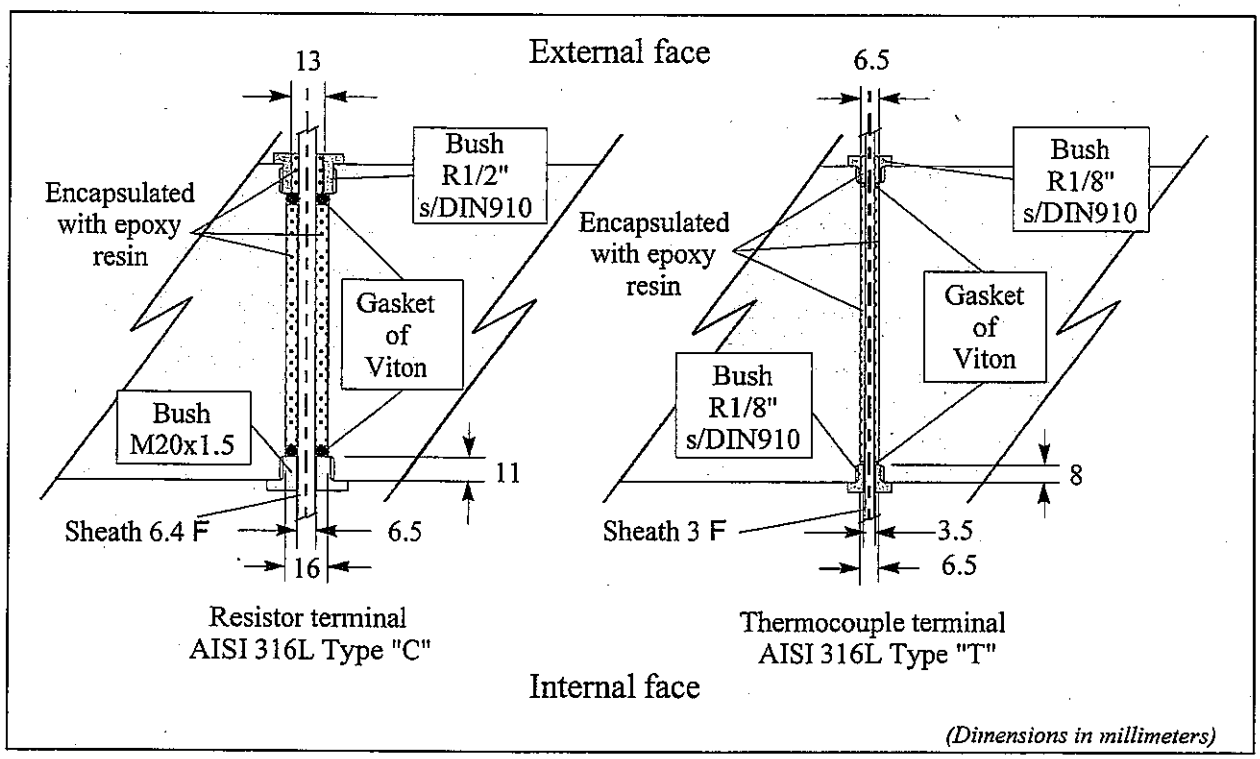

Figure 3-5 : Cable run sealing system.

Electrical characteristics

In order to increase reliability, the system is redundant. Each heater has three independent heating elements, each of which is capable of supplying individually the nominal required power of 4300 W. The elements are of the shielded resistor type and their main characteristics are summarized in Table 3-3.

Table 3-3 : Characteristics of the heating elements.

active conductor	material of the conductor core	Ni-Cr 80/20
	length	52±3% m
	supply voltage	400 V AC
	nominal power	4300±10% W
	insulation	MgO
	sheath material	Inconel 600
	external diameter	4.6 mm
cold terminals	conductor section	6 mm^2
	sheath material	AISI 304 L
	external diameter	6.4 mm

Each heating element is helicoidally wound on the internal reel of the heater, with a total of 25 windings per element and a separation between coils of the same element of 165 mm.

Since temperature is key to the expected life of the elements, 18 thermocouples were installed on the internal reel of the heater to measure the surface temperature of the heating element.

For reliability reasons, all types of electrical connections were avoided in the interior of the heater. The cold terminals of the heating elements are sufficiently long to exit the body of the heater, pass through the concrete plug, and reach the service zone without any electrical connection being made. These terminals, together with the shielded cables of the thermocouples, were placed in a continuous, seamless tube of corrugated Teflon, which extends from the front end cover to the service zone. This tube protects the set of cables against mechanical and corrosive action; it has sufficient flexibility to allow for a certain magnitude of heater movement produced by differential settlement or swelling of the bentonite.

Steel liner

The "in situ" test faithfully reproduces the AGP Granito reference concept, which considers the existence of a continuous steel liner, common to all the canisters emplaced in the same drift. This steel liner consists of a perforated steel tube measuring 15 mm in thickness, providing the space into which the canister is inserted. Given that in the actual design of the AGP Granito concept no consideration is given to the retrievability of the canisters, the function of the steel liner terminates when the canister is introduced; therefore, the deformation of the liner due to swelling of the bentonite is not important.

The steel liner required for the test has a length of 10 m, corresponding to the length of the two heaters plus the 1-m separation between them. Thus, 11 segments of 1 m each were made, designed to be coupled by means of a male/female conical coupling measuring 100 mm in length, machined in the ends of each segment Figure 3-6. The material of the steel liner is conventional alloyed steel for boilers and pressure vessels.

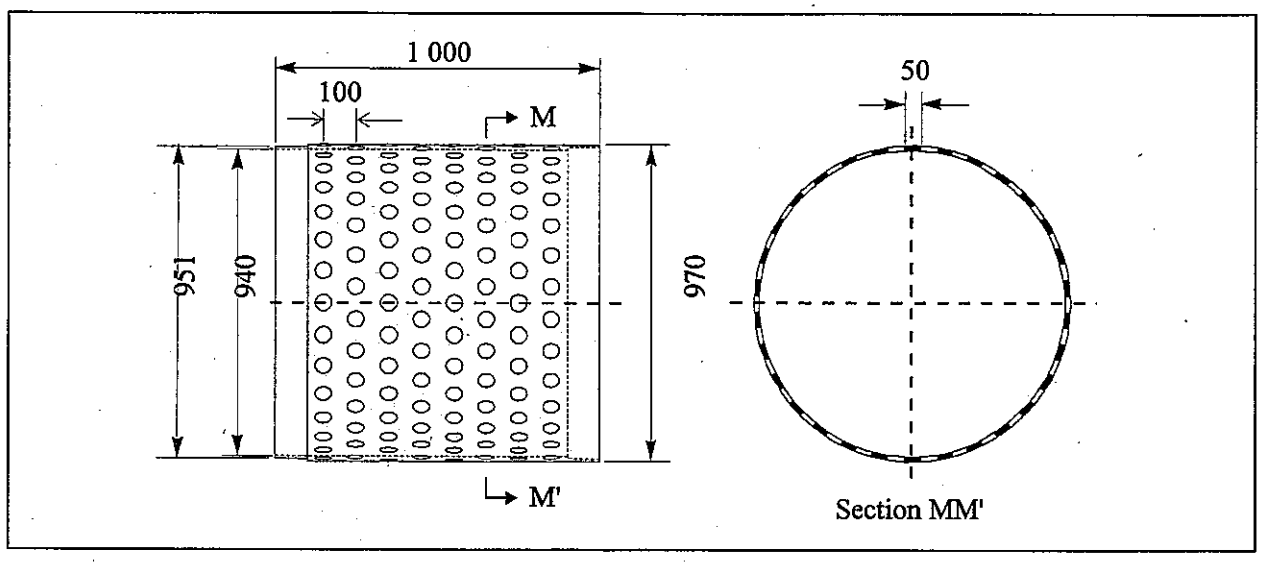

Figure 3-6 : Steel liner.

The inner diameter of the liner is 940 mm; thus there is a gap of 40 mm with respect to the outer diameter of the heaters, a value that was considered sufficient for correct insertion of the heaters, taking into account the normal errors of alignment in an installation operation of this type.

3.2.3 Instrumentation

A total of 632 sensors were installed. Table 3-4 indicates the variables measured, the types of sensors used and the locations of the sensors, by areas.

The sensors in the clay barrier were grouped in a series of cross-sections, as indicated in Figure 3-7: sections A, B1, B2, C, D1, D2, E1, E2, F1, F2, G, H, I, K, L, M1, M2 and N. The sections with an identical letter have similar sensor configurations.

The boreholes BOUS-1, BOUS-2, FBX-1, and FBX-2 were used, along with the 19 boreholes drilled from the interior of the drift, for instrumentation the rock, in particular for hydrogeological and mechanical variations (see Part A of DECOVALEX III, Task 1). Other sensors, such as psychrometers and TDR probes were installed in smaller boreholes, drilled from the drift in areas closer to the wall (up to 2.5 m).

Two examples of the location of sensors in the clay barrier and in the surrounding rock are shown in Figure 3-8 and Figure 3-9, respectively. Each sensor is identified by a code of the type:

AA-BBn-CC

where AA is the code of sensor type (see Table 3-5), BB is the designation of location type (borehole, instrumented section, etc.), n is the order number of section or borehole (where applicable) and CC is the order number within the corresponding section or borehole.

The final location of all the sensors is identified by their coordinates, in the local reference system XYZ indicated in Figure 3-9.

Table 3-4 : Installed sensors (G: granite; B: bentonite; C: heater; S: service zone).

variable (or instrument)	type of sensor	area				total
		G	B	C	S	
Temperature	Thermocouple	62	91	36		189
Total pressure in borehole in rock (3-D)	Vibrating wire	4				4
Total pressure on rock surface	Vibrating wire	30				30
Total pressure on heater	Vibrating wire		6			6
Hydraulic pressure in borehole in rock	Piezoresistive	62				62
Packer pressure in borehole	Piezoresistive	62				62
Pore pressure in bentonite	Vibrating wire		52			52
Water content	Capacitive		58		1	59
Water content	Psychrometer	28	48			76
Water content	TDR	4	20			24
Extensometer in rock	Vibrating wire	2x3				6
Heater displacement	Vibrating wire		9			9
Expansion of bentonite block	Vibrating wire		8			8
Displacement within the bentonite barrier	Potentiometer		2x3			6
Clinometer	LVDT		6x2			12
Crack meter	LVDT	1x3				3
Gas pressure in the bentonite barrier	Magnetic		4			4
Gas flow	Manual measure		6			6
Atmospheric pressure	Piezoresistive				1	1
Velocity of ventilation air	Hot wire				1	1
Resistor intensity	Electric converter				6	6
Resistor voltage	Electric converter				6	6
TOTALS		**261**	**320**	**36**	**15**	**632**

Table 3-5 : Identification of sensor codes.

code	sensor
T	Temperature
P	Total pressure
Q	Pore pressure
SH	Heater displacement
SB	Bentonite block displacement
S	Displacement (general)
3S	Crack meter
PP	Hydraulic pressure of packer in borehole
IT	Clinometer
GP	Gas pressure
GF	Gas flow
WC	Water content (capacitive type)
WP	Water content (psychrometer type)
WT	Water content (TDR type)
AP	Atmospheric pressure (in service zone)
A	Anemometer
V	Voltage meter
C	Electric current meter
Ω	Insulation meter

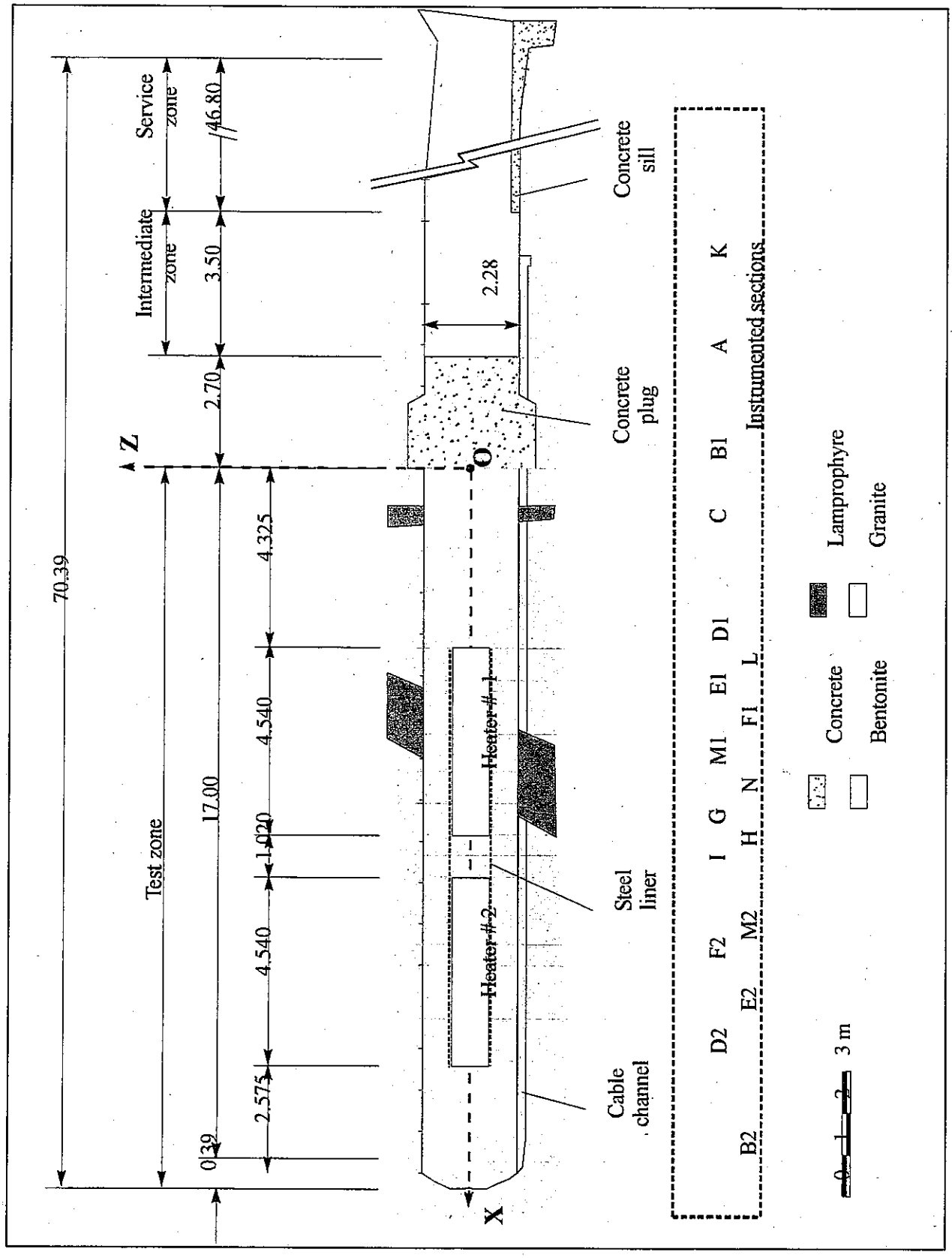

Figure 3-7 : Arrangement of the instrumented sections.

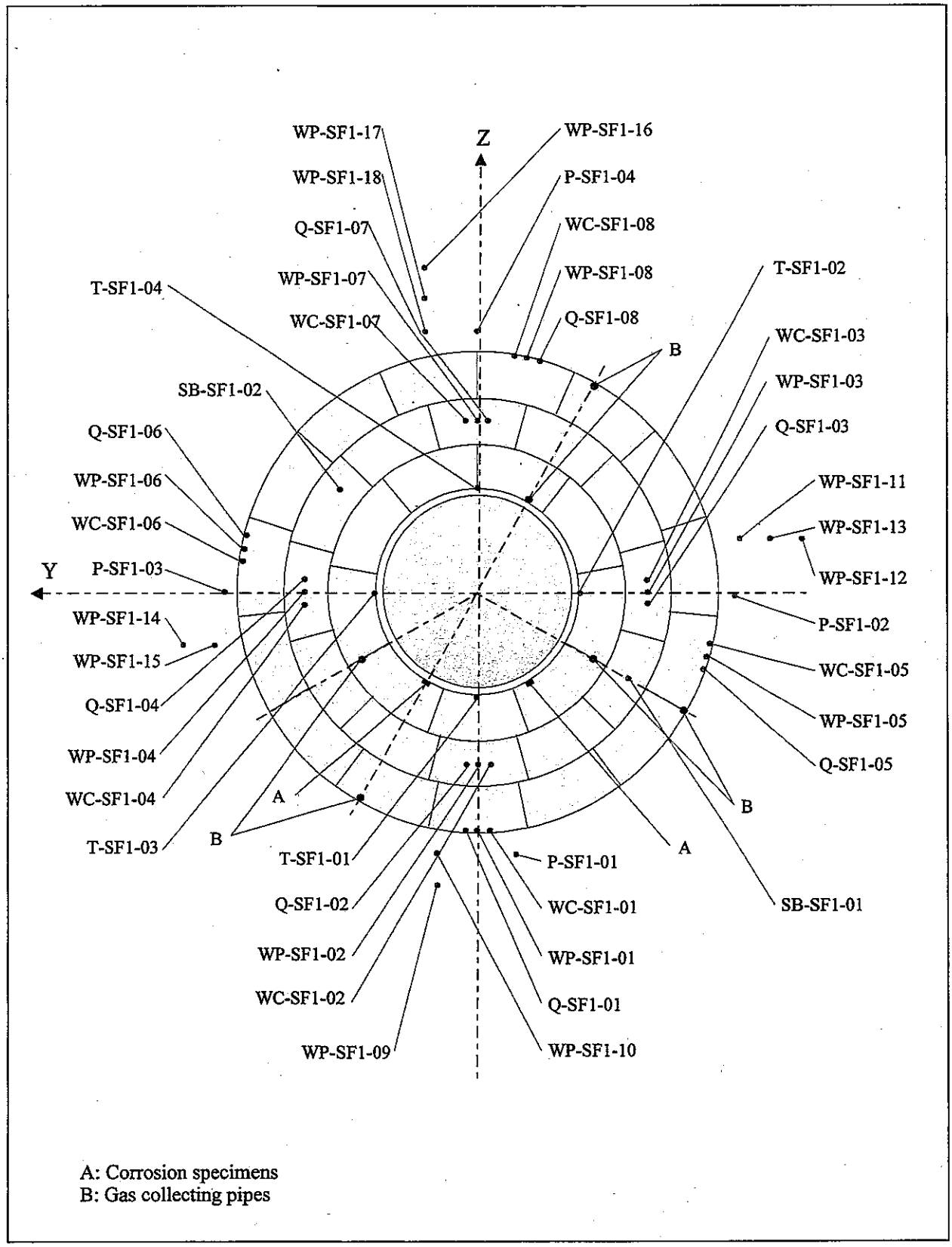

Figure 3-8 : Final location of sensors in instrumented cross-section F1.

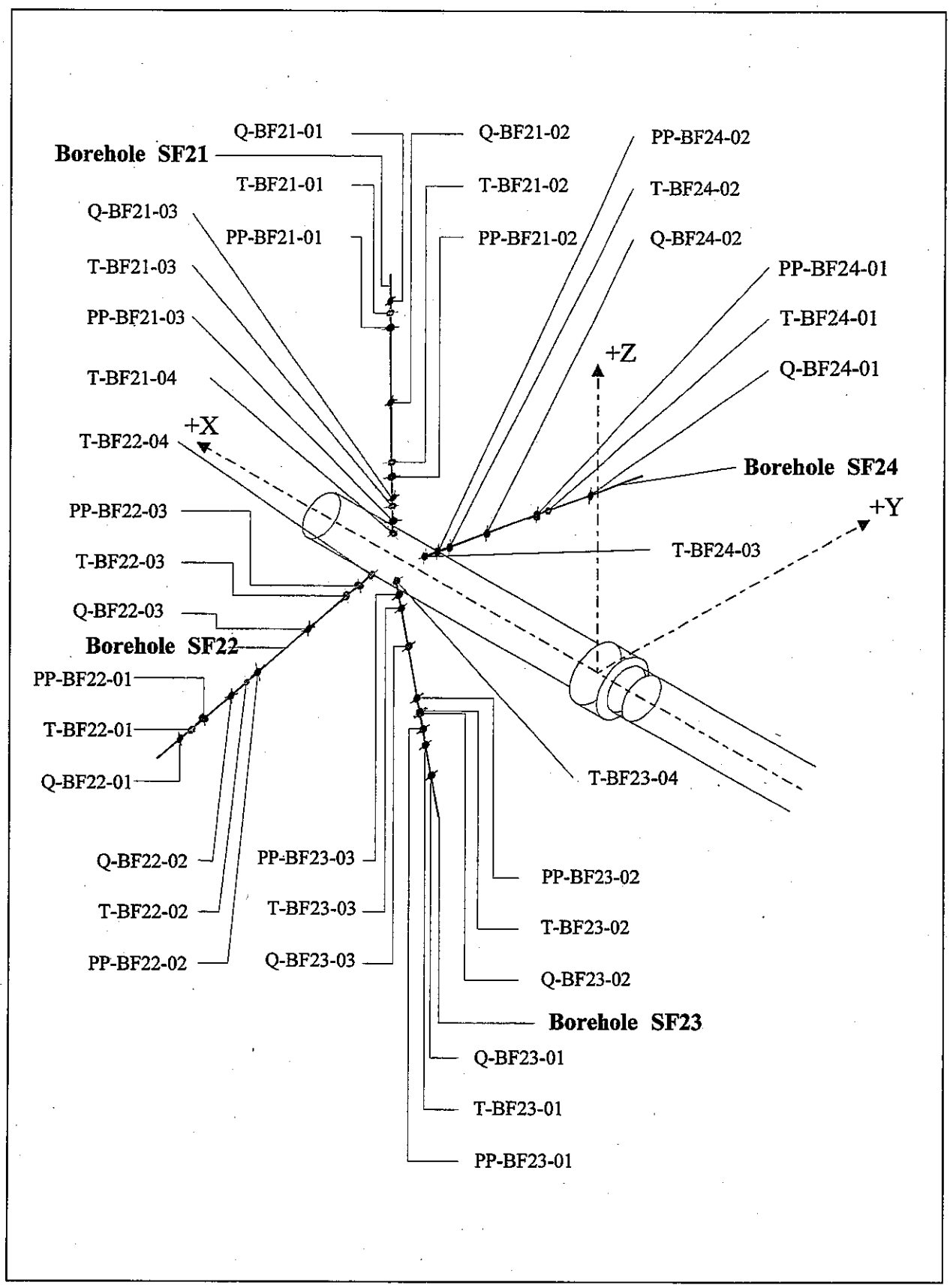

Figure 3-9 : Location of sensors in boreholes SF21, SF22, SF23 and SF24.

3.3 Installation of the clay barrier and the concrete plug

3.3.1 Clay barrier construction

Preliminary tests

Due to the lack of previous experience in an installation of this type, especially in placing the engineered barriers in a horizontal position, a test installation was set up in a simulated drift of concrete (see Figure 3-10) at the AITEMIN facilities in Toledo (Spain). This test was very useful, and served to detect certain important aspects associated with the installation. In particular, these aspects were the stability of the bentonite slices and the accumulative effects of the gap between the blocks themselves and the blocks and the drift.

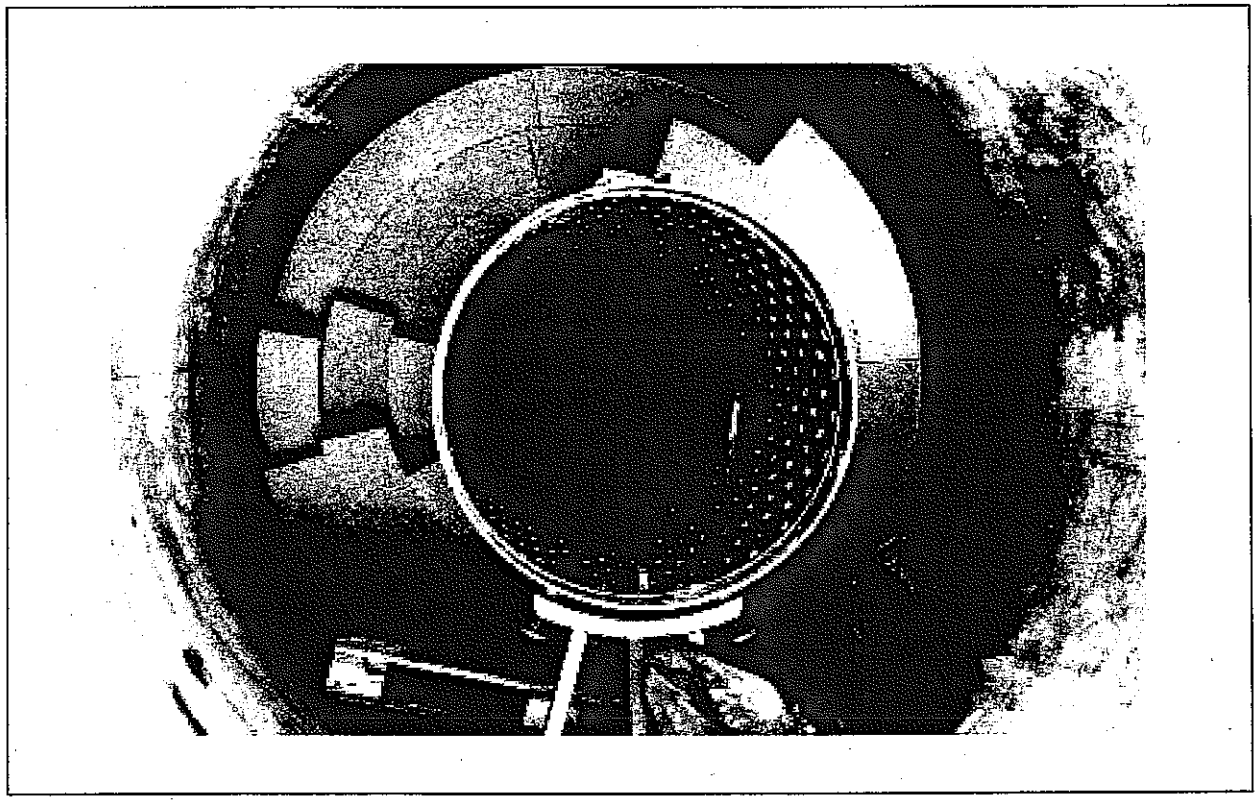

Figure 3-10 : Toledo test installation.

The effects of mechanical degradation of the bentonite blocks due to the humidity of the environment and/or a film of water at the rock surface were studied by laboratory tests and in a tunnel at the GTS. As a result of these experiences, the decision was taken to protect the packages of blocks against humidity; to dry the working area within the drift to the extent possible and to minimize the time the blocks were exposed to the GTS environment, where the relative humidity is practically 100%.

Installation procedure

The barrier was constructed manually, in accordance with the scheduled procedure. The sequence of installation is shown on Figure 3-11. First the steel liner was placed on a provisional support; second, the alignment with the axis of the drift was checked and adjusted; and finally the barrier was constructed around the steel liner, in complete vertical slices, until the space for the heater was enclosed.

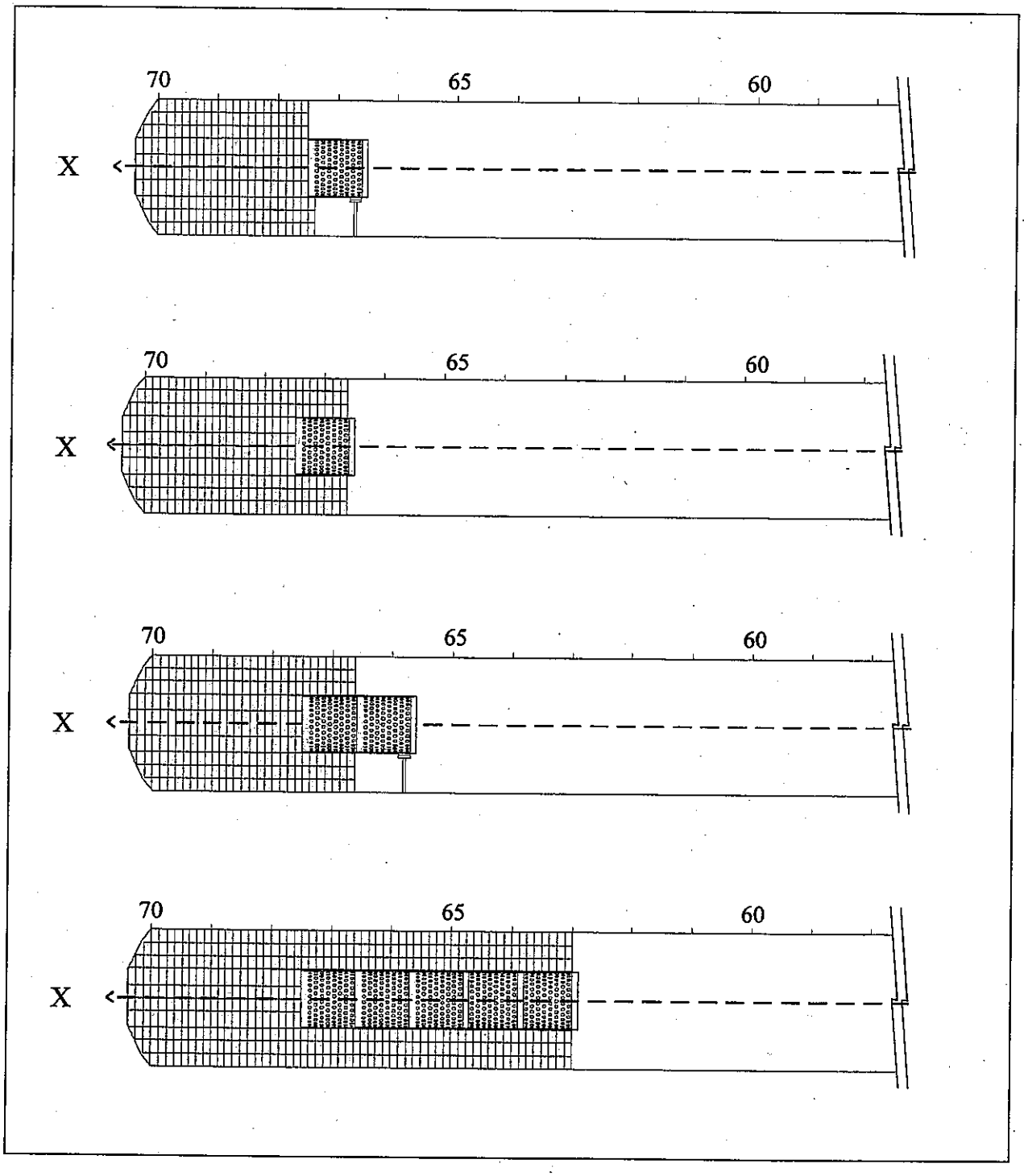

Figure 3-11 : Sequence of clay barrier construction.

The correct alignment of all the segments of the steel liner, with respect to one another and to the drift, is critical in order to avoid difficulties in inserting the heaters. Initially, once aligned, some points were welded in the joint between the liner segments, to ensure and maintain their correct position until the heater was inserted. Later it was decided that it was easier to ensure this alignment by introducing the steel liner into the drift already joined; as a result, up to three joined segments were installed. Figure 3-12 shows the space for the heater, after being enclosed by the construction of the barrier around the steel liner.

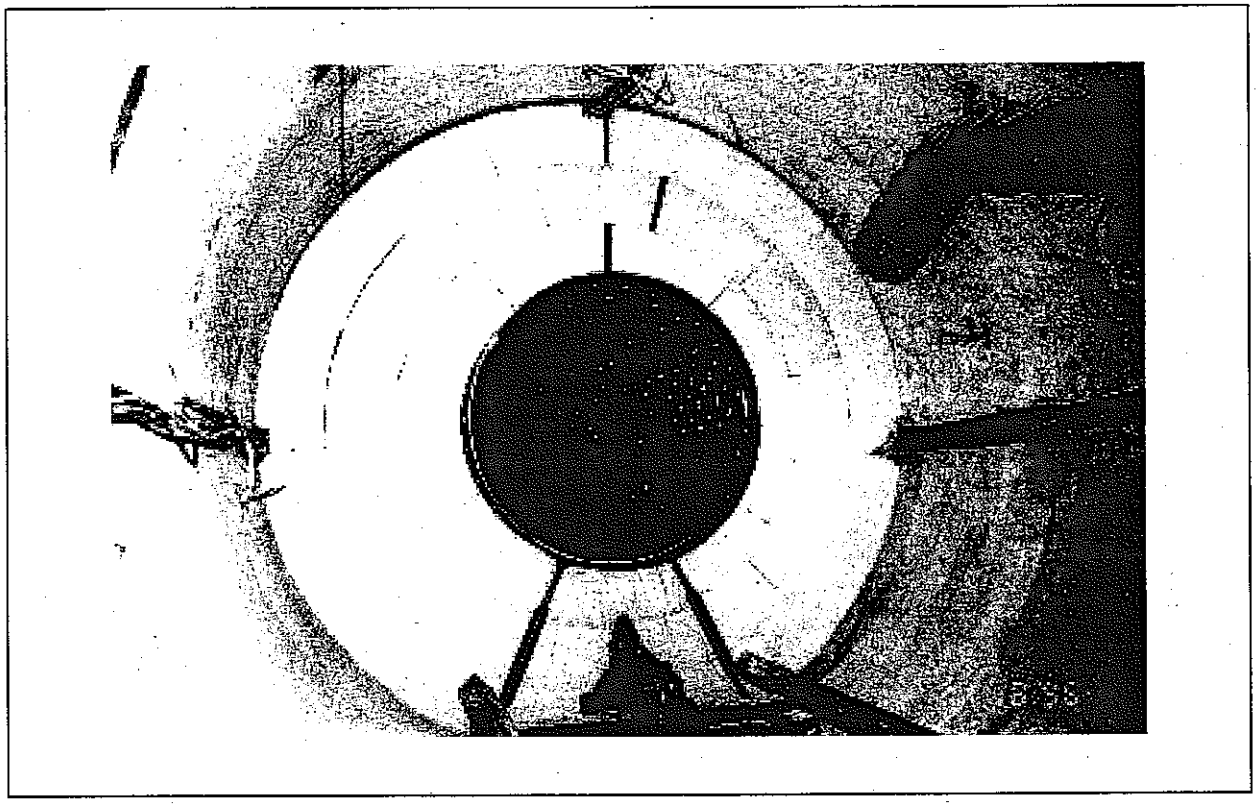

Figure 3-12 : Enclosed space for the heater, after construction of the clay barrier.

In some cases, and especially for the first slices of the installation, it was necessary to wedge the top blocks against the rock to ensure the stability of the slices. The wedges used were of Grimsel granite.

On the other hand, all the gaps existing between the blocks, both by design and as a result of manufacturing tolerances, accumulate at the top part of each slice, resulting in a total gap of approximately 2 to 3 cm. Figure 3-13 represents a typical cross-section of the drift. It maybe seen that, for these reasons, the axis of the steel liner is off-center, displaced some 15 mm. Consequently, the heater is off-center by some 35 mm, the exact deviation depending on the actual diameter of the drift at each point.

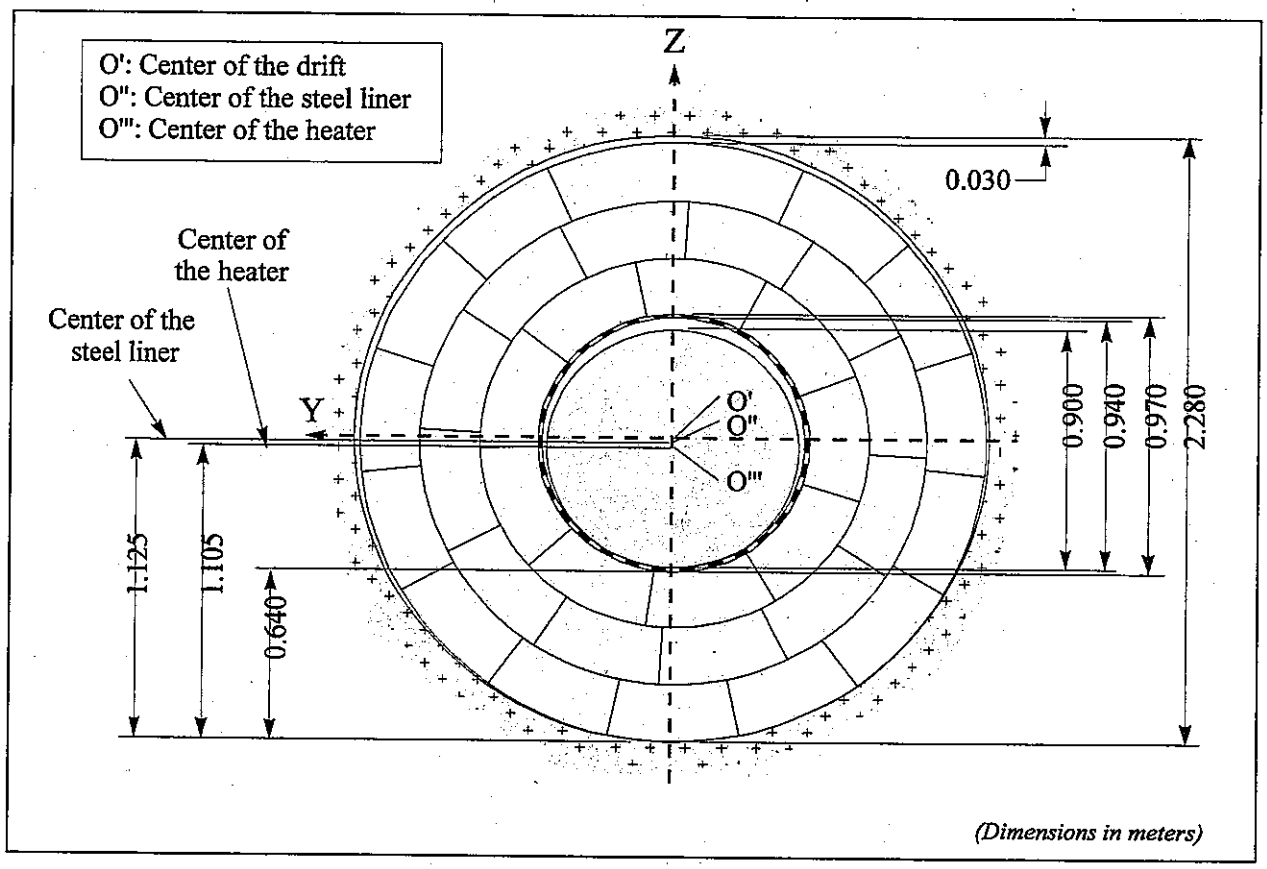

Figure 3-13 : Typical cross section of the clay barrier.

Sensor installation and cabling

The sensors in granite were emplaced before the clay barrier was installed, whereas the sensors in bentonite were installed in mechanically made holes at their pre-assigned positions within the blocks on completion of each slice.

The cables were carried radially from each sensor to the rock surface in a machined groove or channel in the bentonite. All the cables, including those from the sensors in the granite, were grouped into four bundles. The bundles were carried along the rock face at the crown, the invert, and both springlines of the drift. To carry each bundle along the rock face and through the bentonite blocks, a channel equal to the size of the bundle was made in each slice (Figure 3-14). At the crown and the two springlines, the bundles were fastened to the granite with spikes and loops. In the invert, a channel previously made along the entire length of the test zone was used to carry the heater power cables (which are quite rigid and fragile); this arrangement also avoids high initial compression on the cables from the weight of the bentonite barrier. Once all the cables were placed in the invert channel, it was filled with bentonite powder (Figure 3-15).

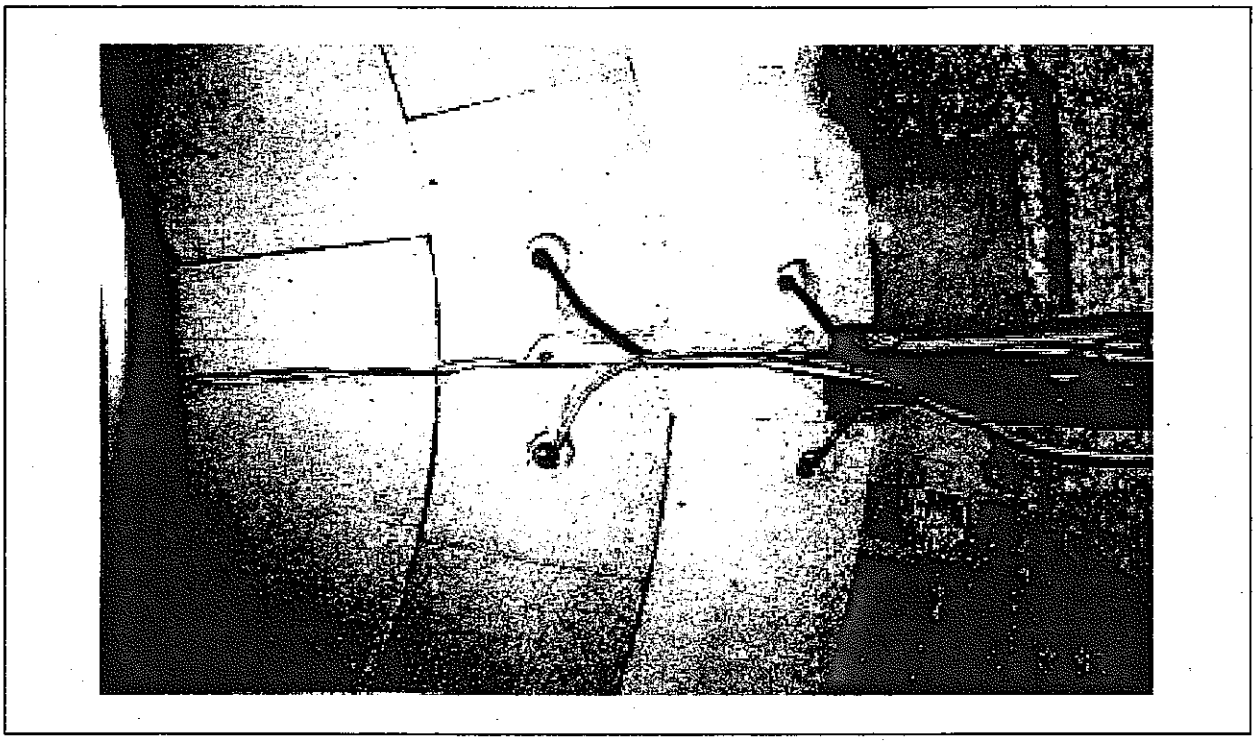

Figure 3-14 : Sensor installation and cabling.

Figure 3-15 : Cable channel in the invert of the drift.

3.3.2 Concrete plug

The test zone was closed with a concrete plug, the geometry of which is shown in Figure 3-16. The plug was designed to resist the swelling pressure of the bentonite. No specification was included for the water tightness or gas tightness of the concrete plug.

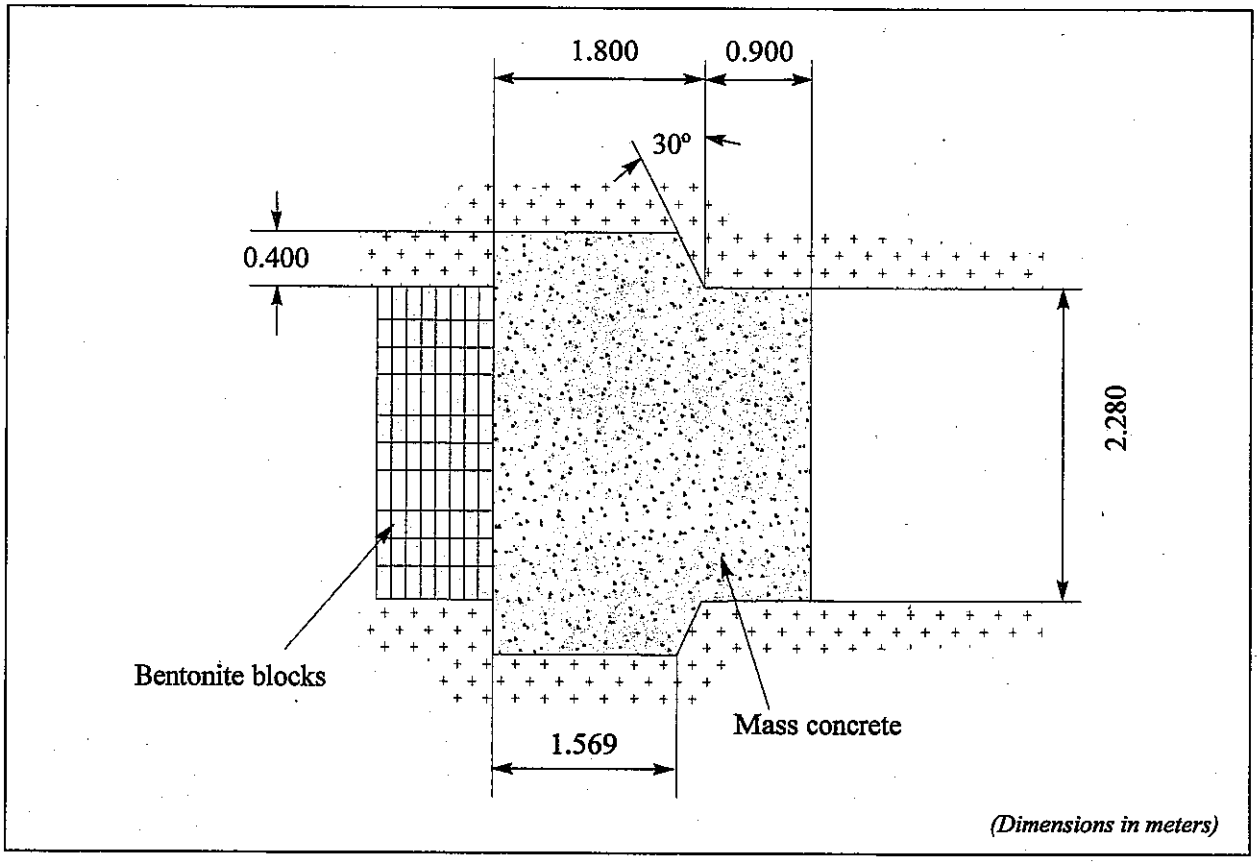

Figure 3-16 : Longitudinal section of the concrete plug.

The plug was constructed with mass concrete, without any reinforcement, to facilitate the planned future dismantling. It was designed to withstand a total force of 2000 t, which corresponds to a swelling pressure of the bentonite of 5 MPa. The concrete used had a low value of hydration heat and minimum shrinkage. Table 3-6 shows the proportions used for the concrete mix.

Table 3-6 : Concrete mix proportions used in plug construction.

component	type	proportions kg/m^3
cement	PCO "Sulfacem" (CEM I 32.5 HS)	160
silica fume	Sikafume HR	60
fine aggregate	Grimsel granite, 4 to 8 mm	660
coarse aggregate	Grimsel granite, 8 to 16 mm	430
sand	Quartz 0.1 to 5.6 mm	800
filler	limestone	170
water	city network	155
superplasticizer	Sikament-12+	13

The plug was concreted in three sections perpendicular to the axis of the drift, such that the filling of the upper part could be checked, at least for a part of the plug. The concrete was pumped from outside the drift and was compacted by vibration. This method did not allow for good concreting of the key, where a void remained, this subsequently being filled by means of injection. Table 3-7 shows the results obtained from the concrete control tests.

Table 3-7 : Results of concrete control tests.

water/cement ratio	0.99
water/total hydraulic materials ratio	0.72
slump (Abrams cone) (mm)	44
density (before setting) (kg/m^3)	2394
air content (%)	0.4
28-day strength (MPa)	47.1

The four bundles of cables pass through the concrete plug inside 200 mm-diameter plastic pipes (Figure 3-17). The pipes were later filled with fine mortar.

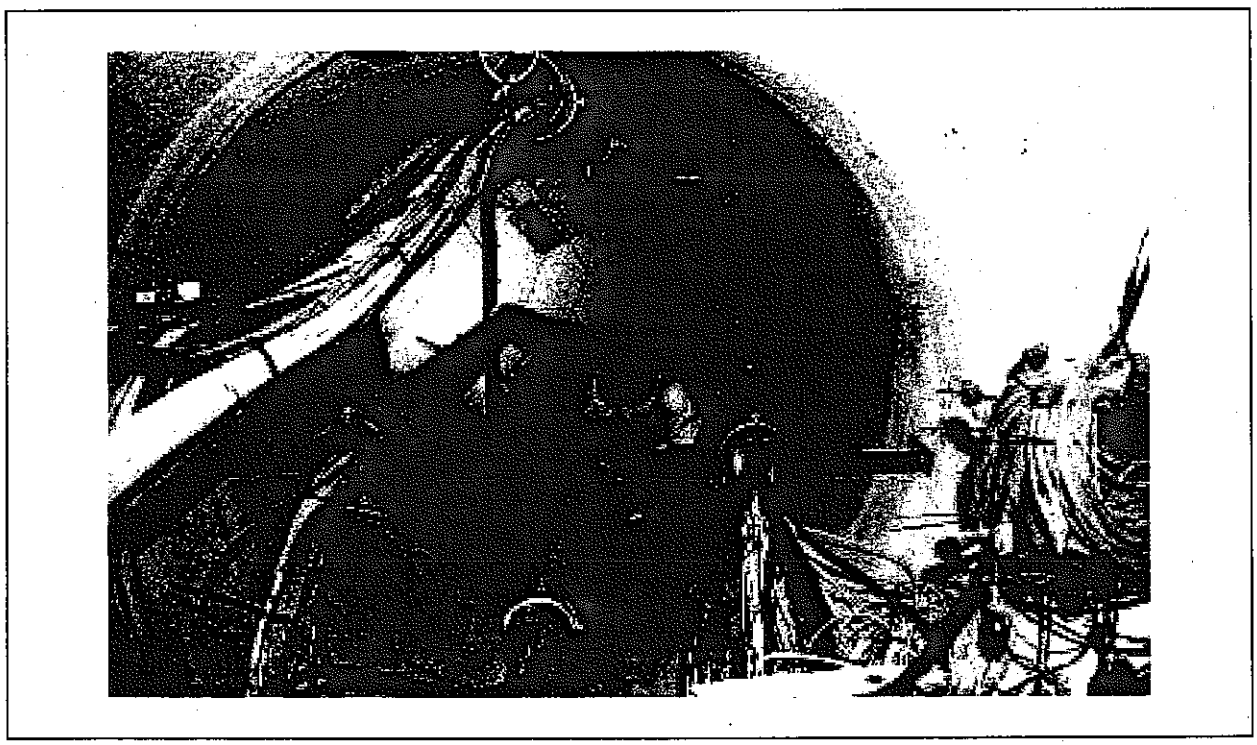

Figure 3-17 : Pipes for concrete plug cable penetrations.

3.3.3 Quality assurance and quality control

Control of the dry density of the clay barrier was fundamental to its construction. The average dry density was to be no more than 1.60 t/m^3, in order not to exceed the maximum swelling pressure of 5 MPa used in the calculations for the test components. On the other hand, it was required not to be less than the minimum considered tolerable, 1.4 t/m^3. Furthermore, knowledge of the actual dry density obtained is necessary for modelling, as well as for the interpretation of the test results. For this reason, during the construction of the clay barrier, the

real mass of bentonite placed and the volume of the drift occupied by each vertical slice of blocks was determined. From these values, the global dry density as well as the percentage of construction gaps for each slice were calculated. The profiles of dry density and construction gaps were drawn from each slice, these being shown in Figure 3-18.

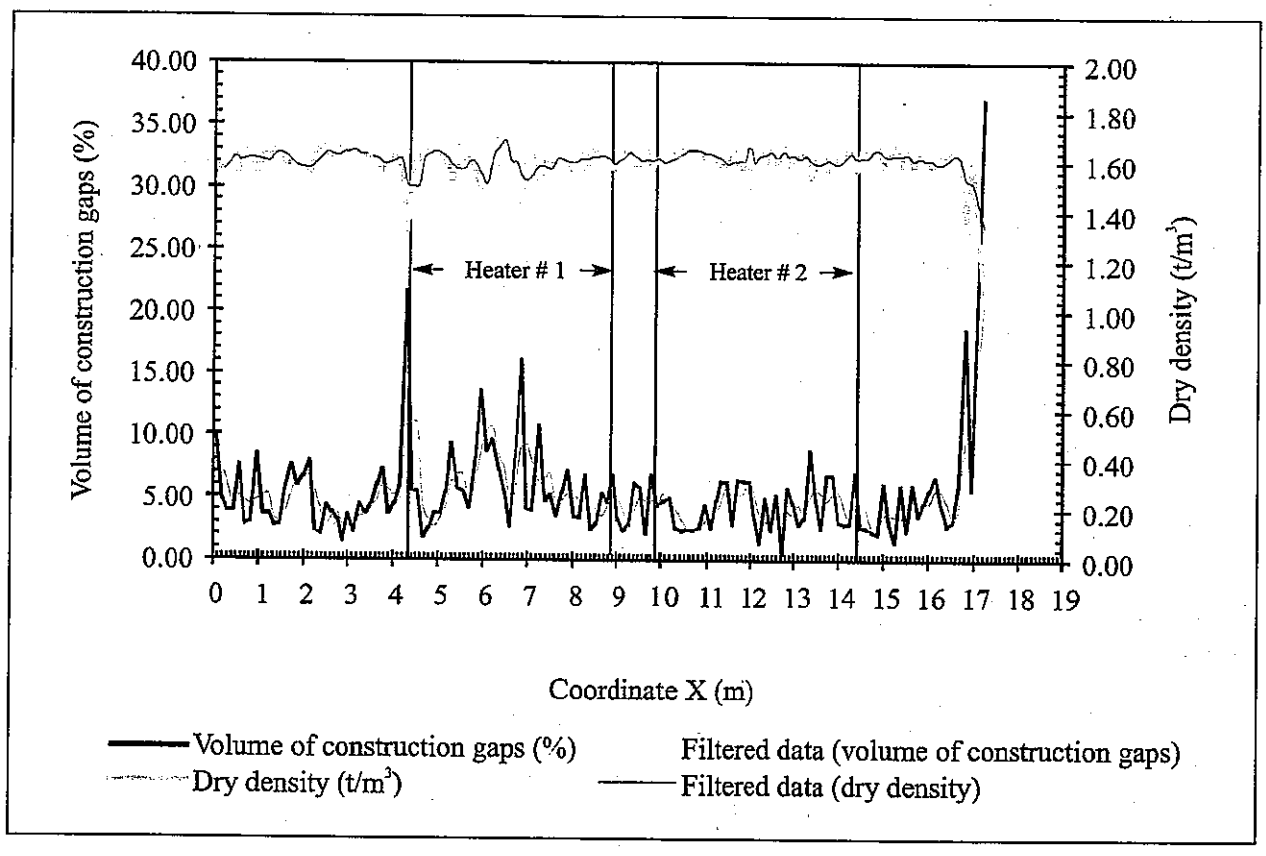

Figure 3-18 : Profiles of dry density and volume of construction gaps in the clay barrier.

A total of 136 slices were installed, made up of 5331 blocks and having an overall mass of 115 716 kg of bentonite. The average values of the barrier are a dry density of 1.60 t/m^3 and a volume of construction gaps of 5.53%. It has been assumed that the barrier maintains the water content (an average of 14.4%) from the fabrication of the blocks.

3.4 Test operation

3.4.1 Initial tests and start-up

The mechanical installation tasks were completed in 16 weeks between 1 July 1996 and 15 October 1996, two weeks ahead of schedule. The assembly and setting up of the data acquisition and control systems were prolonged more than anticipated, until 27 February 1997.

Apart from some short duration tests, the heating (operational) stage began on 27 February 1997, the date identified as "day 0" on the time scale. The sequence of initiation was as follows:

- Throughout an initial period of 20 days a constant power of 1200 W per heater was applied, with the aim of identifying the thermal response of the system and adjusting the control algorithms.

- Over the next 33 days the power was increased to 2000 W per heater and maintained constant to approximate the temperature of 100 °C desired at the surface of the steel liner, but with a limitation on the rate of power increase to reduce thermally-induced stresses.

- Finally, on 21 April 1997 (day 53) the system was switched to the constant temperature control mode, allowing the power to fluctuate freely. Over a period of 8 days, three subsequent steps were performed to adjust the parameters of the control algorithm, the setpoints of the system being established successively at 95°C, 99°C, and 100 °C.

3.4.2 Heating control and operation

Beginning in day 61, the power control system has been automatically regulating the power in the two heaters independently, so as to maintain a constant temperature of 100 °C at the hottest point of the steel liner/bentonite interface, as originally planned.

The reference used by the power control algorithm is the highest temperature value in the sensors located at the surface of the steel liner, which has always been at the center of the bottom line of the heater. Due to the shape of the heater casings, temperatures over 100 °C have been observed at the lids, but these have been discarded, as they are considered to be unique points.

With a view to increasing reliability, the heating system is redundant, and each heater has three independent heating elements, each having the rated nominal power of 4,300 W. During the test, only one of these elements, identified as Resistor A, has been used on each heater on a permanent basis, the other two being kept in reserve. The underlying reason for this was to check the operational life of these elements, which is inversely proportional to their external temperature. In any case, there has not been any failure of the elements after 1000 days (2 years and 9 months, in 27th of November, 2000) of continuous operation.

4 The FEBEX bentonite

In order to characterize the T-H-M behaviour of the FEBEX bentonite, besides the determination of identification properties, two types of tests have been carried out, namely: tests for direct parameter determination and tests for calibration of models. The first type of tests yields values of standard parameters or functions generally required by a mathematical T-H-M model. The second type of tests may be used with backanalysis techniques in order to infer the values of the parameters or functions required by particular mathematical models and to improve the accuracy of parameter determination. The design of these tests, especially the tests for calibration of models, has been guided by the FEBEX "mock-up" and the FEBEX "in-situ" tests. The tests have been carried out mainly by CIEMAT and UPC and the description of the tests and the results obtained have been summarized in two reports. These reports are written in Spanish and in this Section we will try to make them more accessible to the participants. Throughout this Section we will refer to specific Sections of the report by CIEMAT (Villar, 2000) using "CIEMAT-Section" and to specific Sections of the report by UPC (Pintado, 2000) using "UPC-Section".

In the tests carried out by CIEMAT, two types of samples of FEBEX bentonite have been used: unmixed and homogenized. The first type refers to samples taken from one of the bags into which the bentonite was packed. The second type refers to samples taken from the homogeneous mixture of all samples of the first type made by CIEMAT. Results obtained using any of these samples are considered to be representative of the characteristics of the FEBEX bentonite. In the tests that require addition of water, three types of water have been used: distilled water (used by convention and as a reference), granitic water (commercial water representative of the water that will saturate an engineered bentonite barrier) and saline water (water prepared with a chemical composition representative of the pore water inside the bentonite barrier). The chemical composition of the granitic water and of the saline water is given in Table 4-1.

Table 4-1 : Chemical composition of the water used in the tests (in mg/l), and pH.

dissolved ions and pH	granitic	saline
Cl^-	13.1	3550.0
SO_4^{2-}	14.4	1440.0
Br–	0.1	—
NO_3^-	4.8	—
HCO_3^-	144.0	—
SiO2 (aq)	22.2	—
Mg^{2+}	9.4	360.0
Ca^{2+}	44.9	400.8
Na^+	11.0	253.9
K^+	1.0	—
Sr^{2+}	0.09	—
pH	8.3	7.0

In the tests carried out by UPC, the FEBEX bentonite taken from the homogenized sample was always used. Samples were prepared at the water content in equilibrium with the laboratory, which is of w = 13.3 ± 1.3%. Distilled water was used in infiltration tests and for preparing samples with a water content higher than the hygroscopic.

4.1 Origin and general properties

4.1.1 Origin and general aspects

The FEBEX bentonite (also called "Serrata" clay in some FEBEX reports) has been extracted from the Cortijo de Archidona deposit, exploited by Minas de Gádor, S. A., in the zone of Serrata de Níjar (Almería, Spain). This deposit was selected in the ENRESA R&D plans previous to the FEBEX project as the most suitable material for the backfilling and sealing of a HLW repository. Reasons for this selection were its very high content of montmorillonite, large swelling pressure, low permeability, acceptable thermal conductivity, good retention properties and ease of compaction for the fabrication of blocks.

Over several years prior to FEBEX, and following the selection of this deposit as the reference bentonite (called bentonite S-2 in reports and publications), numerous characterization and behavior (thermal, hydraulic, mechanical, and geochemical) studies were performed. As a result, there is an extensive database on the properties of this bentonite. These data were used in the preliminary modelling for the design of the two large-scale tests of the FEBEX project.

Approximately 300 tons of suitably homogenized and conditioned bentonite were stocked for FEBEX. Based on the experience acquired in the aforementioned studies, the selected raw bentonite was required to meet the following specifications:

- Fraction of particles of more than 5 mm, less than 5%, and fraction of particles smaller than 74 μm, greater than 85%.
- Liquid limit greater than 90%.
- Swelling pressure ranging between 3 MPa and 7 MPa, for a dry density of 1.60 g/cm^3.
- Water content, after conditioning, between 12.5% and 15.5%.

The conditioning of the bentonite in the quarry, and later in the factory, was strictly mechanical (homogenization, rock fragment removal, drying, crumbling of clods, and sieving) to obtain a granulated material with the specified characteristics of grain-size distribution and water content. A quality assurance (QA) program was applied to the conditioning process. The conditioned material was packaged in large waterproof bags (about 1300 kg each). During the packaging, a sample of 8 to 10 kg was taken every 2.5 tons of bentonite, for laboratory testing.

However homogeneous it might be, a bentonite deposit has both horizontal and vertical spatial variations. For a research project such as FEBEX, a material as homogeneous as possible must be used and, furthermore, its properties must be determined by specific tests on samples of the same material. Homogenization reduces the uncertainties in modelling, in laboratory results and in the final interpretation of the entire test. For performance assessment (PA) purposes, however, knowledge of the range of variations in the relevant properties of a massive source of bentonite supply is needed. Thus, it is important to compare the properties of clays (known as S-2 bentonite in the earlier studies and FEBEX bentonite in this test) obtained from the same deposit but in two study phases separated by more than five years.

Comparison of the results of the two sets of characterization tests –S-2 bentonite and FEBEX bentonite– indicates that the deposit is very homogeneous. Consequently, it was possible to use certain parameters from the tests on S-2 bentonite for the purposes of the FEBEX test.

In the following sections, several general conclusions on the properties of the bentonite from this deposit are summarized.

4.1.2 Identification properties

The data presented in Table 4-2 are the so-called identification properties (according to the terminology of geotechnical engineering). They provide an initial idea of the type of physico-chemical behavior to be expected in the clay buffers.

It is interesting to notice that the values of the liquid limit for the S-2 and FEBEX bentonites are very similar in the tests performed by CIEMAT, in contrast to those obtained by UPC-DIT for the FEBEX bentonite, which are somewhat lower. In any case, whichever laboratory is considered, the measured values seem to be low for a bentonite with such a high content of montmorillonite and which also has a relatively high concentration of sodium as exchangeable cation.

Regarding differences in the grain-size distributions between the S-2 and FEBEX bentonites, it should be noted that the results obtained from CIEMAT and UPC-DIT differ considerably as regards the content of the < 2 μm fraction (clay size). The proportion of the clay size fraction obtained depends on the previous treatment of the bentonite for the determination of its grain-size distribution. The differences may be explained by the fact that a very strong dispersion procedure, including ultrasounds, was used by CIEMAT, while UPC-DIT employed standard geotechnical techniques.

Table 4-2 : Identification properties.

Property	Bentonite S-2		FEBEX Bentonite		
	CSIC-Zaidín	CIEMAT	CSIC-Zaidín	CIEMAT	UPC-DIT
Water content in equilibrium with the air in the laboratory, in %	—	10 to 13	—	13.7 ± 1.3	13.3 ± 1.3
Liquid limit, in %	—	105 ± 10	—	102 ± 4	93 ± 1
Plastic limit, in %	—	—	—	53 ± 3	47 ± 2
Plasticity index	—	—	—	49 ± 4	46 ± 2
Specific weight	—	2.78	—	2.70 ± 0.04	—
Grain-size distribution, in %					
Fraction less than 74 μm	93 ± 3	86	—	92 ± 1	87
Fraction less than 2 μm	82 ± 6	65 ± 1		68 ± 2	45
Specific surface, in m^2/g					
Total	614 ± 74[1]	516 ± 37[2]	649 ± 5[1]	725 ± 47[1]	—
External, BET	—	37	—	32 ± 3	—

[1] Determined by the Keeling hygroscopicity method
[2] Determined by the methylene blue method

The value obtained for the external specific surface (BET) is somewhat lower than the average values for smectites (as found in the scientific literature).

The low content of the < 2 μm fraction had already been noticed in the first studies performed on the S-2 bentonite. It was proposed at that time that the smaller particles were agglutinated or cemented with colloidal silica (during alteration of the original volcanic material). This would make dispersion of the clay, and consequently separation of the < 2 μm fraction, more difficult. This argument is supported since the most of the silt-sized material, and some of the sand-sized, is formed by "pseudomorphs" of volcanic grains transformed into smectite. The "pseudomorphs" are relatively stable and would moderate the physical behavior of the bentonite: they are identified as smectite from a chemical point of view, but do not have the physical effects of the bentonite. This interpretation may also explain the relatively low values of liquid limit found in tests.

4.1.3 Porosity

(See CIEMAT-2.1) The pore size distribution has been measured using a mercury injection porosimeter with a range of injection pressure from 7 kPa to 210 MPa that allows to measure pore diameters between 200 μm and 0.006 μm. Before placing the samples in the porosimeter, water was eliminated by liophilization, in order to minimize microstructural changes. 45 samples were taken from 15 of the bentonite blocks fabricated for the FEBEX "mock-up" test. These blocks were made using bentonite with a water content of 14.1±1.0 % and uniaxially compacted at pressures of 40-45 MPa which produced a dry density ρ_d = 1.78±0.03 g/cm^3. The samples tested had a dry density of ρ_d = 1.58-1.80 g/cm^3. The result of these porosimetric tests (see Figure 4-1) did not show any significant difference between different positions in a given bentonite block nor between different block types.

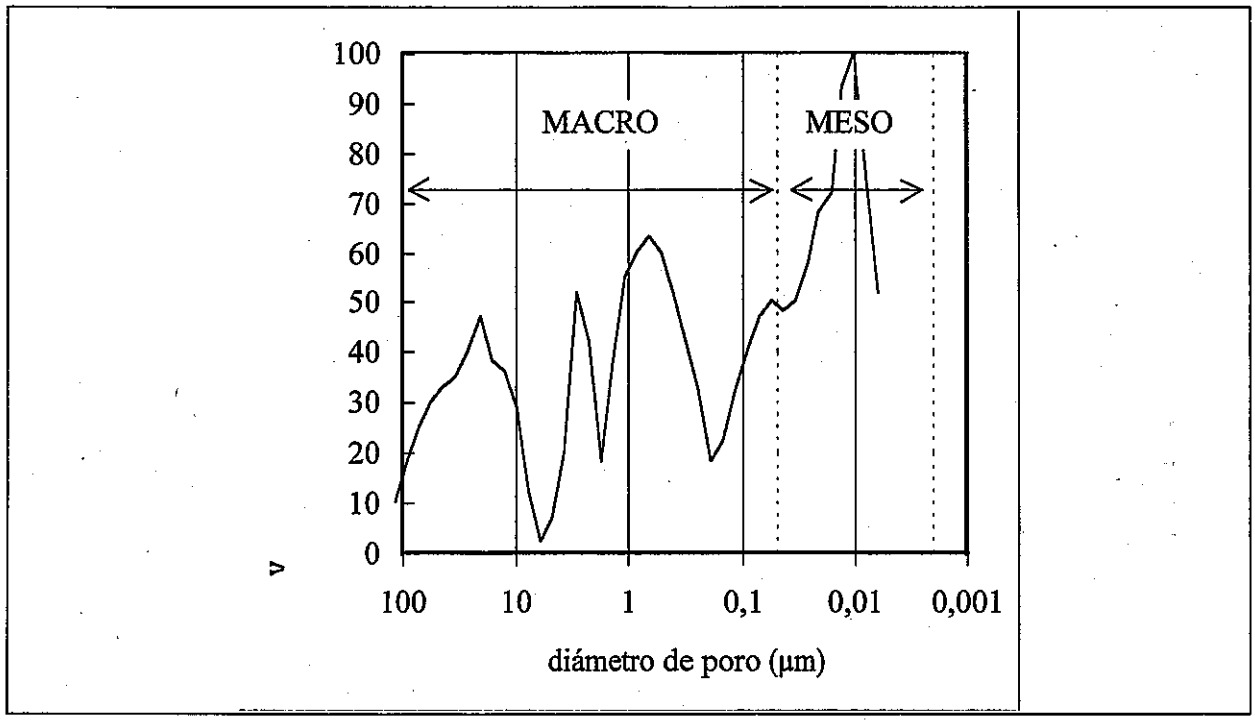

Figure 4-1 : Typical pore size distribution of a sample of compacted FEBEX bentonite (cumulative pore volume per gram in % as a function of pore diameter in %).

4.2 Parameter determination tests

4.2.1 Mechanical properties

4.2.1.1 Strength-unconfined compression and triaxial tests

In the years previous to FEBEX, strength had been determined only on samples of the bentonite S-2. Some of these data are presented herein for informative purposes.

The unconfined compressive strength is 2.5 MPa for samples prepared with a water content at equilibrium with the air in the laboratory (laboratory conditions) and at a density of 1.70 g/cm^3. It was found that unconfined compressive strength increases exponentially with dry density.

Various types of triaxial tests were performed, with saturated and unsaturated samples. The results from the unsaturated samples, prepared at different dry densities with the water content at equilibrium with the laboratory conditions, are presented in Table 4-3.

Table 4-3 : Strength parameters obtained in triaxial tests on unsaturated specimens of bentonite S-2 prepared with a water content in equilibrium with the laboratory conditions and at different initial dry densities.

ρ_d g/cm^3	initial Sr %	range of σ^3 MPa	cohesion MPa	friction angle degrees
1.6	41 – 47	0.5 – 3.0	0.7	25
1.6	41 – 47	3.0 – 10.0	2.8	14
1.6	41 – 47	10.0 – 30.0	4.4	14
1.7	49 – 60	0.5 – 3.0	0.8	30
1.7	49 – 60	3.0 – 10.0	1.0	26
1.7	49 – 60	10.0 – 30.0	3.5	16
1.8	53 – 59	3.0 – 10.0	4.3	16
1.8	53 – 59	10.0 – 30.0	3.6	18
1.9	65 – 79	3.0 – 10.0	4.5	19

4.2.1.2 Compressibility-oedometric tests

Oedometric tests have been performed on samples of the bentonite S-2 for initial dry densities of 1.40 g/cm^3 and 1.60 g/cm^3. Table 4-4 shows the parameters resulting from these tests.

Table 4-4 : Oedometer parameters (C_c = compression index of the virgin compression line, with stress in decimal log scale; C_s = unloading-reloading compression index, with stress in decimal log scale; a_v = virgin confined compression index, with stress in natural scale; $m_v = a_v/(1 + e_0)$, where e_0 is the initial void ratio; and k = saturated permeability)

ρ_d g/cm^3	C_c	C_s	a_v m^2/kN	m_v m^2/kN	k m/s
1.4	0.38	0.20	$2.5\cdot10^{-5}$	$1.7\cdot10^{-5}$	$4.7\cdot10^{-12}$
1.6	0.38	0.33	$2.3\cdot10^{-5}$	$1.4\cdot10^{-5}$	$1.3\cdot10^{-13}$

4.2.1.3 Swelling pressure

Swelling pressure tests were performed using conventional oedometers on samples saturated with distilled water (see CIEMAT-3.1). A regression curve was developed as a function of dry density for the swelling pressure of the FEBEX bentonite, as shown on Figure 4-2, and expressed by the equation

$$P_s = \exp(6.77\,\rho_d - 9.07)$$

where P_s is the swelling pressure in MPa and ρ_d is the dry density in g/cm^3. The deviation of the experimental values with respect to this fitting may be as high as 25 %. The dispersion observed in the values is larger for higher dry densities, this probably being due to technical limitations, as the load capacity of the oedometers is almost exceeded by the swelling pressure.

The swelling pressure values and the regression curve for the bentonite S-2 are also shown in Figure 4-2. The difference in the swelling pressures of the S-2 and the FEBEX bentonites, may be considered negligible for practical purposes.

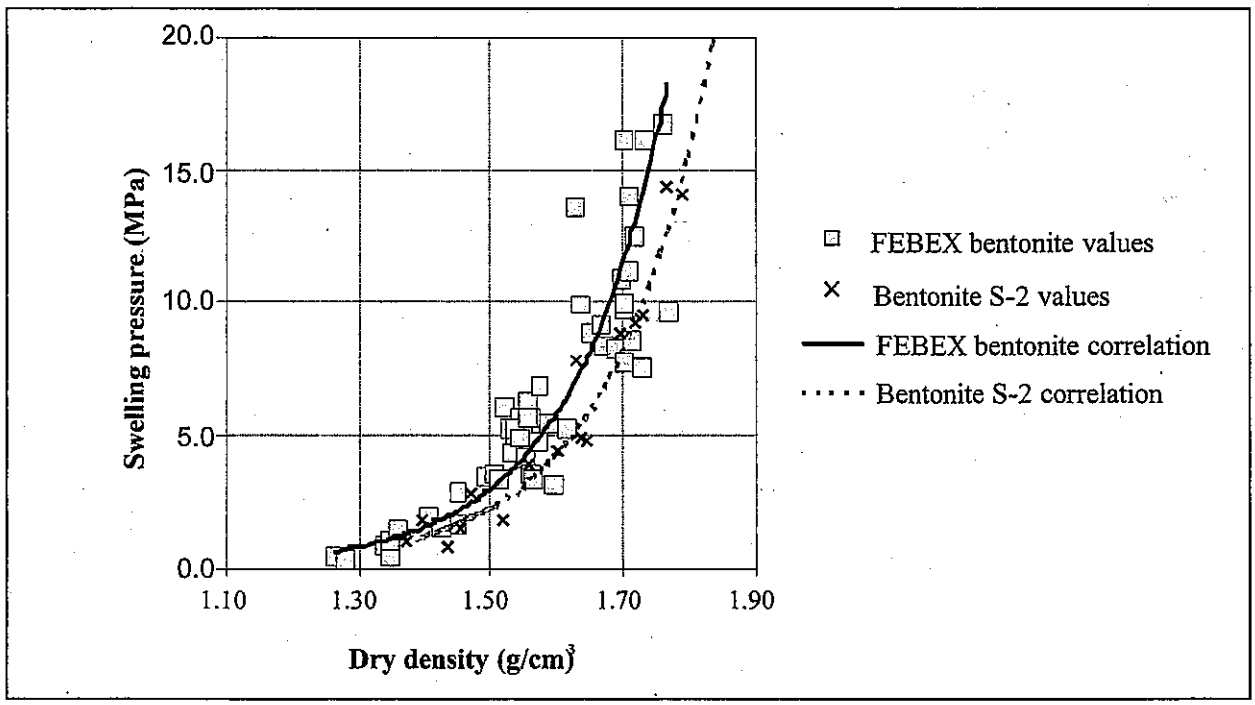

Figure 4-2 : Swelling pressure as a function of dry density

4.2.1.4 Swelling under load

These tests were performed using conventional oedometers on samples of the FEBEX bentonite (see CIEMAT-3.2 and UPC-2.6).

During the pre-operational stage, CIEMAT carried out tests with distilled water on specimens with a nominal dry density of 1.60 g/cm^3. Four of these tests were performed under a load of 0.5 MPa and the other three under a load of 0.9 MPa. Subsequently, several series of swelling

under load tests were performed, in which samples having a nominal dry density of 1.60 g/cm^3 were subjected to different loads ranging between 0.1 and 3.0 MPa. Both granitic and saline water were used to saturate the sample. A commercial granitic water was used. The saline water is a synthetic product having a chemical composition similar to that of the bentonite interstitial water, but simplified to include only the major elements. The chemical composition of both waters is shown in Table 4-5.

Table 4-5 : Chemical composition of the water used in the tests (in mg/l), and pH.

dissolved ions and pH	granitic	saline
Cl^-	13.1	3550.0
SO_4^{2-}	14.4	1440.0
Br–	0.1	—
NO_3^-	4.8	—
HCO_3^-	144.0	—
SiO2 (aq)	22.2	—
Mg^{2+}	9.4	360.0
Ca^{2+}	44.9	400.8
Na^+	11.0	253.9
K^+	1.0	—
Sr^{2+}	0.09	—
pH	8.3	7.0

In addition, some tests have been performed with specimens compacted to nominal dry densities of 1.70 and 1.50 g/cm^3 saturated with granitic water, and some others with specimens compacted to nominal dry densities of 1.70 g/cm^3 and saturated with saline water.

As expected, the specimens compacted to a dry density of 1.50 g/cm^3 undergo strain, on saturation with granitic water, somewhat lower than in the case of specimens compacted to a dry density of 1.60 g/cm^3. Specimens compacted to a dry density of 1.70 g/cm^3 experienced higher swelling strains under the same load, in tests with both saline and granitic water.

Figure 4-3 shows the final swelling strain of the clay in the tests performed with samples compacted to nominal dry densities of 1.60 g/cm^3 and saturated with different kinds of water, along with the fitting for the tests performed with both granitic and saline water. The final values of strain do not seem to be particularly dependent on the kind of water, although in the tests performed with saline water they are somewhat higher than in those performed with granitic water, the values for distilled water being the highest.

Strain (ε, %) as a function of vertical load (σ, MPa) may be approximately expressed by the following equations:

$$\varepsilon = -9.4 + 15.9 \log \sigma \qquad \text{for granitic water}$$
$$\varepsilon = -11.4 + 14.4 \log \sigma \qquad \text{for saline water}$$

UPC-DIT performed 21 flooding-under-load tests on specimens prepared at various dry densities varying between 1.57 g/cm^3 and 1.87 g/cm^3, with an initial water content of 11.7% (water content at equilibrium with laboratory conditions). The specimens were saturated with distilled water while being subjected to a constant load ranging between 0.01 MPa and 10.00 MPa.

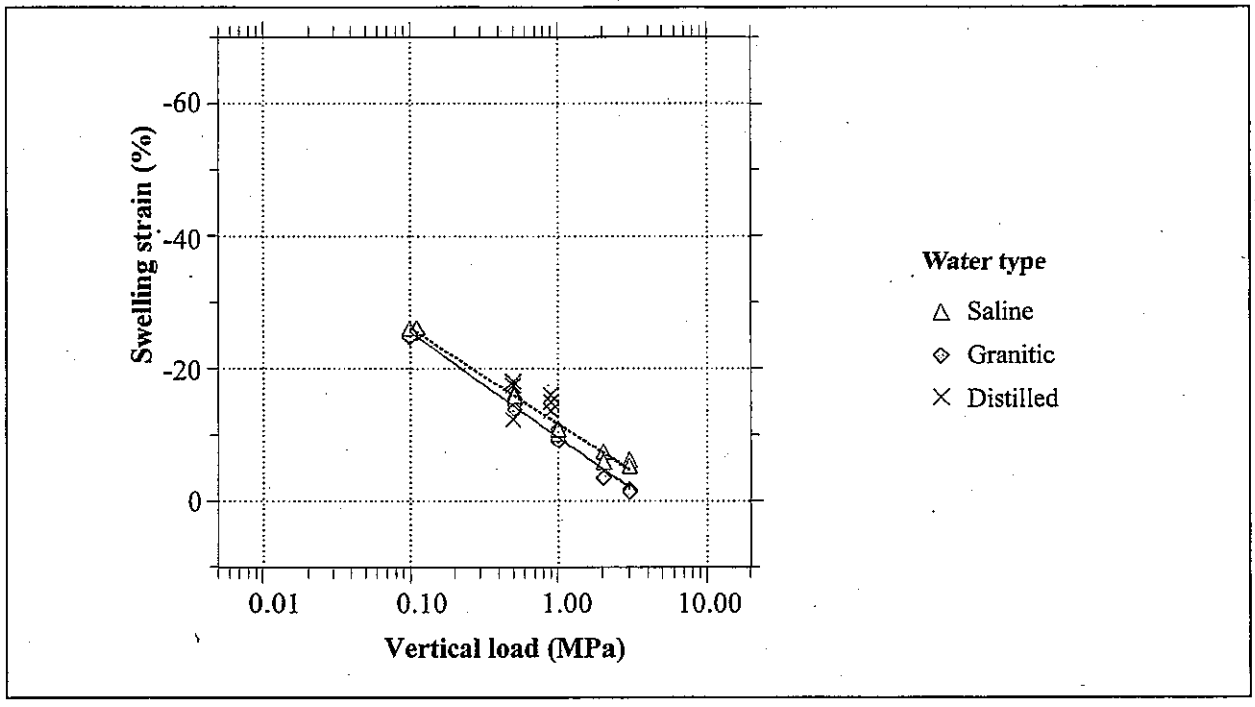

Figure 4-3 : Swelling strain of specimens compacted to dry density 1.60 g/cm^3 on saturation under vertical load with different kinds of water.

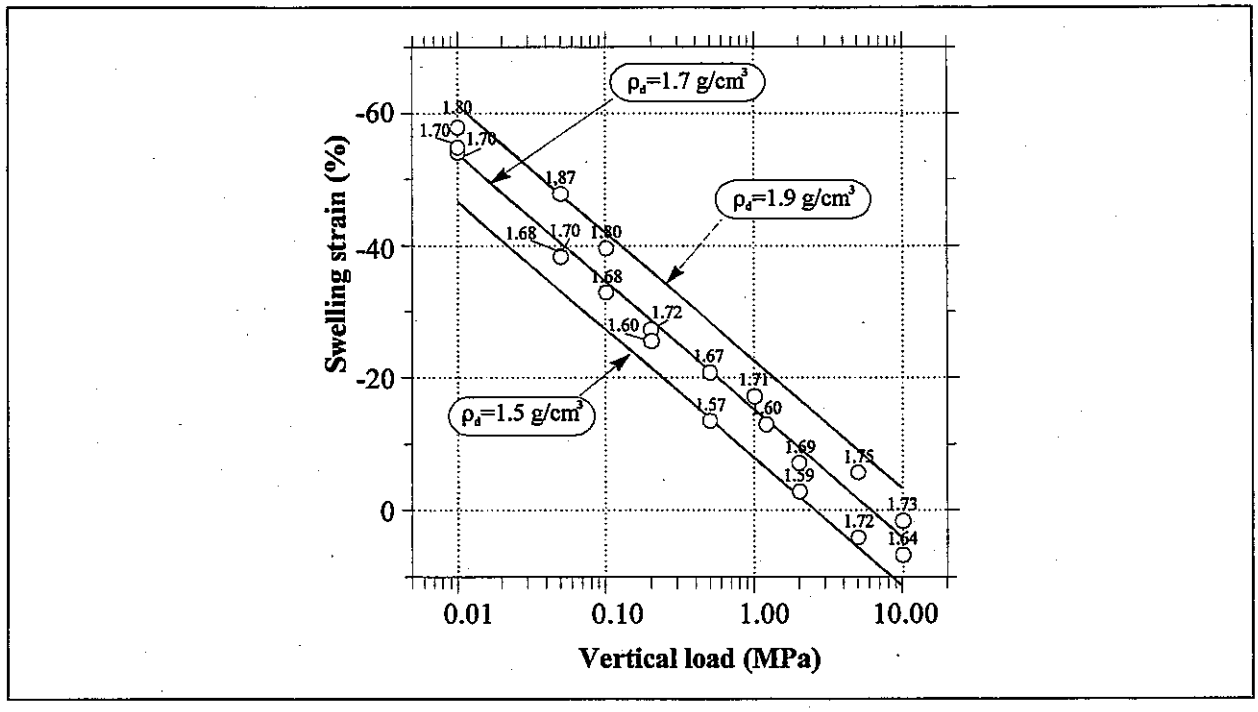

Figure 4-4 : Swelling strain for different applied vertical loads with the value of initial dry density, in g/cm^3, indicated for each point.

The strain (ε, %) induced after saturation is shown in Figure 4-4 and may be approximately expressed by the equation

$$\varepsilon = -46.9 - 19.4 \log \sigma + 36.6\, \rho_d$$

where σ is the vertical load in MPa and ρ_d is the initial dry density in g/cm^3.

The strain values obtained with this equation for a dry density of 1.60 g/cm^3 are slightly higher than those obtained with the fitting used by CIEMAT for tests performed with granitic water. The discrepancy is more marked for low loads, with a maximum difference of 5 percentage points. This would confirm that swelling under saturation with distilled water is somewhat higher than the swelling expected when saturation takes place with granitic water.

4.2.1.5 Elastic shear modulus, G

UPC-DIT determined the elastic shear modulus, G, at small deformations ($10^{-6} \leq \gamma \leq 10^{-4}$) for the FEBEX bentonite (see UPC-2.5). The tests were performed in a resonant column on 10 specimens compacted at various dry densities and degrees of saturation. The results are shown in Table 4-6 and in Figure 4-5.

Table 4-6 : Elastic shear modulus obtained in resonant column tests.

dry density g/cm^3	water content %	degree of saturation %	void ratio	elastic shear modulus, G, in MPa				
				$\sigma_3 = 0.01$ MPa	$\sigma_3 = 0.1$ MPa	$\sigma_3 = 0.2$ MPa	$\sigma_3 = 0.4$ MPa	$\sigma_3 = 0.8$ MPa
1.58	14.7	54	0.757	140	207	245	300	370
1.66	13.6	57	0.668	211	223	270	—	—
1.54	3.4	12	0.802	78	106	174	208	326
1.56	2.8	10	0.777	89	106	138	—	—
1.62	24.6	95	0.717	240	270	—	331	336
1.66	21.3	87	0.677	252	296	370	429	502
1.65	4.7	19	0.685	74	90	137	190	310
1.72	10.4	47	0.615	200	219	293	381	429
1.68	3.7	16	0.652	61	89	141	200	290
1.62	12.7	50	0.713	122	180	240	299	387

4.2.1.6 Compressibility of joints

UPC-DIT performed unconfined compression tests on specimens of the FEBEX bentonite to obtain the relationship between normal stress and displacement in the joints between blocks (see UPC-2.8). The joint displacements were calculated by comparing the average deformations in two specimens for the same level of load: one was a continuous specimen with a height of 7.8 cm and the other was formed by two pieces, each 3.9 cm in height, placed one on top of the other. Each specimen was tested with three different degrees of initial saturation. Figure 4-6 shows the value of the decrease in distance between the joint surfaces of two blocks as a function of the normal load applied, for different degrees of saturation.

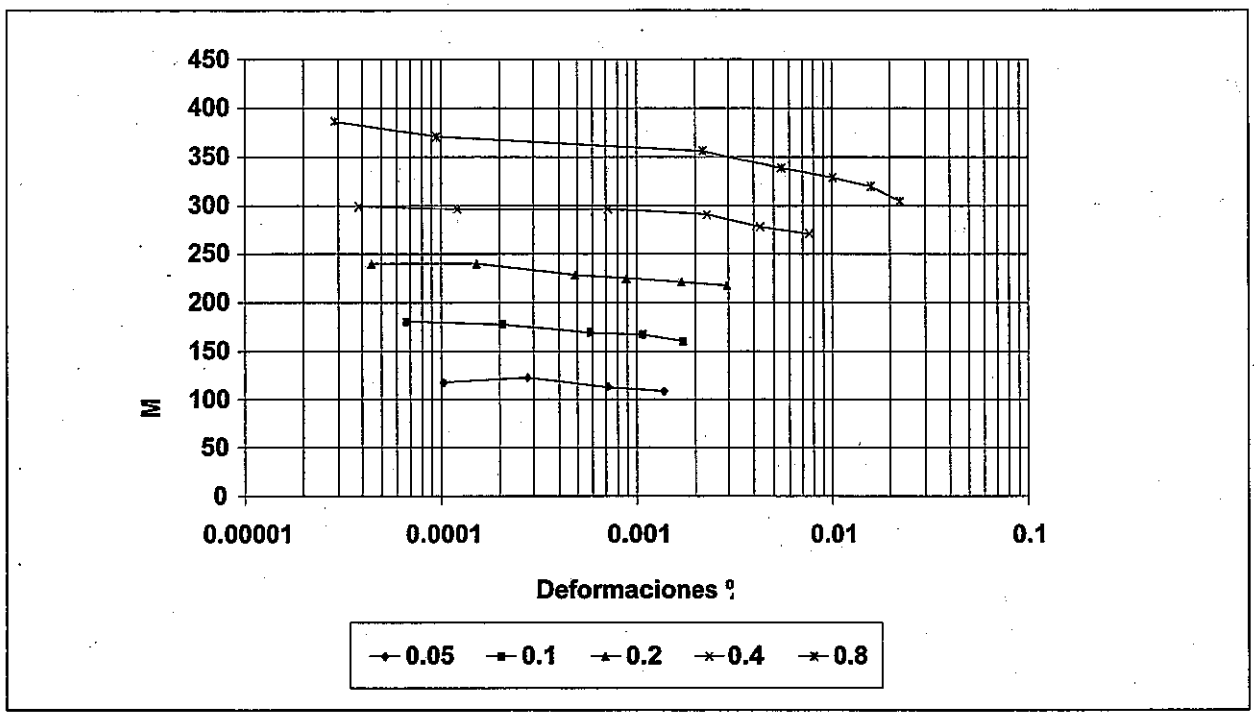

Figure 4-5 : Shear modulus G as a function of the deformation at a degree of saturation of 0.5 and various confining pressures.

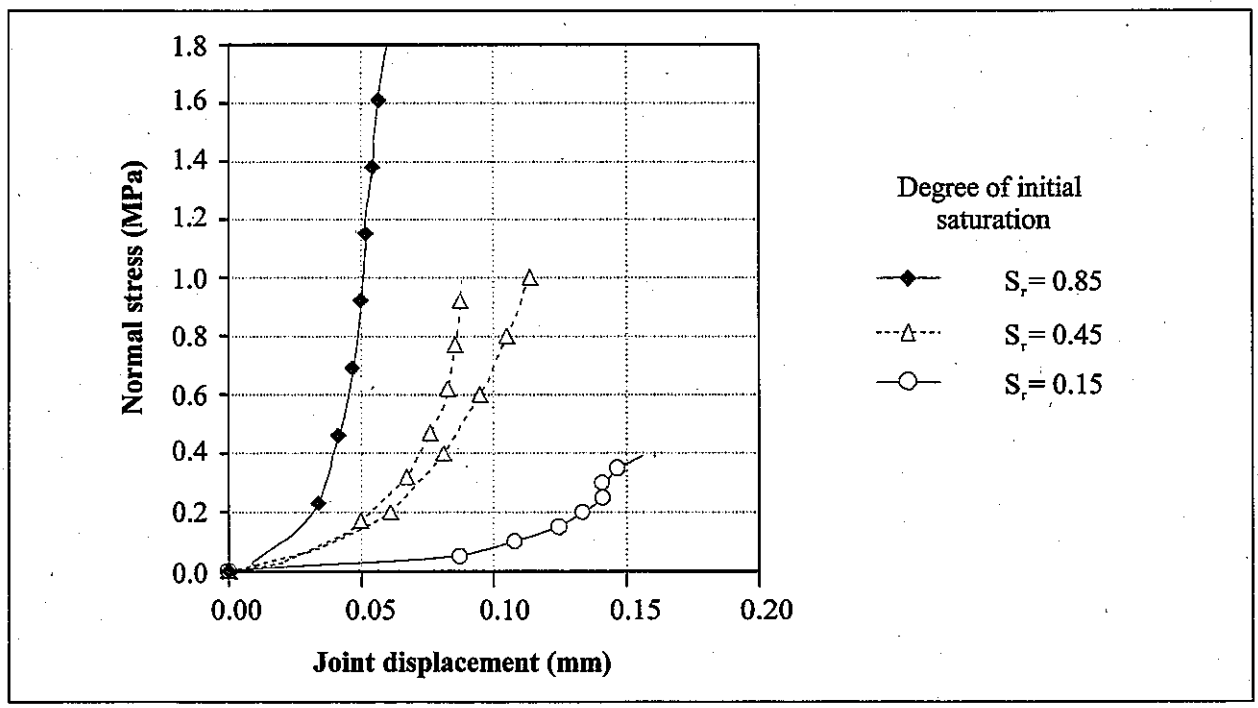

Figure 4-6 : Displacement between joint surfaces for different degrees of saturation.

4.2.2 Hydraulic properties

4.2.2.1 Saturated hydraulic conductivity

An empirical relationship has been obtained, using saturated specimens, for the coefficient of permeability of the FEBEX bentonite as a function of dry density. It was expressed by the following equations

$\log k = -6.00\ \rho_d - 4.09$ $\quad r^2 = 0.97$, 8 points, for ρ_d varying between 1.30 and 1.47 g/cm^3
$\log k = -2.96\ \rho_d - 8.57$ $\quad r^2 = 0.70$, 26 points, for ρ_d varying between 1.47 and 1.84 g/cm^3

where k is the coefficient of permeability for distilled water, in m/s, and ρ_d is the dry density, in g/cm^3 (see CIEMAT-2.3). The variation of the values actually obtained with respect to these fittings is of the order of 30 %.

Figure 4-7 shows the regression lines for the coefficient of permeability of FEBEX bentonite shown above and the points obtained in different determinations. The influence of the water used as permeant has been tested, as well as the influence of the direction of the measurement, parallel or perpendicular to the compaction effort, in the value of the coefficient of permeability. None of these aspects seems to be relevant, with the exception of the use of saline water, that yields a higher hydraulic conductivity.

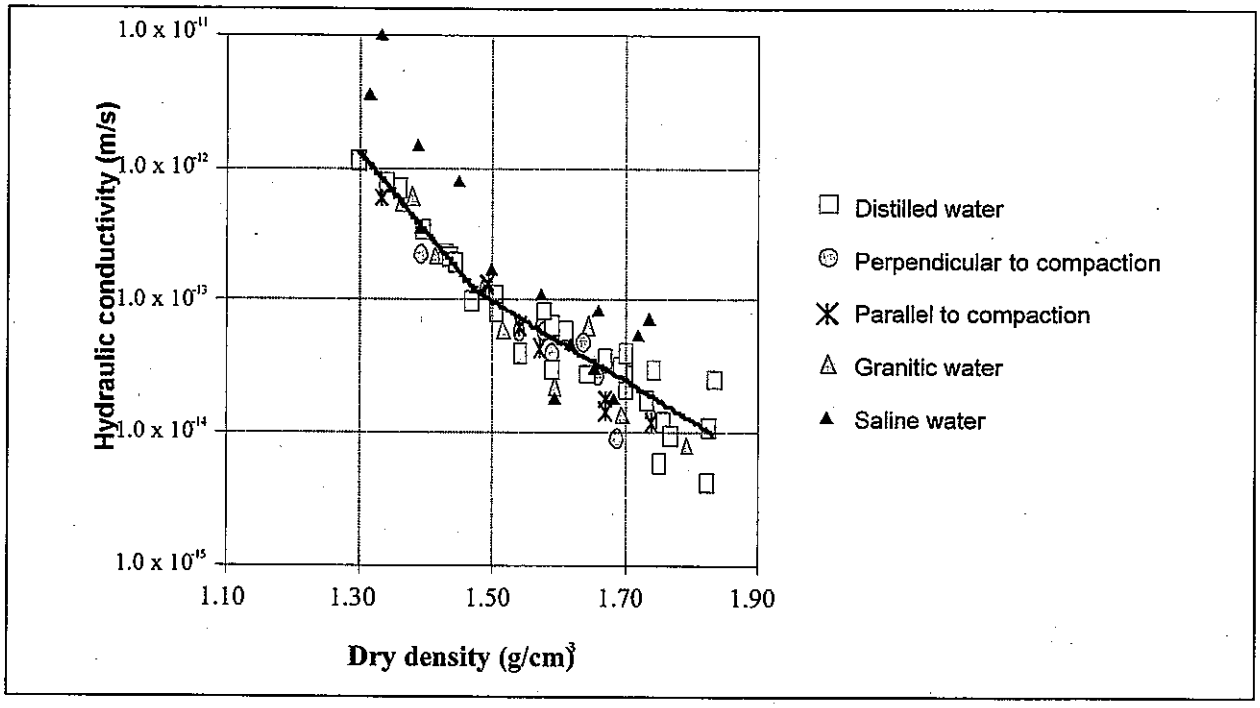

Figure 4-7 : Saturated hydraulic conductivity as a function of dry density.

The data indicate that the FEBEX bentonite is less permeable than the bentonite S-2. However, differences are small: in some cases it is even less than the scattering shown in the same set of tests.

4.2.2.2 Relative permeability

Unsaturated hydraulic conductivity is highly dependent on the degree of saturation (S_r) and may be expressed as the product of relative permeability (k_r) times the saturated hydraulic conductivity. The dependence on the degree of saturation is usually expressed by means of a potential law for the relative permeability: $k_r = S_r^n$.

The water infiltration tests carried out by CIEMAT (see CIEMAT-3.3) in small teflon cells (see Figure 4-8) provide data allowing unsaturated hydraulic conductivity and its dependence on the degree of saturation to be obtained. In the tests, water content throughout the specimen was measured at different times after initiation of the infiltration process. By means of parameter identification techniques similar to those used in groundwater engineering and geophysics, intrinsic permeability and the exponent of the law used to obtain the relative permeability may be estimated. The values obtained were $K = 2.95 \cdot 10^{-21}$ m^2 (for a porosity of 0.4) and n = 4.64 respectively, in the case of samples with an initial dry density of 1.75 g/cm^3.

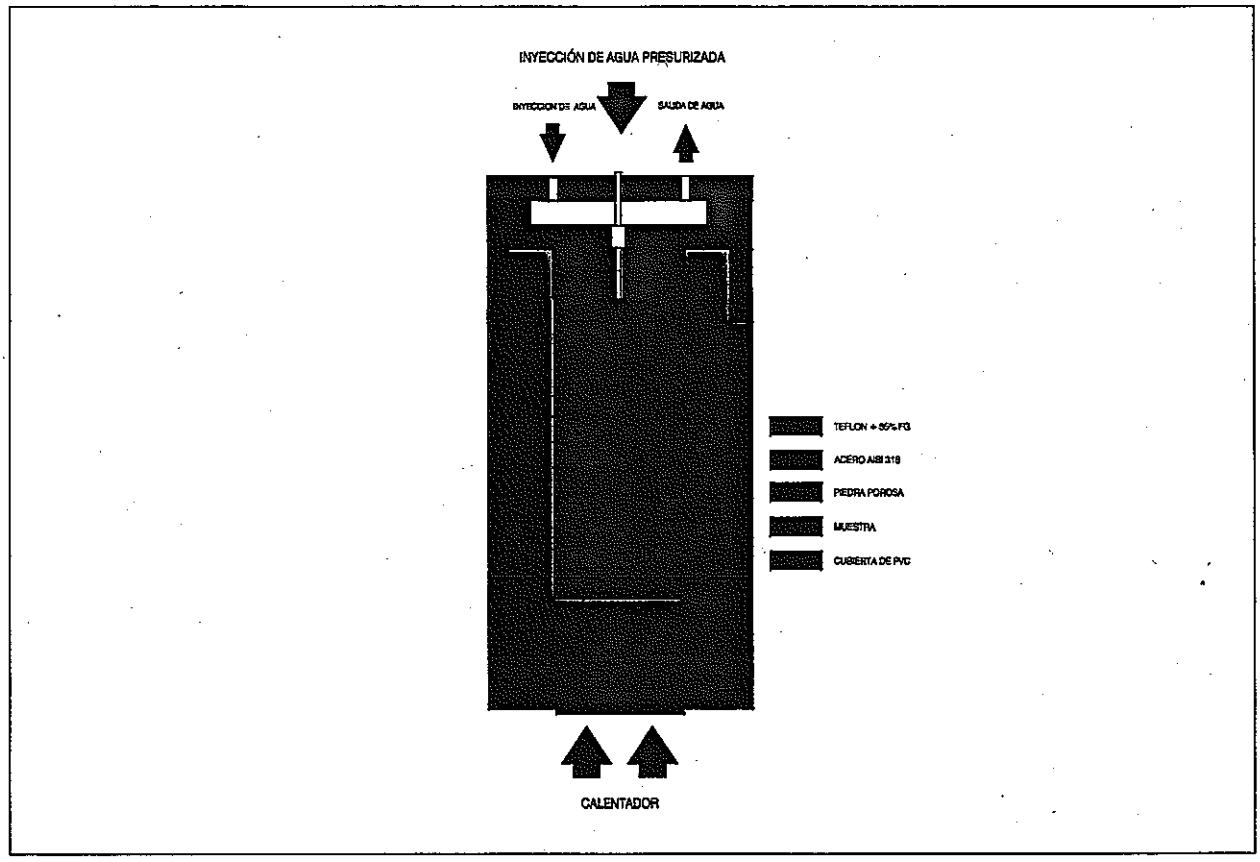

Figure 4-8 : Scheme of the Teflon cell. The lateral walls of the cell are made of Teflon. Water may be enter or leave the cylindrical sample through a porous stone placed on the top of the sample. The openings in the upper steel cap allow the flow of water to or from the porous stone. The lower steel cap allows the heating of the bottom of the sample.

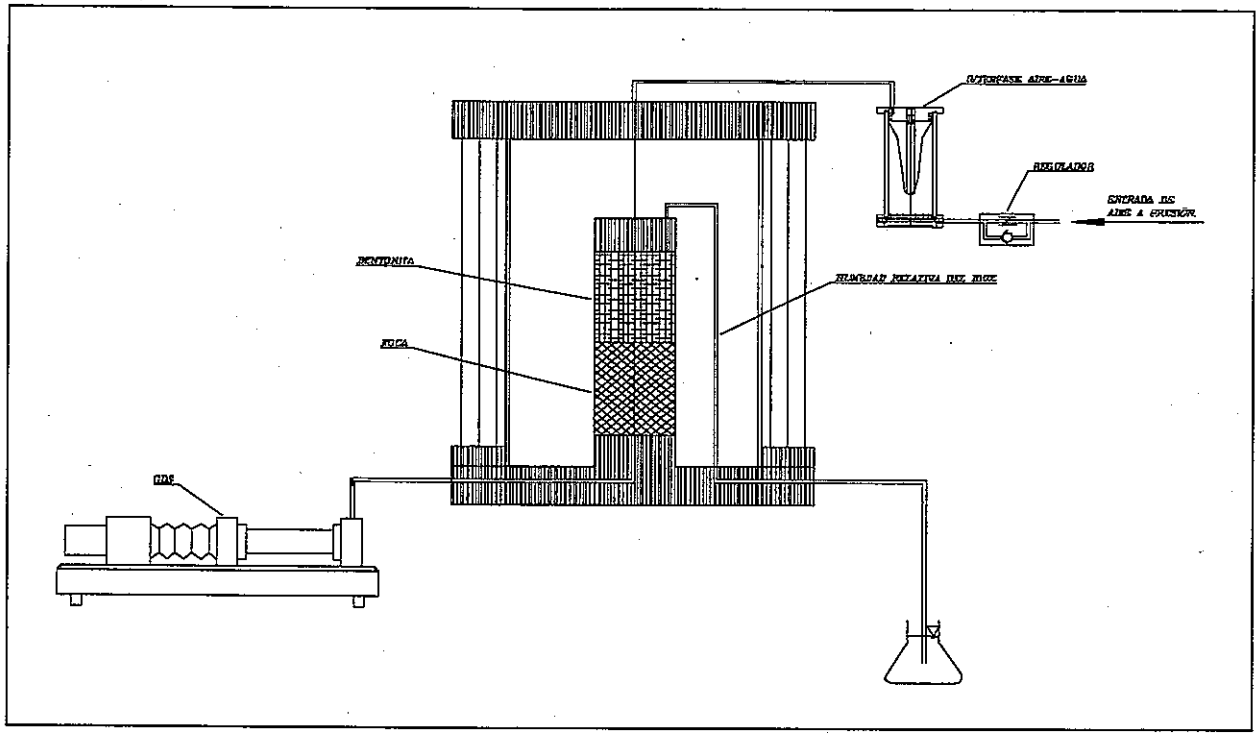

Figure 4-9 : Scheme of the set up used in the infiltration tests.

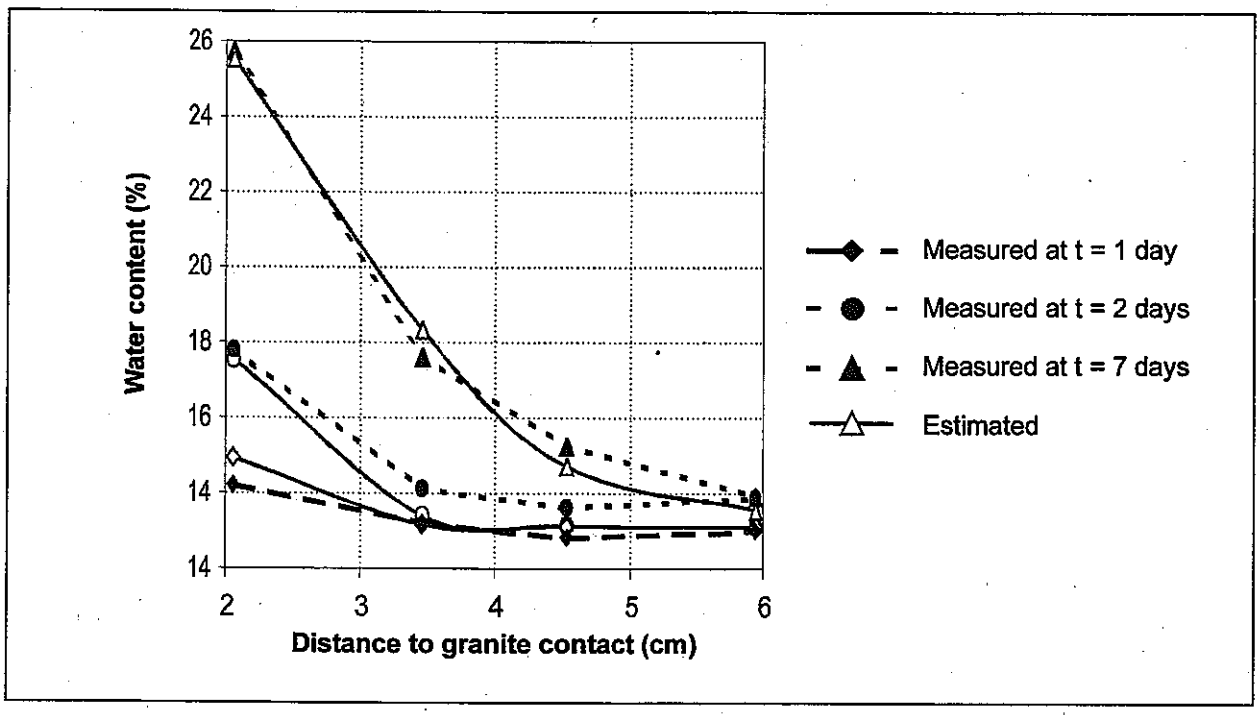

Figure 4-10 : Measured and computed water content in infiltration tests.

Similar infiltration tests have been carried out at UPC-DIT (see UPC-4.1). In this case, in order to study the possibility of desaturation of the surrounding rock at the interface between the bentonite and the granite, a hydraulic gradient was prescribed across a specimen of granite in contact with another specimen of bentonite. The test was carried out in a triaxial cell with a confinement pressure of 0.8 MPa (see Figure 4-9). Specimens were initially compacted at a dry density of 1.76 g/cm^3 and a water content of 13%. No change in the water content of the granite was detected during the test. However, the measurements of water content in the bentonite allow a new value to be estimated for the exponent in the relative permeability law. Figure 4-10 shows how good agreement is achieved between the measurements and numerical model predictions, with the parameters derived from the identification process.

In addition, the unsaturated water conductivity may be estimated in thermo-hydraulic experiments with prescribed heat and water flows (see Section 4.3.1). The summary of values obtained for the parameter "n" in the relative permeability law ($k_r = S_r^n$) is shown in Table 4-7.

Table 4-7 : Exponent in relative permeability law obtained from different types of tests

Test	value of n
Water infiltration in small teflon cells	4.64
Water infiltration in bentonite in contact with granite	3.50
Heat and water flow experiment 1	3.06
Heat and water flow experiment 2	1.10
Heat and water flow experiment 3	1.68

4.2.2.3 Suction–water content relationship at 20 °C

Tests on unconfined samples

CIEMAT has carried out suction–water content tests for the FEBEX bentonite, both in compacted samples and in samples trimmed from blocks (see CIEMAT-2.5). The relationship between suction and water content was initially determined in compacted samples for three different suction values and, subsequently following wetting and drying-wetting paths. UPC tested specimens at various temperatures and suctions between 3 MPa and 700 MPa following similar wetting and drying paths. Figure 4-11 shows the tests results grouped according to initial dry density (ρ_{d0}). Tests with a dry density of 1.67 and 1.75 g/cm^3 were performed by CIEMAT and tests with a dry density of 1.64 g/cm^3 were performed by UPC-DIT (see UPC-2.1). The relationship between suction (s, MPa) and water content (w, %), may be fitted by means of the following equation:

$$w = (45.1\ \rho_{d0} - 39.2) - (18.8\ \rho_{d0} - 20.34) \log s$$

where ρ_{d0} is the initial density in g/cm^3.

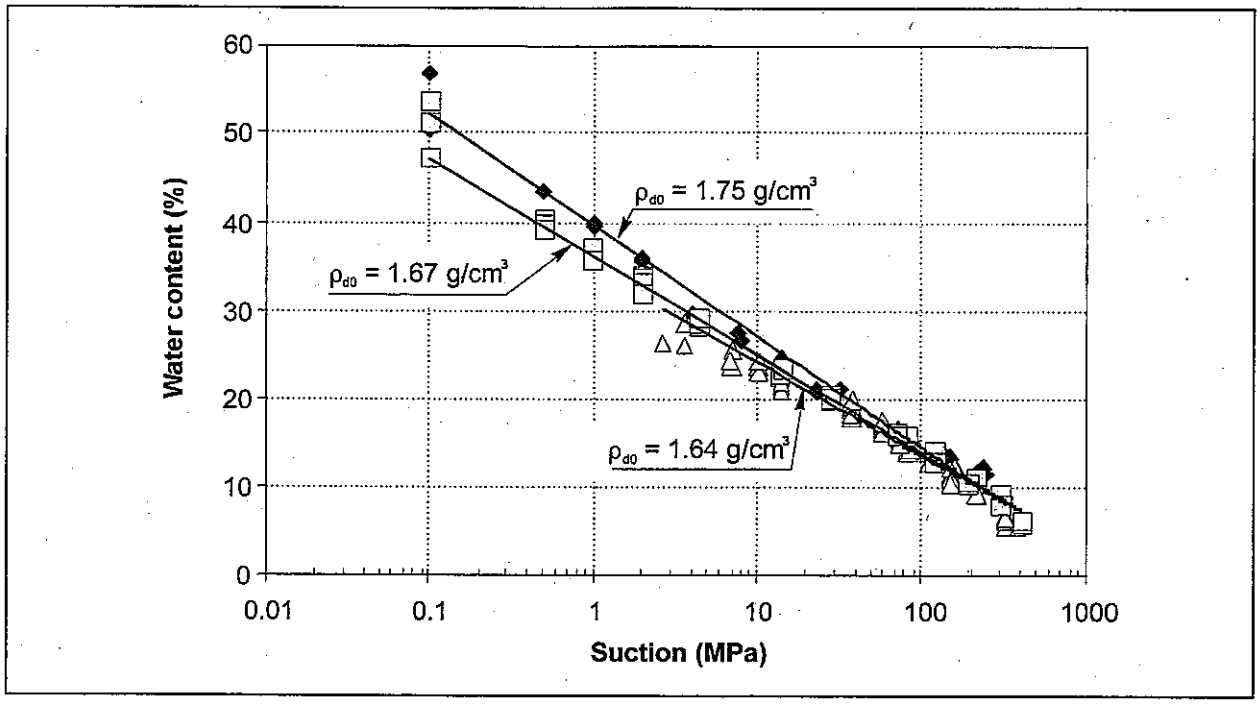

Figure 4-11 : Suction/water content relationship in tests on unconfined samples, for FEBEX bentonite.

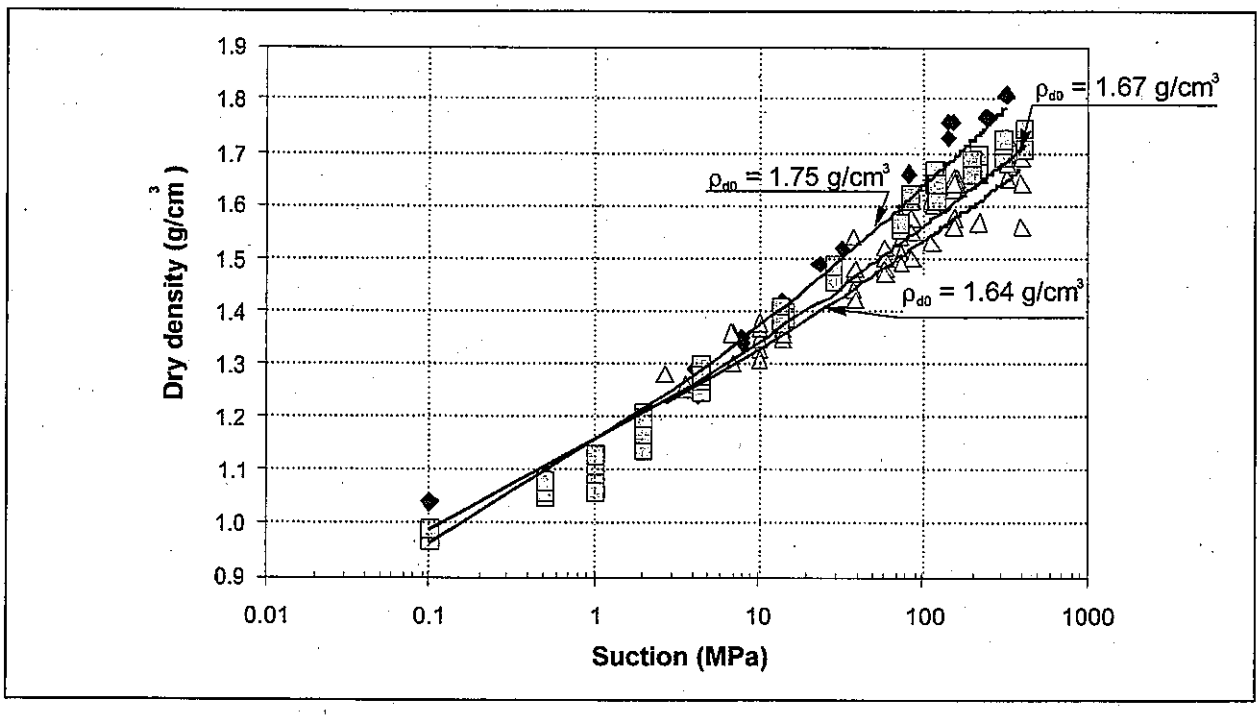

Figure 4-12 : Relationship between dry density and suction in tests on unconfined samples, for FEBEX bentonite.

The volume variations observed with changing suction are important. Figure 4-12 shows the relationship between the dry density and the change in suction for the different samples tested, grouped according to their initial dry densities. The dry density for values of suction ranging from 400 to 0.1 MPa may be obtained through the following expression:

$$\rho_d = 1.15\ s^{0.13\,\rho_{d0} - 0.15}$$

where ρ_{d0} is the initial dry density in g/cm^3 and s is the suction in MPa.

For suctions varying between 2.0 MPa and 385.0 MPa, an empirical equation relating water content and suction was determined for the bentonite S-2

$$w = 36.1 - 12.0 \log s \qquad r^2 = 0.94 \qquad 191 \text{ points}$$

which does not depend on initial dry density. In this equation, w is the water content in %, and s the suction in MPa. Figure 4-13 shows the regression curves for the bentonites (S-2 and FEBEX) and the points obtained by CIEMAT and UPC for each bentonite.

As may be seen, the differences between the two curves are very small, one or two percentage points in the water content, depending on the suction value. Nevertheless, it may be said that there exists a difference that is reflected in the water content in equilibrium with the laboratory conditions, as was indicated in Table 4-2. For all practical purposes, the differences between the two bentonites are very small.

In the low range of suction, water contents determined at a temperature of 72°C are higher than those determined at 20°C. However, the results are limited and more tests are required to quantify the effect of temperature on suction/water content relationship.

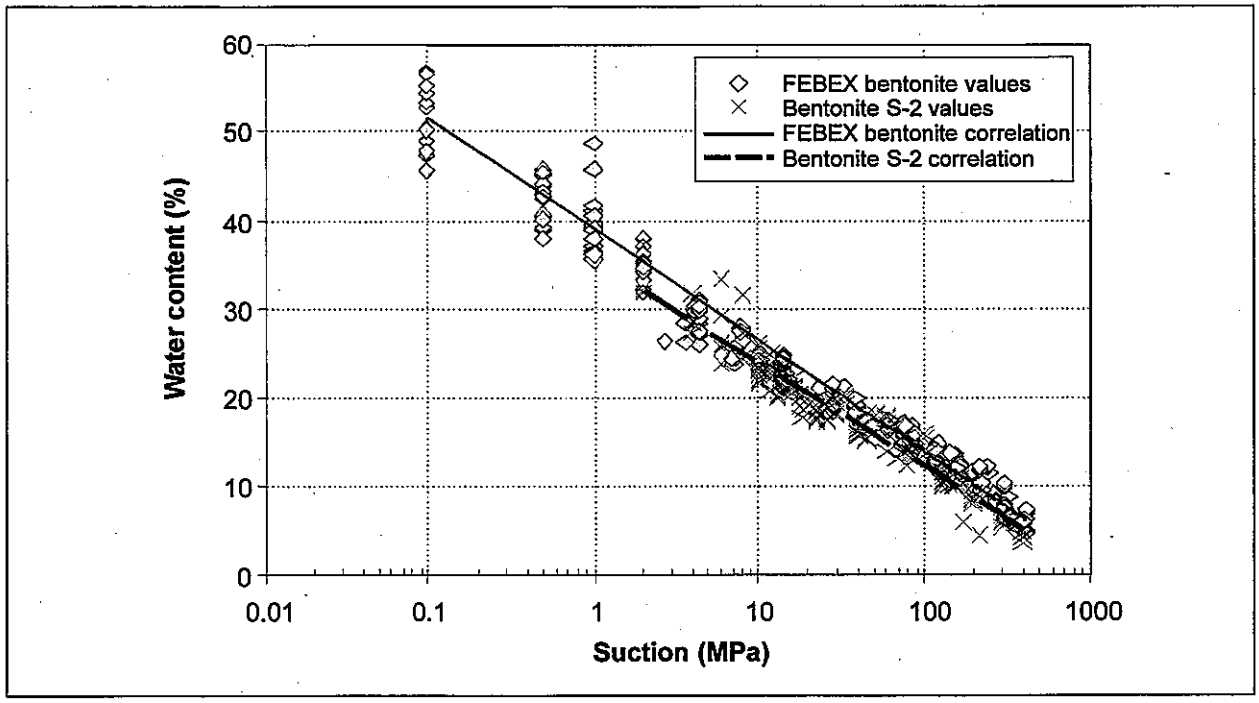

Figure 4-13 : Suction/water content relationship in tests on unconfined samples, for S-2 and FEBEX bentonites.

Tests on confined samples

In unconfined tests, the dry density and structure of the bentonite undergo important changes during the hydration process. However, volume changes are small in a bentonite barrier, and knowledge of the relationship between suction/water content at constant dry density (characteristic or water retention curve) is essential.

To determine the retention curve, two kinds of tests have been performed. CIEMAT used suction controlled oedometers to hinder swelling of the clay, by adding the appropriate loads (see CIEMAT-2.5). UPC designed containers made from sintered metal to fix the volume of the sample, while the water vapor in the clay changes with the atmosphere in which the capsule is placed (see UPC-2.1). In both cases, minor volume changes have occurred.

The retention curves determined may be fitted by means of the van Genuchten expression:

$$S_r = S_{r_0} + (S_{r_{max}} - S_{r_0})\left[1 + (s/P_0)^{\frac{1}{1-\lambda}}\right]^{-\lambda}$$

or to a modification of this expression that is more suitable for higher values of suction:

$$S_r = S_{r_0} + (S_{r_{max}} - S_{r_0})\left[1 + (s/P_0)^{1/(1-\lambda)}\right]^{\lambda}\left[1 - s/P_s\right]^{\lambda_s}$$

where S_{r0} and $S_{r\,max}$ are the residual and maximum degree of saturation and P_0 (MPa), P_s (MPa), λ and λ_s are material parameters. Table 4-8 shows the parameters fitted for the wetting paths, that are plotted together with the experimental points in Figure 4-14. Table 4-9 shows the parameters fitted for the wetting paths, that are plotted together with the experimental points in Figure 4-15.

Table 4-8 : Parameters of the retention curves.

ρ_d range g/cm^3	type of equation (no. in Figure 4-14)	P_0 MPa	λ	S_{r0}	$S_{r\,max}$	P_s MPa	λ_s
1.70 – 1.75	Van Genuchten (1)	90	0.45	0.00	1.00	—	—
1.70 – 1.75	modified van Genuchten (2)	100	0.45	0.01	1.00	1500	0.05
1.60 – 1.65	Van Genuchten (3)	30	0.32	0.10	1.00	—	—
1.60 – 1.65	modified van Genuchten (4)	35	0.30	0.01	1.00	4000	1.5
1.58 – 1.59	Van Genuchten (5)	4.5	0.17	0.00	1.00	—	—
1.58 – 1.59	modified van Genuchten (6)	2.0	0.10	0.01	0.99	1000	1.3

Table 4-9 : Parameters for fitting of the drying paths after saturation.

ρ_d range g/cm^3	type of equation (no. in Figure 4-15)	P_0 MPa	λ	S_{r0}	$S_{r\,max}$	P_s MPa	λ_s
1.70 – 1.75 drying	Van Genuchten (1)	180	0.62	0.0	1.0	—	—
1.70 – 1.75 wetting	modified van Genuchten (2)	100	0.45	0.01	1.0	1500	0.05
1.58 – 1.59 drying	Van Genuchten (3)	30.0	0.15	0.0	1.0	—	—
1.58 – 1.59 wetting	modified van Genuchten (4)	2.0	0.10	0.01	0.99	1000	1.3

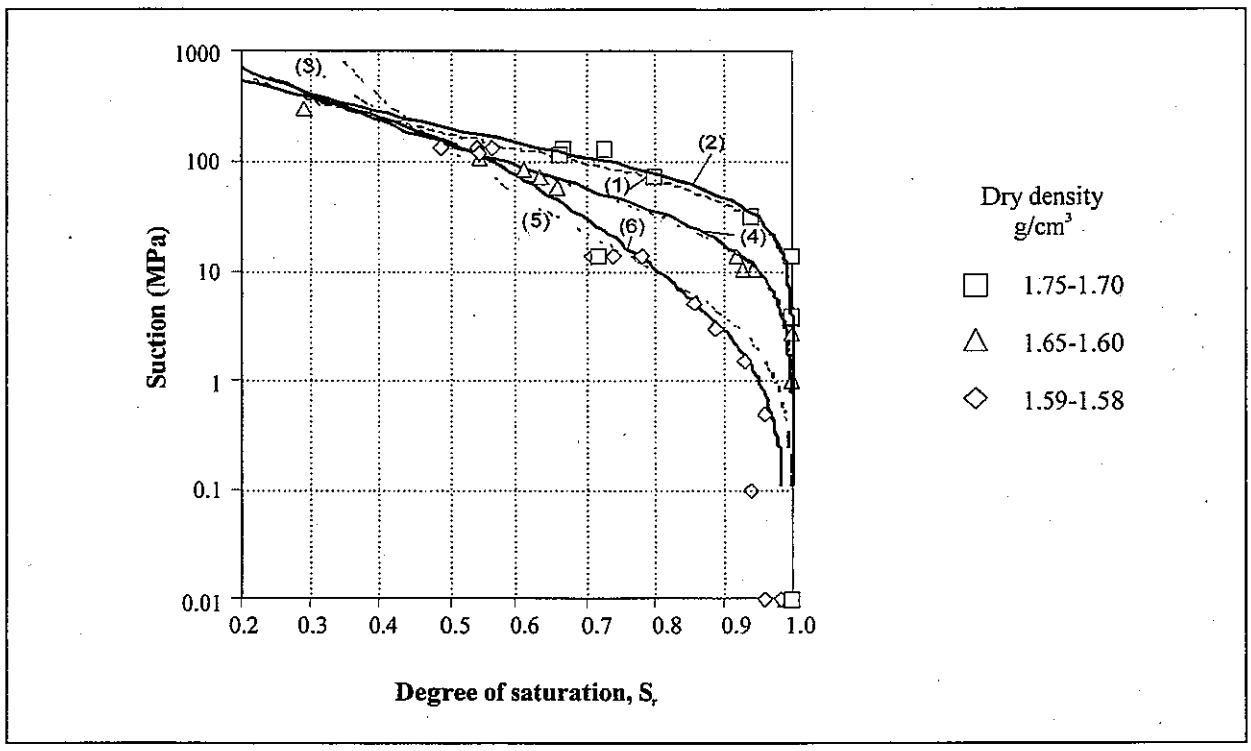

Figure 4-14 : Measured and fitted retention curves in wetting paths performed on confined samples. In parentheses, the number of the equation used in Table 4-8 is shown.

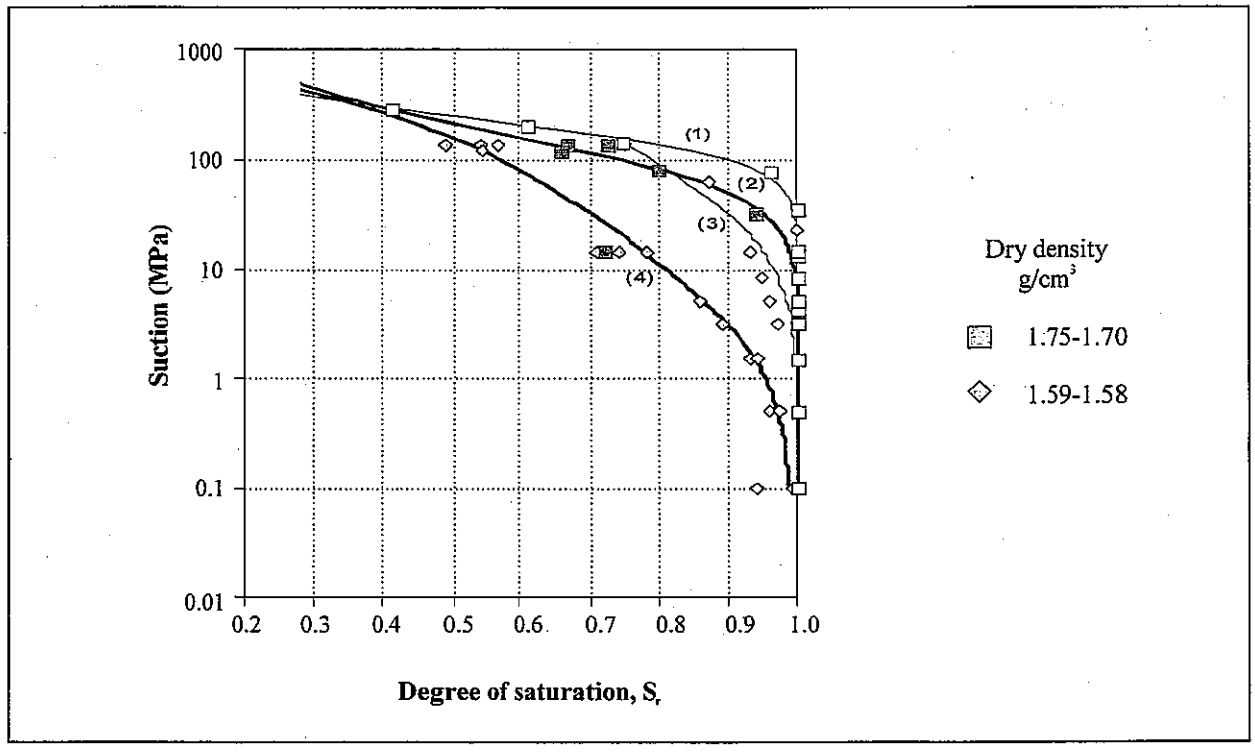

Figure 4-15 : Hysteresis effect on the wetting-drying paths under confined conditions. Bold symbols correspond to wetting paths. In parentheses the numbers of the curves indicated in Table 4-9.

4.2.2.4 Gas permeability

The gas permeability of the compacted clay has been determined using nitrogen gas as a fluid, injected at a low pressure (see CIEMAT-2.4). Specimens of nominal dry densities ranging from 1.50 to 1.70 g/cm^3 and with different water contents have been tested. The values obtained are plotted in Figure 4-16, together with the fitting obtained (valid only for the degree of saturation between 25 and 80 %):

$$K_g = 3.164 \cdot 10^{-6} [e(1 - S_r)]^{4.3} \qquad (r^2 = 0.82, 39 \text{ points})$$

where K_g (m/s) is the gas permeability, e the void ratio and S_r the degree of saturation.

The gas permeability for the same degree of saturation is a function of dry density and decreases with the degree of saturation, for the same dry density. In tests performed with the bentonite equilibrium water content compacted to different dry densities it was observed that gas permeability decreases logarithmically with increasing dry density.

In all of the tests performed, the values of intrinsic permeability obtained (which ranges between 10^{-16} and 10^{-12} m/s) are higher than those obtained when intrinsic permeability is calculated from hydraulic conductivity tests conducted with the clay under saturated conditions (Figure 4-17). This is due to the different structural disposition of the saturated and unsaturated specimens, caused by swelling of the clay as it hydrates. In water flow tests performed under saturated and confined conditions, the bentonite tries to swell and fill the interaggregate pores. Under these conditions, mean pore diameter is close to intra-aggregate pore size (about 0.01 μm). In the case of gas flow under dry conditions, this flow takes place through interaggregate pores with a diameter of more than 1 μm. This difference in accessible pore size may explain the different values of intrinsic permeability that have been derived from water and gas flow.

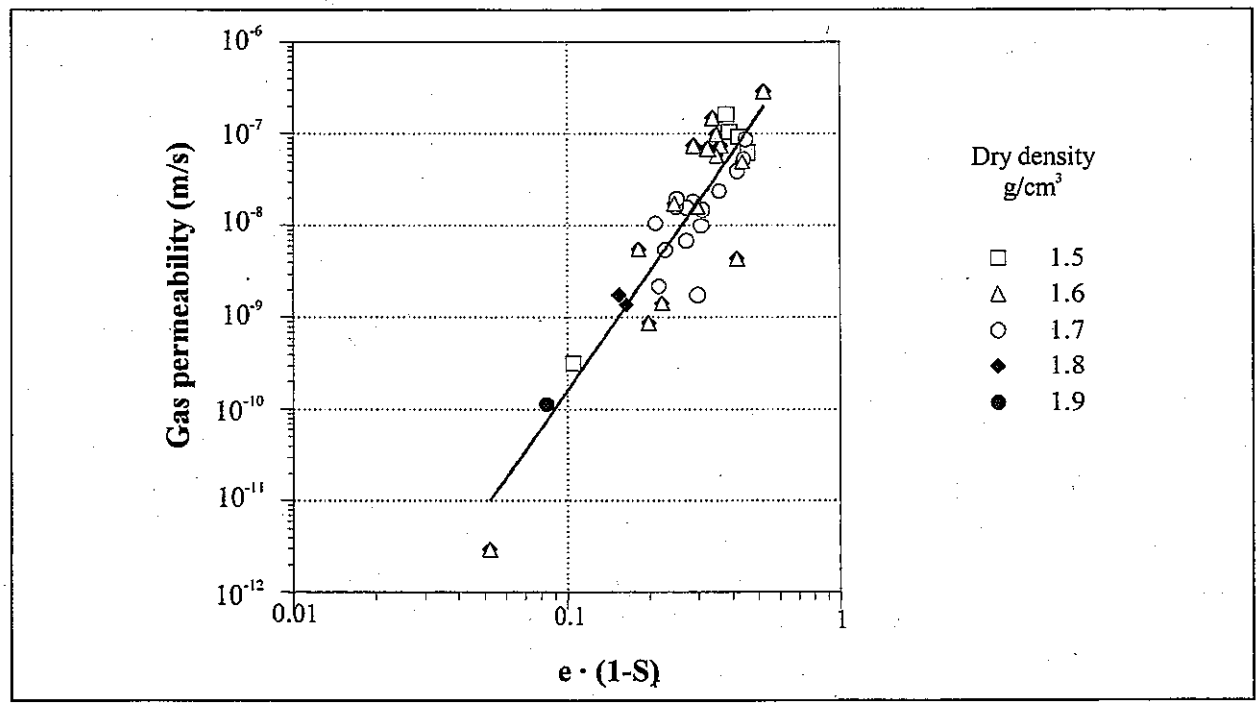

Figure 4-16 : Gas permeability measured in specimens of FEBEX bentonite compacted to different dry densities and with varying water content.

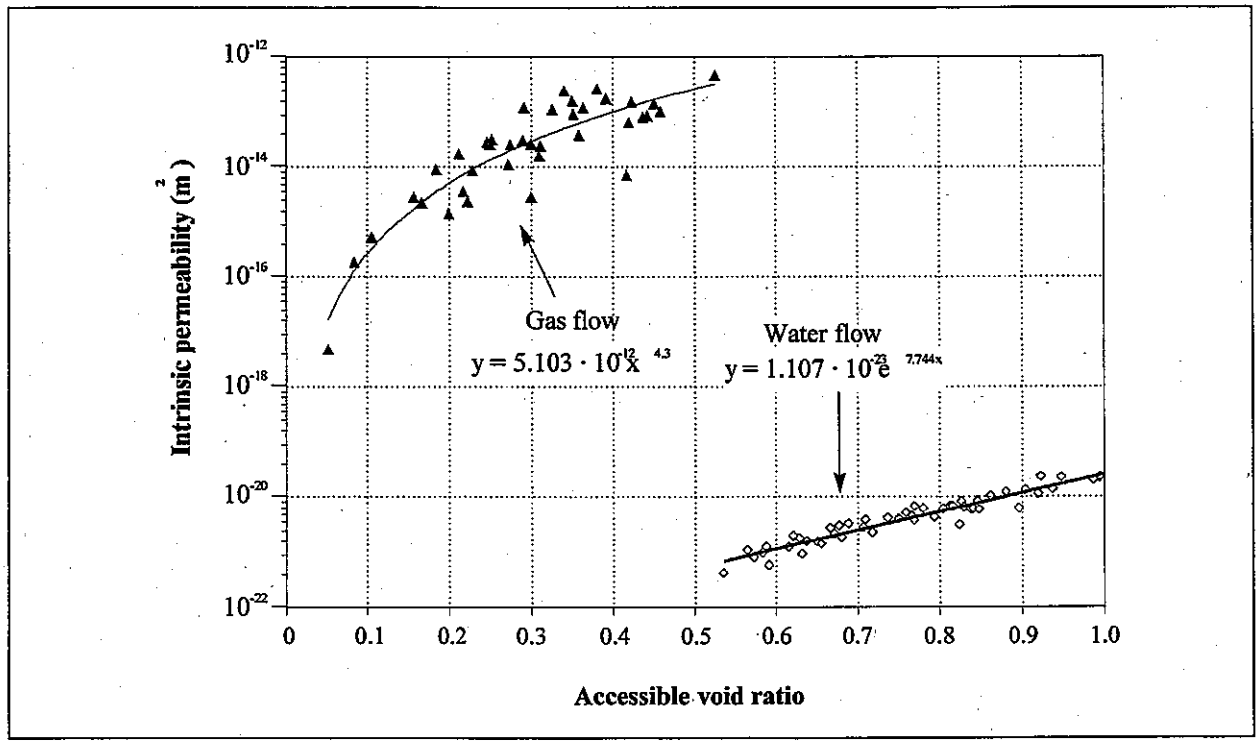

Figure 4-17 : Intrinsic permeability of the compacted clay obtained from saturated water flow and from unsaturated gas flow tests. In gas flow tests, the accessible void ratio indicates the ratio between gas accessible pore volume and particle volume ($e(1-S_r)$).

4.2.3 Thermal properties

4.2.3.1 Specific heat

Specific heat has been determined only for bentonite S-2 (see CIEMAT-2.2). The relationship between specific heat and temperature fit the following equation, in a range of temperatures of between 45°C and 150°C:

$$c_s = 1.38 \cdot T + 732.5$$

where c_s is the specific heat, in J/kg°C, and T is the temperature, in °C.

4.2.3.2 Thermal conductivity

The superficial thermal conductivity of the FEBEX bentonite has been determined in compacted specimens at various nominal dry densities and with different water contents.

Figure 4-18 shows the regression curves of the values of superficial thermal conductivity as a function of the degree of saturation, for bentonites S-2 and FEBEX (see CIEMAT-2.2). A good correlation of the sigmoidal type (Boltzmann) was obtained for the two bentonites by means of the following equation:

$$\lambda = A_2 + \frac{A_1 - A_2}{1 + e^{(S_r - x_0)/d_x}}$$

where λ is the thermal conductivity, in W/m·°K, S_r is the degree of saturation, A_1 is the value of λ for $S_r = 0$, A_2 is the value of λ for $S_r = 1$, x_0 is the degree of saturation for which the thermal conductivity is the average value between the extreme values, and d_x is a parameter. Table 4-10 shows the parameters obtained in the fitting of the curves.

There is a difference between the values measured for FEBEX and S-2 bentonite (see Figure 4-18). This difference is more noticeable for lower values of the degree of saturation. No clear evaluation of the differences is possible, because thermal conductivity increases not only with the water content but also with dry density. In addition, for the bentonite S-2, there are only two points for the lower degrees of saturation. However, taking into account all the experimented points, differences between the two bentonites seem to be small.

Table 4-10 : Parameters for fitting of the drying paths after saturation.

parameter	bentonite S-2	FEBEX bentonite
A_1	0.39 ± 0.08	0.57± 0.02
A_2	1.34 ± 0.06	1.28 ± 0.03
x_0	0.54 ± 0.03	0.65 ± 0.01
d_x	0.15 ± 0.03	0.10 ± 0.02

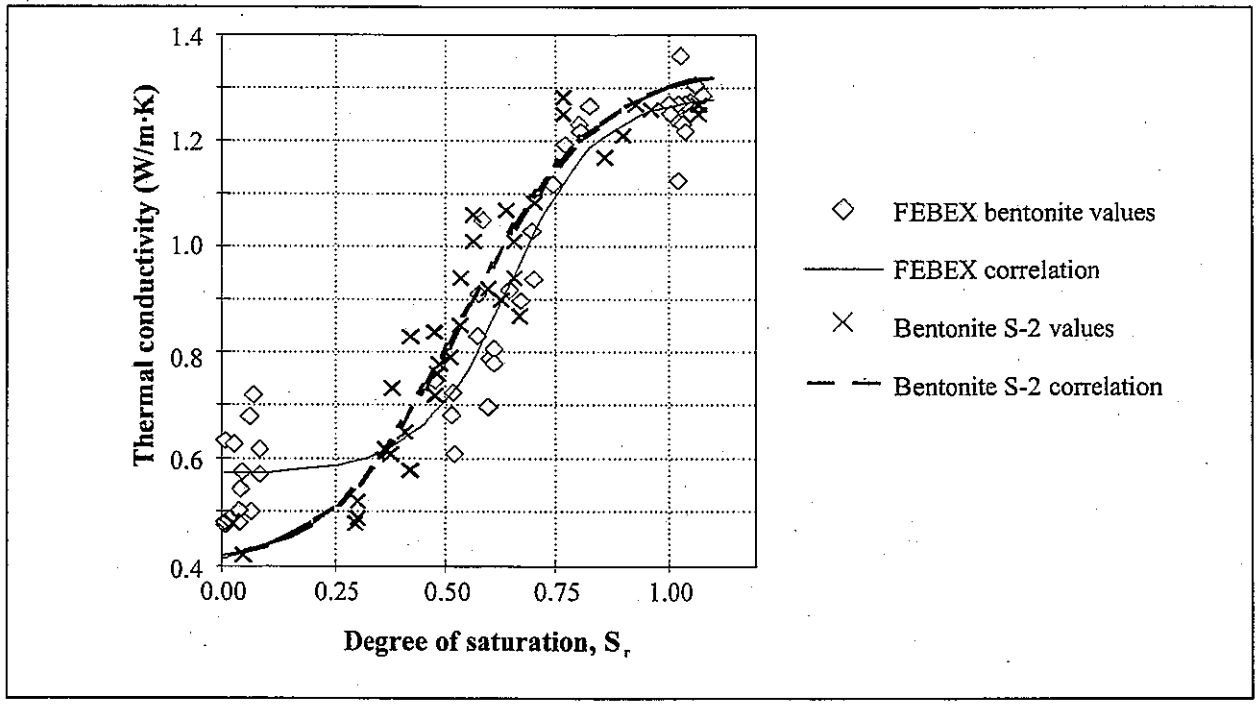

Figure 4-18 : Thermal conductivity as a function of degree of saturation.

4.2.3.3 Coefficient of linear thermal expansion

Measurements of thermal expansion have been carried out on 12 samples of compacted bentonite for initial dry densities ranging between 1.57 and 1.72 g/cm^3 and a water content varying between 12.5 and 25.1 % (see UPC-2.3). The specimens (38 mm in diameter, 76 mm in height) were placed in an isothermal bath with controlled temperature. A latex membrane keeps the overall water content of the soil constant throughout the heating and cooling processes. Temperature varies between 25 and 70 °C. In each test, several cycles of heating and cooling are applied to the sample.

The vertical strains in the first heating path are higher than the strains measured during the second and subsequent cycles. In addition, in each cycle the strains measured during the heating process are higher than those observed throughout the cooling path and, as a result, an accumulation of irreversible strains is observed. The slope of the relationship between temperature and strain is shown in Figure 4-19. This slope increases slightly with temperature.

The following correlations for the linear thermal expansion coefficient have been obtained from this figure:

$$\Delta\varepsilon_z/\Delta T = -0.118\cdot10\text{-}4 + 6.5\cdot10^{-6}\,T \quad \text{(first heating)}$$
$$\Delta\varepsilon_z/\Delta T = -1.265\cdot10\text{-}4 + 6.5\cdot10^{-6}\,T \quad \text{(subsequent heating paths)}$$
$$\Delta\varepsilon_z/\Delta T = -1.538\cdot10\text{-}4 + 6.5\cdot10^{-6}\,T \quad \text{(cooling paths)}$$

where ε_z is the linear strain and T the temperature in °C. At temperatures higher than 55°C, an increase in the dispersion of the results is observed. This dispersion is due to experimental difficulties, such as equipment calibration and specimen sealing.

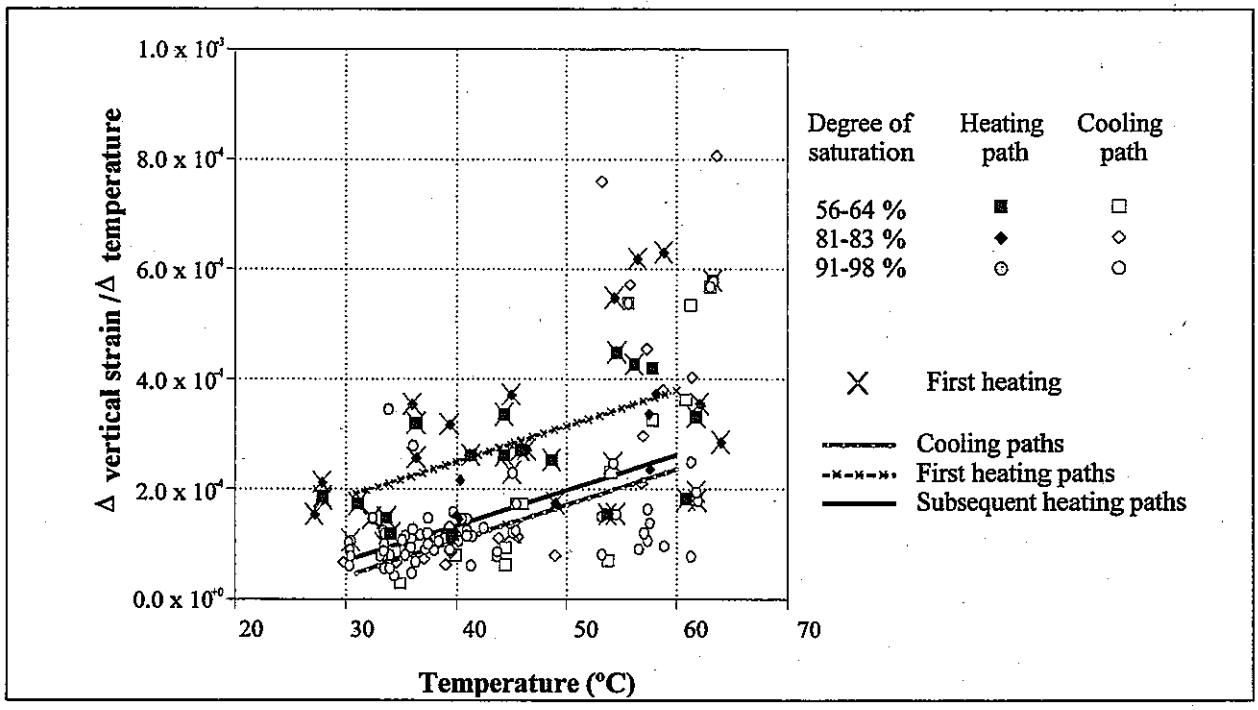

Figure 4-19 : Linear thermal expansion as a function of temperature.

4.3 Thermo-hydro-mechanical tests

4.3.1 Tests for calibration of models by backanalyses. Thrmohydraulic cell.

A general methodology has been developed for the performance of systematic backanalysis of laboratory tests involving the thermohydraulic behaviour of bentonite. The procedure is based on a maximum likelihood approach, which defines a probabilistic framework in which error measurements and the reliability of the parameters identified can be estimated. With a view to identifying the model parameters, an objective function incorporating the differences between measured data and model predictions is minimized (see UPC-2.2). The method is applied to the identification of certain thermal and hydraulic properties of a bentonite specimen, using temperature and water content measurements as input data. The finite element code "CODE BRIGHT" (V2.0) has been used to model the thermohydraulic behaviour of clay. Although the code allows the mechanical behaviour of soils to be studied in a coupled manner, only the thermal and water flow capacities of the code have been used.

A new testing device has been developed to obtain the data required for the identification of certain thermohydraulic parameters. A controlled heat flux is applied at one end of a cylindrical specimen (38 mm in diameter, 76 mm long) and the other end is maintained at constant temperature. A latex membrane, that allows deformation and keeps overall water content constant, and a 5.5 cm thick heat insulating deformable foam surrounds the specimen. In order to ensure knowledge of the heat flux crossing the sample, two specimens symmetrically placed with respect to the heater are used in the tests. The heater is a copper cylinder (38 mm diameter, 50 mm long) with five small electrical resistances inside. A constant power of 2.6 W has been used in the tests, allowing steady temperatures in the range of 70-80 °C to be reached at the hotter end of the specimen. At the cold end, a constant temperature of 30°C is maintained by flowing water in a stainless steel head in contact with the soil. Figure 4-20 shows a scheme of the thermohydraulic cell.

Axisymmetric analyses performed with CODE BRIGHT allowed the effect of lateral loss of heat to be evaluated. It was estimated as 60% of total heater power. This indicates the importance of performing a 2D analysis of the experiment.

During the tests, the temperatures at both ends of the specimen, and at three internal points located at regular intervals, are monitored. At the end of the tests, changes in diameter were measured at some points of the specimen, with an accuracy of up to 0.01 mm. Finally, the soil samples were cut in six small cylinders and the water content of each slice was determined.

Three specimens of bentonite compacted at a dry density of 1.68 g/cm^3 and with water contents of 15.3,16.9 and 17.1 % were tested. The temperatures measured during the heating period for one of the specimens are shown in Figure 4-21. Temperature reaches a quasi-steady regime 10 hours after the start of the test.

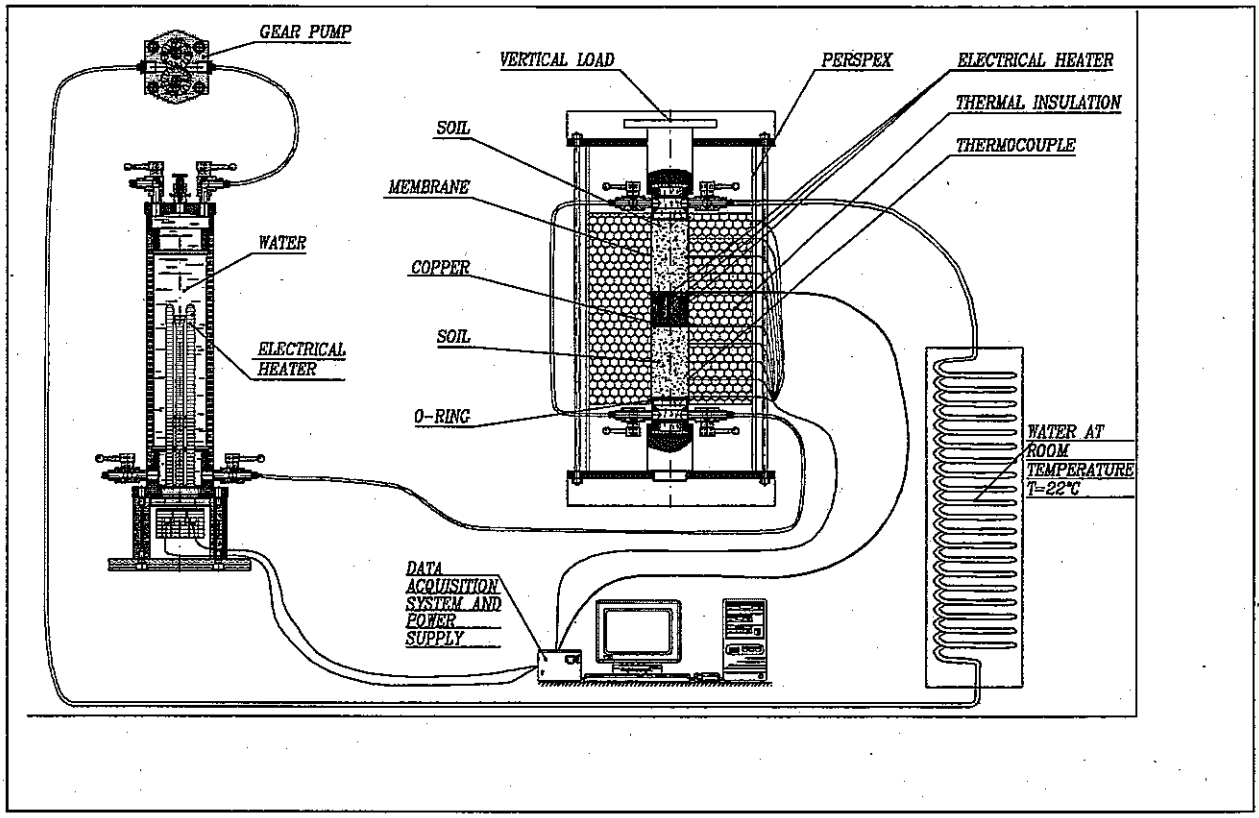

Figure 4-20 : Scheme of the thermohydraulic cell.

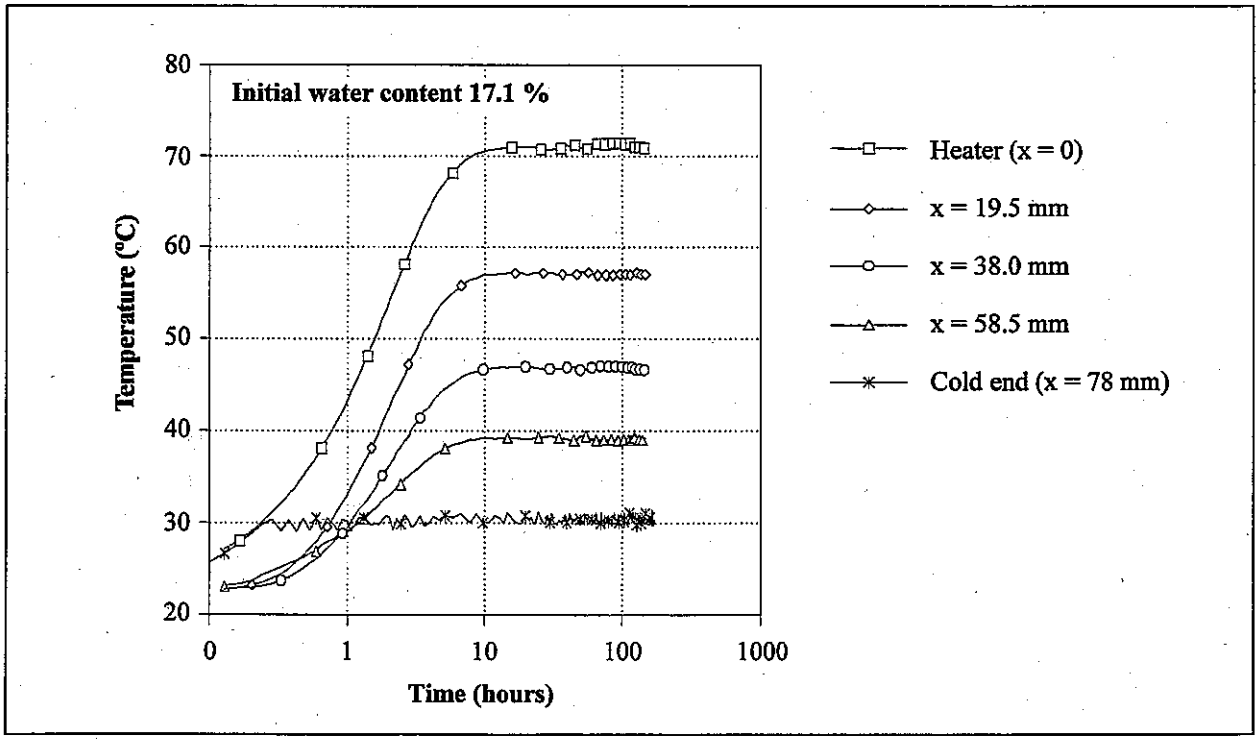

Figure 4-21 : Evolution of temperature in a prescribed heat flow test.

A fully coupled thermo-hydraulic model has been used to simulate the experiment. The temperatures obtained under steady-state conditions and the water content measured at the end of the test have been considered as input data. In each test, three parameters have been identified: the conductivity of bentonite under saturated conditions, λ_{sat}, needed to obtain unsaturated thermal conductivity ($\lambda = (\lambda_{sat})^{Sr} (\lambda_{dry})^{(1-Sr)}$); the tortuosity, τ, (a parameter of the diffusion constant) and the exponent "n" for the unsaturated (relative) permeability law ($k_r=S_r^n$). The thermal conductivity under dry conditions (λ_{dry}) is fixed at 0.47 W/m°C. The parameters obtained during the identification process are similar but not identical in the three tests, as shown in Table 4-11. The values are within the normal range of these parameters. In addition, the identification technique provides a systematic and consistent procedure allowing the parameters that best reproduce the measurements for the selected model to be found. The method also gives an insight into the model structure, and allows the dependence and coupling between parameters to be detected. In the present type of test, analysis of the model structure shows that the values of the parameter "n" that has been obtained entail a higher degree of uncertainty than the values of the other parameters. This is in accordance with the relative influence of water flow in liquid and vapour phases.

Table 4-11 : Exponent n in relative permeability law, tortuosity factor τ and saturated thermal conductivity λ_{sat} obtained from different thermal flow tests.

test	water content	n	τ	λ_{sat} W/m°C
1	15.5	3.06	0.56	1.19
2	16.9	1.10	0.74	1.31
3	17.1	1.08	0.90	1.18

The optimization procedure showed that there are a few combinations of parameters that give similar result in terms of the objective function. This is reasonable, as measured water content is a global quantity, and it is difficult to distinguish between water transported by liquid flow (controlled by "n") and by vapour diffusion (controlled by τ).

Figure 4-22 shows the objective function in terms of the tortuosity factor τ and the exponent "n" for the relative permeability law, for one of the controlled heat flow tests. In order to give the same importance to the sets of measurements for temperature and water content, a weighting procedure has been used to define the objective function. Contours are isolines of the objective function with different combinations of the parameters. The parameter values obtained by backanalysis are located at the minimum of the objective function. The same figure includes points representing the values of the parameters obtained in the other backanalyzed tests. In the case of the hydraulic tests described in Section 4.2.2.2 only the exponent "n" is known. In all cases, the representative points are located in the same area of the objective function, with similar values of error. A set of optimum parameters and laws (see Table 4-12) may be selected taking all the tests into account.

Table 4-12 : Values for the saturated hydraulic conductivity k_{sat}, the relative permeability k_r, the tortuosity factor τ and the thermal conductivity λ.

parameter	value
$k_{sat(porosity=0.4)}$	$2 \cdot 10^{-21}$ m^2
k_r	S_r^3
τ	0.8
λ (W/m°C)	$0.47^{1-Sr}\ 1.15^{Sr}$

This set of parameters has been used to solve the direct problem and to simulate some water infiltration and heat flow tests. Figure 4-23 to Figure 4-26 show that the agreement between the measurements and the model predictions is satisfactory.

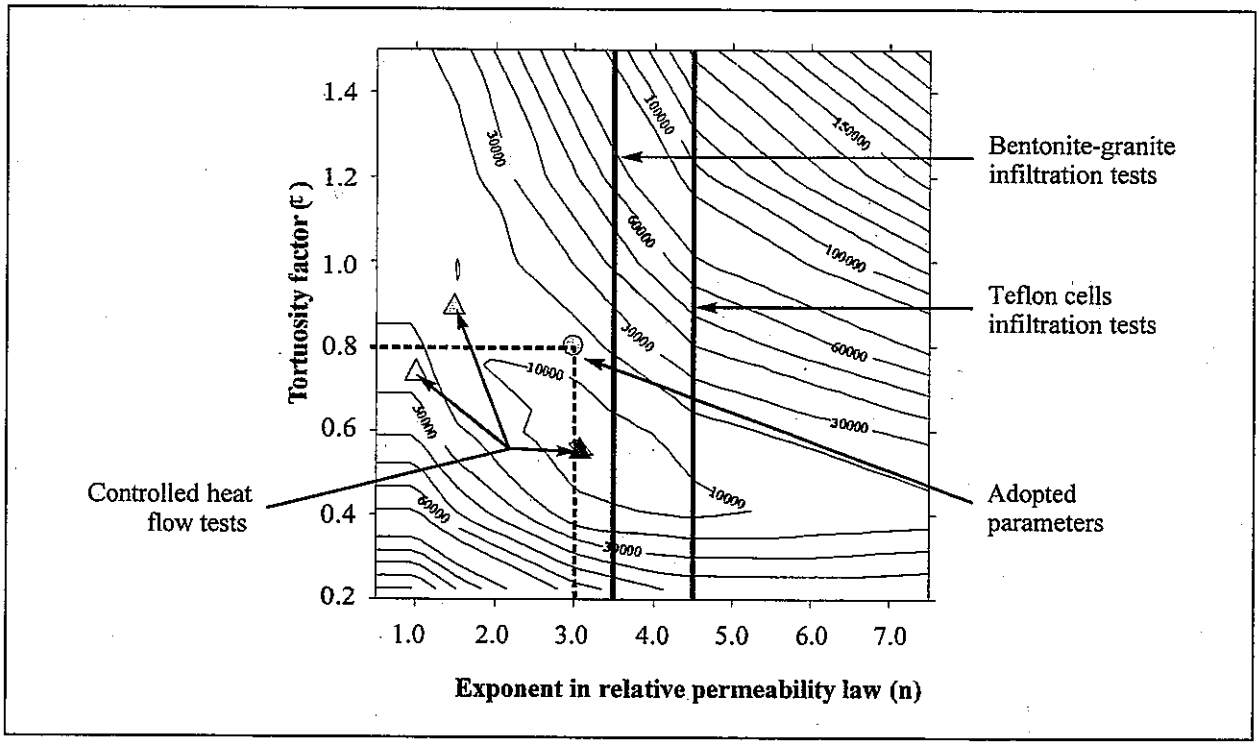

Figure 4-22 : Contour map of objective function in the case of thermal flow test 1 (see details in Table 4-11). The same graph shows the parameter values obtained by backanalyzing different tests.

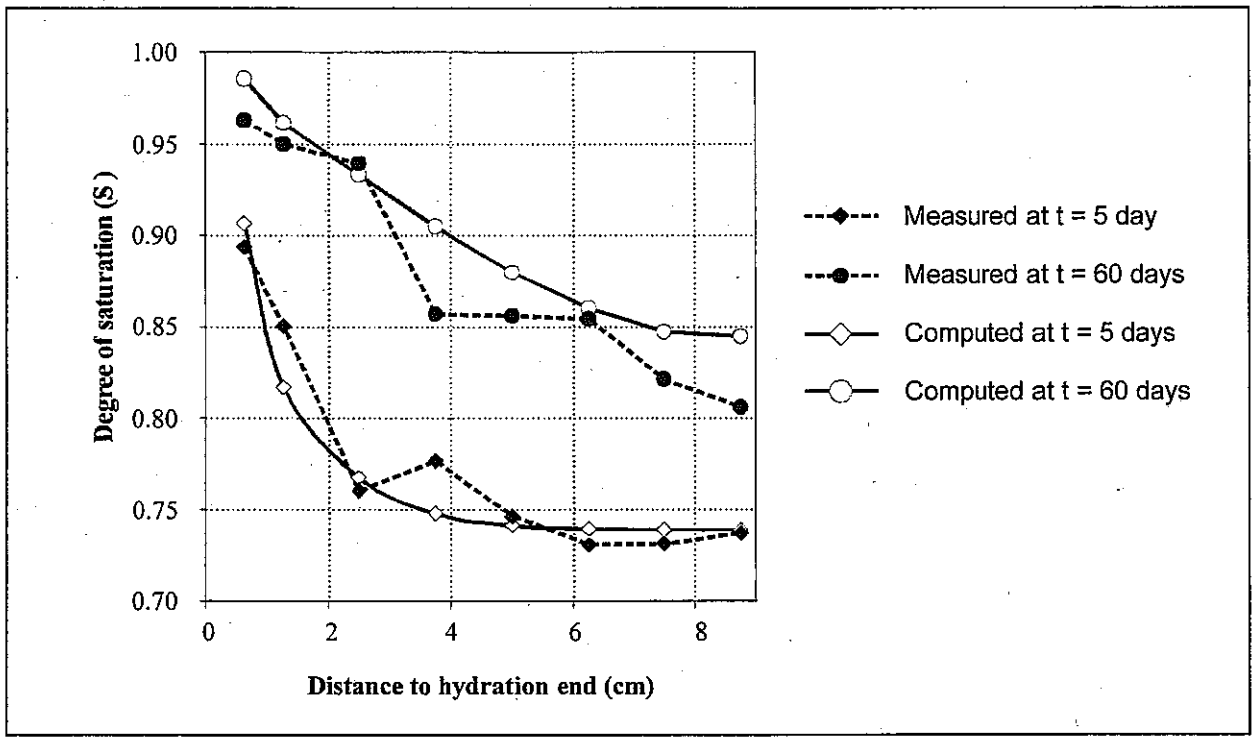

Figure 4-23 : Measured and computed degree of saturation in small cell infiltration tests carried out in CIEMAT, using the final selected parameters.

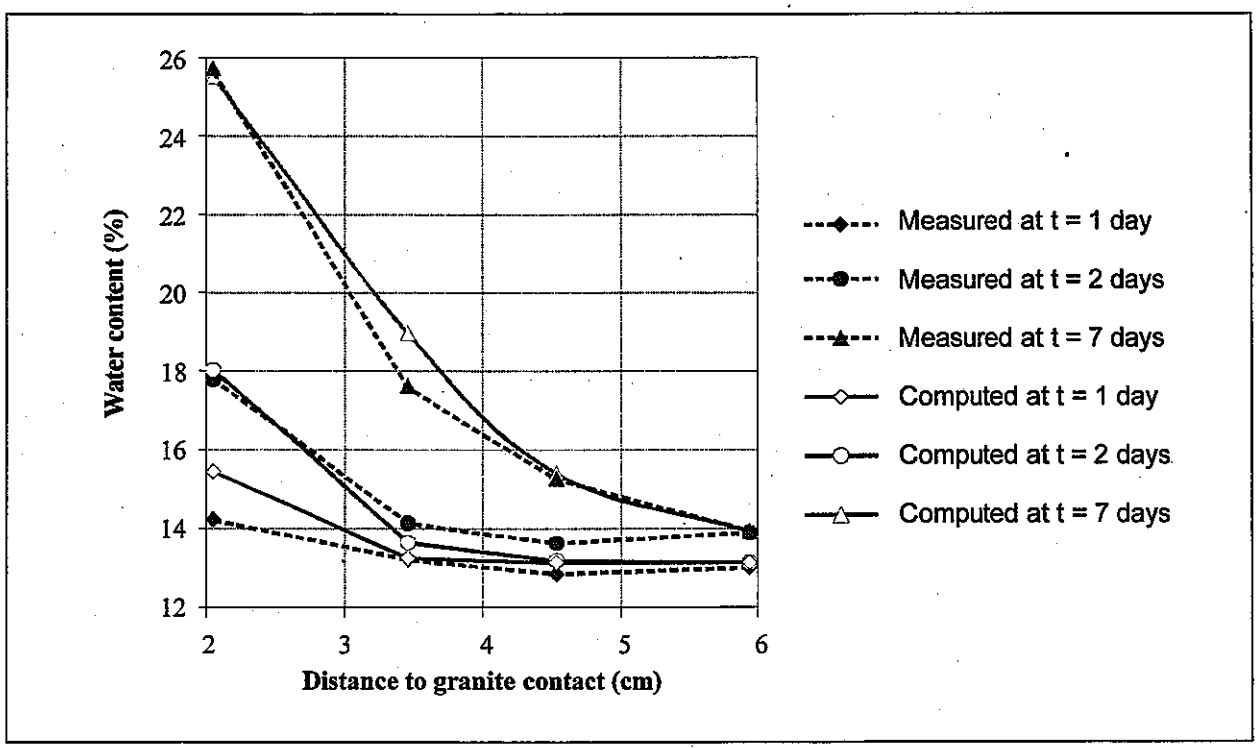

Figure 4-24 : Measured and computed water content in bentonite-granite infiltration tests carried out at UPC, using the final selected parameters.

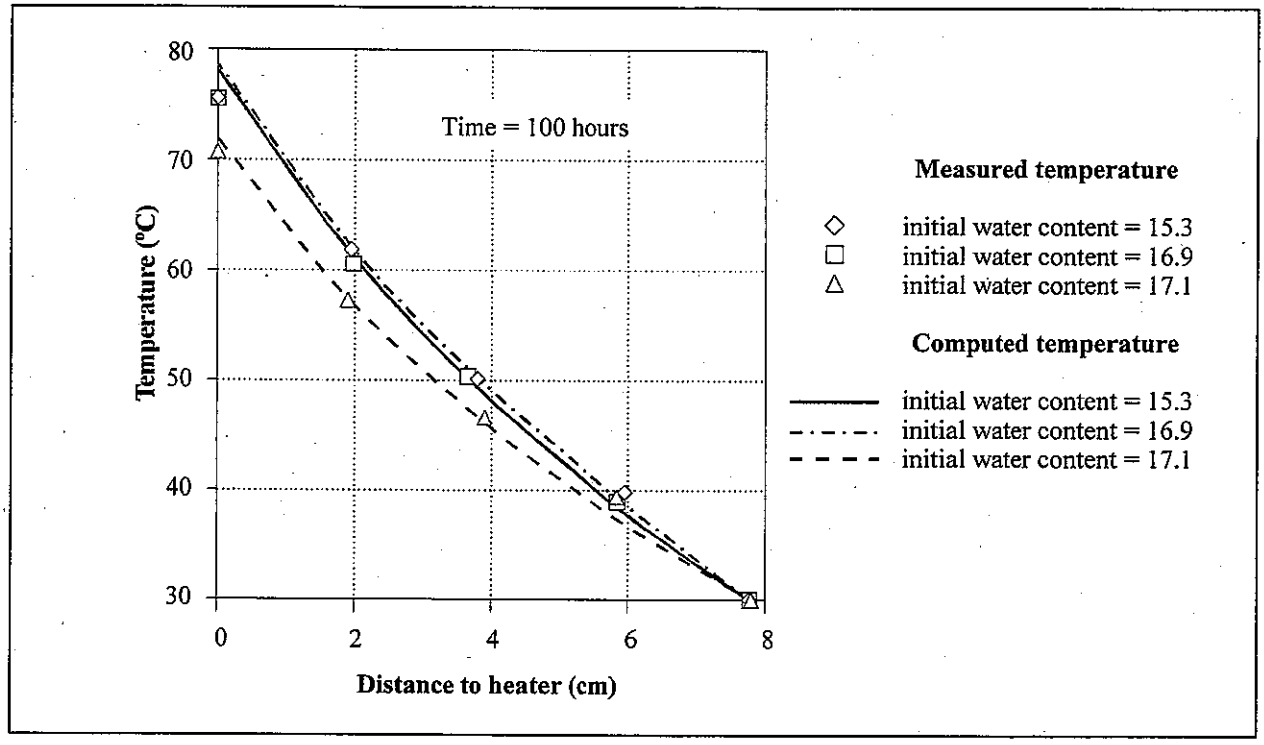

Figure 4-25 : Measured and computed temperature in prescribed heat flow tests, using the final selected parameters.

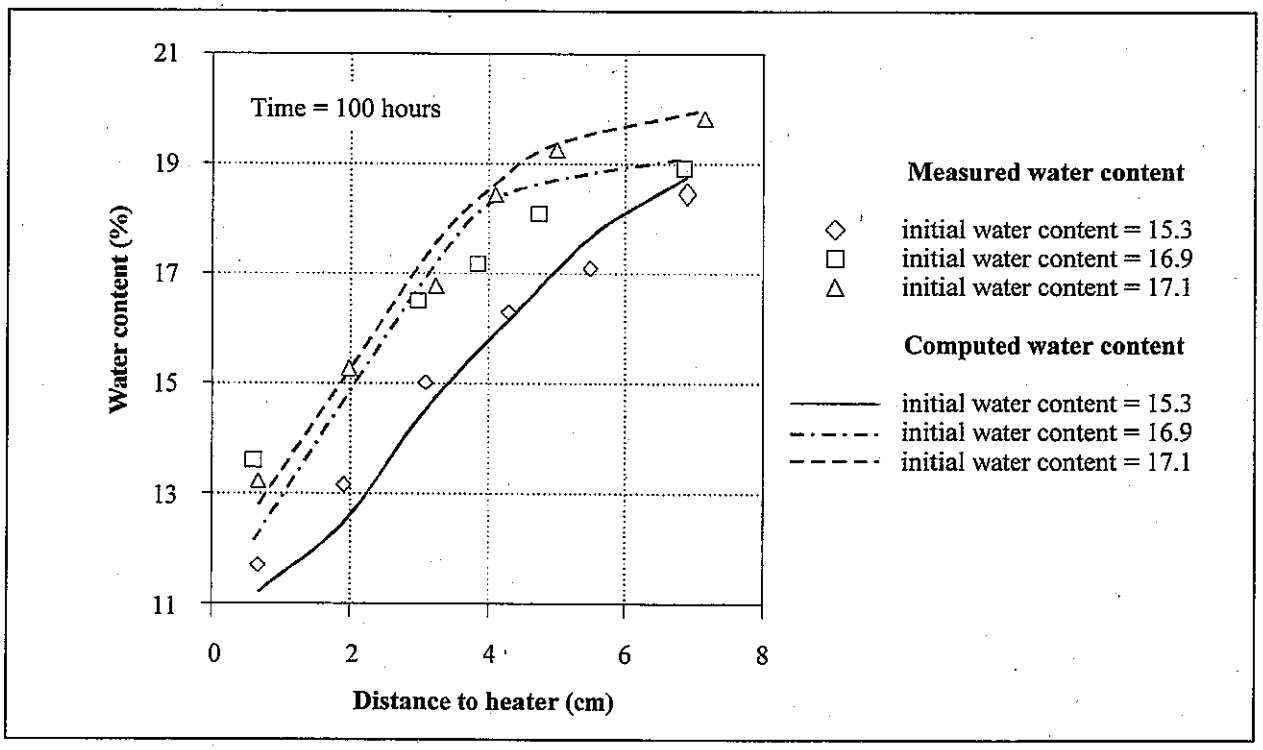

Figure 4-26 : Measured and computed water content in prescribed heat flow tests, using the final selected parameters.

4.3.2 Mechanical properties: oedometric tests with controlled suction

Suction controlled oedometer tests have been performed at CIEMAT (24 tests) (see CIEMAT-4.1) and UPC (5 tests) (see UPC-2.7) on compacted bentonite with a water content in equilibrium with the laboratory conditions, and at dry densities of 1.7 and 1.65 g/cm^3 respectively. Three types of paths have been followed. In the first type, simulating the behaviour of a point near the heater, an initial drying process is followed by a loading path, and finally the bentonite is saturated. In the second type, simulating a point near the external boundary, an initial path of suction decrease is followed by an increase in load. In the third case, aimed at reproducing a swelling pressure test, an attempt was made to maintain the height of the sample constant during a suction reduction path by applying increments of vertical load. Suction is applied, with the relative humidity of the air on the sample being controlled by means of sulfuric acid or salt solutions in the high suction range, and by the axis translation technique in the case of suctions ranging from 0 to 14 MPa.

Figure 4-27, reproduces the results of two of the tests carried out at CIEMAT (EDS3_9 and EDS5_5). The volume changes measured reflect the typical behaviour of compacted clay. It may be observed that for a small value of vertical load the vertical strains on saturation are higher than when a high load is applied. At the same time, the strain under the loading path is higher when the soil is in saturated conditions after reaching important swelling strains. Figure 4-28 and Figure 4-29 show the experimental results in the case of suction decrease paths with different values of applied vertical load and load increase paths with different values of applied suction.

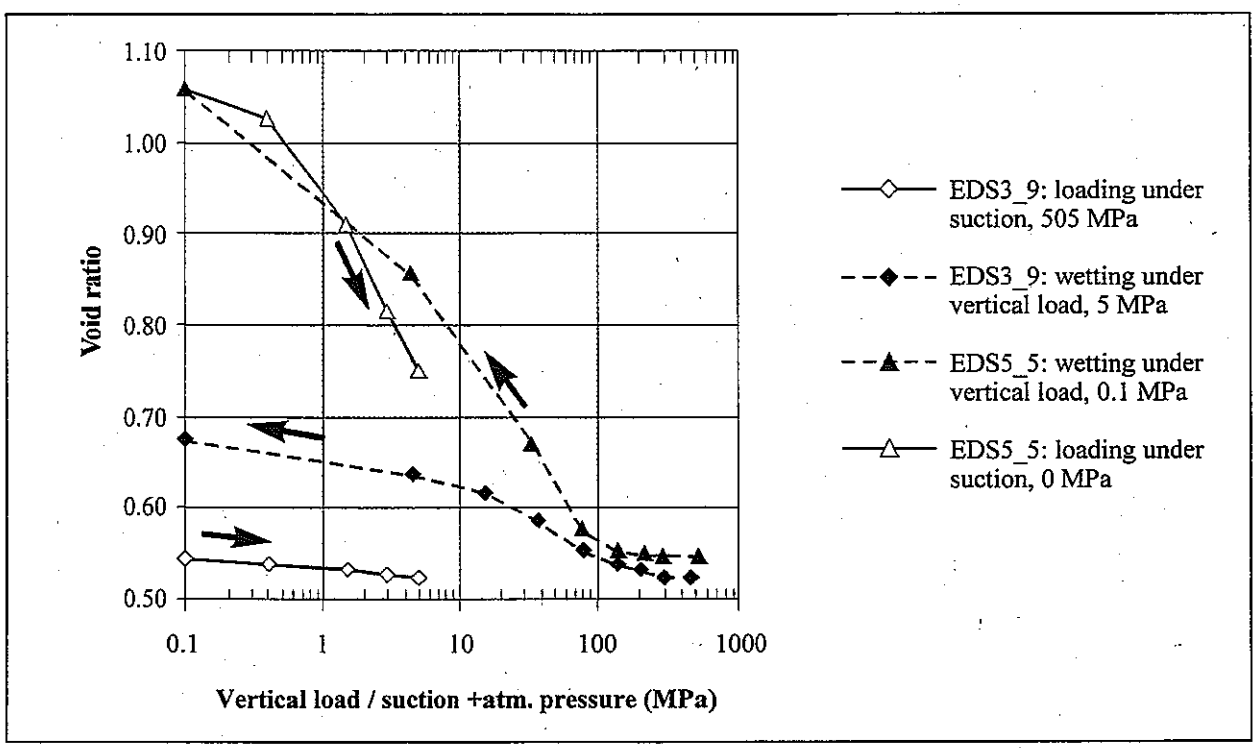

Figure 4-27 : Typical results in two suction controlled oedometer tests on compacted bentonite with an initial density of 1.7 g/cm^3.

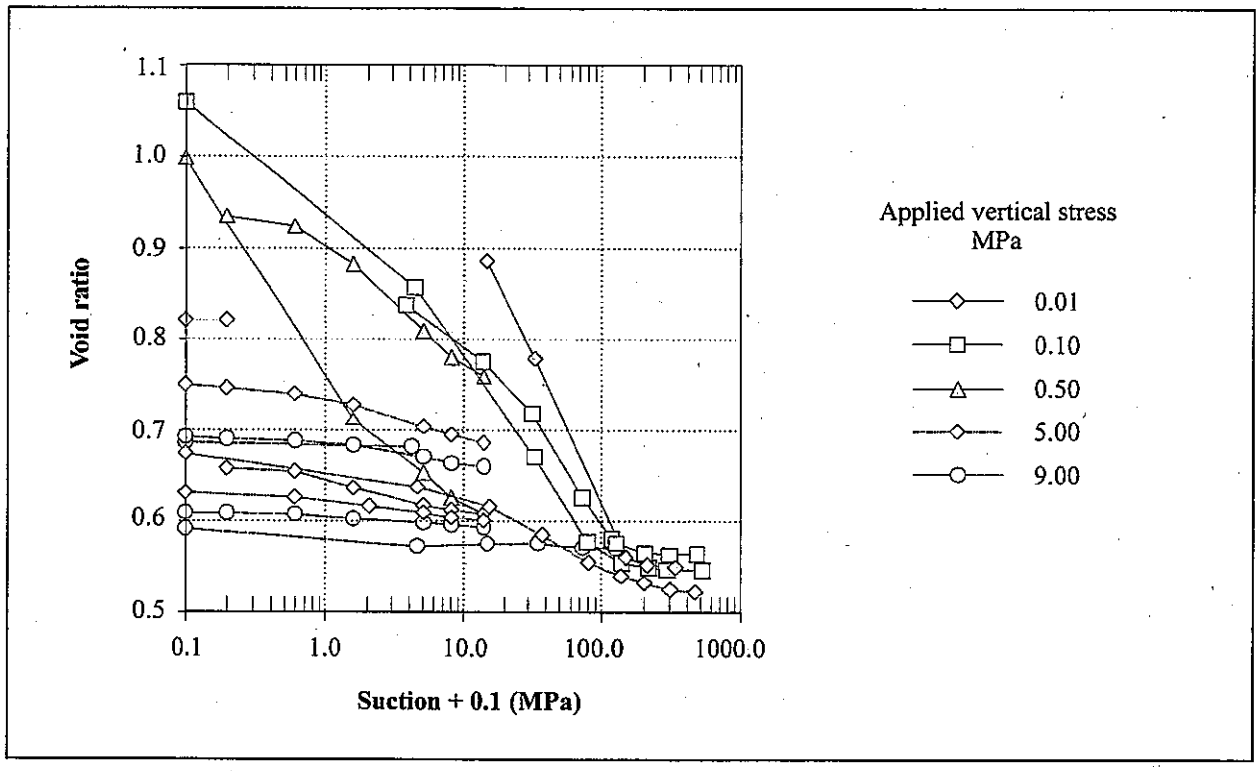

Figure 4-28 : Volume changes measured in suction controlled oedometer tests, in wetting paths under different loads. Initial dry density 1.7 g/cm^3.

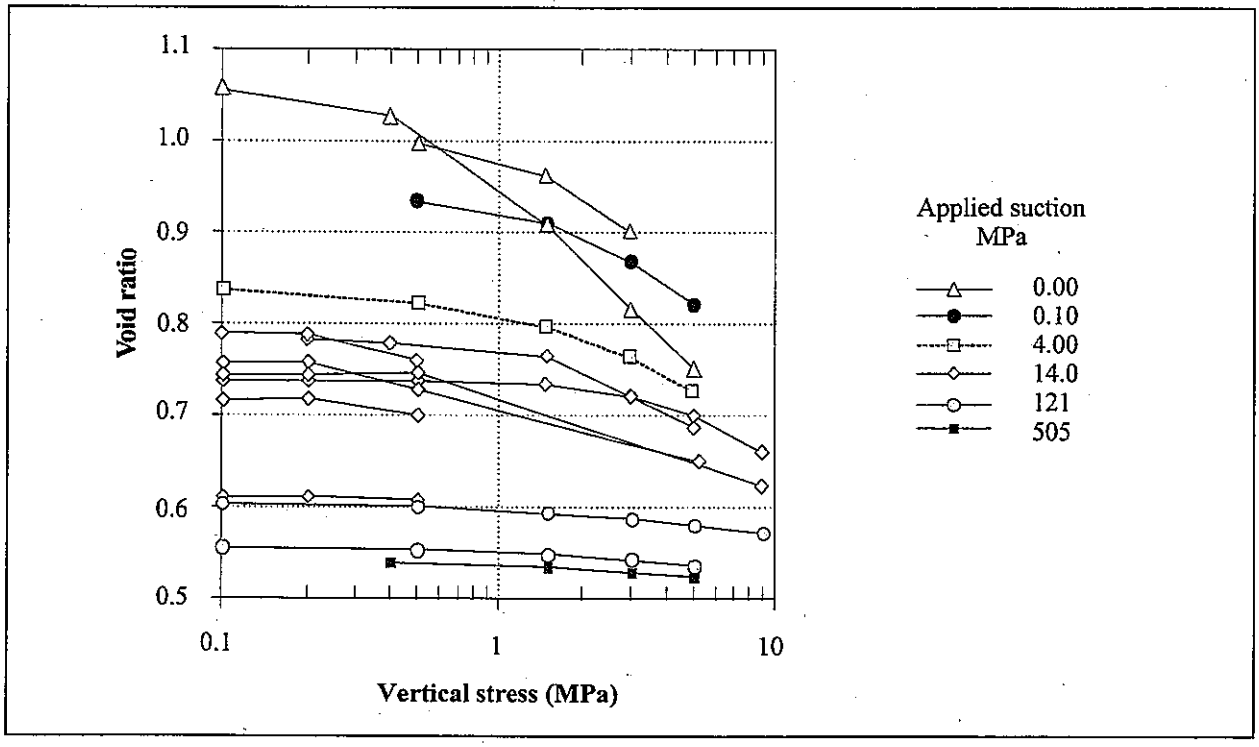

Figure 4-29 : Volume changes measured in suction controlled oedometer tests, in loading paths under different suctions. Initial dry density 1.7 g/cm^3.

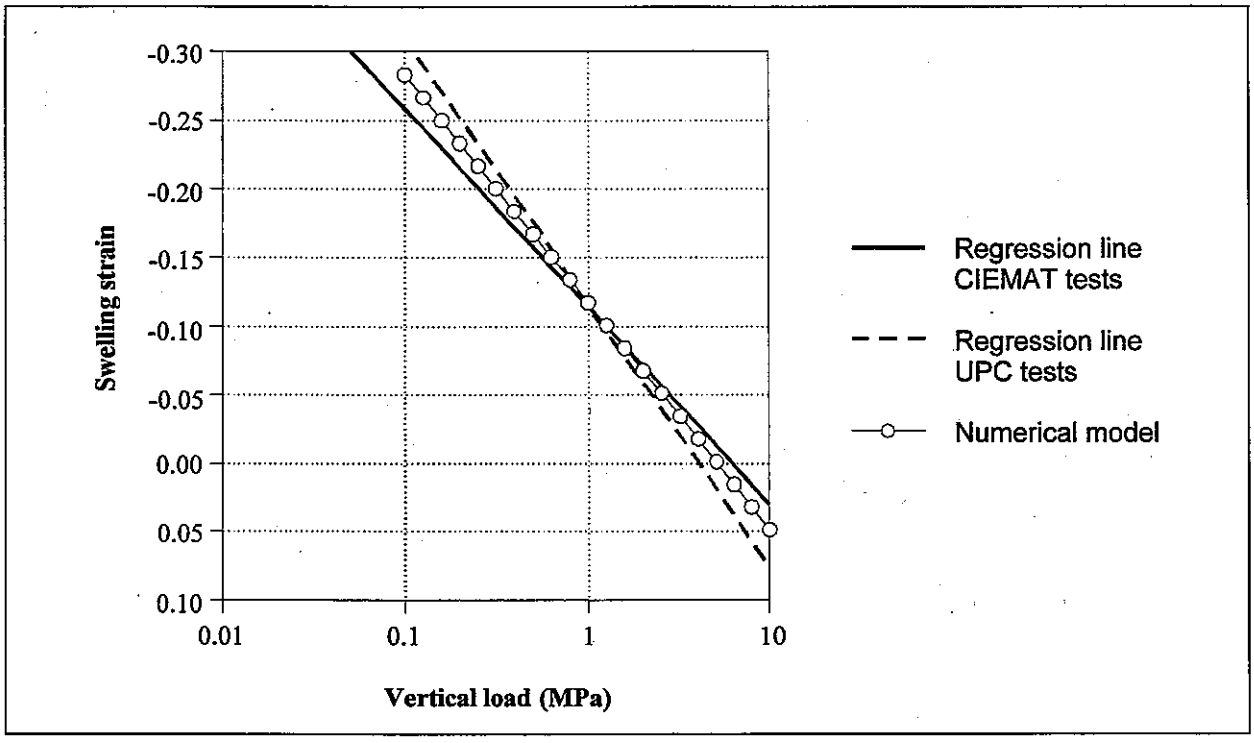

Figure 4-30 : Comparison between swelling strains measured at the CIEMAT and UPC laboratories and computed strains obtained from constitutive equations used in numerical modelling (initial dry density 1.60 g/cm^3).

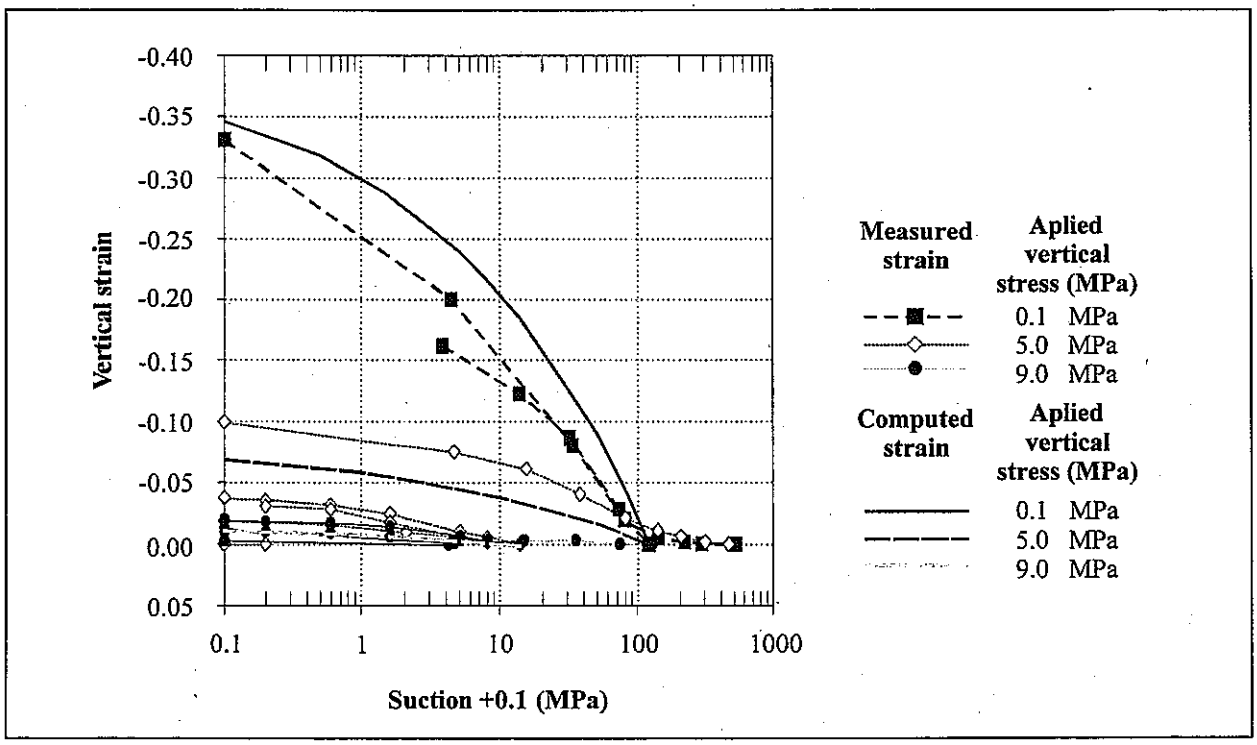

Figure 4-31 : Comparison between swelling strains measured in suction controlled oedometer tests performed by CIEMAT and computed strains obtained from constitutive equations used in numerical modelling.

In order to find the hydromechanical parameters of the constitutive model of the bentonite, tests were simulated by means of a numerical tool (CODE BRIGHT). A trial and error technique was used to reproduce the results of both the swelling pressure and swelling under load tests described in Sections 4.2.1.3 and 4.2.1.4. Figure 4-30 shows a comparison between the numerical model predictions and the swelling strains measured at the CIEMAT and UPC laboratories.

Using the parameters obtained from the swelling tests, the suction controlled oedometer tests may be modeled as a boundary value problem, using CODE BRIGHT. Figure 4-31 shows the results of both experimental and numerical model predictions in the case of wetting paths under different values of applied vertical stresses.

Some general comments may be made concerning the behaviour of the clay when subjected to different stress paths:

- As a result of equipment limitations, the compaction load of the specimens (about 20 MPa) has been higher than the highest external load applied in the oedometers (9 MPa). Furthermore, the samples have shown minor collapse (with suction decreasing to values of between 15 and 5 MPa) only when a high vertical load (9 MPa) is applied.

- High swelling strains have been measured in suction reduction paths in response to minor vertical stresses. The hydration process opens the bentonite structure (pore volume increases) developing irreversible swelling strains, and subsequently an important decrease in stiffness is measured when a vertical load is applied. In these cases, a yield point in the loading paths may be observed at relatively small vertical loads (Figure 4-29).

- Drying of the sample beyond suctions of 120 MPa, does not imply a significant decrease in volume. Furthermore, under suctions higher than this value the external load does not produce any important consolidation of the sample, which remains very stiff. After a drying/wetting cycle the swelling pressure of the clay remains almost unchanged, in keeping with the fact that plastic strains are small in suction increase paths.

4.3.3 Tests to advance knowledge of the THM behaviour of expansive clays

4.3.3.1 Hydraulic tests on joints

Hydraulic tests were performed on specimens in which joints were present, to gain insight into the influence of the joints of the clay barrier on its hydraulic behavior (see CIEMAT-4.2). The analysis included mainly the influence of joints on hydration rate, their sealing capacity (see Figure 4-32) and the modification that they induce on hydraulic conductivity. Different cylindrical cells with water inlet/outlet were used. The specimens were made from four compacted bentonite slices (with final dry densities ranging between 1.61 and 1.23 g/cm^3 and initial water content ranging between 15.0 and 11.7%), some with vertical diametral joints.

The main conclusions of this study are as follows:

- When hydration occurs under a given injection pressure, even if it is low, the volume of water taken up and its distribution inside the clay is controlled by the existence of joints (fissures), their volume and their configuration.

- The clay of the specimens takes the water both from the direct hydration surface and from the block joints. Figure 4-33 shows the final distribution of water content in two hydrated tests, in which four half-sectioned specimens were piled and hydrated from the top, illustrating this observation.

- The volume of water initially taken up depends on hydration pressure.

- Once the joints have been filled with water, the rate of water intake appears not to depend on injection pressure but on the dry density of the clay.

- The sealing of a joint, attained after hydration for 24 hours, is effective against hydraulic pressures of up to 5 MPa.

- Before sealing of the joints is attained, the strain experienced by every slice on saturation is the strain which corresponds to its initial dry density.

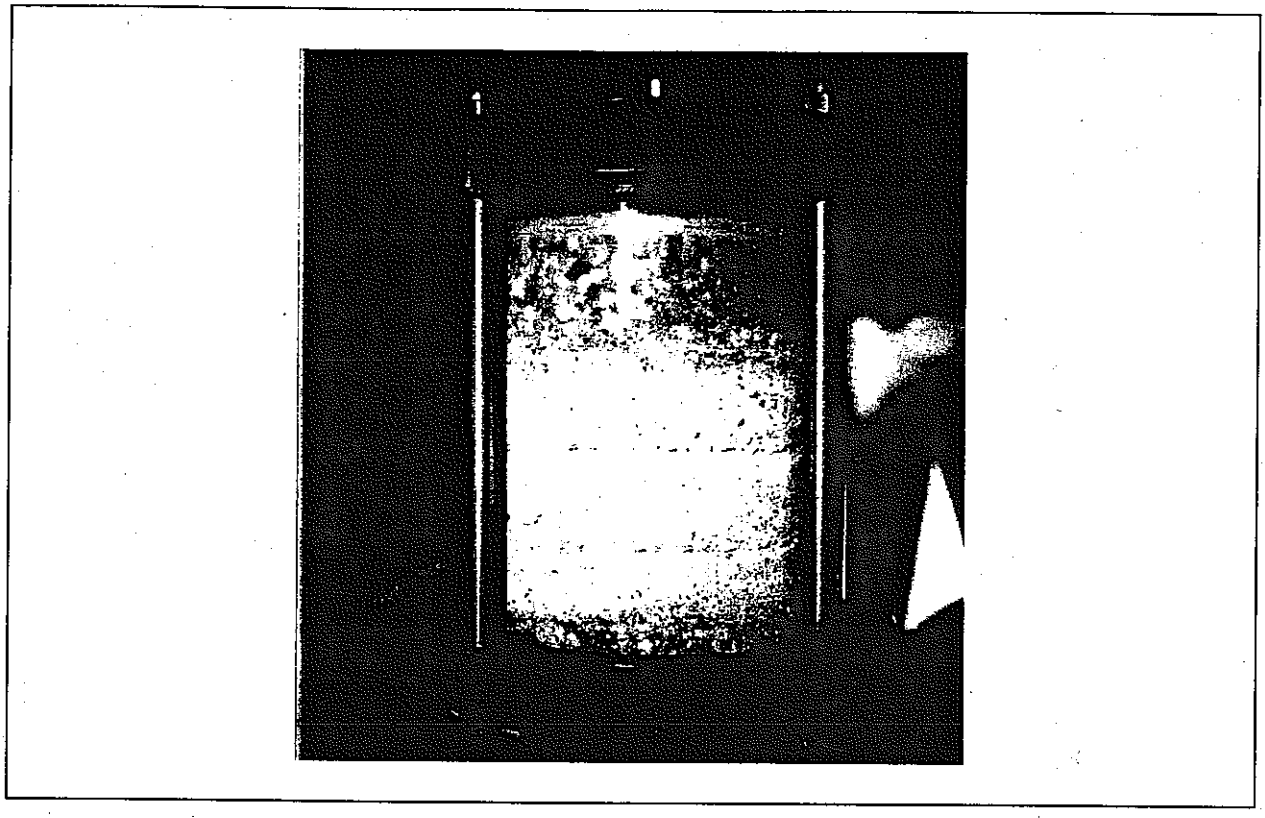

Figure 4-32 : Perspex cell used in joint sealing tests.

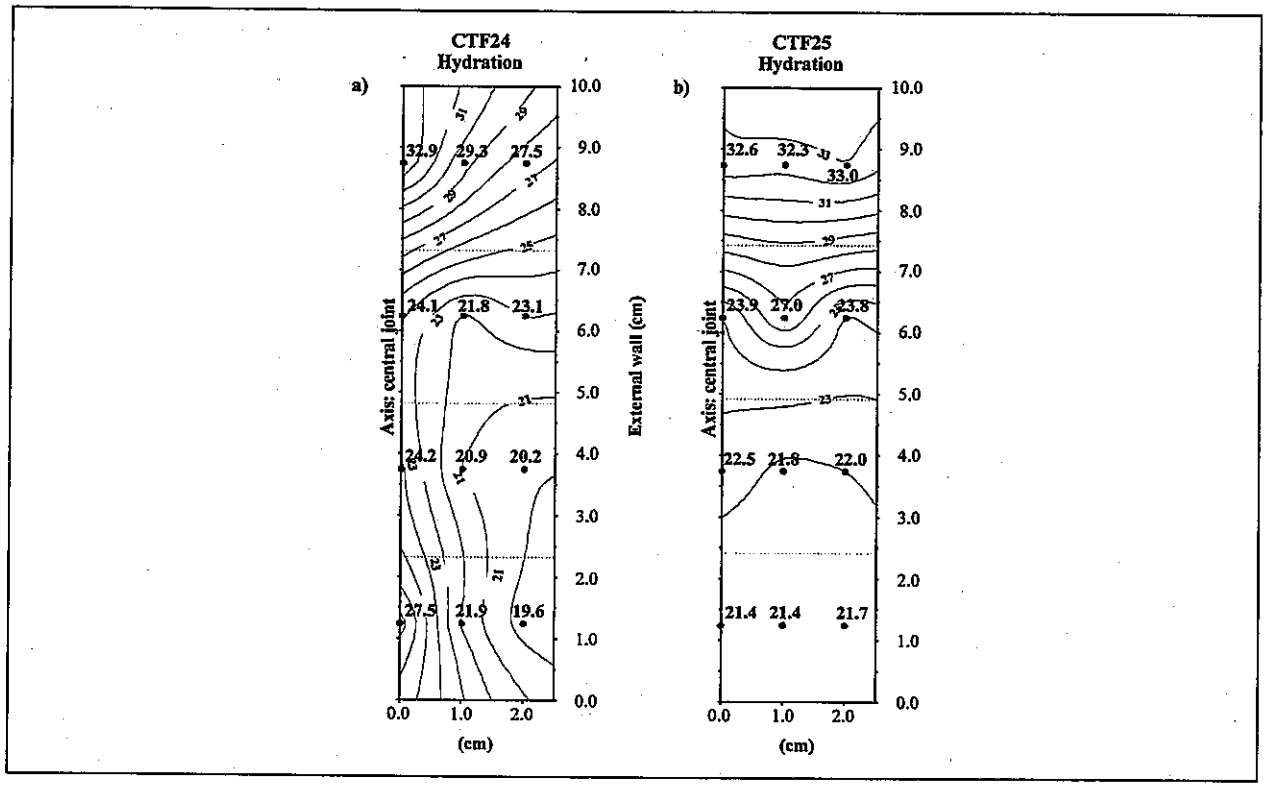

Figure 4-33 : Water content distribution of the clay after two sealing tests (piling of four slices) performed under a hydration pressure of 0.5 MPa and lasting a) 1day, b) 7 days (half section).

4.3.3.2 Suction and temperature controlled oedometer tests

Four oedometer tests including suction decrease and increasing vertical load paths have been performed by CIEMAT (see CIEMAT-4.1) at temperatures of 40 and 60 °C on bentonite compacted at a water content in equilibrium with laboratory conditions and at dry densities of 1.7 and 1.6 g/cm^3. Figure 4-34 shows the evolution of the void ratio during wetting paths starting at a low range of suction (14 MPa), under a vertical stress of 5MPa, and at a high range of suction (120-450 MPa), under a vertical load of 0.1 MPa. Figure 4-35 shows the comparison curves measured at different combinations of suction and temperature, which were maintained constant during the test.

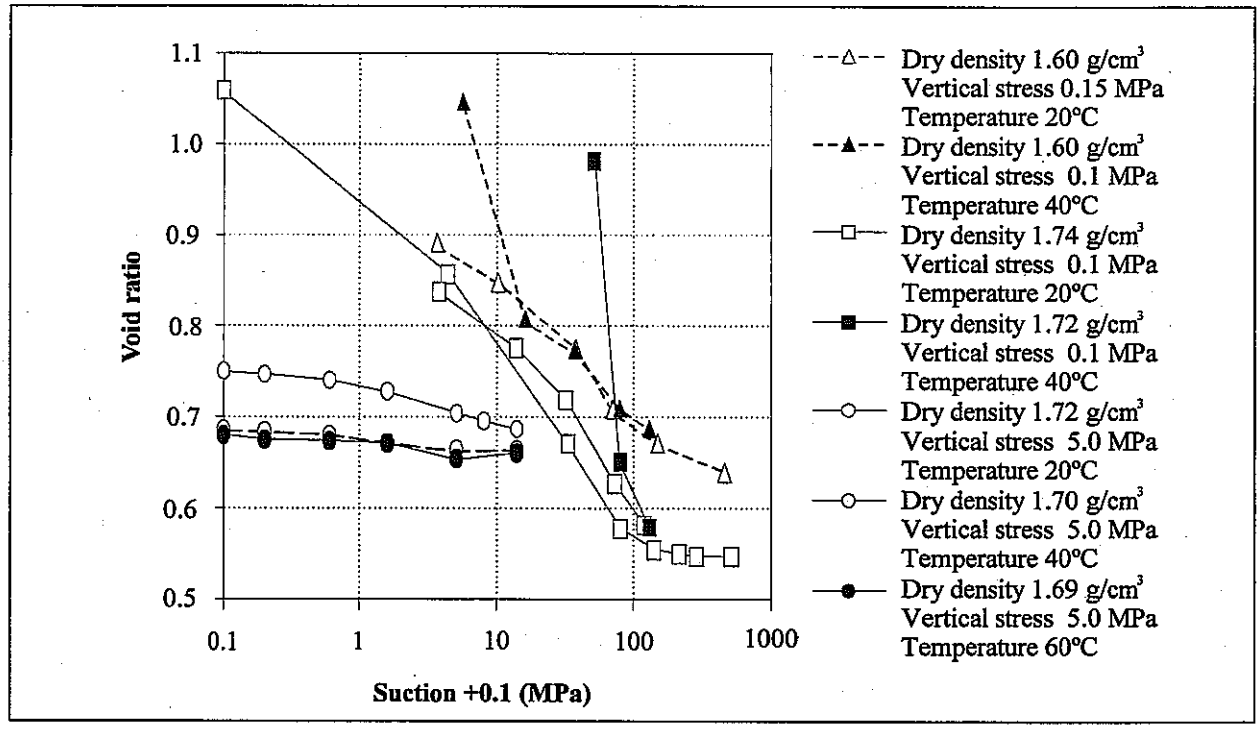

Figure 4-34 : Wetting paths in suction controlled oedometer tests carried out at different temperatures.

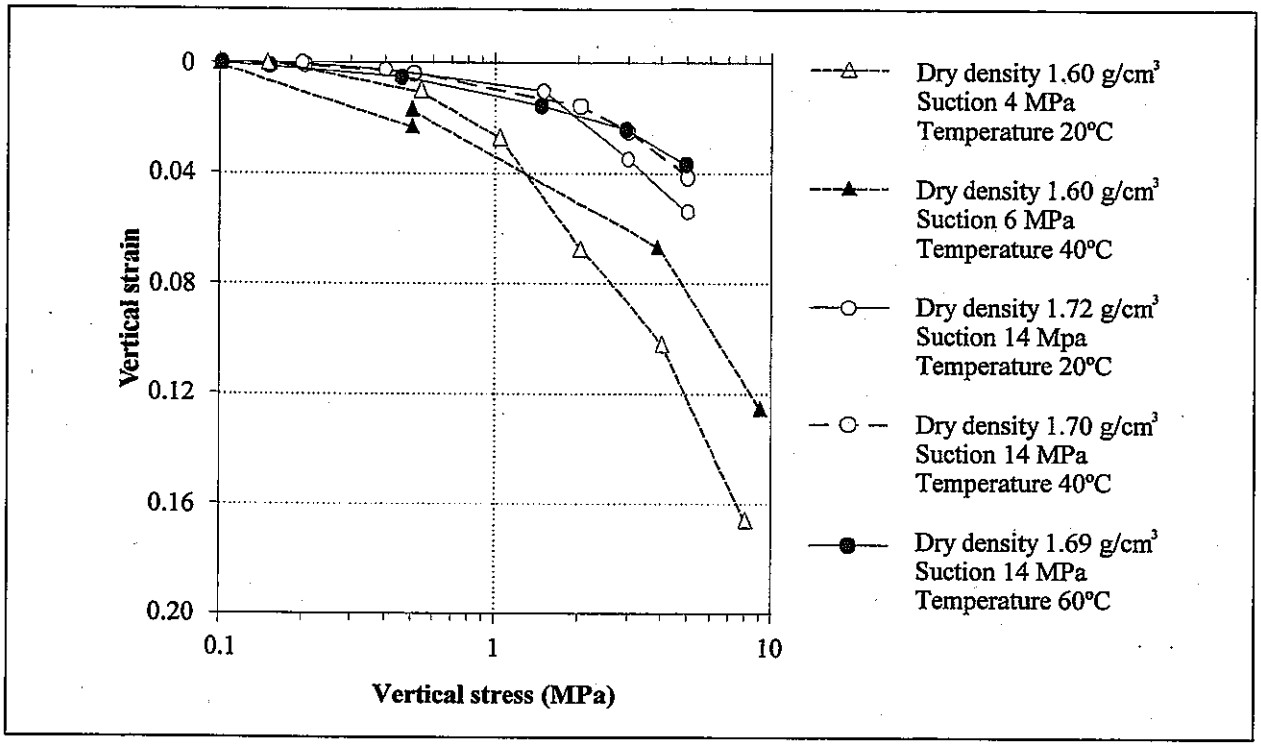

Figure 4-35 : Loading paths in suction controlled oedometer tests carried out at different temperatures.

4.3.4 Tests in thermo-hydraulic cells

The objective of these tests is to analyse the properties of the bentonite and its behaviour under conditions similar to those that will be found in a repository; that is, to subject the material simultaneously to heating and hydration, in opposite directions, for different periods of time.

The tests have been performed in cylindrical hermetic cells of different dimensions:

- Large cells, in which the thickness of the bentonite and the thermal gradient are similar to those of the real case, and the time length of tests are 0.5, 1 and 2 years. No results are yet available.

- Intermediate cells. As saturation will probably not be reached in the large cells, cells of intermediate dimensions have also been used. In these cells, a single bentonite block measuring 13 cm in height and 15 cm in diameter is heated at the top at 100 °C, while being simultaneously hydrated with distilled or granitic water at the bottom, with an injection pressure of 1 MPa (Figure 4-36). The initial dry density and water content of the bentonite are 1.65 g/cm^3 and approximately 14 %, respectively. The quantity of sample is sufficient to allow the bentonite to be sliced into five sections at the end of the test (Figure 4-37). Then, the bentonite porewater is extracted by squeezing techniques. In this way, physical and geochemical characterisation of the solid phase (dry density, water content, soluble salts, exchangeable cations) could be carried out. The test program is devised for study of the phenomena induced separately by the thermal front and the hydration front,

and by the coupling of both fronts, in tests of equal duration. Some results are given in the next Section. The data obtained in these cells have been used to calibrate THG modelling.

- Small cells. In this case, the bentonite specimen measure only 2.5 cm in thickness and 5.0 cm in diameter (Figure 4-38). Saturation is reached after a few days, under an injection pressure of 1 MPa. This has allowed a large number of tests of different duration and conditions to be performed. The initial dry density of the bentonite was 1.65 g/cm^3 and the water content was at equilibrium value under the laboratory relative humidity conditions (around 14 %). Two sets of temperatures (60-35°C and 100-60°C) applied at the heating and hydration ends have been examined, in order to ascertain the effect of temperature on the observed processes. The influence of the chemistry of the hydration water on the processes observed has been verified by using two types of water: granitic and saline (Table 4-5). The saline water has a chemical composition similar to that of the bentonite porewater under saturated conditions, but it is simplified to include only the major elements. The duration of the tests has been related to saturation time. The time needed for saturation has been verified previously, and amounts to 16 days for the tests performed at low temperature and to 10 days for the tests at high temperature.

On completion of the tests, physical, mineralogical and geochemical characterisation of the bentonite in different sections parallel to the heating front was performed. The influence of heating and/or hydration on the physico-chemical and hydro-mechanical properties of the bentonite (hydraulic conductivity and the swelling capacity) and the fabric modifications were also tested. Results are given subsequently.

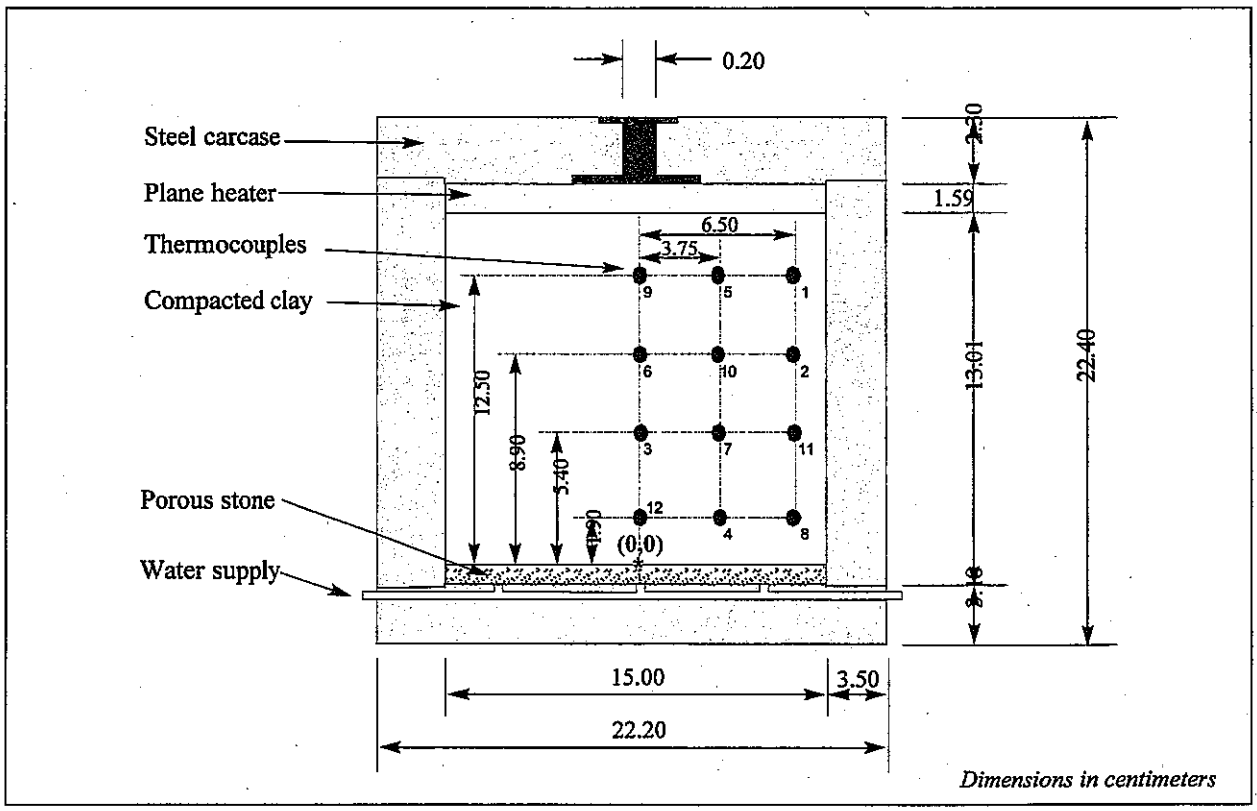

Figure 4-36 : Schematic design of the intermediate cells for THG tests.

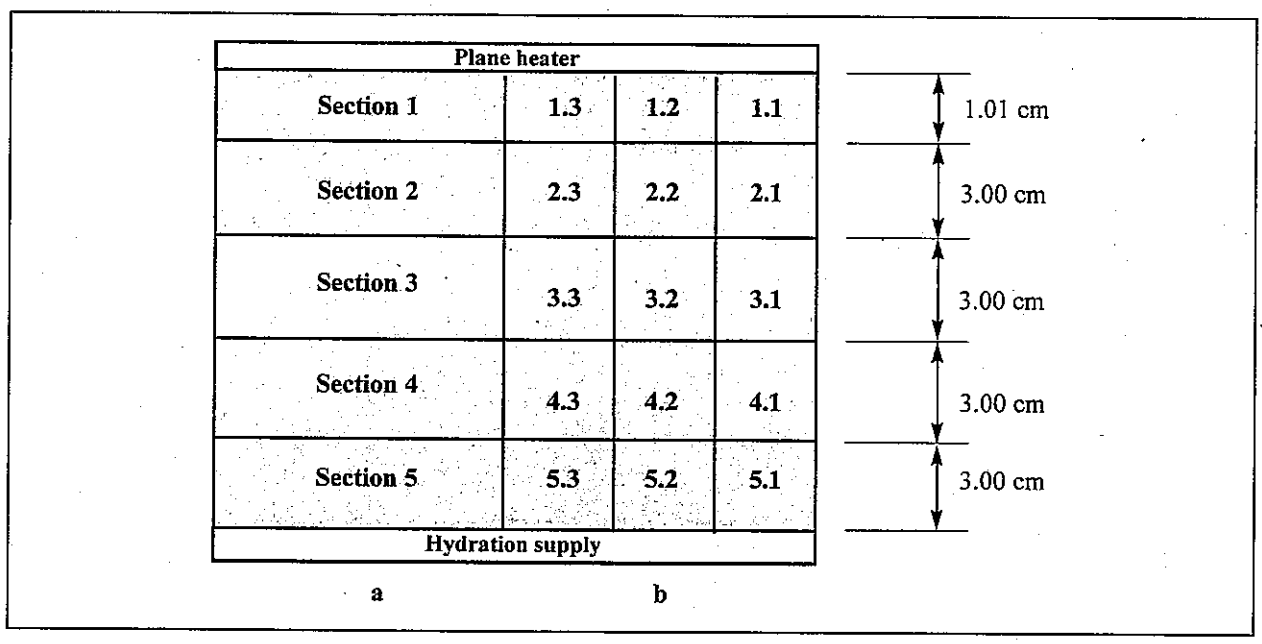

Figure 4-37 : Sampling of the intermediate cells after T-H treatment for: a) porewater analysis by squeezing, b) physical and geochemical characterization of the solid phase.

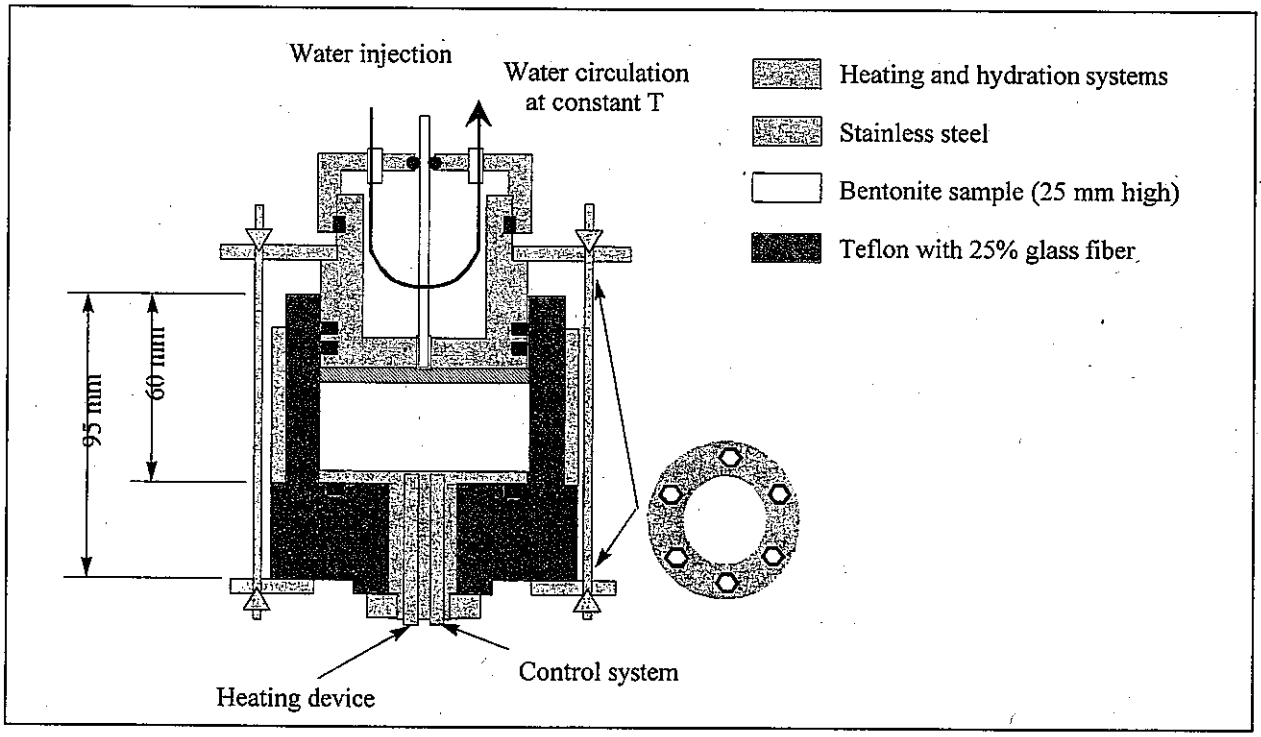

Figure 4-38 : Schematic design of the small cells for THG tests.

4.3.4.1 Intermediate cells

The main objective of these tests is to understand the fundamental mechanisms of water flow and solute transport occurring in a compacted bentonite subjected to simultaneous heating and hydration. Also, the chemical evolution of the bentonite porewater and the hydrogeochemical processes involved in the system (dissolution/precipitation and cation exchange reactions) are studied.

Different tests have been performed, and some are still in progress (Table 4-13). The results presented belong to the transitory state, since saturated conditions have not been reached at the end of the thermohydraulic tests performed.

Table 4-13 : Tests performed with the intermediate cells.

test number	test type	test time (days)	initial conditions				water uptake (cm^3)
			mass (g)	ρ_d (gcm^3)	water content (%)	saturation degree (%)	
CT-22	heating + hydration	26	4298	1.65	13.4	56.7	275
CT-23	heating + hydration	183	4294	1.65	13.3	56.4	486
CT-24	heating	168	4690	1.62	26.5	100	---
CT-26	heating	147	4285	1.65	13.1	55.4	---
CT-27	hydration	148	4247	1.65	13.1	55.4	390
CT-28	heating + hydration	302	4315	1.65	13.9	58.8	in progress
CT-30	hydration	302	4278	1.65	13.9	58.8	in progress

Figure 4-39 and Figure 4-40 show the distribution of temperature and water content in each section analysed, for various tests. The heating source is at the top of the cell (at the right of the following figures) and the hydration supply is at the bottom (to the left of the figures).

Significant changes in dry density, and therefore in porosity, are observed as hydration is induced in these experiments, probably due to the swelling of the bentonite (a slight deformation of the cell, with an increase of volume of the compacted bentonite block, was observed). Consequently, water contents (Figure 4-40) above the saturation water content of the bentonite block initially compacted to a dry density of 1.65 g/cm^3 (23.6 % of water content) were measured.

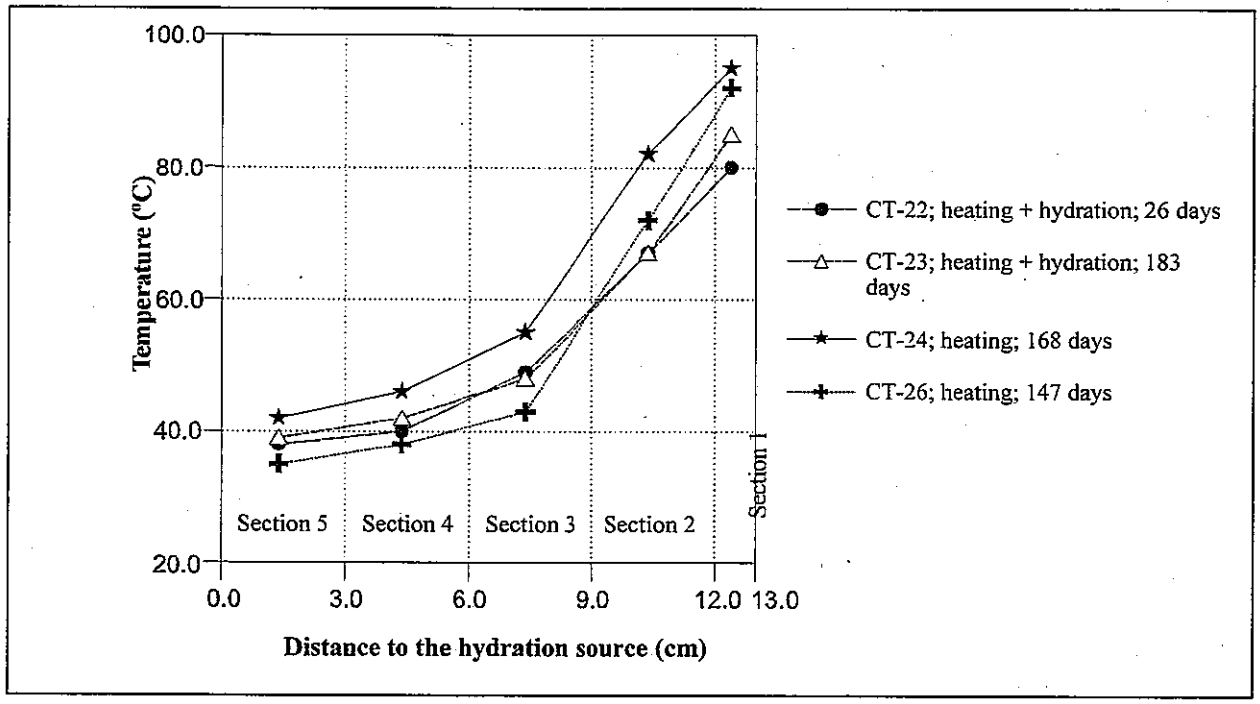

Figure 4-39 : Final temperature distribution in the intermediate cells tests.

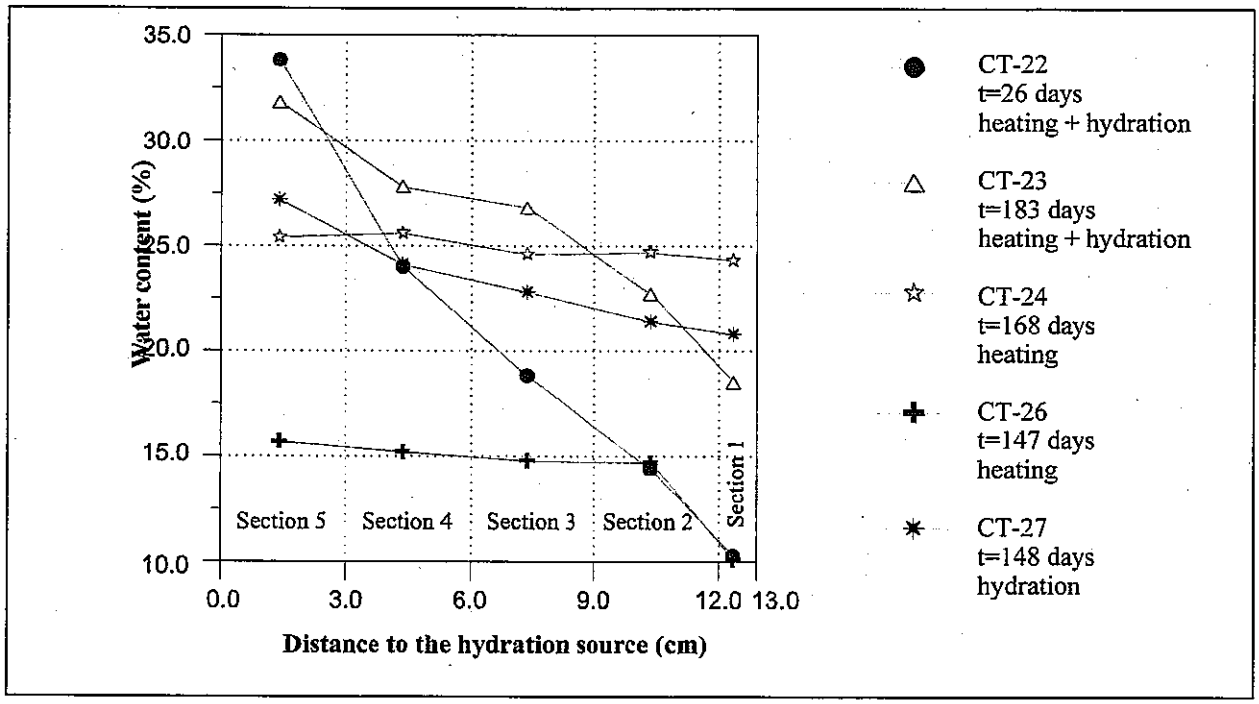

Figure 4-40 : Final water content distribution in the intermediate cells tests.

5 Required results

5.1 Work to be done

Four types of results are required. They refer to:

a) Evolution of heating power
b) Distribution and evolution of relative humidity
c) Distribution and evolution of temperature
d) Evolution of total stresses

a) Evolution of heating power

As described in Section 3.4 (Test operation), a constant power of 1200 W was applied to the heaters during the first 20 days of operation. Power was then increased to 2000 W and maintained constant for an additional period of 33 days. Then, at day 53 the heating system was switched to an automatic constant temperature control mode. Prediction of the power input to both heaters from day 53 onwards is required. The prediction should be given for a period of 1000 days.

b) Distribution and evolution of relative humidity

b1. Distribution of relative humidity (radial direction)

The variation of relative humidity inside the bentonite along the radial distance is required. Three cross sections have been selected to make this prediction (their positions are shown in Figure 3-7):

- Section E1: x = 5.53 m (at heater 1)

  Predictions of relative humidity as a function of radial distance will be given for the following times after day 0) (see Section 3.4 for the definition of day 0):

  t_1: t = 90 days
  t_2: t = 180 days
  t_3: t = 300 days
  t_4: t = 1000 days:

  Four radial directions have been selected for this prediction, namely

  RD1: along positive axis Z (+z)
  RD2: along negative axis Z (–z)
  RD3: along positive axis Y (+y)
  RD4: along negative axis Y (–y)

  (see Figure 3-7, Figure 3-8 and Figure 3-9 for the definition of axis of coordinates).

- Section H: x = 9.50 m (centered between the two heaters)

  Prediction of relative humidity as a function of radial distance will be given for times t_1, t_2, t_3 and t_4 along the radial directions RD1, RD2, RD3 and RD4.

- Section E2: x = 13.44 m (at heater 2)

  Prediction of relative humidity as a function of radial distance will be given for times t_1, t_2, t_3 and t_4 along the radial directions RD1, RD2, RD3 and RD4.

b2. Distribution of relative humidity (longitudinal direction)

The spatial distribution of relative humidity along two lines parallel to the longitudinal axis x are required. These lines are defined by the coordinates:

Line LG1: z = 0; y = –1.08 m
Line RC1: z = 0; y = –0.81 m

Predictions will be given for the two times t_1 and t_4.

b3. Evolution of relative humidity

The evolution of relative humidity along time, within the period (day 0 – day 1000) is required at the following points:

- Section E1: x = 5.53 m (at heater 1)

  Point E1H: coordinates x = 5.53 m; y = –0.52 m; z = 0.00 m
  Point E1C: coordinates x = 5.53 m; y = –0.81 m; z = 0.07 m
  Point E1G: coordinates x = 5.53 m; y = –1.10 m; z = –0.17 m

  (Explanation: E1H means a point in section E1, close to the Heater; E1C means a point in section E1 Centered in the buffer and E1G means a point in section E1 close to the Granite. The three points selected correspond to the actual location of relative humidity sensors of capacitive type: sensors of code WC as explained in Section 3.2.3 Instrumentation).

- Section H: x = 9.50 m (centered between the two heaters)

  Point HH: coordinates x = 9.50 m; y = –0.52 m; z = 0.05 m
  Point HC: coordinates x = 9.50 m; y = –0.81 m; z = 0.05 m
  Point HG: coordinates x = 9.50 m; y = –1.07 m; z = –0.16 m

c) Distribution and evolution of temperature

c1. Distribution of temperature (radial direction)

The variation of temperature inside the bentonite along the radial distance is required. Two cross sections have been selected to make this prediction (their positions are shown in Figure 3-7):

- Section D1: x = 4.42 m (end of heater 1, closest to concrete plug)

  Predictions of the bentonite temperature as a function of radial distance will be given for times t_1 and t_4 along the radial directions RD3 and RD4.

- Section G: x = 8.91 m (end of heater 1, closest to heater 2)

  Predictions of the bentonite temperature as a function of radial distance will be given for times t_1 and t_4 along the radial directions RD3 and RD4.

c2. Distribution of temperature (longitudinal direction)

The spatial distribution of temperature along two lines parallel to the longitudinal axis x are required. These lines are defined by the coordinates:

Line LG1: z = 0; y = –1.14 m
Line RC1: z = 0; y = –0.81 m

Predictions will be given for the two times t_1 and t_4.

c3. Evolution of temperature

The evolution of temperature along time, within the period (day 0 – day 1000) will be given at the following points:

- Section D1: x = 4.42 m (end of heater 1, closest to concrete plug)

  Point D1G: coordinates x = 4.42 m; y = –1.14 m; z = 0.00 m

- Section G: x = 8.91 m (end of heater 1, closest to heater 2)

  Point GG: coordinates x = 8.91 m; y = –1.14 m; z = 0.00 m

d) Evolution of total stresses

The evolution of some specified stress along time, within the period (day 0 – day 1000) is required. The total stress component and the points selected for the prediction are the following.

Section E2,	Point E2G1	(x = 13.45 m; y = –0.28 m; z = –1.19 m).	Radial stress (σ_r)
Section E2,	Point E2H1	(x = 13.28 m; y = 0.00 m; z = –0.48 m).	Radial stress (σ_r)
Section E2,	Point E2G2	(x = 13.46 m; y = –1.19 m; z = 0.00 m).	Radial stress (σ_r)
Section B2,	Point B2G	(x = 17.32 m; y = 0.26 m; z = 0.76 m).	Axial stress (σ_x)

5.2 Output specifications

In order to locate points in the space, the cartesian system of coordinates used is represented in Figure 3-8 will be used. The origin is located on the intersection of the tunnel axis with the surface of the concrete plug in contact with the bentonite barrier. The x-axis is directed along the tunnel axis and points towards the end of the tunnel, nearly to the west. The y-axis is horizontal and points nearly to the south. The z-axis is in the vertical plane that contains the x-axis and points upwards. In order to locate events on time, the origin of time will be on 27 February 1997 at 0:00.

The output data should conform with the document "General Specifications". The following points are recalled: (1) the modelling report should be put in the Word97 file "XXX1B.doc"; (2) output data should be put in the ASCII files "XXX1BNN.txt", where "XXX" stands for the participant's code and "NN" is the file number; (3) data should be arranged in a way similar to that shown in Figure 5-1 to Figure 5-5; and (4) the points provided should be enough to properly define the evolution curve.

The 5 ASCII files where output data should be placed and their content are:

- XXX1B01.txt contains the relative humidity distributions along the 12 (3 sections × 4 radial directions) specified radial directions and 2 longitudinal directions at the 4 specified times.
- XXX1B02.txt contains the relative humidity evolutions at the 6 specified points.
- XXX1B03.txt contains the temperature distributions along the 4 (2 sections × 2 radial directions) specified radial directions and 2 longitudinal directions at the 2 specified times.
- XXX1B04.txt contains the temperature evolutions at the 2 specified points.
- XXX1B05.txt contains the heating power evolution at each heater and the required total stress component evolution at the 4 selected points.

The units to employ in the output files are: (1) coordinates x, y, z in m; (2) time t in days; (3) relative humidity w in %; temperature T °C; (4) total stress component s_x in MPa; and (5) heating power P in W.

```
FILENAME    : XXX1B01.txt
PARTICIPANT: Participant's identification
DATE        : DD.MM.YY

Relative humidity w (%) distributions

section XX along radial direction XX

x (m)       y (m)       z (m)       t = 90 d    t = 180 d   t = 300 d   t = 1000d

0.000E+00   0.000E+00   0.000E+00   0.000E+00   0.000E+00   0.000E+00   0.000E+00
0.000E+00   0.000E+00   0.000E+00   0.000E+00   0.000E+00   0.000E+00   0.000E+00
...         ...         ...         ...         ...         ...         ...

along longitudinal direction XX

x (m)       y (m)       z (m)       t = 90 d    t = 180 d   t = 300 d   t = 1000d

0.000E+00   0.000E+00   0.000E+00   0.000E+00   0.000E+00   0.000E+00   0.000E+00
0.000E+00   0.000E+00   0.000E+00   0.000E+00   0.000E+00   0.000E+00   0.000E+00
...         ...         ...         ...         ...         ...         ...
```

Figure 5-1 : Example of output file "XXX1B01.txt".

```
FILENAME    : XXX1B02.txt
PARTICIPANT: Participant's identification
DATE        : DD.MM.YY

Relative humidity w (%) evolutions

at point XX

x (m)       y (m)       z (m)       t (day)     w (%)

0.000E+00   0.000E+00   0.000E+00   0.000E+00   0.000E+00
0.000E+00   0.000E+00   0.000E+00   0.000E+00   0.000E+00
...         ...         ...         ...         ...

at point XX

x (m)       y (m)       z (m)       t (day)     w (%)

0.000E+00   0.000E+00   0.000E+00   0.000E+00   0.000E+00
0.000E+00   0.000E+00   0.000E+00   0.000E+00   0.000E+00
...         ...         ...         ...         ...
```

Figure 5-2 : Example of output file "XXX1B02.txt".

```
FILENAME    : XXX1B03.txt
PARTICIPANT: Participant's identification
DATE        : DD.MM.YY

Temperature T (°C) distributions

section XX along radial direction XX

x (m)       y (m)       z (m)       t = 90 d    t = 180 d   t = 300 d   t = 1000d

0.000E+00   0.000E+00   0.000E+00   0.000E+00   0.000E+00   0.000E+00   0.000E+00
0.000E+00   0.000E+00   0.000E+00   0.000E+00   0.000E+00   0.000E+00   0.000E+00
...         ...         ...         ...         ...         ...         ...

along longitudinal direction XX

x (m)       y (m)       z (m)       t = 90 d    t = 180 d   t = 300 d   t = 1000d

0.000E+00   0.000E+00   0.000E+00   0.000E+00   0.000E+00   0.000E+00   0.000E+00
0.000E+00   0.000E+00   0.000E+00   0.000E+00   0.000E+00   0.000E+00   0.000E+00
...         ...         ...         ...         ...         ...         ...
```

Figure 5-3 : Example of output file "XXX1B03.txt".

```
FILENAME    : XXX1B04.txt
PARTICIPANT: Participant's identification
DATE        : DD.MM.YY

Temperature T (°C) evolutions

at point XX

x (m)       y (m)       z (m)       t (day)     T (°C)

0.000E+00   0.000E+00   0.000E+00   0.000E+00   0.000E+00
0.000E+00   0.000E+00   0.000E+00   0.000E+00   0.000E+00
...         ...         ...         ...         ...

at point XX

x (m)       y (m)       z (m)       t (day)      T (°C)

0.000E+00   0.000E+00   0.000E+00   0.000E+00   0.000E+00
0.000E+00   0.000E+00   0.000E+00   0.000E+00   0.000E+00
...         ...         ...         ...         ...
```

Figure 5-4 : Example of output file "XXX1B04.txt".

```
FILENAME   : XXX1B05.txt
PARTICIPANT: Participant's identification
DATE       : DD.MM.YY

Heating power P (W) evolutions

t (day)     P1 (W)      P2 (W)

0.000E+00  0.000E+00  0.000E+00
0.000E+00  0.000E+00  0.000E+00
...        ...        ...

Total stress component s_x (radial or axial) (MPa) evolutions

at point XX

x (m)       y (m)       z (m)       t (day)     s_x (MPa)

0.000E+00  0.000E+00  0.000E+00  0.000E+00  0.000E+00
0.000E+00  0.000E+00  0.000E+00  0.000E+00  0.000E+00
...        ...        ...        ...        ...

at point XX

x (m)       y (m)       z (m)       t (day)     s_x (MPa)

0.000E+00  0.000E+00  0.000E+00  0.000E+00  0.000E+00
0.000E+00  0.000E+00  0.000E+00  0.000E+00  0.000E+00
...        ...        ...        ...        ...
```

Figure 5-5 : Example of output file "XXX1B05.txt".

6 References

- Pintado X. (2000) Ensayos THM para el Proyecto FEBEX realizados por la UPC-DIT. UPC, 70-UPC-M-0-03, October 2000.

- Villar M.V. (1999) Ensayos THM para el Proyecto FEBEX. CIEMAT, 70-IMA-L-0-66, March 1999.

別添 - 6

DECOVALEX TASK1

事務局提出書類（検討結果）

Mathematical setting

Constitutive Equations and governing equations

The equivalent continuum model to the fractured medium is introduced by combining the crack tensor theory proposed by Oda (1986) and the constitutive model by Barton and Bandis (1985; BB model). This model can realize the anisotropy of the media by crack tensor theory and the non-linear mechanical and hydraulic behavior by BB model. Thus, the properties are changed heterogeneously and anisotropically through the excavation process.

The Barton-Bandis (BB) model represents the change in the normal and shear stiffness due to the stress change by using *JRC* (Joint Roughness Coefficient) and *JCS* (Joint Compression Strength). By using the JRC_n^I and JCS_n^I (MPa) which is the mean values for each set I, the initial normal stiffness of joint, K_{ni} (MPa/mm), is calculated for each set I,

$$K_{ni}^I = -7.15 + 1.75JRC_n^I + 0.02\left(JCS_n^I / a_j^I\right) \tag{1}$$

where a_j(mm) is the initial joint aperture given by

$$a_j^I = \frac{JRC_n^I}{5}\left(0.2\frac{UCS}{JCS_n^I} - 0.1\right) \tag{2}$$

where *UCS* is the uniaxial compression strength of rock.

The normal stress, σ_n^I, to each set is calculated by $\sigma_{ij}n_i^I n_j^I$ in which σ_{ij} is the calculated stress of each element, and n_i^I is the mean unit normal vector of each set. The normal stiffness of the joint is revised by using the normal stress at each time step.

$$K_n^I = K_{ni}^I\left[1 - \frac{\sigma^I{}_n}{V_m K^I{}_{ni} + \sigma^I{}_n}\right]^{-2} \tag{3}$$

and the shear stiffness is obtained from

$$K_s^I = \frac{100}{L^I}\sigma_n^I \tan\left[JRC_n^I \log_{10}\left(\frac{JCS_n^I}{\sigma^I{}_n}\right) + \phi^I{}_r\right] \tag{4}$$

V_m in the equation (3) is assumed to be the same as a_j^I of the equation (2). L^I is the mean fracture length of the set (mm) and ϕ_r is the residual friction angle.

By using $h^I = K_n^I L^I$, $g^I = K_s^I L^I$, the elastic compliance C_{ijkl} and hydraulic conductivity tensor k_{ij} are calculated by

$$C_{ijkl} = \sum_I \left(\frac{1}{h^I} - \frac{1}{g^I}\right)F_{ijkl}^I + \frac{1}{4g^I}\left(\delta_{ik}F_{jl}^I + \delta_{jk}F_{il}^I + \delta_{il}F_{jk}^I + \delta_{jl}F_{ik}^I\right) \tag{5}$$

$$k_{ij} = \sum_I \frac{1}{12}e'^3\left(P_{kk}^I\delta_{ij} - P_{ij}^I\right) \tag{6}$$

where the summation is carried out for sets. δ_{ij} is the Kronecker delta. F_{ijkl}, F_{ij} and P_{ij} are obtained from

$$F_{ijkl}^{I} = \rho^{I} \frac{\pi}{4} L^{I3} n_i^I n_j^I n_k^I n_l^I \tag{7}$$

$$F_{ij}^{I} = \rho^{I} \frac{\pi}{4} L^{I3} n_i^I n_j^I \tag{8}$$

$$P_{ij}^{I} = \rho^{I} \frac{\pi}{4} L^{I2} n_i^I n_j^I \tag{9}$$

where ρ^I is the fracture density of set I.

The values of F_{ijkl}, F_{ij} and P_{ij} are not changed through the analysis process. The increment of the aperture of the set is given by

$$\Delta V^{I} = \frac{\Delta \sigma_n^I}{K_n^I} \tag{10}$$

The new aperture of the set is revised by

$$e^{I} = e_{\text{int}}^{I} - \Delta V^{I} \tag{11}$$

in which e^I_{int} is estimated from

$$e_{\text{int}}^{I} = \sqrt[3]{\frac{18 \times \mu_l \times K_{mean}}{9.8 \times P_{KK}^{I}}} \tag{12}$$

where μ_l is the viscosity of water. K_{mean} is the mean hydraulic conductivity. The measured hydraulic conductivity at the site is assumed to be the mean one. The distribution of K_{mean} is obtained by the geostatistical approach.

By using the above nonlinear equivalent model, the following coupled equations are solved by the three-dimensional finite element method. The above constitutive law is incorporated into the mechanical, hydraulic and thermal coupling code, THAMES (Ohnishi, et. al., 1985). The continuity equation is given by

$$\left\{ \frac{\rho_l g k_{ij}}{\mu_l} h_{,j} \right\}_{,i} - \rho_{l0} n S r \rho_l g \beta_P \frac{\partial h}{\partial t} - \rho_l \frac{\partial \theta}{\partial \psi} \frac{\partial h}{\partial t} - \rho_l S r \frac{\partial u_{i,i}}{\partial t} = 0 \tag{13}$$

where ρ_l is the density of water, g is the gravitational acceleration. n is the porosity, S_r is the degree of saturation, β_P is the compressibility of water, u_i is the displacement vector, h is the total head and t is the time.

The equilibrium equations are written as

$$\left[\frac{1}{2} T_{ijkl}^{-1} \left(u_{k,l} + u_{l,k} \right) + \chi T_{ijkl}^{-1} C_{kl} \rho_l h \right] + \rho b_i = 0 \tag{14}$$

where $T_{ijkl} = (M_{ijkl} + C_{ijkl})$, in which M_{ijkl} is the elastic compliance of the rock matrix. $C_{ij} = C_{ijkl}\,\delta_{kl}$.

Parameter setting

Fracture data

The geometric information of the fracture sets is mainly obtained from Technical Report 87-14E. Table 1 shows the data used in this analysis. The fracture length is assumed to be one tenth of the mean extent, while the density is assumed to be ten times of the number of fractures per unit length. This is because the mean extent shown in the above report is over 15 m, and it is difficult to assume that such a large fracture acts as a unit for the excavation of Febex tunnel. In this examination, it is assumed that one tenth of the mean extent is influenced by excavation. Thus the influenced distance is a few meters form the drift. The number of the fractures per unit length is obtained by using the thickness of interlying unjointed zone (*b* in Figure 36 in the above report). In order to be consistent with the total amount of the fractures, the density is arranged to be ten times of the real one.
The uniaxial compression strength is set at the average of the values indicated in Table 7-2 of the protocol. JCS is assumed to be 80% of the uniaxial compression strength.
The value of JRC is inferred from the figure of the direct shear test in the report of Interner Bericht 81-01 and the following equation;

$$JRC = [\arctan\frac{\tau}{\sigma_n} - \phi_r][\log_{10}(\frac{JCS}{\sigma_n})]^{-1} \qquad (15)$$

σ_n, τ and ϕ_r are obtained from the figure.
The zone dominated by Lamprophyre is assumed to be consisted by one set, of which direction coincides with the third set. The elements dominated by Lamprophyre are classified as the material number two.

Table 1 Fracture geometry used in the analysis

		System	Density(Num/m^3)	Length(m)	Dip direct./Dip	JRC	JCS(MPa)	UCS(MPa)
Material 1	Set 1	S1+S2	1.00	2.44	155/70	2.99	82.4	103
	Set 2	S3	0.83	1.63	188/81			
	Set 3	K2	1.05	1.83	210/75			
	Set 4	K3	0.72	2.41	258/80			
Material 2	Set3	Lamprophyre	10.5	1.83	210/75	2.81	63.5	79.4

Numerical conditions

Figure 1 shows the finite element mesh used for the analysis.

The upper boundary has a prescribed total water head of 0.8MPa and the other boundaries are set at no flow condition. The mechanical boundary condition is slider condition for all boundaries.

The excavation is carried out as shown in Table 2. The newly created drift wall becomes the zero water pressure condition

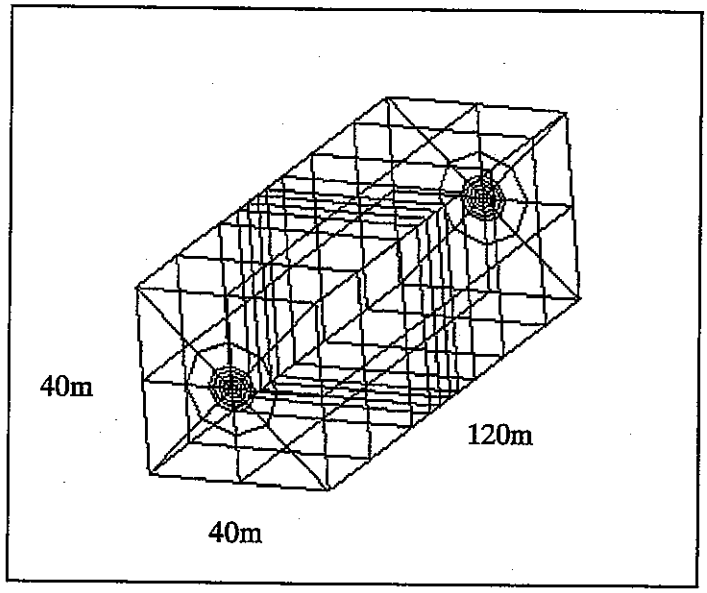

Figure 1 Finite element mesh

Table 2 Excavation schedule

Time(day)	Excavation depth (m)
14	16
22	36
26	50
27	58
28	61.9
29.5	66.65
32.5	71.4
42.5	
53	
73	
100	

Permeability distribution

The hydraulic conductivity at each measurement point is obtained by dividing the transmissivity by the interval. The transmissivities in Tables 6-1 and 6-2 of the protocol are used to get the hydraulic conductivity. Kriging is used to obtain the hydraulic conductivity distribution of entire region. Then the equation (12) is applied to get the initial aperture

distribution of entire region. Then the equation (12) is applied to get the initial aperture distribution. The geometric mean of the hydraulic conductivity used for kriging is 4.4×10^{-11} m/s. Figure 2 shows the resultant initial hydraulic conductivity distribution. The value is indicated by logarithm of the hydraulic conductivity (m/s).

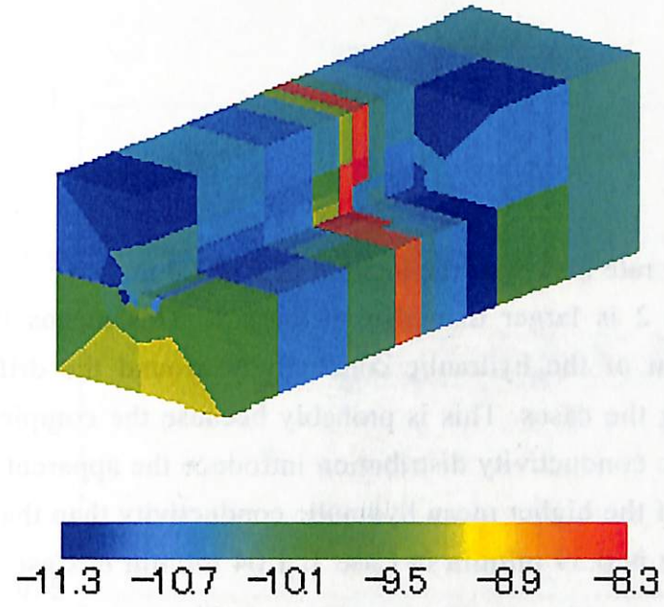

Figure 2 Hydraulic conductivity distribution (log K(m/s))

Other properties

The other mechanical properties are set as shown in Table 3.

Table 3 Mechanical properties used in the analysis

	Young's modulus of intact rock (GPa)	Poisson's ratio
Material 1	32	0.25
Material 2	25	0.25

Analysis cases

Three cases are calculated. The first one is the case in which the above nonlinear anisotropic mechanical and hydraulic properties are used (Case1). The second one is the case that the mechanical property is linear isotropic elastic and the hydraulic one is heterogeneously anisotropic (Case 2). In Case 2, the crack tensor for mechanical property is not considered,

3. The third one is the case in which the deformation is not considered (Case 3). Case 3 is the examination of seepage analysis with excavation. Cases 1 and 2 have homogeneous mechanical property respectively in Lamprophyre zone and the other zone at the initial condition. The hydraulic conductivity is heterogeneous for entire region because of the heterogeneous initial aperture distribution given by kriging. On the other hand, the hydraulic conductivity of Case 3 is homogeneous and constant at $2x10^{-11}$ m/s for entire region. In Cases 2 and 3, the properties are constant through the excavation process, while the mechanical and hydraulic properties are changed though the excavation process in Case 1.Cases 1 and 2 are the calculation of coupled mechanical and hydraulic problem, although Case 3 is only the seepage analysis.

Results

Figure 3 shows the flow rate history at the interval of 50-71.4 m.
The flow rate of Case 2 is larger than that of Case 1. This means that the deformation introduces the reduction of the hydraulic conductivity around the drift. Case3 shows the largest flow rate among the cases. This is probably because the complex flow paths due to heterogeneous hydraulic conductivity distribution introduce the apparent low permeability of the rock mass in spite of the higher mean hydraulic conductivity than that one in Case 3. The flow rate after 100 days is 0.39 ml/min in Case 1, 1.04 ml/min in Case 2 and 7.0 ml/min in Case 3.

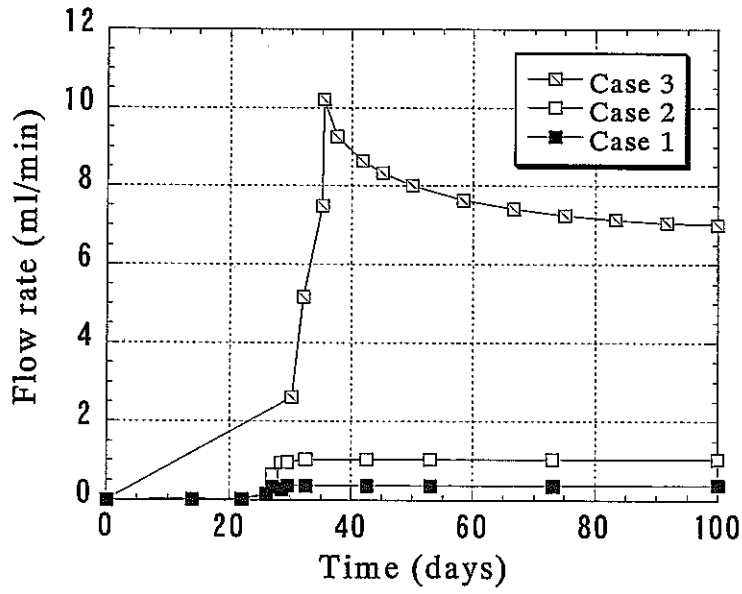

Figure 3 Flow rate from the region between 50 to 71.4 m as a function of time

Figure 4 indicates the pressure history at P3 and P4. The pressure at P4 is drastically changed by excavation in Case1. The negative pressure is happened and the recovers gradually to the initial state. On the other hand, the behavior at P3 in Case 1 is mostly same as the one in Case 2. This means that the influence of excavation at P3 is very small and the nonlinear effect is not occurred. On the other hand, the nonlinear deformation is occurred very much at P4.
Case 2 shows a little increase in pressure just before excavation, while the other cases do not indicate the increase.

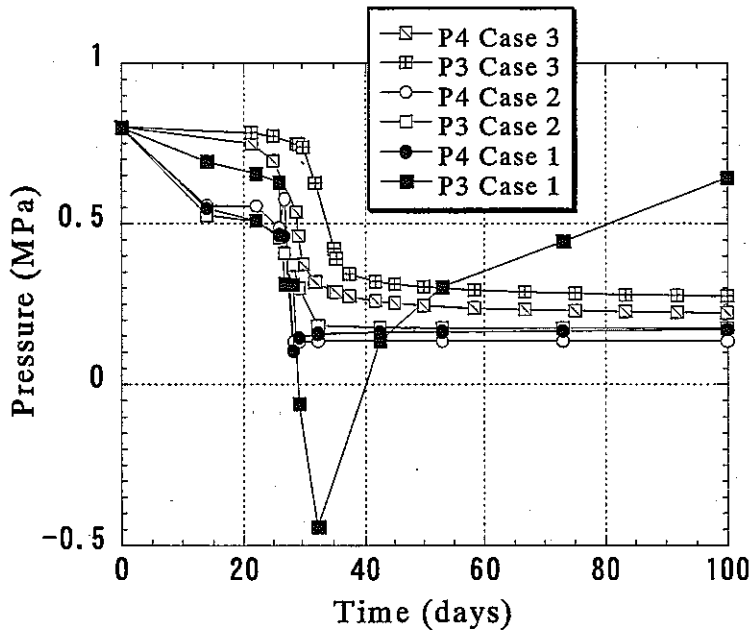

Figure 4 Pressure history at P4 and P3

References

Barton, N, Bandis, S and Bakhtar, K: Strength, Deformation and Conductivity Coupling of Rock Joints, Int. J. Rock M.M.S.G.A, 22,3,pp.121-140, 1985

Oda, M. : An Equivalent Continuum Model for Coupled Stresses and Fluid Flow Analysis in Jointed Rock Masses, Water Resour. Res. Vol. 22, No. 13, pp.1845-1856, 1986

Ohnisi,Y. Shibata,H. Kobayasi,A.,: Development of finite element code for the analysis of coupled thermo-hydro-mechanical behaviors of saturated-unsaturated medium, Proc. Int. Symp. Coupled Porocesses Affectting the Performance of a Nuclear Waste Repository, Berkeley, 263-268,1985.

別添 - 7

DECOVALEX TASK3 BMT1

TASK DEFINITIONS

DECOVALEX III - Task 3 - Bench Mark Test 1 (Final Draft, June 2000)

Implications of T-H-M coupling on the near-field safety of a nuclear waste repository

1. Introduction

The DECOVALEX project is an international co-operative project, initiated by SKI, the Swedish Nuclear Power Inspectorate, to support the development of mathematical models of coupled **T**(Thermal) **H**(Hydrological) **M**(Mechanical) processes in the host rock for potential nuclear fuel waste repositories. During the first stage (May 1992 to March 1995), called DECOVALEX I, the main objective was to develop computer codes for coupled T-H-M processes. In the second stage, called DECOVALEX II, the main objective was to use the computer codes developed in DECOVALEX I to predict and interpret large scale field tests. A third phase of DECOVALEX called DECOVALEX III is now being proposed with two main objectives. The first one is the further validation of codes by simulating large scale experiments as the FEBEX T-H-M experiment performed in Grimsel, Switzerland, and the large scale heater test at Yucca Mountain, Nevada, USA. The second objective is to determine the relevance of THM processes on the safety of a repository. To achieve this objective, benchmark tests are proposed, where typical repository designs, engineered barriers and host rocks are examined.

The benchmark problem defined in this proposal looks at the implications of coupled T-H-M processes on the near-field performance of a repository. The performance of a nuclear waste repository is dependent on two main components:
i) the groundwater flow field since groundwater is recognized as the main agent of contaminant transport from the repository to the biosphere.
ii) the structural integrity of the engineered and geological barriers.

The performance assessment (PA) of a repository is often performed with probabilistic assessment computer codes, using Monte-Carlo simulations. Typically thousands of runs are performed, in order to estimate the probabilistic distribution of a dose to potential receptors. It is thus necessary to simplify the processes involved in the different barriers to contaminant migration. The rock mechanics expert, the engineered barrier expert, and the hydrogeologist usually provide information to the PA analyst on the structural integrity of the rock mass and engineered barriers and the groundwater flow field; this information is then synthetized and simplified by the PA analyst before he (she) defines the input to the PA model. Up to the present time, the above information are provided separately, without considering the coupling between thermal, mechanical processes (implication on structural integrity), and hydraulic processes (implications on flow field). In this benchmark problem, we propose that scoping calculations be performed in order to determine how T-H-M processes can influence the flow field, as well as the structural integrity of the geological and engineered barriers in the near-field of a typical repository .

2. General definition of the problem

Imagine a hypothetical case in which a country is studying the feasibility of constructing a nuclear waste repository in a granitic rock formation at a depth of 1000 m. No particular site has been selected, although investigations have been performed at some experimental areas. For example at one experimental site, galleries were excavated down to a depth of 600 m, and a variety of hydraulic, mechanical, geochemical tests have been performed (figure 1). Of particular relevance to the assessment proposed in this exercise, is a T-H-M experiment which replicates the near field behaviour of the rock mass and buffer around a single waste container (figure 1.b and 1.c). The type of bentonite used in the above experiment and the dimensions of the experimental borehole are comparable with the parameters of the conceptual design (figure 2.b).

Let us further assume, that several site investigations have been performed and a composite picture of the rock mass in this hypothetical country could formed: for example, in general the rock formation down to 600 m is very fractured, with fracture spacing of the order of 0.1 m; at depths greater than 600 m, the degree of fracturing decreases, with fracture spacing of 0.5 to 1 m. Based on the average properties of the rock mass determined from the site investigations, a preliminary design of the repository has been proposed (figure 2). The centreline distance between adjacent tunnels is 10 m and the centreline distance between adjacent inground boreholes for the wastes is 4.44 m. The depth of each borehole is 4.13 m and the diameter is 2.22 m. The overpack for vitrified wastes would be emplaced into the borehole, and a bentonite buffer material would be compacted around the overpack. The details of the borehole are given in figure 2.b. The tunnels would also be backfilled with a mixture of gravel and clay. The PA modeller who studies the near field behaviour is using a Monte Carlo assessment code in order to assess the transport of radionuclides through the engineered barriers to the surrounding rock. She/He wants you, the engineering expert, to give her/him feedback on the following key points:

1. What is the temperature evolution in the near-field?
2. How long would it take for the buffer to resaturate?
3. What are the stresses on the overpack and the buffer ? Will they be structurally stable?
4. How will the permeability and the flow field of the rock mass in the near-field evolve?
5. Is there a potential for rock mass failure in the near-field?
6. What are the uncertainties related to the answers to the above questions, taking into account the variability in the properties of the rock mass?

As a participant in DECOVALEX I and II, you have been developing and applying a coupled T-H-M code in a variety of benchmark problems, and in-situ tests predictions. You decide to use this code as a tool to address the questions raised by the PA modeller. You decide to divide your work in two phases:

1. Calibration of the code with the T-H-M experiment performed at the 550 m-Level gallery at the experimental site, illustrated in figure 1.You consider this step as necessary in building confidence in your code and your understanding of the physical processes.
2. Use of the code to perform scoping calculations of the T-H-M near field behaviour, of the generic design shown in figure 2, in order to specifically give feedback to the PA modeller.

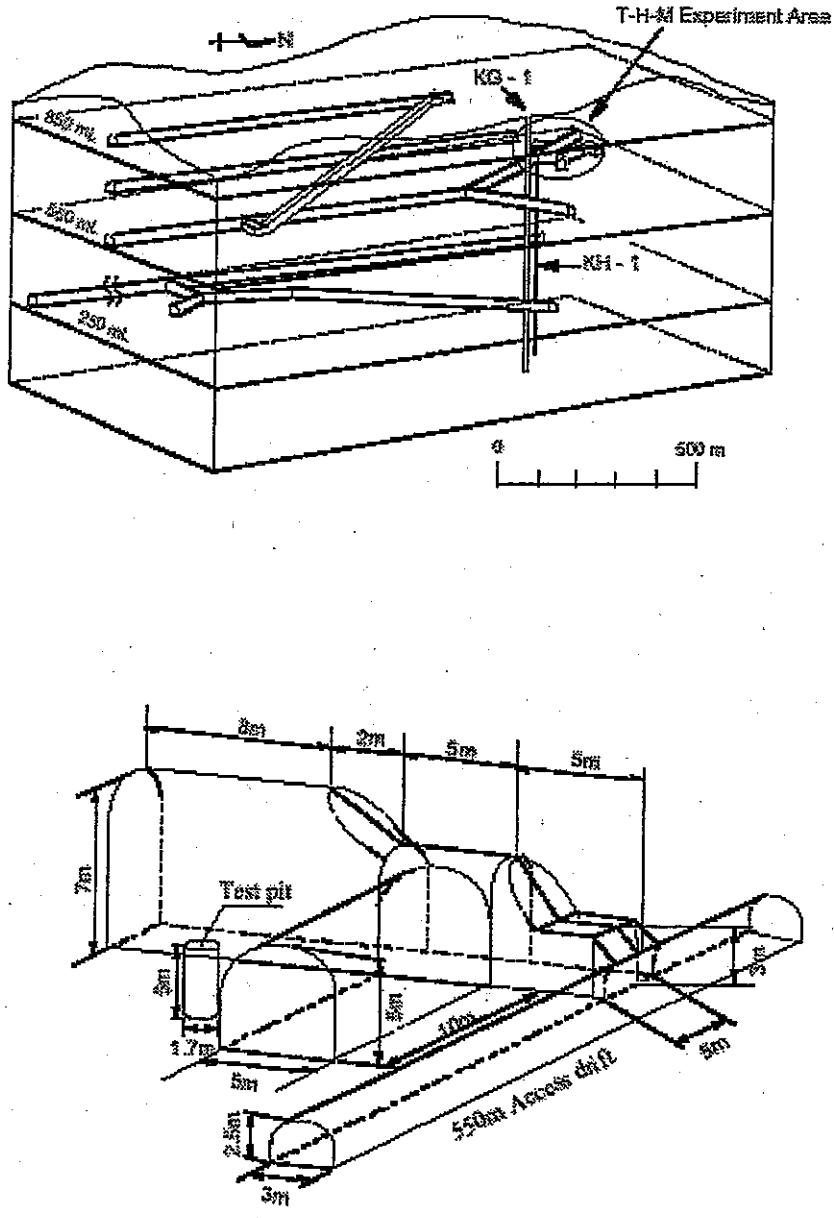

Figure 1 Near-field T-H-M experiment with one single heater

a) Typical tunnel

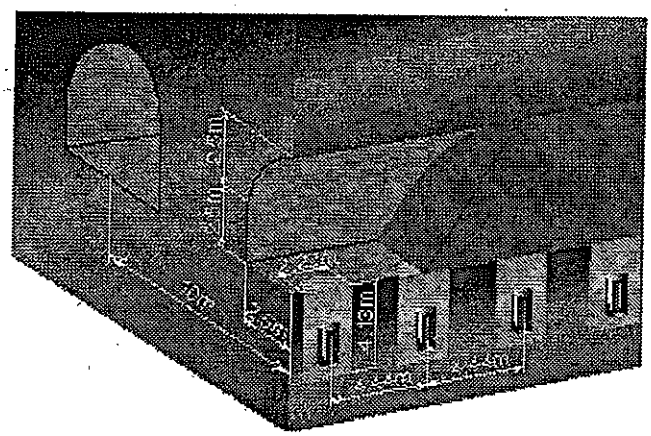

b) Details of borehole

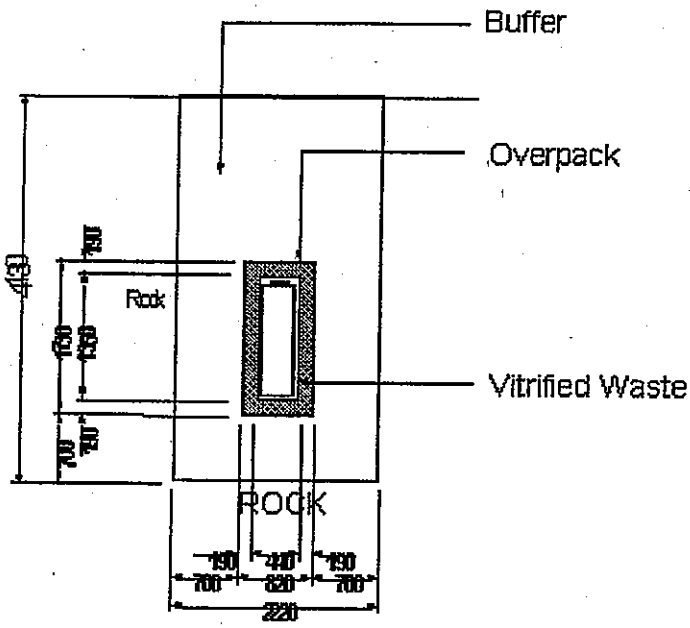

Figure 2 Conceptual design of generic nuclear waste repository

3. Calibration of T-H-M experiment

3.1 General description of the T-H-M experiment

Detailed descriptions of the experiment will be provided to the research teams in separate reports. A general description is given here.

A plan view of the floor of the T-H-M experimental drift in the vicinity of the test hole is shown in figure 3. A cordinate system has been defined, with the x axis corresponding to the East direction, y axis to the North, and z to the upward vertical direction. The floor is set at z= -2.357 m and the centre of the test hole, at the floor elevation, is at cordinates (-10.571,-10.356,-2.357). Four sets of boreholes were drilled in the rock mass prior to the excavation of the borehole. Set 1 (KBH1 to KBH6) is used to monitor the pore pressure and temperature in the rock mass; Set 2 (KBM1 to KBM3) is used to monitor strain and temperature in the rock mass; Set 3 (KBM4 and KBM5) is used to monitor deformation of the rock mass; and Set 3 (KBM6 and KBM7) is used to monitor the displacements in the main fractures near and intersecting the test pit.

A granulated bentonite was compacted directly into the borehole, by layers of 10 cm in thickness. The initial water content (by weight) of the bentonite was 15%. A heater was installed in the test pit, within the bentonite. When bentonite was compacted within the last 50 cm of the pit, a concrete lid was installed in the remaining part; this lid was restrained by vertical steel bars connected to the ceiling of the drift, in order to restrict vertical movements. A dam was then built on the floor, and a water pool of 40 cm was created. The temperature of the water pool was maintained at 12.3 °C during the duration of the experiment. The heating phase of the experiment started when the temperature at the centre of the heater was set to 100°C; this heating phase lasted 258 days. The heater was then turned off, and the cooling phase started; measurements from the sensors were recorded during a period of approximately 180 days.

Sensors to measure water content, temperature, pore pressure, stress and strain in the bentonite were installed at 3 sections DDA, BBC and CD (figure 3).

3.2 Properties of the buffer

The basic T-H-M properties of the buffer material are determined by laboratory tests. These properties include: saturated permeability, thermal conductivity, Young's modulus, water retention curves, isothermal infiltration tests, swelling pressure, moisture flow under thermal gradient tests. The details of the tests and the results are given in a separate report. Typical properties are included here for illustration purposes.

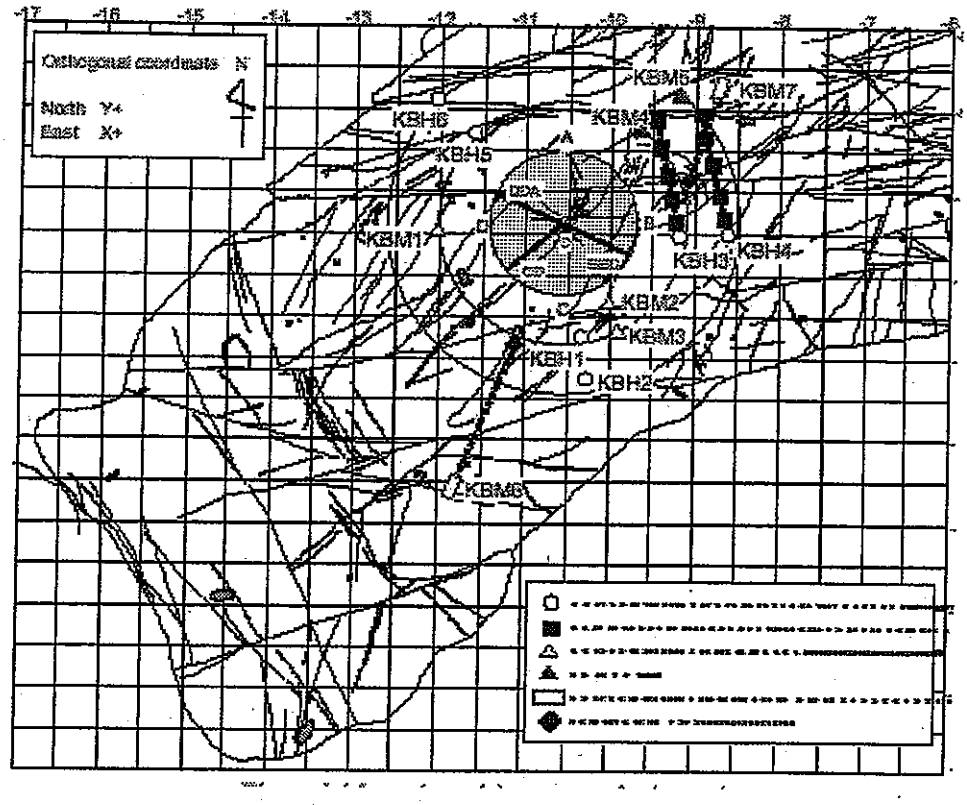

Figure 3 Plan view of the floor of the T-H-M experiment

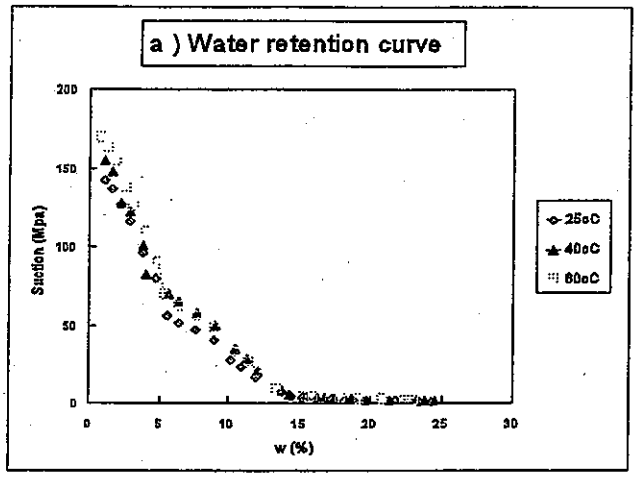

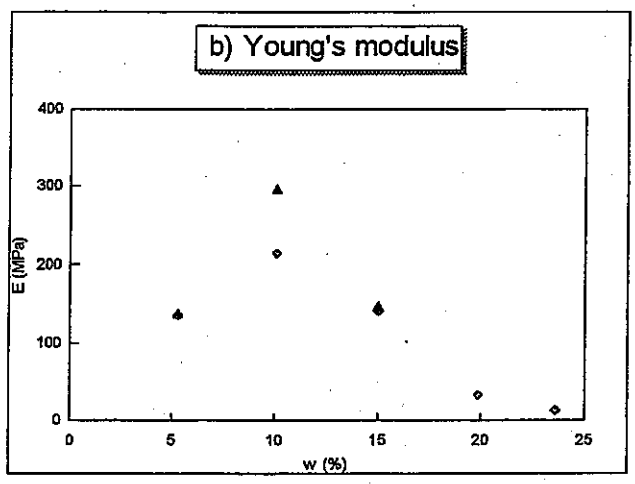

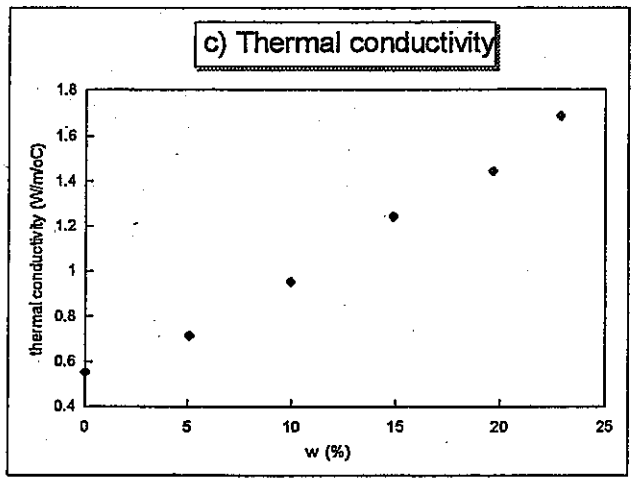

Figure 4 Some typical properties of buffer material

3.3 Rock matrix properties

The basic properties of the rock matrix were determined from laboratory tests on intact samples and will be provided in a separate report. Typical values are:

Density: 2746 kg/m3
Effective porosity: 0.379 %
Young's modulus: 61 GPa
Poisson's ratio: 0.303
Coefficient of linear thermal expansion: 8.21x 10-6 °C
Thermal conductivity:2.54 to 2.71 W/m° K (depends on temperature)
Specific heat: 900 J/kg° K
hydraulic conductivity: 6.6×10^{-14} to 1×10^{-13} m/s
uniaxial compressive strength: 123 Mpa
Tensile strength: 11 Mpa

3.4 Properties of the heater

The basic properties of the overpack are given below:

Density: 7800 kg/m^3
Young's modulus: 200 Gpa
Poisson's ratio: 0.3
Thermal conductivity: 53 W/m° K
Specific heat: 0.46 kJ/kg° K
Coefficient of linear thermal expansion: 1.64×10^{-6} °C^{-1}

3.5 Fracture properties and distribution

Mechanical properties of individual fractures were determined by laboratory tests,on sample of 50 to 95 mm in length.The results, including JRC and JCS, shear strength, shear stiffness are available in a separate report. Typical average values are:

JRC: 8.83
JCS: 105 Mpa

Detailed mapping of the fractures on the floor and roof of the experimental drift, and on the walls of the test hole is reported under separate cover, and will be made available to the research teams. In situ hydraulic test results in the fractured rock mass are also available in a separate report. Figure 3 also shows the most important fractures on the floor of the experimental area.

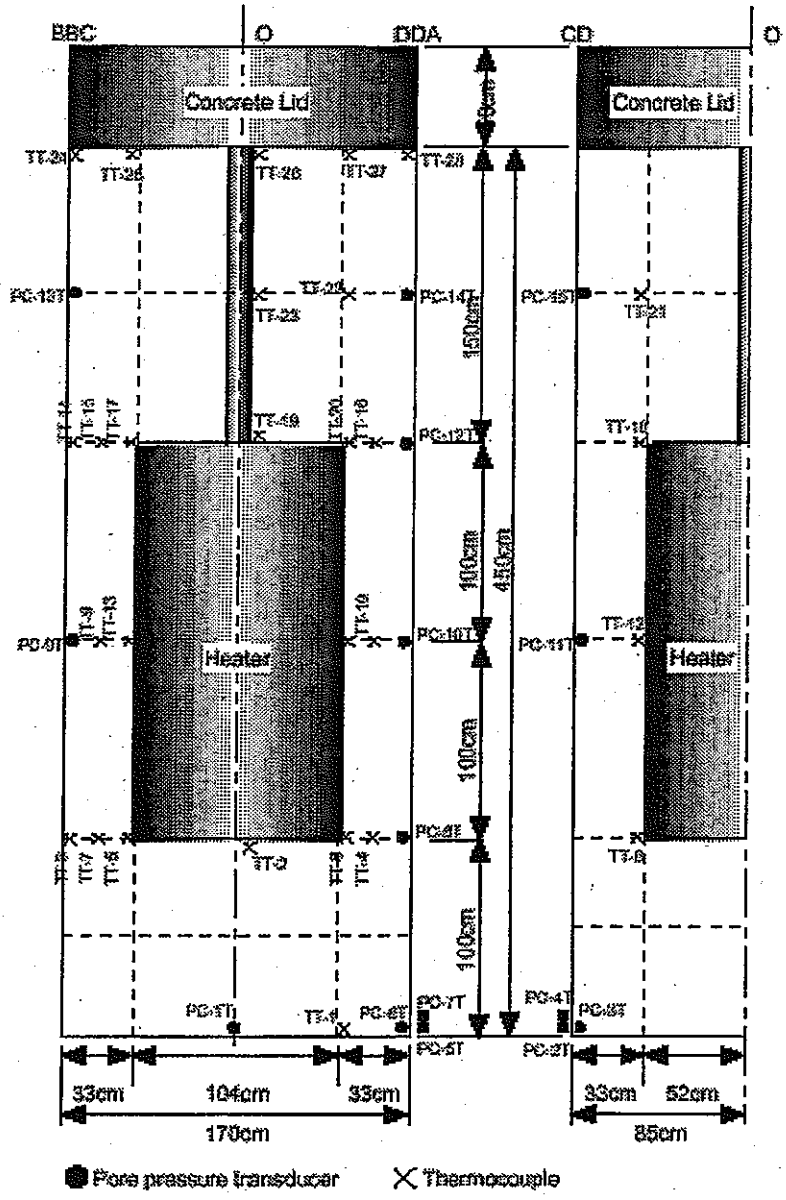

Figure 5 Location of sensors in bentonite - temperature

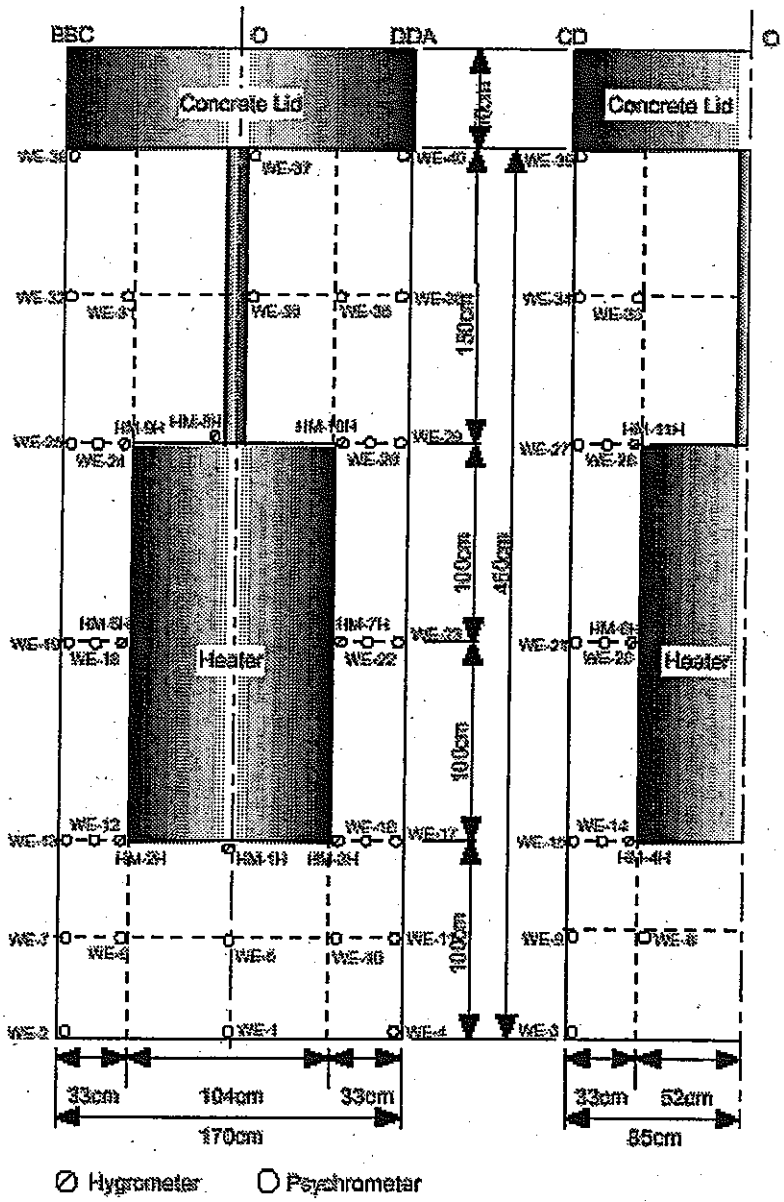

Figure 6 Location of sensors in bentonite - water content

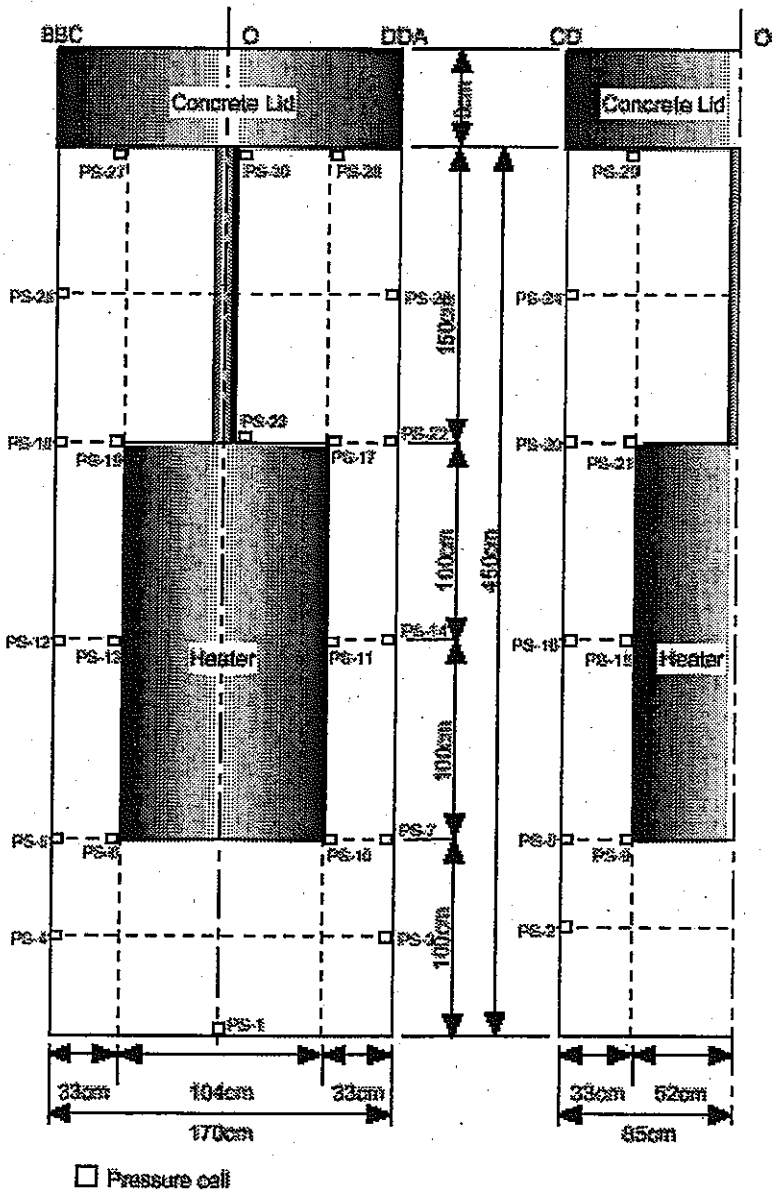

Figure 7 Location of sensors in bentonite - total stress

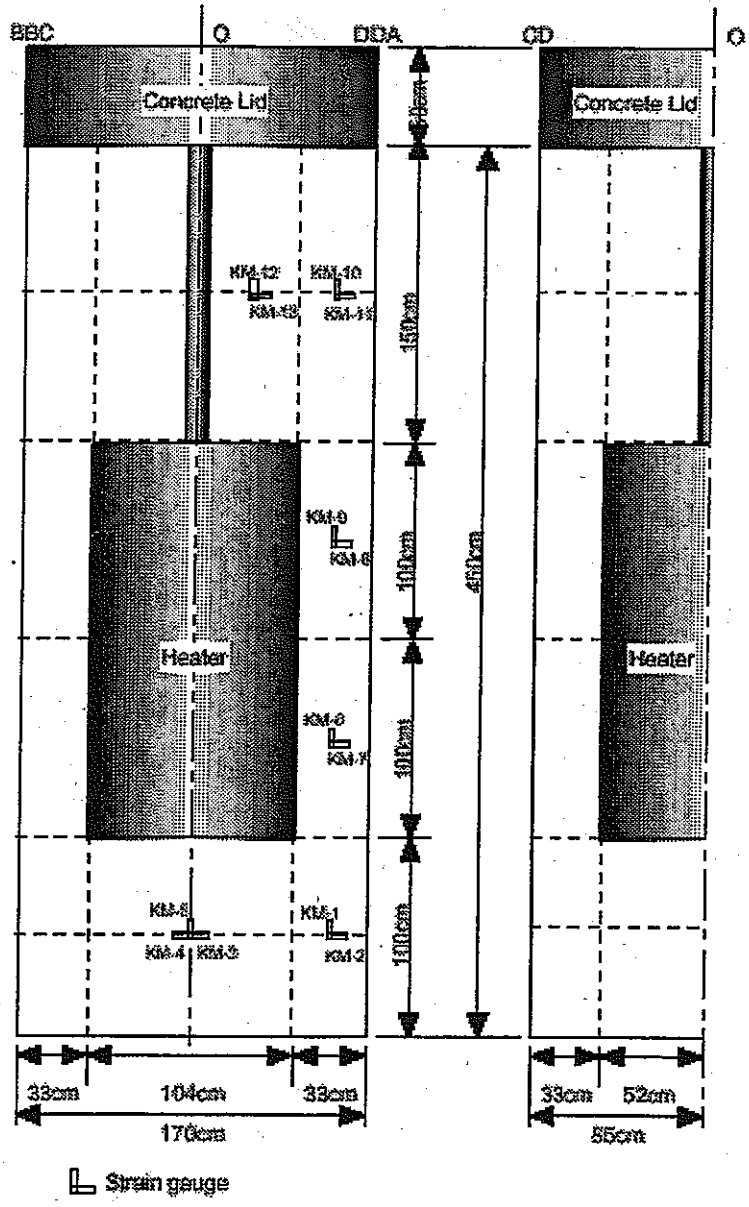

Figure 8 Location of sensors in bentonite - Strain

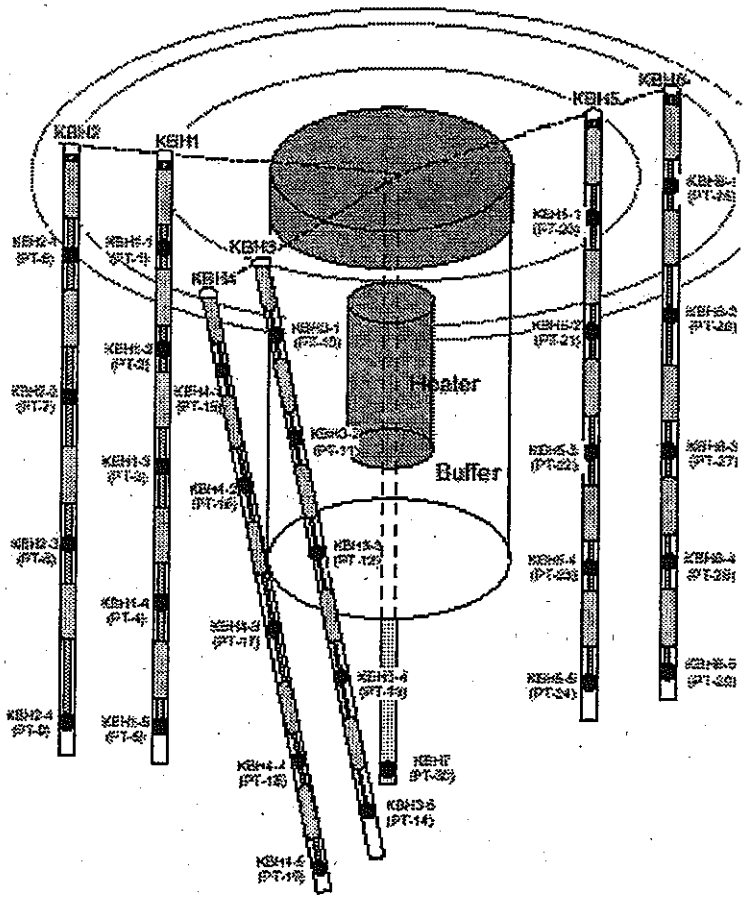

Figure 9 Location of sensors in rock - temperature and pore pressure

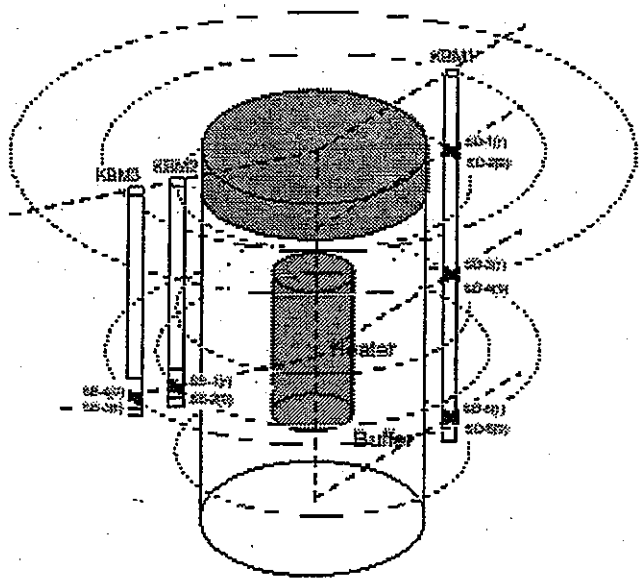

Figure 10 Location of strain gauges in rock

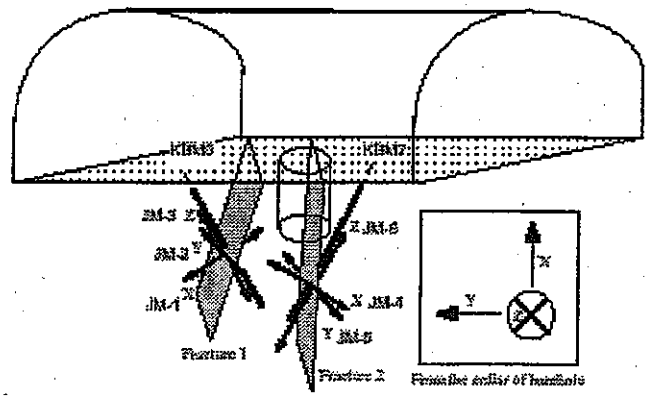

Figure 11 Location of joint deformeters in rock

3.6 Output specifications

The research teams will be provided with experimental time-curve for temperature, displacements, water content, etc. in the buffer and the rock mass at the monitoring points illustrated in figures 5-11 . The research teams will try to calibrate their model with the experimental data. The exact location of the monitoring points and the experimental time curves of the measured parameters will be provided to the research teams.(As an alternative to the full scale calibration exercise, the RT's could perform the simplified 1-D axisymmetric problem, detailed in Appendix I.)

In addition to giving results at the specified points, the RTs shall evaluate these results by discussing the following points:

- Specify which input parameters are needed in your model. Determine which ones are available from laboratory and/or field tests, and which ones were assumed, and justify the values actually used in the calibrated model.
- Discuss and justify how the rock-bentonite and bentonite-heater interface was represented
- Discuss how the site of the calibration exercise is applicable to the generic site to be studied in the second phase of BMT1 (e.g. Are the rock mass properties, the degree of fracturing of the rock mass, the bentonite properties, etc. within the range of properties assumed for the generic site?)

4. Scoping calculations for the near-field of a generic repository

4.1 Conceptual model

From the conceptual design of the repository as shown in figure 2, and assuming repetitive symmetry, one web of the system, comprising one borehole, and a slice of rock and backfill as shown in figure 12 is considered. The applicable boundary conditions for the excavation phase and for the long term phase are differnt, and will be specified in subsequent sections.

4.2 Properties of buffer, rock matrix, overpack and backfill

The properties of the rock matrix and overpack are the same as in the calibration exercise. The buffer is a mixture of sand and bentonite; its properties and the properties of the backfill will be given in separate reports.

4.3 Properties of fractures and degree of fracturing of the rock mass

Parametric studies considering several degree of fracturing of the rock mass :
F0. No fracture.
F1. One horizontal fracture in the midplane of the emplacement borehole
F2. Regular fracture spacing of 1m, in two directions perpendicular to x and z axes

F3. Same as F3, with fracture spacing of 0.5 m
F4. Same as F1 with one vertical fracture 5 m from tunnel
F5. Combination of F1 and F3
For cases F0, F1 and F4, the following initial rock mass effective permeabilities will be considered: 10^{-19}, 10^{-18}, 10^{-17} m^2.

For cases F2, F3 and F4, the generation of the fracture will start at position (0,0,0). Each fracture will have the following properties: JRC= 9; JCS = 105 Mpa, at a laboratory scale of 80 mm; initial hydraulic aperture: 10 μm. The rock matrix will have the properties for intact rock defined in section 3.3 .

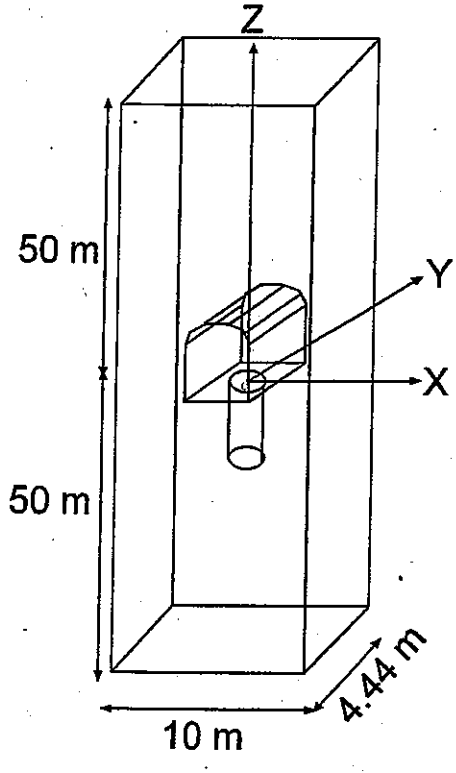

Figure 12 Geometry for near-field scoping calculations

4.4 Excavation effects

The effects of excavation shall be determined by performing a steady-state analysis, with the boundary conditions as illustrated in figure 13. The output of this analysis consists of contours of temperature, pore pressure, permeability, and factor of safety for rock mass failure at sections x=0 and y=0. The permeability function and the failure criterion for the rock mass are given in sections 4.7 and 4.8 respectively.

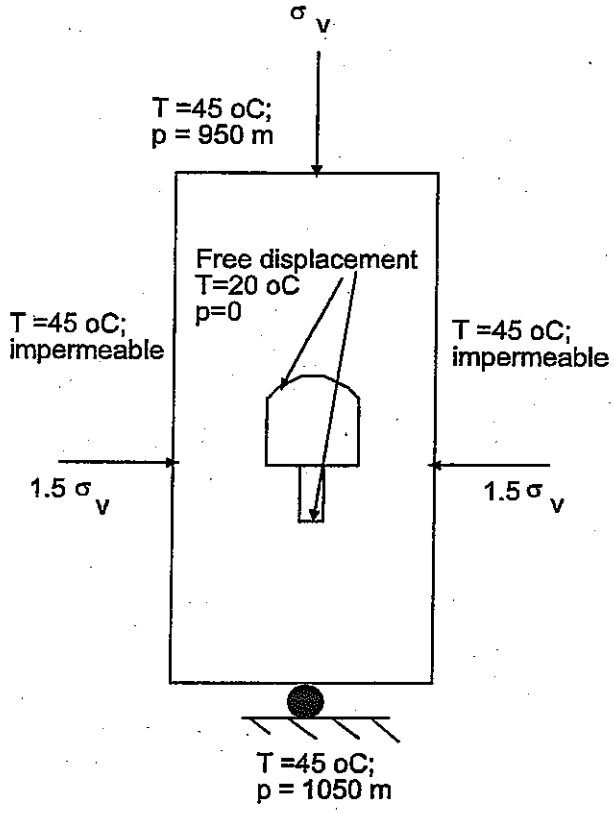

Figure 13 Boundary conditions for excavation analysis

4.5 Transient analysis with emplaced heater, buffer and backfill

A transient analysis shall be performed, assuming that the buffer, backfill and heater are emplaced instantaneously at time t=0. The analysis shall be for a period of 200 years.The results from the steady state analysis for excavation effects for temperature, stresses, and pore pressure in the rock mass shall be used as initial conditions. For the buffer and backfill, the initial stresses are assumed to be zero, the initial temperature is 20 °C, and the initial water content is 15 %. The heat output from the waste is shown in figure 14 and given in tabular form in appendix II. The boundary conditions for the transient analysis are shown in figure 15.

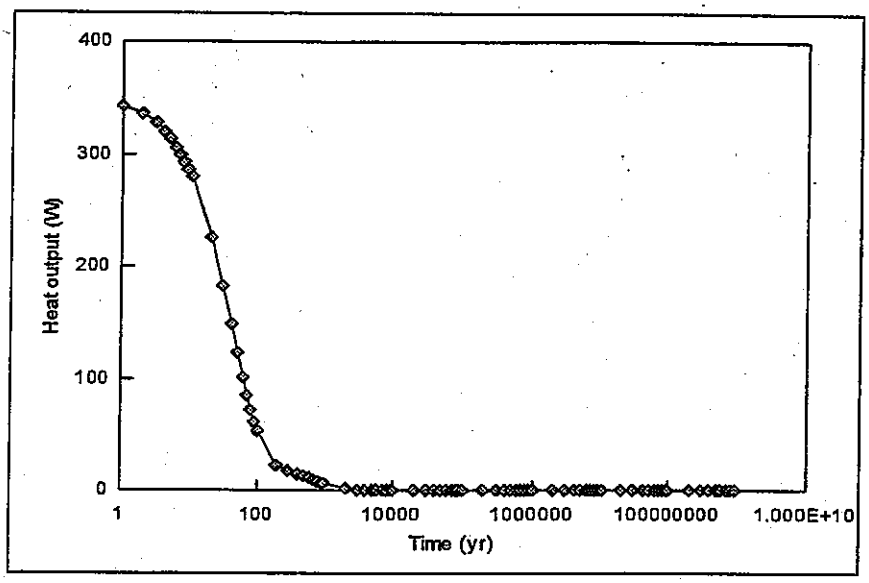

Figure 14 Heat output from the waste

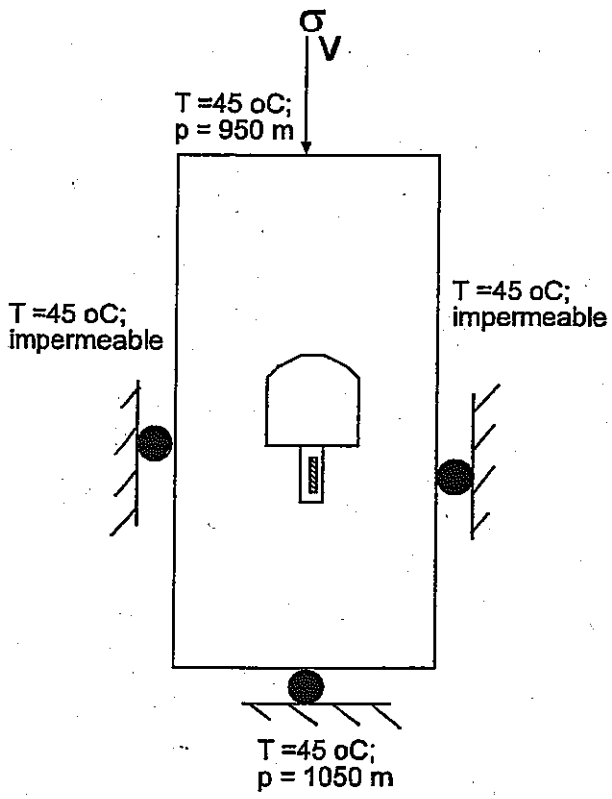

Figure 15 Boundary conditions for transient analysis

4.5.1 Output specifications for buffer and backfill

Time histories of temperature, water content and stresses in the buffer at the output points shown in figure 16 and table 1 will be calculated. The time history of the vertical displacement at B1 shall also be calculated.

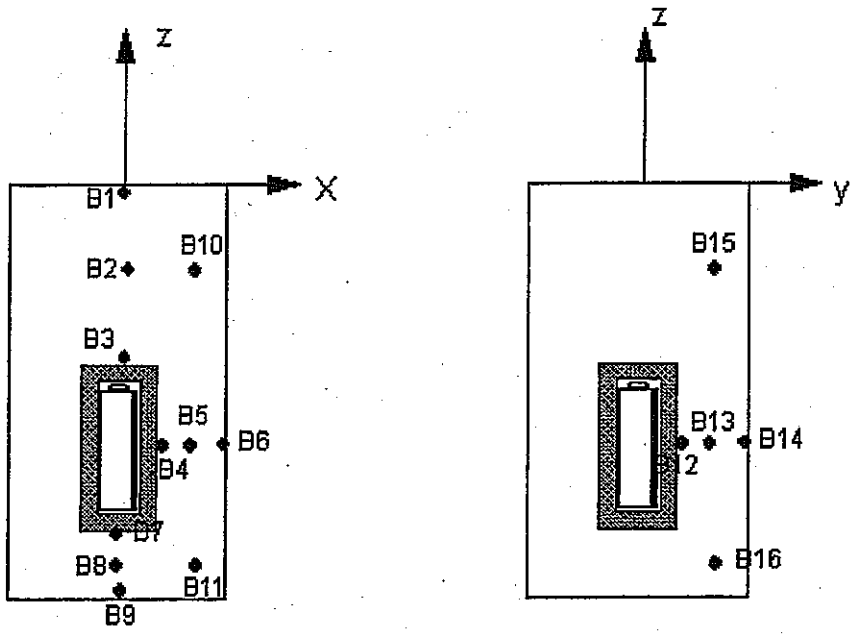

Figure 16 Output points for buffer

Point	x (m)	y (m)	z (m)	Output values
B1	0	0	0	T, θ, σ_{zz}, u_z
B2	0	0	-0.85	T, θ, σ_{xx}, σ_{zz}
B3	0	0	-1.7	T, θ, σ_{xx}, σ_{zz}
B4	0.41	0	-2.665	T, θ, σ_{xx}
B5	0.76	0	-2.655	T, θ, σ_{xx}, σ_{zz}
B6	1.11	0	-2.655	T, θ, σ_{xx}
B7	0	0	-3.43	T, θ, σ_{zz}
B8	0	0	-3.78	T, θ, σ_{xx}, σ_{zz}
B9	0	0	-4.13	T, θ, σ_{zz}
B10	0.76	0	-0.85	T, θ, σ_{xx}, σ_{zz}

B11	0.76	0	-3.78	T, θ, σ_{xx}, σ_{zz}
B12	0	0.41	-2.665	T, θ, σ_{yy}
B13	0	0.76	-2.655	T, θ,σ_{yy}, σ_{zz}
B14	0	1.11	-2.655	T, θ, σ_{yy}
B15	0	0.76	-0.85	T, θ,σ_{yy}, σ_{zz}
B16	0	0.76	-3.78	T, θ,σ_{yy}, σ_{z}

Table 1 Output points for buffer

The contours of temperature and water content in the buffer and backfill, at sections x=0 and y=0 shall be plotted at times: 1 , 2, 4, 8, 16, 32, 64 , 128, and 200 years.

4.5.2 Output specifications for rock mass

Contours at sections: x=0 and y=0 and variations along monitoring lines: x=y=0; z=-0.41 & x=0; z=-0.41 & y=0 will be plotted at times 1 , 2, 4, 8, 16, 32, 64 , 128, and 200 years for the following output parameters:

i) temperature and pore pressure

ii) Factor of safety for rock mass failure

iii) Permeability

4.6 Evaluation of coupling effects

For both the excavation phase, and the long term phase with emplaced buffer, backfill and heater, the analyses shall be performed with increasing degree of complexity of coupling. A comparison matrix will be established in order to compare the implications of various orders of complexity of the coupling, as shown in table 2.

Processes / Output	T	M	H	H-M	T-H	T-M	T-H-M
T evolution		N/A	N/A	N/A			
σ evolution	N/A		N/A		N/A		
k evolution	N/A	N/A	N/A			N/A	
ρ evolution	N/A	N/A				N/A	
θ evolution	N/A					N/A	

Table 2 Comparison matrix for different degree of THM coupling

4.7 Rock mass permeability function

For cases F0, F1 and F4, the rock mass permeability is assumed to be a function of the effective porosity. This function is derived from experimental data on sparsely fractured rock, with a permeabily range of 10^{-19} to 10^{-17} m^2. The permeabily function is shown in figure 17.

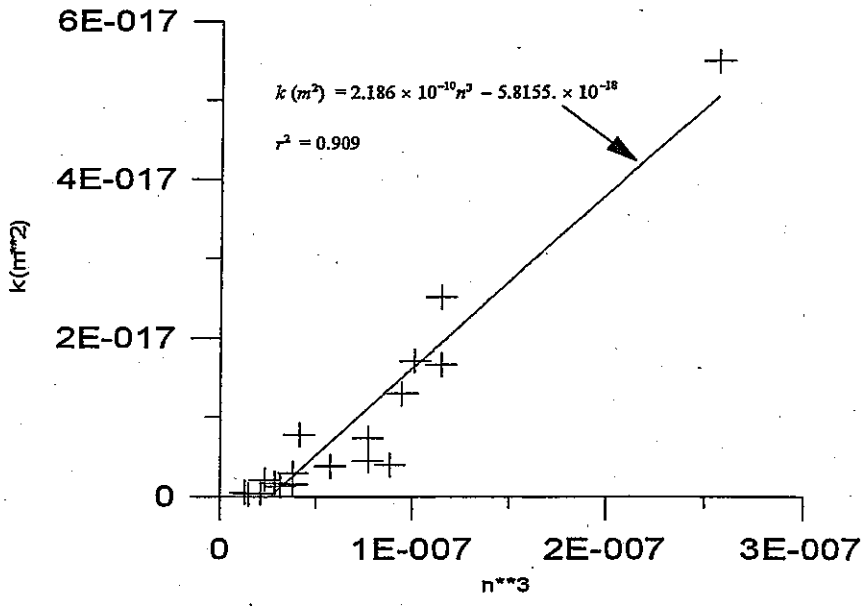

Figure 17 Permeability as a function of effective porosity

4.8 Rock mass failure criterion

We will adopt Hoek and Brown's failure criterion, expressed in term of effective stress:

$$\sigma'_{1f} = \sigma'_3 + \sqrt{m\sigma_c\sigma'_3 + s\sigma_c^2}$$

with:

σ'_{if} = *major effective principal stress at failure*

σ'_3 = *minor effective principal stress*

σ_c = uniaxial compressive strength = 123 Mpa
m, and s are empirical constants:
m= 17.5 and s = 0.19
The effective stress is defined as:

$$\sigma'_{ij} = \sigma_{ij} - p\delta_{ij}$$

with:

σ'_{ij} = *effective stress*

σ_{ij} = *total stress*

δ_{ij} = *Kroenecker delta*

= 1 (*i= j*) *and* 0 (*otherwise*)

p = *pore pressure*

4.9 Interfaces between buffer/rock mass, backfill/rock mass and overpack/buffer

The research teams shall define their own assumptions for the nature of these interfaces, from the experience gained in the calibration of the T-H-M test previously discussed.

4.10 Uncertainty evaluation

Since the buffer and backfill are man-made materials, it is assumed in this exercise that their properties could be considered constant. The most important degree of uncertainty would be related to the characteristics of the rock mass, e.g. the matrix permeability, the rock mass equivalent permeability, the fracture density and possibly orientation. It is hoped that the consideration of different cases in this exercise (F0 to F5) would serve to span a wide span of rock mass characteristics. For example, F0 would constitute a case where no distinctive fracture need to be explicitly included, and the rock mass could be considered as an equivalent porous medium with a range of permeability from 10^{-19} to10^{-17} m^2. F1 would constitute a scenario where one important fracture crosses the borehole, and F2 and F3 would constitute the scenario with ubiquitous fractures. The last task of this BMT1 would be a synthesis of all output results from F1 to F4, where the RTs should compare safety features (i.e. temperature field, time for resaturation,

stress field, permeability change, potential for rock mass failure) between cases F0 to F5. The other source of uncertainty might be the way the interfaces between the buffer/rock mass, backfill/rockmass and overpack/buffer are considered in the model. The RTs should discuss the influence of these interfaces on their results.

5. Proposed schedule and reporting

The following schedule is proposed. For convenience, we will divide BMT1 into the following subtasks:

BMT1-1: Calibration of T-H-M experiment and evaluation of calibration results
BMT1-2: Scoping calculations for F0, F1 and F4
BMT2-3: Scoping calculations for F2, F3 and F5
BMT1-4: Comparison of results for F0 to F5 (effect of rock mass permeability and fracturing); evaluation of the effects of interfaces between different materials.

October, 1999 : Presentation of task definition to FO's and RT's.
April, 1999: Task force group meeting .
June, 2000: RT's present results on BMT1-1. Final task definition sent to FO's and RT's
September, 2000: RT's submit reports on BMT1-1
December 2000: Secretariat, with the assistance of team leader, finalizes comparison report of BMT1-1 for all teams.
January, 2001: RT's present final results of BMT1-1 and preliminary results of BMT1-2
July, 2001: RT's submit reports for BMT1-2
August, 2001: Rt's present results for BMT1-2
April, 2002: RT's present results for BMT1-3 and BMT1-4
July, 2002: RT's submit reports for BMT1-3 and BMT1-4
December, 2002: Secretariat, with the assistance of team leader, finalizes comparison report of BMT1-2 to BMT1-4 for all teams.

Appendix I - Simplified 1-D axisymmetric calibration of T-H-M in-situ experiment

For this exercise, we focus on the THM behaviour of one radial line from the centre of the heater. The geometry of the problem is shown in figure I-1.

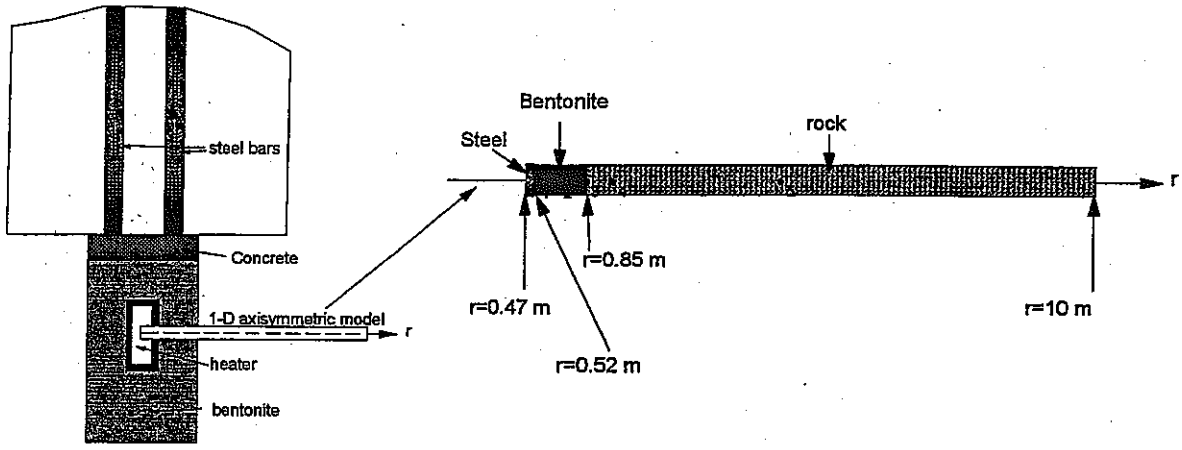

Figure I-1 Geometry of the model

The desired output at 5 points, shown in figure I-1, is detailed in table I-1. Time histories of these output parameters are requested for a heating period of 258 days followed by a cooling period of 180 days .

Point	r (m)	Output
1	0.52	T, u, σ,ε_r, w
2	0.685	T, u, σ,ε_r, w
3	0.85	T, u, σ,ε_r, w
4	1.45	T,u, p, ε_r , ε_t
5	3.	T,u,p

T: temperature (oC) u: radial displacement (m)
p: pore pressure (Pa) w: water content by weight (%)
σ: radial <u>total</u> stress (Pa) ε_r , ε_t: radial and tangential strain (non-dimensional)

Table I-1 Desired output

The boundary conditions are as follows:

At r=0.47 m:

- T=100 °C (during heating) and free temperature (during cooling)
- Free displacement
- Impermeable

At r = 10 m

- T = 12 °C
- u=0
- p=3.9 kPa (equivalent to 0.4 m of water)

The initial conditions are as follows:

- T = 12 °C everywhere
- displacements and stresses are zero everywhere
- p=3.9 kPa in the rock; w=15% in the bentonite

The basic T-H-M properties of the bentonite are determined by laboratory tests by JNC (1997). Depending on the models, input properties additional to the ones determined in the laboratory might be needed. These additional properties were determined by performing calibration of laboratory tests by the research teams involved in task 2C, of DECOVALEX II (Jing et al., 1999). For BMT1, the research teams should refer to these two references to select their input properties. Table 5.1 of Jing et al. summarizes the most important input parameters and should be used as a starting point.

Calibration targets

The following experimental values may be used as calibration targets:

- temperature at points 1, 2 and 3 (figure I-2)
- water content at points 1, 2 and 3 (figure I-3)
- radial stresses at points 1 (figure I-4) and 3 (figure I-5)
- radial strain at point 2 (figure I-6)
- radial and tangential strain at point 4 (figure I -7)

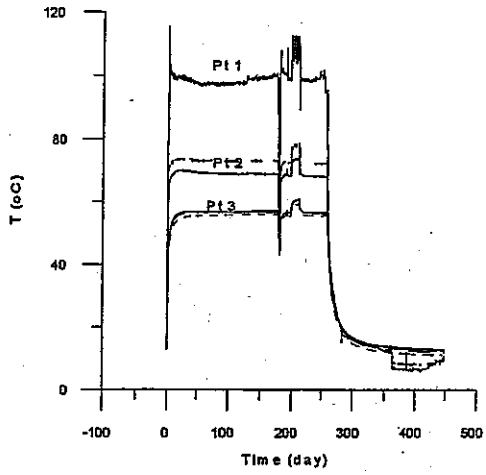

Figure I-2 Temperature at points 1,2 and 3

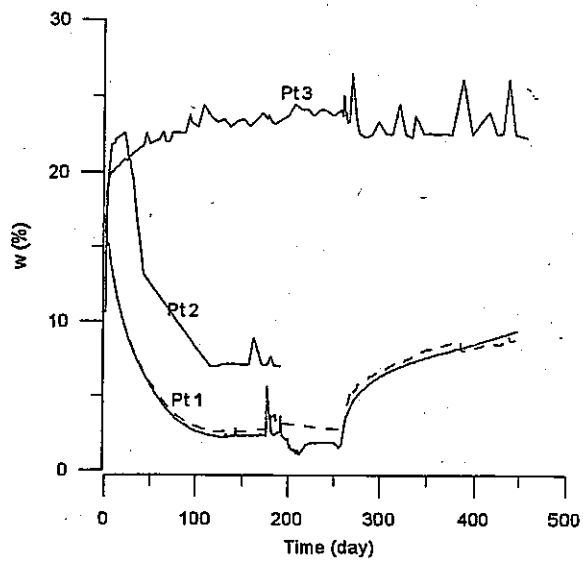

Figure I-3 Water content at point 1,2, 3

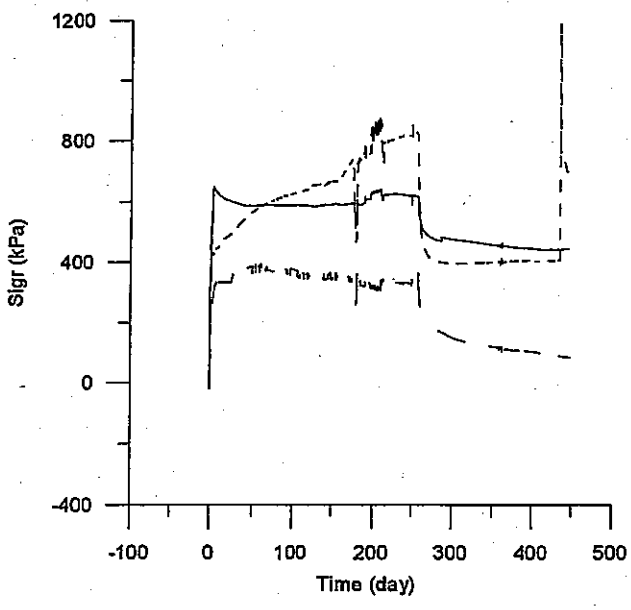

Figure I-4 Total stress at point 1

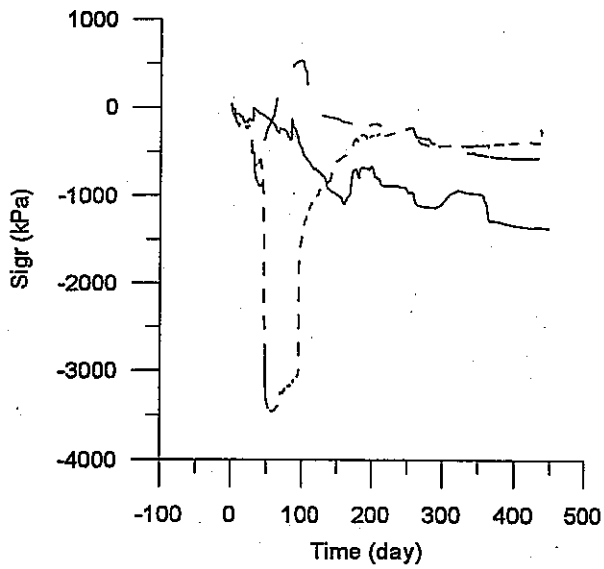

Figure I-5 Total stress at point 3

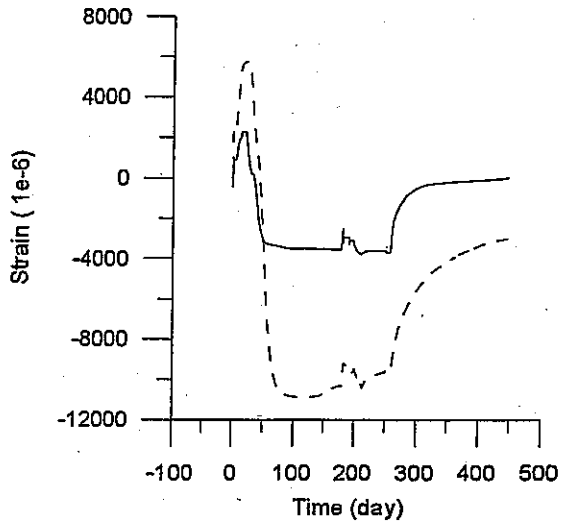

Figure I-6 Radial strain at Point 2

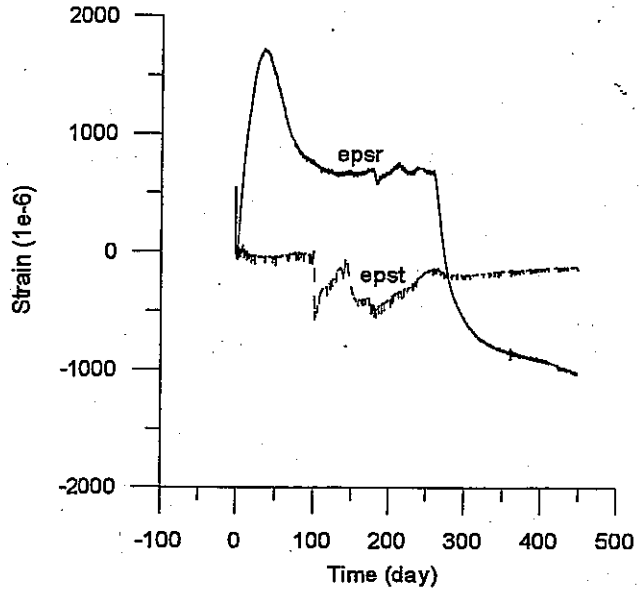

Figure I-7 Strain at point 4

In figures I-2 to I-7, for the same point, there might be several experimental curves shown. These curves come from the recorded results of different sensors at the same radial distance, but at different tangential angles.

Note that according to JNC, stress is positive in compression while strain is positive in tension. In addition, tensile stress measurements (e.g. point 3, figure I-5) are not reliable and are shown for information purpose only.The raw data for figures I-2 to I-7 are extracted from JNC's EXCEL file Buffer.XLS, in the CD handed out in Ottawa in April. There seems to be an error for the sign for sensors PS 11 and PS 13 in that file. This has been corrected; all the 'corrected' data is in the EXCEL file BMT11D.XLS that will be sent to you electronically.

References

1. T. Fujita, M. Chijimatsu, H. Ishikawa, H. Suzuki andK. Matsumoto, 1997, ' Fundamental Properties of Bentonite OT-9607', PNC TN8410 97-0701.

2. L. Jing, O. Stephansson, L. Borgesson, M. Chijimatsu, F. Kautsky, and C-F. Tsang, 1999, ' DECOVALEX II Project - Technical Report - Task 2C', SKI 99:23.

3. M. Chijimatsu, Y. Sugita and T. Fujita, 1999, ' Experimental Results', JNC TN8400 99-034.

Appendix II - Heat output from waste cannister

Time(year)	TOTAL(W/a waste)
0.0E+00	3.51E+02
1.0E+00	3.43E+02
2.0E+00	3.36E+02
3.0E+00	3.28E+02
4.0E+00	3.21E+02
5.0E+00	3.14E+02
6.0E+00	3.07E+02
7.0E+00	3.00E+02
8.0E+00	2.94E+02
9.0E+00	2.87E+02
1.0E+01	2.81E+02
2.0E+01	2.26E+02
3.0E+01	1.83E+02
4.0E+01	1.50E+02
5.0E+01	1.23E+02
6.0E+01	1.02E+02
7.0E+01	8.54E+01
8.0E+01	7.22E+01
9.0E+01	6.18E+01
1.0E+02	5.35E+01
2.0E+02	2.31E+01
3.0E+02	1.76E+01
4.0E+02	1.49E+01
5.0E+02	1.28E+01
6.0E+02	1.10E+01
7.0E+02	9.52E+00
8.0E+02	8.26E+00
9.0E+02	7.19E+00
1.0E+03	6.28E+00
2.0E+03	2.07E+00
3.0E+03	1.17E+00
4.0E+03	9.40E-01
5.0E+03	8.47E-01
6.0E+03	7.86E-01
7.0E+03	7.34E-01
8.0E+03	6.88E-01
9.0E+03	6.46E-01
1.0E+04	6.08E-01
2.0E+04	3.58E-01
3.0E+04	2.44E-01

4.0E+04	1.86E-01
5.0E+04	1.53E-01
6.0E+04	1.33E-01
7.0E+04	1.21E-01
8.0E+04	1.13E-01
9.0E+04	1.08E-01
1.0E+05	1.05E-01
2.0E+05	1.20E-01
3.0E+05	1.35E-01
4.0E+05	1.44E-01
5.0E+05	1.48E-01
6.0E+05	1.48E-01
7.0E+05	1.47E-01
8.0E+05	1.45E-01
9.0E+05	1.41E-01
1.0E+06	1.38E-01
2.0E+06	9.83E-02
3.0E+06	7.12E-02
4.0E+06	5.16E-02
5.0E+06	3.75E-02
6.0E+06	2.72E-02
7.0E+06	1.98E-02
8.0E+06	1.45E-02
9.0E+06	1.06E-02
1.0E+07	7.80E-03
2.0E+07	7.23E-04
3.0E+07	4.47E-04
4.0E+07	4.23E-04
5.0E+07	4.12E-04
6.0E+07	4.04E-04
7.0E+07	3.98E-04
8.0E+07	3.93E-04
9.0E+07	3.89E-04
1.0E+08	3.86E-04
2.0E+08	3.67E-04
3.0E+08	3.55E-04
4.0E+08	3.45E-04
5.0E+08	3.34E-04
6.0E+08	3.25E-04
7.0E+08	3.16E-04
8.0E+08	3.07E-04
9.0E+08	2.99E-04

別添 - 8

DECOVALEX TASK3 BMT1

事務局提出書類（検討結果）

3. Re-evaluation of Kamaishi Mine Modeling by JNC

3.1 Introduction

This section presents the work conducted by the JNC Research team on the first phase of BMT1. The object is to re-evaluate the modeling of the Kamaishi Mine heater test (Chijimatsu et al., 1999). In order to carry out the re-evaluation, the modeling of swelling pressure that took into account the temperature and density dependency based on the laboratory experiment results carried out by Japan Nuclear Cycle Development Institute is performed at first. Then validation of this model is conducted by using the laboratory test and re-evaluation of Kamaishi heater test is carried out by simplified axisymmetric model.

3.2 Temperature and density dependency of swelling pressure

3.2.1 Temperature dependency

Figure 3.1 shows the swelling pressure measurement results (Suzuki and Fujita, 1999). Material of specimen was sand mixture bentonite (B:S=7:3, Dry density is 1.6 g/cm^3). During the swelling pressure measurement, temperature increased step by step as shown Figure 3.1. Table 3.1 shows the final swelling pressure value of each temperature condition. Figure 3.2 shows the relationship between final swelling pressure value and temperature. In these figures, swelling pressure at 60ºC is higher than that at 25ºC in this experiment. However it is assumed that swelling pressure decreases with increases in temperature linearly as shown Figure 3.2 because swelling pressure at 90ºC is lower than that at 25ºC. The function of swelling pressure σ and temperature T is as follows.

$$\sigma = 0.44 - 0.001T \tag{3.1}$$

From this equation (3.1), the swelling pressure at 25ºC is calculated to be 0.415 MPa.

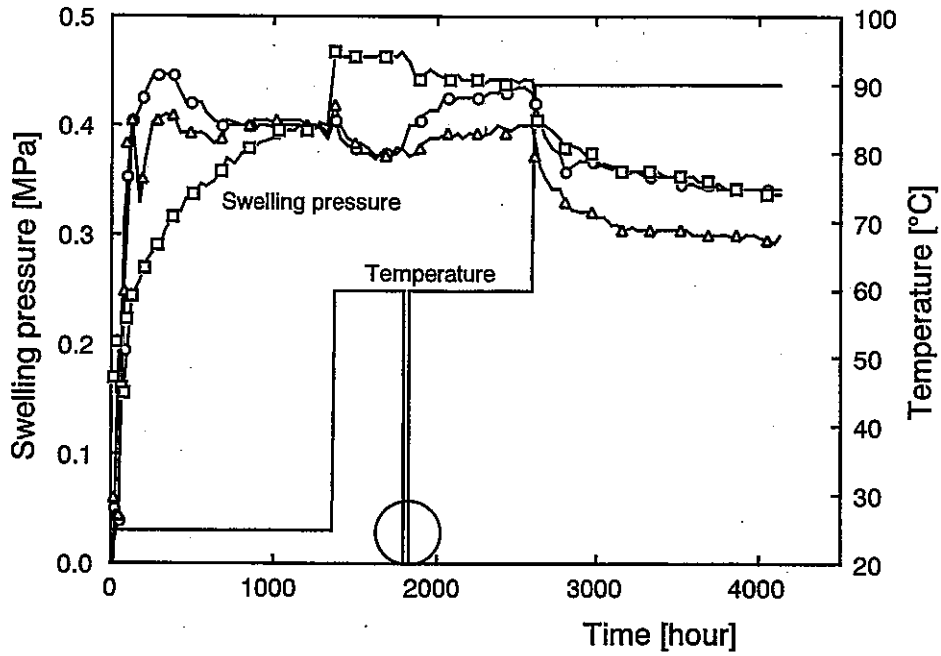

Figure 3.1 Measurement results of swelling pressure with time

Table 3.1 Measurement results of swelling pressure (MPa)

Temperature	25°C	60°C	90°C
Swelling pressure	0.39	0.43	0.34
	0.40	0.40	0.30
	0.40	0.44	0.34

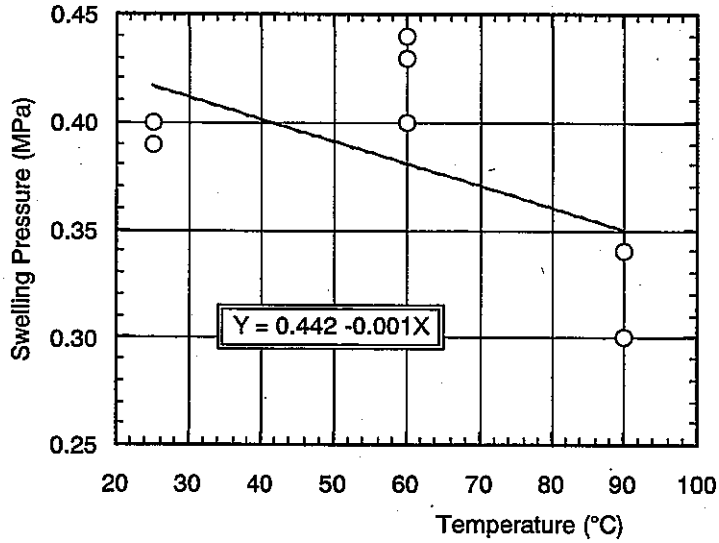

Figure 3.2 Relationship between swelling pressure and temperature

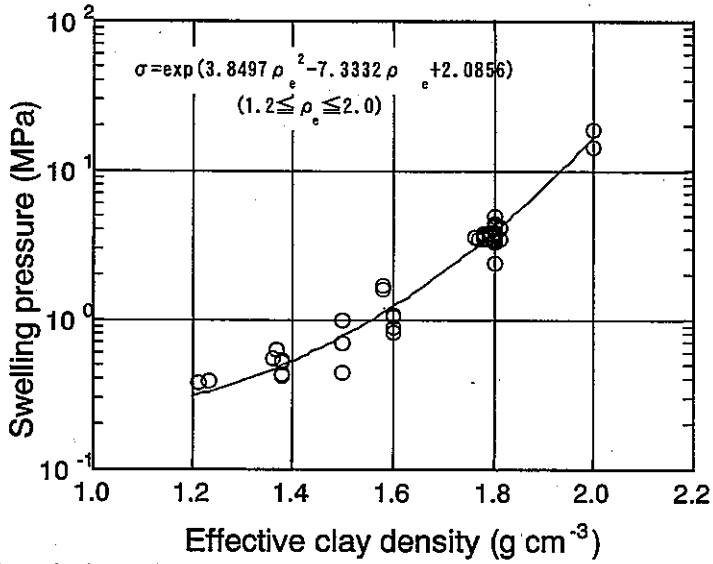

Figure 3.3 Relationship between effective clay density and swelling pressure

3.2.2 Density dependency

Figure 3.3 shows the relationship between swelling pressure and effective clay density. This relationship is expressed by the equation (3.2) (Japan Nuclear Cycle Development Institute, 2000). The effective clay density is calculated by equation (3.3). From the equation (3.2), in the case of sand mixture bentonite (B:S=7:3) at dry density 1.6g/cm^3, effective clay density is 1.368g/cm^3 and swelling pressure is calculated to be 0.48 MPa. Where, density of soil particle is assumed to be 2.65g/cm^3.

$$\sigma = \exp(3.85\rho_e^2 - 7.33\rho_e + 2.09) \quad (3.2)$$

$$\rho_e = \rho_d(100-Rs)/(100-\rho_d Rs/\rho_s) \quad (3.3)$$

where, ρ_e is effective clay density (g/cm^3), ρ_d is dry density (g/cm^3), Rs is mixing ratio at dry weight of sand (%), ρ_s is density of soil particle (g/cm^3).

3.2.3 Modeling of swelling pressure

From above results, it is assumed that swelling pressure is a function of temperature and effective clay density as shown in equation (3.4). In the THM simulation, swelling pressure is modeled as function of water potential as shown in equation (3.5), and coefficient F is estimated by back analysis of laboratory test. Therefore, the estimated coefficient value from the swelling pressure at temperature 25ºC, dry density 1.6 g/cm^3, sand mixing ratio 30% is to be F_o and THM simulation is conducted by using F value shown in equation (3.6).

$$\sigma = \exp(3.85\rho_e^2 - 7.33\rho_e + 2.09) - 0.001T \quad (3.4)$$

$$\sigma = F \mid \Delta\psi \mid \quad (3.5)$$

$$F = F_o \times \left\{ \frac{\exp\left(3.85\rho_e^{\,2} - 7.33\rho_e + 2.09\right) - 0.001T}{\exp\left(3.85\rho_{eo}^{\,2} - 7.33\rho_{eo} + 2.09\right) - 0.001T_o} \right\} \quad (3.6)$$

T_o=25ºC, ρ_{eo}=1.368g/cm^3

3.3 Simulation of laboratory experiment by considering the temperature and density dependency

3.3.1 Simulation of swelling pressure test

Simulation of swelling pressure test at each temperature was conducted and comparison with measurement results was carried out. Simulation was carried out by axisymmetric model as shown in Figure 3.4. The material is sand mixture bentonite with dry density 1.6 g/cm^3. Temperature is 25ºC, 60ºC and 90ºC.

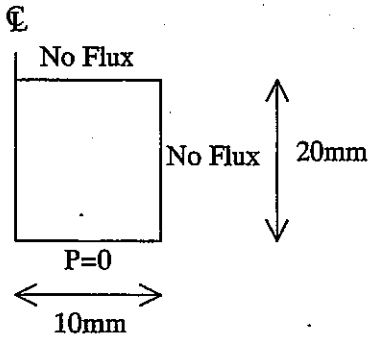

Figure 3.4 Analysis model for swelling pressure test

Figure 3.5 and Figure 3.6 show the water diffusivity and water retention curve, respectively. For the simulation, experimental function (3.7) is adopted for water

diffusivity and van Genuchten model (3.8) is adopted for water retention curve. Table 3.2 shows the coefficients for equations (3.7) and (3.8). Table 3.3 shows the other parameters of sand mixture bentonite.

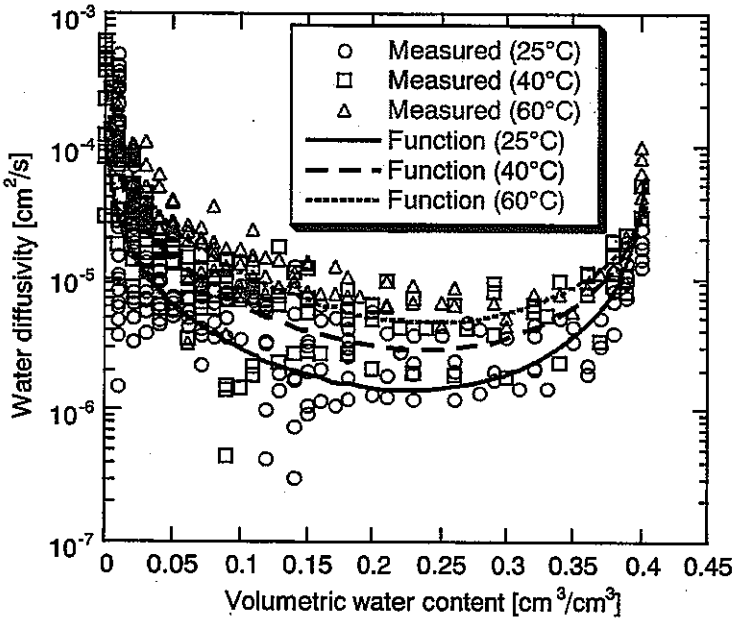

Figure 3.5 Water diffusivity of sand mixture bentonite

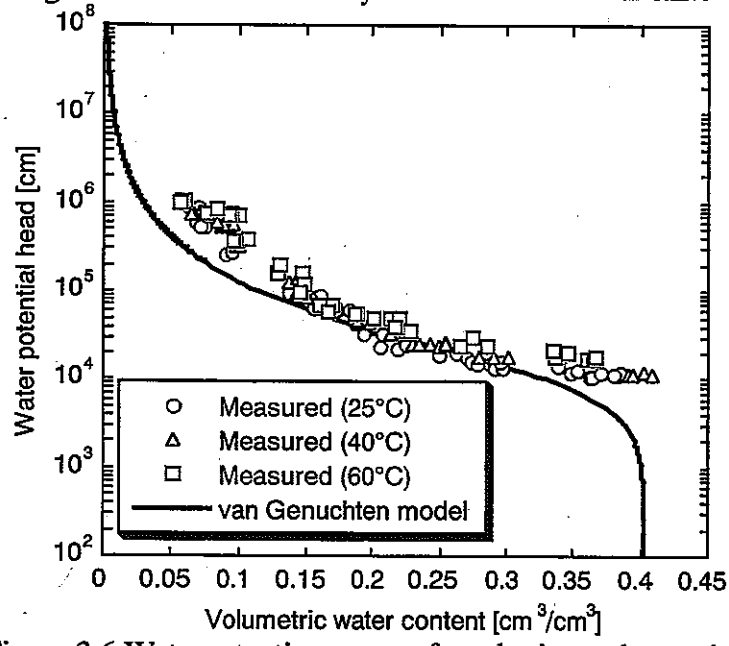

Figure 3.6 Water retention curve of sand mixture bentonite

$$D_\theta = \frac{a_1(\theta - \theta_s)}{(\theta - b_1)(b_1 - \theta_s)} + \frac{a_2\theta}{b_2(\theta - b_2)} \tag{3.7}$$

$$\frac{\theta - \theta_r}{\theta_s - \theta_r} = \left\{1 + |\alpha\psi|^n\right\}^{\left(1-\frac{1}{n}\right)} \tag{3.8}$$

Table 3.2 Coefficients for equations (3.7) and (3.8)

Coefficient	Value
a_1	$2.99 \cdot 10^{-8}T - 3.74 \cdot 10^{-7}$
a_2	$-1.50 \cdot 10^{-8}T + 1.49 \cdot 10^{-7}$
b_1	$-2.49 \cdot 10^{-3}$
b_2	$5.59 \cdot 10^{-4}T + 3.93 \cdot 10^{-1}$
θ_s	0.403
θ_r	0.000
α	$8.0 \cdot 10^{-5}$
n	1.6

Table 3.3 Other parameters

Parameter	Value
Young's modulus (MPa)	50.0
Poisson's ratio	0.3
Intrinsic permeability (m^2)	$4.0 \cdot 10^{-20}$
Thermal conductivity (W/m/K)	$4.44 \cdot 10^{-1} + 1.38 \cdot 10^{-2}\omega + 6.14 \cdot 10^{-3}\omega^2 - 1.69 \cdot 10^{-4}\omega^3$
Specific heat (kJ/kg/K)	$(34.1 + 4.18\omega)/(100 + \omega)$
Thermal expansion coefficient (1/K)	$1.0 \cdot 10^{-5}$
Thermal water diffusivity (m^2/s/K)	$7.0 \cdot 10^{-12}$

Figure 3.7 shows the time history of water potential in each section in the specimen. The legend in the figure shows the distance from the bottom of specimen, that is, the distance from the seepage surface. Figure 3.8 shows the time history of water content in each section in the specimen. Water content in the specimen increases from the closer side of seepage surface. Then specimen becomes saturated after approximately 300 hours past. Figure 3.9 shows the time history of total pressure at each section in the specimen. Because the model that swelling pressure generates with the change of water potential is used, the tendency of swelling pressure generation is similar with the water potential change. Furthermore, swelling pressure becomes constant when the change of water potential is stopped. The swelling pressure value at the seepage side is a little lower than that at opposite side but difference is small. Figure 3.10 shows the time history of strain at each section in the specimen. Positive value shows the compressive strain and negative value shows the tensile strain. Tensile strain occurs near the seepage surface and then compressive strain occurs at the opposite side. Then both tensile and compressive strains decrease with saturating of specimen, and strain becomes zero when specimen is full saturated. Figure 3.11 shows the time history of dry density at each section in the specimen. The dry densities at the bottom side decrease due to the generation of the tensile strain at the early time. On the other hand, dry densities at the upper side increase. The change of dry density also disappears when swelling pressure becomes constant and after that the dry density in the specimen becomes uniformity. Figure 3.12 shows the comparison of swelling pressure between calculated and measured results. Experiments were carried out five times and results show the different swelling pressure value. Therefore, coefficient F_o is estimated to simulate the average swelling pressure value in the measured data as shown in Figure 3.12.

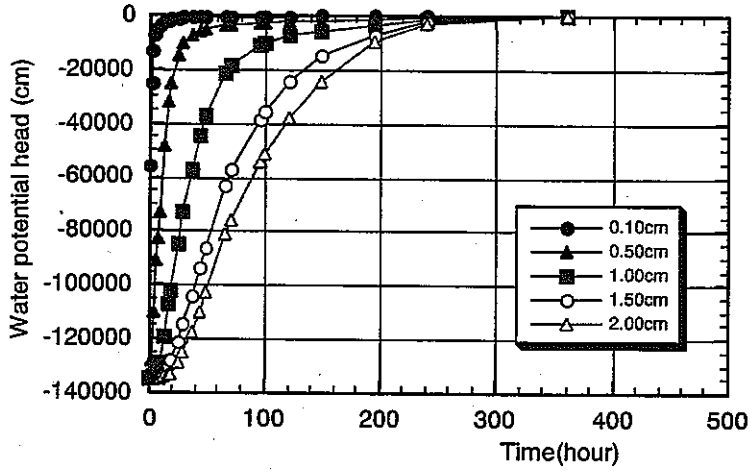

Figure 3.7 Time history of water potential in each section (Temperature is 25ºC)

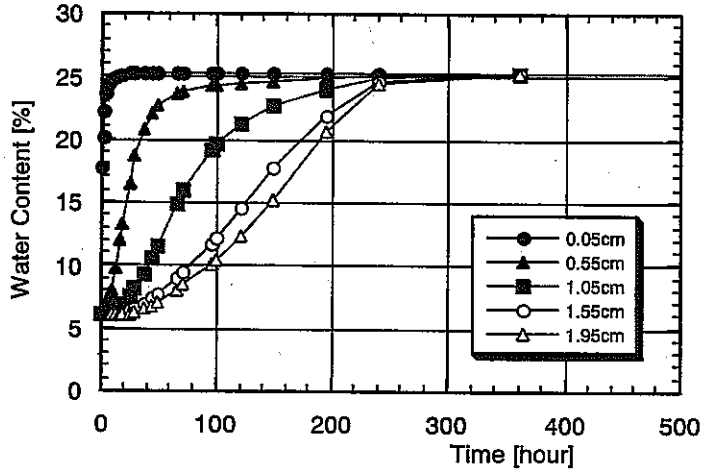

Figure 3.8 Time history of water content in each section (Temperature is 25ºC)

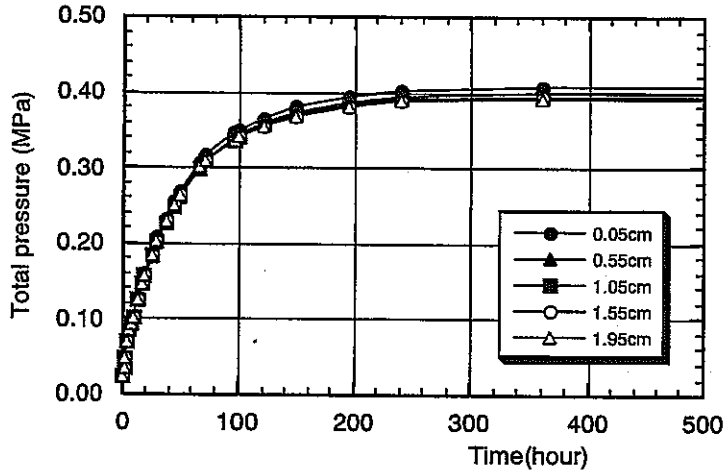

Figure 3.9 Time history of total pressure in each section (Temperature is 25ºC)

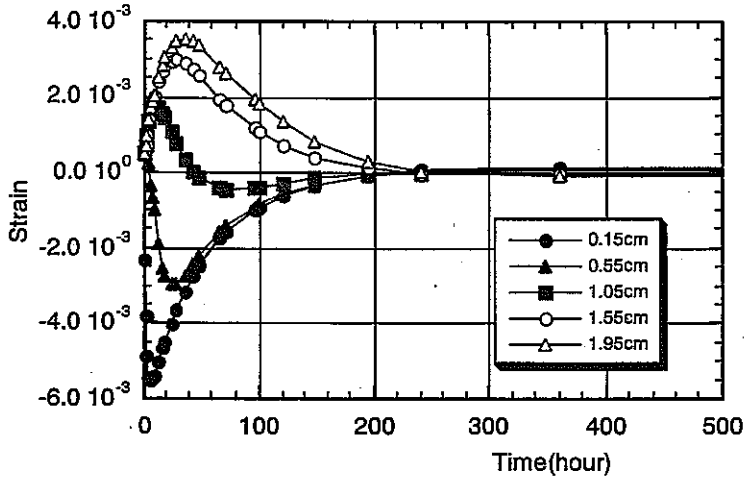

Figure 3.10 Time history of strain in each section (Temperature is 25ºC)

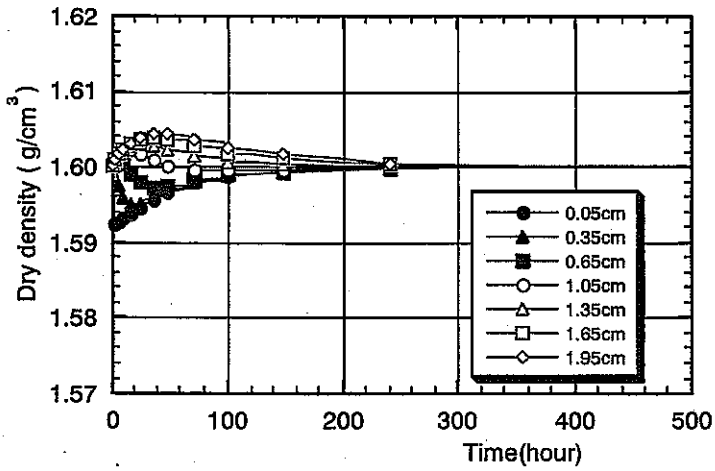

Figure 3.11 Time history of dry density in each section (Temperature is 25ºC)

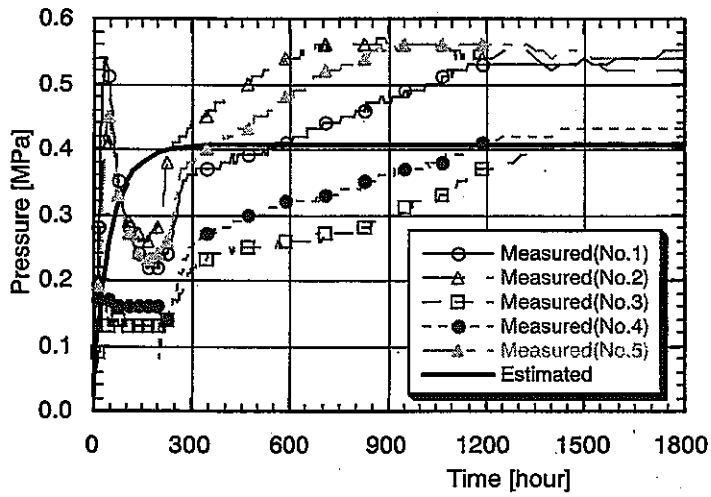

Figure 3.12 Comparison of pressure between analytical and measurement result

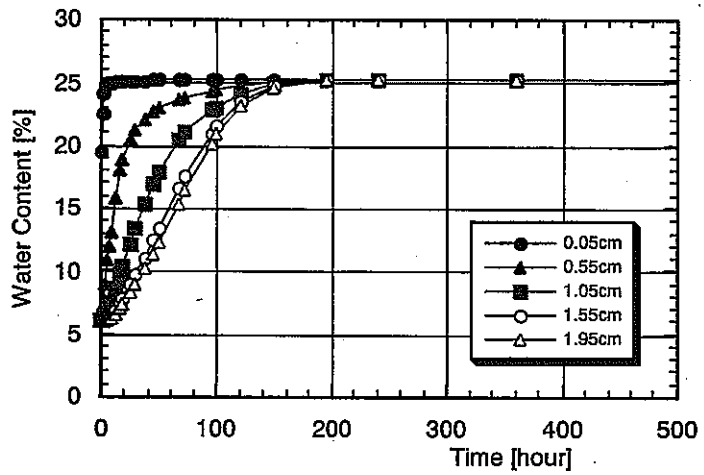

Figure 3.13 Time history of water content in each section (Temperature is 60ºC)

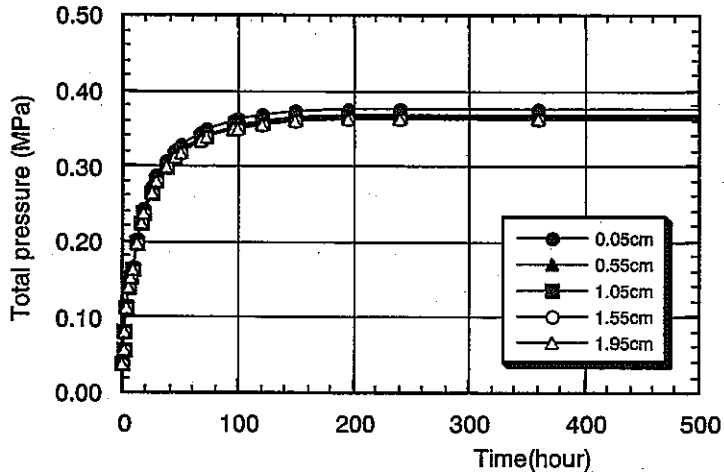

Figure 3.14 Time history of total pressure in each section (Temperature is 60ºC)

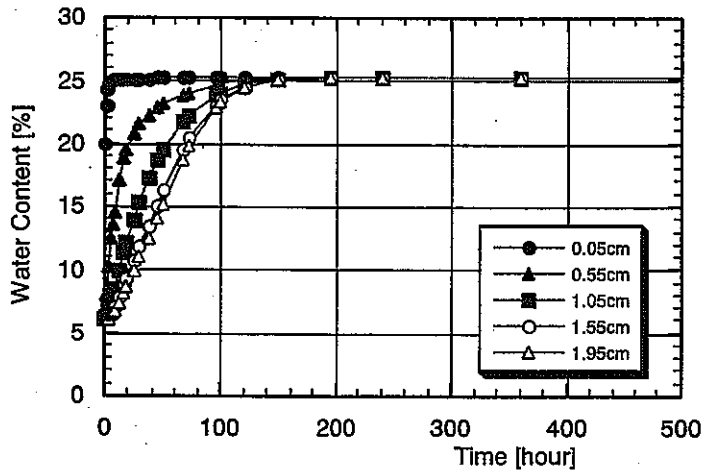

Figure 3.15 Time history of water content in each section (Temperature is 90ºC)

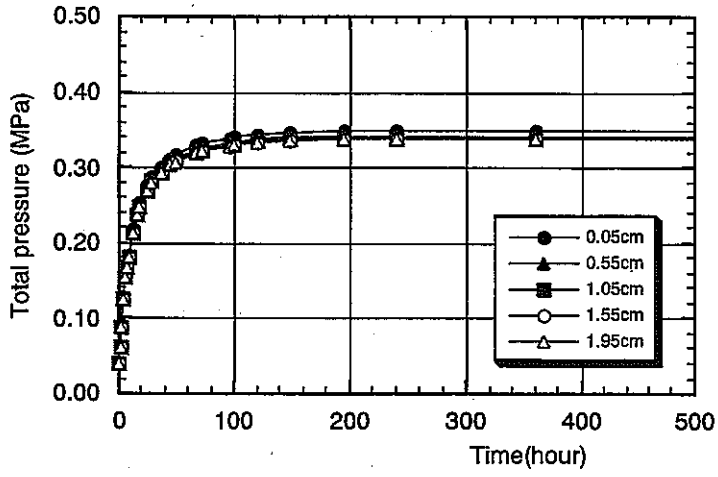

Figure 3.16 Time history of total pressure in each section (Temperature is 90ºC)

Figure 3.13 and Figure 3.14 shows the time history of water content and total pressure at each section in the specimen when the temperature is 60ºC, respectively. Figure 3.15 and Figure 3.16 also shows the time history of water content and total pressure at each section in the specimen when the temperature is 90ºC, respectively. The time when the specimen becomes full saturated is fast with temperture increasing and the time when the swelling pressure becomes constant is also fast. Furthermore, the swelling pressure value decrease with temperature increasing.

3.3.2 Simulation of coupled test in laboratory

(1) Outline of coupled test

Figure 3.17 shows the test apparatus used for coupling test, which consist of the water movement under thermal gradient and water injection (Suzuki et al., 1999). The test apparatus is composed of a specimen, a main unit of 50-mm in diameter and 100-mm in height, a heating chamber, a copper plate, a thermostat with a circulation system, thermocouples, load cells, and a data logger. During the test, the temperature of the thermostat connected to the heating chambers above and below the specimen is controlled at specified temperature. Furthermore, water is injected from the upper side of the specimen at water head of 100cm. Measurement items are total infiltration quantity into the specimen, temperature and swelling pressure. Temperature is measured by thermocouple at locations 0.2, 2.0, 4.0, 6.0, 8.0, 9.8cm from the bottom of the specimen, respectively, with the data logger. Swelling pressure is measured by load cell at locations 1.0, 3.0, 5.0, 7.0, 9.0cm from the bottom of the specimen, respectively, with the data logger. And swelling pressure is also measured at the upper surface of the specimen. The water distribution is obtained by measuring the water content by the oven-dry method after dividing the specimen in the apparatus when test is finished.

(2) Measurement result

Figure 3.18 shows the time history of infiltration quantity into the specimen. From this figure, it is shown that water of 65cc injected into the specimen and injection is almost stopped after 7000hours past from the start. Theoretical maximum infiltration quantity is approximately 60cc. The reason that measured infiltration quantity is larger than theoretical one is considered due to the influence of evaporation of water.

Figure 3.19 shows the time history of swelling pressure. Swelling pressure also becomes constant after 7000hours past from the start and this agrees with infiltration quantity change. The value of swelling pressure is approximately 0.4 MPa at the upper side of specimen and approximately 0.2MPa at the lower side of specimen. That is, swelling pressure at the upper side is higher than that at the lower side. Upper side is the infiltration side and the low temperature side under thermal gradient. After the coupled test was finished, water content distribution was measured and Table 3.4 shows the results. Theoretical saturated water content of this specimen is approximately 25% and it is judged that specimen after coupled test was almost saturated. From Table 3.4, it is shown that water content at the infiltration side and center part of the specimen is higher than other part. The reason of high water content at the infiltration side is due to the swelling at the early stage of coupled test. The reason of high water content at the center part is due to the low dry density of this part by difficulty of uniform manufacturing.

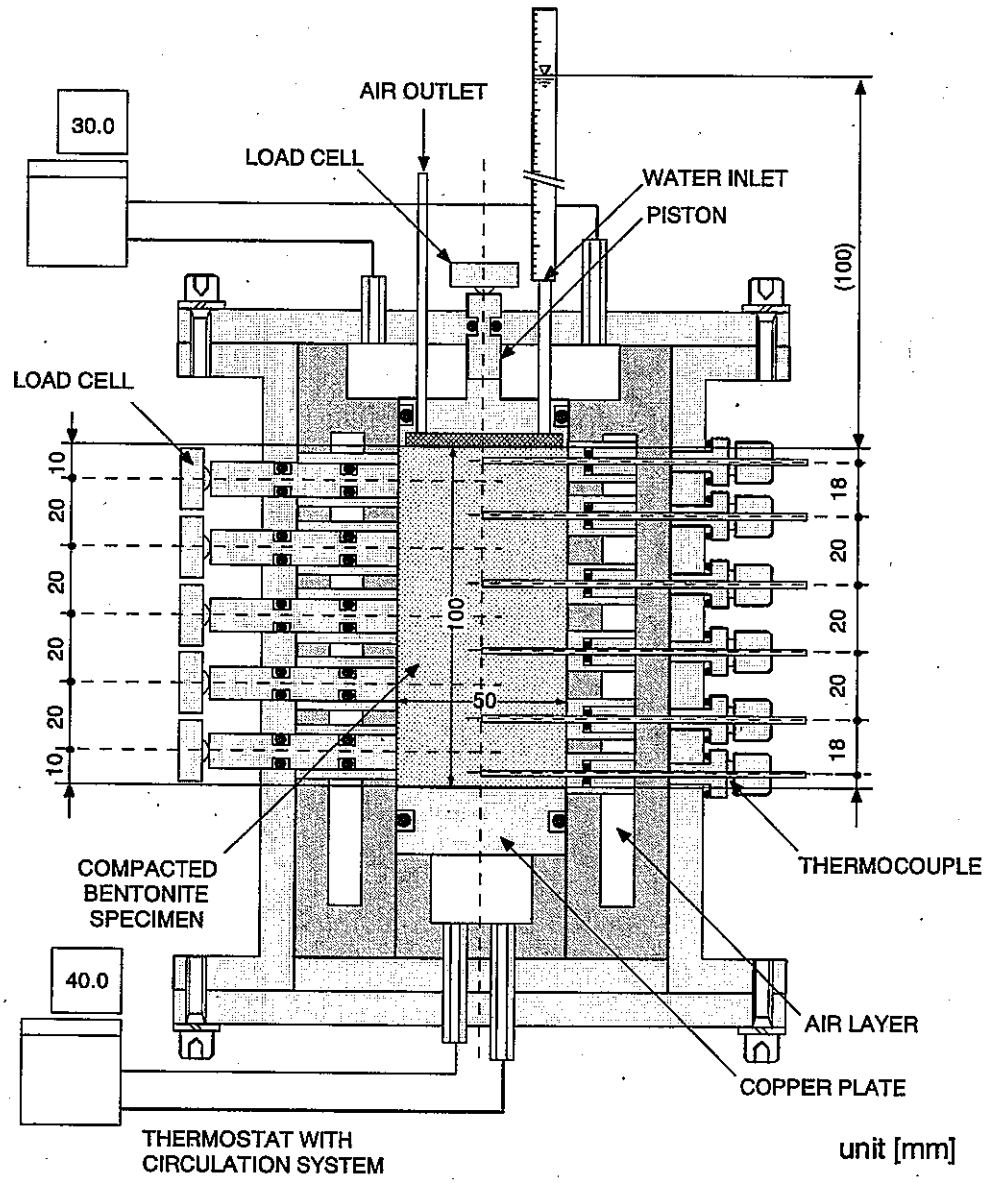

Figure 3.17 Test appratus for coupled test

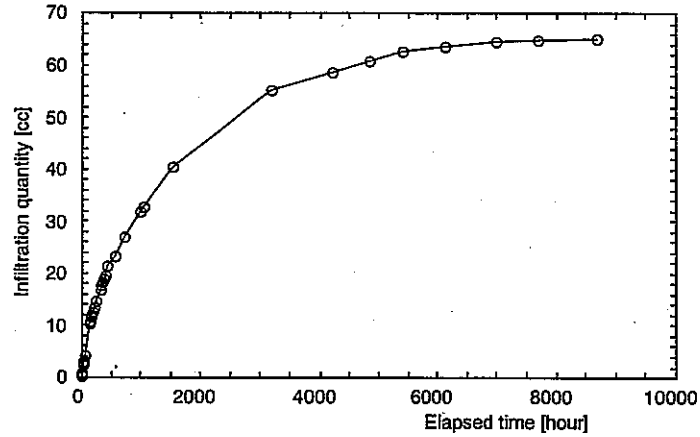

Figure 3.18 Measured infiltration quantity into the specimen

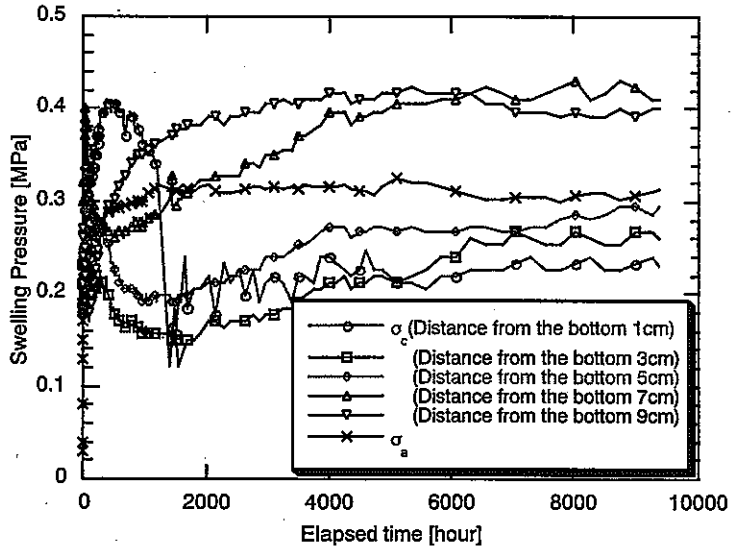

Figure 3.19 Measured swelling pressure

Table 3.4 Measured water content distribution

Distance from the infiltration surface (cm)	Water content (%)
0.5	27.68
1.5	25.27
2.5	25.18
3.5	25.44
4.5	26.20
5.5	26.43
6.5	25.57
7.5	25.63
8.5	24.77
9.5	24.67
Average	25.68

(3) Analysis model

Analysis is carried out by axisymmetric model. Figure 3.20 shows the analysis model. This figure also shows the boundary conditions. About the thermal conditions, upper surface of the model is fixed at 30ºC and bottom surface is fixed at 39ºC. The side of model is adiabatic condition. About the hydraulic conditions, upper surface is

fixed at 100-cm water head and other surfaces are no flow boundaries. The initial water content of bentonite is 6.0%. About the mechanical conditions, all surfaces are fixed to the normal direction.

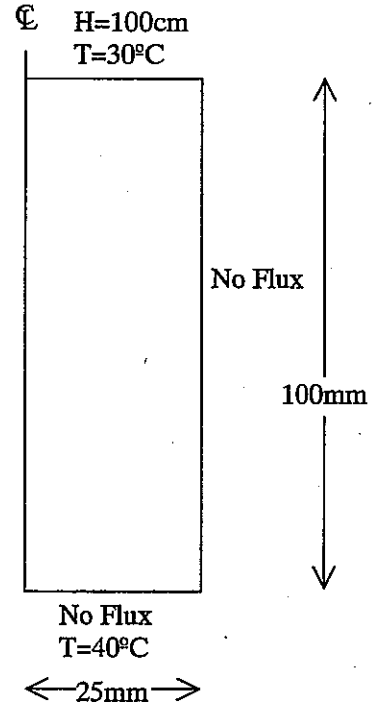

Figure 3.20 Analysis model for coupled test

(4) Analysis results

Figure 3.21 shows the time history of water content in the bentonite. Legend X expresses the distance from the bottom surface of the specimen. That is, X=0cm is the high temperature surface and X=10cm is the low temperature surface. From this figure, it is shown that low temperature side that is infiltration side became saturated earlier than opposite side (This is high temperature side). The water content at the high temperature side decrease at first, however the influence of temperature is small and water content increase after decreasing. After 8000hours from the start, water content change becomes steady state, and water content at the upper side is to be approximately 25%, that is, upper side is saturated. The water content at the lower side is smaller than that at the upper side. Figure 3.22 shows the time history of dry density. From this figure, it is shown that the dry density near the infiltration side becomes low at the early time of experiment due to the swelling, however, the dry density at the high temperature side becomes low finally. From this result, it will be expected that saturated water content at the high temperature side becomes higher than 25%. However, as a result of simulation, water content at the high temperature side becomes lower than 25%. That is, high temperature side is not saturated in this simulation. Figure 3.23 shows the comparison of water infiltration quantity between estimated and measured results. Increasing tendency of estimated result shows the good agreement with that of measured result but final value is different. However estimated water infiltration quantity never be over 60cc because theoretical maximum value of water infiltration quantity is approximately 60cc. Figure 3.24 shows the time history of total pressure in each section. As a result of simulation, total pressure at the high temperature side is lower than that at the low temperature side and this tendency is similar to the measured result.

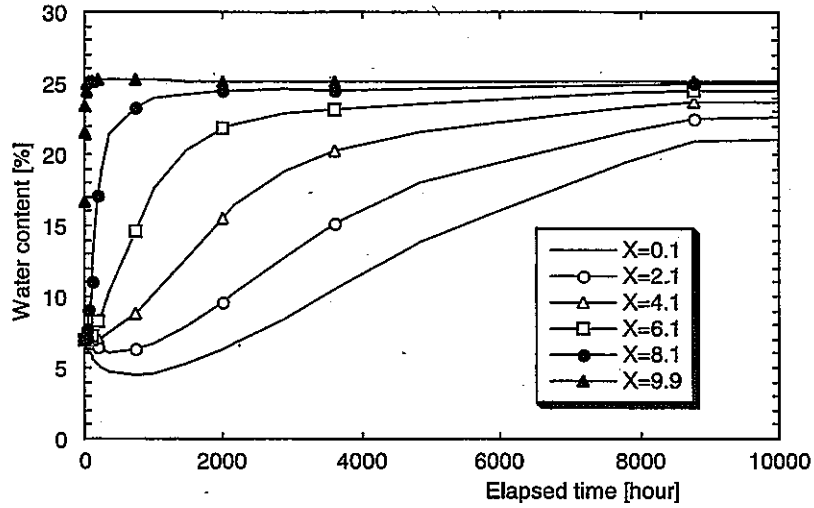

Figure 3.21 Time history of water content by simulation

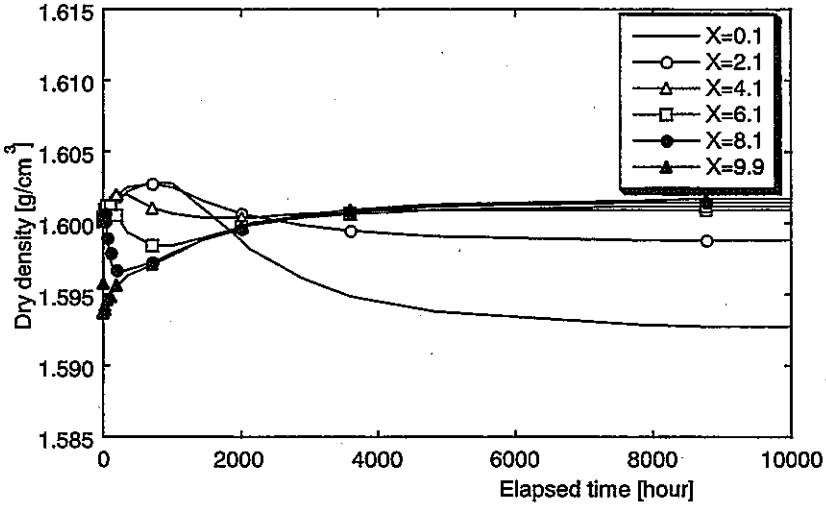

Figure 3.22 Time history of dry density by simulation

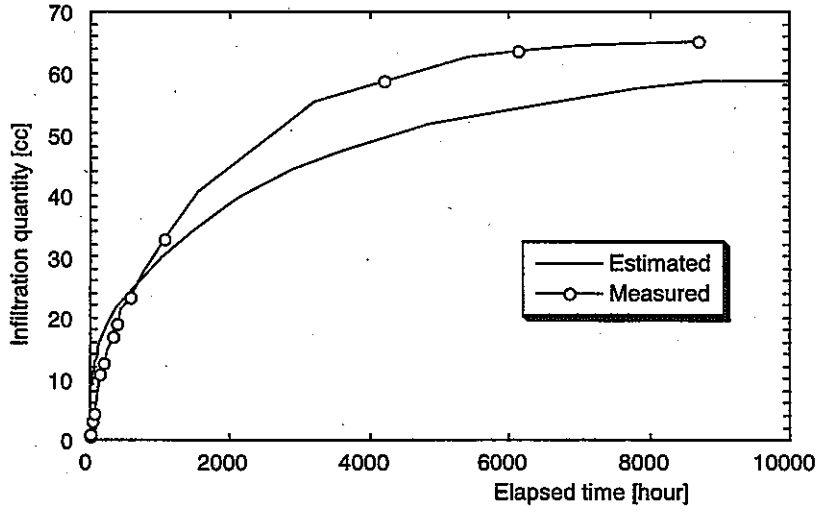

Figure 3.23 Comparison of water infiltration quantity between estimated and measured results

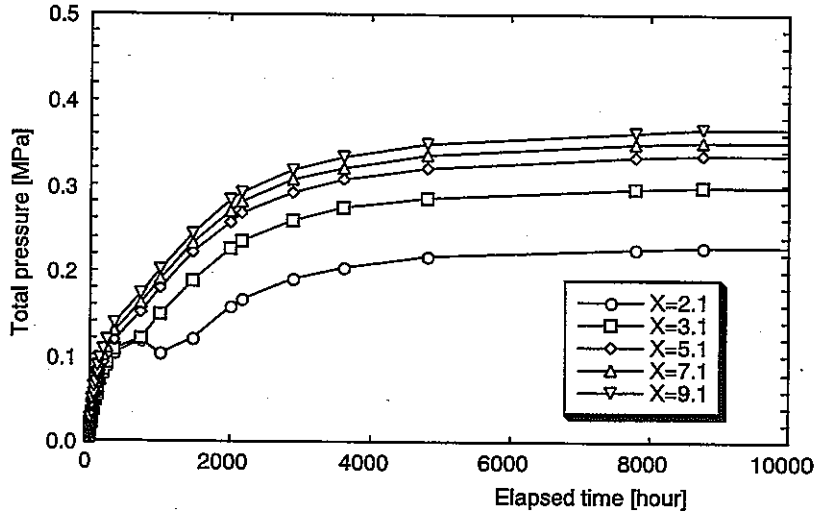

Figure 3.24 Time history of total pressure by simulation

3.4 Re-evaluation of Kamaishi THM experiment

3.4.1 Analysis model

In this section, re-evaluation of Kamaishi THM experiment is presented. Simulation is performed by using a simplified axisymmetric model as shown in Figure 3.25.

Boundary and initial conditions of simulation are as follows.

[Boundary condition]

r = 0.47m

- T = 100 ºC (during heating phase)
- No flow
- No displacement

r = 10m

- T = 12 ºC
- No displacement
- P = 3.9 kPa

[Initial condition]

- T = 12 ºC
- P = 3.9 kPa (in the rock mass)
- ω = 15 % (water content in the bentonite)

Model geometry and boundary conditions are shown in Figure 3.26.

Simulation is performed both in the heating phase (258 days) and the cooling phase (180 days) and output points are shown in Table 3.5.

Table 3.5 Output points

Point	r (m)
1	0.52
2	0.685
3	0.85
4	1.45

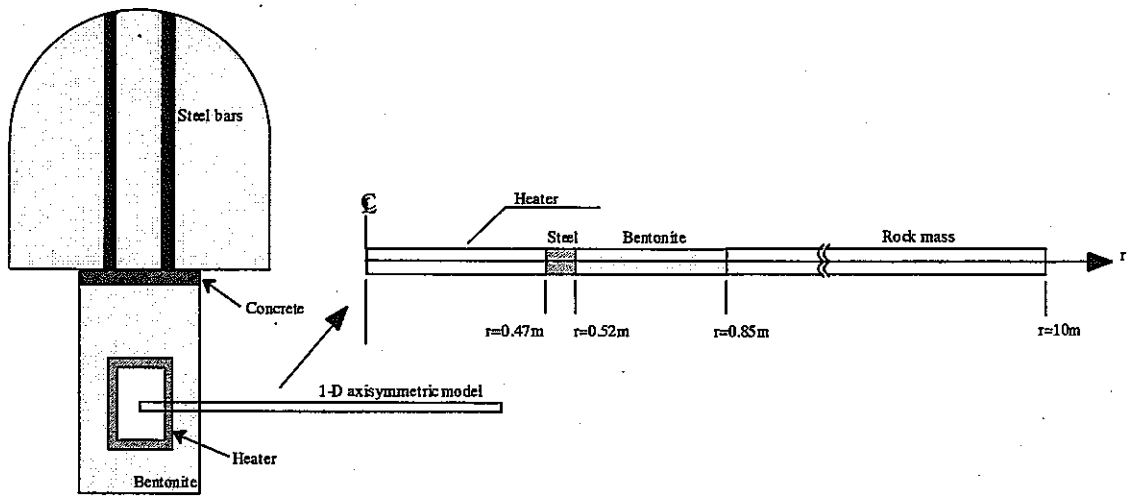

Figure 3.25 Analysis model for calibration of Kamaishi THM experiment

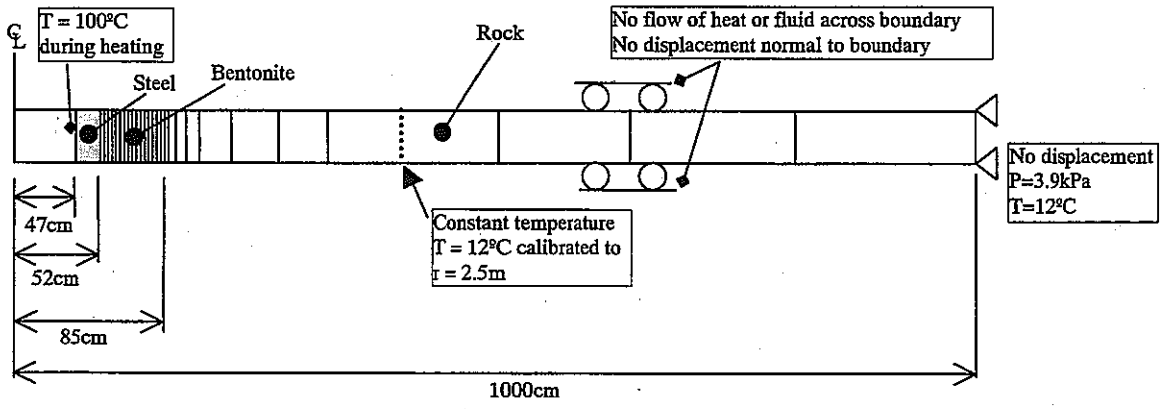

Figure 3.26 Model geometry and boundary conditions

3.4.2 Parameters for simulation

Many parameters of bentonite are obtained by laboratory tests directly (Fujita et al., 1997). The water diffusivity is a function of volumetric water content and temperature. The water potential is a function of volumetric water content. These relationships are determined by laboratory tests. The thermal water diffusivity and parameters for swelling pressure are determined by back analysis of laboratory test. Furthermore, thermal expansion coefficient is calibrated newly.

(1) Water diffusivity and water retention curve

The intrinsic permeability K [m^2] and the water diffusivity $D_{\theta l}$[cm^2/s] of bentonite are shown in equations (3.9) and (3.10). The intrinsic permeability is obtained by permeability test and water diffusivity is obtained by infiltration test directly. The water diffusivity is assumed the sum of vapor diffusivity $D_{\theta v}$ and liquid diffusivity $D_{\theta l}$, and functional equation is obtained as shown in equation (3.10). Figure 3.27 shows the measured water diffusivity value and function value.

$$K = 2.00 \times 10^{-20} \tag{3.9}$$

$$D_\theta = D_{\theta v} + D_{\theta l}$$
$$= \frac{(3.68\times10^{-8}T - 2.08\times10^{-7})(\theta - \theta_s)}{(\theta + 1.00\times10^{-3})(-1.00\times10^{-3} - \theta_s)} + \frac{\theta(-3.58\times10^{-9}T - 2.19\times10^{-7})}{0.41(\theta - 0.41)} \quad (3.10)$$

where, θ_s is a saturated volumetric water content.

The water potential is measured by thermocouple psychrometer. The relation between the water potential and the water content is called the water retention curve. This relation is very important for the simulation of unsaturated flow. In this simulation, the real experimental values are used as tabular except at full saturation where the water potential is set to 0. Figure 3.28 shows the measured water potential and water retention curve that is used for simulation.

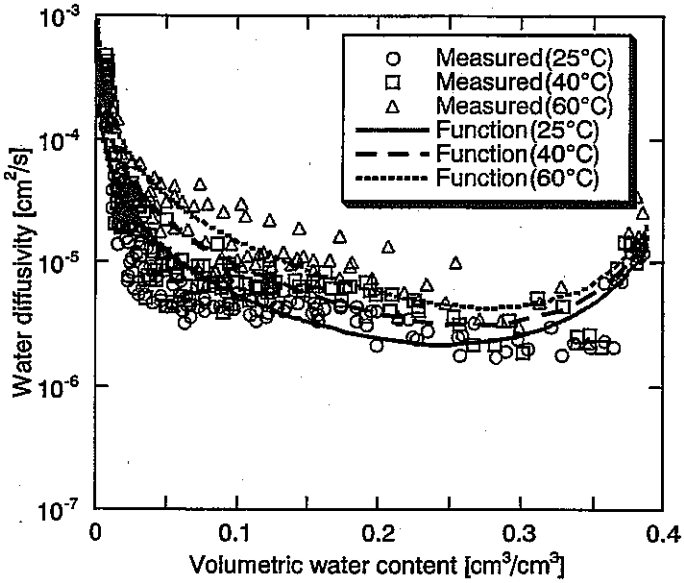

Figure 3.27 Measured and functional water diffusivity

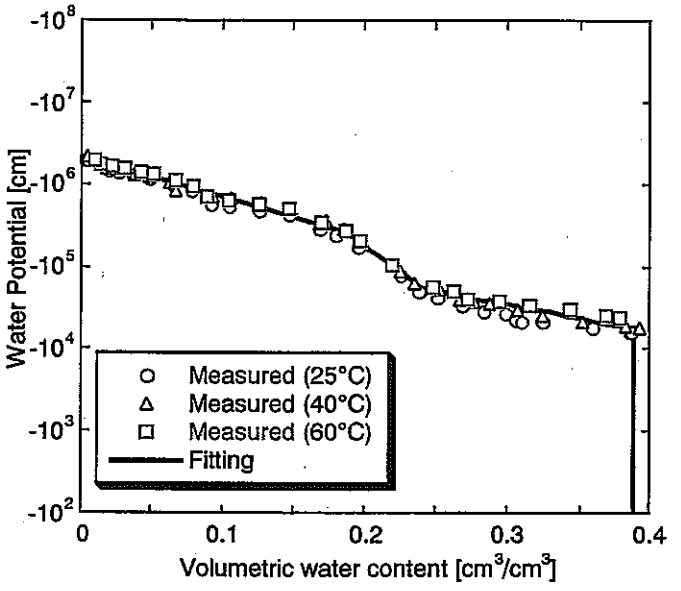

Figure 3.28 Water retention curve for simulation

(2) Thermal water diffusivity

The thermal water diffusivity D_T [cm^2/s℃] is assumed to be a function of temperature as shown in equation (3.11).

$$D_T = D_{To} \exp\left(\alpha_T \frac{T - T_o}{T_o}\right) \tag{3.11}$$

where, D_{To} is a thermal water diffusivity at the reference temperature T_o, α_T is a coefficient.

These parameters are obtained by back analysis of laboratory test. As a result of back analysis, following parameters are determined.

$$D_{To} = 1.0 \cdot 10^{-7} \tag{3.12}$$
$$\alpha_T = 0.1 \tag{3.13}$$
$$T_o = 10\ ^{\circ}\mathrm{C} \tag{3.14}$$

(3) Parameter for swelling pressure

Parameters for swelling pressure F is calibrated by the results of Kamaishi THM experiment. The thermal expansion coefficient α [1/K] of bentonite is also calibrated by Kamaishi THM experiment. Determined values are as follows. As a result of calibration by in-situ THM experiment, the thermal expansion coefficient of bentonite is increased from $1.0 \cdot 10^{-6}$ (Rutqvist et al., 2000) to$1.0 \cdot 10^{-5}$, and swelling pressure parameter F is decreased from 0.190 to 0.010.

$$F = 0.010 \tag{3.15}$$
$$\alpha = 1.0 \cdot 10^{-5} \tag{3.16}$$

(4) Other parameters

Table 3.6 shows the other parameters. In this simulation, three materials (steel (heater), bentonite and rock mass) are considered. The young's modulus E, the specific heat c and the thermal conductivity λ of bentonite are the function of water content ω.

Table 3.6 Parameters for simulation

Parameter	Heater	Bentonite	Rock mass
Young's modulus [MPa]	$2.0 \cdot 10^5$	Equation (3.17)	$2.81 \cdot 10^4$
Poisson's ratio [-]	0.3	0.3	0.3
Density [g/cm^3]	7.80	2.04	2.75
Intrinsic permeability [m^2]	$1.0 \cdot 10^{-27}$	$2.0 \cdot 10^{-20}$	$1.98 \cdot 10^{-16}$
Specific heat [kJ/kg/K]	0.46	Equation (3.18)	0.833
Thermal conductivity [W/m/K]	53.0	Equation (3.19)	2.71
Thermal expansion coefficient [1/K]	$1.64 \cdot 10^{-6}$	Equation (3.16)	$1.0 \cdot 10^{-6}$

$$E = 254.9 - 8.854\omega \tag{3.17}$$

$$c = \frac{42.6 + 4.18\omega}{100 + \omega} \tag{3.18}$$

$$\lambda = 0.050\omega + 0.503 \tag{3.19}$$

3.4.3 Analysis result

Figure 3.29, Figure 3.30, Figure 3.31 and Figure 3.32 show the analysis results. Figure 3.29 shows the time history of temperature at each output point. The outer thermal boundary of the model is defined to be located at 10m. However, in order to match the observed temperature, the constant temperature boundary had to be applied closer to the heat source. As a result, the constant temperature boundary was calibrated to be located at a radius of 2.5m. During the heating phase, the temperatures at the all points increase rapidly and become constant early time. Furthermore, decrement of temperature in the cooling phase is also rapid and these become constant immediately. Figure 3.30 shows the time history of water content in the bentonite and Figure 3.31 shows the time history of stress in the bentonite. The stresses during heating phase are rising at all points and stress at the output point 1 is the largest. The stress at the point 1 decreases suddenly just after the heater is turned off. However, it increases gradually with increasing of water content in the bentonite. The stresses at the points 2 and 3 increase continuously even after the heater is turned off. Figure 3.32 shows the time history of strain both in the bentonite and rock mass. Positive value shows the tension and negative value shows the compression. The compressive strain occurs in the bentonite just after the start of experiment and tensile strain occurs in the rock mass. When heater is turned off, both absolute values are only decreased.

Figure 3.33 to Figure 3.37 shows the comparison between calculated and measured results. Figure 3.33 shows the comparison of temperature and Figure 3.34 shows the comparison of water content. Calculated temperature is good agreement with measured one. Calculated water content is almost good agreement with measured one except for the point 2. Figure 3.35 shows the time history of stress at the point 1 that is near the heater. Measured values are different with the directions but show the same tendency. That is, the stress increases during the heating phase and it decreases when the heater is turned off. The calculated result shows the same tendency and it is almost good agreement with the results measured at BBC section. Figure 3.36 and Figure 3.37 shows the comparison of strain in the bentonite and rock mass. Measured value show the high tensile strain just after the experiment is started but this is not appeared in the simulation. However, the tendency of variation after that is almost similar, even though the absolute values about the bentonite are different. Furthermore, in the rock mass, compressive strain measured just after the heater is turned off but it does not occur in the simulation. The reasons may be that the mechanical constitutive law is inappropriate and unsuitable properties are used about the bentonite and rock mass, and so on.

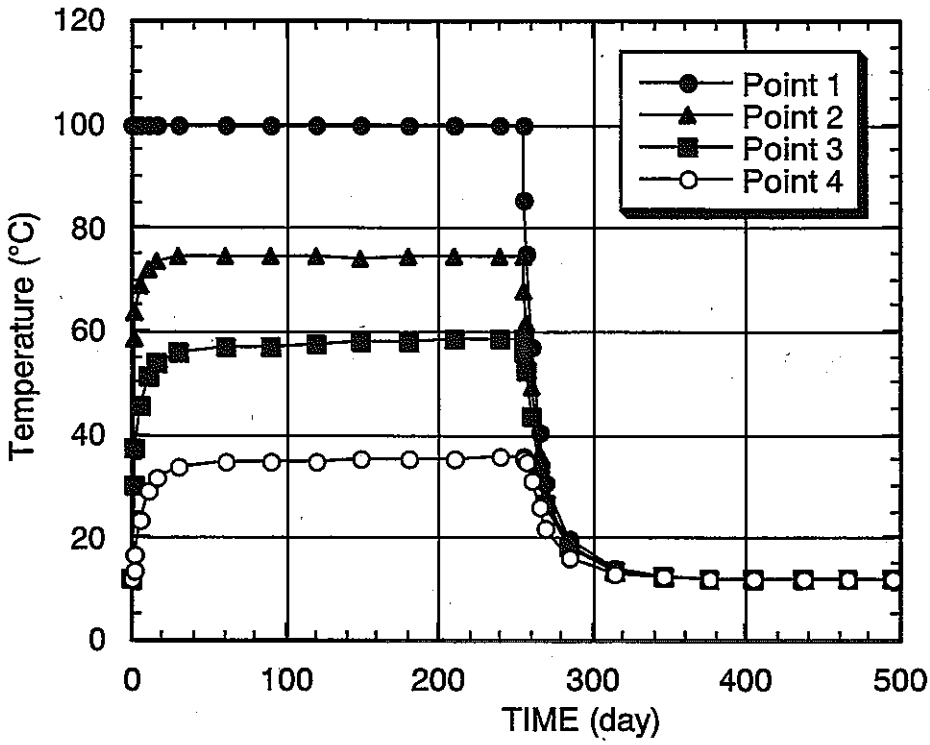

Figure 3.29 Time history of temperature at each point by simulation

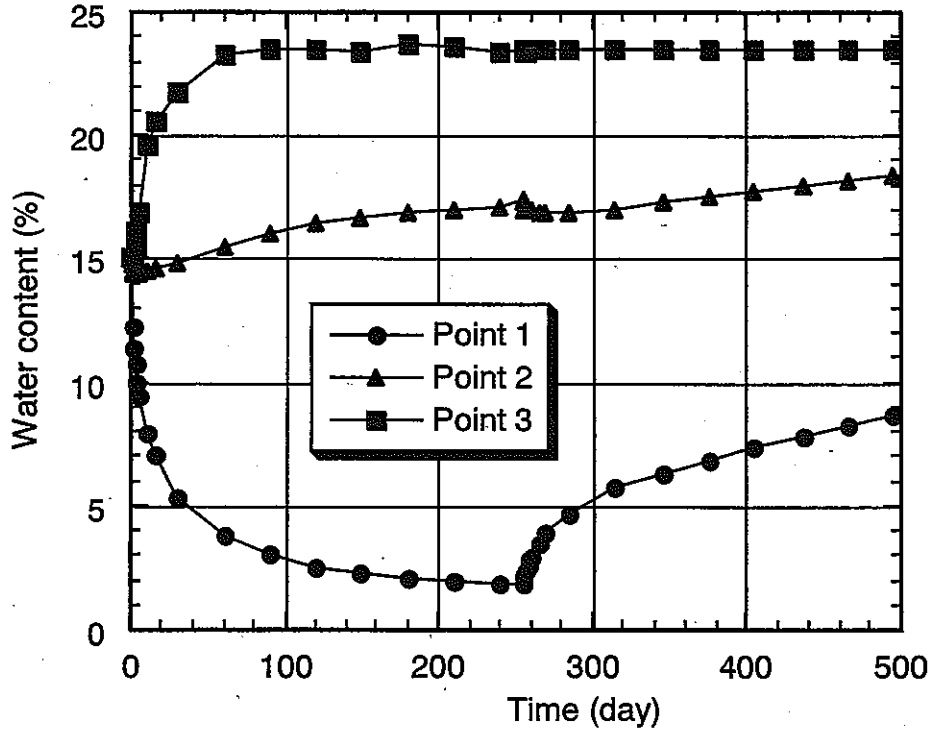

Figure 3.30 Time history of water content at each point by simulation

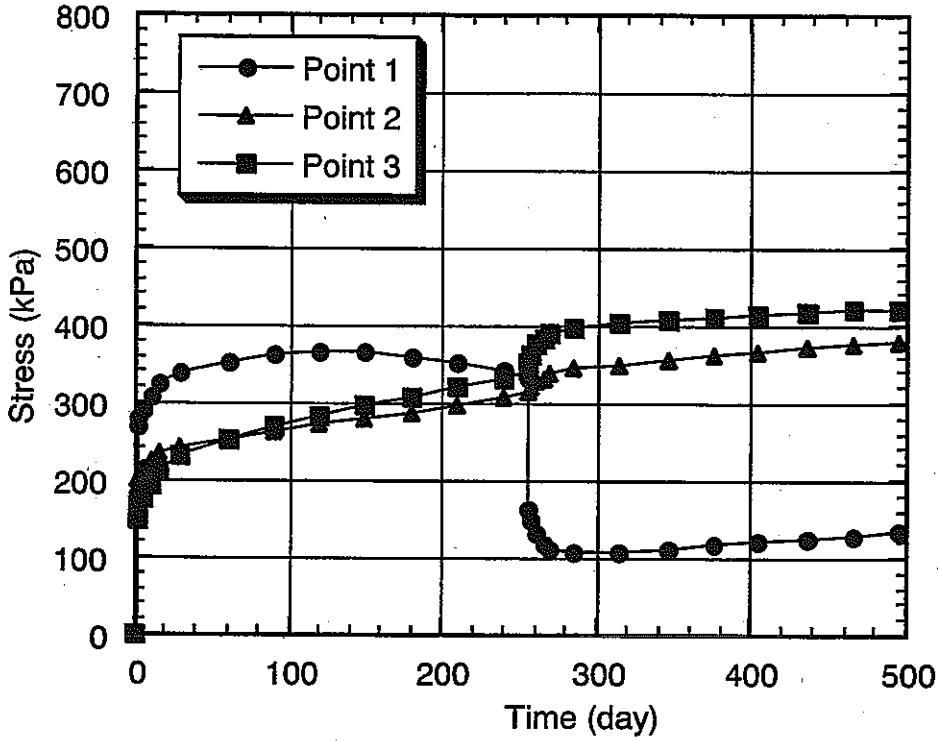

Figure 3.31 Time history of stress at each point by simulation

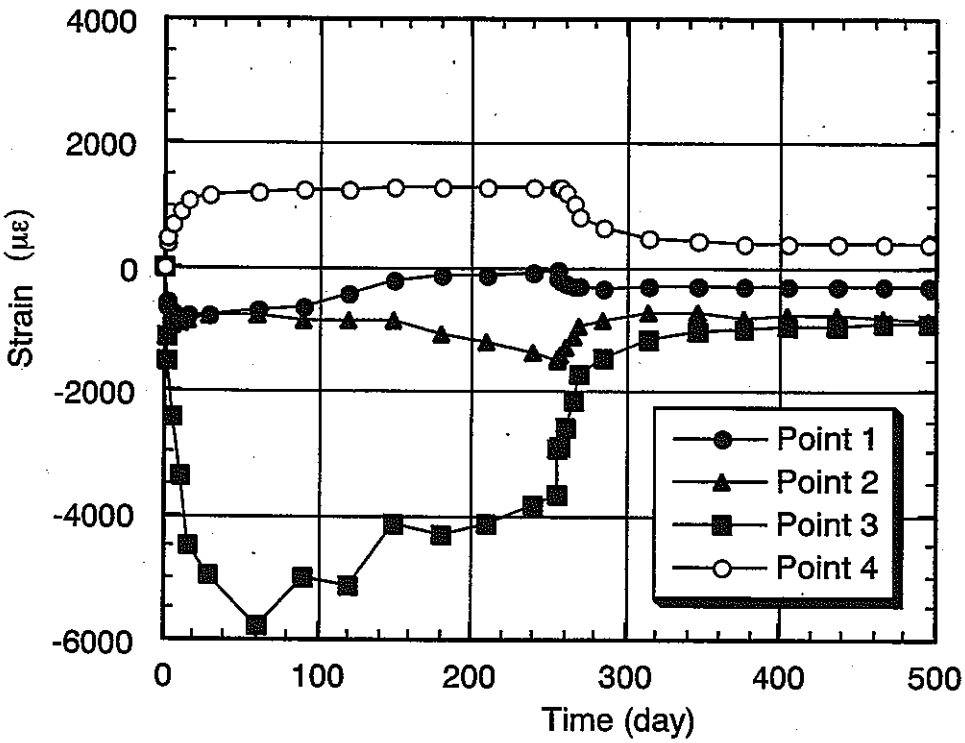

Figure 3.32 Time history of strain at each point by simulation

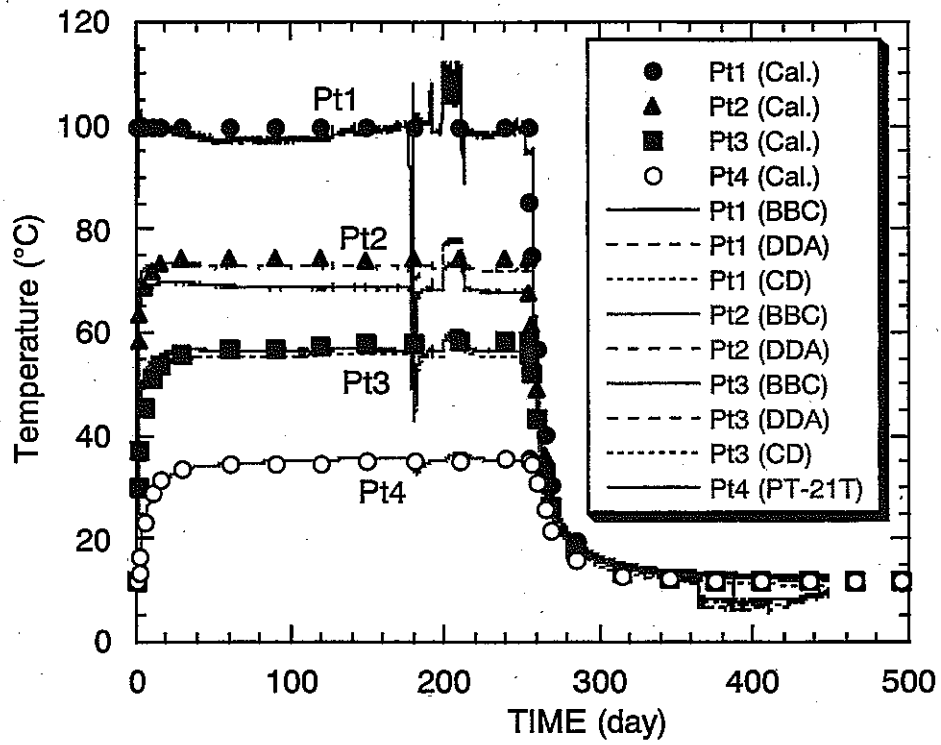

Figure 3.33 Comparison of temperature between measured and calculated results

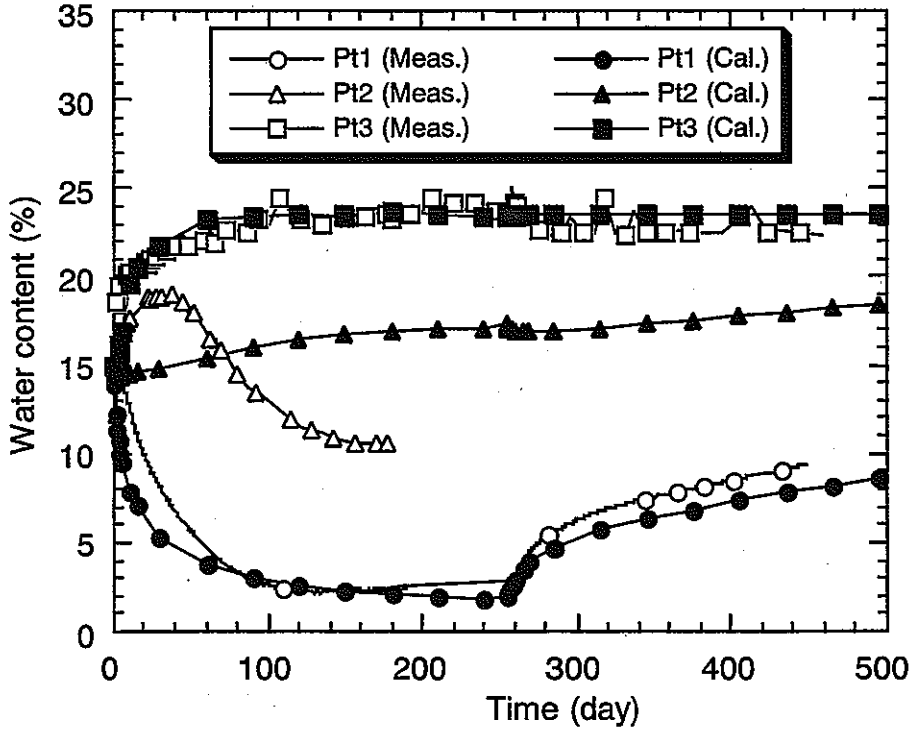

Figure 3.34 Comparison of water content between measured and calculated results

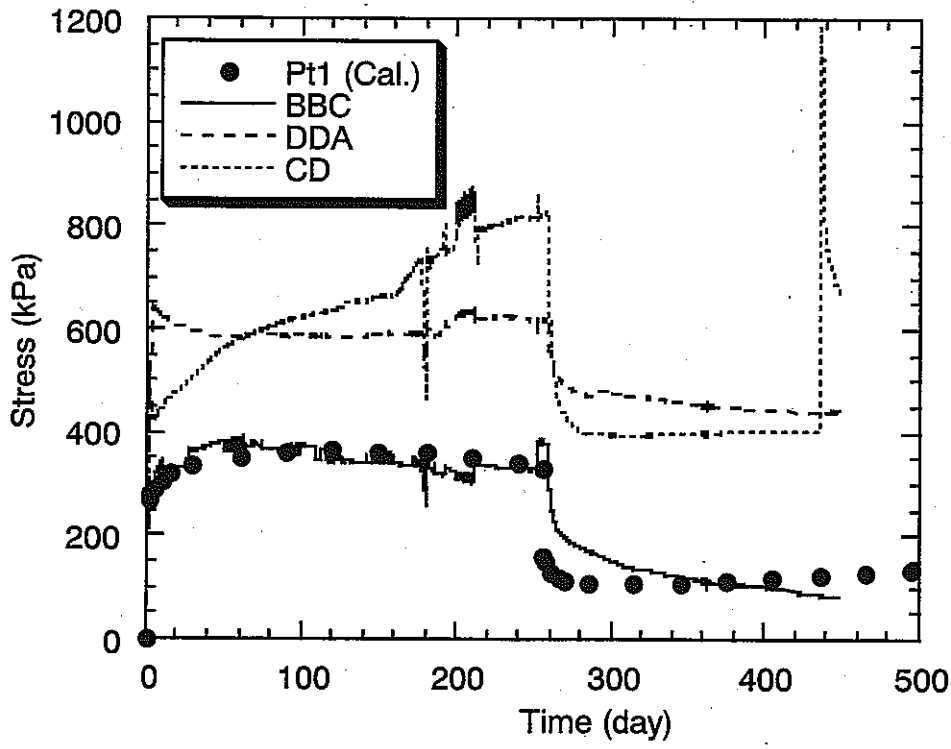

Figure 3.35 Comparison of stress between measured and calculated results

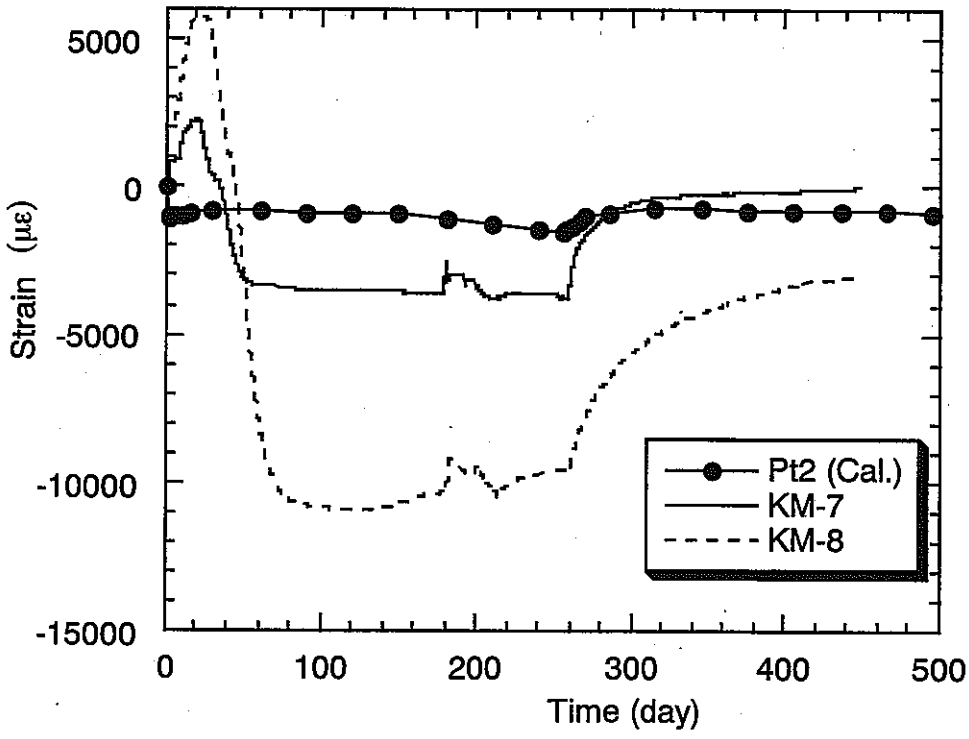

Figure 3.36 Comparison of strain in the buffer between measured and calculated results

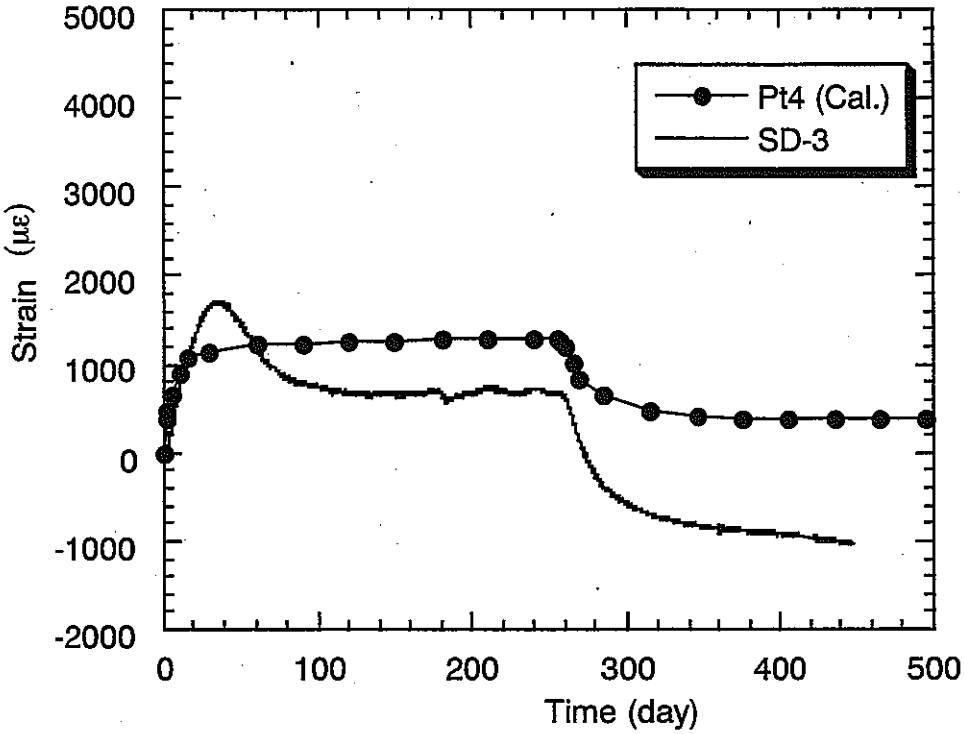

Figure 3.37 Comparison of strain in the rock mass between measured and calculated results

3.5 Summary

In this section, modeling of swelling pressure that took account the temperature and the density dependency was adopted. This model was validated using the laboratory-scale coupled test and show the good agreement with measured data. Using this model, re-calibration of Kamaishi THM experiment was performed. Although the model geometry is simplified to the field test environment, the simulation results show the similar tendency with the measured results. In this re-evaluation, the mechanical behavior was the main focus for simulation. In order to capture the observed mechanical behavior in simulation, thermal expansion coefficient and swelling pressure parameter were calibrated from the in-situ measurement results. As results, the swelling pressure parameter was decreased from the former parameter that was obtained by back analysis of laboratory test. Then, the decreased sweling pressure parameter and the increased thermal expansion coefficient of the bentonite gave a good agreement with the observed mechanical behavior of the bentonite. From these results, it is suggested that a reasonable prediction of the mechanical behavior will be able to be done if bentonite parameters are properly obtained by the laboratory test. Furthermore, more reasonable unsaturated mechanical constitutive law of bentonite will be needed to evaluate the mechanical behavior more properly.

3.6 References

Chijimatsu M., Sugita Y., Fujita T. and Amemiya K., Coupled thermo-hydro-mechanical experiment at Kamaishi mine, Technical note 15-99-02, Experimental results, Japan Nuclear Cycle Development Institute, JNC TN8400 99-034 (1999).

Fujita T., Chijimatsu M., Ishikawa H., Suzuki H. and Matsumoto K., Coupled thermo-hydro-mechanical experiment at Kamaishi mine, Technical note 11-96-04, Fundamental properties of bentonite OT-9607, Japan Nuclear Cycle Development Institute, JNC TN8410 97-071 (1997).

Japan Nuclear Cycle Development Institute, Second progress report on research and development for the geological disposal of HLW in Japan, H12: project to establish the scientific and technical basis for HLW disposal in Japan, JNC TN1410 2000-001.

Rutqvist J., Börgesson L., Chijimatsu M., Nguyen T. S., Jing L., Noorishad J. and Tsang C.-F., Coupled thermo-hydro-mechanical Analysis of a Heater Test in Fractured Rock and Bentonite at Kamaishi Mine – Comparison of Field Results to Predictions of Four Finite Element Codes. *Int. J. Rock mech. Min. Sci.* In press (2000).

Suzuki H. and Fujita T., Swelling characteristics of buffer material, Japan Nuclear Cycle Development Institute, JNC TN8400 99-038 (1999) (in Japanese).

Suzuki H., Chijimatsu M. and Fujita T., Measurement of water movement under a thermal gradient and swelling pressure of buffer material, Japan Japan Nuclear Cycle Development Institute, JNC TN8400 99-020 (1999) (in Japanese).

別添 - 9

DECOVALEX TASK3 BMT2
TASK DEFINITIONS

DECOVALEX III

Bench Mark Test 2

Understanding the Impact of Upscaling THM processes on Performance Assessment

alternatively known as

The THM Upscaling Bench Mark Test

Test case description
Annex 1 - Problem Definition

Version 6, 08/12/2000

REVISION RECORD

Date	Version	Status	Comments
12/1/2000	2.0	Issued	Annex 1 amended to include text relating to the bentonite backfill Annex 2 amended to include data on fracture lengths.. Annex 3 and Appendix giving details of bentonite testing methods and properties added.
10/2/2000	3.0	Issued	Figure on page 5 amended to include dimensions of seabed and water depth etc. Third line of in situ stress data was incorrectly shown as Hmin should have been Hmax.
21/3/2000	4.0	Issued	Additional dimensional data were supplied that relate to Figure on page 5.
15/11/2000	5.0	Issued	Case description: clarified objectives, better defined performance measures and updated time schedule. Annex 1 Problem definitions modified with a new heat source. Annex 2-3 Data modifications
08/12/2000	6	Issued	Some missing text (equations 1 and 2) in annex 1 and additional data have been introduced

Contents

Test case description

1. Aims

The thrust of the proposed research is a quantitative examination of the quality of estimates of repository host rock performance using large-scale performance assessment models. In this context, the definition of a large-scale model is one in which the geometrical and physical properties of the host rock are characterised using upscaled models, parameters and values. The definition of the upscaling is not prescribed, but an assumption is made a priori that the large-scale models will be based on continuum representations. The major concern is to establish a sound basis for using such models for host rocks in which discrete features such as fractures and faults dominate the hydraulic behaviour of the rock.

The research programme is focussed specifically on determinations of performance assessment for the host rock that are dependent on the use of models of coupled THM processes. The chosen determinants may relate to the magnitudes and rates of fluid through-flow or travel time statistics for radionuclide migration, among others.

Given this initial point, the project has two, closely integrated aims:

- To understand how an explicit acknowledgement of the need for upscaling of coupled processes alters the approach to performance assessment modelling and the analysis of the model results;

- To understand the uncertainty and bias inherent in the outputs from performance assessment models in which the upscaling of THM parameters is either implicit or explicit.

More specifically:

- The BMT assesses a problem of relevance to repository performance with a potential THM impact in the far-field. All judgements regarding importance etc. should be done with the PA-context in mind. In particular:

- The BMT should help explore how different means of simplifying the geometrical detail of a site, with its implications on model parameters, ("upscaling") impacts model predictions of relevance to repository performance.

- The BMT should explore to what extent the THM-coupling needs to be considered in relation to PA-measures.

- The BMT should compare the uncertainties in upscaling (both to uncertainty on how to upscale or uncertainty that arises due to the upscaling processes) and consideration of THM couplings with the inherrent uncertainty and spatial variability of the site specific data.

- It is an essential component of the BMT that individual teams not only produce numerical results but are forced to make their own judgements and to provide the proper justification for their conclusions based on their analysis. The different teams will then jointly assess the different conclusions.

Finally it should be understood that conclusions drawn will partly be specific to the problem analysed, in particular as it mainly concerns a 2D application. This means that specific conclusions may have limited applicability to real problems in 3D. Still the methodology used and developed within the BMT should be useful for analysing yet more complicated problems.

2. Methodology

The objective of the project is not to define how to upscale THM processes for a heterogeneous rock but to determine how the upscaling process impacts on the calculation of performance assessment measures. The research teams chosen to carry out the project will not be invited to develop new upscaling rules (although this may arise as a by-product of the research). Rather, they will be requested to apply their normal rules (or strategies) for model parameterisation to the generation of a coupled HM model for a specific performance assessment problem. The chosen problem must allow quantitative checks on the adequacy of the various model outputs and the experimental design must explain the observed features in them.

The issues to be resolved by the experimental design can be summarised as:

- How much information is lost (or conversely retained) during the modelling process in the translation from the small to the large scale?

- How important is the choice of upscaling strategy to the attainment of acceptable performance assessment model results?

- How significant are the contributions of THM processes to the overall uncertainty in the output performance measures and how sophisticated must a large-scale THM model be to capture the main contributions to risk?

To answer the first of these questions, it will be necessary to create a reference problem in which all the components of the small-scale behaviour are available for inclusion in the calculation of the large-scale response of the host rock volume. This reference problem will provide the focal point for the comparison of the alternative upscaled model results obtained by the different research teams. A synthetic host rock based on a particular rock mass has been formulated that will permit detailed summary (statistical) knowledge of the rock mass characteristics to be transmitted to the research teams. The nature of the reference problem definition will impact on the reference model results and the accuracy of the upscaling analysis (to answer issue 1) will depend on how far participating groups are willing to refine the spatial articulation of the rock mass distribution. While it will not be possible to state with

absolute confidence that the results from the research teams are representative of real rock systems, the model outputs should represent the current state of knowledge for the modelled rock mass. The second question will be answered by the intercomparison of the results obtained by the different research teams in answer to question one. The final question will be answered through studies of the contributions to uncertainty and bias from the application of different models and modelling assumptions using the statistical information on rock properties to characterise the rock mass.

Initially, to gain insights into the answers to each of the questions posed it is appropriate to consider only two-dimensional systems. The computational complexity of three-dimensional calculations would introduce a computational overhead that could excessively constrain the progress of the research. However, extensions to three dimensions will eventually be necessary and the lessons learnt from the proposed two-dimensional studies should be used in the later stages of the project to address a three-dimensional equivalent problem. Clearly, the inclusion of this element of the project will depend on the success and progress of the initial work in two dimensions.

The reference case definition as given is rather detailed, but yet stochastic. Still, determining upscaling rules is a deterministic process and different rules may possibly result depending on the from where you start. This will to some extent make it more difficult to compare analyses of the different teams. However, considering the BMT objectives there will not be a further defined reference case for BMT 2. *Each team should derive, and justify, their own upscaling rules, and then each team will apply those rules to the analysis of the site.*

3. Tasks

To achieve the required outcome from this bench mark test, three phases of work are envisaged: reference problem analysis; uncertainty analysis; and, three-dimensional analysis. The proposed research is to be completed within a collaborative research programme and has been defined as a set of six tasks (five technical and one administrative). Each task is to be completed within a six month period. The primary tasks will be performed independently by the different research teams and at the end of each task the results will be drawn together and inferences made about the adequacy or otherwise of the alternative approaches taken.

Depending on the results obtained and their reliability, the output from each task will be used to guide the development of the subsequent tasks. The intention is that each task should require no more than four months work within any six months. The remaining two months in each period will be available for the integration of results and for extensions to the research to enhance the output from the overall programme. Some code developments should be anticipated at each stage, particularly for the processing of model inputs and outputs. The total project period is three years.

Each period will terminate with a workshop at which the research team representatives will discuss the results from the completed task in detail. The six tasks comprise:

Task 1: Inception. The reference case has been created to include several characteristics expected in actual fractured rock and will allow alternative boundary conditions to be imposed. A description of the reference problem is provided in Annex 1. Data for typical fractured rock formations have been used to constrain the description of the reference case and these are defined in Annex 2. By way of illustration, it may be anticipated that models developed by the teams could include at the finest scale between 10,000 and 100,000 individual features (fractures) in the domain to be upscaled (an area of 100m x 100m). Layering of geological strata is represented and a single fault zone has been included.

The adoption of suitable boundary conditions for the model domain is critical to the success of the research and some time will need to be devoted to their determination. Boundary conditions should be imposed by a large regional model in which the upscaling domain is embedded. The main requirement is that a clear time dependent THM response can be expected that is both physically realistic and, in a computational sense, feasible.

The scenario for the perturbation of the reference model is based on thermal disturbance based on a simple HLW disposal scenario in the designated rock volume. Heat production rates for ten thousand years have been prescribed for single canisters and the number of canisters is prescribed. The performance measures are provided in Annex 1. This will allow preliminary identification of the proposed methods and codes that will be employed by the research teams. It may also be used to establish methods of data entry to the simulation codes. A review of the different modelling approaches will allow the programme co-ordinators to identify best practicable means for performing the various comparisons required in the subsequent tasks.

If time permits, the research teams could be expected to investigate the impact of retaining individual or small sets of the intermediate scale features during upscaling.

The first workshop will be used to discuss the initial appraisal of the reference case data sets by the research teams, to identify specific problems and to ensure that the programme of work for Task 2 is clearly understood.

Task 2: Upscaling For this task the research teams will take the data set for the reference case, the given boundary conditions for the embedding model and the performance measures and use these to develop their models. The objectives in this task are twofold. The first objective is for each research team to develop the most accurate model they can of the reference case. The second objective is to develop the most parsimonious model (or models) of the reference domain using suitable upscaling strategies that are assumed to lead to models that capture the performance characteristics of the system.

A methodological statement will be required from each research team describing the issues addressed in the development of the models, the basis for any simplifications made in developing both models, a statement of computational efficiency and a comparison of the 'accurate' and 'parsimonious' model results with the required performance measures. The statements should be returned to the secretariat in advance of the workshop and inter-comparison of the results completed for discussion..

The teams have total freedom in this problem to define grid resolutions, time stepping etc. needed to obtain well conditioned output for the comparison phase.

Task 3: Evaluation By the start of this task, the research teams should have been made aware of the actual results from the other team's outputs. It may be expected that the comparison will show differences and the teams will be required in this task to establish the reasons for these and where appropriate to redevelop their modelling strategy to improve results. The aim of this task is therefore to refine individual team methodologies and to establish optimal practices for the simplification of models that are efficient and unbiased, at least for the performance measures defined.

Finally, the teams will be required to perform simulations for a small number of alternative boundary conditions to explore the generality of the methods developed.

Task 4: Importance Analysis The research teams are being provided with statistical and tabulated data (for well characterised discrete features) describing the internal structure of a region of host rock. The given statistical data will provide sufficient information to undertake simulation experiments aimed at quantifying the uncertainty in the predictions of the rock and fluid behaviour employing the model upscaling strategies identified in Tasks 2 and 3.

Most importantly, the modelling teams will be invited to explore the sensitivity of their results to different sets of coupled processes. This can be carried out by selectively including and excluding different processes to explore their relative impact.

The outcome of this task will be sufficient data from the different modelling activities to permit a comparison of the uncertainty and possible biases inherent in THM modelling. It should also permit general statements to be made on the added value accruing from the inclusion of additional THM components in performance assessment models.

Task 5: 3D Extensions. Depending on how far each of the teams has progressed with the Uncertainty analysis, the aim here should be to repeat the reference case analysis (Task 1/2) but this time in three dimensions. The size of the problem tackled may need to be reduced to allow some results to be ready for the workshop. The lessons learnt from the 2D cases should provide useful guidance in the setting up of this task and its completion.

Task 6: Final Reporting. This task will allow the project to be completed on time, write-ups to be prepared and incomplete sections of the work to be finalised.

A final workshop will be needed to draw out the main conclusions from the research and to prepare a final report.

3. Timescale

The project is assumed to commence on the 1st September, 1999 and for a planning meeting at the start of Task 1 to be established in either September or October, 1999. Thereafter activities should run at six monthly intervals.

The schedule of tasks and timetable is as follows:

Task 1:	Inception	: Start Oct 1999	End Sep 2000
Task 2:	Full Upscaling	: Start Sep 2000	End Feb 2001
Task 3:	Evaluation	: Start Feb 2001	End May 2001
Task 4:	Uncertainty Analysis	: Start May 2001	End Dec 2001
Task 5:	3D Extensions	: Start Dec 2001	End Mar 2001
Task 6:	Final Reporting	: Start Apr 2002	End Sept 2002

4. Deliverables and Milestones

Each Task will be monitored at the midpoint interval through a research team meeting. A report on the task results will be submitted prior to the workshop to the Secretariat.

A presentation of the results for the task will be made at the workshop. The date for the workshops will be set to coincide with the end of each task period.

Milestones are clearly identified by the dates for the workshops.

Annex 1 Problem Definition

The reference problem geometry is shown on the drawing below (Figure 1). This comprises a large-scale model based essentially on Sellafield, Cumbria, UK and an embedded small-scale model based loosely on a high level waste repository. It is assumed that the HLW (heat source) is encased within resaturated bentonite within a repository drift shown as a simple horizontal body. (NB no attempt is made to represent repository detail such as deposition holes etc.). The repository sits within a low permeability fractured rock unit which is overlain by a second low permeability fractured rock unit that extends to ground surface. A vertical fracture zone cuts both rock units but lies beyond the end of the repository tunnel.

Performance measures

The research teams are asked to predict performance measures using the following strategy.

In several different publications Cvetkociv et al. (1999) shows that the breakthrough along a single streamline essentially depends upon two different parameters

$$\tau = \int 1/v(s)ds \text{ and} \qquad (1)$$

$$\beta = \int 1/(v(s)b(s))ds = \int 1/(Q_2(s))ds \qquad (2)$$

where v(s) is the fluid velocity along the streamline, b(s) the fracture aperture and $Q_2(s)$ (m^2/s) the specific flow rate. (The total flow rate in fracture Q is given by $\int Q_2(w)dw$ integrated perpendicular to the streamlines in the fracture). Interpretation of the parameters in Equations (1) and (2) are that the τ is the transit time (distribution) for a particle(s) in the flowing water and β describes the retardation capacity of the rock matrix. The parameter β is called the "transport resistance".

In practice it turns out that β is by far the most important parameter of the two since it relates tothe possibilities for interaction between the flowing water and the rock matrix. In the safety assessments carried out in Sweden and Finland, it is this retention (diffusion into the matrix combined with sorption inside the matrix) which actually has any affect on reducing releases It can be shown that β is equal to the product $a_w t_w$ used to in the far-field migration code used in SKB SR 97 (SKB, 1999), WL/Q used in safety assessments in Finland (see e.g. Vieno and Nordman, 1999) or $a_r L/q$ used in SKI SITE-94 (SKI, 1996).

Consequently teams are asked to provide *both* "transit time (τ) distributions" and "transport resistance (β) distributions " .

1. Flow and transport occurs only in the fractures of the rock. At the local-scale, rock matrix diffusion, absorption, adsorption, dispersion, diffusion and mass decay do not arise in the host rock.

2. Flow velocities, to be used for estimating transit times according to equation (1) are defined for a single fracture as q/a where q is the flux per unit width of fracture and a is the hydraulic aperture. Flow velocity is therefore assumed to be independent of distance from a fracture wall.

3. In order to estimate transport resistance(β) according to equation 2 one should note that this can be achieved by calculating "travel times" using a "flow velocity" of q (i.e. not dividing by a) in discrete fracture models or by setting porosity equal to unity in porous medium models.

4. Flow through the repository volume is characterised as single porosity, Darcian continuum flow. The effective porosity of the repository fill is taken to be the bulk porosity of the bentonite. No account of the presence of the canisters is required for particle pathway calculations.

5. Particle migration in the repository volume is by advection.

6. The research teams must define the upscaled particles migration characteristics based on their own upscaling rules.

Particle starting points and masses

1. Particles are to be distributed uniformly over the repository volume..

2. Particles are to be released as three pulses at times t=0, t=1000, t=10000 yrs.

3. The number of particles used for simulation is left to the discretion of the research teams but should be sufficient to plot temporal and spatial breakthroughs that provide good estimates of the output measures

Output surfaces and measures

a) Two output surfaces are identified for breakthrough observations

   1. A perimeter surface at 50m from the boundary (wall/floor/roof) of the repository.

   2. The land/sea floor surface.

b) Mean transit time from the repositoryto the output surfaces for the following quantile ranges (0-10%), (10-20%), (20-40%), (40-60%), (60-100%)

c) Mean transport resistance from the repository to the output surfaces for the following quantile ranges ranges (0-10%), (10-20%), (20-40%), (40-60%), (60-100%)

d) Cumulative particle density (Nr of particles per unit area/length) at the output surfaces for the following quantile ranges (0-10%), (10-20%), (20-40%), (40-60%), (60-100%)

e) Graphs showing cumulative net outflows through the repository boundary, the 50m-perimeter surface and the land/sea floor surface should also be provided.

Data

To achieve this team are asked to devise methods of homogenizing/upscaling relevant properties. The relevant data, and boundary conditions, for the rock formations and fault based on Sellafield data is given in Annex 2. The data is in the form of statistical distributions of properties. The regional flows will come for the large-scale model (coupled or uncoupled) and the regional stress field, i.e. boundary condition, will be assumed to be constant.

Distance of left-hand edge of repository from right-hand edge of vertical fault - 10 m. Distance of left-hand edge of repository from left-hand boundary of model - 2.5 km. Distance between top of repository and bottom of Formation 2 is 20 m. The ground surface is flat and 100 m above sea level'.

The terms 'Max spacing vertical' and 'Mean spacing vertical' in the Discontinuity Data section of Annex 2 Sources of Data - are unclear as to whether they were measured perpendicular to the joint sets or measured along a vertical borehole?

They were measured from vertical boreholes but then corrected using a Terzaghi correction to true spacings measured perpendicular to the fracture set.

Fault Zone = Faulted Longlands Farm Member

		Cluster Analysis			Mean Plane	
Set	Number of fractures	Fisher Kw	Variability	Confifence	Dip	Azimuth
1	207	6.8	33.9	2.5	8	021
2	83	11	26.8	3.1	76	330
3	81	13	24.4	2.8	72	021
4	77	6.9	33.5	4.1	74	085

Data from SA/97/052 Figure A.9.

Formation 2 = Altered Longlands Farm Member

		Cluster Analysis			Mean Plane	
Set	Number of fractures	Fisher Kw	Variability	Confifence	Dip	Azimuth
1	49	7.2	32.8	5	25	028
2	21	9.4	28.6	6.5	81	156

3	40	11	26.1	4.3	72	020
4	23	8.1	31	6.8	68	090

Data from SA/97/052 Figure A.12.

Formation 1 = Bulk Longlands Farm Member

		Cluster Analysis			Mean Plane	
Set	Number of fractures	Fisher Kw	Variability	Confifence	Dip	Azimuth
1	283	5.9	36.2	2.3	8	145
2	130	9	29.3	2.7	88	148
3	126	10	27.1	2.5	76	021
4	128	10	27.6	2.5	69	087

Data from SA/97/052 Figure A.15.

Repository disturbance

The repository is assumed to comprise 60 canisters of HLW uniformly distributed over a horizontal repository area of 100 m x 100 m embedded in compacted bentonite. Figure 2 shows the heat evolution versus time for each canister.

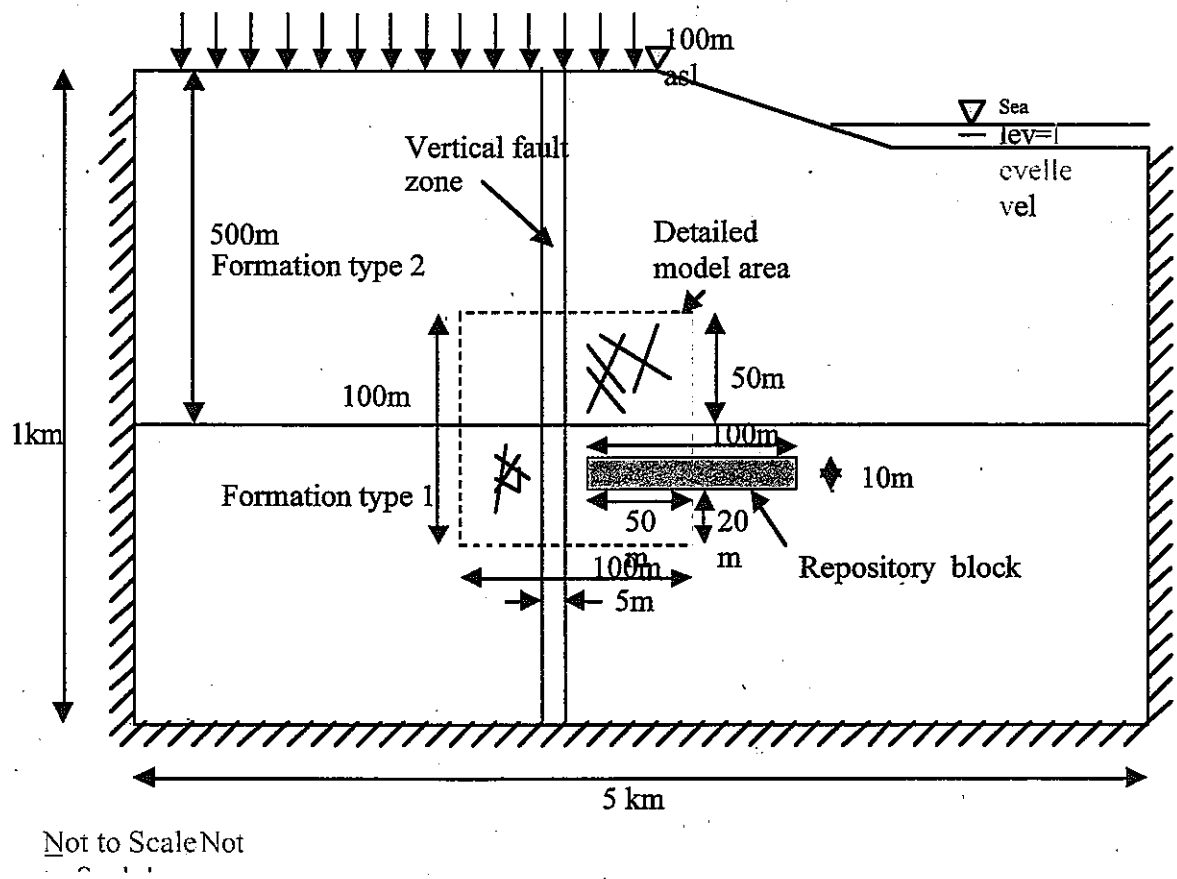

Figure 1: The reference problem

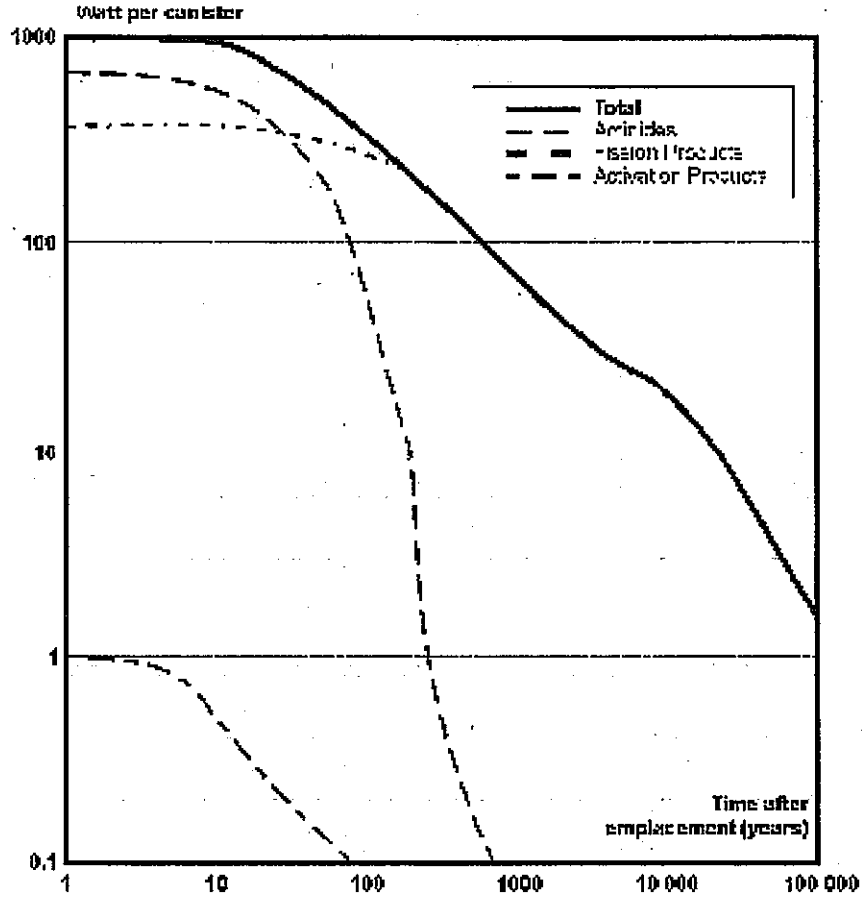

Figure 2 - Heat evolution versus time for a single canister.

References

Cvetkovic, V., Selroos, J. O. & Cheng, H., 1999. Transport of reactive tracers in rock fractures. Journal of Fluid Mechanics, Vol. 378, pp. 335-356.

SKB, 1999a. SR 97 – Post-closure safety. Deep repository for spent nuclear fuel. Main Report (Volumes I and II). Svensk Kärnbränslehantering AB, Stockholm.

SKI (1996). The SKI Deep Repository Performance Assessment Research Project SITE-94. SKI Report 96:36. Swedish Nuclear Power Inspectorate

Vieno T och Nordman H, 1999. Safety assessment of spent fuel disposal in Hästholmen, Kivetty, Olkiluoto and Romuvaara TILA-99, Posiva Oy, Helsinki, Finland.

DECOVALEX III
Bench Mark Test 2

and

BENCHPAR
Work Package 3

Understanding the Impact of Upscaling THM processes on Performance Assessment

alternatively known as

The THM Upscaling Bench Mark Test

Annex 2 - Sources of Data
Annex 2 - Appendix
Annex 3 - Bentonite Properties
Annex 3 - Appendix

Version 5, 16/11/2000

REVISION RECORD

Date	Version	Status	Comments
12/1/2000	2.0	Issued	Annex 1 amended to include text relating to the bentonite backfill Annex 2 amended to include data on fracture lengths.. Annex 3 and Appendix giving details of bentonite testing methods and properties added.
10/2/2000	3.0	Issued	Figure on page 5 amended to include dimensions of seabed and water depth etc. Third line of in situ stress data was incorrectly shown as Hmin should have been Hmax.
21/3/2000	4.0	Issued	Additional dimensional data were supplied that relate to Figure on page 5.
4/10/2000	5.0	Draft	Front page, reference to BENCHPAR added. 4. Distance from top of repository to base of Formation 2 set at 20m not 10m. 4. Ground surface flat and at 100m above sea level. 7. Top hydraulic boundary condition set so that water table coincides with ground surface. 7. Correction to vertical stress equation, 8. Inclusion of section on conceptual model of groundwater flow. 8. Reference to standard tables of water density and viscosity as function of temperature. 9. Inclusion of a section on short interval hydraulic properties. 9. Change reference to source of discontinuity data 10. Replacement of original fracture length data. 10. Addition of fracture density data. 11. More detail given relating to upscaling of rock mass hydraulic properties. 11. Joint compliance data redefined. 13.Inclusion of Nirex 1997f reference. 13. Inclusion of Weast reference. 13. amendment to Nirex 1997b reference. Inclusion of Appendix 2. 14. Figure 3 replaced. 15. Figure 4 replaced.

			Inclusion of calculated joint parameters from KTH. Inclusion of Appendix to Annex 2.

Contents

Annex 2 Sources of data

Introduction

The large-scale model for Bench Mark Test 2 (BMT2) comprises four rock volumes; a lower and upper low permeability fractured rock mass and a fault zone which passes vertically through both rock units. For convenience the fault zone may be subdivided into two parts that lie within each of the rock units. The data for parameterising the rock mass and in-situ stress state in BMT2 are based on site characterisation of the area near Sellafield, Cumbria, England, undertaken by United Kingdom Nirex Limited (Nirex). Geotechnical data for the lower and upper rock units and the entire fault zone are based on data for the Longlands Farm Member, Altered Longlands Farm Member and the Faulted Longlands Farm Member respectively [Nirex 1997a]. Hydrogeological data for the lower and upper rock units and the lower and upper parts of the fault zone are based on upscaled and calibrated data from the Fleming Hall Formation, Near-surface BVG, and Faulted Fleming Hall Formation, Faulted Near-Surface BVG in Nirex 97 [Nirex 1997b]. Data on the length scales of the fractures is taken from Nirex [1997e]. The in-situ stress data are taken from Nirex [1997c]. Thermal data are taken from Nirex [1997d].

These data sets are all three dimensional. In order to get the most out of BMT2, which is assumed to be a 2D exercise, it is proposed that the plane of the section should be orientated along σ_{Hmax} (159/339). This is also close to the direction of one of the fracture sets in each of the rock types which can therefore be ignored in the 2D representation.

Data for the repository itself are based on a generic HLW repository backfilled with bentonite. At time zero it is assumed that the bentonite has fully resaturated. Data for the bentonite is the same as in DECOVALEX III BMT1 and is based on bentonite used for the FEBEX experiment, see Annex 3 and Annex 3 Appendix.

Boundary conditions

Hydraulic Boundary conditions of the large-scale model

The base and sides are no flow boundaries. It is assumed that water table is at the ground surface.

Mechanical boundary conditions of the large-scale model

The rock volume in-situ stress state has the intermediate principal stress vertical. The 2D section is in the plane of σ_{Hmax}, and σ_{Hmin} is perpendicular to the plane of the section.

$\sigma_{vertical}$	0.02494D + 0.26622	MPa
σ_{Hmin}	0.019961D – 0.31619	MPa
σ_{Hmax}	0.03113D + 1.88747	MPa

where D is the vertical distance in metres from the top surface of the large-scale model (Nirex, 1997c).

Thermal boundary conditions of large-scale model

The air temperature at sea level is assumed to be a constant at 11°C. For ground surfaces above sea level the adiabatic lapse is 6.2°C/km. Sea temperature is a constant at 11°C.

Basal heat flow is 54 mW/m^2.

No thermal heat flow is assumed through the sides of the large-scale model. All thermal data are from Nirex [1997d].

Conceptual model of Groundwater Flow

At the Sellafield site used to parameterise the Bench Mark Test only a subset of the total number of fractures are hydraulically active. Those that were active and intersected by boreholes were designated 'Flowing Features' or 'Flow Zones'. They were found to have a characteristic fracture infill mineralogy. Examination of cores showed that other fractures also showed the same infill mineralogy and were believed to be potentially capable of carry groundwater flow but were not hydraulically active where they were intersected by the boreholes. These fractures were termed 'Potentially Flowing Features'. Figure 3 compares the position of Flow Zones and Potentially Flowing Features with transmissivity data derived form short interval tests [1.56 m length scale]. There is a clear relationship between potential flowing features and high tranmissivity derived from short interval testing and the flow zones are themselves a subset of the potential flowing features. The Stonely Wave reflection coefficient, which is related to fracture aperture, also shows a relationship to potential flowing features.

Groundwater Properties

Groundwater is assumed to be freshwater with a density of 0.998 kg/m^3 at STP.

Equation of state for groundwater density and viscosity should make use of standard tables, for example Weast [1981].

Material Properties

All data are from Nirex [1997c].

Formation 1 (Based on Bulk Longlands Farm Member).

Material properties	Core Data			Wireline data		
	Max	Min	Mean	Max	Min	Mean
UCS (MPa)	308.8	29.1	157.0			
Young's Modulus (GPa)	97.50	73.80	84.60	99.56	31.17	69.08
Poisson's Ratio	0.25	0.22	0.24	0.354	0.168	0.263
Effective Porosity (%)	4.53	0.05	0.86	12.66	0.01	5.19
Saturated density (Mg/m^3)	2.92	2.66	2.75			
Hoek-Brown m	9.78	3.171	7.453			
Hoek-Brown s	1.71	0.63	1.062			
Bulk density (Mg/m^3)				2.82	2.58	2.69
Compressional sonic velocity (km/s)				6.59	3.89	5.60
Shear sonic velocity (km/s)				3.84	2.11	3.18

Formation 2 (based on Altered Longlands Farm Member)

Material properties	Core Data			Wireline data		
	Max	Min	Mean	Max	Min	Mean
UCS (MPa)	41.0	38.1	39.6			
Young's Modulus (GPa)				75.70	31.52	46.93
Poisson's Ratio				0.371	0.115	0.287
Effective Porosity (%)	10.41	2.48	5.70	34.03	0.92	9.67
Saturated density (Mg/m^3)	2.75	2.70	2.65			
Hoek-Brown m						
Hoek-Brown s						
Bulk density (Mg/m^3)				2.94	2.50	2.69
Compressional sonic velocity (km/s)				5.90	3.63	4.81
Shear sonic velocity (km/s)				3.34	2.13	2.61

Fault zone (based on Faulted Longlands Farm Member)

Material properties	Core Data			Wireline data		
	Max	Min	Mean	Max	Min	Mean
UCS (MPa)	157.8	104.2	128.4			
Young's Modulus (GPa)			60.00	91.46	24.70	62.62
Poisson's Ratio			0.23	0.350	0.165	0.262
Effective Porosity (%)	1.12	0.06	0.44	18.09	0.01	6.24
Saturated density (Mg/m^3)	2.77	2.69	2.73			
Hoek-Brown m			24.1			
Hoek-Brown s			0.65			
Bulk density (Mg/m^3)				2.92	2.49	2.67
Compressional sonic velocity (km/s)				6.45	3.43	5.36
Shear sonic velocity (km/s)				3.70	1.93	3.04

Discontinuity Data

The following tables of data are from Nirex [1997a].

Formation 1 (Based on Bulk Longlands Farm Member).

	Mean dip (º)	Dip direction (º)	Max spacing vertical (m)	Mean spacing vertical (m)
Set 1	08	145	5.35	0.29
Set 2	88	148	2.21	0.26
Set 3	76	021	2.01	0.28
Set 4	69	087	3.54	0.31

Formation 2 (based on Altered Longlands Farm Member)

	Mean dip (º)	Dip direction (º)	Max spacing vertical (m)	Mean spacing vertical (m)
Set 1	25	028	4.29	0.51
Set 2	81	156	2.5	0.35
Set 3	72	020	3.83	0.28
Set 4	68	090	2.26	0.41

Fault Zone (based on Faulted Longlands Farm Member)

	Mean dip (º)	Dip direction (º)	Max spacing vertical (m)	Mean spacing vertical (m)
Set 1	08	021	1.43	0.18
Set 2	76	150	1.41	0.18
Set 3	72	021	1.06	0.19
Set 4	74	085	1.32	0.22

Fracture lengths

In the previous version of this Annex, fracture length data was supplied separately for each Formation and the Fault. An updated data set is provided here which should be used for both Formations and the Fault.

The data was obtained from analysis of 1-dimensional scan-line data at outcrop, 2-dimensional outcrop trace maps and 2-dimensional aerial photography lineaments [Nirex 1997e, page 46]. Combined data sets obtained from the above sources, for all fracture orientations, show a power law distribution of fracture lengths (Figure 4) such that the number of fractures per km^2 of length greater than L(m) is given by:

$$N = CL^{-D}$$

where

N number of fractures per km^2 of length L(m)
C $4\ 10^6$
D 2.2 [+/- 0.2] [Note fractal dimension is for a 2-dimensional fracture network]

These data sets did not include fractures of very small trace length. For consistency it is recommended that the above relationship should not be extrapolated to fractures with trace lengths less than 0.5 m, see Figure 4.

Fracture Density

Fracture density has been shown to be a function of sampling technique, in particular the lower cut-off in the smallest fracture size included in the fracture sample is directly related to fracture density, see Figure 5.

Compilation of outcrop, borehole, aerial photography and structural maps suggests that the relationship for 2-dimensional surfaces is of the form [Nirex 1997f]:

$$\text{density } (m^{-1}) \quad \acute{a} \quad x^{-E}$$

where

x cut off (m)
E is a power law exponent = 1

Using Figure 5 fracture density (2-dimensional) can be derived for any specified fracture cut-off length. The same relationship should be taken as representative of both Formations and the Fault.

As noted in the previous section it is recommended that a lower cut-off in fracture length used in modelling should be set at 0.5 m.

Extent of fracture Overlap / Underlap

There is no numerical data for fracture overlap / underlap. However, Figures 6 and 7 show fracture trace maps of outcrops which provide schematic information on the extent of fracture overlap / underlap [Nirex 1997e]. The same relationship should be taken as typical of both Formations and the Fault.

Fracture terminations

The following fracture terminations were noted during the outcrop fracture mapping. They should be taken as applying to both Formations and the Fault. The letters refer to the terminations seen at each end of a fracture. Data from Nirex [1997e].

Notes
T = Intersection with another fracture.
R = Termination in rock.
U = Unknown termination (obscured or beyond outcrop).
RT/TR = sum of fractures with terminations such as R-----T or T-----R.

Outcrop	TT no	TT %	UT/TU no	UT/TU %	RT/TR no	RT/TR %	RR	RR %	RU/UR no	RU/UR %	UU no	UU %	sum
CH5	69	63	14	13	25	23	1	1	0	0	1	1	110
Ch22	51	43	20	17	27	23	7	6	9	8	5	4	119
Ch37	58	55	24	8	80	28	18	6	6	2	1	0	286
SCI0	42	36	28	24	34	29	5	4	7	6	1	1	117
Lb31	73	49	5	3	56	38	11	7	2	1	1	1	148
TRIa	8	17	19	40	10	21	0	0	7	15	3	6	47
Combined	301	48	110	13	232	28	42	5	31	4	12	1	827

Rock Mass properties

Data are from Nirex [1997c].

	Formation 1	Formation 2	Fault Zone	Notes
NGI Q value	44.55	5.58	9.07	
RMR value	71.79	60.96	63.49	based on RMR=12log$_{10}$(Q)+52
Hoek-Brown m value	6.21	4.22	4.62	
Hoek-Brown s value	0.04	0.01	0.02	calculated for undisturbed rock assuming high-quality blasting
E_{mass} GPa	65	44	44	

Rock Mass hydraulic properties

Data are from Nirex [1997b Table 5.2].

Calibrated equivalent permeability.

The method used to derive these upscaled caibrated equivalent continuum values is described in the separate document entitled "Derivation of upscaled permeability data for Formations 1, 2 and the Fault in DECOVALEX III BMT2".

Rock Unit	mean(k) m^2	mean $\log_{10}$k	std dev $\log_{10}$k
Formation 2 (Near-surface BVG)	$8.51\ 10^{-14}$	-13.070	0.604
Fault Zone in Formation 2 (Faulted Near-surface BVG)	$2.69\ 10^{-13}$	-12.570	0.604
Formation 1 (Fleming Hall Formation)	$5.67\ 10^{-18}$	-17.246	0.480
Fault Zone in Formation 1 (Faulted Fleming Hall Formation)	$4.54\ 10^{-18}$	-17.343	0.865

Short Interval Hydraulic properties

One hundred contiguous short interval pulse tests were carried out within Formation 2. They were carried out at a length-scale of 1.56 m. The relationship of the derived transmissivities to other properties of the fracture network is shown in Figure 3. The individual results are tabulated in Table 1, and illustrated in Figures 3 and 7. Data from Armitage et al [1996].

Discontinuity mechanical properties

An expanded data set of joint discontinuity data is provided in Table 2. Data from NGI [1996]. Note that data is not complete for all fracture sets in each Formation and the Fault.

Joint Compliance Data

The CSFT test subjects the rock joint to a realistic effective normal stress while a the same time measuring the permeability and the degree of closure. Subsequently the joint is sheared while recording the dilation/contraction and any changes in permeability. There are only a small number of measurements tests available which should be used for both Formations and the Fault.

In each test the joint was subjected to three load-unload cycles (normal stress alone). On the 4th cycle the joint was sheared 3 mm under normal stress appropriate to the depth of the sample in the borehole. At each stress level the flow through the joint was monitored and converted to an eqiivalent smooth-wall conducting aperture. To prevent reaction formation water compositions were used.

Sample no/BH/depth	joint dip	JCS MPA	JRC	ör	Normal stress MPA	Joint conducting aperture on 3rd cycle ì m	Shear displacement mm	Normal stress MPa	Joint conducting aperture after shearing ì m
3/bh2/503.57	70	87.1	5.44	28.7	24	125	2.8	15.0	75
5/bh4/609.92	75	264.55	4.22	25.3	31	8	3.1	9.7	13
6/bh5/691.71	59	*	3.00	*	30	6	3.0	17.4	40
7/bh5/805.54	72	*	4.00	*	30	5	5.5	16.6	15
229/RCF1/808.18	72	198318	3.46	47.0	30	3	3.0	20.0	
449/RCF3/878.26	80	124.22	5.65	56.0	30	3	3.0	20.0	

From Nirex [1995 Tables 4.9, 4.10], NGI [1996,Table 1].
* not obtained because of delicate fracture infills.

Further details are as follows.

Sample 229

Profile of the tested joint, Figure 9.
Normal displacement during loading-unloading cycles Figure 10.
Joint permeability during loading-unloading cycles, Figure 11.
Equivalent smooth-wall conducting aperture during loading-unloading cycles, Figure 12.
Equivalent mechanical aperture during load-unloading cycles, Figure 13.
Dilation during shear displacement, Figure 14.
Permeability change during shear displacement, Figure 15.
Equivalent mechanical aperture during shear displacement, Figure 16
Equivalent smooth-wall conducting aperture during shearing, Figure 17.

Sample 449
Profile of the tested joint, Figure 18.
Normal displacement during loading-unloading cycles Figure 19.
Joint permeability during loading-unloading cycles, Figure 20.
Equivalent smooth-wall conducting aperture during loading-unloading cycles, Figure 21.
Equivalent mechanical aperture during load-unloading cycles, Figure 22.
Dilation during shear displacement, Figure 23.
Permeability change during shear displacement, Figure 24.
Equivalent mechanical aperture during shear displacement, Figure 25.
Equivalent smooth-wall conducting aperture during shearing, Figure 26.

Sample 5
Normal displacement during loading-unloading cycles Figure 27.
Equivalent smooth-wall conducting aperture during loading-unloading cycles, Figure 27.
Equivalent smooth-wall conducting aperture during shearing, Figure 29.

Sample 7
Equivalent smooth-wall conducting aperture during loading-unloading cycles, Figure 28.
Equivalent mechanical aperture during shear displacement, Figure 28.
Equivalent smooth-wall conducting aperture during shearing, Figure 29.

The following additional parameters were calculated from the above data by KTH.

Sample	Joint normal stiffness (GPa/m)	Joint shear stiffness (GPa/m)	Hydraulic aperture at zero stress (μm)	Residual Hydraulic aperture (μm)	Mechanical aperture at zero normal stress (μm)
Sample 229	577(fig.9,pp.30)	577(assumed to be same as normal)	32(fig.11,pp32)	23(fig.11,pp32)	32(fig.12,pp33)
Sample 449	234(fig.18,pp.39)	234(assumed to be same as normal)	59(fig.20,pp41)	22(fig.20,pp41)	67(fig.21,pp42)
Sample 5	500(fig26,pp47)	500(assumed to be same as normal)	100(fig.26(lower),pp.47)	14(fig.26(lower),pp.47)	140(inferred from fig.26(upper),pp47)
Sample 7	500(assumed to be same as sample 5)	500(assumed to be same as normal)	68(fig.27(upper),pp.48)	13(fig.27(upper),pp.48)	68(fig.27(lower),pp.48)
Mean value	434	434	65	18	77

Notes

These four samples should be used as representative of both Formations and the Fault.

The joint normal stiffness was calculated using the 3rd cycle of each experiment (by the secant method).

Joint shear stiffness was assumed to be the same as joint normal stiffness because there was no shear loading data.

Rock Mass Thermal Properties

The following figures apply to all rock units.

thermal conductivity	2.29	W/mK	for air dried samples
specific heat capacity	798	J/kg/K	for air dried samples

heat production by radioactive decay 2.0 ì W/m^3

The following apply to the groundwater.

thermal conductivity	0.61	W/mK
specific heat capacity	4185.2	J/kg/K

Data are from Nirex [1997d].

References

Armitage P., Holton D., Jefferies N.L., Myatt B.J., Wilcock P.M., 1996, Groundwater flow through fractured rock at Sellafield, EUR 16870 EN.

ENRESA, 1998, FEBEX: Bentonite Origin, properties and fabrication of blocks. ENRESA Report no. 05/98.

NGI 1993, Geotechnical (CSFT) laboratory testing of BVG joint samples from boreholes RCF1 and RCF3. NGI Report 931005-102/2.

NGI 1997, Rock joint strength data summary sheets for boreholes RCF 1, 2, 3, and PRZ 2. NGI Report 961020-10/2.

Nirex. 1995. Geotechnical studies at Sellafield, Executive summary of NGI/WSA work from 1990-1994. Nirex Report 801.

Nirex. 1997a. Data summary sheets in support of gross geotechnical predictions. Nirex Report SA/97/052.

Nirex. 1997b. An assessment of the post-closure performance of a deep waste repository at Sellafield: Volume 2 – Hydrogeological model development – Effective parameters. Nirex Report S/97/012.

Nirex. 1997c. Assessment of the in-situ stress field at Sellafield. Nirex Report S/97/003.

Nirex. 1997d. Thermal data for use in modelling and their preliminary interpretation. Nirex Report SA/97/074.

Nirex. 1997e. The lithological and discontinuity characteristics of the Borrowdale Volcanic Group at outcrop in the Craghouse Park and Latterbarrow areas. Nirex Report SA/97/029.

Nirex 1997f. Evaluation of heterogeneity and scaling of fractures in the Borrowdale Volcanic group n the Sellafield area. Nirex Report SA/97/028.

Nirex 1997g, the hydrogeology of the Sellafield area: 1997 update. Nirex Science Report S/97/008.

Weast R.C. (editor) 1981 CRC Handbook of Chemistry and Physics. CRC Press Inc, Boca Raton, Florida.

Table 1. Short interval hydraulic pulse tests. These all relate to Formation 2. The tests form a contiguous sequence with test 1 the deepest and test 100 the shallowest. from Armitage et al [1996]. See also Figure 3 and Figure 8.

Category 1 = No pulse generated, because of rapid leak-off of fluid into formation.
Category 2 = Pressure fully recovers during the 1.5 hour monitoring period.
Category 3 = Pressure recovers by at least 50% by the end of the 1.5 hour monitoring period.
category 4 = Pressure recovers by less than 50% by the end of the 1.5 hour monitoring period.

Test Number	Category	Pulse height (kPa)	Transmissivity (m^2s^{-1})
100	4	1247	2.00E-12
99	4	1264	2.30E-12
98	4	1250	1.60E-13
97	4	1265	3.10E-12
96	4	1215	6.20E-13
95	4	1277	1.60E-13
94	4	1255	2.10E-13
93	4	1238	6.70E-13
92	4	1259	8.30E-14
91	3	1173	3.10E-13
90	4	1244	7.80E-16
89	4	1234	8.80E-14
88	2	1013	4.30E-11
87	3	1284	9.50E-13
86	3	1162	2.50E-13
85	4	1276	1.60E-12
84	4	1243	1.20E-13
83	4	1227	1.50E-13
82	4	1233	2.10E-12
81	4	1231	1.40E-12
80	4	1243	1.70E-12
79	4	1271	5.40E-13
78	4	1206	7.20E-13
77	2	77	3.00E-09
76	4	1233	7.40E-14
75	4	1267	1.10E-12
74	4	1202	1.90E-12
73	4	1234	1.90E-13
72	4	1270	1.10E-13
71	4	1249	1.00E-12
70	4	1239	7.30E-14
69	4	1252	1.30E-13
68	4	1244	1.20E-12
67	4	1166	1.60E-13
66	4	1230	2.00E-12
65	4	1229	1.30E-13
64	4	1243	1.30E-12
63	4	1196	5.20E-13
62	4	1190	4.10E-13
61	4	1245	1.50E-13
60	2	633	1.00E-10
59	3	1232	1.40E-12

58	3	951	8.50E-13
57	4	1272	3.90E-13
56	4	1166	2.70E-13
55	4	1276	4.50E-13
54	4	1216	2.50E-13
53	2	1198	6.00E-11
52	2	1139	2.90E-10
51	4	1305	3.10E-14
50	4	1241	3.60E-13
49	3	1306	9.40E-13
48	4	1270	1.70E-13
47	3	1251	9.10E-13
46	2	1191	7.40E-11
45	2	412	1.30E-10
44	22	429	2.80E-10
43	2	555	4.70E-10
42	4	640	1.20E-12
41	4	1340	5.60E-13
40	3	1252	1.50E-12
39	4	1281	1.50E-12
38	4	1188	1.90E-14
37	3	1316	1.30E-12
36	4	1288	3.60E-12
35	4	960	2.60E-13
34	3	1004	1.60E-12
33	3	1269	1.60E-12
32	3	997	1.90E-12
31	3	961	2.50E-12
30	4	1061	4.90E-13
29	3	970	1.70E-12
28	3	590	2.50E-12
27	3	1015	2.00E-12
26	3	1052	1.60E-12
25	4	953	3.10E-12
24	4	928	2.30E-12
23	4	972	5.20E-13
22	1	No pulse	>E-9
21	1	No pulse	>E-9
20	3	996	1.70E-12
19	1	No pulse	>E-9
18	3	1005	1.60E-12
17	3	978	2.70E-12
16	1	No pulse	>E-9
15	1	No pulse	>E-9
14	3	909	4.60E-12
13	1	1016	4.80E-12
12	1	1039	4.20E-12
11	3	1059	2.00E-12
10	4	1025	2.00E-12
9	4	1045	2.50E-12
8	4	1173	1.60E-12
7	3	1133	1.60E-12
6	3	1059	1.40E-12
5	3	1096	5.40E-13
4	4	1146	2.80E-13
3	4	1046	1.00E-12

2	4	1023	2.30E-12
1	3	1079	9.00E-13

Table 2. Discontinuity mechanical properties. All data is taken from NGI [1996], Tables as indicated in right most column. Note Formation 2 = ALFM = Altered Longlands Farm Member, Formation 1 = BLFM = Bulk Longlands Farm Member, Fault = FLFM = Faulted Longlands Farm Member..

Formation	Joint set	Depth in Bh	Bh No	Dip (°)	dip direction (°)	Mean joint amp. (mm)	Mean joint length (mm)	Mass (g)	Area (cm^2)	Mean tilt angle (°)	Joint rebound number	Rock rebound number	Basic friction angle (°)	Rock unit weight (kN/m^3)	Table number
ALFM	3	503.62	RCF3	83	178	5.3	201.0	1670.20	189.1	49.6	22.2	44.8	28.4	26.9	c10-c12
ALFM	3	512.96	RCF3	57	21	3.6	136.8	864.60	113.8	42.0	32.9	41.6	34.2	22.4	c10-c12
ALFM	3	526.75	RCF3	83	190	4.2	224.0	858.40	150.4	56.5	43.0	50.4	34.8	25.5	c10-c12
ALFM	4	526.35	RCF3	84	271	5.3	134.0	959.00	143.5	50.0	28.2	50.4	34.8	25.5	c13-c15
Mean										49.5	31.6	46.8	33.1	25.1	
BLFM	1	432.41	RCF1	31	118	1.1	84.0	697.50	57.2	38.2	35.9	36.4	33.9	26.2	a7-a9
BLFM	1	523.31	RCF1	49	185	3.0	142.0	2094.70	109.3	48.0	36.0	53.2	30.0	26.0	a7-a9
BLFM	1	588.55	RCF2	43	352	1.4	73.1	218.90	46.2	59.8	32.4	42.0	34.2	26.4	b10-b12
BLFM	1	573.03	RCF3	42	128	1.9	94.2	626.20	78.1	29.2	37.8	63.4	30.3	25.9	c16-c18
BLFM	1	593.89	RCF3	46	44	2.0	118.0	879.90	93.0	52.5	33.1	50.4	34.5	25.9	c16-c18
BLFM	1	507.72	PRZ2	24	64	2.4	104.7	373.89	65.5	57.0	35.7	63.8	31.8	26.2	d1-d3
BLFM	1	540.42	PRZ2	26	93	5.5	91.0	314.28	61.1	63.5	52.4	66.2	35.2	24.8	d1-d3
BLFM	1	543.74	PRZ2	3	155	0.8	76.7	265.70	48.6	38.2	37.7	59.7	36.7	25.2	d1-d3
BLFM	2	430.98	RCF2	84	344	1.3	115.0	323.90	73.2	43.5	42.9	65.8	27.0	27.3	b13-b15
BLFM	2	459.22	RCF2	76	338	1.8	114.0	751.50	69.0	44.8	46.8	66.6	36.8	25.8	b13-b15
BLFM	2	582.89	RCF2	64	348	3.5	96.0	280.00	53.4	62.8	25.0	54.0	35.5	26.2	b13-b15
BLFM	2	603.49	RCF2	76	314	2.1	110.7	556.60	77.7	63.2	49.5	60.6	31.5	27.2	b13-b15
BLFM	2	584.68	RCF3	80	326	2.0	156.2	1380.10	145.7	53.3	51.2	69.4	34.0	27.1	c17-c19
BLFM	2	600.97	RCF3	63	265	2.4	170.7	614.80	100.4	40.3	51.9	68.6	27.0	26.5	c17-c19
BLFM	2	604.47	RCF3	61	329	3.4	163.0	510.10	86.5	41.8	59.1	64.6	34.3	28.4	c17-c19
BLFM	2	625.08	RCF3	85	325	2.0	216.1	412.10	143.1	69.8	49.0	69.3	34.9	27.0	c17-c19
BLFM	2	648.31	RCF3	66	345	3.4	173.0	946.10	143.4	68.1	57.0	64.0	29.4	27.3	c17-c19
BLFM	2	574.36	RCF3	75	325	6.3	307.0	1528.10	220.1			68.6	36.3	27.4	c17-c19
BLFM	2	499.56	PRZ2	60	138	2.4	90.7	503.70	60.7	58.0	35.3	64.4	34.0	25.4	d4-d6
BLFM	2	540.00	PRZ2	84	130	2.1	116.0	327.60	70.4	41.8	54.2	61.0	27.2	25.6	d4-d6
BLFM	3	584.54	RCF1	72	186	3.5	113.0	984.80	67.2	49.5	23.8	52.8	34.2	25.9	a10-a12
BLFM	3	591.55	RCF1	55	124	3.1	103.0	677.20	75.7	54.3	50.0	62.4	36.5	25.7	a10-a12
BLFM	3	441.96	RCF2	69	16	1.8	97.0	440.40	57.8	62.3	41.0	63.2	34.2	26.3	b16-b18

BLFM	3	449.99 RCF2	70	43	4.6	108.0	374.50	59.9	46.2	45.5	65.4	30.2	27.4	b16-b18
BLFM	3	571.69 RCF2	52	44	1.8	78.7	373.20	49.4	45.8	47.2	58.2	33.2	26.7	b16-b18
BLFM	3	603.74 RCF2	62	21	1.0	92.8	638.20	60.6	48.5	48.3	57.8	32.7	26.3	b16-b18
BLFM	3	546.80 RCF3	70	3	3.7	202.5	1147.00	155.2	48.8	58.8	63.4	28.8	27.4	c20-c22
BLFM	3	624.95 RCF3	71	23	1.9	223.0	2379.00	155.6	39.5	38.5	69.3	34.9	27.0	c20-c22
BLFM	3	639.22 RCF3	72	18	5.9	225.0	1314.30	189.2	57.4	57.4	69.2	32.3	27.0	c20-c22
BLFM	3	656.31 RCF3	66	25	4.1	122.8	719.70	110.3	31.1	31.1	58.8	35.3	27.3	c20-c22
BLFM	3	518.80 PRZ2	80	251	2.7	99.3	428.48	65.0	50.0	44.3	63.4	30.5	26.0	d7-d9
BLFM	3	556.51 PRZ2	88	194	2.3	104.0	446.15	66.4	45.5	47.8	57.2	34.2	27.6	d7-d9
BLFM	4	458.36 RCF1	62	93	2.4	143.0	1215.10	117.6	64.9	30.6	42.0	34.7	29.0	a13-15
BLFM	4	466.56 RCF1	65	104	2.0	137.3	1097.30	107.5	61.1	44.7	67.6	33.5	26.3	a13-15
BLFM	4	460.97 RCF2	67	110	2.4	181.0	1024.30	109.9	64.0	28.8	66.0	33.8	26.6	b19-21
BLFM	4	636.38 RCF3	54	54	1.3	122.0	520.30	101.8	52.0	59.8	69.4	33.8	26.3	c23-c25
mean									51.3	43.4	61.1	33.0	26.6	
FLFM	1	520.80 RCF2	40	315	1.4	80.0	236.00	40.1	39.3	46.6	56.6	28.8	27.4	b1-b3
FLFM	2	538.54 RCF1	68	334	6.7	230.0	590.20	131.7	71.2	40.2	62.8	30.5	26.2	a1-a3
FLFM	2	478.82 RCF2	79	323	2.2	94.0	775.00	55.2	48.9	44.8	58.2	35.0	26.8	b4-b6
FLFM	2	491.31 RCF2	77	139	10.5	281.0	667.70	169.4	64.3	56.4	63.6	33.8	27.6	b4-b6
FLFM	2	519.90 RCF2	70	123	2.2	152.6	514.50	104.0	58.0	49.0	67.2	32.3	26.0	b4-b6
FLFM	2	557.37 RCF2	61	325	1.4	90.3	783.00	58.1	56.2	37.1	61.7	30.5	26.5	b4-b6
FLFM	2	456.58 RCF3	80	339	11.1	347.0	2290.60	273.3	69.7	37.4	52.2	26.8	26.0	c1-c3
FLFM	2	463.78 RCF3	76	352	2.5	304.0	1683.90	222.9		46.6	66.6	33.5	27.0	c1-c3
FLFM	3	563.87 RCF1	86	42	4.0	120.0	952.00	148.9	40.8	34.2	50.4	33.3	27.0	a4-a6
FLFM	3	541.88 RCF1	52	41	3.3	135.0	814.00	102.0	48.0	46.8	66.2	29.3	26.5	a4-a6
FLFM	3	443.49 RCF3	66	30	3.4	158.0	892.80	136.2	57.5	48.8	54.0	34.5	27.3	c4-c6
FLFM	4	512.15 RCF2	57	59	1.7	92.0	407.00	55.1	36.0	16.2	65.0	35.0	26.6	b7-b9
FLFM	4	448.89 RCF3	50	78	1.5	129.0	703.60	73.1	33.5	42.9	46.2	28.5	22.1	c7-c9
FLFM	4	482.39 RCF3	61	82	2.1	164.0	1541.10	135.7	41.6	47.7	57.6	27.8	27.8	c7-c9
mean									51.2	42.5	59.2	31.4	26.5	

Table 2. Continued

Formation	Joint set	Depth in BH	BH	$JCS_{(0)}$ (MPa)	Normal stress (MPa)	Residual friction angle (°)	JRC at joint length tested	300mm divided by joint length tested	Extrapolated JRC_{300} vaules 300mm	Extrapolated JCS_{300} values 300 mm (MPa)	Table number
ALFM	3	503.62	RCF3	34.32	3.64E-04	18.3	6.29	1.49	5.98	31.82	c10-c12
ALFM	3	512.96	RCF3	45.55	4.11E-04	30.0	2.38	2.19	2.29	43.07	c10-c12
ALFM	3	526.75	RCF3	94.39	1.71E-04	31.9	4.29	1.34	4.18	90.91	c10-c12
ALFM	4	526.35	RCF3	43.93	2.71E-04	26.0	4.61	2.24	4.28	39.30	c13-c15
mean						26.7	4.3	1.7	4.2	55.3	
BLFM	1	432.41	RCF1	68.82	7.39E-04	33.6	0.92	3.57	0.90	66.44	a7-a9
BLFM	1	523.31	RCF1	68.18	8.41E-04	23.5	4.98	2.11	4.63	60.97	a7-a9
BLFM	1	588.55	RCF2	57.91	1.18E-04	29.6	5.30	4.10	4.56	46.26	b10-b12
BLFM	1	573.03	RCF3	74.39	5.99E-04	22.2	1.37	3.18	1.33	70.94	c16-c18
BLFM	1	593.89	RCF3	58.13	3.44E-09	27.6	4.76	2.54	4.35	50.89	c16-c18
BLFM	1	507.72	PRZ2	68.09	1.66E-04	23.0	6.06	2.87	5.33	56.23	d1-d3
BLFM	1	540.42	PRZ2	142.42	1.00E-04	31.0	5.28	3.30	4.65	117.91	d1-d3
BLFM	1	543.74	PRZ2	70.15	3.31E-04	29.3	1.67	3.91	1.59	65.53	d1-d3
BLFM	2	430.98	RCF2	109.81	2.28E-04	20.0	4.13	2.61	3.81	97.51	b13-b15
BLFM	2	459.22	RCF2	118.18	5.38E-04	30.9	2.61	2.63	2.48	109.56	b13-b15
BLFM	2	582.89	RCF2	38.58	1.07E-04	24.8	6.85	3.13	5.86	30.53	b13-b15
BLFM	2	603.49	RCF2	156.61	1.43E-04	27.8	5.85	2.71	5.21	131.46	b13-b15
BLFM	2	584.68	RCF3	170.22	3.32E-04	28.8	4.30	1.92	4.06	156.48	c17-c19
BLFM	2	600.97	RCF3	166.08	3.49E-04	22.1	3.20	1.76	3.09	157.32	c17-c19
BLFM	2	604.47	RCF3	306.92	3.21E-04	32.6	1.54	1.84	1.51	298.40	c17-c19
BLFM	2	625.08	RCF3	149.36	3.37E-05	29.0	6.13	1.39	5.89	140.62	c17-c19
BLFM	2	648.31	RCF3	239.53	9.00E-05	27.2	6.36	1.73	5.93	215.64	c17-c19
BLFM	2	574.36	RCF3					0.98			c17-c19
BLFM	2	499.56	PRZ2	62.95	2.29E-04	25.0	6.07	3.31	5.25	50.83	d4-d6
BLFM	2	540.00	PRZ2	170.22	2.54E-04	25.0	2.89	2.59	2.73	156.77	d4-d6
BLFM	3	584.54	RCF1	35.68	6.06E-04	23.2	5.51	2.65	4.95	30.36	a10-a12
BLFM	3	591.55	RCF1	138.29	2.99E-04	32.5	3.84	2.91	3.54	122.26	a10-a12

BLFM	3	441.96 RCF2	90.97	1.61E-04	27.2	6.11	3.09	5.32	73.97	b16-b18
BLFM	3	449.99 RCF2	127.97	2.94E-04	24.1	3.92	2.78	3.62	113.49	b16-b18
BLFM	3	571.69 RCF2	131.53	3.60E-04	29.4	2.94	3.81	2.72	116.86	b16-b18
BLFM	3	603.74 RCF2	134.23	4.53E-04	29.4	3.49	3.23	3.21	118.72	b16-b18
BLFM	3	546.80 RCF3	267.78	3.14E-04	27.3	3.62	1.48	3.52	256.60	c20-c22
BLFM	3	624.95 RCF3	84.09	8.93E-04	26.0	2.71	1.35	2.67	82.09	c20-c22
BLFM	3	639.22 RCF3	236.50	4.52E-04	28.9	1.16	1.33	1.15	234.15	c20-c22
BLFM	3	656.31 RCF3	57.17	3.61E-04	25.9	2.97	2.44	2.81	52.80	c20-c22
BLFM	3	518.80 PRZ2	105.58	2.67E-04	24.5	4.56	3.02	4.12	90.76	d7-d9
BLFM	3	556.51 PRZ2	148.24	3.24E-04	30.9	2.58	2.88	2.44	136.58	d7-d9
BLFM	4	458.36 RCF1	61.79	1.82E-04	29.3	6.44	2.10	5.86	53.54	a13-15
BLFM	4	466.56 RCF1	110.80	2.34E-04	26.7	6.06	2.18	5.51	96.13	a13-15
BLFM	4	460.97 RCF2	48.32	1.76E-04	22.5	7.62	1.66	7.06	43.05	b19-21
BLFM	4	636.38 RCF3	247.75	1.90E-04	31.0	3.43	2.46	3.22	225.85	c23-c25
mean			123.52	0.00	27.19	4.21	2.54	3.85	112.21	
FLFM	1	520.80 RCF2	136.03	3.46E-04	25.3	2.51	3.75	2.35	123.15	b1-b3
FLFM	2	538.54 RCF1	86.47	4.56E-05	23.3	7.63	1.30	7.33	81.36	a1-a3
FLFM	2	478.82 RCF2	116.56	5.95E-04	30.5	3.50	3.19	3.22	103.20	b4-b6
FLFM	2	491.31 RCF2	239.80	7.27E-05	31.5	5.03	1.07	4.99	237.44	b4-b6
FLFM	2	519.90 RCF2	135.24	1.36E-04	26.9	5.19	1.97	4.84	121.74	b4-b6
FLFM	2	557.37 RCF2	75.02	4.09E-04	22.5	6.40	3.32	5.49	59.58	b4-b6
FLFM	2	456.58 RCF3	73.40	9.89E-05	21.1	8.27	0.86	8.48	76.10	c1-c3
FLFM	2	463.78 RCF3	130.98		27.5		0.99			c1-c3
FLFM	3	563.87 RCF1	66.46	3.59E-04	26.9	2.64	2.50	2.52	61.80	a4-a6
FLFM	3	541.88 RCF1	126.29	3.50E-04	23.4	4.42	2.22	4.12	113.60	a4-a6
FLFM	3	443.49 RCF3	152.18	1.86E-04	32.6	4.21	1.90	3.99	140.33	c4-c6
FLFM	4	512.15 RCF2	24.50	4.74E-04	20.0	3.40	3.26	3.14	21.72	b7-b9
FLFM	4	448.89 RCF3	69.87	6.56E-04	27.1	1.28	2.33	1.25	67.65	c7-c9
FLFM	4	482.39 RCF3	150.29	6.23E-04	24.4	3.20	1.83	3.08	141.82	c7-c9
mean			113.08	0.00	25.93	4.44	2.18	4.22	103.81	

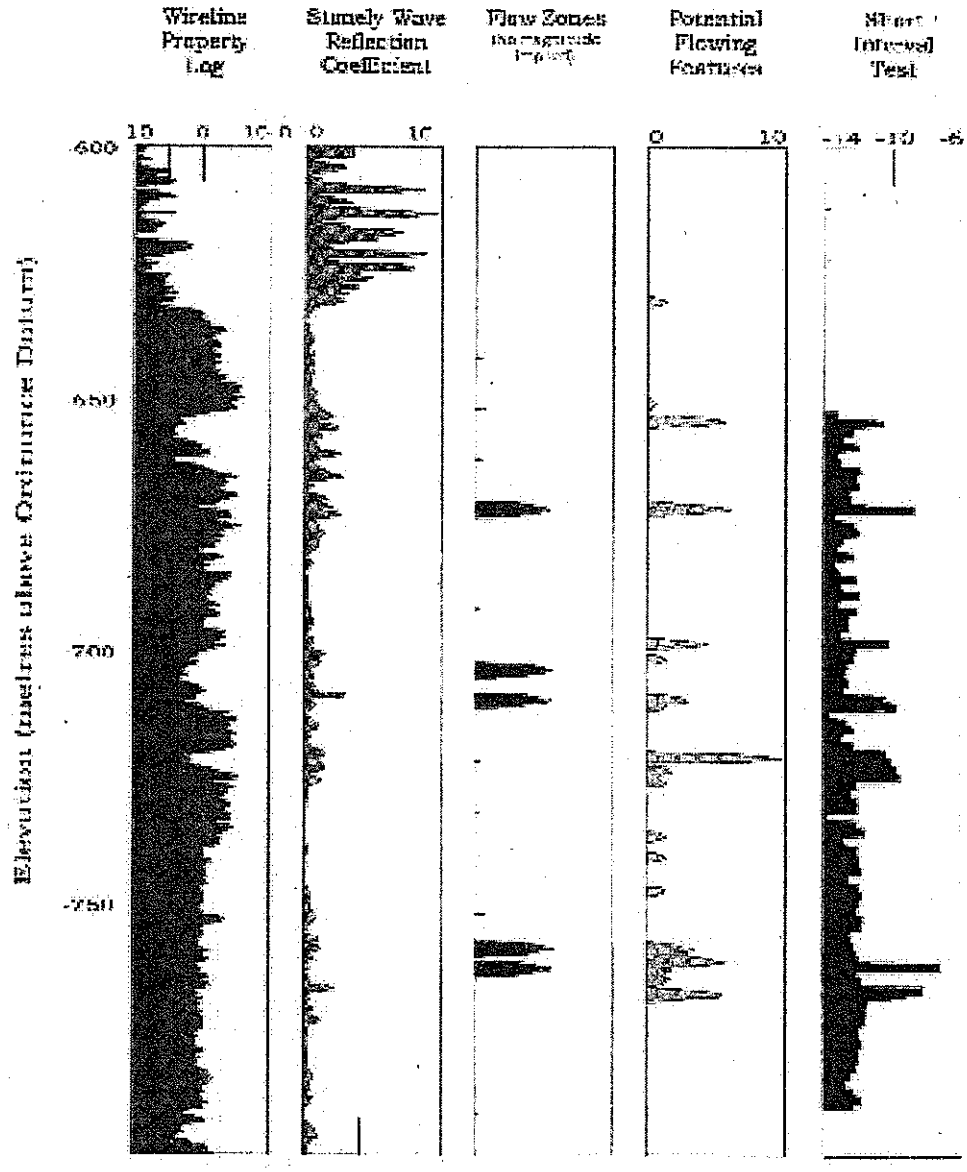

Figure 3. Some hydrogeological properties of the the Borrowdale Volcanic Group (Formations 1 and 2) in Borehole RCF3. Shown are the position of Flow Zones identifed from large length-scale testing, Potential Flowing Features which have the same fracture infill mineralogy as the Flow Zones, and the transmissivity obtained from short interval hydraulic tsting undertaken at a length-scale of 1.56 m. Also shown is the Stonely Wave reflection coefficient which is related to fracture aperture. From Nirex 1997g Figure 19].

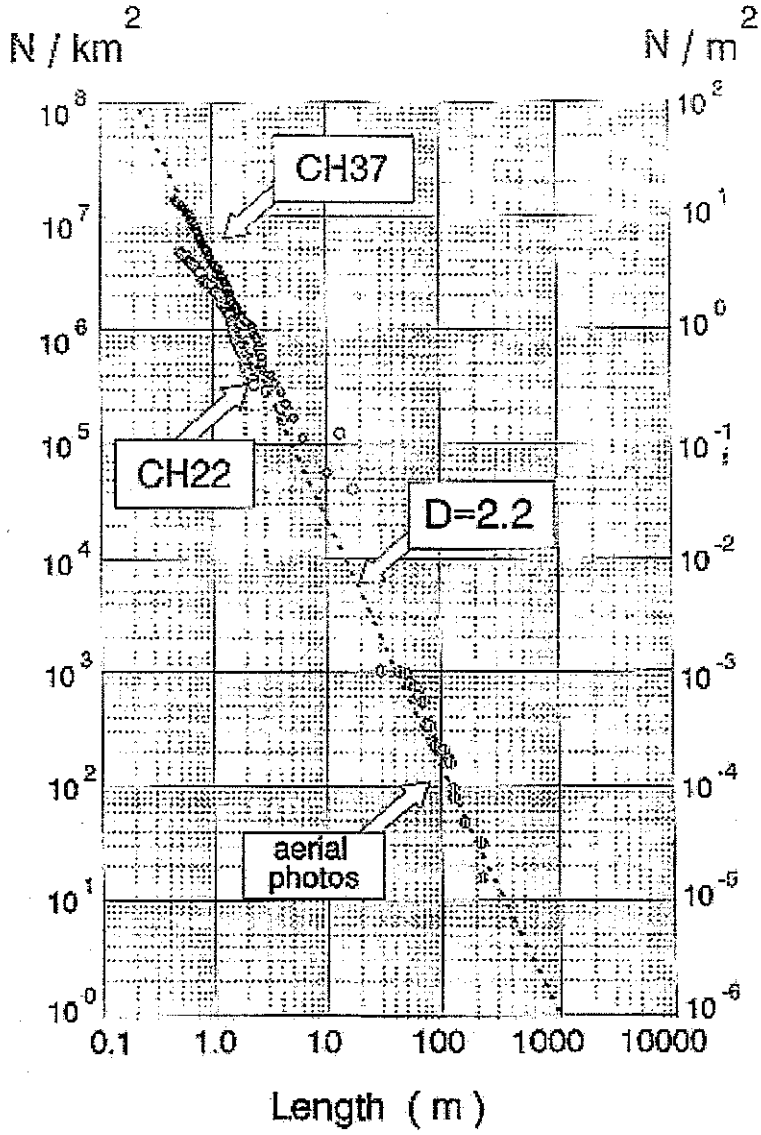

Figure 4. Plot of fractures greater than some length [m] against number of fractures per km^2 obtained from outcrop fracture mapping and aerial photo interpretation. Data fall on a straight line establishing a power law relationship for trace length over the range 0.5 m to 250 m. The relationship is relevant to fractures lengths in both Formations and the Fault. From Nirex [1997e, Figure 5.5].

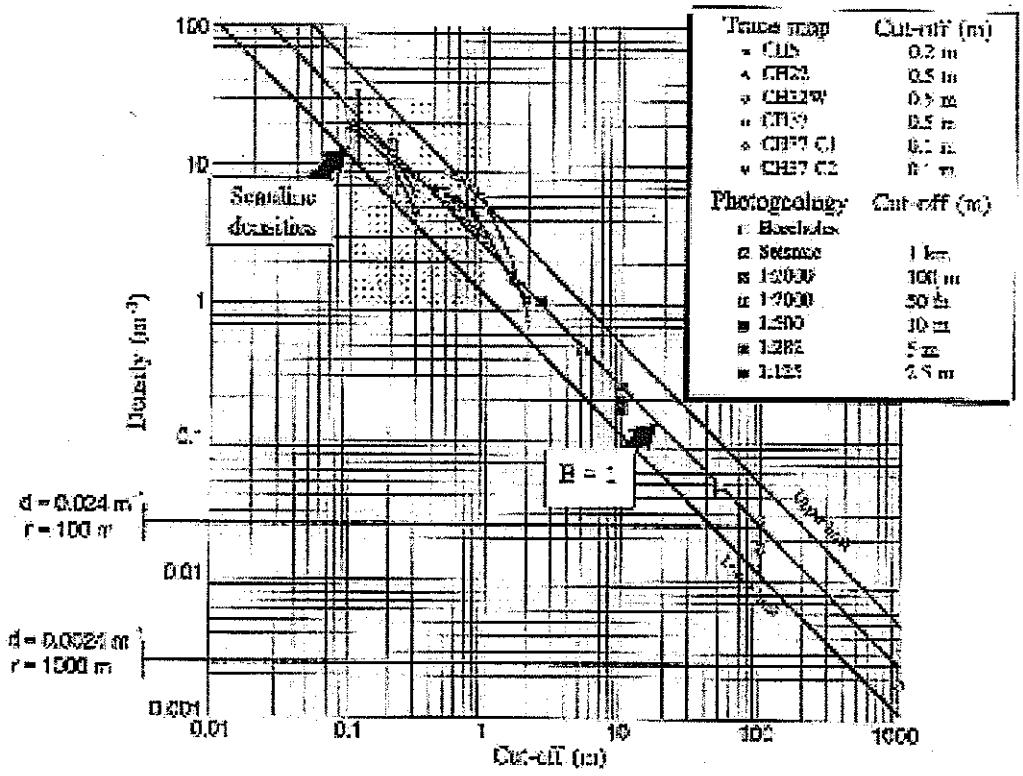

Figure 5. 2-dimensional fracture density as a function of lower fracture trace length cut-off. data obtained from outcrop trace maps, borehole logging, photogeology and seismic data. The slope of the best fit line -E = 1.0. Two extrapolations for lower trace length cut-offs of 100 m and 1 km give densities of 0.024 m^{-1} and 0.0024 m^{-1} respectively. From Nirex [1997e Figure 5.7].

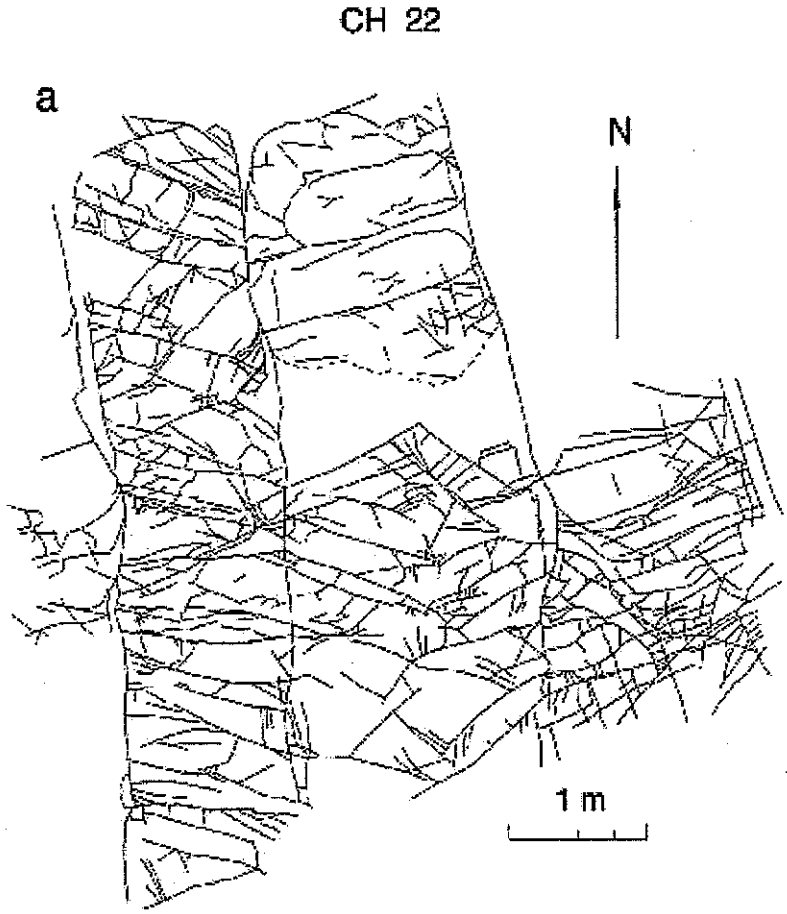

Figure 6. Fracture mapping of outcrop CH22.

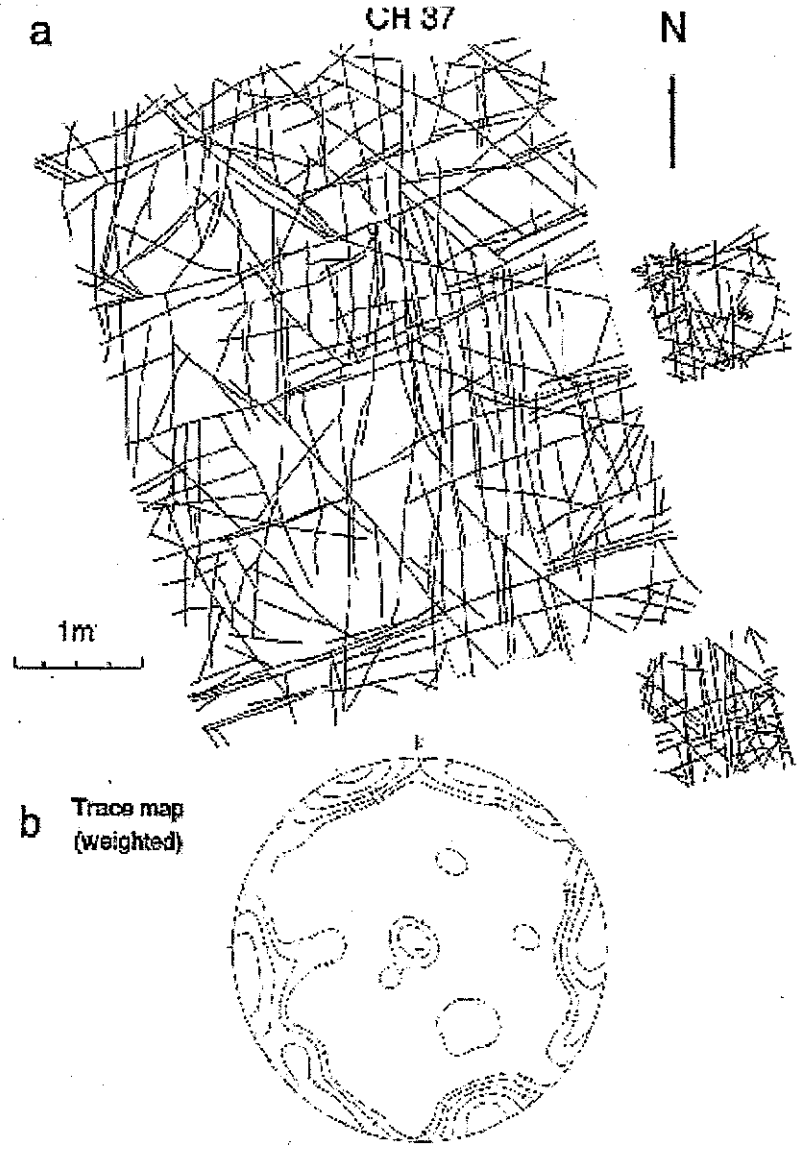

Figure 7. Fracture mapping of outcrop CH37.

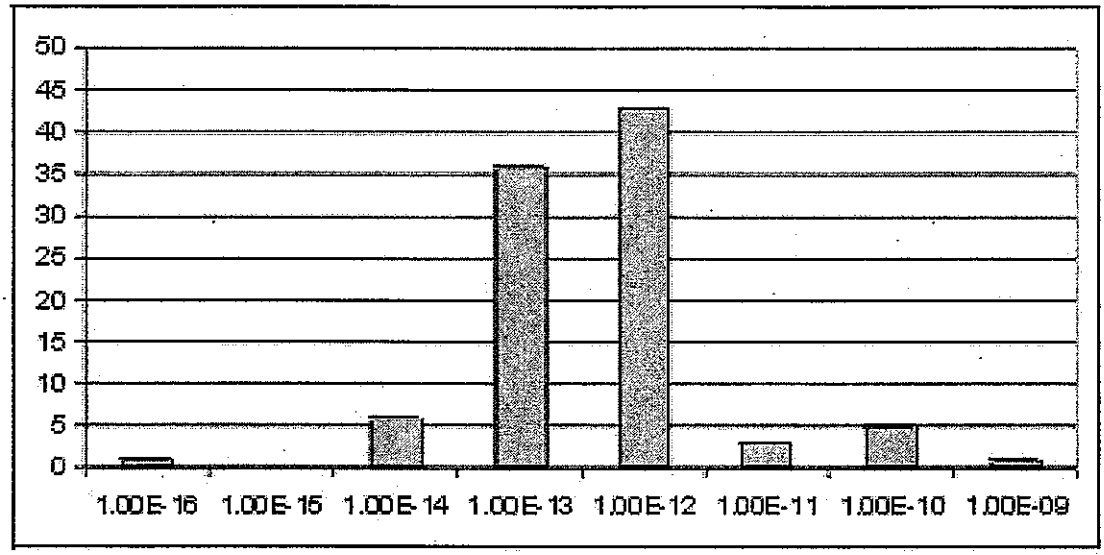

Figure 8. Histogram of short interval hydraulic transmissivity.

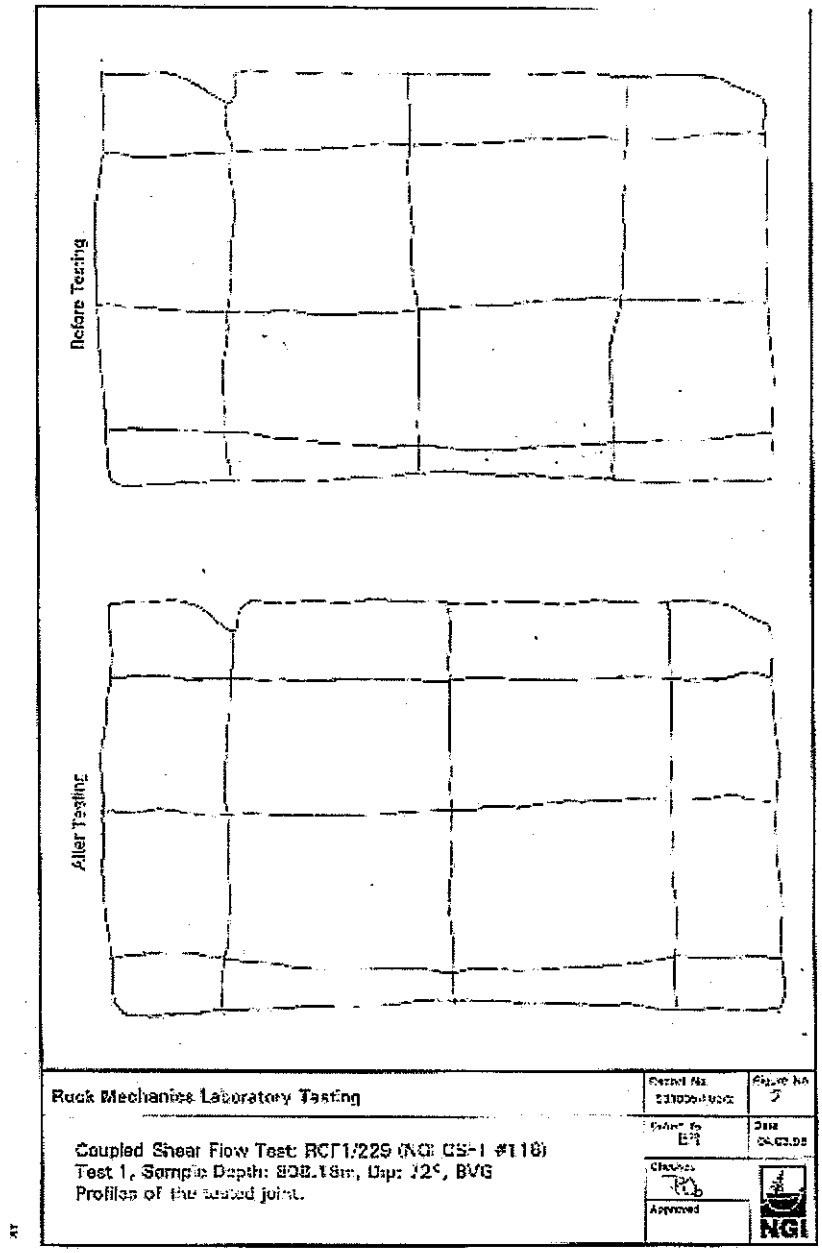

Figure 9. Profile of joint 229, from NGI [1993, Figure 2].

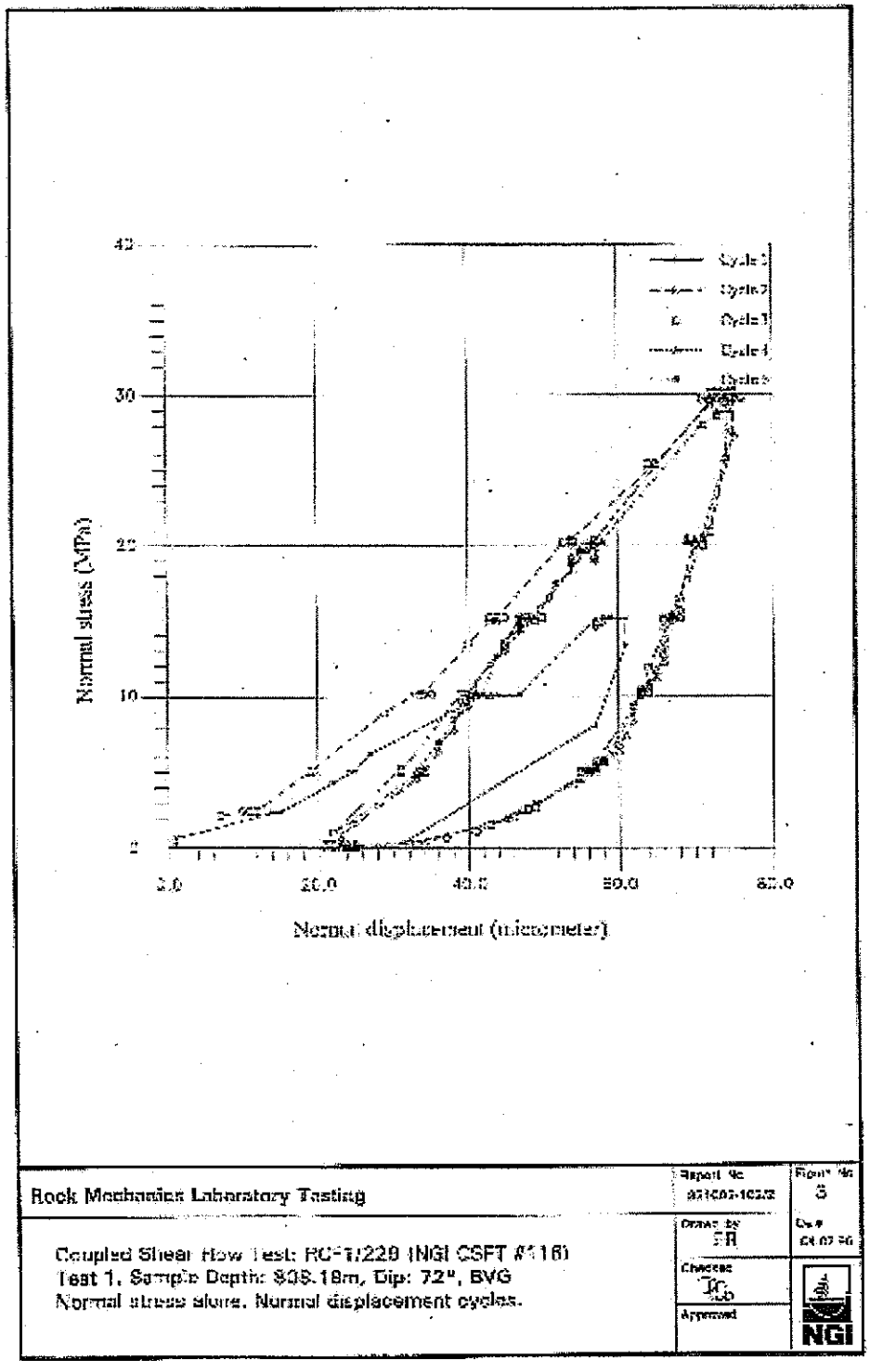

Figure 10. Normal displacement during loading-unloading cycles for sample 229, from NGI [1993, Figure 3].

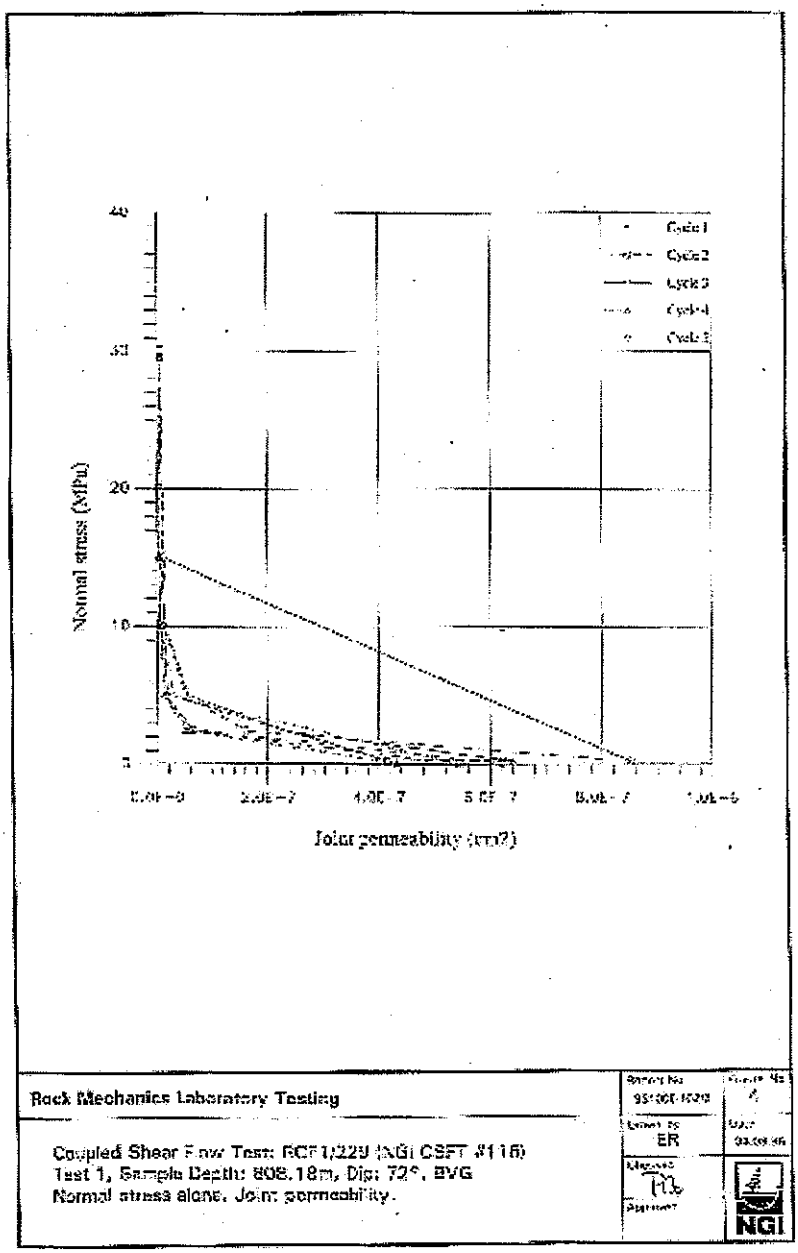

Figure 11. Joint permeability during loading-unloading cycles for sample 229, from NGI [1993, Figure 4].

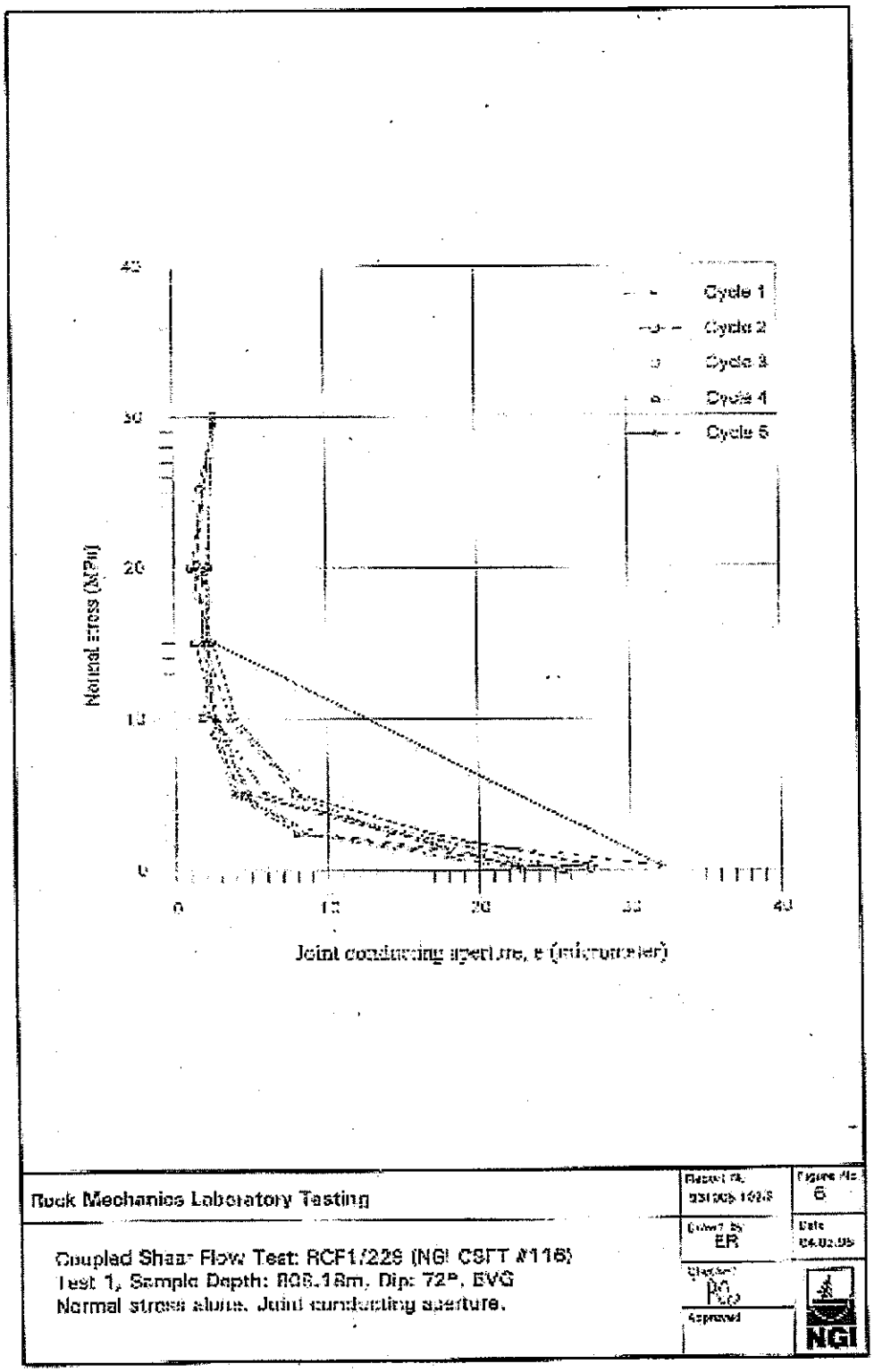

Figure 12. Equivalent smooth-wall conducting aperture during loading-unloading cycles for sample 229, from NGI [1993, Figure 6].

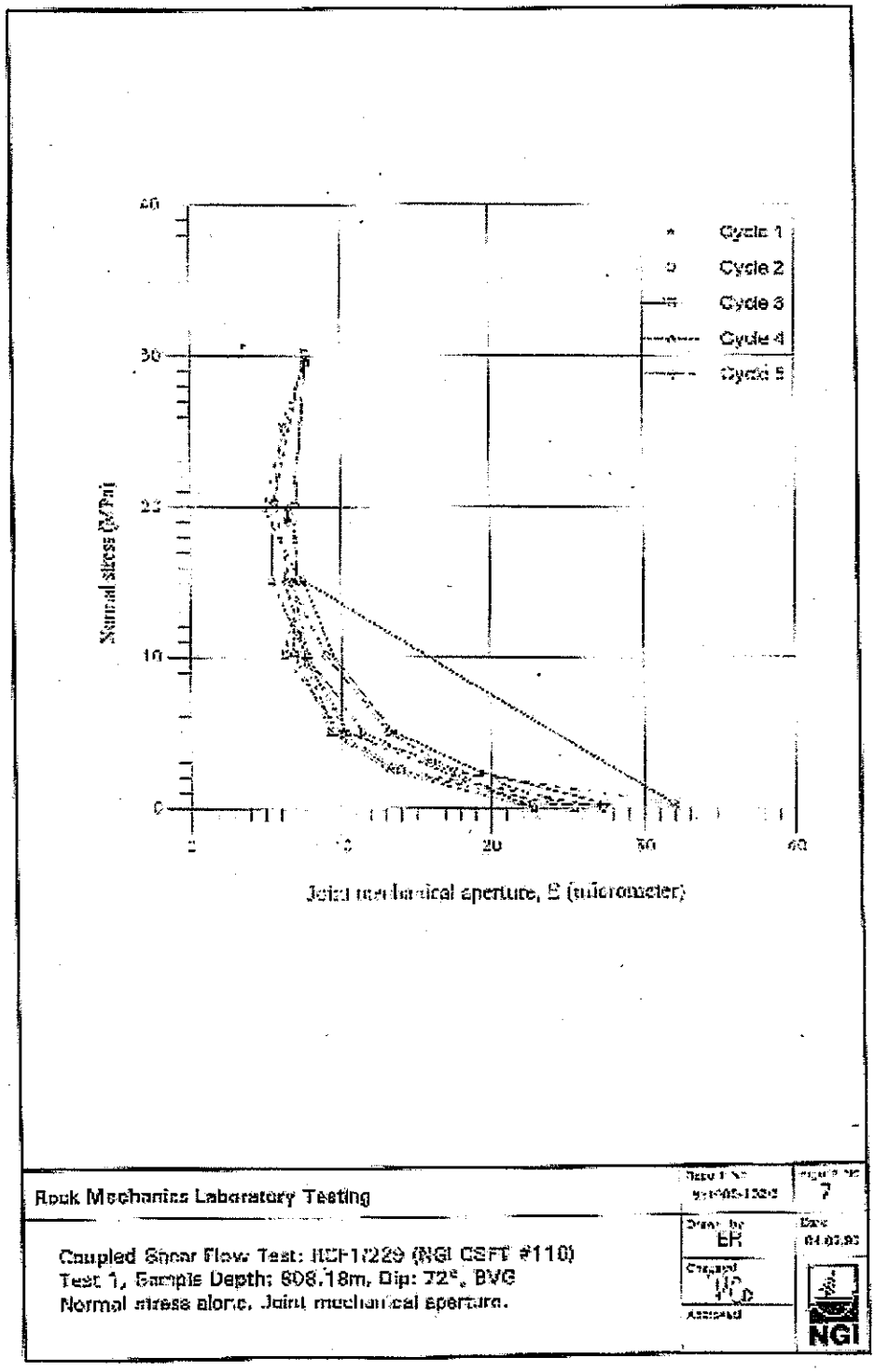

Figure 13. Equivalent mechanical aperture during load-unloading cycles for sample 229, from NGI [1993, Figure 7].

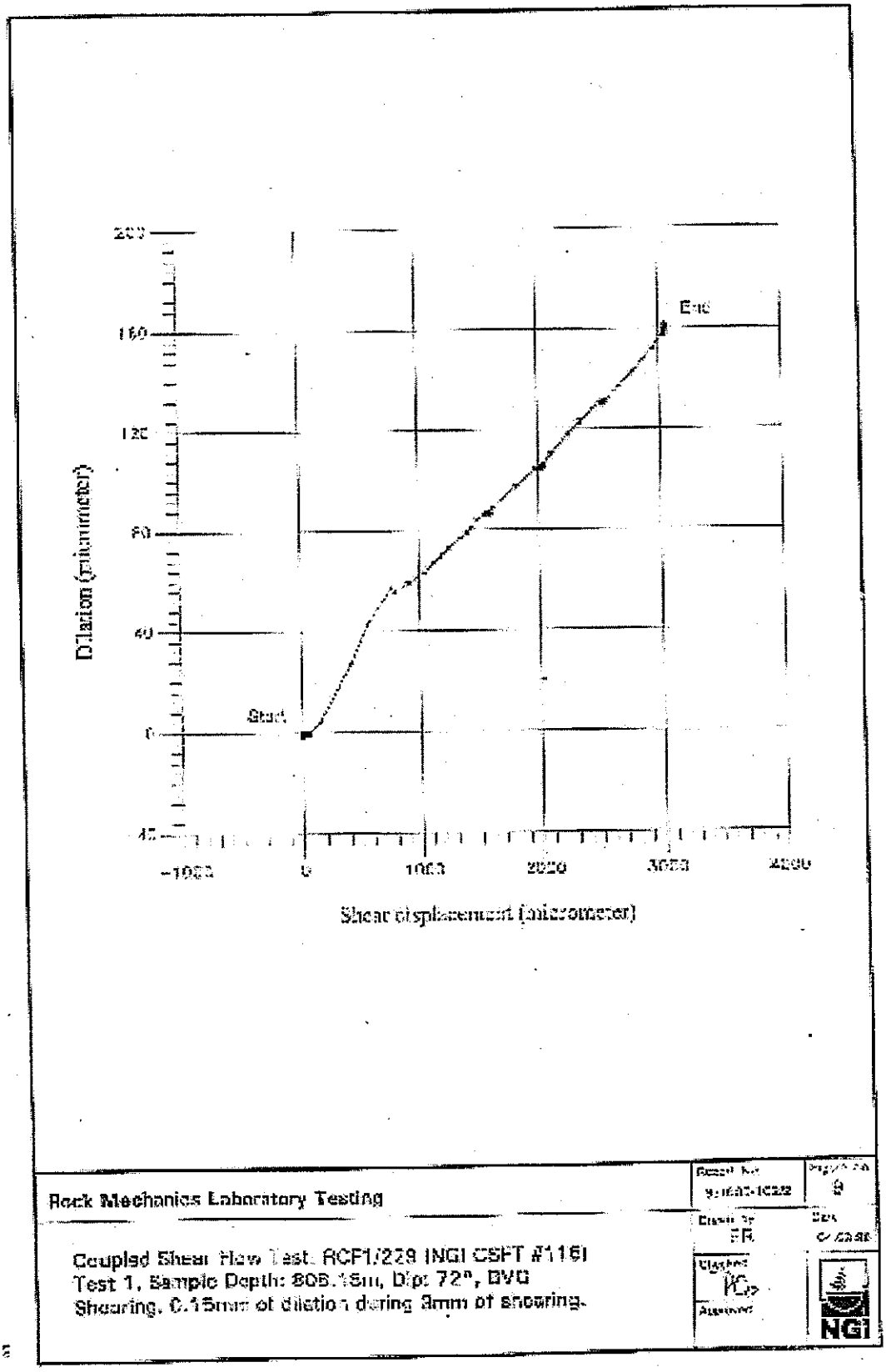

Figure 14. Dilation during shear displacement for sample 229, from NGI [1993, Figure 9].

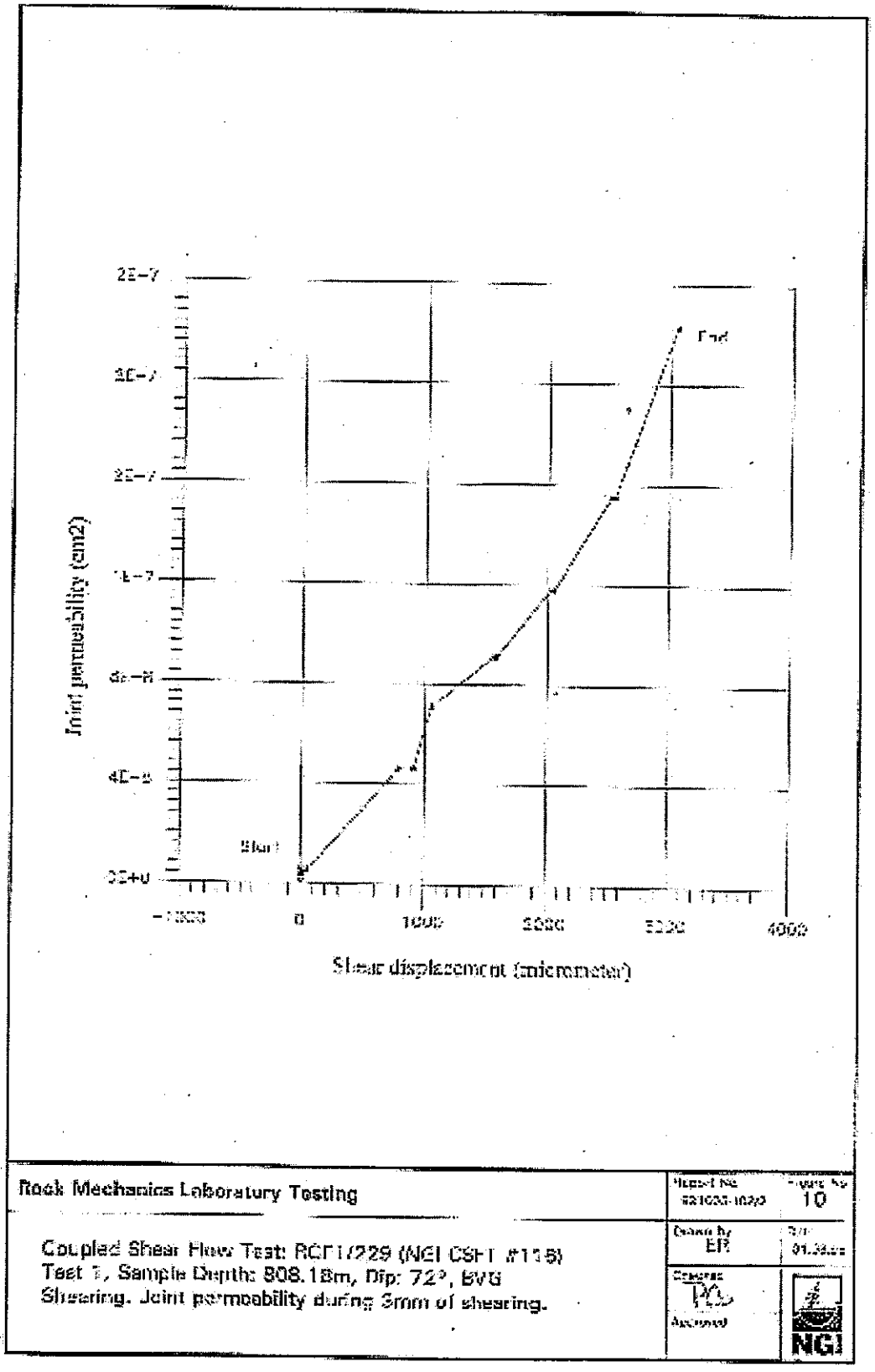

Figure 15. Permeability change during shear displacement for sample 229, from NGI [1993, Figure 10].

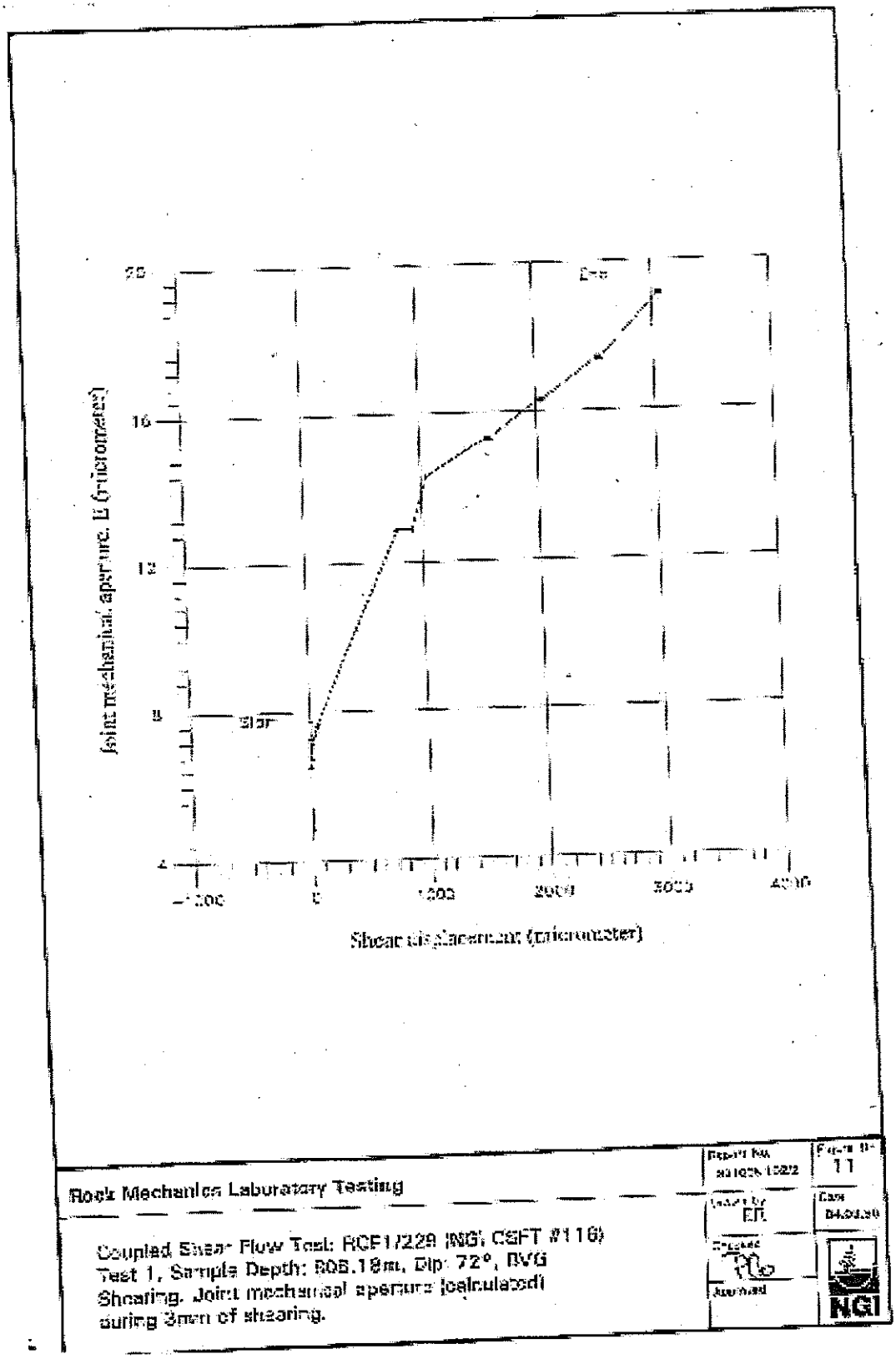

Figure 16. Equivalent mechanical aperture during shear displacement for sample 229, from NGI [1993, Figure 11].

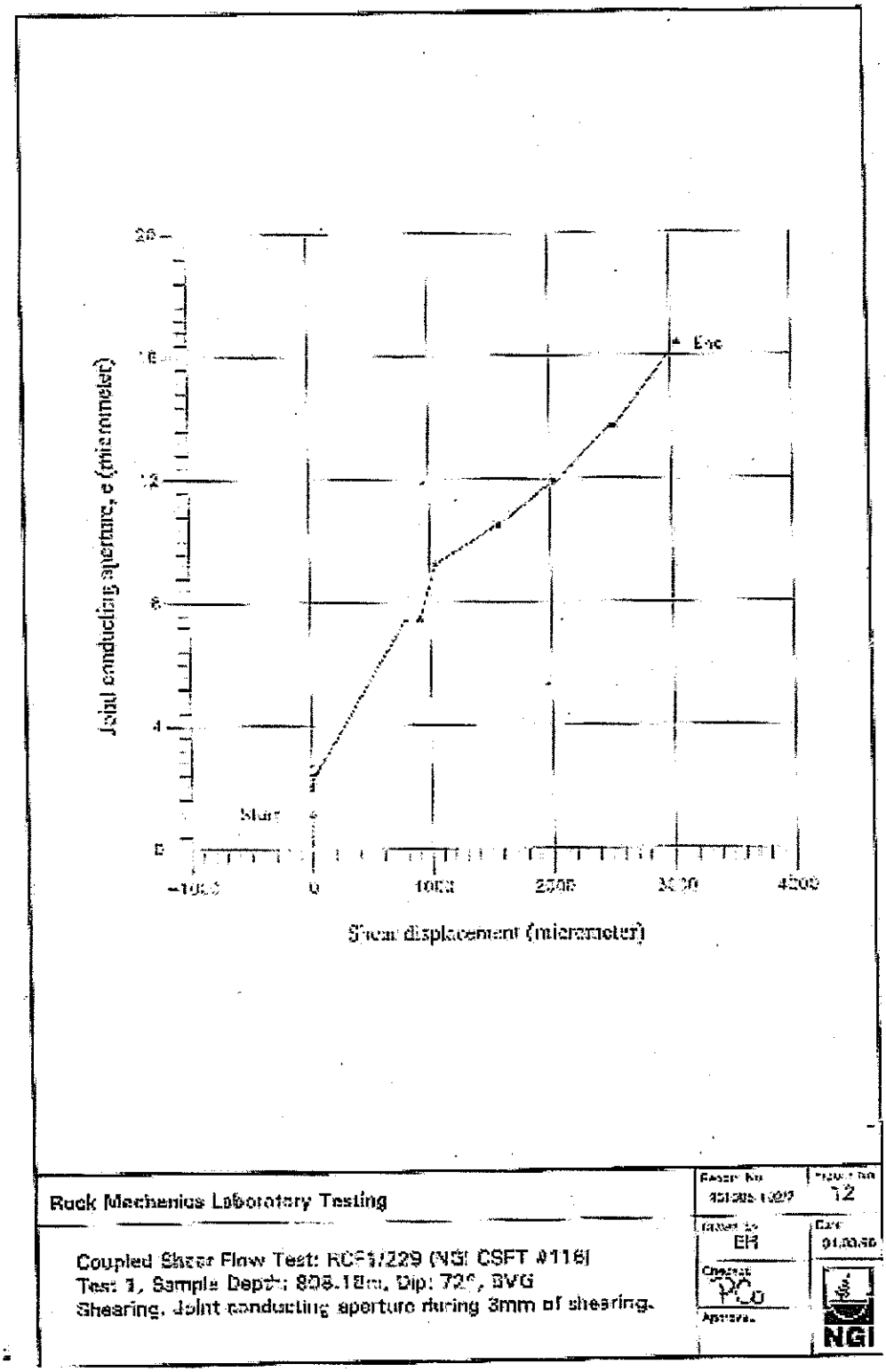

Figure 17. Equivalent smooth-wall conducting aperture during shearing for sample 229, from NGI [1993, Figure 12].

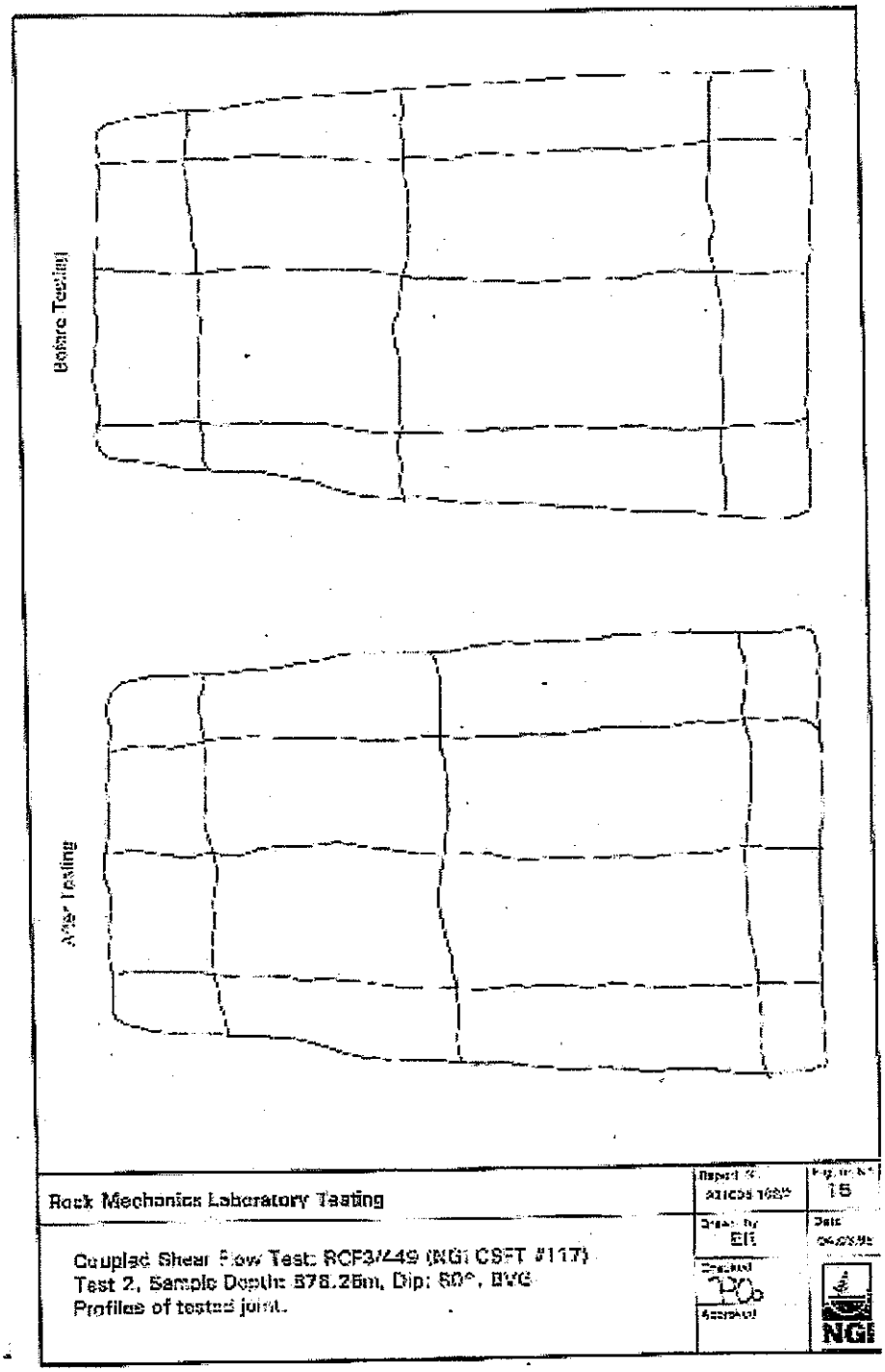

Figure 18. Profile of the joint sample 449, from NGI [1993, Figure 17].

Annex 3 Properties of the FEBEX Bentonite

Note this Annex and related Appendices are derived from a data provided by Martin Alonso and Alcoverro in a document entitled 'BENCHMARK 3.2 FEBEX MOCK-UP TEST. The text description is taken unchanged from Section 4 of the above report and the Appendices are taken unchanged from the Appendix to the above report.

Properties of the FEBEX Bentonite

As a result of the R&D programs of ENRESA previous to the FEBEX project, a site for the extraction of bentonite was selected in Almería. A comprehensive series of characterization tests as well as thermal, hydraulic, mechanic and geochemical tests have been performed using the bentonite first selected by ENRESA (this bentonite is called S-2 in reports and publications). Among these tests, the tests performed using small thermohydraulic cells (one of which was used in BM 2.2) may be mentioned. As a result, there is a comprehensive data base of the properties of this bentonite that has been used in the preliminary modellings for the two large scale tests of the FEBEX project.

The bentonite actually used in the FEBEX project (called "Serrata" in some FEBEX documents) was also extracted from the same site in Almería. For the FEBEX project, about 300 tones of properly homogenized and treated bentonite were purchased. Based on the experience from previous studies, it was required for the bentonite to comply with the following specifications:

- Grain sizes greater than 5 mm less than 5% and grain sizes less than 74 ì m greater than 85%.
- Liquid limit larger than 90%.
- Swelling pressure between 3 and 7 MPa for a dry density of 1.60 g/cm^3.
- Water content after the mechanical treatment (see below) between 12.5 and 15.5%.

The bentonite, both at the quarry and at the factory, was mechanically grinded until a granular material with the desired properties was obtained. The material was packed in big impervious bags of about 1300 kg. The whole process has been subjected to a quality control program.

Using the FEBEX bentonite, a series of new experiments has been performed. Despite the fact that both the FEBEX and S-2 bentonites come from the same site, their properties, although similar, are not identical. In order to provide the maximum information and to be able to establish a link with BM 2.2, the properties of both bentonites will be given. However, when available, the properties of the FEBEX bentonite should be used for this BM. Properties of the S-2 bentonite should be used only when they are not yet available for the FEBEX bentonite.

Identification properties

A comparison of the identification properties for the S-2 and FEBEX bentonites obtained by various laboratories is made in Appendix A1.

Mechanical properties

Several mechanical properties obtained for the S-2 and FEBEX bentonite are presented below. In some cases, the expressions of curve fittings to experimental data are also indicated. Partners, however, are free to use their own fittings. More details may be found in [2].

- The results of a series of uniaxial compression and triaxial tests performed on S-2 bentonite are summarized in Appendix A2.

- The results of a series of swelling pressure tests performed on FEBEX bentonite as well as their mean values are gathered in Appendix A3. The following correlation has been determined in tests using S-2 bentonite:
  $P_s = \exp(5.9\,\tilde{n}_d - 7.9)$
  where P_s is the swelling pressure in MPa and $\tilde{n}_d$ is the dry density in g/cm^3. The swelling pressures for the FEBEX bentonite appear to be higher to the ones predicted by the above formula (about 7% for $\tilde{n}_d$ = 1.60 g/cm^3 and about 10% for $\tilde{n}_d$ = 1.70 g/cm^3). As reported in [3], CIEMAT has performed a series of tests on FEBEX bentonite for a wide range of dry densities using distilled water to saturate the sample. The effect of both the compaction direction anisotropy and the kind of water used to saturate the sample (distilled or granitic) was checked, but no differences have been observed up to date. The following expression of a regression curve for the FEBEX bentonite is also reported in [3]:
  $P_s = \exp(6.7\,\tilde{n}_d - 9.2)$
  where the same symbols as before have been used.

- The results of a series of swelling under load tests performed on FEBEX bentonite for vertical loads of 0.5 and 0.9 MPa made by CIEMAT may be consulted in Appendix A4. On the other hand, 21 swelling under load tests performed on samples prepared at various dry densities ranging from 1.57 to 1.87 g/cm^3, with an initial water content of 11.7 % (in equilibrium with the laboratory atmosphere) have been made by UPC using FEBEX bentonite. Vertical loads ranged from 0.01 to 10.00 MPa. The deformation measured after saturation was reached, may be described by the expression:
  $\mathring{a} = -0.4693 - 0.1935 \log(\acute{o}) + 0.3659\,\tilde{n}_d$
  where å is the swelling deformation at saturation, ó is the vertical load in MPa and $\tilde{n}_d$ is the initial dry density in g/cm^3.

- A comprehensive series of suction controlled oedometric tests was given in the definition of Benchmark 2.2, [4] "Suction controlled oedometric tests (CIEMAT)" (taken from [5]).

- The small strain elastic shear modulus of samples of FEBEX bentonite compacted at different dry densities and degrees of saturation was determined by UPC. The results are given in Appendix A5.

The stiffness of the joints between blocks has also been investigated by UPC. To this end, 4 unconfined compression tests were performed in cylindrical samples (diameter 38 mm, length 78 mm) compacted at a dry density of 1.63 g/cm^3. The displacement of the joint has been determined by subtracting, at the same load, the deformation of a solid sample from the deformation of a sample including a central joint. The table below shows the results for the unconfined compression strength and elastic modulus:

Sr (%)	ó$_{joint}$ (MPa)	ó$_{no\ joint}$ (MPa)	E$_{joint}$ (MPa)
15	0.82	0.49	78
45	2.19	2.18	377
45	2.68	2.23	436
85	4.43	4.76	601

In this table, Sr is the degree of saturation, $_{joint}$ is the strength of the sample which includes a horizontal joint, $_{no\ joint}$ is the strength of the sample without joint and E$_{joint}$ is the elastic modulus of the joint at = 0.5%.

Hydraulic properties

Relevant hydraulic properties of the S-2 and FEBEX bentonites are summarised below. In some cases, analytical expressions for suitable correlations are available. Partners are however free to select their own approximations. Details may be found in [2].

- The saturated hydraulic conductivity of the S-2 bentonite as a function of the dry density has been found to be well reproduced by the following expressions:
  log(k) = –8.14 ñ$_d$ – 0.72 (1.1 ñ$_d$ 1.4 g/cm^3)
  log(k) = –2.97 ñ$_d$ – 8.29 (1.4 ñ$_d$ 1.9 g/cm^3)
  where k is the permeability coefficient in m/s and ñ$_d$ is the dry density in g/cm^3. Concerning the FEBEX bentonite, the results of a series of permeability tests may be found in Appendix A6. The permeability coefficient obtained using the previous formulae are about 1.5 greater than the values observed for the FEBEX bentonite. It is reported in [3] that checks of the effect of anisotropy with respect to the compaction direction as well as the effect of the permeating fluid (distilled or granitic water) have been made, but no important differences have been found. In appendix A6, the results of a series of oedometric tests made by UPC on samples of FEBEX bentonite used for the swelling under load tests are also presented. In [4] "Hydraulic saturated conductivity (CIEMAT)" (taken from [5]),

the hydraulic saturated conductivity was given as a function of temperature for dry densities of 1.60 and 1.70 g/cm^3.

- Based on backanalysis of data concerning infiltration test made by CIEMAT using S-2 bentonite, UPC derived the following expression for the relative permeability:
  $k_{rl} = (Sr)^3$
  where k_{rl} is the relative permeability and Sr is the degree of saturation.

- For the S-2 bentonite, CIEMAT determined the following expression of the water retention curve:
  $w = 36.1 - 12.0 \log(s)$ (2.0 s 385.0 MPa)
  where w is the water content and s is the suction. In order to check if this relationship obtained for the S-2 bentonite was also valid for the FEBEX bentonite, CIEMAT performed a series of tests, whose results are summaized in Appendix A7. Using these data, the following expression for the water retention curve of the FEBEX bentonite was derived:
  $w = 40.68 - 14.26 \log(s)$ (3 s 700 MPa)
  where the same symbols as before have been used.
  In [3] it is reported that using FEBEX bentonite samples compacted to various initial dry densities, UPC has obtained the following relation:
  $w = 40.7 - 6.2 \log(s)$ (15 s 700 MPa)
  whereas CIEMAT, following a wetting path from the "as compacted" condition (150 MPa) down to a suction of 0.1 MPa, has obtained the following relation:
  $w = 38.9 - 5.2 \log(s)$ (0.1 s 130 MPa)
  where the same symbols as before have been used. Additional data concerning water retention curves may be found in [4] "Water retention curves (CIEMAT)" (taken from [5]) and "Water retention curves (UPC)" (taken from [6]).

Thermal properties

Data concerning the thermal behaviour of both the S-2 and the FEBEX bentonites are summarised below. As before, some correlations with experimental data are presented. Additional details may be found in [2].

- For the S-2 bentonite, the following expression of the specific heat has been fitted to experimental data:
  $c_s = 1.38\,T + 732.5$ (45 T 150 °C)
  where c_s is the specific heat in J/kg°C and T is the temperature in °C.

- For the S-2 bentonite, the following expression for the thermal conductivity has been fitted to experimental data:

$$\lambda = 1.34 - \frac{0.95}{1 + exp[(Sr - 0.54)/0.15]}$$

where ë is the thermal conductivity in W/m· K and Sr is the degree of saturation. Similarly, for the FEBEX bentonite and using the experimental data given in Appendix A8, the following expression has been obtained:

$$\lambda = 1.30 - \frac{0.75}{1 + exp[(Sr - 0.67)/0.11]}$$

where the same symbols as before have been used. This expression has been slightly modified in [3], where it reads:

$$\lambda = 1.31 - \frac{0.79}{1 + exp[(Sr - 0.63)/0.13]}$$

Additional data are given in [4] "Thermal conductivity (CIEMAT)" (taken from [5]).

- For the FEBEX bentonite, UPC performed tests to determine the linear coefficient of thermal expansion. For samples with a dry density of 1.70 g/cm^3 and water content of 13.5 %, the linear coefficient of thermal expansion is 1· 10^{-4} in the range of temperatures varying from 14.8 to 51.0 °C. The table below summarises the results:

sample	ñ$_d$ (g/cm^3)	w (%)	T range (°C)	á (1/°C)
090996a	1.68	14.42	22.6-14.8	5· 10^{-5}
090996a	1.68	14.42	16.6-41.0	8· 10^{-5}
120996e	1.71	12.53	31.0-51.0	21· 10^{-5}
120996e	1.71	12.53	51.0-41.0	6· 10^{-5}

where is ñ$_d$ the dry density, w is the water content and is the linear coefficient of thermal expansion. Additional data are given in [4] "Thermal expansion (UPC)" (taken from [6]).

References

1. ENRESA (1997): FEBEX. Etapa Preoperacional. Informe de Síntesis. Publicación técnica núm. 09/97. Madrid.

2. Villar, M.V.; Lloret, A.; Linares, J.; Pérez, A. et al. (1997): FEBEX. Bentonita (Origen, Propiedades y Fabricación de Bloques). CIEMAT Technical Report 70-IMA-M-3-3. Madrid. 140 pp.

3. Villar, M.V.; Lloret, A.; Cuevas, J.; Yllera, A.; Fernández, A.M. and Jiménez de Cisneros, C.: FEBEX project: Laboratory Experiments. In: Haijtink, B. and Davies, C. (1998): In situ testing in underground research laboratories for radioactive waste disposal. Proceedings of a cluster seminar held in Alden Biesen, Belgium, 10 and 11 December 1997. European Commission, Nuclear Science and Technology. DOC XII/015/98-EN.

4. Alonso, E.E. and Alcoverro, J. (1997): CATSIUS CLAY. BM 2.2 Small scale wetting-heating test on compacted bentonite. Benchmark definition.

5. CIEMAT REPORT. CEC Contract FI2W-CT91-0102 (DOEO). Modelling and validation of the thermal-hydraulic-mechanical and geochemical behaviour of the caly barrier. Final report 1991 – 1994. CIEMAT. DIRECCIÓN DE TECNOLOGÍA. TÉCNICAS GEOLÓGICA. Madrid 1994.

6. UPC REPORT. THM Laboratory tests in FEBEX phase 3. 70-UPC-L-3-01. Barcelona 1996.

Appendix to Annex 3 FEBEX Bentonite Properties

A1 Identification properties

The table below shows the identification properties of the S-2 and FEBEX bentonites, according to tests performed at different laboratories. The large differences between the percentages of grains with sizes less than 2 ì m found by CIEMAT and UPC may be due to the different degree of dispersion of these particles achieved during the tests.

Property	S-2 bentonite CSIC	S-2 bentonite CIEMAT	FEBEX bentonite CIEMAT	FEBEX bentonite UPC	FEBEX bentonite CSIC	units
Eq. water content (lab)		10-13	13.7±1.3			%
Liquid limit		105±10	102±4	93±1		%
Plastic limit			53±3			%
Plasticity index			49±4			%
Specific weight		2.78	2.71±0.04			-
Granulometry						
less than 74 ì m	93±3	86	92±1	87		%
less than 2 ì m	82±6	65±1	68±2	45		%
Specific surface						
total	614±74	516±37			640-659	m^2/g
external, BET		37	32±3			m^2/g

A2 Strength parameters in uniaxial compression and triaxial tests

Simple compression tests performed in S-2 bentonite using cylindrical samples (diameter of 38 mm, height of 78 mm) with a loading rate of 2% of deformation per minute showed that the uniaxial compression strength raises exponentially with the dry density. For a dry density of 1.70 g/cm^3 and equilibrium water content under laboratory relative humidity conditions, the uniaxial compression strength is 25 kg/cm^2. Maximum strengths are obtained for water contents about 20%.

The following table shows the results of triaxial tests performed on unsaturated samples (at the laboratory equilibrium water content) for different initial dry densities.

ñ$_d$ (g/cm^3)	initial Sr (%)	ó$_3$ interval (MPa)	cohesion (MPa)	frict. angle (°)
1.6	41-47	0.5-3.0	0.7	25
1.6	41-47	3.0-10.0	2.8	14
1.6	41-47	10.0-30.0	4.4	14
1.7	49-60	0.5-3.0	0.8	30
1.7	49-60	3.0-10.0	1.0	26
1.7	49-60	10.0-30.0	3.5	16
1.8	53-59	3.0-10.0	4.3	16
1.8	53-59	10.0-30.0	3.6	18
1.9	65-79	3.0-10.0	4.5	19

A3 Swelling pressures

Using FEBEX bentonite, a series of oedometric tests have been performed on 11 samples (F) and on 5 samples (A) taken from a homogeneized batch. The following table shows the swelling pressure P_s obtained in these tests for dry densities of 1.60 and 1.70 g/cm^3.

Sample	$\tilde{n}_d$ (g/cm^3)	init w (%)	final w (%)	P_s (kg/cm^2)	$\tilde{n}_d$ (g/cm^3)	init w (%)	final w (%)	P_s (kg/cm^2)
F-2	1.59	15.2	29.5	>58	1.71	15.6	29.6	108
F-18	1.59	15.5	27.5	>62	1.70	15.0	29.4	83
	1.58	16.1	29.4	>50				
F-37	1.58	14.5	32.4	42	1.71	12.7	27.8	111
F-59	1.60	13.0	30.5	49				
F-65	1.58	15.0	30.1	>60				
F-75	1.60	11.2	29.2	30	1.70	12.7	28.4	77
	1.59	12.2	29.2	52	1.70	12.3	27.5	97
F-79	1.59	13.1	32.5	41				
F-93	1.59	13.8	29.9	36				
	1.59	14.0	29.7	>>56				
F-102	1.60			>56	1.69	14.8	28.4	105
F-109	1.57	14.3	29.6	52				
F-119	1.58	13.5	30.1	54	1.70	12.5	28.2	99
	1.60	12.5	28.4	52				
MEAN	1.59±0.01	13.9±1.4	29.9±1.3	50±9	1.70±0.01	13.4±1.4	28.5±0.8	97±13
A-1	1.61	13.0	29.9	32	1.72	13.4	29.0	85
	1.61	13.7	28.3	>68				
A-2	1.64	12.0	26.7	52				
A-3	1.62	13.0	31.0	54	1.72	12.8	27.2	124
A-4	1.62	13.0	30.2	56				
A-5	1.60	14.5	31.9	34	1.72	13.4	28.2	96
	1.62	12.7	27.5	48				
MEAN	1.62±0.01	13.1±0.8	29.4±1.9	48±13	1.72±0.00	13.2±0.3	28.1±0.9	102±20

A4 Swelling under load tests

Using FEBEX bentonite, seven swelling under load tests have been performed taking samples from a homogeneized batch. All samples were prepared at a nominal dry density of 1.60 g/cm^3.

Sample	v. load (MPa)	$\tilde{n}_d$ (g/cm^3)	init w (%)	final w (%)	swelling strain (%)
A-1	0.5	1.62	13.2	39.3	17.8
A-2	0.5	1.60	14.7	40.1	17.2
A-4	0.5	1.62	13.7	38.3	17.8
A-5	0.5	1.62	14.0	39.1	17.2
MEAN		1.61±0.01	13.9±0.6	39.2±0.7	17.5±0.3
A-2	0.9	1.59	14.2	36.7	15.9
A-3	0.9	1.61	13.8	36.6	14.7
A-4	0.9	1.59	15.0	37.2	13.4
MEAN		1.60±0.01	14.3±0.6	36.8±0.3	14.7±1.3

A5 Elastic shear modulus

For the FEBEX bentonite, UPC determined the elastic shear modulus G for small strains (10^{-6} ã 10^{-4}). The tests were performed, using a resonant column, on 10 samples compacted at different dry densities, degrees of saturation and confining pressures. The table below shows the results obtained.

				Shear modulus G (MPa)				
ñd (g/cm^3)	w (%)	Sr (%)	e	ó3 = 0.01 (MPa)	ó3 = 0.1 (MPa)	ó3 = 0.2 (MPa)	ó3 = 0.4 (MPa)	ó3 = 0.8 (MPa)
1.58	14.7	54	0.757	140	207	245	300	370
1.66	13.6	57	0.668	211	223	270		
1.54	3.4	12	0.802	78	106	174	208	326
1.56	2.8	10	0.777	89	106	138		
1.62	24.6	95	0.717	240	270		331	336
1.66	21.3	87	0.677	252	296	370	429	502
1.65	4.7	19	0.685	74	90	137	190	310
1.72	10.4	47	0.615	200	219	293	381	429
1.68	3.7	16	0.652	61	89	141	200	290
1.62	12.7	50	0.713	122	180	240	299	387

A6 Saturated hydraulic conductivity

For the FEBEX bentonite, and using non homogeneized samples, a series of permeability tests were carried out. The cylindrical samples (diameter of 5.0 cm and height of 2.5 cm) were confined between two porous stones and, using a water pressure of 0.6 MPa, were hydrated from both ends until saturation was reached. Afterwards, water pressure was raised in the lower porous stone. Pressures of 5.2 MPa (for $\tilde{n}_d$ = 1.60 g/cm^3) and 7.2 MPa (for $\tilde{n}_d$ = 1.70 g/cm^3) were applied and, when the steady state was reached, the water flow was determined. Using Darcy's formula, the following table was prepared:

sample	$\tilde{n}_d$ (g/cm^3)	init w (%)	k (x10^{-14} m/s)	$\tilde{n}_d$ (g/cm^3)	init w (%)	k (x10^{-14} m/s)
F-2	1.59	14.8	3.1	1.70	14.8	3.8
F-18	1.60	15.0	5.9	1.70	15.1	2.9
F-37	1.60	13.3	6.0	1.70	13.4	3.8
F-75	1.61	11.7	5.9	1.69	11.7	3.2
F-109	1.59	12.5	6.4	1.70	11.9	4.1
F-119	1.58	14.0	8.3	1.67	14.5	3.7
MEAN	**1.60**	**13.5**	**5.9**	**1.69**	**13.6**	**3.6**
STD DEV	**0.01**	**1.3**	**1.7**	**0.01**	**1.5**	**0.4**

UPC performed also a series of oedometric tests at the end of the swelling under load tests once saturation was completed. In order to compute the saturated hydraulic permeability, the following expression was used to match the recorded sample deformations

$$\delta = \delta_0 + \frac{2H\Delta\sigma}{E_m} U(t, c_v, H) + 2Hc_\alpha \log(t/t_{90}); \qquad c_v = \frac{kE_m}{\gamma_w}$$

In this expression ä is the settlement of the sample, ä$_0$ is the instantaneous settlement due to the elastic compressibility of the testing device and of the sample support, $2H$ is the height of the sample, E_m is the confined modulus of deformation, $U(t, c_v, H)$ is the degree of consolidation according to Terzaghi's theory, $c_{\ddot{a}}$ is the secondary consolidation coefficient, t the time, t_{90} is the time for the 90% of primary consolidation, c_v is the consolidation coefficient, k is the permeability and ã$_w$ is the specific weight of water. For times less than t_{90} the secondary consolidation has been assumed to be negligible. The results of the backanalysis performed are presented in the following table:

$\tilde{n}_d$ (g/cm^3)	e_i	$\acute{o}_i$ (MPa)	$\acute{o}_f$ (MPa)	c_v (10^{-3} cm^2/s)	E_m (MPa)	k (m/s)	$c_{\acute{a}}$ (10^{-3})	$\ddot{a}_0$ (m)	$\mathring{a}_r$ (m)
1.15	1.417	0.01	0.1	4.39	4.42	$9.9 \cdot 10^{-10}$	3.26	597	6.6
1.12	1.473	0.01	0.1	4.47	4.90	$9.12 \cdot 10^{-10}$	3.37	446	12.0
1.36	1.036	0.2	1.0	0.0415	18.27	$2.27 \cdot 10^{-12}$	6.00	273	15.4
1.39	0.999	0.5	1.0	0.0320	42.46	$7.53 \cdot 10^{-13}$	1.99	43	5.5

where $\tilde{n}_d$ is the initial dry density, e_i is the initial void ratio, $\acute{o}_i$ is the initial load, $\acute{o}_f$ is the final load, c_v is the consolidation coefficient, E_m is the confined deformation modulus, k is the permeability, c is the secondary consolidation coefficient, $\ddot{a}_0$ is the instantaneous settlement of the sample and $\mathring{a}_r$ is the difference between the measures values and the analytical approximation.

A7 Water retention curves

The following table summarizes the results of a series of tests performed on FEBEX bentonite in order to check if the expression for the water retention curve obtained for the S-2 bentonite was also valid for FEBEX bentonite. Each sample was tested twice and the values on the table represent their mean value. The last column shows the value obtained using the formula derived for the S-2 bentonite

sample	init w (%)	s (MPa)	$ó_d$ (g/cm^3)	final w (%)	final Sr (%)	w* (%)
F-2	14.8	255.5	1.65	9.0	39	7.8
F-17	16.0	255.5	1.61	9.0	36	7.8
F-37	13.3	255.5	1.63	9.1	38	7.8
F-59	12.7	255.5	1.63	9.2	38	7.8
F-75	11.7	260.6	1.62	8.3	34	7.7
A-1	14.4	260.6	1.65	8.4	36	7.7
A-5	14.5	260.6	1.65	8.3	35	7.7
F-2	14.8	138.6	1.61	13.2	52	10.9
F-17	16.0	138.6	1.62	13.3	55	10.9
F-37	13.3	138.6	1.60	13.0	51	10.9
F-59	12.7	138.6	1.60	12.8	49	10.9
F-75	11.7	144.1	1.60	10.9	43	10.8
F-109	11.9	143.3	1.62	11.1	45	10.8
F-119	12.3	143.3	1.63	11.5	47	10.8
A-1	14.4	144.1	1.63	11.7	48	10.8
A-5	14.5	144.1	1.62	11.6	48	10.8
70-IMA-3-4-0	13.1	143.3	1.62	11.5	47	10.8
F-109	11.9	126.6	1.60	12.1	48	11.4
F-119	12.3	126.6	1.59	12.7	49	11.4
70-IMA-3-4-0	13.1	126.6	1.60	12.3	48	11.4

sample	init w (%)	s (MPa)	$ó_d$ (g/cm^3)	final w (%)	final Sr (%)	w* (%)
F-2	14.8	14.5	1.39	22.7	65	22.5
F-17	16.0	14.5	1.43	22.6	69	22.5
F-37	13.3	14.5	1.35	22.6	61	22.5
F-59	12.7	14.5	1.36	22.8	62	22.5
F-75	11.7	14.0	1.35	21.9	59	22.6
F-109	11.9	14.9	1.35	21.9	59	22.3
F-119	12.3	14.9	1.35	22.2	60	22.3
A-1	14.4	14.0	1.34	22.4	60	22.6
A-5	14.5	14.0	1.35	22.4	61	22.6
70-IMA-3-4-0	13.1	14.9	1.36	22.0	60	22.3

A8 Thermal conductivity

The table below shows the results of a series of tests performed on 37 samples taken from 11 samples of FEBEX bentonite. The measurements were performed in the direction of compaction.

sample	ód (g/cm^3)	w (%)	Sr (%)	ë (W/m·K)	ñd (g/cm^3)	w (%)	Sr (%)	ë (W/m·K)
F-18	1.53	1.7	6	0.5013				
F-37	1.55	0.9	3	0.4797				
F-75					1.66	1.9	8	0.6195
F-75					1.67	0.1	0	0.6356
F-75					1.72	0.5	2	0.6293
F-109	1.53	0.1	0	0.4841				
F-18	1.60	1.0	4	0.5473				
F-37	1.60	2.0	8	0.5738				
F-109	1.58	0.1	0	0.4771				
F-119	1.59	1.1	4	0.5763				
F-2	1.59	15.5	60	0.6978	1.74	13.7	67	0.8992
F-18	1.60	15.5	61	0.7824	1.71	15.0	70	0.9402
F-37	1.63	12.6	52	0.7261	1.73	11.9	57	0.8339
F-75	1.60	13.1	51	0.6825	1.72	12.9	61	0.8077
F-102	1.59	15.4	60	0.6995				
F-119	1.60	13.3	52	0.6114	1.70	13.1	60	0.7923
F-2	1.62	26.0	105	1.2754	1.73	21.6	104	1.2183
F-17	1.63	25.3	104	1.2726	1.75	20.4	101	1.2450
F-37	1.62	26.2	106	1.3043	1.72	21.6	102	1.1247
F-59	1.64	25.4	106	1.3069	1.76	20.5	104	1.2342
F-75	1.61	25.8	103	1.3619	1.69	22.7	103	1.2717
F-79	1.61	27.1	108	1.2854	1.71	22.6	103	1.2541
F-102	1.59	27.4	106	1.2613	1.70	21.8	100	1.2709
F-119	1.60	26.6	104	1.2472	1.69	22.3	101	1.2531

The same tests were performed on FEBEX bentonite using the homogeneized sample 70-IMA-3-4-0. Two measurements were carried out: in the direction of compaction

(ë) and in a direction perpendicular to it (ë). The results are given in the following table:

ρ_d (g/cm^3)	w (%)	Sr (%)	ë (W/m·K)	ë (W/m·K)
1.51	15	51	0.7621	0.7077
1.58	15	57	0.8114	0.7283
1.63	15	62	0.9550	0.8934
1.65	15	64	1.0003	0.8940
1.69	15	68	0.9531	0.9525
1.52	20	70	0.9128	0.9030
1.59	20	77	1.1187	0.9930
1.65	20	85	1.1851	1.1622
1.67	20	88	1.1405	1.1686
1.72	20	95	1.4319	1.3918
1.52	25	87	1.0913	1.1517

There are no important differences between the values obtained in a direction parallel to the compaction direction and those obtained in a direction perpendicular to it.